Proceedings of the 10th Italian Conference

Sensors and Microsystems

A G Mignani | R Falciai | C Di Natale | A D'Amico

Editors

World Scientific

Proceedings of the 10th Italian Conference

Sensors and Microsystems

Proceedings of the 10th Italian Conference

Sensors and Microsystems

Firenze, Italy 15 – 17 February 2005

Editors

A G Mignani
CNR-IFAC, Italy

R Falciai
CNR-IFAC, Italy

C Di Natale
University of Rome "Tor Vergata", Italy

A D'Amico
University of Rome "Tor Vergata", Italy

World Scientific

NEW JERSEY • LONDON • SINGAPORE • BEIJING • SHANGHAI • HONG KONG • TAIPEI • CHENNAI

Published by

World Scientific Publishing Co. Pte. Ltd.

5 Toh Tuck Link, Singapore 596224

USA office: 27 Warren Street, Suite 401-402, Hackensack, NJ 07601

UK office: 57 Shelton Street, Covent Garden, London WC2H 9HE

British Library Cataloguing-in-Publication Data
A catalogue record for this book is available from the British Library.

SENSORS AND MICROSYSTEMS
Proceedings of the 10th Italian Conference

ISBN-13 978-981-283-352-5
ISBN-10 981-283-352-8

Printed in Singapore by World Scientific Printers

FOREWORD

This volume collects the papers presented at the 10th Italian Conference on Sensors and Microsystems held in Firenze, February 15-17, 2006.
The conference was organized by the Italian Association of Sensors and Microsystems (AISEM) with the local organization of the Institute of Applied Physics "N. Carrara" of the National Research Council (CNR).
The Italian Conference on Sensors and Microsystems is now an established event offering a unique interdisciplinary forum in Italy for experts in fields such as physics, chemistry, biology, engineering, and material science. The proceedings volume, published since the first edition by World Scientific, are a testimonial of the Italian contribution to key research areas of all major disciplines related to sensors, including: sensors and actuators; materials and process technologies; signal monitoring, acquisition, and conditioning; data processing and pattern recognition techniques; microsystems, micromachinery, and other applications.

The 10th edition of the conference consisted of a plenary session, nine oral sessions and two poster sessions. The 158 papers, 14 of which invited, offer a compendium of the most significant theoretical and experimental results in the field of sensors and of the major collaborative ventures between academic and industrial research groups.

Anna Grazia Mignani and Riccardo Falciai
CNR – Institute of Applied Physics "N. Carrara", Firenze

Arnaldo D'Amico and Corrado Di Natale
Department of Electronic Engineering, University of Rome Tor Vergata

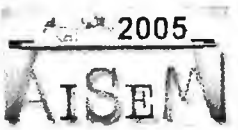

CONFERENCE ORGANISERS

Anna Grazia Mignani Riccardo Falciai

CNR – Istituto di Fisica Applicata 'Nello Carrara', Firenze

STEERING COMMITTEE

A. D'Amico
Università di Roma 'Tor Vergata',

L. Campanella
Università di Roma 'La Sapienza'

P. De Gasperis
CNR-IMM-PSM, Roma

C. Mari
Università di Milano

G. Martinelli
Università di Ferrara

U. Mastromatteo
ST Microelectronics, Castelletto (MI)

A.G. Mignani
CNR-IFAC, Firenze

M. Prudenziati
Università di Modena

G. Sberveglieri
Università di Brescia

P. Siciliano
CNR-IMM-IME, Lecce

G. Soncini
Università di Trento

SCIENTIFIC COMMITTEE

M.C. Carotta
Università di Ferrara

P. Dario
Scuola Superiore S. Anna, Pisa

F. Davide
Telecom Italia, Roma

A. Diligenti
Università di Pisa

C. Di Natale
Università di Roma 'Tor Vergata'

L. Dori
CNR-IMM-LAMEL, Bologna

G. Faglia
Università di Brescia

C. Malvicino
CRFiat Orbassano (To)

M. Mascini
Università di Firenze

N. Minnaja
Polo Navacchio SpA, Cascina (PI)

G. Palleschi
Università di Roma 'Tor Vergata'

F. Villa
ST Microelctronics, Castelletto (Mi)

M. Zen
ITC-IRST, Trento

LOCAL ORGANISING COMMITTEE

L. Ciaccheri C. Cucci B. Radicati C. Trono

CNR-IFAC, Firenze

C. Pardini
ICVBC

R. Zacchi
IVaLSA

CNR – Area di Ricerca di Firenze

SUPPORTING ORGANISATIONS

Società Italiana di Ottica e Fotonica
http://siof.ifac.cnr.it/

Network of Excellence on Micro-Optics
http://www.micro-optics.org/

CONFERENCE SPONSORS

Acqiris
http://www.acqiris.com/index.jsp

ENTE
CASSA DI RISPARMIO
DI FIRENZE

Ente Cassa di Risparmio di Firenze
http://www.entecarifirenze.it/online/html/asp/index.asp

AGRIPECCIOLI
http://www.agripeccioli.it/

AlphaPhotonics
http://alfaphotonicsweb.free.fr/index.htm

G. Gambetti Kenologia, srl
http://www.gambetti.it/default.php

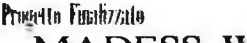

CNR – Progetto Finalizzato MADESS II
http://www.madess.cnr.it/

National Instruments, Italy
http://digital.ni.com/worldwide/italy.nsf/main?readform

COMSOL, Inc.
http://www.comsol.com/

Technobiochip s.c.a r.l.
http://www.technobiochip.com/

CONTENTS

GAS SENSORS

CHEMICAL SENSOR ARRAYS

MICROFABRICATION AND MICROSYSTEMS

SYSTEMS, NETWORKS AND ELECTRONIC INTERFACES

INVITED TALKS

COMPUTER SCREEN PHOTO-ASSISTED TECHNIQUES: PRINCIPLES AND APPLICATIONS

Daniel Filippini and Ingemar Lundström

Division of Applied Physics,
Linköping University, Linköping, Sweden
e-mail: ingemar@ifm.liu.se

A tutorial description is made of the recently introduced computer screen photo assisted technique (CSPT). The technique is based on the use of a (computer) screen as a light source in physical experiments and for colorimetric assays. In the present contribution we concentrate on the colorimetric applications of CSPT. We describe how the so called rgb- colors produced by the screen can be used together with a web camera to obtain spectral information, both for transmitted and reflected light from a sample. Fingerprinting of colored samples is further enhanced by the use of the information in all three channels of the web camera, enabling as an example the separation of light emission (fluorescence) and absorption for a given dye. A short discussion of the physics behind CSPT is given. The evaluation of test strips used to determine a number of parameters in urine for medical diagnostic purposes is given as an example of one of the interesting application areas of CSPT. It is also pointed out that the CSPT platform is suitable for mobile applications (palmtops, mobile phones) and furthermore inherently compatible with internet based control and evaluation of diagnostic tests both for medical and environmental purposes.

1. Introduction

Control of scientific experiments and internet based information transmission and retrieval are but a few possible areas of applications of computers. One feature of the computer, or rather of the screen used together with the computer hard- and software, has not been explored in detail yet. This relates to the use of the screen as a programmable light source for physical experiments and for colorimetric measurements. We have during the last couple of years explored such possibilities and demonstrated the versatility of what we call computer screen photo assisted techniques, or CSPT for short [1-6]. In the present contribution we describe the principles of CSPT and give an overview of the applications demonstrated so far. The light from a screen is determined by the so called color index, (r, g, b). The size of the three coefficients determine the intensity of the three primary colors, red, green and blue, possible to excite in each of the pixels of the screen.
Since the combination of r, g, and b is easily controlled by the computer, as well as the area of the screen lit up, we have an extremely versatile light source at no extra cost, with the following features:

Light source of any color, intensity and shape through choice of color index
Programmed scanning of colors possible without extra devices
Programmed movement of light spots without extra devices
Chopped light source created by programming, or by refresh frequency (CRTs)
Data collection and evaluation integrated with the light source
Data collected either electronically or optically (web camera)

The last point above is particularly interesting since it suggests a new completely computer based platform for optical measurements. One such possibility explored in some detail is colorimetric medical diagnostic tests. The uses of CSPT so far can be summarized as follows:

Scanning light pulse techniques (for the creation of "chemical images" with semiconductor structures) [1, 2]
Colorimetric bio- and chemical assays (for medical diagnostics and environmental monitoring) [3, 4, 7]
Detection of (multicolor) fluorescence in (micro) arrays [5, 8]

In the first of the three points above the screen is used alone without the web camera as a light source for the evaluation of large area catalytic metal-insulator-semiconductor structures for chemical sensing. These measurements illustrate, among others, the use of the screen to provide a scanning light spot, i.e. its possibility to provide a light source of any shape and location. We will, however, in the present contribution concentrate on the use of the computer screen and web camera combination as a commonly available platform for the evaluation of colorimetric tests of interest e.g. health care in general, but perhaps for primary health care units and even individual homes in particular.

A simple and inexpensive methodology for the observation of gas induced color changes in colorimetric sensing layers was recently demonstrated by Suslick et.al [9, 10]. They used the flat bed scanner to obtain (digitized) images of porphyrins before and after exposure to volatiles and where able to detect color changes caused by organic molecules. The CSPT approach differs in two aspects. It utilizes an even more common light source, the computer screen, and furthermore provides the possibility of scanning the colors of the light source in contrast to the white light used in the flat bed scanners. Additionally, the combination of camera filters and screen spectral radiances allow more spectral bands of analysis than in simply tri-chromatic recording, enabling to endure the inherent analytical weaknesses of the system.

2. The CSPT platform for the evaluation of colorimetric tests

The colors created by a computer screen are not monochromatic but consist of the combination of three broad band primary colors. This holds both for CRT- and LCD-based screens, although the generation mechanisms are different in the two cases. In CRT-based screens the colors are determined by the excitation of three different phosphorescent pigment areas, whereas in LCD-based screens the colors are controlled by the modulation of the intensity of background light through polarization changes caused by liquid crystals, and three broad band filters [11, 12]. The physical background of the computer-web camera setup for the measurements of light transmission, reflection, scattering, fluorescence, etc. is illustrated in Fig. 1.

This figure illustrates a sequence of colors obtained from the computer screen at different rgb-triplexes used to excite the screen. The rgb - values describe the intensity of the different primaries in 256 levels. Some of the rgb - combinations are indicated in the drawing. The bottom row is a part of a sequence of web-camera images of spots of different dyes exposed to the sequence of colors illustrated by the top row.

The platform itself is illustrated in Fig. 2 where it is indicated that the computer is used both to provide the light source and to present the results of the measurements, i.e. the images from the web camera at the same time. Furthermore the display window contains also the graphical user interface, commanding e.g. the selection of regions of interest in the obtained images. By using blank (white, transparent) wells/spots and specific calibration rows (or by comparison with reference spots) in the assay CSPT becomes independent of the computer/web camera platform. Measurements start by tuning the assay to the specific screen/camera combination used. One simple way to use the data is to calculate the average intensity in the three different camera channels for each region of interest, which as an example can be each spot or well in an array, disregarding a small region at its edges to compensate for edge effects. This masking is especially important for measurements in the wells of microtiterplates.

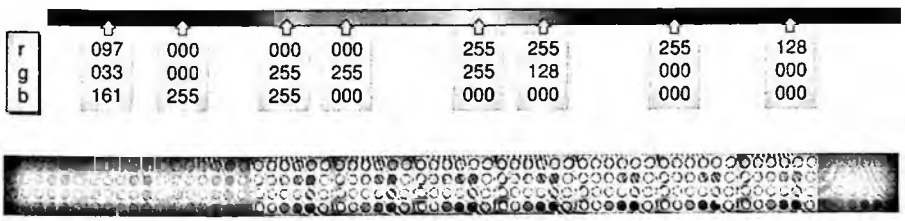

Fig. 1 Upper row: Illustration of one possible sequence of colors produced from a light window in a computer screen. The sequence is obtained by programming the computer using either data collection software (LabView, MatLab,..) or video files or specially composed slide shows, all providing simple ways to obtain the wanted color sequence. Some of the rgb-values corresponding to a given color are indicated. The screen was a CRT-based screen in the example. Lower row: Selected image frames from the web camera taken through an array of dots of different colors with increasing density towards the right. The column at far right contains transparent dots used as references

Fig. 2 Schematics of the computer-web camera platform for the measurement of colored samples. A light window in the computer screen illuminates a test array (solid and dry) or an array containing liquids (as in a microtiterplate, schematically shown bottom left). Measurements on liquid samples are performed through the use of a mirror (set at 45 degrees) allowing a horizontal mounting of the test plate.The images of the array obtained by the web camera for the different colors from the light window (see Fig. 1) can be stored as a video file for further treatment and analysis

The average intensities in each channel are added and divided by the sum of the average intensities obtained from the transparent reference points (which in case of aqueous samples can be the buffer, etc. in which the analysis is performed). In this way we obtain a result which can be compared with that of light transmission as measured by a spectrophotometer. The outcome plotted as a function of "color index" contains interestingly enough information, which is similar to monochromatic spectra, as illustrated in Fig. 3. The results in Fig. 3 were obtained from images as those shown in Fig. 1 and from separate measurements on each spot with a spectrophotometer.

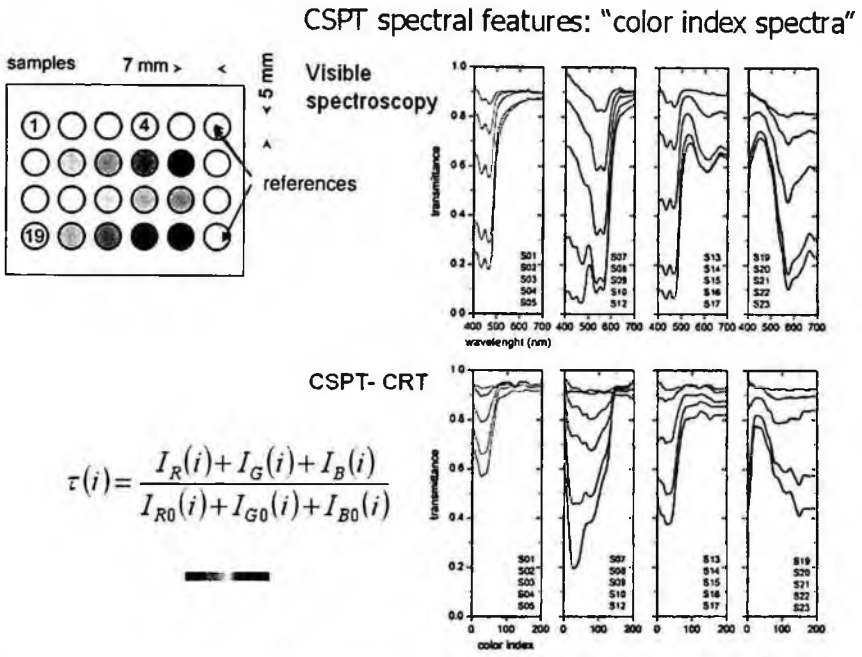

$$\tau(i) = \frac{I_R(i) + I_G(i) + I_B(i)}{I_{R0}(i) + I_{G0}(i) + I_{B0}(i)}$$

Fig. 3 Comparison between normal transmission spectra obtained with a spectrophotometer (Spectra Physics; narrow band monochromatic light) and the "color index spectra" obtained with the computer - web camera combination. Each color index is a combination of the three r, g and b values. The 200 different colors were created using a software making a sequence of colors caused the rainbow sequence [13]. τ(i) is the transmission at color index i as described in the text. The array tested consisted of 20 colored spots of different colors and hues on a plastic film and a column of transparent spots (i. e. the film itself) used as references (upper left). The numbers refer to the identification of the spectra to the right. The collection of spectra for each color shows the transmission of the light for the five different hues of each color.

3. Reflectance measurements

Many simple and fast "colorimetric" analyses are based on test strips which reflectance are measured. It is therefore necessary for the computer – web camera (CSPT) platform to be able to perform well also in such situations to provide a viable alternative to e.g. medical diagnostic tests performed in the primary health care. Figure 4 shows the result of reflectance measurements with the CSPT setup and results obtained with a conventional instrument for color evaluation of surfaces. In this case the CSPT setup appears to give more detailed information than the normal reflectance measurements. The reflectance ρ was calculated as the sum of the intensities in the three camera channels divided by the sum of the intensities obtained from the reference, the paper on which the colored strips were produced. We will

return to the reflectance measurements later when we discuss one of the applications of CSPT, namely the reading of (multi parameter) test strips used in primary health care units and in individual homes.

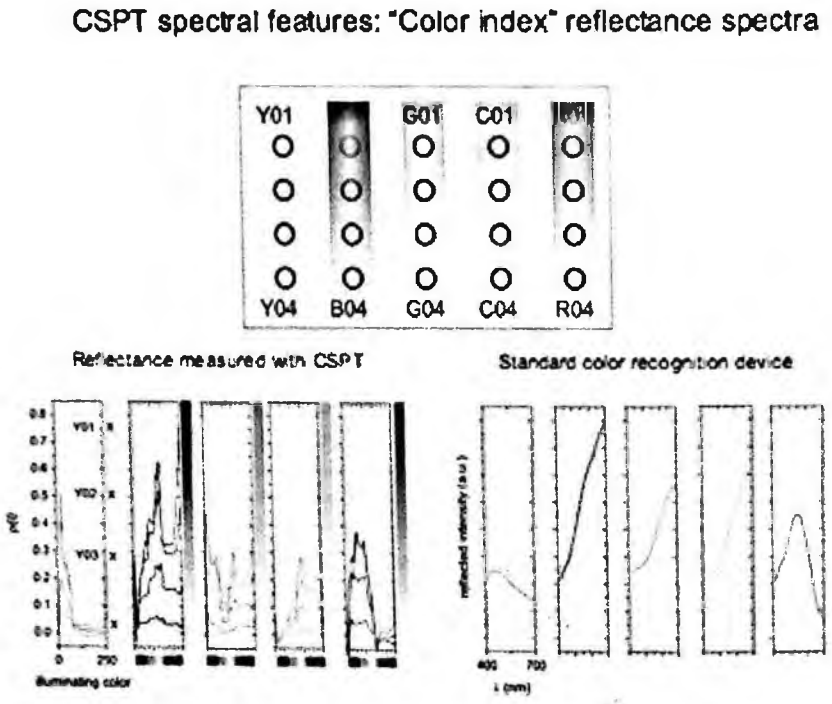

Fig. 4 Reflectance measurements with the computer screen- web camera platform. In this case a sequence of 250 different colors was used to illuminate the test strips consisting of selected spots of different colors made on opaque white paper (top picture). The reflectance was calculated in a way similar to the transmission shown in Fig.3. The measurements were made at four different spots for each color (circles in the top picture, crosses in the bottom left picture. The reflectance for each of the strongest colored points measured with a standard device is shown at the bottom right.

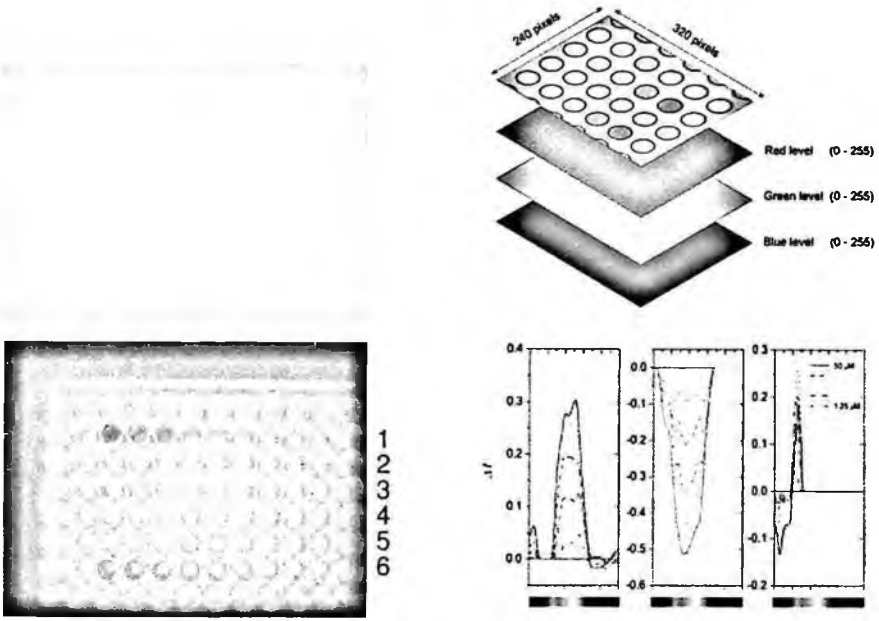

Fig. 5 Upper left image: Light window in the computer screen having in this case a yellow color with (r, g, b) = (255,255, 10). Lower left image: Image of part of a microtiterplate at the yellow illumination. The plate contained solutions of six different dyes with decreasing concentrations, 1mM to 1μM from left to right. The dyes were 1: aniline; 2: fluorescein; 3: acridine orange; 4: cy 3; 5: rhodamin; 6: cy 5.
Upper right image: Illustration of the fact that each image frame contains information in the three different channels of the web camera. Lower right image: The intensities recorded in the different channels after transmission of light with different colors (see bars at the bottom of each individual channel recording) through rhodamine compared to the light passing through a reference (pure water). The yellow areas indicate "extra" light intensity, i.e. fluorescence.

4. Detection of fluorescence and computer generated color contrasts

Experiments on colored spots or solutions of colored substances in (microtiterplate) wells yield web camera images, which often show different colors from that of the light window. This is due to two effects. Since the colors generated by the computer screen are composed by red, green and blue primaries a strong absorption of one of the primaries will yield images composed of the remaining ones. An example of this is the absorption of computer generated yellow light by a red pigment like rhodamin. A strong red color is observed as illustrated by the left hand side of Fig. 5. One obvious explanation for this is that since rhodamin absorbs most of the g-component of yellow light a red color remains (yellowish colors are characterized by large intensities of red and green, and a relatively small blue intensity. An interesting

question arises, however. Since rhodamin has also a red fluorescence some of the observed red color in the image may emanate from the fluorescence instead. We can here make use of the fact that information is stored in all of the three individual web camera channels, as illustrated in Fig. 5 (upper right). The red, green and blue intensities are stored individually, again in 256 levels. The recorded intensities in the individual channels at different illuminating colors for the wells containing rhodamin are shown in Fig. 5 (lower right). They are shown as the difference between the observed light intensities after transmission through the solution with the dye and the light intensity after passage through a reference well containing pure distilled water. A positive difference means that light is created in the sample. This is seen very clearly in the red channel of the web camera where a positive difference is observed for many of the illuminating colors. The cause of this is the large absorption of green part of the colors, causing fluorescence. It should be pointed out, however, that the details of the observed intensities in the different camera channels depend on the position of the absorption and emission spectra of the dyes with respect to the camera filters. The positive difference observed in the blue channel has no simple explanation as that in the red channel, but depend most probably on the specific nature of the rgb-colors and the position of the blue camera filter.

The computer can be used to further enhance results like those described by Fig. 5 by reconstructing the color images, giving the absorption (negative difference) a positive value and create a color describing the absorption (i.e. assign to the measured decrease in a given channel a positive color index in proportion to the size of the decrease). In the same way we can do for the positive differences. The results of such a reconstruction for the six dyes of Fig. 5 is shown in Fig.6.

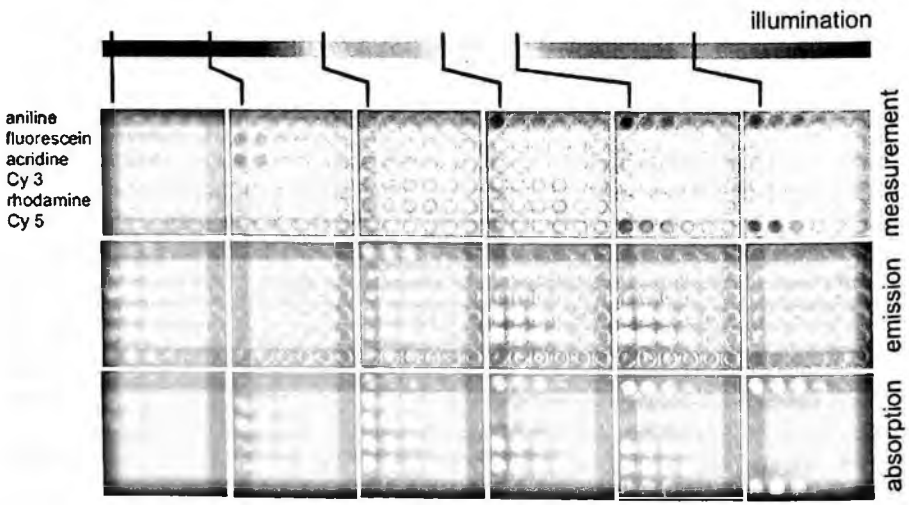

Fig. 6 Reconstructed assay image (see text for details)

5. CSPT reflectance evaluation of color test strips for medical diagnostics

The similarity between the "color index reflectance spectra" and normal reflectance spectra is illustrated in Fig. 4. Even here it is possible to extend the discriminatory possibilities of the CSPT platform further by using the information in the three camera channels individually, as in the "spectral fingerprinting" described in the previous section. This is particularly useful for classification purposes, when we like to use the platform for the determination of colors produced by blood, serum, saliva or urine samples interacting with test strips of different kinds. One way of utilizing the three channels is to connect the three individual intensity spectra into one continuous set of data. For the colored strips in Fig. 4 the data set corresponding to the measurements at the largest hue for each of the strips is presented to the left in Fig. 7. The differences between the differently colored strips are of course already seen in this figure. In order to more generally establish the possibility of the CSPT platform to classify different colors pattern recognition was made on the data. The 765 data points for each of the selected hues in Fig. 4 (one for each illuminating color in each of the camera channels) evaluated with principal component analysis [14] give the result to the right in Fig. 7. The colors are well separated, except for the smallest hues as expected. A check of the performance of the CSPT platform for medical diagnostic tests was made with a commercial multi parameter test for urine. An experiment was designed to find out the inherent performance of the platform in classifying the parameters of interest without the complication of the uncertainty of using real samples.

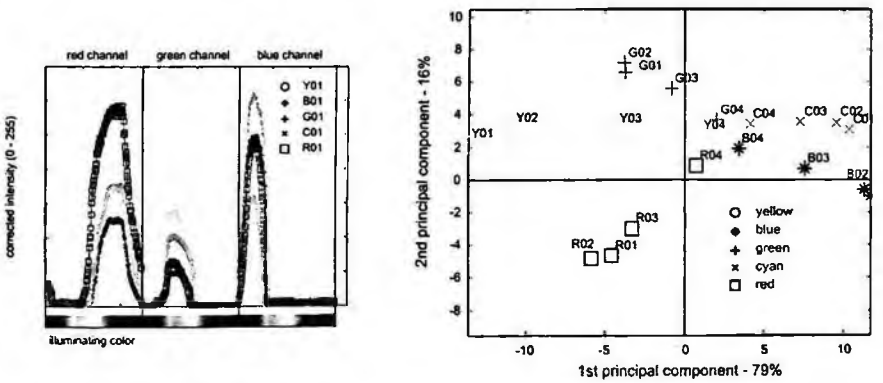

Fig. 7 Evaluation of reflectance measurements using information in the three different camera channels. The average intensities in each channel of the light reflected from the selected spots is shown in the left hand figure. Data are shown for the largest hue of each color strip in Fig. 2. The data set consists of the intensities of the light in each of the three camera channels at each of the 255 illuminating colors (i.e. 765 points per evaluated spot). The right hand figure shows the first two principal components of data like that to the left for all of the four hues selected in Fig. 4.[15]

The color sequence used to obtain the data in Fig. 4 and Fig. 7 consists of 255 combinations of rgb-values. Such long sequences contain redundant information and it is possible to use much shorter sequences in practice and also to optimize them for a given application [13]. In the evaluation of the Combur test to be described a sequence of 15 colors was thus used. The evaluation was not a clinical trial but aimed at checking the instrumental quality of the CSPT for evaluating such kind of colorimetric tests. Accordingly, clinical samples were not used at this point. Instead, synthetic samples generated as color printouts of possible assay outcomes were used. Standard scanning and printing procedures imply an inherent color degradation that makes the task of distinguishing different colors more demanding for CSPT. The results of such an evaluation become therefore a conservative estimation of the actual performance. The different synthetic test results evaluated are shown in Fig. 8 together with a schematic of the experimental setup. With these 5 different sets of indicators most of the outcomes of the assay are represented (nitrites were not possible due to the poor color reproduction in the printouts), enabling a full range estimation of the instrumental capabilities of CSPT for this application. In the CSPT measurement the image of the test strip together with the calibration (evaluation) chart is acquired in synchronism with each screen color of the illuminating sequence. The illuminating sequence used in this study was a non-optimal 15 colors set (Fig. 8) empirically chosen for satisfying a good sample classification in a short time.

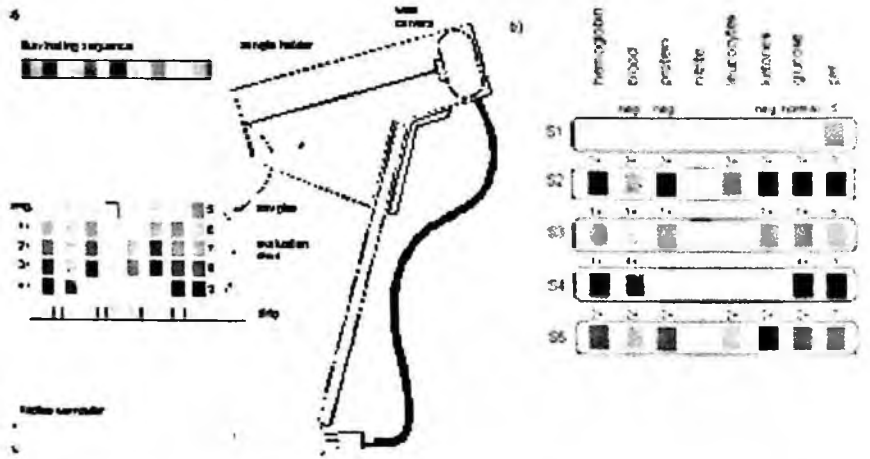

Fig. 8 Experiment using an illuminating sequence consisting of 15 colors created by a laptop computer. A schematic drawing of the experimental setup is shown. It is indicated that the web camera take images of the calibration chart provided by the manufacturer and the test strip at the same time. The test results were generated by a computer and printed on white paper. Five different combinations of test results were evaluated

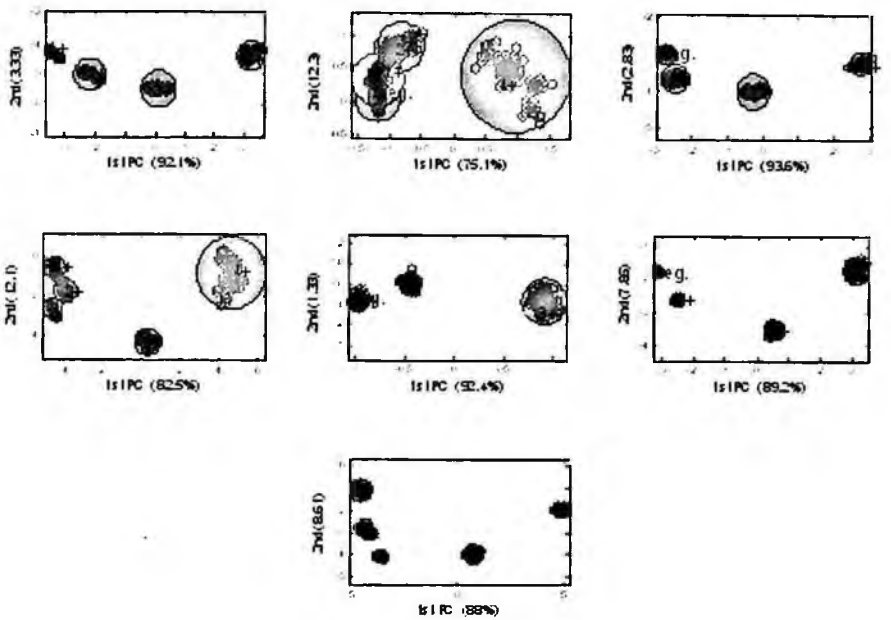

Fig. 9 Collection of principal component plots for seven parameters of interest to measure in urine. The blue clusters represent the "test" results for a number of different strips (3-5) for low values of the parameters and a pH of 6 (see the text for further description).

Here we only present one overall result showing the classification of "samples" with "low" values. The classification was again made by principle component analysis. One new measurement of the calibration chart was made each time a new strip was evaluated (in total 100 strips). The green circles in Fig. 9 illustrate the uncertainty in the measurements of the colors of the calibration chart. In most cases that uncertainty is much smaller than the distance between the (calibration) clusters for the different classes of samples (characterized by 1+, 2+, etc.). One exception is that for blood (in the urine) where the uncertainty in calibration makes it possible to only distinguishes with certainty the highest value (4+). This is due to the granular and uneven appearance of the colors of the blood assay as seen in Fig. 8. Altogether 580 classifications were made in the experiment with only 13 wrong classifications. Eleven of these occurred for glucose at 2+, which is not expected from the results in Fig. 9. In comparison the analysis of the same test strips done with only white light ("normal colorimetry") gave 60 miss classifications. A more thorough analysis of the performance of CSPT for the evaluation of diagnostic test strips is under preparation.

6. Possibilities in primary health care

The use of test strips and visual comparison with a calibration chart is of interest mainly for self tests without instrumentation. Most manufacturers of test strips for blood, urine, etc. provide also a reader for their strips performing the reflectance measurements and giving a numerical reading of the actual test result. The need for a new platform, although simple and generally available, may seem somewhat superficial. It is interesting to note, however, that there is a plethora of instruments available, as many as there are different types (and manufacturers) of test strips. Even in a primary care unit where a large number of instruments may be available it will be cost effective to use the same platform for all of the tests. This is even more true if the different test strips can be combined into one specifically made test card for the CSPT platform, designed to measure key parameters in (drops of) blood, urine, saliva,... A vision for the future is therefore a "Screenlab" replacing a number of instruments and test cards as illustrated in Fig. 10.

Fig. 10 There are many different solitary instruments and test strips and test cards available for fast diagnostic tests as illustrated by the collage to the left of the figure. These can be replaced by a properly developed test card to be used together with the computer screen and the web camera as illustrated to the right. The concept termed "Screenlab" is under development by RGB Technologies in Sweden.

7. Discussion

The CSPT concept is very versatile and consists of many more possibilities than described in this presentation. The CSPT-platform, as schematically illustrated in Fig.2, is based on already available platforms as standard computer sets of any kind: desktops, laptops, palm tops or even mobile telephones. Many optical phenomena may be evaluated (absorption, reflection, light scattering, emission). Any material

(polymer, hydrogel, insulator, semiconductor, solution,...) can be used as indicator material. Any color reaction can be employed as indicator. Applications are possible both in gas and liquid phase: Medical diagnostics based on blood, saliva, urine, sweat, breath and body odors and environmental monitoring of air and water can be made. In the future this may be possible also with the computer in individual homes.

Although not stressed in the present contribution, the use of mobile solutions for colorimetric assays is interesting not only for distributed medical diagnostics but also for the use of CSPT for environmental monitoring based on the already distributed network of mobile phones. CSPT also offers a natural internet embedded operation suitable with distributed evaluation and centralized administration. It is also highly customizable. The application is defined by the sensing assay (e.g. medical diagnostics or environmental monitoring) but the platform is always similar. In principle it does not require to install any specific software, just the regular internet browser would be enough, enabling centralized and secure processing of the generated results. It is compatible with several commercially available sensing technologies (e.g. ELISA assays, fluorescent assays, test strips, lateral flow devices, etc.). The best possible use of the CSPT platform requires, however, the development of tailor made test formats, the size and assay colors chosen to optimize the performance of the screen – web camera combination.
A few other observations are that by optimizing the computer generated color sequence defined molecules can be efficiently recognized in comparison to other molecules, i.e. providing a kind of molecular fingerprinting. For fluorescent samples the absorption and emission may be separated by the computer using the information in the three camera channels as described in Section 4.

The RGB-colors consist of linear combinations of three primary colors, and in principle it would be enough with three suitably chosen colors to get the best possible classification of a given substance. Since, however, in a general analysis there are several colors to distinguish and sometimes small shifts in the spectra of the samples, the use of a longer sequence of closely spaced colors optimize the evaluation. Even for the classification of one single substance the optimum sequence appears to contain more than three rgb-combinations. The reasons for this may be an increased signal to noise ratio by repeating the measurements at more linear combinations which could be similar to repeating an optimal three color sequence a number of times, a possibility not tested yet. Furthermore some non- linear effects in the color generation can not be excluded at present. More work has thus to be done to understand and optimize the performance of computer screen generated light in physical experiments and colorimetric tests. Regardless of the level of detailed understanding CSPT can, however, be used as a practical tool in many applications involving multiple sensing spots, like in optical electronic noses and for multi parameter diagnostic tests.

Acknowledgements

The participation in the 10th National Symposium on Sensors and Microsystems was made possible through an individual senior grant to IL from the Swedish Foundation for Strategic Research (SSF). The study of the physics and development of applications of CSPT are supported by grants from the Swedish Research Council (VR) and the Swedish Agency for Innovation Systems (VINNOVA).

References

[1] D. Filippini and I. Lundström, Chemical imaging by a computer screen aided scanning light pulse technique, J. Appl. Phys. 81 (2002), 3891-3893.

[2] D. Filippini and I. Lundström, Chemical images generated by large area homogeneous illumination of metal–insulator–semiconductor structures, J. Appl. Phys. 82 (2003), 3791 - 3793.

[3] D. Filippini, S. P. S. Svensson and I. Lundström, Computer screen as a programmable light source for visible absorption characterization of (bio)chemical assays, Chem. Commun. 2003 (2003), 240-241

[4] D. Filippini, T. P. M. Andersson, S. P. S. Svensson and I. Lundström, "Microplate based biosensing with a computer screen aided technique", Biosensors and Bioelectronics 19 (2003), 35-41.

[5] D. Filippini, J. Bakker, I. Lundström, Fingerprinting of fluorescent substances for diagnostic purposes using computer screen illumination, Sensors and Actuators B (2005), in press.

[6] D. Filippini, I. Lundström, Adaptive illumination in computer screen assisted spectral fingerprinting, Appl. Phys. Lett. (2005), in press.

[7] A. Suska, D. Filippini, T. Andersson, I. Lundström, Generation of biochemical response patterns of different substances using a whole cell assay with multiplesignalling pathways, Biosensors and Bioelectronics (2005), in press.

[8] D. Filippini, P. Åsberg, P. Nilsson, O. Inganäs, I. Lundström, Computer screen photo-assisted detection of complementary DNA strands using a luminescent zwitterionic polythiophene derivative, Sensors and Actuators B (2005), in press.

[9] N. A. Rakow and K.S. Suslick, A colorimetric sensor array for odor visualization, Nature 406 (2000) 710-713.

[10] K.S. Suslick, N. A. Rakow and A. Sen, Colorimetric sensor assays for molecular recognition, Tetrahedron, 60 (2004), 11133-11138.

[11] J. Gibson, M. Fairchild, Colorimetric characterization of three computer displays (LCD and CRT), Munsell color science laboratory report, 2000, pp. 1–40.

[12] R. Jackson, L. MacDonald, K. Freeman, Computer Generated Color, Wiley, 1994.

[13] D. Filippini, J. Manzano, I. Lundström, LCD-aided computer screen photo-assisted technique for colorimetric assays evaluation, Sensors and Actuators B 103 (2004), 158-164.

[14] I. T. Jolliffe, Principal Component Analysis, Springer-Verlag, New York, 1986

[15] D. Filippini, G. Comina, I. Lundström, Computer screen photo-assisted reflectance fingerprinting, Sensors and Actuators B (2005), in press.

ELECTROCHEMICAL DNA BIOSENSORS FOR HYBRIDIZATION DETECTION BASED ON ENZYME AMPLIFICATION

FAUSTO LUCARELLI AND MARCO MASCINI

Dipartimento di Chimica
Università degli Studi di Firenze
Via della Lastruccia 3, 50019, Sesto Fiorentino, Firenze, Italy
Email: marco.mascini@unifi.it

Introduction

The field of molecular diagnostics has expanded rapidly over the past decade. Applications range from the detection of mutations responsible for human inherited disorders, disease-causing and food-contaminating viruses and research into bacteria and forensics.

Detection of infectious species and genetic mutations at the molecular level opens up the possibility of performing reliable diagnosis even before any symptom of a disease appears. Additionally, the development of novel therapeutics based on the regulation of gene expression provides revolutionary new opportunities in the area of pharmaceutical science.

In order to improve patient care, molecular diagnostics laboratories have been challenged to develop new tests that are reliable, cost-effective and accurate and to optimise existing protocols by making them faster and more economical.

Conventional methods for the analysis of specific gene sequences are based on either direct sequencing or DNA hybridisation. Because of its simplicity, DNA hybridisation is more commonly used in the diagnostic laboratory than the direct sequencing method. In DNA hybridisation, the target gene sequence is identified by a DNA probe that can form a double-stranded hybrid with its complementary nucleic acid with high efficiency and extremely high specificity in the presence of a mixture of many different, non-complementary, nucleic acids. DNA probes are single-stranded oligonucleotides, labelled with either radioactive or non-radioactive material, which provide detectable signals indicating DNA hybridisation. Radioactive labels are extremely sensitive, but have the obvious disadvantages of short shelf life, risks associated with exposure of personnel to radiation, cost, storage and disposal problems. On the other hand, non-radioactive probes, such as enzymatic or luminescence labels, are less sensitive and flexible in terms of design and application, but are clearly safer and more environmentally friendly.

Over the past few years, advances in robotics, microfluidics, electronics and high resolution optics have driven the impressive development of both DNA microarrays and real-time PCR systems. The majority of commercial microarrays (pioneered by Affymetrix Inc. with their *GeneChip*® [http://www.affymetrix.com]) and all real-time PCR instruments (e.g., ABI Prism® 7900HT Sequence Detection System, [http://www.appliedbiosystems.com]) rely upon the detection and quantitation of a fluorescent reporter, whose signal increases proportionally to the amount of hybridised target or amplified PCR product. Detection thus requires imaging equipment or fluorescence readers that are generally very expensive.

In addition to these technologies which are already impacting on the market, new commercial research tools are expected to have a major influence in coming years. The recent appearance on the diagnostic market of electrochemical DNA microarrays (e.g., Motorola eSensor™ DNA Detection System [http://www.motorola.com/lifesciences/esensor/] and Xanthon Xpression Analysis System [http://www.xanthoninc.com]) bears witness to the enormous potential of electrode-based genosensors. Electrochemical devices are highly sensitive, inexpensive, easy-to-use, portable and compatible with microfabrication technologies. Moreover, in contrast with optical detection schemes, the electrical responses are independent of sample turbidity. In order to make DNA testing more convenient, more economically feasible and ultimately more widely used, the appealing promise of electrochemical detection technologies is thus driving an intense research effort by hundreds of laboratories world-wide.

A genosensor is a biosensor which employs an immobilised oligonucleotide as the bio-recognition element. Specifically, electrochemical genosensors rely upon the conversion of the base-pair recognition event into a useful electrical signal. Typically, the design of an electrochemical genosensor involves immobilisation of the DNA probe, hybridisation with the target sequence, labelling and electrochemical investigation of the surface. Optimisation of each step is required to improve the overall performance of the devices. However, deviations from this general scheme have to be considered when using modified magnetic beads for electrochemical genosensing.

Recent progresses in the development of electrochemical genosensors have been summarised in some excellent reviews (Pividori *et al.*, 2000; Yang *et al.*, 1997; Wang J., 2000; Palecek and Fojta., 2001; Palecek E., 2002; Vercoutere and Akeson, 2002; Drummond *et al.*, 2003; Kerman *et al.*, 2004).

This paper will describe electrochemical DNA biosensors recently developed in our laboratory using screen-printed gold electrodes as transducers. The biosensor format involved the modification of the gold surfaces through chemisorption of a 25-mer thiol-tethered DNA probe and a spacer thiol, 6-mercapto-1-hexanol. An enzyme-amplified detection scheme, based on the coupling of a streptavidin-alkaline phosphatase conjugate and biotinylated target sequences was then applied (Figure 1). The enzyme catalysed the hydrolysis of the electro-inactive α-naphthyl

phosphate to α-naphthol and then differential pulse voltammetry was used for the detection of this electroactive product.

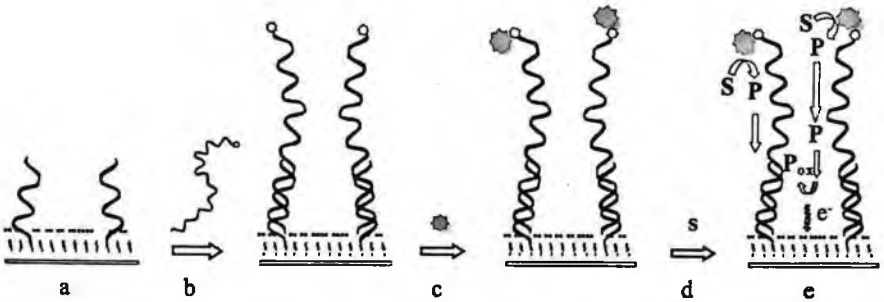

Figure 1.. Schematic representation of the electrochemical genoassay. a) Probe-modified screen-printed gold electrode; b) hybridisation with a 5'-biotinylated, thermally denatured, amplicon; c) Affinity coupling of the biotinylated hybrid with the streptavidin-conjugated alkaline phosphatase; d) Incubation with the enzymatic substrate; e) electrochemical detection.

This procedure, optimised using synthetic oligonucleotides, was finally applied to the detection of a typical genetic construct present in the majority of GMOs currently on the market: the 35S promoter. Such a sequence, used as a model analyte, was extracted from the pBI121 plasmid, amplified by PCR and analysed with the genosensor.

Materials and Methods

1.1. Materials and Reagents

Dithiothreitol (DTT), 6-mercapto-1-hexanol (MCH), streptavidin-alkaline phosphatase, α-naphthyl phosphate, bovine serum albumin (BSA), saline sodium citrate (SSC), diethanolamine, formamide and dextran sulphate were obtained from Sigma-Aldrich. Di-sodium hydrogenphosphate, potassium ferrocyanide, sulphuric acid, magnesium and potassium chloride were purchased from Merck. NAP-10 columns of Sephadex G-25 and *Taq* polymerase were obtained from Amersham Pharmacia Biotech. MilliQ water was used throughout this work. Synthetic oligonucleotides and primers used for PCR amplifications were obtained from MWG Biotech AG:

Probe (DNA-SH):	5' HS-$(CH_2)_6$-GGC CAT CGT TGA AGA TGC CTC TGC C -3'
Target:	5' biotin-GGC AGA GGC ATC TTC AAC GAT GGC C -3'
Non-complementary:	5' biotin-TCA CGC AGC TCA GCA GGC CCT -3'
P35S top primer:	5' - GCT CCT ACA AAT GCC ATC A – 3'
P35S bottom primer:	5' biotin-GAT AGT GGG ATT GTG CGT CA -3'
Lectin top primer:	5'-TGC CGA AGC AAC CCA AAC ATG ATC C-3'
Lectin bottom primer:	5' biotin-GCC CAT CTG CAA GCC TIT TTG TG -3'

All oligonucleotide stock solutions were prepared in 0.5 mol/L phosphate buffer (pH 7) and stored frozen.

1.2. DNA amplification by polymerase chain reaction (PCR)

The pBI121 plasmid incorporating the 35S promoter sequence was extracted from *E. Coli* using a QIAprep Kit (Qiagen), according to the manufacturer's protocol. A 195 bp region of the 35S promoter was then amplified using a DNA Thermal Cycler PTC-150 (MJ Research Inc.) following the procedure described by Pietsch and co-workers (1997). Briefly, each amplification reaction was carried out in a 10 mmol/L Tris-HCl solution (pH 8.3) containing 50 mmol/L of KCl, 1.5 mmol/L of $MgCl_2$, 50 μmol/L of each deoxynucleoside triphosphate, 400 nmol/L of each primer, 4 U of *Taq* polymerase and 20 ng of the pBI121 template (final volume 100 μL). After the first denaturation step (4 min at 95°C), the subsequent 40 cycles consisted of 1min of denaturation at 94°C, 1 min of annealing at 54°C and 1 min of extension at 72°C. A final extension at 72°C for 4 min was also included. Successful amplification was confirmed by gel electrophoresis.

A 217 bp fragment of the lectin gene was also amplified following the procedure reported by Pietsch *et al.* (1997) using genomic DNA extracted from soybean powder (0% Roundup Ready ™ CRM; Fluka). The PCR products were purified using Microcon® PCR kits (Millipore) according to the manufacturer's protocol. Amplicon concentrations were finally determined by fluorescence measurements, using the Picogreen™ dye and a TD-700 fluorometer (Analytical Control).

1.3. Screen-printing of gold electrodes

The electrochemical cells were planar three electrode strips, based on a gold working electrode, a carbon auxiliary electrode and a silver pseudo-reference electrode. The electrodes were screen-printed in house using a DEK 248 screen-printing machine (DEK). Silver-based (Electrodag PF-410) and graphite-based (Electrodag 423 SS) polymeric inks were obtained from Acheson Italiana; the gold-based ink (R-464 (DPM-78)) was obtained from Ercon Inc. and the insulating ink (Vinylfast 36-100) from Argon. A polyester flexible film (Autostat CT5), obtained from Autotype, was used as the printing substrate.

The silver ink was printed first in order to obtain the conductive tracks and the silver pseudo-reference electrode. Carbon and gold inks were then used to print the auxiliary and working electrode, respectively. After each step, silver, carbon and gold inks were cured at 120° C for 10 min. The insulating ink was finally used to define the working electrode surface (Æ = 3 mm). A curing period of 20 min at 70° C was applied.

To facilitate handling, the screen-printed electrochemical cells were attached to a rigid polycarbonate-based support. Each electrode was treated as disposable after use.

1.4. Purification of thiol-derivatised oligonucleotides

Prior to use, the thiol-modified oligonucleotides were treated with DTT. This reagent allowed reduction and cleavage of oligo dimers eventually obtained by oxidative coupling of two DNA-SH molecules (i.e. DNA-S-S-DNA). The lyophilised oligonucleotides were dissolved in a 0.17 mol/L phosphate buffer solution (pH 8) containing 0.04 mol/L of DTT. The reaction was allowed to proceed for 16 h at room temperature (Patolsky *et al.*, 2001). The thiolated DNA was then purified by elution through a NAP-10 column of Sephadex G-25 using 0.5 mol/L phosphate buffer (pH 7). DNA-SH stock solutions (26 μmol/L) were prepared in the same buffer and stored frozen.

1.5. Bio-modification of the sensor surface

Using the planar screen-printed electrode as a drop-on sensor, 10 μL of the thiolated oligonucleotide solution (1 μmol/L in 0.5 mol/L phosphate buffer) were placed on the gold working electrode surface. Chemisorption was allowed to proceed overnight (»16 h). During this period, the electrodes were stored in petri dishes to protect the solutions from evaporation.

The immobilisation step was followed by a post-treatment with MCH. A 10 μL drop of the 1 mmol/L aqueous solution of MCH was placed onto the DNA-modified working electrode surface for 1 hour. Prior to hybridisation reaction, the modified electrodes were washed twice with 15 μL of 2xSSC buffer.

1.6. Hybridisation with synthetic oligonucleotides and PCR-amplified samples

The probe-modified gold electrodes were exposed to a 10 μL drop of the biotinylated target sequence solution (buffered with 2xSSC) for 20 min. A biotinylated non-complementary sequence was used as the negative control. After hybridisation, the sensors were washed twice with 15 μL of DEA buffer (0.1 mol/L diethanolamine, 1 mmol/L $MgCl_2$, 0.1 mol/L KCl; pH 9.6).

After purification and reconstitution with MilliQ water, DNA samples obtained by PCR amplification were diluted 1:5 with 2xSSC buffer or "hybridisation buffer A" (i.e. 5xSSC, 20 mmol/L phosphate-buffered saline, 45% V/V formamide, 5 % w/w sodium dextran sulphate, pH 7.4). The double-stranded DNAs were thermally denatured using a boiling water bath (5 min at +100°C). Amplicon strand re-annealing was then retarded by cooling the sample in an ice-water bath for 5 min. A 10 mL aliquot of this solution was finally placed directly onto the probe-modified surface for 1 hour after which the sensors were washed twice using 15 μL of DEA buffer.

1.7 Hybrid labelling with alkaline phosphatase and electrochemical detection

The biotinylated hybrid obtained at the electrode surface was reacted with a 10 μL drop of solution containing 1 U/mL of the streptavidin-alkaline phosphatase

conjugate and 8 mg/mL of BSA in DEA buffer. After 20 minutes, the sensors were washed twice with 15 μL of DEA buffer.

The planar electrochemical cell was then covered with 150 μL of an α-naphthyl phosphate solution (1 mg/mL in DEA buffer). After 20 minutes of incubation, the oxidation signal of the enzymatically-produced α-naphthol was measured by DPV (modulation time = 0.05 s; interval time = 0.15 s; step potential = 5 mV; modulation amplitude = 70 mV; potential scan: from 0.0 to +0.6 V). The naphthol peak height was taken as the analytical signal. All electrochemical measurements were performed with a μAUTOLAB type II digital potentiostat/galvanostat (Eco Chemie). All potentials were referred to the silver pseudo-reference electrode. The experiments were carried out at room temperature (25°C).

2. Results

2.1. Electrochemical characterisation of the screen-printed gold electrodes

The screen-printed gold electrodes were firstly characterised by cyclic voltammetry in 0.5 mol/L H_2SO_4. Characteristic gold oxide formation and reduction peaks were found near +1.35 V and +0.65 V *vs.* Ag, respectively (data not shown). The electrochemically active surface of the screen-printed gold sensors was also evaluated by cyclic voltammetry, in the presence of the ferrocyanide redox probe. The Randles-Sevcik equation:

$$i_p = (2.687 \times 10^5)\, n^{3/2} A\, D^{1/2} C\, v^{1/2}$$

was used for the calculations. In the equation i_p is the ferrocyanide peak current (A), n the number of electrons involved, A the electrode area (cm^2), D the diffusion coefficient (= 6.50×10^{-6} cm^2/s [Heyrovsky, 1966]), C the concentration (mol /cm^3) and v the scan rate (V/s). An electrochemically active surface of 5.77 ± 0.16 mm^2 was calculated from the results (geometrical area = 7.07 mm^2). Additionally, the small relative standard deviation found for these measurements (2.8 % [n = 9]) indicated the good reproducibility of the screen-printing process.

Although mechanical or electrochemical cleaning of the gold surface is usually recommended, both thiol-tethered DNA probe immobilisation and naphthol electrochemistry were not found to be significantly affected by surface pretreatments (data not shown). Hence, the screen-printed gold electrodes were used as produced.

2.2. Electrochemical investigation of the probe-modified surface

The influence of probe coverage on the hybridisation reaction was the first parameter to be investigated. This effect was firstly examined by varying DNA-SH concentration. A series of sensors was exposed to thiolated oligonucleotide solutions (0.1, 0.6, 1, 3 μmol/L in 0.5 mol/L phosphate buffer), with chemisorption allowed to proceed overnight. Voltammetric data, summarised in Figure 2, show that excellent specific *vs.* non-specific signal ratios could be obtained even using the lowest DNA-SH concentration (i.e. 0.1 μmol/L). However, the most favourable ratio was

obtained using the 1 μmol/L concentration; this value was used for all subsequent experiments.
In the graph, it is also interesting to note that the signals measured at sensors exposed to the non-complementary sequence and pure hybridisation buffer were nearly the same. Therefore, the non-specific binding of the non-complementary sequence was assumed to be negligible, with any observed signal exclusively originating from the minimal non-specific adsorption of the enzymatic conjugate.

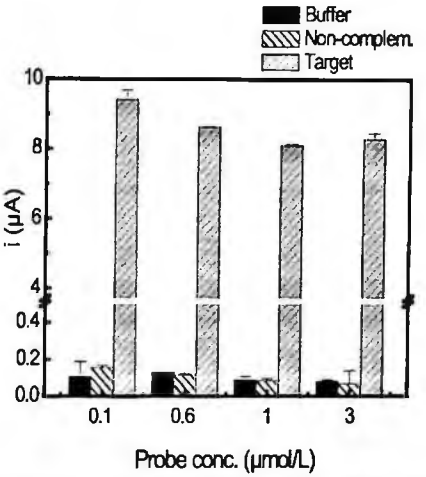

Figure 2. Influence of probe concentration on hybridisation reaction. DNA-SH immobilisation: 10 μL (0.1, 0.6, 1, 3 μmol/L in 0.5 mol/L phosphate buffer) onto the gold working electrode surface overnight. MCH treatment: 10 μL (1 mmol/L aqueous solution) onto the DNA-modified surface for 1 h. Target and non-complementary concentration: 12 nmol/L in 2xSSC buffer. Other conditions as described in the Materials and Methods section. The bars are the average of at least three measurements and the error bars the corresponding standard deviation.

Typical voltammetric responses for probe-modified electrodes exposed to buffer, non-complementary and target sequence solutions are given in Figure 3.
The features of immobilisation kinetics were also investigated. Different sets of gold electrodes were exposed to thiol-modified DNA solutions (10 μL, 1 μmol/L in 0.5 mol/L phosphate buffer) for increasingly amounts of time (1, 2, 4, 19 h). The results, plotted in Figure 4 as a function of the immobilisation period, show that the most favourable specific *vs.* non-specific signal ratios were obtained after an overnight immobilisation. This chemisorption time was used for all subsequent experiments.

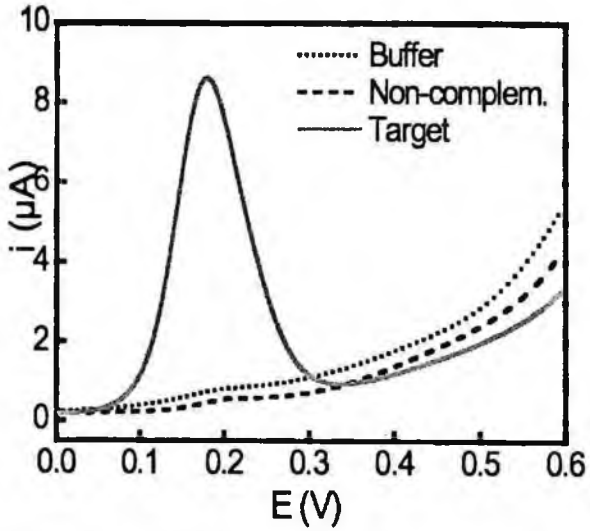

Figure 3. DPV signals for probe-modified electrodes exposed to buffer, non-complementary and target sequence solutions. DNA-SH concentration: 1 μmol/L. Other experimental conditions as reported in Figure 2.

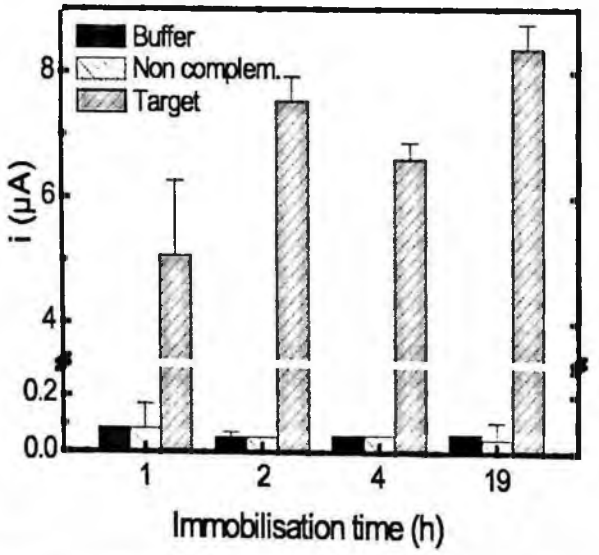

Figure 4. Influence of probe immobilisation time on hybridisation reaction. DNA-SH immobilisation: 10 μL (1 μmol/L in 0.5 mol/L phosphate buffer) on the gold working electrode surface for 1, 2, 4, 19 h. Other conditions as reported in Figure 2.

Preparation of mixed monolayers of a thiol-modified DNA probe and a spacer thiol by way of a two-step method was introduced by Herne and Tarlov in 1997. Use of 6-mercapto-1-hexanol (MCH) and its influence on analytical signals were explored. Two different sets of probe-modified electrodes were processed simultaneously but, in one case, the use of MCH was omitted. Both sets of sensors were then exposed to increasingly amounts of the biotinylated target sequence. Figure 5 shows the corresponding calibration plots. When the MCH treatment was omitted and hybridisation was directly attempted, only 50 % or less signal was obtained; within the 0-12 nmol/L concentration range the sensitivity of detection decreased from 0.655 to 0.310 μA/(nmol/L).

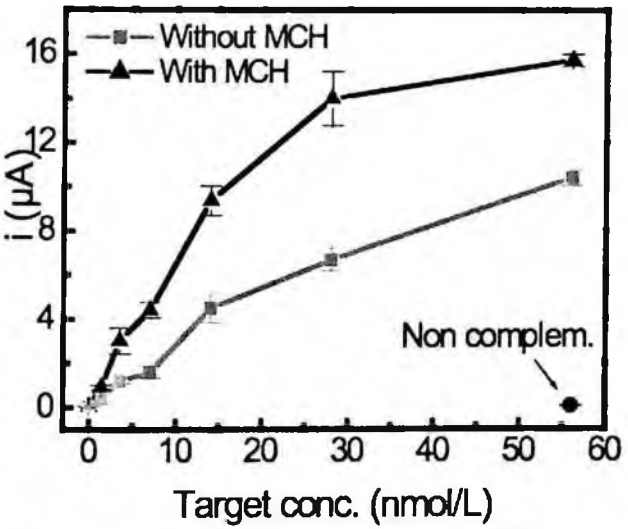

Figure 5. *Influence of MCH post-treatment on hybridisation reaction. DNA-SH concentration: 1 μmol/L. Other experimental conditions as reported in Figure 2. Each point represents the mean of at least three measurements and the error bars the corresponding standard deviation.*

2.3. Labelling with alkaline phosphatase

A number of electrochemical genosensors reported in the literature rely on the use of avidin-enzyme conjugates (Xu *et al.*, 2001; Patolsky *et al.*, 1999; Patolsky *et al.*, 2001). However, when using the avidin-alkaline phosphatase conjugate for labelling the hybrid-modified screen-printed gold electrodes a dramatic non-specific signal was observed (Figure 6, bars A). In an attempt to limit the non-specific adsorption of the avidin-conjugate, BSA was used as the blocking agent (Gizeli and Lowe, 1996; Fähnrich *et al.*, 2003). Different uses of this protein were also compared: a) preliminary blocking of the electrode surface with BSA followed by exposure to the enzymatic conjugate [two steps interaction] ; b) direct exposure of the surface to a BSA/ avidin-alkaline phosphatase mixture [one step interaction]. In both cases, the

specific *vs.* non-specific signal ratio was slightly improved; however, the results were far from being satisfactory (bars B and C in Figure 6). On the other hand, excellent results were obtained using the other commercially available conjugate, streptavidin-alkaline phosphatase, in combination with BSA (bars D in Figure 6). A favourable specific *vs.* non-specific signal ratio of 150 was found using such a conjugate. A solution containing the streptavidin-alkaline phosphatase conjugate and 8 mg/mL of BSA in DEA buffer was used for all subsequent experiments.

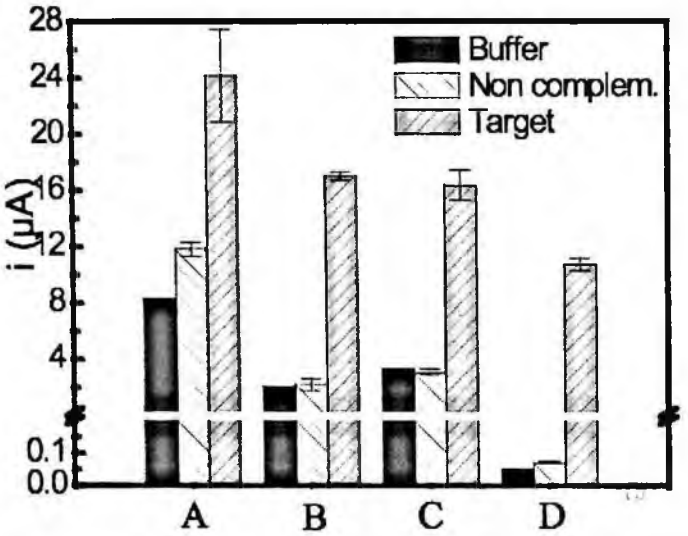

Figure 6. Labelling with alkaline phosphatase (AP): comparison between different enzymatic conjugates and use of BSA as the blocking agent. The modified sensors (DNA-SH concentration: 1 μmol/L) were exposed to: avidin-AP (1 U/mL in DEA buffer) for 20 min (bars A); BSA (8 mg/mL in DEA buffer) for 1h followed by avidin-AP (1 U/mL in DEA buffer) for 20 min (bars B); avidin-AP/BSA mixture (1 U/mL and 8 mg/mL in DEA buffer, respectively) for 20 min (bars C); streptavidin-AP/BSA mixture (1 U/mL and 8 mg/mL in DEA buffer, respectively) for 20 min (bars D). Other conditions as in Figure.2.

In order to further optimise the analytical assay, the influence of the enzymatic conjugate concentration on electrochemical signals was also investigated. A series of sensors was exposed to increasingly amounts of streptavidin-alkaline phosphatase (0.25, 0.5, 1, 2.5 U/mL) while keeping constant BSA concentration (8 mg/mL in DEA buffer). Experimental results (not shown) demonstrated how both the current due to the non-specific adsorption of the conjugate and that due to its specific coupling with the biotinylated hybrid increased with the streptavidin-alkaline phosphatase concentration. These data suggested that optimal analytical signal (compatibly with minimal non-specific adsorption of the conjugate) could be achieved using the 1 U/mL concentration. This value was used for all subsequent experiments.

The influence of the enzymatic substrate concentration on electroanalytical signals was additionally assessed. The a-naphthyl phosphate concentration was increased by orders of magnitude (0, 0.01, 0.1, 1, 10 mg/mL) while checking the current responses for both the target and the non-complementary sequence. The specific signals increased with the substrate concentration up to 1 mg/mL; therefore, this value was used for all subsequent experiments. On the other hand, the non-specific signals were still negligible even using 10 mg/mL of a-naphthyl phosphate.

2.4 Optimisation of hybridisation time

The last issue to consider was the influence of the hybridisation time. Linear dependence of the response on hybridisation time was observed up to 10 min, with the maximum signal achieved after 20 min (Figure 7). Therefore, this hybridisation time was used for all experiments involving the use of synthetic oligonucleotides.

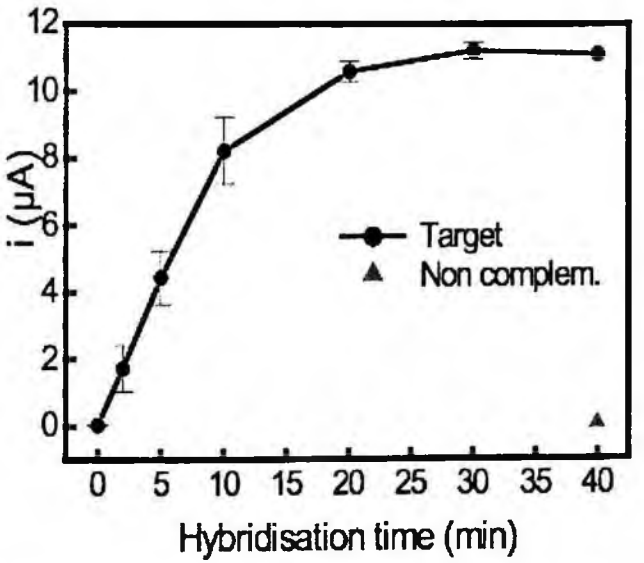

Figure 7. Influence of hybridisation time on electrochemical signals. The probe-modified sensors (DNA-SH concentration: 1 μmol/L) were reacted with 10 μL of the biotinylated target for 0, 2, 5, 10, 20, 30, 40 min (40 min only for the non-complementary sequence). Other conditions as reported in Figure 2. Each point represents the mean of at least three measurements and the error bars the corresponding standard deviation.

2.5 Calibration plot for synthetic oligonucleotides

To elucidate the analytical performance of the electrochemical geno-assay, a calibration experiment was finally designed. The voltammetric signals linearly increased ($R^2 = 0.986$) with the target concentration up to 25 nmol/L and then more gradually, until a plateau was reached (data not shown).

The experiments performed using the biotinylated non-complementary sequence further confirmed the selectivity of the sensor, with the non-specific signal being negligible even at the highest investigated concentration (1230 nmol/L). The reproducibility of the measurements (evaluated as relative standard deviation over 4 results) was 12%; a detection limit of 0.25 nmol/L of oligonucleotide target sequence (i.e. 1.5 x 10^9 target molecules in 10 μL of sample solution) was estimated.

2.6 Hybridisation with PCR amplified samples

PCR amplified targets were 195 bp fragments of the 35S promoter. A biotinylated fragment of the lectin gene (217 bp) was used as the negative control. The PCR mix (i.e. the solution containing primers, deoxynucleosides triphosphate, *Taq* polymerase, etc., but lacking the 35S template) was used as a further negative control and considered as the blank of the measurement.

Firstly, amplicon analysis was carried out in the conditions optimised for synthetic oligonucleotides (20 min of hybridisation in 2xSSC buffer). The only difference consisted in thermal denaturation of the samples which was required in order to let the biotin labelled strand hybridise with the immobilised probe. The results, reported in Table 1, demonstrated the sensitivity of the genosensor, with the target sequence (100 nmol/L) giving rise to an average signal which was 13-fold bigger than that observed for the negative control (100 nmol/L). The selectivity of the biosensing interface was also confirmed: negative control and blank gave substantially similar results.

Table 1. *Genosensor responses for PCR amplified targets (35S amplicons) and negative controls (PCR blanks, lectin amplicons and 2xSSC buffer, respectively)*.*

Sample	Signal (nA)
Target	161 ± 15
Target	149 ± 25
Target	151 ± 15
Target	150 ± 30
Target	151 ± 11
Blank	16 ± 3
Blank	13 ± 1
Blank	11 ± 2
Negative control	6 ± 1
Negative control	18 ± 4
Negative control	10 ± 5
2xSSC	7 ± 2

**The samples were purified and reconstituted with 2xSSC buffer. After thermal denaturation, target (100 nmol/L), negative control (100 nmol/L), blank and 2xSSC buffer solutions were interacted with the probe-modified electrodes (DNA-SH concentration: 1 μmol/L) for 20 min. Other conditions as reported in Figure 2.*

As shown in Figure 8, linear correlation (R^2 = 0.986) between amplicon concentration and electrochemical signal was found within the 0-120 nmol/L range. The detection limit of the assay, considered as the lowest analysed concentration which produces a signal distinguishable from blank and negative controls (S/N=3), was 15 nmol/L (i.e. 9.0 x10^{10} target molecules in 10 μL of sample solution).

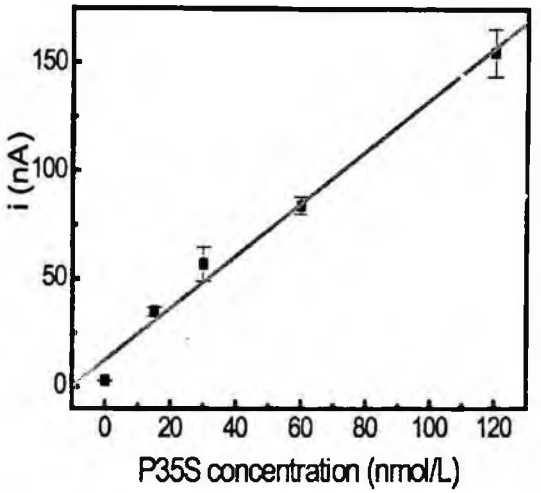

Figure 8. Calibration plot for 35S amplicons. Probe-modified electrodes were exposed to purified and thermally denatured target solutions 0, 15, 30, 60, 120 nmol/L in 2xSSC buffer. Other conditions as reported in Table 1. Each point represents the mean of at least three measurements and the error bars the corresponding standard deviation.

In order to increase the sensitivity of the analytical procedure, both the hybridisation buffer and the hybridisation time were modified. The new hybridisation buffer (denoted as "hybridisation buffer A") was 5xSSC, 20 mM phosphate-buffered saline and contained 45% V/V of formamide and 5% w/w of sodium dextran sulfate (Xu *et al.*, 2001). A hybridisation time of 1 h was selected during these experiments. The analytical results are reported in Table 2.

Table 2. Genosensor responses for PCR amplified targets (35S amplicons) and negative controls (PCR blanks, lectin amplicons and hybridisation buffer A, respectively).*

Sample	Concentration (nmol/L)	Signal (μA)
Target	100	1.63 ± 0.08
Target	100	2.13 ± 0.44
Target	100	2.21 ± 0.39
Target	100	2.28 ± 0.67
Target	8	0.39 ± 0.02

Target	8	0.45 ± 0.14
Target	8	0.48 ± 0.11
Blank	-	0.02 ± 0.01
Negative control	100	0.02 ± 0.01
Negative control	100	0.03 ± 0.02
Negative control	100	0.06 ± 0.04
Hybrid. buffer A	-	0.02 ± 0.01

**The samples were purified and reconstituted with hybridisation buffer A. After thermal denaturation, target (8 and 100 nmol/L), negative control (100 nmol/L), blank and hybridisation buffer A solutions were interacted with the probe-modified electrodes for 1 h. Other conditions as reported in Table 1.*

A favourable specific *vs.* non-specific signal ratio of about 70 was obtained when using the hybridisation buffer A. It is also interesting to note that the non-specific interaction of the non-complementary amplicon was not significantly enhanced, despite the extreme hybridisation conditions adopted. Furthermore, correct classification of the 35S samples became possible even when a concentration as low as 8 nmol/L was tested. A detection limit of 1 nmol/L (i.e. 6.0×10^9 target molecules in 10 μL of sample solution) was calculated for these experimental conditions. Interestingly, such a value approached the one found for synthetic oligonucleotides.

3. Discussion

The electrochemically active surface of the screen-printed gold electrodes was found to be 5.77 ± 0.16 mm^2. When comparing this value with the geometrical area of each sensor (7.07 mm^2) an apparent roughness factor of about 0.82 could be calculated. Such a low factor (which is the ratio between microscopic and geometrical area [Bard and Faulkner, 2001]) can be explained considering that only a part of the surface comprises gold readily available for the electrochemical reaction, while the residual is probably blocked by the binding polymer. Despite this view of the screen-printed gold surface, each electrode does not act as an array of microelectrodes.

The features of the immobilisation process were explored with the aim of maximising the sensitivity and selectivity of the voltammetric assay. Investigation of DNA-SH immobilisation kinetics clearly demonstrated that the chemisorption of a thiol-tethered oligonucleotide is a relatively fast process, with the surface coverage reaching a plateau after about 2h exposures. This observation is fully consistent with XPS and SPR data, obtained immobilising 25-mer thiol-tethered oligonucleotides onto evaporated gold films (Herne and Tarlov, 1997; Peterlinz et al., 1997). Therefore, it was concluded that the chemisorption of thiolated molecules on the

screen-printed gold surface was not significantly disturbed by the binding polymer of the gold ink.
Neutron reflectivity measurements of Levicky and co-workers (1998) demonstrated that, after treatment with the MCH spacer, thiol-tethered oligonucleotides were lifted off the surface, the S atom becoming the only anchoring point. In this work, the significant improvement of sensitivity that followed the treatment with MCH (Figure 5) was also attributed to dramatic changes of probe interfacial bio-architecture, as described by Levicky et al.
Enzyme labels have been widely used in affinity biosensors, particularly in immunosensors. Use of such labels greatly amplify the hybridisation signals and thus offers considerable promise for ultrasensitive detection of DNA hybridisation. When comparing the two commercially available alkaline phosphatase derivatives, the streptavidin-AP conjugate offered the most favourable specific vs. non-specific signal ratio. The experimental results displayed in Figure 6 can be rationalised when considering the isoelectric point (pI) of both the enzyme-conjugates and the blocking agent. In DEA buffer (pH 9.6) the avidin conjugate is positively charged (pI 10.5). Therefore, its electrostatic interaction with the negatively charged DNA backbone is expected to be considerable and responsible for the observed non-specific signal. When using this label, BSA (pI 5.2) is unlikely to be an effective blocking agent because of its negative charge in DEA buffer.
Unlike avidin, streptavidin has no carbohydrate side chains and has a lower isoelectric point (pI 5.0). As a result, streptavidin exhibits lower levels of non-specific adsorption than avidin.

PCR amplified targets were 195 bp fragments of the 35S promoter (Figure 9):

5' - **GCT CCT ACA AAT GCC ATC** ATT GCG ATA AAG GAA A<u>GG CCA TCG TTG AAG ATG CCT CTG CC</u>G ACA GTG GTC CCA AAG ATG GAC CCC CAC CCA CGA GGA GCA TCG TGG AAA AAG AAG ACG TTC CAA CCA CGT CTT CAA AGC AAG TGG ATT GAT GTG ATA TCT CCA CTG ACG TAA GGG **ATG ACG CAC AAT CCC ACT ATC** – 3'

Figure 9. *PCR amplified sequence. Bases denoted in bold indicate the top and bottom primer, respectively. Underlined bases indicate the region corresponding to the immobilised probe.*

The region of complementarity with the immobilised probe resided in the inner part of the amplicon, far from the end corresponding to the top primer. This choice further ensured the specificity of the assay. Given a selected couple of primers, the PCR process might be poorly selective, resulting in the amplification of an unwanted DNA region. Therefore, false positive signals would be obtained using an immobilised probe having the same sequence as the primer.

When using the 2xSSC buffer, the detection limit found for the PCR products was significantly lower than that found for synthetic oligonucleotides (0.25 vs. 15

nmol/L). Amplicon sister strand re-annealing in solution (which competes with hybridisation to the capture probe at the electrode surface) and the higher steric hindrance of the amplified target sequence probably played an important role. Longer hybridisation times and a specific hybridisation buffer were used in order to increase the sensitivity of the analytical assay. All constituents of hybridisation buffer A (5xSSC, phosphate-buffered saline, formamide and sodium dextran sulphate) are known to positively influence the rate of hybridisation reaction. This rate is strongly dependent on ionic strength. Formamide is known to decrease the melting temperature of nucleic acid duplexes, thus allowing efficient hybridisation at lower temperatures. On the other hand, dextran sulphate is an inert polymer that, by excluding the DNA from its own volume occupied in solution, effectively increases the concentration of the target DNA (Hames and Higgins, 1985). When using the modified procedure, the detection limit was improved by one order of magnitude (1 nmol/L) and approached the value found for synthetic oligonucleotides.

4. Conclusions

This paper describes an electrochemical genosensor developed by self-assembling a mixed monolayer of a thiol-tethered oligonucleotide and MCH onto disposable screen-printed gold electrodes. No chemical or physical treatment of the electrode surfaces was required prior to immobilisation of the synthetic DNA probe, thus greatly simplifying the use of these transducers for the bioanalytical assay.

The experimental results showed that the immobilisation of the DNA probe was relatively fast and that the binding polymer of the gold ink did not significantly interfere with the chemisorption process. Formation of DNASH/MCH mixed monolayers was used to improve the hybridisation efficiency of the DNA probe.

The detection scheme used, based on the enzymatic amplification of hybridisation signals, led to highly sensitive detection of the target sequence. Non-specific signals were minimised using an appropriate enzymatic conjugate (streptavidin-AP) coupled with an efficient blocking agent (BSA). The genosensor response was found to be linearly related ($R^2 = 0.986$) to the oligonucleotide target concentration between 0 and 25 nmol/L; a detection limit of 0.25 nmol/L was estimated. Although similar detection limits have been recently reported in the literature, such results were often achieved at the cost of more complex procedures.

Moving from proof-of-concept experiments to real sample analysis, the analytical procedure was further optimised and then applied to the detection of biotinylated amplicons of the 35S promoter (195 bp). The results showed that the genosensor enabled sensitive and specific recognition of the amplified sequences (detection limit = 1 nmol/L).

References

Bard A.J. and Faulkner L.R., 2001. *Electrochemical Methods: Fundamentals and Applications* (second edition). Wiley, New York, pp. 167, 369, 598.

Drummond T.G., Hill M.G., Barton J.K., 2003. Electrochemical DNA sensors. *Nat. Biotechnol.* **21** (10) 1192-1199.

Fähnrich K. A., Pravda M. and G. Guilbault, 2003. Disposable amperometric immunosensor for the detection of polycyclic aromatic hydrocarbons (PAHs) using screen-printed electrodes. *Biosens. Bioelectron.* **18**, (1), 73-82.

Gizeli E., Lowe C. R., 1996. Immunosensors. *Curr. Opin. Biotechnol.* **7**, (1), 66-71.

Hames B.D. & Higgins S.J., 1985. *Nucleic acid hybridisation – a practical approach.* Oxford University Press, Oxford, p. 78.

Herne T.M. and Tarlov M.J., 1997. Characterisation of DNA probes immobilised on gold surfaces. *J. Am. Chem. Soc.* **119**, 8916-8920.

Kerman K., Kobayashi M., Tamiya E., 2004. Recent trends in electrochemical DNA biosensor technology. *Meas. Sci. Technol.* **15**, R1-R11.

Levicky R., Herne T.M., M.J. Tarlov, Satija S.K., 1998. Using self-assembly to control the structure of DNA monolayers on gold: a neutron reflectivity study. *J. Am. Chem. Soc.* **120**, 9787-9792.

Palecek E., Fojta M., 2001. Detecting DNA hybridisation and damage. *Anal. Chem.* **73**, 74A-83A.

Palecek E., 2002. Past, present and future of nucleic acids electrochemistry. *Talanta* **56**, 809-819.

Patolsky F., Katz E., Bardea A., Willner I., 1999. Enzyme-linked amplified electrochemical sensing of oligonucleotide-DNA interactions by means of the precipitation of an insoluble product and using impedance spectroscopy. *Langmuir* **15**, 3703-3706.

Patolsky F., Lichtenstein A., Willner I., 2001. Detection of single-base DNA mutations by enzyme-amplified electronic transduction. *Nature Biotechnol.* **19**, 253-257.

Peterlinz K.A., Georgiadis R.M., Herne T.M., Tarlov M.J., 1997. Observation of hybridisation and dehybridisation of thiol-tethered DNA using two-colour surface plasmon resonance spectroscopy. *J. Am. Chem. Soc.* **119**, 3401-3402.

Pietsch, K., Waiblinger, U., Brodmann, P., Wurlz, A., 1997. Screeningverfahren zur identifizierung gentechnisch veränderter pflanzlicher lebensmittel. *Deutsche Lebensmittel RundschauHelf* **2**, 35-38.

Pividori M.I., Merkoci A., Alegret S., 2000. Electrochemical genosensor design: immobilisation of oligonucleotides onto transducer surfaces and detection methods. *Biosens. Bioelectron.* **15**, 291-303.

Vercoutere W., Akeson M., 2002. Biosensors for DNA sequence detection. *Curr. Opin. Chem. Biol.* **6**, 816-822.

Wang J., 2000. Survey and Summary. From DNA biosensors to gene chips. *Nucleic Acids Res.* **28** (16), 3011-3016.

Xu D.-K., Huang K., Liu Z., Liu Y., Ma L., 2001. Microfabricated disposable DNA sensors based on enzymatic amplification electrochemical detection. *Electroanalysis* **13** (10), 882-887.

Yang M., McGovern M.E., Thompson M., 1997. Genosensor technology and the detection of interfacial nucleic acid chemistry. *Anal. Chim. Acta* **346**, 259-275.

DIRECT ELECTRON TRANSPORT BETWEEN PHOTOSYSTEM II AND MODIFIED GOLD ELECTRODES[a]

J. MALY

Department of Biology, University of J.E.Purkyne, CZ-40001 Usti nad Labem, CZ

M. ILIE, E. CIANCI, V. FOGLIETTI,

CNR-IFN, Via Cineto Romano 42, Roma I-00156, Italy

L.DELLA SETA, M.R.MONTEREALI, K.PUNAKIVI, W.VASTARELLA AND R.PILLOTON[b]

ENEA-CR-Casaccia, Via Anguillarese 301, I-00060 S.Maria di Galeria Rome, Italy

Photosystem II providing direct electron transport with electrodeposited poly(mercapto-p-benzoquinone) was immobilised onto modified gold electrodes. The properties of the biosensor were characterized using linear sweep voltammetry, atomic force microscopy and photo-induced chronoamperometry. I_0=9nM and LOD=0.7nM for DCMU showed improved sensitivity compared to all previously studied PSII biosensors

1. Introduction

The vast majority of used herbicides blocks the electron transport in the PSII (see abbreviations at the end of the text) complex due to their specific binding [1], which results in inhibition of photosynthesis. A biosensor for detection of triazine-, urea- and phenolic- herbicides has been developed with isolated PSII particles from the thermophilic cyanobacterium *Synechococcus bigranulatus*, immobilised on the surface of a Clark electrode [2]. Oxygen evolution due to PSII activity during a red light short pulse decreased proportionally to herbicide concentration in the medium. An advanced PSII biosensor has been then developed using graphite SPE [3] and amperometric detection of an artificial

[a] This work was supported partly by COSMIC (ENEA Target Project on Biosensors and Bioelectronics), by Italian Ministry of Research (FIRB2001), by the project 522/001274 of Grant Agency of the Czech Republic, by the project IBIS of Czech Ministry of Industry and Trade and by a grant from TRIL Program of the International Centre for Theoretical Physics, Trieste.

[b] Corresponding author. Tel.: +390630483814; fax: +390630484096.
E-mail address: Pilloton@casaccia.enea.it - www.biosensing.net

electron acceptor (DQ). Cross-linking of PSII in a gel matrix of BSA and GA restricted the performances of such a biosensor because of the slow diffusion of mediator and decreased sensitivity to herbicides. An oriented monolayer of recombinant PSII with a tag of six histidine residues has been then used [4, 5] as sensing part of biosensor. Improved properties such as fast inhibitor transport, increased sensitivity, spatially controlled and reversible immobilisation were obtained. Despite that, the main drawback was still found in blocking effect of dense PSII monolayer towards the diffusion of red-ox mediators [6]. A common strategy for obtaining direct red-ox control over the protein is usually based on its attachment to conductive polymers and DET. Under natural conditions, electrons are taken from PSII by membrane soluble plastoquinones, which binds inside of so-called Q_B pocket of PSII. Therefore, the most suitable molecular wire should end with the quinone group which could fit Q_B pocket and could easily drain photo-generated electrons. The spontaneous self-assembling of thiolated quinones like SBQ on gold surface has already been widely described [7-9]. Unfortunately, such monolayer could not be used for DET [10], since the length of the polymer (approx. 4.4 Å [8]) was not sufficient to reach the red-ox reaction center of the protein. The use of a spacer between the quinone group and the electrode greatly affected the reversibility of the red-ox reaction which decreased with the distance from the electrode [9]. On the contrary, SBQ can undergo the electrochemical polymerization on gold electrode [10-12]. Such conducting polymer, polySBQ, has been already used for DET in many enzymes (e.g. xanthine oxidase, pyruvate oxidase, D-aminoacid oxidase) [10-12].

2. Materials and methods

SBQ was prepared as previously described by Alcalay [13] and electrodeposited on SPE from a saturated solution in 25mM nitrogen bubbled PB (pH =7.4) at E =+650mV. CV was used for determination of the red-ox properties of polySBQ film. Au SPE with a deposited polySBQ layer was immersed in PB (25mM, 100mM KCl) bubbled (15 min) with nitrogen and cycled between ±1V vs.Ag/AgCl. For the purpose of the AFM topographic measurements (Digital Instruments D3100), a μ-array (7x7) of gold electrodes deposited by optical lithography and

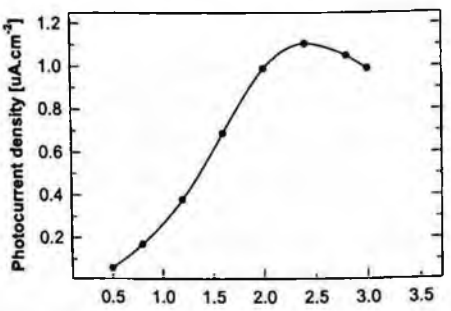

Figure 1. The effectiveness of DET vs the number of immobilized quinone moieties.

chemical vapour deposition on silicon substrate [14] was also used. The scanned surface was of 1μmx1μm. Immobilization of PSII particles [2] has been done by incubation of polySBQ modified electrodes in MESB [2] containing PSII equivalent of 30μg Chl mL^{-1} at 4°C in darkness for 20 minutes.

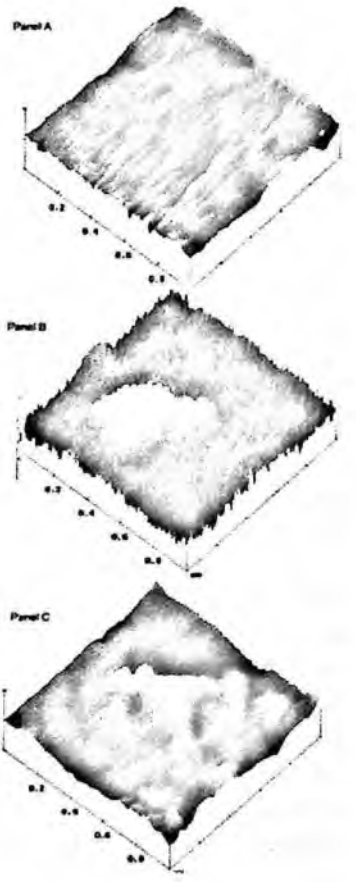

Figure 2: AFM images (see text).

3. Results and discussion

Electrochemical deposition of SBQ on AuWE showed an initial increase of anodic current (up to about 2 min) followed by the current decline till a lower steady state. Such electrochemical behaviour was typical for any free sulfhydryl containing molecules [4]. During the initial phase, the fast creation of monolayer was observed. With the prolonging time of oxidation, the multilayer structure as well as polymerisation process occurred (Surface plasmon resonance data during electrochemical oxidation not sown). The immobilization of the quinone group as well as the ability to exchange the electrons between the red-ox groups and electrode surface was controlled by CV. A quasi-reversible red-ox peak pair of quinone moieties was observed at E =-126mV with anodic peak centred at E_a=-107mV and cathodic at E_c=-146mV vs.Ag/AgCl (pH=7,4). The position of peak pair is in agreement with other authors [7, 8]. The peak position as well the charge transferred over the anodic or cathodic peaks remained unchanged up to 2 hours of repetitive cycling showing the stability of immobilized layer. The linear dependence between the red-ox potential and pH was observed between pH=5.4–8.4 (20mM PB, 100mM KCl). The slope of the linear dependence was -59mV/pH unit (data not shown). Such observation is in agreement with [7-10] and shows the 2-electron-2-proton red-ox reaction: $Q+2e^-+2H^+ \leftrightarrows H_2Q$. Since the diameter of one μ-electrode in array was 70μm and the charge transferred over anodic peak (obtained after 20 minutes of SBQ electro-oxidation) was

$Q=7,7mC\cdot cm^{-2}$, taking two electron red-ox reaction, than equivalent number of immobilized quinone moieties resulted to be $2,4\times10^{16}$ molecules$\cdot cm^{-2}$ ($3,98\times10^{-8}$ mol$\cdot cm^{-2}$). The photo-current generated by PSII immobilised trough the polySBQ layer is reported vs. the number of the quinone moieties in fig.1. Almost identical value was described [10] as an ideal value for DET for xanthine oxidase. Furthermore, as already shown, the typical experimental values [7-9] obtained for self-assembled monolayer of SBQ on gold were about two orders lower, close to the theoretical calculated value $5,7\times10^{-10}$ mol$\cdot cm^{-2}$ for vertically bound SBQ through the S-Au bond [15]. Therefore, the quantity of quinone moieties obtained with a 20 min electro-oxidation overcame the number necessary for an ideal monolayer by a factor of about 68. Therefore, assuming the polymerization process under ideal conditions, where linear polymerization from each SBQ molecule immobilized on gold is expected, we obtained chains containing 68 monomers which means chains about 30nm long (the SBQ is approx 4.4 Å long [8]). The AuWEs μ-array on silicon substrate [14] was selected since each electrode was individually addressable and the surface roughness of gold was substantially low (average roughness 3.5nm, Fig.2A). The surface appearance of electrode markedly changed after electro-deposition of the polySBQ layer as reported in Fig.2B. We found out needle-like structures with an average width of about 1nm or less. The average length varied from 7nm, in case of individual needle, up to 34nm in the case of crowded clusters. Interestingly, this value is quite close to 30nm which was previously obtained by electrochemical experiments. The AFM scans were stable when repeating on the same place which shows a strong attachment of the polymer on the electrode surface. After loading PSII, the needle-like structures diminished under the protein deposition (Fig.2C); round shapes have been noticed with relative average height in the range of 10nm. We supposed they were PSII molecules trapped by each needle-shaped polymer chain. In contrast, no such deposit was observed on unmodified gold electrode immersed in the same solution of PSII which shows that changes in polySBQ modified electrode were due to immobilized protein. Again, the AFM scans were repeatable, indicating a strong adherence of PSII to polySBQ layer. PSII itself is a big membrane protein (X-Y dimer core dimensions 17,2×9,7nm [16]) surrounded by all the remaining thylakoid membrane as well as the detergent micelle when isolated. Thus no strict homogeneity in size of immobilized PSII particles could be expected as usual in case of water soluble proteins. Therefore we were not able to observe AFM topography consisting of individually recognizable protein units. Instead, the superimposing effect caused by hydrophilic adherence to polySBQ layer,

rests of thylakoid membranes as well as the detergent and PSII itself determined the irregular hill-like structures which were observed. The photo-activity of PSII-polySBQ-AuWE was determined using a flow cell and screen printed gold electrodes. The illumination of PSII-polySBQ-AuWE with a LED (100μmol photons $m^{-2}s^{-1}$, λ=650nm, E=+250mV vs.Ag/AgCl) resulted in a photo-generated current (Fig.1,3). No detectable photo-generated current was observable, when polySQB-AuWE was illuminated under the same conditions. Time required to achieve 95% of the steady state was less than 5s. Here, we observed a big difference when compared with MET described in a previous paper [3]. In the former case, the velocity of the electrode reaction was restricted only by the rate of the enzyme reaction and by charge transport along the polySBQ layer. From CV measurements described above was clear, that the transduction of charge through polymer was very fast, since $\Delta E=E_a-E_c=39mV$. Thus we could assume that the velocity of the electrode response was only due to the rate of the enzymatic reaction. On the other hand, in the case of MET, the velocity of the electrode response was due to diffusion of red-ox mediator in the PSII-BSA-GA gel and the steady state was then achieved within several minutes under the same conditions [3,5]. Figure 3B reports the calibration curve obtained with the herbicide DCMU and Figure 3A shows an example of the inhibition effect on the photo-generated signal due to DET of PSII. I_{50}=9nM and LOD=0.7nM for DCMU shows improved sensitivity [17] compared to all previously studied PSII biosensors.

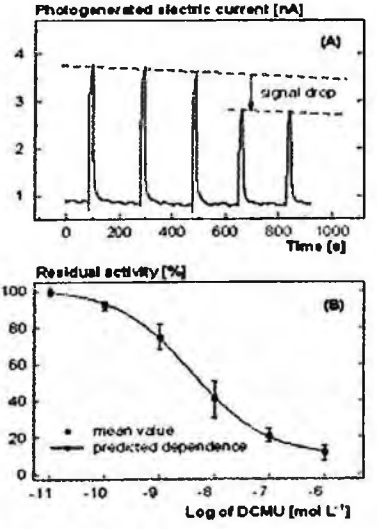

Figure 3. A) Inhibition of PSII-polySBQ-AuWE as the response to addition of 3nM DCMU. **B)** Calibration curve for DCMU.

Conclusions

A conductive polySBQ layer was synthesized on the surface of (i) Au SPE, (ii) Au μ-electrodes in an array using a simple electro-oxidation process. The basic red-ox as well as morphology properties of polymer film were determined using electrochemistry and scanning probe microscopy. PSII isolated from thermophilic bacteria *Synechococcus bigranulatus* was immobilized on polySBQ-AuWE. Resulting PSII-polySBQ-AuWE showed photo-inducible

DET at the potential E=+250mV vs. Ag/AgCl. Basic properties of this process were studied. As the result: (i) the charge transport from PSII to gold WE was fast and dominated by the rate of the PSII enzymatic reaction; ii) I_{50} and LOD showed improved sensitivity compared to all previous PSII biosensors.

Abbreviations

AFM:atomic force microscopy; **AuWE**:gold working electrode; **BSA**:bovine serum albumin; **BSA-GA-PSII**:crosslinked PSII in a gel matrix of BSA and GA; **Chl**:chlorophyl; **CV**: linear sweep voltammetry; **DCMU**:diuron; **DET**:direct electron transport; **DQ**:tetramethyl-p-benzoquinone; **GA**:glutaraldehyde; **I_{50}**:dose causing 50% inhibition; **LED**:Light emitting diode; **LOD**:limit of detection; **MES**:2-(N-morpholino) ethanesulfonic acid; **MESB**:40mM MES, 100mM NaCl, 15mM $CaCl_2$, 15mM $MgCl_2$, 50μM chloramphenicol, 0.03%Dodecylmaltoside, pH=6.5; **MET**:Mediated Electron Transport; **PB**:phosphate buffer; **polySBQ**:poly(mercapto-p-benzoquinone) **polySBQ-AuWE**:poly(mercapto-p-benzoquinone) deposited on Au; **PSII**:photosystem II; **PSII-polySBQ-AuWE**:poly(mercapto-p-benzoquinone) on Au with immobilized PSII; **Q_B**:quinone binding site of PSII; **SBQ**:sulfobenzoquinone; **SPE**:screen printed electrode;

References

1. Draber W., Tietjen K., Kluth J.F. & Trebst A. (1991) Angewandte Chemie International Edition (English) 30, 1621-1633
2. Koblížek M., Masojídek J., Komenda J., Kučera T., Pilloton R., Mattoo A.K. & Giardi M.T. (1998) Biotechnology and Bioengineering 60, 664-669
3. Koblízek M., Malý J., Masojídek J., Komenda J., Kučera T., Giardi, M.T. Mattoo A.K. & Pilloton R. (2001) Biotechnology and Bioengincering 78, 110-116
4. J.Maly, A.Masci, J.Masojidek, M.Sugiura and R.Pilloton, (2004) Analytical Letters, Vol. 37, No. 8., pp. 1676–1687
5. J.Maly, C.Di Meo, M. De Francesco, A. Masci, J. Masojidek, M. Sugiura, A. Volpe, R. Pilloton (2004) Bioelectrochemistry, Vol/Issue 63/1-2 pp. 271-275,
6. J. Maly, J. Krejci, M. Ilie, L. Jakubka, J. Masojıdek, R. Pilloton, K. Sameh, P. Steffan, Z. Stryhal, M. Sugiura, Anal Bioanal Chem (2005) 381: 1558–1567
7. Sato Y., Fujita M., Mizutani F., Uosaki K.; J.Electroanal.Chem.409(1996)145-154
8. Chan E.W.L., Yousaf M. N., Mrksich M., J.Phys.Chem.A 2000, 104, 9315-9320
9. Hong H., Park W., Yu E., J.Electroanal.Chem.476 (1999) 177-181
10. Arai G., Takahashi S., Yasumori I., J.Electroanal.Chem. 410 (1996) 173-179
11. Arai G., Noma T., Habu H., Yasumori I., J.Electroanal.Chem. 464 (1999) 143-148
12. Arai G., Noma T., Hayashi M., Yasumori I., J.Electroanal.Chem.452 (1998) 43-48
13. Alcalay W., Hel. Chim. Acta, Vol XXX, II 578-585 (1947)
14. J. Maly, M. Ilie, V. Foglietti, E. Cianci, A. Minotti, L. Nardi, A. Masci, W. Vastarella and R. Pilloton; Sens. & Act. (2005) in press
15. Stern D.A., Wellner E., Salaita G.N., Laguren-Davidson L., Lu F., Batina N., Frank D. G., Zapien D.C., Walton N., Hubbard A.T., J. Am. Chem. Soc. 110 (1988) 4885
16. K. Bacon, in: Advances in Photosynthesis, vol. 10, Photobiochemistry and Photobiophysics, Kluwer Academic Publishers, Dordrecht, 2001, pp.278-279
17. J. Maly, J. Masojidek, A. Masci, M. Ilie, E. Cianci, V. Foglietti, W. Vastarella, R. Pilloton; (2005) Biosensors and Bioelectronics, in press

SILICON BASED PHYSICAL AND BIOPHYSICAL MICROSYSTEMS: TWO CASE STUDIES

B. MARGESIN, L. LORENZELLI, M. ZEN
ITC-irst Microsystems Division, Via Sommarive 18, Povo 38050, Trento, Italy.

G. SONCINI
Department of Information Tecnologies, University of Trento
Via Sommarive 14, Povo 38050, Trento, Italy.

ITC-irst Microsystems Division is since many years active in the design and fabrication, at prototype level and small volume production, of silicon integrated microsystems. In this paper we present two examples of recently developed microsystems: a new type of RF MEMS switch and an ISFET based Bioelectronic Microsystem for monitoring cellular metabolic activity.

The RF MEMS switch, which has been named "Symmetric Toggle Switch", is a capacitive microswitch based on a push–pull mechanism and utilizes torsion springs and levers, placed symmetrically and transverse to CPW line. It presents low actuation voltage and high isolation, and has been designed for high RF power and reliability applications in telecommunication.

The Bioelectronic microsystem uses ISFET arrays for extracellular acidification monitoring with VLSI read out electronics. The system is also intended for electrophysiological measurements by monitoring, extracellularly, the electrical activity from a network of neurons coupled to the microtransducer array substrate. The proposed system should be able to measure the electrical activity, as well as the metabolic activity, of a neuronal cell population by means of ISFET devices.

1. RF MEMS Switches

1.1. *Introduction*

The importance of RF MEMS switches in high value space and commercial telecommunication applications has been well established by the vast amount of literature published over the last decade [1,2]. In comparison to conventional switching devices, MEMS switches exhibit superior electrical performance and low power consumption on a size scale commensurate with solid-state devices. In

electrostatically actuated MEMS switches, whose basic microstructure is presented in fig. 1, the use of low resistivity metal beams and 2÷5 μm of air gap between the switching elements result in low insertion loss (< 0.2dB) and high isolation (>20dB).

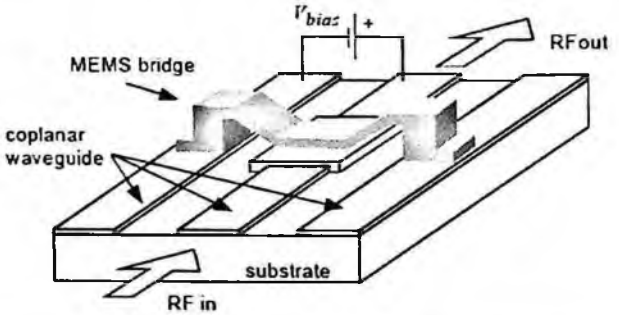

Fig. 1. Basic microstructure of the electrostatically actuated RF MEMS switch

The inevitable I-V non-linearities associated with semiconductor junctions in PIN diodes and GaAs FETs are non-existent; except for the minor hysterises in C-V characteristics of shunt switches. The high levels of integration, no measurable harmonics or intermodulations and negligible quiescent current, improves the overall performance. However, higher actuation voltage (>10V), low RF power handling capability, switching speed and reliability are the issues, which undermine the potential RF MEMS switch applications.

In order to achieve low actuation voltage, the conventional fixed-fixed or fixed-free beam design approach leads to various trade-offs among the critical parameters [2] and complex fabrication process. In electrostatically actuated MEMS switches, the pull-in voltage is a function of the gap between the movable beam and actuation electrode, the actuation area and the spring constant of the beam. Among the three variables spring constant presents more flexibility in achieving low pull-in voltage without affecting the switch performance and insignificant increase in dimensions. However lowering the spring constant adversely affects the switching speed and makes devices susceptible to self-biasing, external shocks and vibrations.

In this paragraph we describe the so-called "Symmetric Toggle Switch", which makes use of thin torsion springs and levers to achieve low actuation or pull-in voltage and higher isolation. The push-pull mechanism ensures immunity to self biasing and external vibrations. The symmetry about the transmission line improves the mechanical and electrical characteristics of the device.

1.2. The symmetric toggle switch

Fig. 2 shows a schematic 3D view of the symmetric toggle switch, whose functional details are illustrated in the 1D cross sectional view.

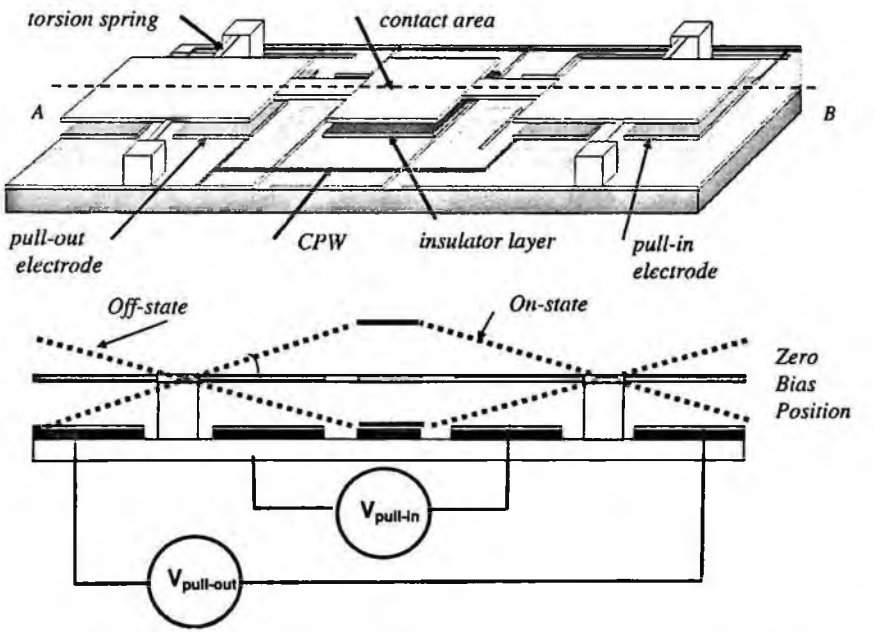

Fig. 2. Schemaic 3D view and 1D cross sectional view of the Simmetric Toggle Switch

The movable bridge structure consists of the central contacting area, which is connected to rectangular torsion micro-actuators on either side by levers. As

shown by the 1D cross sectional view in Fig.2, the pull-out electrodes (outer pair) are biased to keep the beam clamped in the up state, which corresponds to the switch "on" state. The transmission loss in a capacitive shunt switch is determined by C_{off} capacitance between the beam and CPW central conductor. The pullout mechanism increases the gap height to more than the zero bias gap, thus improving the transmission significantly. Also, the switch is impervious to the external vibrations and self-actuation, if the pullout voltage is higher than the RF-signal magnitude (V_{rms}). The pull-in electrodes (inner pair) when biased to a voltage $\geq$ Vpull-in threshold voltage, brings the beam in contact with the dielectric layer on top of the transmission line, capacitively coupling the RF signal to ground. The switch is in the "off" state. The pull-in threshold voltage is a function of the microactuator top and bottom electrode dimensions, gap height, torsion spring and connecting lever dimensions.

1.3. Prototype development

In the design of microwave switches, actuation voltage and RF performance are the primary considerations. In order to optimize the device, a dedicated analytical model has been developed and used to guide the overall device microstructure design [3]. Designed details of the microstructures have been validated by using conventional MEMS simulation tools, mainly CONVENTOR and ANSYS.

In order to demonstrate the fabrication feasibility a few devices with lever length ranging from 200 to 400μm and contact areas ranging from 200 to 400μm in length and 50 to 70μm in width were micromachined using the seven masks proprietary IRST RF MEMS process already described in ref. 4. One of the prototypes chip is shown in fig. 3 togheter with SEM micrographs of the most significant structural details.

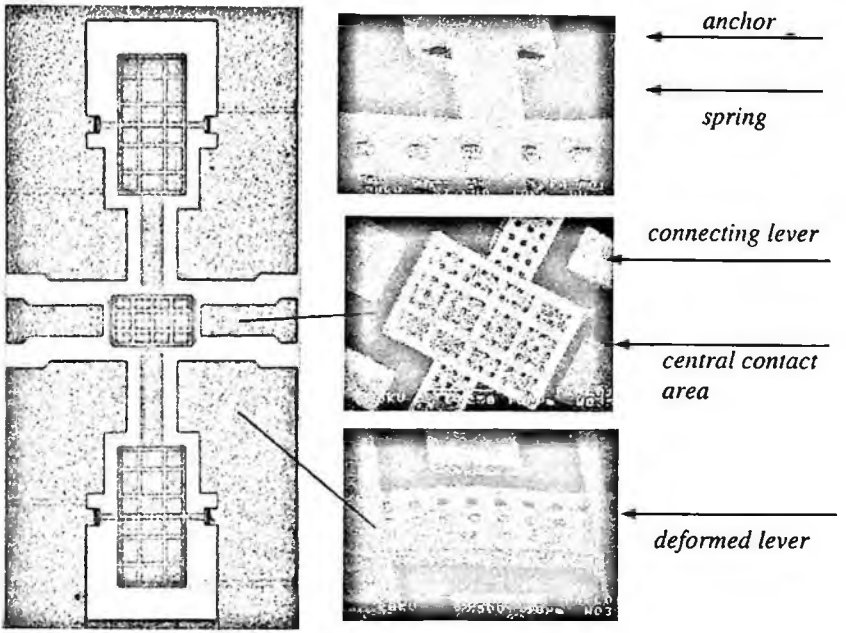

Fig. 3. Simmetric Toggle Switch prototype

Characterization for the fabricated devices was carried out using an experimental setup consisting of HP Vector Network Analyzer (8719D) and Agilent 4156C (Percision Semiconductor Analyzer used as voltage sweep source). The first measurements showed that the actuation voltages for devices are higher than expected. SEM analysis showed that this is related to residual stresses in the materials which induce deformation of the mobile plate and lever. The most critical technological steps have been revised in order to relieve the stresses and the consequently induced deformation of the layers.

2. Bioelectronic Microsystems

2.1. *Introduction*

In the last decade, fundamental advances in the fabrication technology of cell-based microsystems have demonstrated the feasibility to utilize living cells

as primary transducers to detect biologically active agents [5]. The main motivation for the development of such systems originates from the interest to screen analytes from physiological effects. Recent advances in MEMS technology that combines micromachining with new microtransducer realization methodologies and aforementioned in-vitro culture techniques, has allowed the behavioral study of cell populations and neuron cultures grown on appropriately functionalized substrates and sensors, in a controlled way. Thus, real time in-vitro investigations of the physiological state of a cell population in a broad area of biomedical applications, ranging from basic research to various fields of pharmacological analyses, can be performed. Complex systems, constituted by arrays of electrochemical transducers eventually combining micromachined structures for cell culture guidance can be envisaged.

Aim of this paper is to illustrate a microsystem designed for multisite monitoring of the physiological state of a cell population. The microsystem, consists of an array of spatially distributed ISFETs and gold microelectrodes designed to monitor the electrochemical activity of cells and neurons.

2.2. *Characteristics of the microsensor chip*

The core of the system, described in detail in ref. [6], consists of a sensor chip bonded by means of a surface mounted device (SMD) package on a printed circuit board with a flow injection micro-chamber. In general, the design of the microsensor module requires a fabrication process, both technologically reliable and economically suitable to be integrated with different technologies such as microelectrode fabrication and micromachining. In our case, the utilized technological process is a modified ion sensitive field effect transistor complementary metal nitride oxide semiconductor (ISFET/CMNOS) technology, whose basic structure is shown in fig. 4. The chemical sensing layer consists of stoichiometric Si3N4.

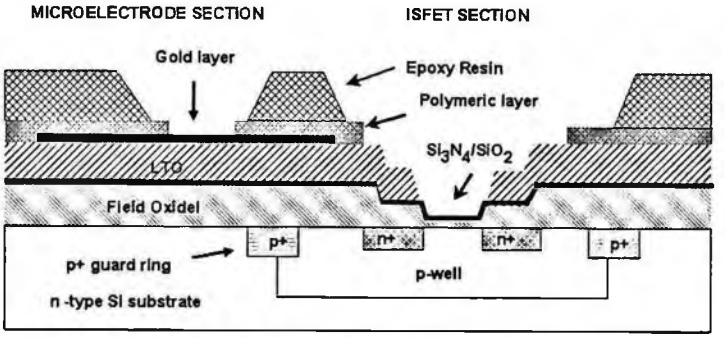

Fig. 4. IRST ISFET/CMNOS technology

Different microsystems designed for multisite monitoring of the physiological state of a cell population have been developed. microsystem, shown in Fig. 5 consists of an array of 40 ISFETs and 20 gold microelectrodes and has been designed to monitor the electrical activity of neurons. This is achieved by direct coupling of the neuronal culture with the ISFET sensitive layer and by utilising gold microelectrodes for neuronal electrical stimulation. Cell cultures can be grown either, by traditional laboratory methods, on the membrane of commercial wells positioned onto the sensor chip surface or directly onto the sensor chip surface. An integrated CMOS multiplexer, consisting of a current-mode preamplifier with a multiplexing stage, which provides analog channels for signal monitoring, has been implemented with the purpose of getting a bias circuit small in size, stable and easily integrated and connected to external data acquisition systems.

In a first evaluation phase, a set of experimental measurements have been performed for characterizing the electrical and metabolic activity of a cell population with particular emphasis on electrophysiological measurements for pharmacological applications. For this purpose, two different cellular lines (Cheratinocytes and CHO cells) have been chosen as test cell cultures and small pH variations induced by the metabolic activity of the cells have been monitored

by the ISFETs both in normal conditions and under the addition of a toxicological agent, as described in detail in ref. [7]. The results obtained are in agreement with the expected values calculated considering the number of cell per unit area, the protons generated per second, the cell-sensor distance and the buffer capacity of the medium.

Fig. 5. (a) Microsystem for neuron electrical activity monitoring; (b) ISFET array; (c) chip detail

3. Conclusions

A microsystem based on ISFET arrays for extracellular acidification monitoring with VLSI read out electronics has been developed. The system is also intended for electrophysiological measurements by monitoring, extracellularly, the electrical activity from a network of neurons coupled to the microtransducer array substrate. The proposed system should be able to measure the electrical activity, as well as the metabolic activity, of a neuronal cell population by means of ISFET devices. Moreover, the electrical activity of the neurons can be stimulated (and also recorded) by using the conventional gold microelectrodes.

Although, the device is not already optimized it provides, taking advantage of the specialized fabrication tools for the microfluidics and microsensors array, new assays in electrophysiological measurements and in pharmaceutical screening. Future work will be devoted to the validation of the proposed

automated microsystem with particular emphasis on pharmacological applications and to the integration of cell guidance methodologies to re-designed micromachined microsystems.

Aknowledgements

The RF Microswitch work has been supported by the PAT-CNR project "Ricerca e Formazione in Microsistemi".

The Bioelectronic Microsystem work has been supported by the Italian Ministry for Scientific and Technological Research and was developed with a collaborative research activity including University, research institutions and private companies.

References

1. G. M. Reibeiz and J. B Muldavin,. "*MEMS switches and switch circuits*". IEEE Microwave Magazine, December 2001, pp. 59 - 71.

2. H.A.C Tilmanns, 2002. *MEMS components for wireless communication.* Euro sensors XVI, 16th Euro. Conf. On Solid State Trans., September 15-18, Prague, Czech Republic, 1-34.

3. K. J. Rangra, B. Margesin, L. Lorenzelli, F. Giacomozzi, C. Collini, G. Soncini "*Simmetric Togglke Switch: a new type of RF MEMS Switch for Telecommunication applications*" Sensors and Actuators A (to be published)

4. F. Giacomozzi, L. Lorenzelli, B. Margesin, G. Turco, R. Marcelli *"MEMS Technology for RF Switches"* Proc. AISEM 2004 (to be published).

5. Lorenz, M. Despont, P. Vettiger, P. Renaud H., *"Fabrication of photoplastic high-aspect ratio microparts and micromolds using SU8 UV resist"* , Microsystem Technologies, 4, pp.143-146, (1998)

6. Martinoia, et. al., *"Development of ISFET array-based microsystems for bioelectrochemical measurements of cell populations"*, Biosensors & Bioelectronics, 16 1043–1050, (2001)

7. M. O. Heuschkel, *"Fabrication of multi-electrode array devices for electrophysiological monitoring of in-vitro cell/tissue cultures"*, Hartung-Gorre Verlag, Konstanz, Germany, Series in Microsystems Vol. 13, pp. 188, (2001)

BIOSENSORS

PREPARATION AND CHARACTERIZATION OF GOD BIOSENSORS BASED ON NANOMATERIALS

A. Curulli

Istituto per lo Studio dei Materiali Nanostrutturati, ISMN – CNR, Via del Castro Laurenziano 7, 00161 Roma

F. Valentini

Dip.to di Chimica, Università 'Tor Vergata', Via della Ricerca Scientifica 1, 00133 Roma

S. Kaciulis, G. Padeletti, L. Pandolfi, M. Viticoli, A. Cusmà

Istituto per lo Studio dei Materiali Nanostrutturati, ISMN – CNR, C.P. 10, 00016 Monterotondo Stazione, Roma

The immobilization of GOD enzyme on a series of different substrates (Si wafers, nanostructured TiO_2 films and Au nanotubes) has been investigated by means of X-ray photoelectron spectroscopy and atomic force microscopy. The peak-fitting analysis of main XPS lines enabled us to identify the GOD signals and to compare the enzyme's entrapment on different substrates. The highest amount of entrapped enzyme was registered on the surface of nanostructured TiO_2 films prepared by using MOCVD technique. Preliminary electrochemical studies of glucose oxidase, immobilised on titanium oxide films, were carried out in order to investigate the direct electrochemistry and the possibility to employ GOD/TiO_2 structures in biosensing devices.

1. Introduction

The behaviour of enzymes, immobilized on various solid surfaces, has been investigated amply in recent years. Spatial organization, ordering, morphology, and activity of enzyme molecules in artificial molecular systems are crucial issues for the development of high-performance enzyme biosensors. Molecular level fabrication of enzyme biosensors is based on the ability to immobilize only the monolayer or submonolayer of enzymes on the surface, while retaining full enzymatic activity.

Nanotechnology has been defined as a technology that arises from the exploitation of novel and improved properties, phenomena and processes, taking place in the intermediate scale between the atomic/molecular and bulk behaviour (1 - 100 nm). The immobilization of single or clustered molecules of glucose oxidase (GOD) enzyme on nanostructured surfaces represents an important step in the production of glucose-responsive biosensors with a direct electrochemistry. In this study, two nano-structured materials (Au nanotubes and TiO_2 thin film) have been compared with common Si wafer substrate. The immobilization of GOD on these substrates was performed by using conventional methods of entrapment [1-2].

2. Experimental

2.1 Sample Preparation

Three different types of substrates were used for the enzyme's immobilization: Si wafer, Au nanotubes [3], nanostructured film of TiO_2 on Si substrate. The GOD enzyme molecules were immobilized on the surface of Au nanotubes by self assembling method (SAM). The membranes containing Au nanotubes were immersed for 17h in 2 x 10^{-3}M of MEA (2-mercaptoethylamine) or MPA (3-mercaptopropionic acid), using absolute ethanol as solvent. Upon removal from the solution, these samples were rinsed with absolute ethanol and dried in a nitrogen stream.

The self-assembled cysteamine monolayers were soaked for 2h in a solution of glutaraldehyde (commercial solution diluted 100-times in phosphate buffers solution) at room temperature. The resulting monolayers were rinsed with phosphate buffer solution and placed for 2h in a solution of GOD (1g/l) at pH 7.0 in 0.1M phosphate buffer. The terminal carboxylic acid groups of MPA modified gold surfaces were activated by immersion for 2h in a pH 3.5 MES (2-morpholinoethanesufonic acid) buffer solution containing 2mM EDC (1-Ethyl-3-(3-dimethylaminopropyl)-carbodiimide) and 5 mM NHS (*N*-Hydroxysuccinimide). Then the surface was rinsed with buffer and immediately placed in a solution of GOD in phosphate buffer. The samples were incubated for 2h in 1 g/l GOD solution, after that were rinsed with phosphate buffer and used immediately or stored at 4 °C in buffer solution

After the realization of Si electrodes modified with TiO_2, the GOD was immobilized on electrode surface. The enzyme immobilization was performed by dip-coating, introducing the TiO_2 modified electrodes in 0.1 M phosphate buffer (pH = 7) GOD aqueous solution (1 g/l) overnight at room temperature. After the elimination of free (not adsorbed) GOD, the TiO_2-GOD electrodes were dried at room temperature and, if not used immediately, stored at 4 °C. After the enzyme immobilization, functionalised TiO_2-GOD samples were used as working electrodes.

An identical procedure was used for the immobilization of GOD on plain Si substrate. In Tab. 1 is reported the description of investigated samples:

Substrate	GOD Solution	GOD solution concentration
Si wafer	1) Bi-distilled water	x 1 (as in biosensors)
	2) Bi-distilled water	x 10
	3) Phosphate buffer solution	x 10
Au nanotubes	1) Bi-distilled water	x 10
	2) Phosphate buffer solution	x 10
TiO_2 film	1) Bi-distilled water	x 10
	2) Phosphate buffer solution	x 10

2.2 Sample Characterization

AFM analysis was performed in air by means of a Dimension 3100 Digital Instruments Microscope, equipped with an optical deflection system in combination with Si cantilevers and tips, working in tapping mode. Topographic

images have been recorded with a resolution of 512 x 512 data points over the scanning areas of 3 x 3 and 2 x 2 μm^2 for the Au nanotubes and TiO_2 films, respectively. The surfaces were characterized by means of the excursion peak-valley, registered in the scanning area (Zr) of the average surface roughness (Ra), relative to a reference central plane, and a standard deviation of the z values (rms) within the given area.

An Escalab MkII (VG Scientific), equipped with a 5-channeltron detection system and a standard Al K_α excitation source ($h\nu$ = 1486.6 eV), was employed for XPS measurements. The spectra were acquired in constant analyser energy mode, at pass-energy of 20 eV. After the acquisition, the peak fitting of the spectra was performed by using synthetic peaks composed of symmetric, mixed Gaussian-Lorentzian curves.

2.3 Electrochemical measurements

The electrochemical measurements were carried out in electrochemical cell equipped with three electrodes, described in details elsewhere [2]. Cyclic voltammetry was run in 0.1 M phosphate buffer solution, at pH 7.0, at different scan rate, ranging from 10 to 500 mV/s, by using an Amel Polarographic Analyzer Model 433.

3. Results and discussions

3.1 AFM characterization

The AFM images of Au nanotubes before and after the coverage with GOD in phosphate buffer solution are shown in Fig. 1. The shape of the single nanotubes (with estimated diameter of about 50 nm) is visible in both cases, evidencing that the GOD was immobilized following the morphology of the substrate. A similar behaviour of this enzyme was observed in the samples on TiO_2 nanostructured films. The mean size of the grains of titanium oxide surface without enzyme was about 30 nm, while after the GOD immobilization this size became about 40 nm. This result confirms the maintenance of the nano-scaled morphology of the substrate after the immobilization of biomolecules.

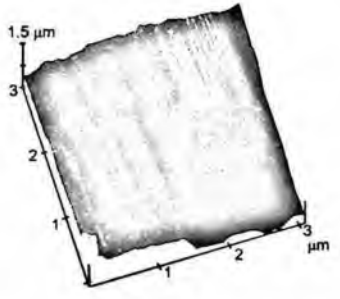

Figure 1. AFM image of Au nanotubes without enzyme.

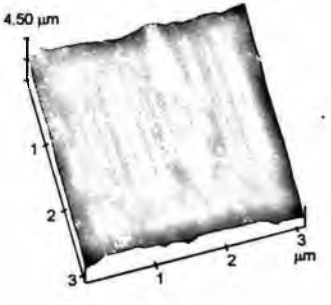

Figure 2. AFM image of Au nanotubes with GOD enzyme deposited from buffer solution with pH = 7.

3.2 XPS characterization

The surface analysis of the samples on Si substrate detected the presence of the chemical elements (C, O and N) attributable to the GOD enzyme, while the signal of Si 2p originated from the uncovered substrate areas. In Fig. 3 are showed the results of the peak-fitting for the C 1s spectrum of the sample deposited from GOD solution (with a concentration x 1) in bi-distilled water.

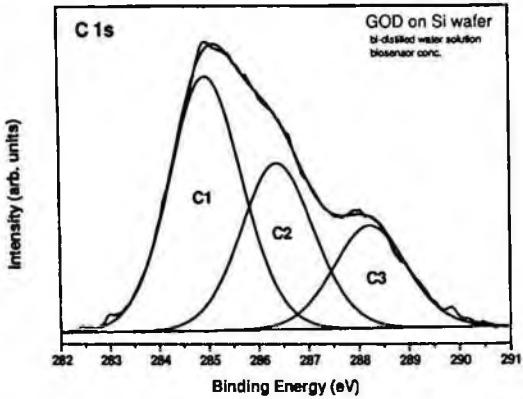

Figure 3. Deconvolution of C 1s spectrum of the GOD sample on Si. The enzyme was immobilized from bi-distilled water solution.

Three components (C1, C2 and C3) were necessary to fit the experimental spectrum. These three peaks correspond to the aliphatic bond CH-CH (BE = 285.0 eV), to the carbon bonded with nitrogen (N-CH-C=O) in the amidic group and to the oxydrilic group C-OH (BE = 286.4 eV), and to the acid carbon of the amidic group (N-CH-C=O) (BE = 288.3 eV), respectively [4]. The analysis of the binding energies of the N 1s (BE = 400.7 eV) and O 1s (BE = 532.6 eV) peaks has revealed that these elements are definitely attributable to the enzyme. Excluding the aliphatic carbon C1 that can be also caused by the surface contamination, all other elements and their related chemical states, can be used as the fingerprints of GOD enzyme.

The surface covering parameter C can be defined as the ratio between the atomic percentages of the element corresponding to the substrate (Si, Ti or Au) and an element chosen as the fingerprint of GOD enzyme.

The C values, calculated for the samples on Si by using the concentrations (see Tab. 1) of C2, C3 and N peaks, are shown in Fig. 4.

From this figure it is possible to note that the coverage in the samples, obtained from the solution of GOD in water, is lower than in the ones from phosphate buffer solution with the same concentration of enzyme. As it can be expected, a higher concentration of GOD in the solution corresponds to the higher coverage of the substrate.

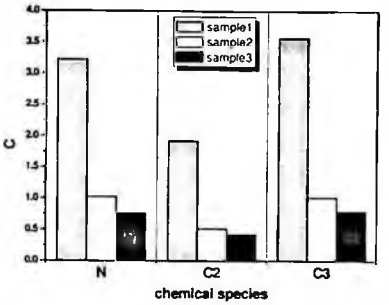

Figure 4. Coverage parameter for the samples on Si substrate.

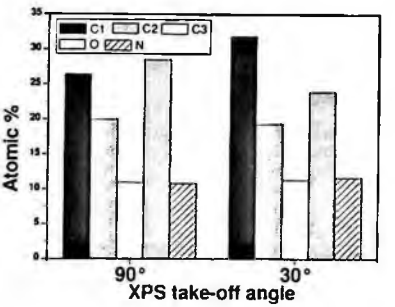

Figure 5. Atomic concentrations of chemical species, measured at different XPS take-off angles for the GOD sample, deposited from phosphate buffer solution on TiO_2 nanostructured film.

Qualitatively similar results of the enzyme coverage were obtained for the samples on Au nanotubes and TiO_2 nanostructured films. Particularly for the last case, a complete coverage of the substrate surface has been found in the samples prepared from GOD in phosphate buffer solution. Therefore, the nanostructured TiO_2 can be indicated as a very promising substrate for the immobilization of enzyme without any intermediary.

From the comparison of XPS data, acquired at two different angles of photoelectron take-off, it is possible to recognize the elements located on the surface and in the deeper sublayer of the sample. The atomic percentages of C1, C2, C3, N and O for the sample, where GOD from phosphate buffer solution was immobilized on TiO_2 film, are reported in Fig. 5. An increase of the atomic concentration with a change of the photoelectron take-off angle from 90° to 30° corresponds to the elements predominant on the surface. On the contrary, a concentration decrease is caused by the location of the corresponding element in the inner sublayer. As it is possible to note from Fig. 6, a significant decrease of the oxygen concentration is registered when the angle is reduced. This result can be explained only supposing that the main interaction between the enzyme and substrate surface is based on the bonds of the OH- groups of GOD.

3.3 Electrochemical characterization

Direct electron transfer in GOD on gold nanotubes and on modified Si-electrodes was observed. A cyclic voltammetry results (Fig. 6) of the GOD/TiO_2, TiO_2 and GOD/glassy carbon electrodes show three pairs of stable and well-defined redox peaks of the direct electron transfer. The potentials of these peaks, centred at –500 and –400 mV for the GOD/TiO_2 electrode, are consistent with reported values for free FAD and redox FAD centre for flavoenzyme [5]. The peak positions remain constant as the scan rate increases

(Fig. 7), while the redox peak currents are proportional to the scan rate in the range lower than 100 mV/s, indicating a typical surface-controlled quasi-reversible process [6].

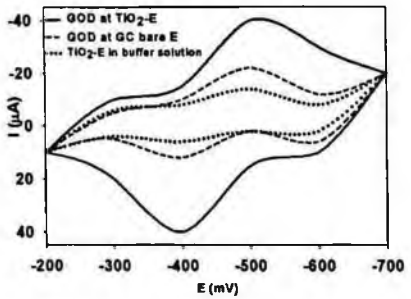

Figure 6. Cyclic voltamograms of the GOD/TiO_2, TiO_2 and GOD/glassy carbon electrodes

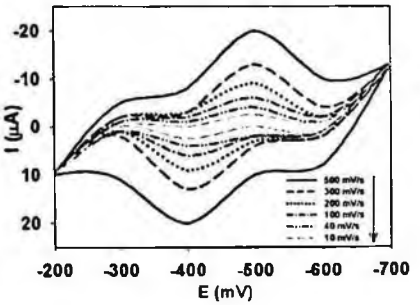

Figure 7. Cyclic voltamograms registered at different scan rates for the GOD/TiO_2 electrode.

4. Conclusions

Solid surface, modified with nanomaterials, seem to be a very promising system for the third-generation biosensors. Nanostructured TiO_2 layers and gold nanotubes provide an efficient immobilization platforms for the GOD enzyme, without the use of any mediators. The results of XPS study demonstrate, how these materials can satisfy the main requirements necessary for the optimised biosensing: the homogeneity and complete coverage of the substrate.

GOD, immobilized on nanostructured surfaces, has been characterized by direct voltammetric responses. The direct electron transfer between the enzyme and the electrodes was enhanced by nanostructured substrate.

References

1. A. Curulli, F. Valentini, G. Padeletti, S. Kaciulis, A. Cusmà, D. Caschera, G. Palleschi, Sens. Actuators B (2005), in press.
2. A. Curulli, F. Valentini, G. Padeletti, A. Cusmà, D. Caschera, G. Palleschi, Sens. Actuators B (2005), in press.
3. P. Kohli, M. Wirtz, C. R. Martin. Electroanalysis (2004), 16, 1-2 pg 9-19
4. A. Griffith, A. Gliele, G. Beamson, J.M. Cooper, Phys. Chem. B (1997), 101, p. 2092-2100
5. Q. Chi, J.D. Zhang, S.J. Dong and E.K. Wang, Electrochimica Acta, 39 (1994) 2431
6. J. Bard Electroanalytical Chemistry, Marcel Dekker, New York.

DETECTION OF PATHOGENIC BACTERIA BY MEANS OF AN ELECTROCHEMICAL GENOASSAY

M. L. DEL GIALLO, F. LUCARELLI, I. PALCHETTI, G. MARRAZZA*, M. MASCINI

Dipartimento di Chimica, Università degli Studi di Firenze, Polo Scientifico, via della Lastruccia 3, 50019 Sesto Fiorentino, Firenze, Italy

This paper describes the use of oligonucleotide-modified screen-printed gold electrodes for the enzyme-amplified sensing of DNA sequences that identify pathogenic bacteria. Particular attention was given to design of the capture probe sequence, in order to obtain the highest hybridisation yield at the sensor surface. Moreover, probe surface densities were observed to deeply determine the bio-recognition capabilities of the immobilised probes. The electrochemical genoassay allowed specific detection of the PCR-amplified targets (388 bp).

1. Introduction

In recent years, highly publicised outbreaks of severe food borne illness has underscored the importance of rigorously testing, in real time, raw materials and finished food products for the presence of pathogenic bacteria. Therefore, rapid and accurate analytical methods are required in order to detect the presence of such biological contaminants. This work describes the use of an enzyme-based electrochemical genosensor for the highly sensitive detection of the sequences identifying *Salmonella spp.* The new analytical method relied on the use of screen-printed gold electrodes which were modified using thiol-tethered oligonucleotide probes [1,2]. The sequences related to the bacteria of interest (e.g., *Salmonella spp.* and *Listeria monocytogenes*) were obtained from the corresponding genomic DNAs through PCR amplification.
According to Fig. 1, unmodified PCR products (b) were captured at the sensor interface (a) via sandwich hybridisation with surface-tethered probe and a biotinylated signaling probe. The resulting biotinylated hybrid (c) was coupled with a streptavidin-alkaline phosphatase conjugate (d) and then exposed to an α-naphthyl phosphate solution (e). Differential pulse voltammetry was finally used to detected the α-naphthol signal (f).

2. Experimental

2.1. *Reagents*

All reagents were of analytical grade. MilliQ water was used throughout this work. Synthetic oligonucleotides were obtained from MWG Biotech AG:
Surface-immobilised probe: 5'- HS-$(CH_2)_6$-AAAAAAGCGCGCGAACGG -3'

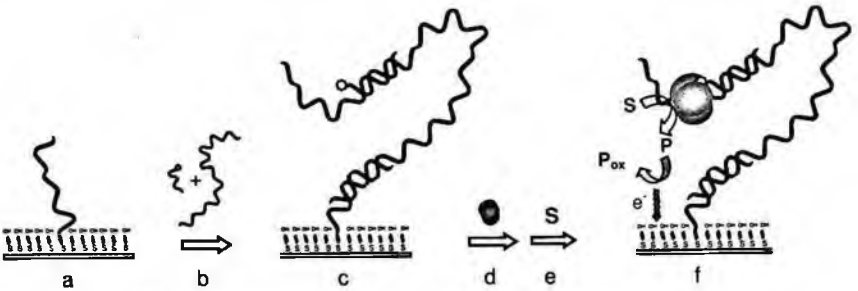

Figure 1. Schematic representation of the electrochemical genoassay.

Signaling probe: 5' - TTTGTGAACTTTATTGGCGG-biotin-TEG - 3'
Oligo target: 5'-CCGCCAATAAAGTTCACAAAACGCCGTTCGCGCGC-3'
Non-complementary oligo: 5'- GGCAGAGGCATCTTCAACGATGGCC – 3'
A 388 bp region of the gene invA of *Salmonella spp.* was amplified from the corresponding genomic DNA using the following primers:
Fw: 5'-GCCGCGCGCGAACGGCGAAG-3'
Rev: 5'-ATCCCGGCAGAGTTCCCATT-3'

2.2. Bio-modification of the sensor surface

Materials and procedures to screen-print the gold electrode transducers are described in [1]. The gold surface of the working electrode was modified by interaction with 10 µL of the thiolated probe solution (0.05 µmol/L [unless otherwise stated] in 0.5 mol/L phosphate buffer; 16 h) The immobilisation step was followed by treatment with a spacer thiol (MCH, 10 µL, 1 mmol/L aqueous solution; 1 h). Prior to hybridisation reaction, the modified electrodes were washed twice with 15 µL of phosphate buffer.

2.3. Hybridisation with synthetic oligonucleotides and PCR-amplified samples

Both synthetic oligonucleotides and PCR products were analysed using a sandwich hybridisation format. The samples were diluted to the desired concentration using a 0.5 mol/L phosphate buffer that contained 0.15 µmol/L of the biotinylated signaling probe. Double-stranded amplicons were thermally denatured by using a boiling water bath (5 min at 100°C); amplicon strand re-annealing was retarded by cooling the sample in an ice water bath (5 min). A 10 µL aliquot of these solutions was finally incubated with the probe-modified electrodes for 1 hour. PCR blank and non-complementary oligomers and PCR products were used as negative controls.

2.3. Labelling with alkaline phosphatase and electrochemical detection

The biotinylated hybrid was reacted with 10 µL of a solution containing 1 U/mL of the streptavidin-alkaline phosphatase conjugate and 8 mg/mL of BSA (blocking agent) in DEA buffer. After 20 minutes, the sensors were washed twice with 15 µL of DEA buffer.

The planar electrochemical cell was then incubated with 150 µL of an α-naphthyl phosphate solution (1 mg/mL in DEA buffer). After 20 minutes, the oxidation signal of the enzymatically-produced α-naphthol was measured by DPV (modulation time = 0.05 s; interval time = 0.15 s; step potential = 5 mV; modulation amplitude = 70 mV; potential scan: from 0.0 to +0.6 V). All electrochemical measurements were performed with a µAUTOLAB type II (Eco Chemie). The experiments were carried out at room temperature (25°C).

3. Results and discussion

When testing the performance of the genosensor using synthetic oligonucleotides (Fig. 2), the signal was found to be linearly related (R^2 = 0.991) to the target concentration between 0 and 15 nmol/L; a detection limit of 0.4 nmol/L was estimated (S/N = 3). The absence of any non-specific signal for 15 nmol/L of the non-complementary oligomer confirmed the specificity of the assay.

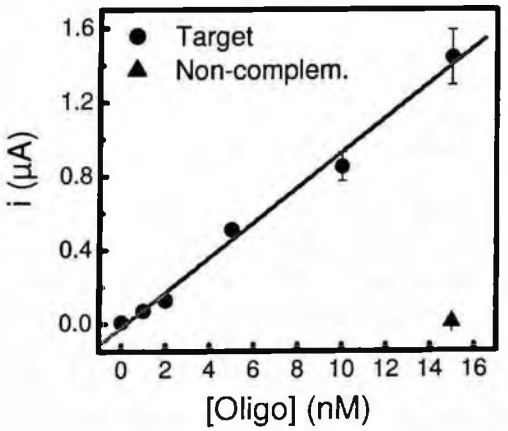

Figure 2. Calibration plot for synthetic oligonucleotides.

Most of work was devoted to the optimisation of the assay for Salmonella's amplicons. In contrast to previously studied cases [1,2] the analysis of such long PCR-amplified samples (388 bp) required some important modifications of the analytical procedure. The use of a capture probe which recognised one of the end of the long amplicon was essential for ensuring a higher hybridisation efficiency at the sensor surface. Moreover, the selectivity of the bio-recognition process was substantially improved using a short (12 mer) probe [3]. Its additional $-(A)_6-$ spacer was introduced to further minimise the steric interference of the electrode surface (data not shown).

In order to explore the hybridisation capabilities of the surface-immobilised probe over a wide range of surface densities, the concentration of the capture probe solution was first varied by orders of magnitude (0.002, 0.02, 0.2, 2 μmol/L) and then by smaller steps (0.01, 0.02, 0.05, 0.1, 0.2 μmol/L).

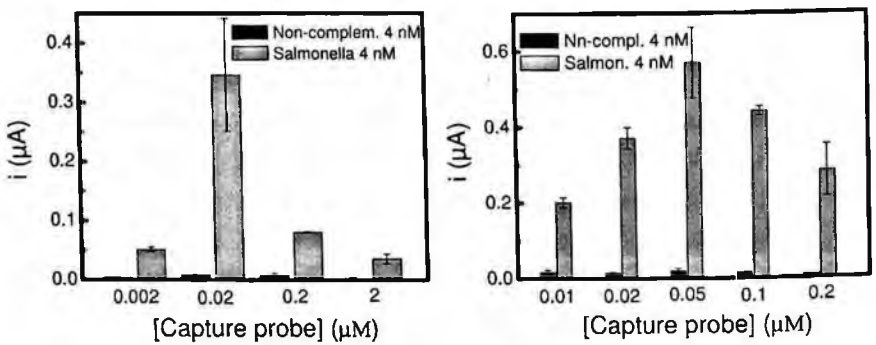

Figure 3. Influence of capture probe conc. on analytical signals.

As shown in Fig. 3, the highest hybridisation yield was obtained using a 0.05 μmol/L probe solution. The diminished analytical signals observed using both lower and higher concentrations of the thiolated probe, can be explained as follows. Electrodic surfaces characterised by low probe densities clearly possessed a limited number of bio-recognition sites, so that only a few amplified strands could be captured. In contrast, higher surface densities caused steric and electrostatic interference between tightly packed probes and incoming target DNA [4].

The influence of hybridisation time on analytical signals was additionally investigated. The hybridisation process was found to reach a plateau after 30 min (Fig. 4). Therefore, this time was chosen for all subsequent experiments.

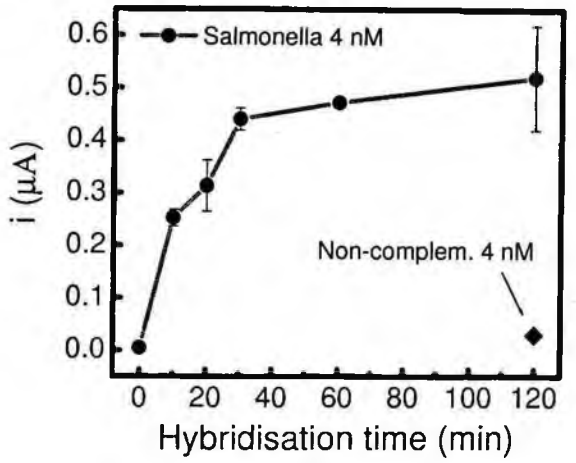

Figure 4. Influence of hybridisation time on analytical signals.

Fig. 5 demonstrates that specific detection of the target sequences was possible even diluting ~ 500 fold the PCR-amplified products. The selectivity of the assay was again confirmed by analysing PCR products unrelated to the immobilised probe.

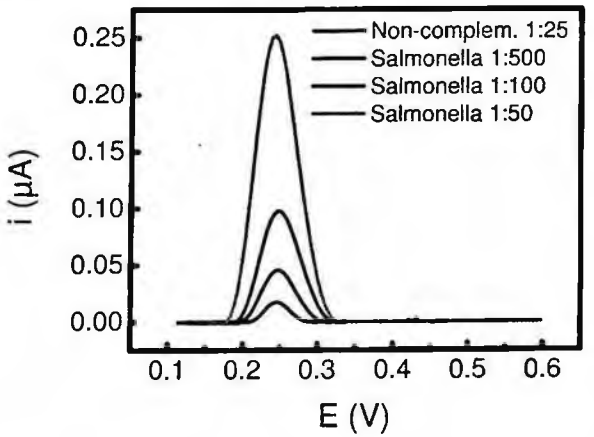

Figure 5. Analysis of complementary and non-complementary PCR samples at different dilution levels.

4. Conclusions

The electrochemical genosensor described in this paper allowed highly sensitive detection of the sequences identifying *Salmonella spp*. Work is currently in progress to applied this method for the detection of other pathogens (*E. coli 0157:H7, Lysteria monocytogenes and Staphylococcus aureus*) and integrate multiple sensors on a single screen-printed platform. Such an electrode array should lead to significant advantages in terms of reliability, cost, speed and simplicity of the detection of specific DNA sequences. Simultaneous detection of several bacterial strains should be additionally feasible. An interesting application of the proposed electrochemical genoassay could be the identification of pathogenic bacteria in food processing plants.

References

1. G. Carpini, F. Lucarelli, G. Marrazza, M. Mascini. *Biosens. Bioelectron.* **20**, 167, (2004).
2. F. Lucarelli, G. Marrazza, M. Mascini. *Biosens. Bioelectron.* (2004) in press.
3. L. Alfonta, Singh A.K., I. Willner. *Anal. Chem.* **73**, 91, (2001).
4. E. Huang; M. Satjapipat; S. Han; F. Zhou. *Langmuir*, **17**, 1215, (2001).

BIOMIMETIC RECEPTORS FOR PESTICIDES: COMPARISON OF COMPUTATIONAL AND EXPERIMENTAL DATA

MARCELLO MASCINI*, MICHELE DEL CARLO ALESSIA PEPE, MIRIAM DE GREGORIO AND DARIO COMPAGNONE
Università di Teramo, Dipartimento di Scienze degli Alimenti , 64023 Teramo, Italy

**Corresponding author: mmascini@unite.it*

The idea at the base of this study was to test bio-mimicking receptors computationally designed for compounds of evident toxicity like pesticides. Three tetrapeptides, with different estimated binding energy versus pesticides, were used for the experimental approach. The affinity toward two different pesticides, one carbamate (CM) and one organophosphate (OP), was tested using an electrochemical bioassay for AChE inhibitors. Concentrations, incubation time, and ionic strength of the oligopeptide-pesticide solution were evaluated using the electrochemical screening method. This study showed a nicely dependence between the estimated binding energy calculated by computational modeling and the ability of the tetrapeptides to bind the pesticides in solution. Particularly one of them (the tetrapeptide His-Gly-Ser-Ala) appeared as good candidate for the development of affinity systems for OP pesticides.

1. Introduction

The detection and quantification of Carbamates (CM) and organophosphates (OP) pesticides levels in samples requires sensitive analysis techniques to satisfy the current and proposed regulations (1). Biological matrices are often characterized by high amounts of fat and low levels of pesticide contamination, therefore most of the multiresidues analytical procedures consist in an extraction step and clean-up followed by GC-ECD or GC-MS (2,3).

There is a need for fast and inexpensive testing devices for pesticide detection. Biosensors have been widely exploited in this field and a review has been recently published (4). One of the approaches to their developments assumes the determination of pesticide inhibition on acetylcholinesterases (AChEs) coupled with the electrochemical determination of the enzyme product (5–9).

Our research is oriented to develop biomimetic receptors able to mimic the active site of AChE, either as binding or catalytic site. These receptors are envisaged as new ligand in biosensors design.

In a previous work (10), both the classes of pesticide (CM and OP) were designed and their affinity toward the AChE active site were tested by a computational approach (GOLD© , Genetic Optimisation for Ligand Docking software) (11). We studied the binding energy and the three-dimensional structure of the complex between CM/OP pesticides and the AChE active site. The obtained results represented the basis for development of artificial oligopeptides. After a series of tetrapeptides were designed and their affinity

toward pesticides was tested by computational approach using Leapfrog® algorithm a module from Sybyl® Sofware (12-13). In this work three tetrapeptides, with different binding energy versus pesticides, were selected for the experimental approach. The affinity toward two different pesticides, one carbamate (CM) and one organophosphate (OP), was tested using an electrochemical biosensor for AChE inhibitors (14). Concentrations, incubation time, and ionic strength of the oligopeptide-pesticide solution were evaluated using this electrochemical screening method.

2. Experimental

Reagents

AChE (EC 3.1.1.7) from Electric Eel (type IV V-S, 970 U/ml), Choline Oxidase from Alcaligenes sp. (EC 1.1.3.17) methanol and all the other reagents were obtained from Sigma Aldrich (Milan, Italy). Dichlorvos and carbaryl were purchased from Riedel de Haen (Milan, Italy). The pesticide stock solution was prepapred in methanol. The oligopeptides were synthesized from EspiKem Srl (Italy) and were the following:

A: [N] Ser-Ala-Gly-Glu [C]
B: [N] His-Gly-Ser-Ala [C]
C: [N] Glu-Pro-Ser-Ala [C]
NC:[N]Asn-Phe-Gln-Gly-Phe[C]

The negative control (NC) was an oligopeptide selective for dioxins (15). The electrochemical measurements were carried out with a Palm SenseTM hand held potentiostat using screen printed electrodes obtained from Palm SenseTM (Amsterdam, Holland).

Inhibition assay

The inhibitory effect of pesticides on AChE was evaluated comparing the decrease of the current produced by the reduction of the electrochemical mediator Prussian Blue.

The biochemical-electrochemical pathway used to determine the inhibition consisted of two enzymatic reactions (I & II) generating a chemical oxidation (III) determined by cathodic chronoamperometry (IV).

(I) Acetylcholine + H_2O →Acetic Acid + Choline (Enzyme I: AChE)
(II) Choline + 2 O_2 + H_2O→ 2 H_2O_2 + Betaine (Enzyme II: Choline oxidase)
(III)2Fe^{2+} + H_2O_2 → 2Fe^{3+} + 2OH^- (Chemical oxidation)
(IV) Fe (III) + e^-→ Fe (II)(Electrochemical reduction)

Standard and peptide-pesticide solution were measured according to the following experimental scheme: first a blank sample was measured and the current recorded, then the pesticide, either standard or with peptide in solution was measured in duplicate, finally a second blank measurement completed the protocol. The average current of the blank sample (I_0) and the average current of the contaminated sample (I_I) were used to calculate the inhibition % according to the equation: $I\%=100*(Io-I_I)/Io$

The assay consisted in the addition of an aliquot of pesticide or pesticide-peptide solution to an AchE solution (0.125 U/ml). The incubation was allowed to proceed for an optimised period of time (10 minutes) and thereafter 0.3 mM of acetylcholine was added to the solution; after 2 minutes, 100 µl were placed on the biosensor surface and the steady state current recorded for 2 minutes.

The limit of detection (LOD) of this method was respectively for dichlorvos 0.090µM with $I_{50\%}$=1µM and for carbaryl 1.250µM with $I_{50\%}$=3µM.

The biosensor was previously polarised in phosphate buffer solution, pH 7.4 KCl 100 mM, at -50 mV vs Ag/AgCl pseudo-reference electrode. After each measurement the biosensor surface was rinsed with phosphate buffer.

The ability of the oligopeptides to subtract pesticides in solution were evaluated using the following equation: SP%= [(P-PF)/P]*100, where SP was the percentage of Pesticide Subtracted (pesticide in solution no more able to inhibit AchE), P was the signal obtained from Pesticide without oligopeptide (Peptide blank) and PF was the signal obtained from the Pesticide Free in solution after the interaction with the oligopeptide.

3. Results and Discussion

This set of experiments was finalised to gain an understanding of the selectivity of new pesticides receptors by comparing the results obtained with the pesticide solution vs pesticide-peptide solution. The quantitative evaluation of different pesticide/peptide molecular ratio (MR) of the solution is reported in Table 1.

All the pesticides gave a good interaction at MR of 1:1000. Only using a MR of 1:100 the differences between the peptides went up matching the results obtained by computer modelling. At the MR of 1:50 the sensibility of the method decrease but the interaction pesticide-peptide remained proportional to the computational binding score.

Table 1. Results expressed as SP% (pesticide in solution no more able to inhibit AchE) using dichlorvos (OP) pesticide. NC=negative control, MR= pesticide/peptide molecular ratio. In the last row is reported the estimated binding energy calculated by molecular modeling. The relative standard deviation, obtained from 3 measurements, was within 10%.

Dichlorvos concentration	**A 100μM SP (%)**	**B 100μM SP (%)**	**C 100μM SP (%)**	**NC 100μM SP (%)**	**MR**
0.100μM	100	100	100	0	1:1000
1.000μM	42	48	39	4	1:100
2.000μM	17	28	13	2	1:50
Binding Score (KJ/mol) vs dichlorvos	***96***	***165***	***9***		
Binding Score (KJ/mol) vs carbaryl	***133***	***86***	***3***		

The oligopeptide selectivity vs OP and CM was carried out using the four oligopeptides A, B, C and NC vs dichlorvos and (Figure 1).

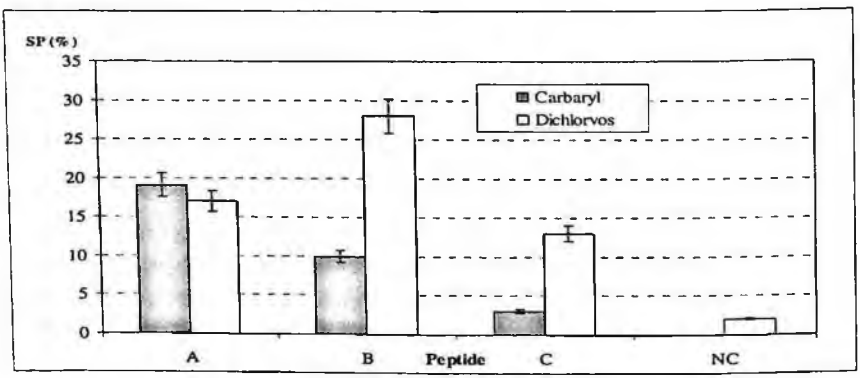

Figure 1. Results expressed as SP% (pesticide in solution no more able to inhibit AchE) using dichlorvos (OP) and carbaryl (CM) pesticides. NC=negative control, MR=1:50. The relative standard deviation, obtained from 3 measurements, was within 10%.

As shown in Figure 1 also for carbaryl the ability of the oligopeptides to subtract the pesticide (SP%) seemed nicely dependent on the estimated binding energy calcuted by computational modeling. Finally, as reported in Table 2, modulating time and ionic strength we obtained an increase of the signal.
80% of SP was obtained when 16 hours of incubation and no KCl were used as incubation conditions. This data may suggest slow kinetic in peptide-pesticide complex formation and a rationale dependence on the medium ionic strength.

Table 2. Effect of ionic strength and time. Results expressed as SP% (pesticide in solution no more able to inhibit AchE) using peptide B and NC vs dichlorvos at a MR of 1:100. The relative standard deviation, obtained from 3 measurements, was within 10%.

KCl concentration	B SP%		NC SP%	
mM	10 min	960 min	10 min	960 min
0	45	80	0	4
100	48	52	2	3

4. Conclusions

This study showed a nicely dependence between the estimated binding energy calculated by computational modelling and the ability of the tetrapeptides to bind the pesticides. Particularly one of them (the tetrapeptide His-Gly-Ser-Ala) appeared as good candidate for the development of affinity systems for OP pesticides.

Acknowledgments

The authors would like to express their gratitude to Dr. Beining Chen at Sheffield University for her contribution to the work.

References

1. European Directive 2001/57/CE
2. Blasco C, Fernandez M, Pico Y, Font G J. (2004) Chrom A 1030(1-2):77-85

3. Chiron S, Rodriguez A, Fernandez-Alba A (1998) J. Chrom A 823(1-2):97-107
4. Trojanowicz M (2002) Electroanal 14:1311-1328
5. Palchetti I, Cagnini A, Del Carlo M, Coppi C, Mascini M, Turner APF (1997) Anal Chim Acta 337:315–21.
6. Bachmann TT, Leca B, Vilatte F, Marty JL, Fournier D, Schmid RD (2000) Biosensor & Bioelectronics 15:193-202
7. Del Carlo M, Mascini M, Compagnone D, Pepe A, Mascini M (2002) J Agric Food Chem, 50: 7206-7210
8. Del Carlo M, Mascini M, Pepe A, Diletti G, Compagnone D (2004) Food Chem 84:651-656
9. Snejdarkova M, Svobodova L, Evtugyn G, Budnikov H, Karyakin A, Nikolelis DP, Hianik T (2004) Anal Chim Acta 514:79–88
10. M. Mascini,, M. Del Carlo and D. Compagnone (2004) Sensors and Microsystems: Proceedings of the 9th Italian Conference (World Scientific)
11. M. L. Verdonk, J. C. Cole, M. J. Hartshorn, C. W. Murray, R. D. Taylor (2003) Proteins, 52 (4), 603
12. A. W. R. Payne, R. C. Glen (1993) J. Mol. Graph., 11 , 74
13. P. J. Goodford (1985) J. Med. Chem., 28, 849
14. M. Del Carlo, A. Pepe, M. Mascini, M. De Gregorio, A. Visconti & D. Compagnone (2005) Anal Bioanal Chem Available online
15. M. Mascini, A. Macagnano, D. Monti, M. Del Carlo, R. Paolesse, B. Chen, P. Warner, A. D'Amico, C. Di Natale and D. Compagnone (2004) Biosensors and Bioelectronics, 20, 1203–1210

DETECTION OF A CLINICALLY RELEVANT TP53 GENE MUTATION USING DNA LABEL-FREE BIOSENSORS

D. DELL'ATTI, M. MINUNNI, S. TOMBELLI, M. MASCINI
Università degli Studi di Firenze, Dipartimento di Chimica,Polo Scientifico, Via della Lastruccia 3, 50019 Sesto Fiorentino, Firenze (Italy)

M. ADAMI
Elbatech, Via Roma 10, 57030 Marciana (LI)

The development of piezoelectric and optical DNA-based sensing for the detection of point mutations of the TP53 tumor suppressor gene is presented. The sensing is based on the hybridization reaction between the immobilized probe and the target in solution. The mutation is detected since differences in the hybridization signal can be detected when the probe hybridizes the fully complementary or the mutated sequence.

The immobilization chemistry is performed by thiol-dextran-streptavidin coupling and then the biotinylated probe is added.

On the gold surface of the quartz crystal used for piezoelectric sensing, the specific probe sequence is immobilized, while the sensor chip of the optical device BIACORE X was modified by immobilizing, on the two flow cells, two different probes, differing only in one base. One probe is the same as in the piezoelectric sensor and the second probe contains the sequence carrying the mutation of interest. The hybridization reaction with two different target sequences (fully complementary and mutated) was performed. The analytical parameters of the systems were studied.

1. INTRODUCTION

The piezoelectric and the optical biosensor system are able to detect a specific DNA sequence without any label through a DNA probe immobilized on the sensor gold surface[2, 5, 6, 7]. This probe permits the molecular recognition of the complementary sequence in solution through the hybridization reaction.

In clinical diagnostics there is a great interest for these devices because they are able to detect SNPs (Single Nucleotide Polymorphisms) responsible for many pathologies derived from genetic alterations[5, 8].

The p53 tumor suppressor gene (which codes for a phosphoprotein of 393 amino acids) has proven to be one of the genes most often mutated in human cancers. It involves mainly point mutations leading to amino acid substitutions in the central region of the protein which impair its normal functions. There are three hot-spot codons, 175, 248 and 273, which are involved in mutational events. We have investigated the mutation of the codon 248 that is a CpG mutation. In particular, this mutation is responsible for causing colorectal carcinogenesis [2].

The sensing is based on the hybridization reaction between the immobilized probe and the target in solution. The mutation detection is detected since differences in the hybridization signal can be detected when the probe hybridizes the fully complementary or the mutated sequence[1, 5, 8].

2. EXPERIMENTAL SECTION

2.1. Apparatus and Reagents

In the case of the piezoelectric biosensor, 9.5 MHz AT-Cut quartz crystals (14 mm) with gold evaporated (42.6mm^2 area) on both sides, purchased by Crystal Manufactoring (USA) were used. The quartz crystal analyser was the commercially available multiple-channels QCMagic by Elbatech (Marciana, Livorno, Italy).

For the optical biosensor (SPR) BIACORE X^{TM} instrumentation was used, together with Sensor Chip CM5 (Biacore AB Uppsala, Sweden).

11-mercaptoundecanol was from Sigma (Milan,Italy), Dextran 500 was from Amersham Biosciences (Uppsala, Sweden), (+)/–epichloridin and *N*-hydroxysucciminide was purchased from Fluka (Milan, Italy). Ethanol and all the reagents for the buffers were purchased from Merk (Italy).

Two different buffers were used: one for the probe immobilization (NaCl 300mM, Na_2HPO_4 20mM, EDTA 0.1 mM, pH 7.4) and one for the target hybridization (NaCl 150mM, Na_2HPO_4 20mM, EDTA 0.1 mM, pH 7.4).

Oligonucleotides were purchased from MWG Biotech (Milan, Italy).

Probe A: 5'- biotin-TGG GCG GCA TGA ACC GGA GGC CCA TC -3'
Probe B:5'-biotin-TGG GCG GCA TGA ACC AGA GGC CCA TC -3'
Target C: 5'- GAT GGG CCT CTG GTT CAT GCC GCC CA – 3'
Target D: 5'- GAT GGG CCT CCG GTT CAT GCC GCC CA - 3'
(negative control): 5'-GGC AGA GGC ATC TTC AAC ATG GCC-3'

2.2. Immobilization of the probe on the sensors surface

The immobilisation method was the same for both biosensors. The principle of this procedure is to take advantage of the strong affinity between biotin and streptavidin. An oligonucletidic biotinylated probe was used and the streptavidin was immobilised on the gold surface, previously modified with thiol and carboxylated dextran in the case of the piezoelectric biosensor. The details of the immobilisation procedure are reported in literature[1, 3, 4, 8].

2.3. Hybridization reaction

Piezoelectric biosensor: Once the probe A was immobilised on the gold surface, the hybridisation reaction was conducted by adding 100 µL of the target solution to the cell where the crystal with the immobilised probe is located.

The reaction was monitored for 10 minutes. This time is retained adeguate to obtain a good analytical signal in a brief measurement time (Minunni et al. 2003). After 10 minutes the oligonucleotide was removed and the surface washed with hybridization buffer to eliminate the unbound oligonucleotide. The analytical signal was given by the frequency shift between the final value of the hybridization buffer and its value before the hybridization. In this way the value depends only on the oligonucleotide bound to the probe.

After each hybridization cycle, the probe was regenerated by 1 mM HCl solution (1 min) to allow sensor re-use. In this way it was possible to use the crystal for 15 cycles of hybridization.

Optical biosensor: The gold sensor chip CM5, was already modified with thiol and dextran. So, to couple the biotinylated probe, streptavidin was first immobilized on the previously modified surfaces (Wang et al. 2004). Then, two different probes, differing only in one base, were immobilized on the sensor gold surface, onto the two different flow cells (Fc1 and Fc2 carried probe B and probe A, respectively). Flow rate was 5 µl/min and working temperature was 25°C.

Then the target solution (C) was injected over the two cells simultaneously. Target C was fully complementary to probe (B) immobilized on cell 1 and mutated as regards to probe A immobilized on cell 2.

Hybridisation experiments were performed by injecting 25 µl of the target solution at a flow rate of 5 µl/min. The reaction was monitored for five minutes and then the sensor chip was automatically washed with buffer to remove the unbound DNA material. The analytical signal reported as Resonance Units (RU), was derived by the difference between the final value and the value recorded before the hybridization (baseline).

The single stranded probe was regenerated by injecting 1 mM HCl solution (2 µl).

3. Results and discussion

The optimization of the sensors was similar for both systems: they were studied in terms of the main analytical parameters such as specificity, sensitivity, reproducibility, stability, etc.

The specificity was tested adding 1 µM solution of a non-complementary sequence (26-mer), used as negative control. No remarkable hybridization signal was obtained with both sensors evidencing the high specificity of the sensors.

Piezoelectric biosensor: the probe A was successfully immobilized on the sensor gold surface, in agreement with our previous work[8].

A calibration curve of p53 full-complementary target (D) was produced. Each point of the curve is the average of three measurements at the same concentration.

The reproducibility of measurements was tested repeating the same concentration of the p53 target for three times on the same crystal. This for each tested concentration.

In order to evaluate the stability of the sensor system, the baseline value was monitored after each measurement cycle. The difference between the maximum and the minimum baseline was around 50 Hz after 15 hybridization/regeneration cycles, indicating a good stability of the sensor.

To compare the hybridization response with full–complementary oligonucleotide a calibration curve with the mutated (mismatch) oligonucleotide (C) was produced. The mismatch signal was always lower than full-complementary signal, as expected[5, 8].

The results obtained with the fully complementary and mutated oligonucleotides are shown in figure 1.The applied concentration range was 0.125-1 µM.

Optical biosensor: Two different probes, differing only in one base, were immobilized on the sensor gold surface, on the two different flow cells (Fc1 and Fc2 carried probe B and probe A, respectively).

The calibration curves obtained by flowing the target solution over the two different cells are shown in figure 2. The concentration range was 0.0125-0.6 µM.

It was possible to discriminate the signals for a concentration higher than 0.125 µM.

Each point of the curve is the average of three measurements at the same concentration.

The reproducibility of measurements was tested repeating each tested concentration of the target for three times, in one day. The system demonstrated an high reproducibility with a CV of 1.5 % for both cells.

The stability of the modified chips was monitored by observing the baseline value after each hybridization-regeneration cycle. In 30 measurements a baseline variation of less than 20 RU for each cells was observed.

4. Conclusion

The piezoelectric and optical DNA biosensors have been optimized to detect a point mutation in the TP53 gene. The hybridization reaction was detected in real time with good reproducibility for both the sensors.

It was possible to discriminate the mutated sequence. In the optical biosensor the lower concentration tested was 0.0125 μM, while the piezoelectric sensor was 10 times less sensitive since it was possible to detect the two curves for a concentration higher than 0.125 μM.

The optimized sensors resulted very promising for further analysis of real samples of PCR amplified genomic DNA, extracted from patients affected by colorectal cancers.

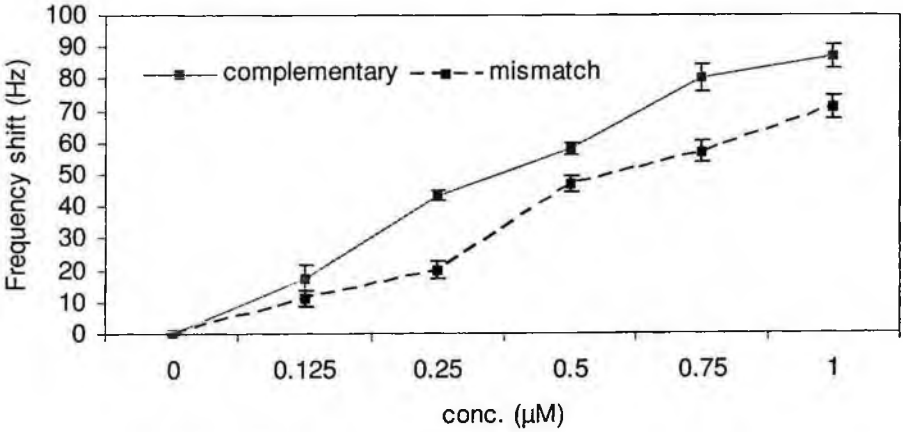

Fig. 1. Calibration curves obtained with probe A immobilized on the quartz crystal. (—) complementary target (C) ; (- - -) mismatch target (D).

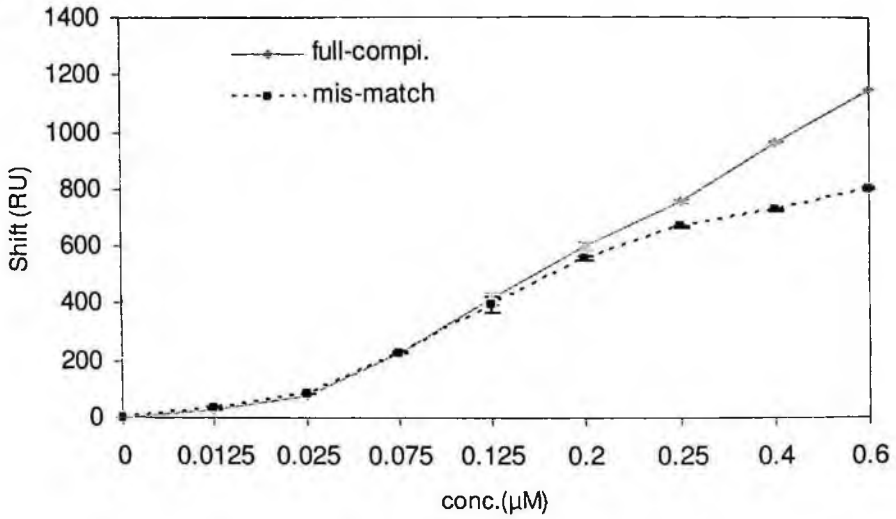

Fig. 2. Calibration curves obtained with probe B on cell 1 and probe A on cell 2 (SPR).

References

1. E. Giakoumaki, M.Minunni, S. Tombelli, I. E. Tothill, M. Mascini, P. Bogani, M. Buiatti Analysis of amplified nucleic acids by Surface Plasmon Resonance: application to genetically modified food detection *Biosensor and Bioelectronics* 2003; **19**: 337-344.
2. T. Jang, M. Minunni, M. Mascini, Toward fast and inexpensive molecular diagnostic. The case of TP53. *Clinica Chimica Acta* 2004;**343**: 45-60
3. I. Mannelli, M. Minunni, S, Tombelli and M. Mascini, Quartz Crystal Microbalance (QCM) Affinity Biosensor for Genetically Modified Organisms (GMOs) Detection, *Biosensor and Bioelectronics* 2003; **18 Issue 2-3**: 129-140
4. E. Mariotti, M. Minunni_and M. Mascini, Surface Plasmon Resonance (SPR) Biosensor for Genetically Modified Organism (GMOs) Detection, *Analytica Chimica Acta* 2002; **453**:165-172,
5. M. Minunni, S. Tombelli, R. Scielzi, I. Mannelli, M. Mascini, C. Gaudiano Detection of beta-Thalassemia by a DNA Piezoelectric Biosensor Coupled with PCR, *Analytica Chimica Acta* 2003; **481 (1)**: 55-64
6. R. Wang, S. Tombelli, M. Minunni, M.M. Spiriti, M. Mascini, Immobilisation of DNA probes for the development of SPR-based sensing, *Biosensor and Bioelectronics* 2004; **20 (5)**: 967-974.
7. J. Wang, Survey and Summary. From DNA biosensors to gene chips, *Nuclei Acids Research,***2000**, 28 (16), 3011-3016.

8. Tombelli S., M. Mascini, L. Braccini, M. Anichini and Anthony P. F. Turner Coupling of a DNA piezoelectric biosensor and polymerase chain reaction to detect apolipoprotein E polymorphisms *Biosensors and Bioelectronics* 2000; **15**:363-370

ADSORPTION OF POLY(L-LYSINE) ON Si_3N_4-GATE OF ISFET BASED DNA SENSORS

L. BANDIERA, G. CELLERE, A. DE TONI, A. PACCAGNELLA
Department of Information Engineering, Padova University, Italy
S. CAGNIN, G. LANFRANCHI
Cribi Biotechnology Center, Padova University, Italy
L. LORENZELLI
ITC-IRST Microsystems Division, Trento Italy

Field effect transistors (FET) are candidates for a new generation of fully electrical DNA sensors [1,2,3]. However, experimental data and theoretical models are still missing concerning the interaction among sensor surfaces, promoting polymers, and DNA. In this work we have studied the self-assembled monolayer of polypeptide poly(L-lysine) (PLL), which is used to control the specific adsorption of DNA onto the gate surface of Ion Sensitive Field Effect Transistor (ISFET), with silicon nitride (Si_3N_4) as the gate sensitive area. We have analyzed the adsorption of PLL, which has a fixed positive charge per monomer, through electrical measurements.

1. Introduction

Surface-based methods are attractive approaches for the electrical detection of biopolymers since they allow for label–free detection and can lead to the integration of the sensor in the planar silicon technology, which is the basis of most microelectronic devices such as amplifiers and microprocessors [1,2,3]. Most studies of biological to silicon interfaces have used SiO_2 [1] or Au [3] as uppermost layers. In this paper we study the adsorption of poly(L-lysine) (PLL) onto gate insulator surface of ISFET with Si_3N_4 as sensitive material [2]. We propose a model to estimate the interface electrochemical potential variation and the PLL charge. The model takes into account the modification in proton concentration at the Si_3N_4/electrolyte interface after PLL adsorption.

2. The interface model

A schematic representation of ISFET/PLL system is depicted in fig. 1. The Si_3N_4/electrolyte interface can be described by assuming that only silanol and basic primary amine sites play a rule in the surface/electrolyte equilibrium [4]. Under this hypothesis the system is well described by site-binding theory [4] and the potential drop ϕ_{ei} for unit area at the electrolyte/insulator interface can be written as:

$$\phi_{eo} = \frac{q}{Ceq} \cdot \left[N_{sil} \cdot f_a(\phi_{eo}, pH) + N_{nit} \cdot f_b(\phi_{eo}, pH) \right] \quad (1)$$

where $f_a(\phi_{eo}, pH)$ and $f_b(\phi_{eo}, pH)$ are suitable setting functions [4]. N_{sil} and N_{nit} are the surface densities of the silanol and of the primary amine sites, respectively. C_{eq} is the total capacitance of the insulator/electrolyte interface, and q is the elementary charge.

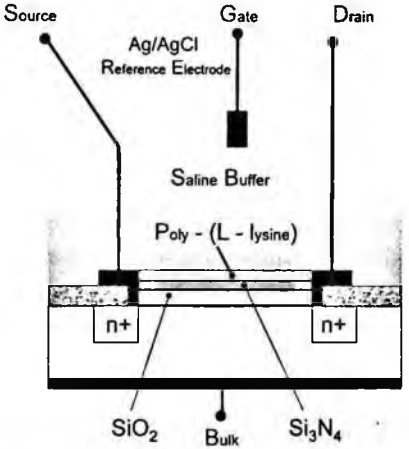

Figure 1: Sketch of n-channel ISFET with its active gate area covered by poly(l-lysine) layer.

Eq (1) states that the potential ϕ_{eo} can be modelled as a non-linear function of pH (and ϕ_{eo} itself). The threshold voltage of the ISFET can be written as:

$$V_{th}(ISFET) = V_{th}(MOSFET) + E_{ref} + \phi_{lj} + \chi_e - \varphi_{ei} - \frac{\phi_m}{q} \quad (2)$$

where $V_{th}(MOSFET)$ is the "natural" threshold voltage of the MOS equivalent system (that is, with metal gate instead of the electrolyte), E_{ref} is the potential of the reference electrode, ϕ_{lj}, is the liquid junction potential between the reference solution and the electrolyte, χ_e is the surface dipole potential, ϕ_{ei} is the potential of the electrolyte/insulator interface, and ϕ_m is the semiconductor work function. This model was developed [4] in the case of a pure saline solution as electrolyte, without any molecular adsorption on the surface. Therefore, in our case to describe the system we should use a modified expression of (2), which includes the potential drop across the PLL layer (φ_{pll}), after PLL adsorption:

$$V_{th}(ISFET, pll) = V_{th}(MOSFET) + E_{ref} + \phi_{lj} + \chi_e - \varphi_{ei,pll} - \frac{\phi_m}{q} - \varphi_{pll} \quad (3)$$

where $\varphi_{ei,pll}$ represent the potential of Si_3N_4/solution interface after PLL adsorption. We are supposing that adsorption of PLL onto the Si_3N_4 surface,

controlled by the solution pH, follows the reversible adsorption reaction as expressed according to eq. (4), that is valid for a glass surface [5]:

$$L + S_{sil} \cdot nH_2O \xleftrightarrow{Ke} L \cdot S_{sil} + nH_2O \tag{4}$$

where L represents a lysine molecule from one of the PLL chains in solution, S_{sil} is an active silanol site (out of N_{occ} overall occupied sites), nH_2O represents n water molecules (which are released from a surface site to the surrounding saline solution as a result of the adsorption of the lysine monomer, and adsorbed to the surface if the lysine is desorbed), and K_e represents the equilibrium constant for the process. If we suppose that N_{occ} is only a negligible part of N_{sil} (that is, the total number of silanol groups of the Si_3N_4 gate surface), the surface insulator charge still follows eq. (1). Under this assumption, we can assume the adsorbed PLL layer as a positive thin charged layer at distance d_{pll}=6 nm from the Si_3N_4/electrolyte interface (Atomic Force Microscope measurements of d_{pll} are not shown here for brevity). Since only N_{occ} sites out of N_{sil} are occupied, the Si_3N_4 surface is also in direct contact with the saline solution which permeates the PLL layer. Noticeably, $d_{pll}>L_d$=1nm, that is the Debye length in saline solution.

Fig 2 sketches the resulting charge distribution: ρ_{mos} is the charge density in the semiconductor, ρ_s is the charge density at the electrolyte/insulator interface, and ρ_{pll} is the charge due to positive PLL monomers, assumed to be constant and at the distance d_{pll} from the ISFET surface. The charge neutrality of the structure leads to the following expression for the surface charge densities:

$$\rho_s + \rho_{mos} + \rho_{pll} + \rho_{d,pll} + \rho_{d,s} = 0 \tag{5}$$

where $\rho_{d,s}$ and $\rho_{d,pll}$ are the charge distribution in Stern and Gouy-Chapmann layers of Si_3N_4/electrolyte and electrolyte/PLL/electrolyte interfaces, respectively (these are not shown in fig. 2 for clarity). As a simplifying condition, we assume that the potential linearly drops inside the thin local layer of electrolyte between the PLL and the sensor surface. Boltzmann distribution predicts that the proton concentration at the insulator surface is related to its concentration just outside the PLL layer. Hence the pH_s at the insulator surface depends on the potential through the PLL layer following [1]:

$$pH_{ohp1-2} = pH_{ext} + \frac{\phi_{pll} \cdot q}{2.3 \cdot k \cdot T} \tag{6}$$

where $pH_{ohl\text{-}2f}$ is the pH between the double layers at the Si_3N_4/electrolyte and PLL/electrolyte interfaces, and pH_{ext} is the pH on the outermost surface of the PL layer. By using eqs. (1), (3), and (5), we can evaluate the effective potential drop across the PLL layer ϕ_{pll} and the potential across the insulator/electrolyte

interface $\phi_{ei,pll}$. Finally, the Si_3N_4/electrolyte and electrolyte/PLL/electrolyte interfaces are described as a capacitors, which take into account the Gouy-Chapmann and Helmhotz layers, C_{Gouy} and C_{Helm} evaluated as in [4]:

$$C_{Helm} = \frac{\varepsilon_{IHP} \cdot \varepsilon_{OHP}}{\varepsilon_{IHP} \cdot d_{IHP} + \varepsilon_{OHP} \cdot d_{OHP}}, \quad C_{Gouy} \approx \frac{\sqrt{8 \cdot \varepsilon_w \cdot k \cdot T \cdot C_{bulk}}}{2 \cdot V_t}, \text{ and } C_{dl} = C_{Helm} // C_{Gouy} \tag{7}$$

where ε_{ihp} and ε_{ohp} are the inner and outer Helmholtz plane permittivities, respectively; d_{ihp} and d_{ohp} are the insulator-nonhydrated and the insulator-hydrated ion distances, respectively; ε_w is the permittivity of the electrolyte; C_{bulk} is the ion concentration in the electrolyte, and $V_t = kT/q$ is the thermal voltage. We adopt here a one dimensional model of the ISFET in equilibrium, so that the possible variations of electric field along the channel (from source to drain) are neglected.

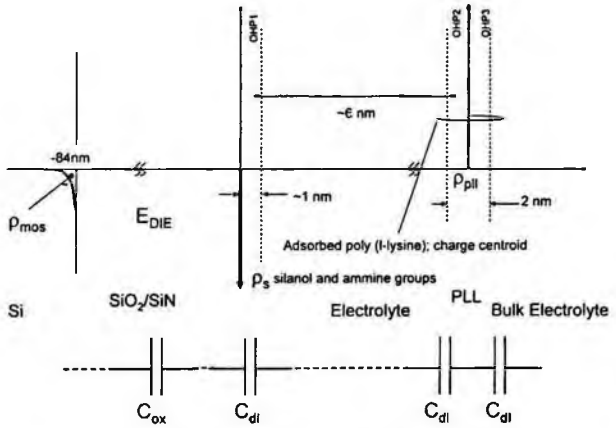

Figure 2: Schematic representation of the charge distribution assumed in the one dimensional model of the ISFET/PLL layer/electrolyte system, and the equivalent electric circuit of the structure. The interfaces are schematized by equivalent double layer capacitance.

3. Results and Discussion

3.1. *Devices and Preparation of the PLL Multilayer Coated ISFET Surface*

We have used n-channel ISFETs, with gate dielectric made by a SiO_2/ Si_3N_4 stack (with 84 nm electrical equivalent thickness), Si_3N_4 being the outermost layer. In order to prepare the ISFET surface to PLL adsorption, we have first performed a treatment of the Si_3N_4 surface: after cleaning with HF (2%), the surface was bathed on a wash solution (280 ml of 6.25 M NaOH with 420 ml of 95% ethanol) for 1 h in an orbital shaker. The sensors were then rinsed in ddH_2O

and then dried by centrifuging for 1 min at 100 rpm. The sensitive area was functionalized with 0.2 mg/ml PLL (pH=7, PLL-hydrobromide, MW 70,000-150,000, Sigma), rinsed with ddH_2O and dried for 5 min at 45° C. The poly-L-lysine features positively charged monomers due to the presence of a free amino group in each lysine. After PLL coating, ISFET surface features both carboxyl and amino groups that permit immobilization of biomolecules.

3.2. *Electrical Measurements*

As a first step, we have characterized the ISFETs as a function of pH to evaluate the number of superficial active sites. The ISFET ion sensitivity, defined as ΔV_{th}/°pH, is related to the ratio between N_{sil} and N_{nit}, to the number of active sites, and to C_{ox}, the SiO_2/ Si_3N_4 capacitance. Therefore, it strongly depends on the fabrication process but it is limited to around 58 mV/°pH for thermodynamic reasons [4]. Following the procedure presented in [4], from the pH sensitivity we can evaluate the ammine and silanol site density as N_{nit}= $2x10^{18}m^{-2}$ and N_{sil}=$3x10^{18}m^{-2}$, respectively.

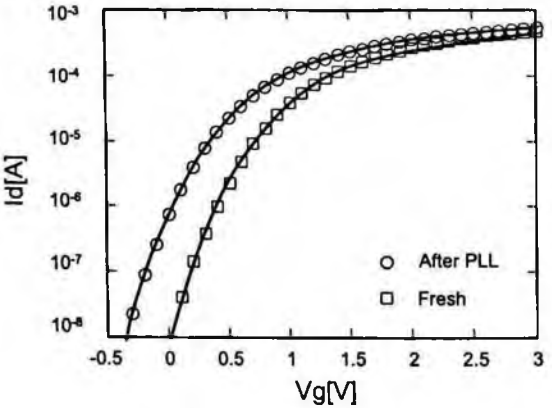

Figure 3: trans-characteristics of the ISFET before and after adsorption of PLL onto the gate insulator surface.

Fig. 3 shows I_{ds}-V_{gs} curves taken at V_{ds}=100 mV before and after adsorption of poly (l-lysine). The logarithmic Y-axis scale emphasise the sub-threshold behaviour. Experimentally we observe a rigid shift of I_{ds} to lower voltages after deposition, but no variation in sub-threshold slope is observed. This indicates that the PLL adsorption on the Si_3N_4 gate surface modified both the Helmholtz and diffused layers, but no interface state is generated. The shift toward negative V_{gs} is expected for adsorption of positive charge to n-channel ISFET.

The threshold voltage shift caused by the PLL layer can be written as $\delta V_{th}=V_{th}(ISFET,pll)-V_{th}(ISFET)$ and depends not only on the amount of

adsorbed PLL but also on the ISFET ion sensitivity. The device shown in fig. 3 shows δV_{th}~0.15V, corresponding to a PLL charge of Q_{pll}~1.5 x 10^{-4}C/m^2. On a 10-devices set, we statistically found Q_{pll}=(1.59±0.65)x10^{-4}C/m^2, equivalent to N_{occ}~10^{15} m^{-2} active sites; such a value confirms our hypothesis that the number of PLL occupied sites, N_{occ}, is much lower than the total number of silanol sites, N_{sil} (~10^{18}/cm^2). It is interesting to note that this charge corresponds to 20 lysines/nm^2, that is comparable to the saturation concentration observed for PLL adsorption on glass microspheres [5]. From our measurements the maximum expected threshold voltage variation induced by PLL adsorption onto Si_3N_4 surface is related to the highest possible sensitivity value, and δV_{th} corresponds to roughly -0.22V for a sensitivity of 58 mV/°pH.

4. Conclusions

In this work, silicon nitride ISFETs have been used for electrical detection of biomolecules. Experimentally, after the deposition of the PLL, ISFETs feature a V_{th} shift to more negative voltages. A detailed interface model that describes the ISFET/PLL system have has been developed. The model accurately predicts the charge of PLL layer, taking into account not only the potential drop due to PLL adsorption, but also the variation of pH on the ISFET surface induced by the PLL layer itself. Our model demonstrates that the PLL charged layer, other than modifying the Helmontz and diffuse layers, also changes the proton density (i.e. the local pH) at the insulator/electrolyte interface. The calculated PLL charge is statistically (1.59±0.65)x10^{-4}C/m^2, corresponding to 20 lysines/nm^2.

5. References

1. F.Pouthas, C. Gentil, D. Cote, G. Zeck, B. Straub "Spatially resolved electronic detection of biopolymers", Phys. Rev. E 70, 2004.
2. G.Cellere, L.Bandiera, S. Cagnin, A. Paccagnella, G. Lanfranchi, L. Lorenzelli "ISFET-based detection of cDNA perfect or partial matching kinetics" proceedings of Biosensors, 2004.
3. D. Kim, Y. Jeong, H. Park, J. Shin, P. Choi, J. Lee, and G. Lim "An FET-type charge sensor for highly sensitive detection of DNA sequence" Biosensors and Bioelectronics, Vol 20, 2004.
4. Grattarolla and Massobrio "Bioelectronics Handbook, MOSFETs, Biosensors, and Neurons" McGraw-Hill, 2002.
5. R.A. Lautor, Jr, Sharon D. trembley, Yuan Tian, Gary C. Lickfiel, and A.P. Wheeler "Determination of apparent thermodynamic parameters for adsorption of midchain peptidyl residue onto a glass surface" J. Biomed. Mater. Res. 49, 58, 2000.

A NEW POLYMERIC IMMOBILIZER FOR ENZYMES SUITABLE FOR SPR DETECTION SCHEME

G. MARGHERI[1], E. GIORGETTI[1], T. DEL ROSSO[1], S. SOTTINI[1], E. VAZQUÉZ[2], I. MOGGIO[2], E. ARIAS[2], J. ROMERO[2], P. FALCIANI[3]

[1]*Istituto dei Sistemi Complessi-CNR,Via Panciatichi 64,50127,Firenze,Italy*

[2]*Centro de Investigación en Química Aplicada[1]Centro de Investigación en Química AplicadaBoulevard Enrique Reyna 140, 25100 Saltillo, Mexico*

[3]*Galileo Avionica S.p.A.,Via A.Einstein 35,50013,Campi Bisenzio (Firenze)Italy*

Abstract

Conjugated polymers (CP) are a class of organic substances of increasing interest for their electroluminescence photoluminescence and nonlinearity properties . Some other properties of these molecules can be exploited to fix enzymes for biosensors. In this work, we investigate the immobilization property of a new class of modified polyphenil-ethynilenes (pPE). In these polymers, a glycol thioester group has been added to favour both the immobilization of enzymes and their filmability by self-assembly (SA) method. As a first glance, we choose to study the immobilization of the enzyme glucose-oxidase (GOD), responsible of the catalytic reaction of glucose, that is a well-known process and successfully applied in a wide class of glucose sensors. First, the enzymatic activity and stability of SA layers on dielectric substrates was demonstrated. Then, the behaviour of immobilized enzyme was tested in a Surface Plasmon Resonance (SPR) detection scheme as a fast and highly sensitive tool to monitor the interface enzymatic reaction. To this goal, gold-pPE/GOD multilayers were made and put in contact with a solution of glucose in water. Then, they were coupled in a Kretschmann configuration to a propagating surface plasmon by using light at 850 and 633 nm wavelengths. A well resolved angle shift was detected with both wavelengths, putting in evidence the set-on of the catalytic reaction of glucose These encouraging tests indicate that the new pPEs can be excellent and stable immobilizers of enzymes, and are able to preserve their activity. This can be combined with high resolution optical techniques as SPR to give attractive alternatives to the existing systems or for their implementation.

1. Introduction

Conjugated polymers (CP) are a class of organic substances of increasing interest in several fields, thanks to the π-electron delocalization through the conjugated backbone[1]. For example, poly(diacetylenes) and poly(tiophenes) exhibit well established electro-photoconductive and nonlinear properties[2].

The same materials can be exploited also for other purposes, one of the most promising being that of optical biosensors. An optical biosensor could be obtained by immobilizing an enzyme on a molecule which presents specific optical properties (absorption or fluorescence), that could change as a consequence of conformational changes due to the molecular recognition by the enzyme[3]. Alternatively, the presence of a certain chemical specie can be

recognized indirectly from the presence of the reaction products of the enzymatic catalysis, that change the dispersive and/or absorptive properties of the functionalized interface for some spatial extent. In both cases the capability of firmly immobilizing the enzyme is of basic interest, together with the requirements of good and simple filmability of the immobilizer, the layers' stability and preservation of enzyme activity. To fulfill these goals, we designed a new sequenced poly(phenylethynylene) analogous to the polymer already investigated for its photoluminescence properties[4], but where the flexible sequence is a glycol thioester group (pPEG3OC12-sqS), whose sulphur atoms are likely to favour the interactions with enzymes due to their known specific affinity for amminoacids, and enhance the self-assembly process on substrates. As target enzyme we chose the glucose oxidase (GOD) ,whose catalytic reaction of glucose is well established and employed also in the realization of a broad serie of commercial products for home and clinic diagnosis of glycemia[5].
In particular, we checked the enzymatic activity of multilayer pPEs functionalized with GOD with standard assay methods. Then, we prepared GOD-functionalized films on gold, with the aim of investigating the recognition of glucose present in water solutions with the Surface Plasmon Resonance technique as a fast and highly resolving optical tool to monitor the interface enzymatic reaction.

2. Experimentals

2.1 Synthesis and films preparation

pPEG3OC12-sqS (structure in Fig. 1) was synthesized according to the same route reported in Ref. (4). Thin polymer films were deposited on glass or quartz substrates previously treated with a sulfochromic solution for at least one day, washed with distilled water, sonicated in H_2O and then dried in oven at about 60°C.

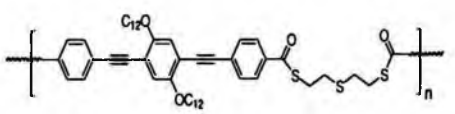

pPEG3OC12-sqS

Figure 1. Molecular unit of pPEG3OC12-sqS

For the polymer deposition, the substrate was immersed in $CHCl_3$ solution (concentration of 1 g/l) for 20 min at room temperature, washed with distilled water and dried with a gentle flux of air.

For the enzyme deposition, a 1 g/l water solution was prepared and adjusted with HCl at the pH value of 5.5, corresponding to the maximum enzymatic activity of glucose oxidase. Two different kinds of multilayers were prepared. In one configuration, the multilayer is built by alternating in several routes one

layer of pPEG3OC12-sqS and one of GOD, while in the second configuration a serie of four pPEG3OC12-sqS layers is deposited, with a final cover with a GOD layer (stratification named in the following (pPEG3OC12sqS)$_4$/GOD). The enzymatic activity of the films was evaluated by UV-Vis spectroscopy according to a standard assay method[6]. The test mixture composed of o-dianosidine, horseradish peroxidase and β-D-glucose was prepared and stabilized at 35 °C in the UV-Vis cell. Then the film was incubated in the test solution in 9 cycles of 20 seconds each, so achieving the typical kinetic shown in Fig. 2, which refers to a

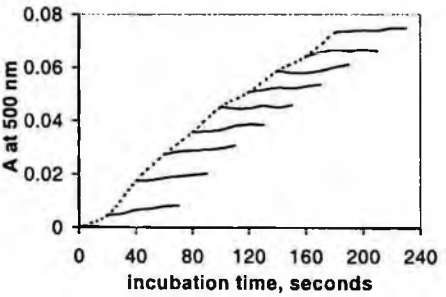

Figure 2. Absorbance vs time of glucose-dianisyne-peroxidase solution for 9 incubation cycles of immobilized GOD on pPEG3OC12sqS)$_4$ films

(pPEG3OC12sqS)$_4$/GOD film. This kind of multilayer resulted to exhibit the highest activity. The lack of a sigmoid behaviour in the kinetic excludes the possibility of even a partial dissolution of the enzyme. To summarize, these tests indicate that the enzyme is active in the multilayer, it is firmly immobilized by the polymer and is able to start the glucose catalysis.

2.2. SPR study

Biosensoring tests were performed using SPR technique in Kretschmann configuration[7]. The apparatus is shown in Fig. 3 using focused light at the wavelength of 850 nm.

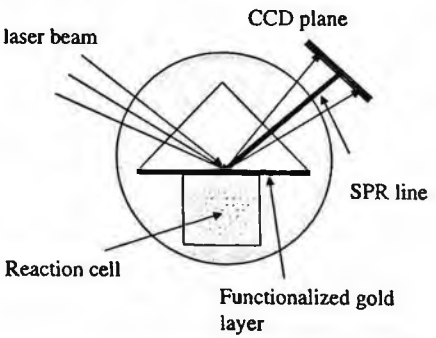

Figure 3. Scheme of the Kretschmann coupling prism used for the SPR tests

A BK7 prism was first coated with a gold layer obtained by electron gun evaporation, then a (pPEG3OC12-sqS)$_4$/GOD was deposited on the metal layer with the procedure outlined in 2.1.

The hypothenuse was coupled to the liquid contained in a small reaction cell. The output is acquired with a proper software, and a successive processing gives the reflectivity of the optical stratification on a predetermined horizontal scan line of the CCD. The resolving power of the apparatus was 0.011°/pixel.

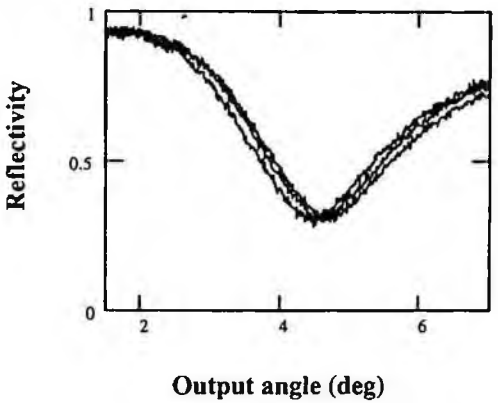

Figure 4. SPR curves after the injection of glucose in the reaction cell.The curves were recorded in 1 min. The radiation wavelength was 850 nm.

A pre-set measurement, with only deionized water in the cell, was performed on a similar non-functionalized gold layer to measure the thickness and dielectric constant. of the metal layers, so achieving the values ε = -28+1.5i and 35 nm. Then, measurements on gold-pPEG3OC12-sqS)$_4$/GOD multilayers were performed, after the injection of a glucose-water solution in the cell, with a concentration of 90 mg/l.

Fig. 4 reports the reflectivity vs. incident angle curves at different times after the injection of the glucose solution in the reaction cell. The shift of the plasma angle indicates that the refractive index of the solution-enzyme interface is increasing in time. After some minutes, the shift goes to a regime value of 0.18°. Further measurements were also performed with the light of a He-Ne laser (633 nm wavelength). Even if the lower wavelength gives rise to a wider resonance, angular shifts were evident and well beyond the resolving power of the apparatus. To confirm the local character of the variation of the solution refractive index, a subsequent set of measurements was performed, in which a glass sample covered with SA (pPEG3OC12-sqS)$_4$/GOD multilayer was immersed in a saturated water-glucose solution, that was put in contact with the gold coated hypothenuse of the Kretschmann prism without functionalization Then, we monitored the minimum shift with time in two different measurements, and after 10 minutes we observed only a shift as small as 0.02°, thus excluding any significant volume variation of the refractive index.

3. Conclusions

In this work we have investigated the capability of a modified poly(pheynylethynylene) (pPE) to immobilize enzymes, chosing as a starting point the interaction with glucose oxidase (GOD) for its well-known role in the development of glucose sensors. Thanks to the presence of sulphur, the added glycole thioester groups have been demonstrated to favour both the binding with GOD as well as the self-assembly on glasses and on metals. Self-assembled pPE multilayers have been made with different supramolecular arrangements, and GOD was immobilized on them .Tests were performed to check the activity of the immobilized enzyme and the stability of the SA multilayers. SPR tests were also performed on gold functionalized layers with immobilized GOD, put in contact with a glucose-water solution. Well resolved angular shifts of the absorption line were achieved at two different wavelengths (633 and 850 nm), evidencing just in some seconds the set-on of the glucose catalysis at the functionalized interface, whose local character was confirmed by successive tests performed with non-functionalized gold coated Kretschmann prisms.

This work was financially supported by CONACyT through the projects 43166 and the Program of Collaboration CNR-CONACyT and by C.I.Q.A. (project F80340).

References

1. H.S. Nalwa, Handbook of Organic Conductive Molecules and Polymers, J. Wiley and Sons Ltd., West Sussex, 1997.
2. G.Margheri,E.Giorgetti,S.Sottini,G.Toci "Nonlinear chacacterization of nanometer-thick dielectric layers bt Surface Plasmon Resonance techniques",JOSA B, Vol. 20, n°4, p.741 (2003).
3. A review of the immobilization of enzyme in electropolymerized films, J. Electroanal. Chem. 362, 1-12.
4. C. Espinosa, I. Moggio, E. Arias-Marín, J. Romero-García, R. Cruz-Silva, J. Le Moigne and C. Ortiz-Cisneros, Synth. Met., 139 (2003) 157.
5. H.M.Heise,P.Abel "Clinical analysis: glucose" from "Encyclopedia of analytical science" 2nd edition Elsevier, 2004.
6. I.H. Segel, "Enzyme Kinetics", J. Wiley and Sons, New York, 1975.
7. H.Raether "Surface plasmons on smooth and rough surfaces and on gratings" Springer-Verlag, Vol. 111, 1988.

PROTEIN-LIGAND INTERACTION DETECTION BY POROUS SILICON OPTICAL SENSOR

LUCA DE STEFANO*, LUCIA ROTIROTI AND IVO RENDINA

Institute for Microelectronics and Microsystems, Department of Naples, National Council of Research, Via P. Castellino 111, 80131 Naples, Italy

LUIGI MORETTI

"Mediterranea" University of Reggio Calabria, Località Feo di Vito, 89060 Reggio Calabria, Italy

VIVIANA SCOGNAMIGLIO, MOSÈ ROSSI, AND SABATO D'AURIA

Institute of Protein Biochemistry, National Council of Research, Via P. Castellino 111, 80131 Naples, Italy

Molecular binding between the glutamine binding-protein (GlnBP) from *Escherichia coli* and L-glutamine (Gln) is detected by means of an optical biosensor based on porous silicon nano-technology. The binding event is revealed as a wavelength shift in the reflectivity spectrum of a porous silicon optical microcavity (PSMC). Exploiting the hydrophobic interaction between GlnBP and the porous silicon surface "as etched", we avoid any preliminary surface functionalization process. The unmodified porous silicon optical microcavity, infiltrated by the protein, results stable to oxidation for few cycles of wet measurements.

Keywords: Porous silicon, optical biosensor, optical microcavity, L-glutamine, proteins.

1. Introduction

The interaction between an analyte and a biological recognition system is normally detected in biosensors by the transducer element which converts the molecular event into a measurable effect, such as an electrical or optical signal. Recently, lot of experimental work, exploiting the worth noting properties of porous silicon (PSi) in chemical and biological sensing, has been reported (Dancil et al., 1999; De Stefano et al., 2004).

PSi is an almost ideal material as transducer due to its porous structure, with hydrogen terminated surface, having a specific area of the order of 200 –

* Author to whom correspondence should be addressed: luca.destefano@na.imm.cnr.it

500 m^2 cm^{-3}, so that a very effective interaction with several adsorbates is assured. Moreover, PSi is an available and low cost material, completely compatible with standard IC processes. Therefore, it could usefully be employed in the so-called smart sensors (De Stefano et al., 2004).

Optical sensing devices in PSi are based on changes in its physical properties, such as photoluminescence or reflectance, due to the interaction with the target analytes. Some researchers have chemically or physically modified the Si-H surface sites in order to enhance the sensor selectivity through specific interactions (Dancil et al., 1999, Yin et al., 2004). The common approach is to create a covalent bond between the porous silicon surface and the biomolecules which specifically recognize the target analytes (Hart et al., 2003). Sensitive label-free biosensors are highly requested for applications in high throughput drug monitoring and diseases diagnostics: unlabeled analytes require in fact easy sample preparation. For this reason, many label-free optical biosensors have been proposed, mainly falling into two categories: optical interferometers and surface plasmon resonance devices (F. S. Ligler and C. A. Rowe Taitt (Eds.), 2004).

PSi structures are realized by electrochemical etching of a silicon (Si) wafer in a hydrofluoridic acid solution. It is well known that the porous silicon "as-etched" has a Si-H terminated surface due to the Si dissolution process (L. Canham Ed., 1997). From a chemical point of view, the Si-H bonds make the PSi surface strongly hydrophobic and very reactive. On the other hand, ligand binding proteins are good candidates when designing highly specific biosensors for small analytes: in particular, the Glutamine-binding protein from E. coli is a monomeric protein composed of 224 amino-acid residues (26 kDa) responsible for the first step in the active transport of L-glutamine across the cytoplasmic membrane. GlnBP consists of two similar globular domains, the large domain (residues 1 to 84 and 186 to 224) and the small domain (residues 90 to 180), linked by two peptide. Each domain contains a central core of beta-sheet flanked by alpha-helices which is a typical beta/alpha/beta protein structure. The deep cleft formed between the two domains contains the ligand-binding site. Of the naturally occurring amino acids, only glutamine is bound by GlnBP with a dissociation constant Kd of 3×10^{-7} M (Hsiao et al., 1996). When in contact with the hydrogenated porous silicon surface, the GlnBP adopts a structure which promotes the hydrophobic interactions, and, as a consequence, it temporary attaches to the PSi. The GlnBP from E. coli can sufficiently strongly interacts with the porous silicon surface and also works as molecular probe for the detection of L-glutamine. Glutamine is a major source of nitrogen and

carbon in cell culture media. Thus, glutamine monitoring is important in bioprocess control.

In this communication, we report some preliminary data on the development of a reagentless microsensor for optical detection of L-glutamine (Gln) based on the interaction between unmodified porous silicon monolayer and GlnBP.

2. Material and Methods

Porous silicon is also very attractive for the possibility of fabricating single layer, like Fabry-Perot interferometers, and multilayers, such as Bragg or rugate filters, structures exploiting high quality optical response (Theiss, 1997). In this study we used as sensor a $\lambda/2$ optical microcavity sandwiched between 7 Bragg reflectors realized alternating layers with high and low refractive indices.

The PSMC was obtained by electrochemical etch in a HF-based solution. A highly doped p+-silicon, <100> oriented, 0.01 Ω cm resistivity, 400 μm thick was used. The silicon was etched using a 50 % HF : ethanol = 1 : 1 solution in dark and at room temperature. Before anodization the substrate was placed in HF solution to remove the native oxide.

A current density of 400 mA/cm^2 for 0.8 s was applied to obtain the high refractive index layer with a porosity of 75 % while one of 80 mA/cm^2 was applied for 1.87 s for the low index layer with a porosity of 67 %. The optical microcavity is a low refractive index layer. This structure has a characteristic resonance peak at 1089 nm in the middle of a 295 nm stop band.

The optical set-up required for our sensing experiments was very simple (see Figure 1): a tungsten lamp (400 nm < λ < 1800 nm) inquired, through an optical fibre and a collimator, the sensor closed in a glass vial which can be fluxed by liquids or gases. The reflected beam is collected by an objective, coupled into a multimode fibre, and then directed in an optical spectrum analyser (Ando, AQ6315A). The reflectivity spectra have been measured with a resolution of 0.2 nm.

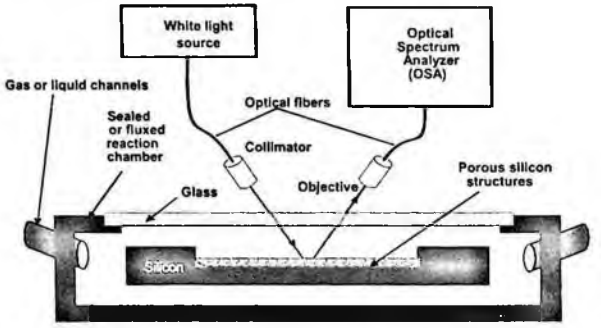

Figure 1. The experimental set-up

The presence of Si-H bonds on the porous silicon surface has been monitored by means of infrared spectroscopy with a Fourier transform spectrometer (FT-IR Nicolet Nexus) (Socrates, 2001).

2.1. *preparation and purification of GlnBP*

GlnBP from E. coli was prepared and purified according to standard procedure (Dattelbaum et al., 2001). The protein concentration was determined by the method of Bradford (Bradford, 1976) on a double beam Cary 1E spectrophotometer (Varian, Mulgrade, Victoria, Australia) with bovine serum albumin as standard.

2.2. *Labeling of GlnBP*

A solution of homogenous GlnBP 2.0 mg/ml in 1.0 ml of 0.1 M bicarbonate buffer, pH 9.0 was mixed with 10 µl of Fluorescein Isothiocyanate (FITC) (Molecular Probes) solution in N, N-Dimethylformamide DMF (1.0 µg FITC/100 µl DMF). The reaction mixture was incubated for 1 h at 30 °C and the labeled protein was separated from unreacted probe by passing over a Sephadex G-25 column equilibrated in 50 mM phosphate buffer, 100 mM NaCl, pH 7.0.

To assess the protein penetration into the pores we spotted on the porous silicon chip 20 µl of 1.0 mM sodium bicarbonate buffer containing the dye labeled protein. For ligand-protein interaction measurement we prepared a 20 mM L-glutamine in the same buffer solution.

3. Eexperimental setup

Since the hydrophobic interaction is the only binding mechanism between the PSi and the GlnBP, it is crucial to assess the presence of Si-H bonds in the samples before spotting the protein on them. Figure 2 shows the FT-IR spectrum of the porous silicon monolayer as etched: the characteristic peaks of Si-H bonds at 910 cm^{-1} and 2100 cm^{-1} are clearly visible, while Si-O-Si peaks at 1050-1100 cm^{-1} are not present.

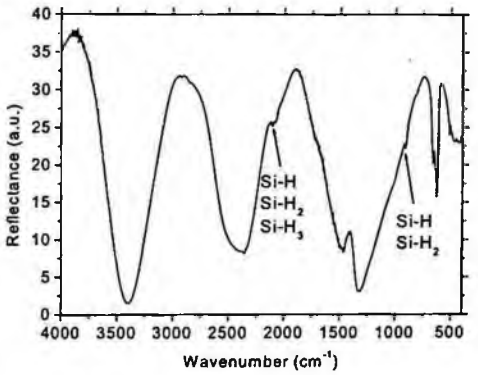

Figure 2: Infrared spectrum of porous silicon as etched measured in reflectance mode.

When the biological matter (refractive index n≅1.45) interacts with the porous silicon structure, it substitutes the air (n=1) into the pores, causing an increase of the average refractive index, which results in a shift towards longer wavelengths of the reflectivity spectrum.

We have firstly verified the penetration of GlnBP, labeled with FITC, into the porous silicon pore. In Figure 3-a is shown the porous silicon as-etched under UV illumination. No fluorescence signal can be detected. In Figure 3-b, the adsorbed labeled-protein is clearly visible.

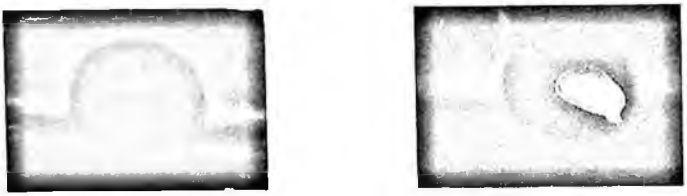

a) b)

Figure 3: a) Porous silicon chip as-etched illuminated by a UV lamp. b) Porous silicon chip after a drop of solution containing the labelled-GlnBP has been adsorbed into it.

We have also qualitatively tested the strength of hydrophobic bond between the protein and the porous silicon surface. We have washed the chip with the spotted protein several times by hands in demi-water. After five rinses, the fluorescence zone on the porous surface starts to decrease in size and intensity.

We have also checked, by FT-IR spectroscopy, that the PSi surface covered by the protein shows a good stability toward aqueous oxidation: after water immersions, the characteristic peak of Si-O-Si bonds did not appear in the FT-IR spectrum. In the presence of L-glutamine, the GlnBP undergoes to a large conformational change in its global structure to accommodate the ligand inside the binding site. The ligand binding is detected as a shift in wavelength of the peak of resonance, corresponding to a refractive index change. The experimental measurement to detect the binding of Gln to GlnBP is a three step procedure: firstly, we have registered the optical spectrum of the porous silicon layer as etched in presence of the buffer solution; then we have repeated the measurement after the GlnBP absorption on the chip surface and, finally, after the Gln solution has been spotted on it. The organic material excess has been removed by a further rinse in the buffer solution. In Figure 4 the shifts induced by each step in the peak of resonance of the reflectivity spectrum are reported. A well defined red-shift of 15 nm, due to protein-ligand interaction, has been registered.

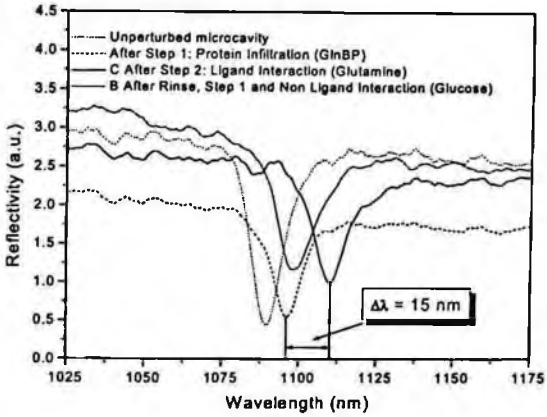

Figure 4: Shift of the peak of resonance of the optical microcavity due to ligand-protein interaction. Dot curve (a): porous silicon as-etched. Dashed curve (b): porous silicon + protein. Continuous curve (c): porous silicon + protein + glutamine. Wavelength shift between curve (b) and curve (c) is 15 nm.

A control measurement has been made using a solution containing a different molecule, such as glucose: a very small peak shift has been recorded in the reflectivity spectrum respect to the one obtained after the GlnBP absorption on the chip surface (step two).

4. Conclusion

In conclusions, in this work we have presented some preliminary data useful for the development of an optical protein-based microsensor, based on porous silicon nano-technology, for the detection of L-glutamine. We do not make use of a surface functionalization step, but just exploit a direct hydrophobic interaction, to immobilize in the porous silicon the L-glutamine binding protein of Escherichia Coli, which selectively recognizes the target analyte.

References

1. Bradford, M.M. (1976), "A rapid and sensitive method for the quantitation of microgram quantities of protein utilizing the principle of protein-dye binding", Anal Biochem, 72, 248-254.
2. L. Canham Ed., Properties of porous silicon (1997), IEE Inspec, London, United Kingdom.
3. Dancil K.-P. S., Greiner D. P., and Sailor M. J. (1999), "A Porous Silicon Optical Biosensor: Detection of Reversible Binding of IgG to a Protein A-Modified Surface", J. Am. Chem. Soc. 121, 7925-7930.
4. Dattelbaum, J.D.; Lakowicz, J.R. (2001), "Optical determination of glutamine using a genetically engineered protein", Anal Biochem, 291, 89-95.
5. De Stefano L., Moretti L., Rendina I., Rossi A. M., Tundo S. (2004), "Smart optical sensors for chemical substances based on porous silicon technology", Appl. Opt. 43, No. 1, 167-172.
6. De Stefano L., Moretti L., Rossi A. M., Rocchia M., Lamberti A., Longo O., Arcari P., Rendina I., (2004), "Optical sensors for vapors, liquids, and biological molecules based on porous silicon technology", IEEE Trans. Nanotech. Vol. 3 n. 1, 49-54.
7. Hart B. R., Letant S. E., Kane S. R., Hadi M. Z., Shields S. J. and Reynolds J. G. (2003), "New method for attachment of biomolecules to porous silicon", Chem. Comm., 322-323.
8. Hsiao C.D., Sun Y.J., Rose J., Wang B.C. (1996), "The crystal structure of glutamine-binding protein from Escherichia coli", J. Mol. Biol. 262 (2), 225-242.
9. F. S. Ligler and C. A. Rowe Taitt (Eds.), Optical Biosensors: Present and Future (2004), Elsevier, Amsterdam, The Netherlands.
10. Socrates G., Infrared and Raman characteristic Group Frequencies (2001), Wiley, England.
11. Theiss W. (1997), "Optical properties of porous silicon", Surface Science Reports 29, 91-192.
12. Tolosa L., Ge X., Rao G. (2003), "Reagentless optical sensing of glutamine using a dual-emitting glutamine-binding protein", Anal Biochem. 314 (2), 199-205.
13. Yin H.B., Brown T., Gref R., Wilkinson J.S., Melvin T. (2004), "Chemical modification and micropatterning of Si (100) with oligonucleotides", Microelectronic Engineering 73-74, 830-836.

LIVING FUNCTIONS MONITORING

CATHECTOR: A GAMMA-RAY DETECTOR IN A CATHETER

R. SCAFÈ*, G. IURLARO, L. MONTANI, A. SANTAGATA, N. BURGIO, D. DELLA SALA

Casaccia Research Centre, ENEA, Rome, Italy

G. ALONGE, S. DE VITO, T. FASOLINO

Portici Research Centre, ENEA, Naples, Italy

This work is aimed to study the feasibility of a low energy gamma-ray detector for nuclear medicine to be inserted into a body cavity, duct, or vessel. The small dimension detector concept is based on a CsI:Tl scintillation crystal coupled to a Si Avalanche Photodiode (APD) mounted in a catheter. Due to the availability of ^{99m}Tc in nuclear medicine departments, 140 keV photons have been considered for detector design. At this energy the response concerns a more extended volume nearby the cathector than in the case of beta emitting radiotracers. Monte Carlo simulations have been performed and results have then been compared to experimental ones. The latter have been obtained using a ^{57}Co radioisotopic source and a laboratory setup including a detector having dimensions not optimized coupled to a low-noise conventional electronics. Count rates and sensitivities have been measured approaching a point source to the detector along some paths and considering different background irradiation levels.

1. Introduction

Scintigraphy in Single Photon Emission Computer Tomography (SPECT) modality is a well established functional diagnostic nuclear medicine technique [1]. The cathector idea consists of a few millimeter detector which can be introduced in a cavity, duct or vessel of the human body. Such a detector would allow localizing internal lesions [2-3], even of small dimensions, situated in the cavity proximity which could not be detected with similar sensitivity using a common device, positioned outside the body. We have performed some preliminary measurements using a laboratory setup and simulated through Monte Carlo models the detector response both in the experimental geometry and in conditions more similar to the clinical ones [4].

* Corresponding author: scafe@casaccia.enea.it; Ph: +3906-3048-3434; Fax: +3906-3048-3989

2. Equipment and Method

Figure 1 shows the detector made of a CsI(Tl) crystal 2.85x2.85x5.00 mm^3 manufactured by Hilger Crystals [5], wrapped by us in a reflective/diffusive coating and coupled to an Hamamatsu S8664-55 Si-APD with 10.6x9.0 mm^2 overall dimensions and 5x5 mm^2 active area [6]. The device was mounted on a BNC connector plugged into a Tennelec TC171 FET Preamplifier [7]. Measurements were performed using two ^{57}Co (E_γ=122-136keV; aboundances=89-11%, respectively) 1mm diameter point sources to simulate the lesion and a background. Some lucite blocks were positioned nearby the detector to simulate a scattered background radiation. Experiments were performed moving the lesion-source on a rectilinear trajectory with respect to the crystal. Further measurements performed along two curvilinear trajectories gave similar results, also due to the small value of the maximum angle between source and detector (14°) which can be considered well representative of realistic anatomical situations.

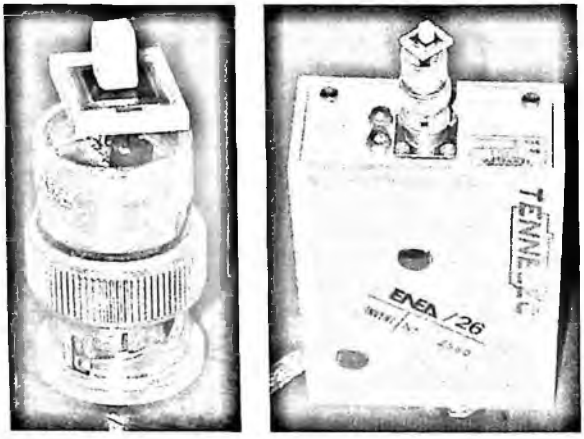

Figure 1 The detector used for preliminary measurements. On the left the scintillation crystal on the APD mounted on the BNC connector and, on the right, the device connected to the preamplifier.

In principle the detector response is mainly affected by three factors: (i) the geometric efficiency, depending on the inverse of the square of source-crystal distance, (ii) the Compton scattering in tissues and (iii) the crystal geometry and orientation with respect to the source. We have preliminarily evaluated the latter effect computing the fraction of photons undergoing a photoelectric absorption

both vs. crystal thickness and vs. orientation between the crystal and the incident photon, supposed passing from its centre [8].

Figure 2 reports the results obtained for 2mm and 5mm crystal heights. Calculations have been repeated including a 0.2mm thick tungsten absorber on the crystal top, in order to reduce the background contribution to the count rate (Fig. 3).

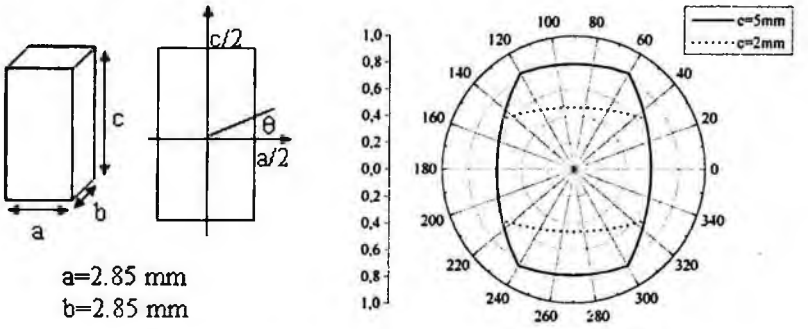

Figure 2 Fraction of photoelectric absorption vs. incident angle for two crystal heights.

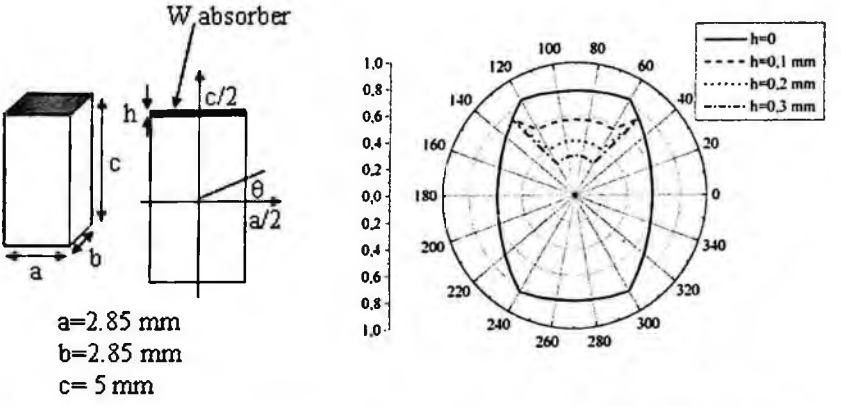

Figure 3 Fraction of photoelectric absorption vs. incident angle for different absorber thickness.

3. Results

The localization capability of such a detector has been evaluated considering the gradient modulus of the count rate as a function of source to crystal distance (Figure 4). Measurements made in presence of different background levels have given similar results.

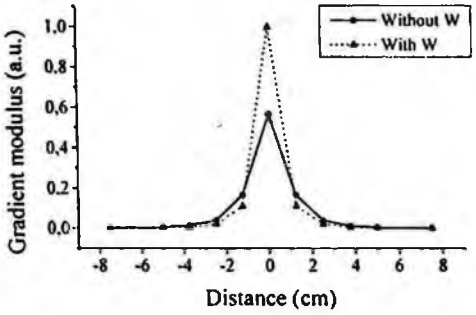

Figure 4 Modulus of count rate gradient as a function of source to detector distance with and without a 0.2mm thick W absorber on the crystal top face.

Figure 5 shows pulse height spectra measured with the lesion-source positioned at the crystal transverse axis for different backgrounds. The higher peak corresponds to the 122-136keV doublet, while the lower represents the convolution of Cs and I fluorescence escape lines around 90keV. Energy resolution at 122 keV resulted in the range 13-14% FWHM.

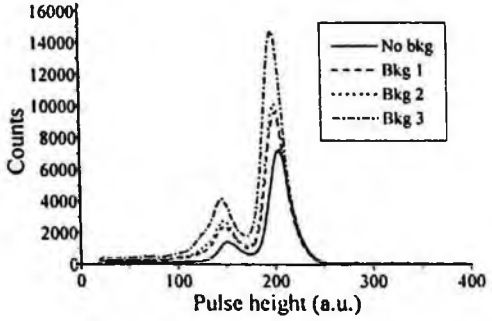

Figure 5 ^{57}Co pulse height spectra at 122 keV for different backgrounds.

The use of a tungsten absorber on the crystal top gives rise to a third peak on the pulse height spectrum corresponding to the W fluorescence line (59 keV) as shown in figure 6. Note that the peak area depends on the source-detector relative position and on the background intensity.

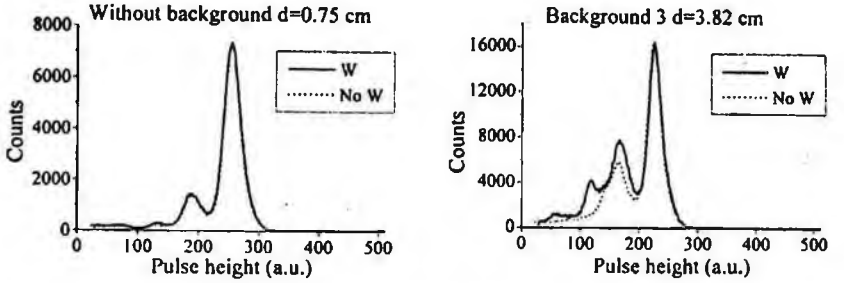

Figure 6 ^{57}Co pulse height spectra with and without the 0.2mm W absorber positioned on the crystal top. Left: cases without background and minimum source-crystal distance. Right: maximum considered background and maximum distance.

Monte Carlo simulations have been performed reproducing the described experimental conditions. Figure 7 compares experimental and simulated results in terms of count rate vs. source to crystal distance in presence and absence of a background irradiation. A quite good agreement is shown, apart from cases of minimum distances in which a discrepancy up to 30% is present.

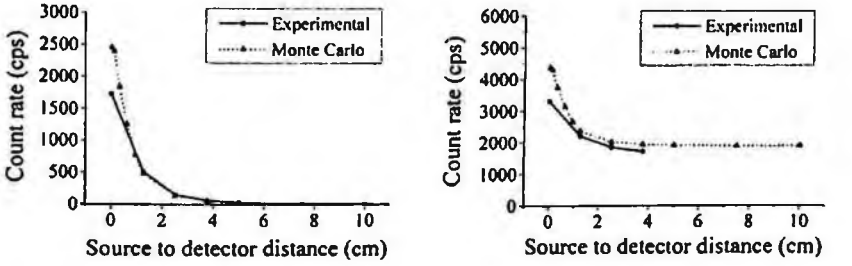

Figure 7 Comparison between experimental and simulated results in terms of count rate as a function of source to detector distance in absence (top) and in presence (bottom) of an irradiation background.

4. Conclusion

A method for lesion localization has been tested, based on the count rate variation as a function of lesion distance of a small dimension scintigraphic detector. Experimental and simulated results have been compared showing a satisfactory agreement which will be further improved. Simulations of conditions more similar to the clinical ones will be performed. The possibility of

using an absorber layer to reduce the background signal and to get information of the lesion position from the absorber fluorescence peak on the energy spectrum will be further investigated.

Acknowledgment

This work was supported by ENEA under project P466 "Functional Imaging in Nuclear Medicine and Biology".

References

[1] S. Webb, "The physics of medical imaging", Institute of Physics Publishing, Bristol and Philadelphia, 1988, pp 142-318.
[2] J.R.Davies et al.: "Molecular and Metabolic Imaging of Atherosclerosis"; J Nucl Med, 45-11 (2004) pp.1898-1907.
[3] T.Mukai et al.: "A catheter-based radiation detector for endovascular detection of atheromatous plaques"; Eur J Nucl Med Mol Imaging, 31 (2004) pp.1299–1303.
[4] J.F. Briesmeister (Editor): "MCNP4C – A general Monte Carlo N Particles transport code", Los Alamos National Laboratory Report, LA-13709-M 200.
[5] Spectra-Physics, Hilger Crystals, Westwood, Margate, Kent, U.K.
[6] Hamamatsu Photonics K.K.: "Si APD S8664 series data sheet"; KAPD1012E02, Sep.2003 DN, Japan.
[7] R.Scafè et al.: "Silicon avalanche photodiodes evaluation for low-energy single-photon scintillation readout", Eurosensors XVIII, Digest of technical papers, Palombi Editore, Rome, 2004, ISBN 88-7621-282-5.
[8] M.J. Berger et al.: "XCOM: Photon Cross Sections Database", NIST Standard Reference Database 8 (XGAM), National Institute of Standards and Technology, USA.

IRDA-BASED HEART FREQUENCY MONITORING FOR MOBILE HEALTHCARE APPLICATIONS

P. LIVRERI, G.M. DI BLASI, G. TERRAZZINO

Dipartimento di Ingegneria Elettrica, Università degli Studi di Palermo, Viale delle Scienze – Edificio 9, Palermo, 90128, Italy

Recent advances in mobile technologies have greatly extended traditional communication technologies to mobile devices. Besides, thanks to VLSI integration technologies, mobile devices with high power calculation are more and more frequent available on the consumer market. So, it is possible to fit these devices with healthcare environments, which are obviously "mobile" where doctors and nurses do not have fixed workspaces. The aim of this study is to design and implement a mobile system for patient heartbeat monitoring, and to up-to-date an electronic case sheet, consultable by every hospital PCs for remote control of patient heart frequency.

1. Introduction

Nowadays, the telemedicine is an operating reality, thanks to the recent advances in electronics, telecommunications and informatics fields which create new prospects to prevention and healthcare applications by using biomedical sensors [1,2]. In particular, mobile technologies can be determinant in these medical sectors where continuous monitoring and specialist assistance are important for patient's care and life [3-5]. Wireless patient monitoring systems increase not only the mobility of patients and medical personnel but also the healthcare quality [6].

The biomedical sensors market offers many solutions in telemedicine field, in a position to satisfy several demands, overall in telecardiology. Infact, electrocardiogram (ECG) detectors, which transfers ECG data by the aid of telephone line or GPRS/Internet, are largely available but to prohibitive costs [7]. So, the market possible solutions don't allow to join the real-time medical monitoring and health service requirements with the all possible uses of consumer PCs or PDAs [8].

In this context, we developed a system capable to monitor continuously patient heartbeat and to transfer collected data or processed by them in real-time by using a mobile device, and, eventually, to interface with the same patient by learning additional news. To get an efficient and fast, but overall simple and

economic, connection between patient and medical personnel in any time and any site, we used a mobile device as notebook or PDA. This solution allows to implement telemedical specific functions with mobile calculator normal ones.

2. Telemedicine Principles

The telemedicine main objective is always to realize an efficient system by solving the problems of emergency medicine and permitting territorial decentralization of specialist competences. This opportunity is given by solutions and services based on telematics technology developed to medicine. So, local monitoring and remote hospital treatment are born as two branches of telemedicine, creating a system which can be schematized as Figure 1, where it is possible to distinguish three main components: a physiological parameter (e.g. heartbeat) gathering device, a mobile calculator device called patient unit, and a medical workstation.

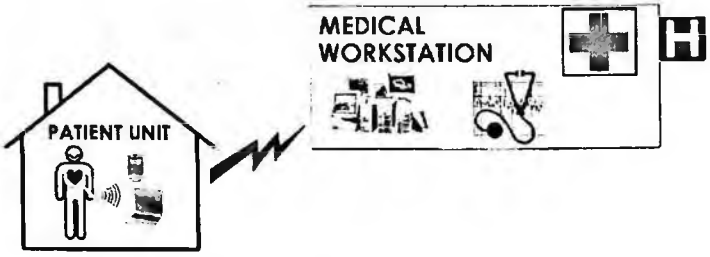

Figure 1. Telemedicine project.

The possibility to associate the frequency heart monitor device to notebook or PDA is able to realize a system with high power calculation, very flexible, light and more economic than traditional systems. The use of a PC or PDA in the telemedicine can represent the future of any physiological parameter monitoring, adding only a set of devices connected by parallel, serial, USB and IrDA ports or Bluetooth. Besides, collected data can be locally and directly processed and the results sent to one o more specialist medical workstations for necessary treatments, by permitting to seek the advice of more medical experts to the patient undependably to their distance. The advantages are also for medical personnel, as they can directly know, through a simple hospital LAN connection, all data coming from the patient units and monitor their health in real-time. WLAN and UMTS evolution are promoting more and more telemedicine applications, to allow largely hospital cost reductions.

3. IrDA-based Heart Frequency Monitoring Project

The implementing system must be in a position to gather the patient heartbeat, to evaluate heartbeats number in real-time and to transmit evaluated heart frequency to mobile device, which gets a job to elaborate and send data to hospital medical workstation.

However, in this system, an human physiologic information has to be converted into electrical signal and, simultaneously, to digitalize this information ready to use in a digital system, the project is divided in two parts, as shown in Figure 2. The analog part acquires heartbeats and amplifies gathered signal to render compatible with digital one. The digital part permits to evaluate heartbeat frequency and sends this information to notebook by using IrDA port.

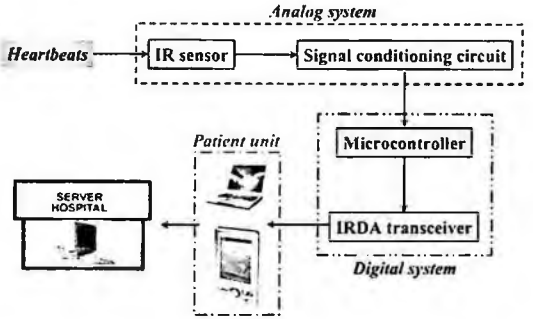

Figure 2. Diagram block of IrDA-based heart frequency monitoring system.

3.1. *Analog Part Implementation*

To convert blood vessels pressure into electrical signal containing beat number per minutes, a commercial sensor is used. A LED diode, used to emitter infrared light, and an infrared photoresistor, used to receive LED emitted radiation, inserted into a clip for ear lobe, compose this sensor. The change of ear lobe thickness, due to blood flow, permits to alter luminous radiation quantity which arrives to receiver photoresistor from transmitter diode. So, the light presence or not on photo receiver indicates heartbeat existence.

However, photoresistor electrical signal contains a large DC component (blue line) due, principally, to human tissue presence, and a low AC component (red line) due to heartbeat, as shown Figure 3. The use of a pass-high filter, implemented with an RC network, allows to eliminate the DC component and to consider only the AC one. The AC signal has an amplitude equal to 20mV, so it is possible make compatible with TTL logic by using an amplifier with a

clipping limit circuit. The obtained signal is ready to be elaborated by system digital part.

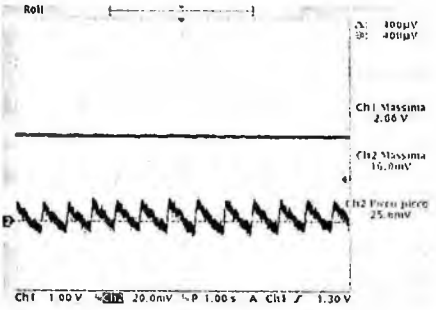

Figure 3. Electrical signal coming from commercial sensor.

3.2. *Digital Part Implementation*

The main element of digital part is a microcontroller (Microchip Technology PIC16F84). The microcontroller evaluates the time between two heartbeats in real time and with sufficient precision, permitting to know the instantaneous heart frequency and to estimate heartbeats number per minute. Besides, the microcontroller manages the IrDA controller (Microchip Technology MCP2120) to transmit through an IR transceiver realized by an LED emitter diode.

4. Prototype Implementation and Results

The IrDA-based heart frequency monitoring laboratory prototype is shown in Figure 4.

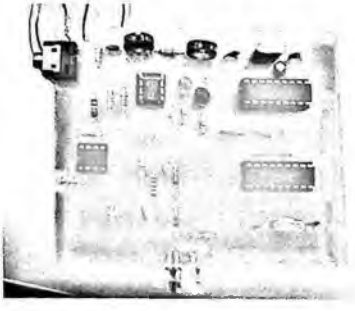

Figure 4. The developed laboratory prototype.

It has been necessary to implement a communication software driver to manage the IrDA port of mobile device. In our test the mobile device is a PC notebook based on Microsoft® Windows®XP operating system, as shown in Figure 5.

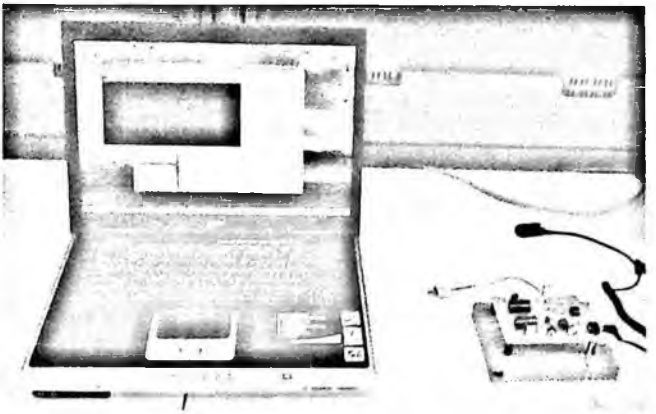

Figure 5. The prototype test system.

After testing communication channel reliability, the heart frequency monitoring prototype starts to send data as shown Figure 6.

Figure 6. Heart frequency monitoring prototype data.

In this figure, first datum represents estimated beats number per minute (bpm), obtained by second datum which is the time t_C between two heartbeats expressed in milliseconds. The mathematical relationship between two data is given by:

$$bpm = 60 \cdot \frac{1}{t_C}. \quad (1)$$

Differently from commercial heart frequency monitor device, this prototype estimates beats number per minute only heart beats couple and not averaged on more heartbeats. Infact, it is possible to notice that estimated heartbeats number changes even if it remains nearly previous evaluated value. That is a physiological normal condition because it can be little difference of time between two successive heartbeats couple.

References

1. M.R. Neuman and C. Liu, "Biomedical Sensors in Interventional Systems: Present Problems and Future Strategies", *Proceedings of the IEEE* **vol. 76 n. 9**, (1988).
2. G.L. Coté, R.M. Lec and M.V. Pishko, "Emerging Biomedical Sensing Technologies and Their Applications", *IEEE Sensors Journal* **vol. 3 n. 3**, (2003).
3. E. Kafeza, D.K.W. Chiu, S.C. Cheung and M. Kafeza, "Alerts in Mobile Healthcare Applications: Requirements and Pilot Study", *IEEE Transactions on Information Technology in Biomedicine* **vol. 8 n. 2**, (2004).
4. Y. Lin, I. Jan, P. Chow-In Ko, Y. Chen, J. Wong and G. Jan, "A Wireless PDA-Based Physiological Monitoring System for Patient Transport", *IEEE Transactions on Information Technology in Biomedicine* **vol. 8 n. 4**, (2004).
5. C.S. Pattichis, E. Kyriacou, S. Voskarides, M.S. Pattichis, R. Istepanian and C.N. Schizas, "Wireless telemedicine systems: an overview", *IEEE Antennas Propag. Mag.* **vol. 44**, pp. 143-153, (2002).
6. S.P. Nelwan, T.B. van Dam, P. Klootwijk and S.H. Meij, "Ubiquitous mobile access to real-time patient monitoring data", *Comput. Cardiology* **vol. 29**, pp. 557-560, (2002).
7. J. Dong and H. Zhu, "Mobile ECG detector through GPRS/Internet", *Proceedings on the 17th IEEE Symposium on Computer-Based Medical Systems (CBMS'04)*, (2004).
8. S. Fischer, T.E. Stewart, S. Mehta, R. Wax and S.E. Lapinsky, "Handheld Computing in Medicine", *J. Amer. Med. Inform. Assoc.* **vol. 10 n. 2**, pp. 139-149, (2003).

AN INNOVATIVE REMOTE HEALTH MONITORING SYSTEM

ALESSANDRO CONVERTINO, AGOSTINO GIORGIO, ANNA GINA PERRI
Politecnico di Bari, Dipartimento di Elettronica/ Laboratorio di Dispositivi Elettronici, Via E. Orabona, 4, 70125 Bari (ITALY)

A system intended to bring about innovation in remote health monitoring in terms of simplicity, economy and effectiveness in both domestic and hospital applications has been designed and prototyped.
It allows real-time rescue in case of emergency without the necessity for data to be constantly monitored by a medical; the unit performing a real time diagnosing electronically. When an emergency sign is detected through the real-time diagnosing system, the system sends a warning message to persons able to arrange for his/her rescue. A GPS system also provides the patient's coordinates.
The system might be useful not only to GPs but also to sportsmen. Thanks to its characteristics it can help reduce hospitalization rates and length of stays thereby improving health costs and quality of life.

1. Introduction

Nowdays, there is a growing need for inexpensive and reliable health monitoring devices [1], able to record data, to analyse them real time and, if possible, to transmit them to a receiving unit by wireless technology, but the market still does not seem to offer any reliable GPRS or Bluetooth-based, effective and low-cost health-monitoring telemetric systems.

In fact, though telemetric systems are already used in hospitals, they do not seem to fully exploit all the potential of modern technology and seem to suffer from some important limitations. In fact, many devices are specifically intended for emergencies [2] and can transmit ECG results, as well as those from the monitoring of some other parameters. Such systems are inadequate for continuous health monitoring, not easy to use and have to be managed only by qualified operators, which makes them unsuited for personal use and domestic applications. Suffice it here to mention some examples, such as the systems developed for the Ambulance and the Emergency-112 projects, where data are transmitted via GSM (with the employment of many hardware components), which results in high operating costs due to GSM time-based billing.

Current telemedicine implementation also employs WAP technology of mobile phones [3]. Such systems use "store and forward" communication, since their limited bandwidth makes real-time continuous monitoring impossible.

One of the existing systems suited for personal use and home care is the so called "teleheart system", which transmits ECG results via modem to a receiving centre using the telephone network. However, that system seems to present users with some problems as well: it only applies to ECG results and patients are compelled to keep close to the telephone socket, so that the continuous monitoring of heart activity is in fact impossible. Besides, since teleheart systems are not highly automated, expertise is needed to use them.

ECG transmission by means of handhelds is also widely known, but such a method depends on the availability of a palmtop computer and applies to a limited number of parameters with little diagnostic value.

Therefore, one of the limitations of existing devices lies in the fact that they are not portable or, better said, wearable. Another problem is connected to the necessity for an operator to analyse data while they are being collected, which results in high costs in terms of both personnel and telephone fares. Besides this common devices only allow to monitor ECG, saturation and some other parameters separately, otherwise extraordinary bandwidth would be needed in order to transfer all data, especially via GSM (at the limited speed of 9200 kbit/s). GPRS and UMTS technologies result from the development of GSM transmission of packet data.

The new telemonitoring system developed by the authors is intended to solve all problems of known technology resulting from the combination of the latest suitable telecommunication solutions (GPRS and Bluetooth) with new algorithms and solutions for automatic real-time diagnosis, cost-effectiveness (both in terms of purchase price and data transmission/analysis) and simplicity of use (the patient will be able to wear it).

The designed system also aims at allowing real-time rescue operations in case of emergency without the necessity for data to be constantly monitored.

For this purpose the new system has been equipped with highly developed firmware which enables automated functioning and complex decision-making. It is indeed able to prevent lethal risks thanks to an automatic warning system. All this occurs automatically without any intervention by the user.

The special management software enables to monitor any number of patients simultaneously leaving them free to move, as well as to create and manage an electronic case sheet for each of them.

The system meets the needs of both patients and their families. It can be suitably used in hospitals, nursing and care homes, and might be useful not only to GPs but also to sportsmen. Thanks to its characteristics it can help reduce hospitalization rates and length of stays thereby improving health costs and quality of life. Patients at risk monitored are indeed free to do anything they can with the same chance of getting aid and surviving as patients treated at hospital.

2. The new system description

The new telemonitoring system allows real-time rescue in case of emergency without the necessity for data to be constantly monitored by a medical thanks to a reliable, real-time, automatic electrodiagnostic service and alarm system to alert medical staff, families or anyone able to arrange for rescue operations.

The system is able to monitor (via GPRS and/or Bluetooth) the most relevant health parameters and environmental factors affecting health, also leaving patients free to move and allowing prompt aid.

Each monitored patient is given a case sheet on a Personal Computer (PC) functioning as a server (online doctor). Data can also be downloaded by any other PC, handheld or smartphone equipped with a browser. The system reliability rests on the use of a distributed server environment, which allows its functions non to depend on a single PC and gives more online doctors the chance to use them simultaneously.

The whole system consists of three hardware units and a management software properly developed. The units are:

- Elastic band: the sensors for the measurement of health parameters are embedded in an elastic band to be fastened round the patient's chest;
- Portable Unit (PU), having the following characteristics: wearable, wireless (GPRS/Bluetooth) and wireline (internet) connection, transmission, continuous or sampled or on demand, GPS satellite localization, real-time information devices, automatic diagnosing system, automatic alarm service, on board memory, USB port for data transfer, rechargeable battery
- Relocable Unit (RU): GPRS/Bluetooth Dongle (on PC server, i.e. online doctor);
- Management Software: GPS mapping, address and telephone number of nearest hospital, simultaneous monitoring of more than one patient, remote (computerized) medical visits and consultation service, creation and direct access to electronic case sheets (login and password).

In Figure 1 there is a picture of the PU; the very small dimensions are remarkable, even if it is only a prototype and more reduction in dimensions is possible.

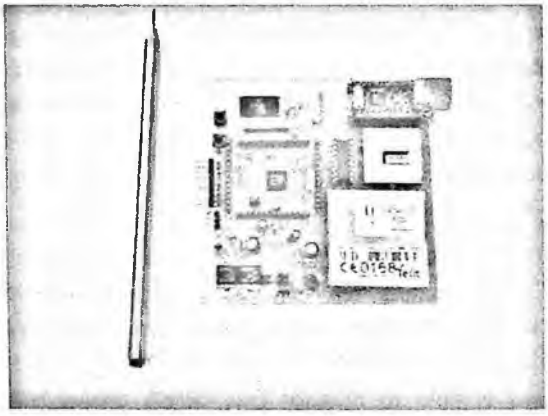

Figure 1 – A picture of the Portable Unit (PU), the main part of the telemonitoring system

The monitorable parameters are: electrocardiogram (6 derivations), heart frequency, respiratory frequency, body kinetics, body temperature, oxygen saturation of hemoglobin (non invasive), environmental pressure, temperature and humidity , position (GPS), arterial pressure. Moreover, results and diagnosis of any examination can be uploaded into the patient's case sheet by the server PC where the management program is installed. A non-invasive measuring device for glucose is also being developed.

3. The functioning: description and examples

The system, in particular the PU, collects data continuously. These are stored in an on-board flash memory and then analysed real-time with an on-board automatic diagnosis program. Data can be sent to the local receiver, directly to the PC server (online doctor), or to an internet server, which allows anyone to download them by his/her own login and password.

Data can be transmitted as follows:

1. real time continuously;
2. at programmable intervals (for 30 seconds every hour, for example);
3. automatically, when a danger is identified by the alarm system;
4. on demand, i.e. whenever required by the monitoring centre;
5. offline (not real-time), i.e. by downloading previously recorded (over 24 hours, for example) data to a PC.

In all cases patients do not need to do anything but supply power by simply switching on.

When an emergency sign is detected through the real-time diagnosing system, the PU automatically sends a warning message, indicating also the diagnosis, to one person (or even more) who is able to verify the patient's health status and arrange for his/her rescue. In order to make rescue operations as prompt as possible, the PU by its GPS receiver also provides the patient's coordinates and the Management Software provides real-time a map indicating the position of the patient.

In Figure 2 there is a picture of an electrocardiogram transmitted by Bluetooth and plotted on a Personal Computer by the proper developed management software.

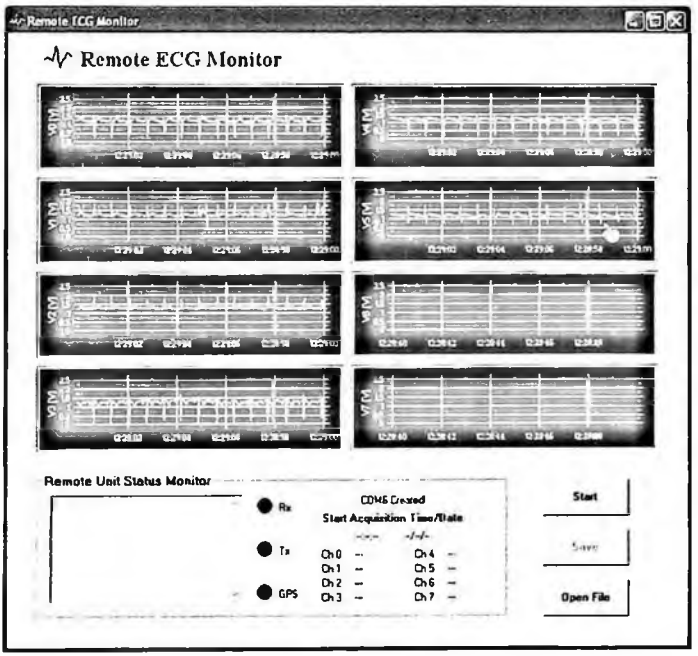

Figure 2. Example of acquisition by Bluetooth of an electrocardiogram

4. Conclusions and future development

An innovative remote health monitoring system has been designed and prototyped. The main advantages of the designed system are:

a. to monitor the most relevant health parameters and environmental factors affecting health, leaving patients free to move;
b. to avoid the necessity for data to be constantly monitored by professionals, allowing also the simultaneous monitoring of patients and, then, providing cost effectiveness;
c. to implement a reliable, real-time, automatic electro-diagnostic and alarm service allowing to arrange for rescue operations.

The main future tasks are:
1. to further reduce dimensions using a microcontroller with the USB interface embedded or FPGA architecture and a GPRS/GPS integrated module;
2. to further improve the performances of the analog filters using DSP;
3. to employ wireless sensors to make the system more and more comfortable;
4. to employ UMTS to perform remote medical visits.

References

1. E. Jovanov, A. O'Donnel Lords, D. Raskovic, P.G. Cox, R. Adhami, F. Andrasik, *IEEE Engineering in Medicine and Biology Magazine*, 49, (2003).
2. S. Pavlopoulos, E. Kyriacou, A. Berler, S. Dembeyiotis, D. Koutsouris, *IEEE Transactions on Information Technology in Biomedicine*, Vol. 2, no. 4, 101, (1998).
3. Hung, Y.T. Zhang, *IEEE Transactions on Information Technology in Biomedicine*, vol. 7, no. 2, 101, (2003)

APPLICATION OF OPTICAL FIBRE BRAGG GRATING TO ASSESS THE PERFORMANCE OF A NOVEL DENTAL IMPLANT SYSTEM

I. ABE[1], L. CARVALHO[2,3], M. W. SCHILLER[1], P. CARVALHO[2], P. LOPES[1], J. A. SIMÕES[2], J. L. PINTO[1].

1-Departamento de Física, Universidade de Aveiro, 3810-193 Aveiro, Portugal
2-Departamento de Engenharia Mecânica, Universidade de Aveiro, 3810-193 Aveiro, Portugal
3-Instituto Superior de Ciências da Saúde Norte , 4585-116 Gandra PRD, Portugal

The main aim of this work was to conceive a more reliable dental implant system to improve the load mechanism transfer from the implant to the surrounding bone media for better long term fixation. There are several design approaches to achieve this goal, such as coating the implant with bioactive materials, changing the implant's geometry or using different materials. In this work, optical Fibre Bragg Grating (FBG) sensors have been used to dynamically measure the bone response to mechanical impact in implants and evaluate load transfer.

1. Introduction

Optical Fibre Bragg Grating (FBG) sensors technology has increasingly been applied in the recent years in several practical applications since they exhibit interesting advantages such as high sensitivity, geometric versatility, electromagnetic immunity, and compactness [1].

The numerical results in Carvalho et al. [2] have suggested that an implant attached to bone, made with two different materials, might induce a more similar strain pattern as a natural tooth-bone system than other options. A more physiological strain pattern will allow bone to be well stimulated for healthy continuous process of bone remodeling [3] and good long term fixation.

In order to demonstrate that hypothesis, FBG were used to measure the strain patterns, at several locations, in bone surface, around implants attached to bovine fresh bones. Macro models of dental implants, fabricated based on the Brånemark system of Nobel Biocare, have been used.

2. Materials and Methods

Three types of dental implant macro models were manufactured, having a length of 40 mm and a diameter of 15 mm. All of them had the same overall geometry, based on the model standard of Brånemark system of Nobel Biocare, but were made combining different materials. The first one was made only in steel alloy (type 1), the second was made combining steel alloy and plastic ABS (type 2) and the third one was made only in plastic ABS (type 3) (Fig.1).

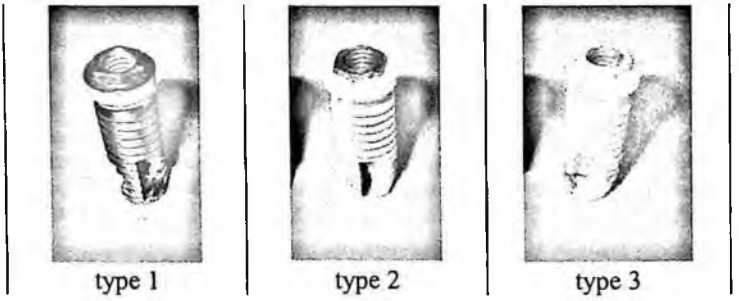

Fig.1: Macromodels of dental implants

They were screwed in bovine fresh cancellous bone, with a maximum torque of 35 N.cm. The two sensorial FBG were glued onto the surface of the bone, along a vertical line parallel to the longitudinal axis of the implant 23mm away and 17.5mm apart from each other. FBG 1 was located at half height of the implant, while FBG 2 was approximately at the level of the lower end of the implant.

Fig.2 – General view of the experimental setup, exhibiting the bovine bone with the FBG glued onto its surface and with the implant screwed into it.

The bone was settled in a support, to avoid displacements. The dynamic load was simulated by the strike of a mass of 172g, dropped by gravity from a height of 270mm. The dynamic response was recorded and analysed, in order to obtain the strain pattern induced by the three implants.

The Fibre Bragg Gratings (FBG) used, were recorded by illuminating the fibre with UV radiation in standard telecommunications fibre optic with 125μm of cladding diameter. The estimated length of the grating was 2mm.
The signal has been measured using a dedicated opto-electronic system, that dynamically demodulates optical intensity for a signal of a few kHz.
It is based on the matching of two spectral responses: one of a broad filter (transmission) and another of a FBG (reflection) (Fig.3) [4].

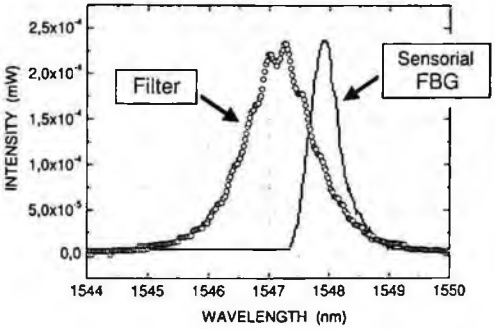

Fig.3 – Filter and FBG spectra

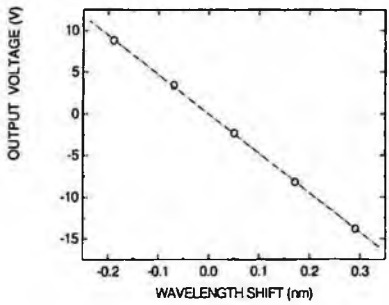

Fig.4 – Calibration line: –slope=50V/nm

The latter one, when shifting according to applied stress, originates different optical intensities at the system's photodetector. The voltage output, normalized with input optical power to avoid undesired and meaningless output fluctuations. The optoelectronic system was also tested for linearity between strain and output voltage. Although any curve would be acceptable and would provide a calibration procedure, the test resulted in a straight line with slope equal to 50V/nm.
The acquisition system acquires data at a sample rate of 100 KHz and is able to detect dynamic signals with frequency components until 5KHz.
Sensitivity as well as dynamic band is determined by the filter slope shown in Fig.4.
Resolution and bandwidth are determined by the FBG optical power, so a high power ASE source has been used instead of a LED.
The conversion of voltage data into strain data was carried out using the slope value of the curve in Fig.4 (50 V/nm) and the known factor of 1,2 pm/με [1].

This latter value has been obtained in previous work and is confirmed by the literature [1]. The resulting constant is **50/3** με/V.

3. Results and Discussion

From the data acquired, it was obtained and displayed in Table 1, the strain distribution, with time, for each implant. For each implant, the strain was measured at the surface of the bone, at two points, FBG 1 and FBG 2.
For all implants and considering the two measuring point, the impact load was the same, as mentioned above.

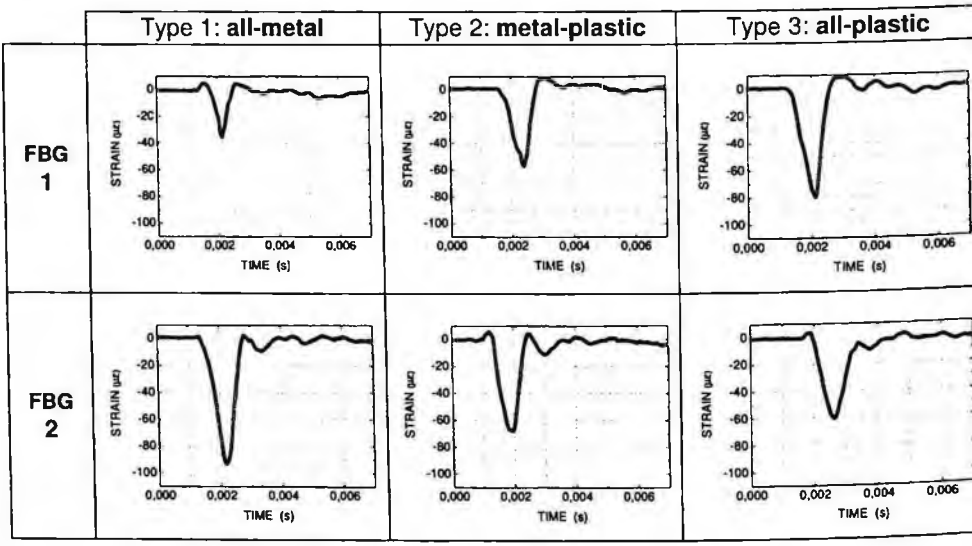

Table 1 – Strain distribution as a function of acquisition time for the three types of dental implants and for the two measuring points.

For all the implants and considering the two measuring points, they present the same strain pattern. For the type 1, the strain is mainly transmitted at the apical region of the implant. Instead of the type 3, the strain is mainly transmitted at the neck of the implant. It is type 2 that presents a more uniform strain distribution. This indicates that the strain impact is not equally transmitted in space, meaning that some parts of the surrounding bone are subject to higher stress values, that could result in bone damage.

Highly localized strain is undesirable since it endangers bone fixation around the implant. An equally distributed strain around the implant can stimulate positively bone remodelling and thus a good long-term dental implant fixation.
These results could only be made possible due to the use of small sized, well localized strain sensors as FBGs are. Around them a complete optical and electronic setup had to be designed and implemented having in account the high degree of sensitivity, stability and accuracy required.

Conclusions

It was implemented an optical and electronic setup with a good sensitivity, stability and accuracy for measure dynamic strains, in biomechanics applications.
Results have shown that a combination of plastic and metal alloy can induce more physiological strains inside the bone, in the same way the alveolar bone, adjacent to a natural tooth does. It is the physiological strain level in bone that could stimulate positively the remodeling process and guaranties a long term fixation of dental implants.

Acknowledgments

This work was supported by FCT — Fundação para a Ciência e Tecnologia (Portugal), through project POCTI/42474/EME/2001 and scholarship SFRH/BPD/14513/2003.

The authors acknowledge to Instituto de Investigação for funding Marcelo W. Schiller.
The authors acknowledge to PRODEP III, Acção 5.3 (supported by the Portuguese Government and the European Fund) for funding Lídia Carvalho.

The authors would also like to thank Dr. Jean Carlos Cardozo da Silva for his work on the 1st version of the opto-electronic device for dynamic measurements.

References

1. A. Othonos, "Fibre Bragg Grating", Rev. Scient. Instrum, 68(12), pp.4309-4341, 1997.

2. Carvalho, L., Pereira, J., Ramos, A. e Simões, J. A.,, "Sistema de implante dentário não convencional: um estudo preliminar", Métodos Numéricos en Ingeniería, pp. 74 (in CD-ROM) Ingeniería V, J. M. Goicolea, C. Mota Soares, M. Pastor e G. Bugeda (Eds.), Sociedade Española de Métodos Numéricos en Ingeniería, 2002.

3. D. R. Carter, "The relationship between in vivo strains and cortical bone remodelling", *CRC Crit. Rev. Biomed. Engr.*, **8** (1), 1983.

4. S. M. Melle, K. Liu, R. M. Mesures, "A Practical Fiber Optic Bragg GratingStrain Gauge System", APPLIED OPTICS, v.32, n.19, pp 3601-3609,1993.

A NEW SMART SENSOR FOR NON INVASIVE BLOOD'S GLUCOSE MONITORING

ROBERTO DIANA, AGOSTINO GIORGIO, ANNA GINA PERRI

Dipartimento di Elettrotecnica ed Elettronica, Politecnico di Bari, Via E. Orabona 4, 70125 Bari, Italy

The impedance spectroscopy is a very promising technique for monitoring the blood glucose, very useful when frequent measurements are required. Our approach for monitoring the glucose level changes makes use of an AC analysis of the skin impedance over a wide frequency range, which is scanned until the optimal frequency, corresponding to the best sensitivity, has been reached. Our sensor has been optimized to work in frequency range 1-200MHz, in which the best performances in terms of electrical changes in the blood can be provided.

1. Introduction

It is well known that high values of blood glucose can indicate serious illnesses, such as diabetes, which in the long-term can produce several complications affecting many body tissues and organs.

Frequent blood glucose measurements allow the proper administration of insulin, so improving the health and reducing the possibility of complications for diabetics. Therefore, a system for blood glucose monitoring, providing detailed information throughout the day, is required. A number of alternative strategies are available, most of them based on invasive or semi-invasive approaches.

Non-invasive glucose monitoring based approaches are very attractive, particularly for patients which require frequent measurements without any inconvenience [1]. There are several methods which are based on non invasive approaches. The most interesting technologies are the 1) near infrared light (NIR) spectroscopy, 2) far infrared radiation (FIR) spectroscopy, 3) reverse iontophoresis, 4) optical rotation of polarized light, 5) impedance spectroscopy. Each method has technical problems to overcome.

The NIR spectroscopy [2] makes use of a light source with wavelengths in the near infrared spectrum. The glucose produces, at each wavelength, an absorption of a small amount of the light, which can be investigated by spectroscopy techniques. Unfortunately, this approach requires frequent

recalibrations especially after alterations in the blood hemoglobin level or state of hydration.

The FIR Spectroscopy measures the absorption of the far infrared radiation contained in natural thermal emissions by blood glucose. The blood glucose level can be spectroscopically determined by comparing measured and predicted amounts of thermal energy at the skin surface. The main problem of the FIR spectroscopy is related to the very small level of the thermal emission.

The reverse iontophoresis makes use of an electric current to extract and measure tissue fluid from the skin. The method can not be applied for quick variations of the blood glucose levels, because the glucose level in the fluid does not follow rapidly the glucose variations in the blood.

The polarimetry measures the optical rotation of polarized light. When polarized light passes through a fluid that contains glucose, the plane of polarization rotates proportionate to the glucose concentration. This method can be applied to measure the glucose level of the aqueous humor of the eye. The polarimetry suffers from a small signal level which does not allow to obtain high values of sensitivity. Moreover, quick shifting in the blood glucose levels can not be investigated because of the lag time between blood and aqueous humor glucose concentrations.

One of the most important non-invasive approach for blood glucose monitoring is the impedance spectroscopy, which can investigate the relaxation processes of complex systems in an extremely wide range of characteristic times from 10^{-12} to 10^{4} s. In particular, the impedance spectroscopy is sensitive to intermolecular interactions and can monitor cooperative processes.

As reported in [3], the glucose concentration can not be measured directly, since any change in the blood glucose does not affect the dielectric spectrum in the MHz frequency band. The measurement can be made, therefore, only indirectly, by measuring the AC conductivity change which is related to the blood's glucose levels [4]. This conductivity variation affects the electric polarization of cell membranes, thus resulting in the skin permittivity change.

In order to not lose the sensitivity to this effect, we must choose a working frequency not greater than 200 MHz. At the same time, the working frequency has not to be too low in order to avoid the electrode polarization. This paper describes a new blood glucose sensor, based on the impedance spectroscopy technique, which performs the investigation in AC mode and operating in the frequency range between 1 and 200 MHz.

2. Sensor architecture

The general scheme of our sensor is shown in Fig. 1.

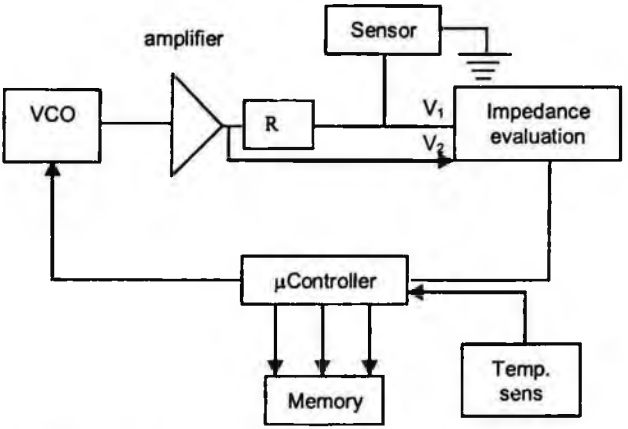

Figure 1. General scheme of the impedance spectroscopy based blood glucose sensor under investigation

The sensor evaluates the glucose level by comparing a sine signal with the same signal passed through the passive filter constituted by the skin impedance and the resistor R. The skin impedance, which depends on the glucose concentration, is calculated by the following, well known, voltage divider based relationship:

$$z = R\frac{V_1}{V_2 - V_1} \tag{1}$$

The above calculation has to be made for several values of frequency in the range 1-200MHz, in order to evaluate the impedance minimum which provides the best sensor sensitivity. To investigate this wide frequency range a suitable voltage controlled oscillator (VCO) has been designed to provide a sine signal with a high linearity. The output signal, coming from the impedance evaluation block, can be processed by the microcontroller which finds the minimum frequency and stores it in a semiconductor memory. The general scheme is,

then, constituted by an analog part, which provides the high frequency sine signal, and a digital section which processes this signal.
The Eqn. (1) can be easily solved in log forms. To this purpose, the impedance evaluation block is constituted by two differential and two logarithmic amplifiers, as shown in Figure 2:

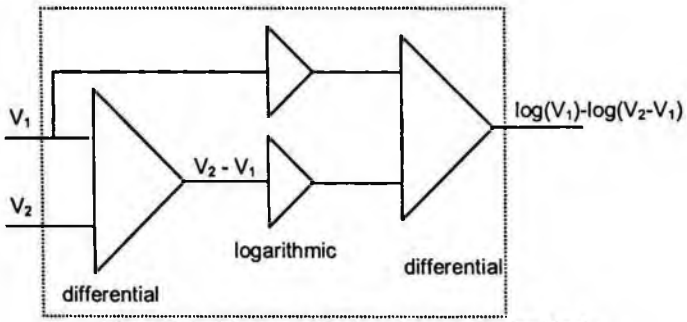

Figure 2. Architecture of the impedance evaluation block

The VCO has to produce a sine function with a frequency changing in a wide range. We have designed an oscillator by using a high frequency programmable waveform generator (Maxim MAX038) operating up to 20MHz output frequency. In order to raise the operating frequency, we have used three voltage output multipliers (AD835) which have been set to work as frequency doublers. The architecture of our oscillator is shown in following figure:

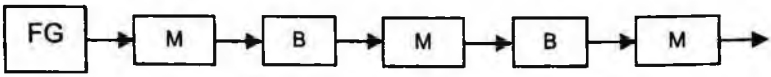

Figure 3. Architecture of the high frequency voltage controlled oscillator

where:

FG=frequency oscillator (MAX038);
M=Frequency doubler (AD835);
B=Buffer (AD8075)

3. Conclusions

We have presented the architecture of an impedance spectroscopy based blood glucose sensor. The sensor is designed to make a continue noninvasive analysis and is more comfortable then other solutions for patients which require frequent measurements without any pain. The device is constituted by commercial integrated circuit and is, then, compact, light and easily transportable.

References

1. A. Caduff, E. Hirt, Y. Feldman, Z. Ali, L. Heinemann, *Biosens. and Bioelectron.*, 1 (2003)
2. K. Maruo, M. Tsurugi, J. Chin, T. Ota, H. Arimoto, Y. Yamada, M. Tamura, M. Ishii, and Y. Ozaki, *IEEE J. of Selected Topics in Quantum Electronics*, **9**, 322 (2003)
3. K. Fuchs, and U. Kaatze, *J. Phys. Chem.*, **B105**, 2036 (2001).
4. Hayashi, Y., Livshits, L., Caduff, A., Feldman, Y., *J. Phys. D: App. Phys.* **35**, 1 (2002).

A NEW DILATATION SENSOR FOR RESPIRATION RATE MEASUREMENT

DOTT. RIC. G. GELAO, PROF. ING. A. GIORGIO, PROF. ING. A. G. PERRI, DOTT. M. QUINTO

Dipartimento Elettrotecnica ed Elettronica, Politecnico di Bari,
Via Orabona 4, Bari 70125, Italia
E-mail: perri@poliba.it; http://www.dispositivielettronici.com

Automatic breathing detection is an important medical issue in apnea syndrome in newborn and/or quite old people, or to detect the response of body to physical activity. We detect the breathing using a conductive rubber to sense chest displacement. At the best of our knowledge, this is the first sensor based on the conductive rubber specifically designed to measure the breathing frequency. The conductive rubbers offer quite cheap and sensitive devices for dilatation measurement.
Signal detection is easier than in piezo sensor, compared to inductive displacement it is more simple. We expect it could be more rugged than inductive sensors and then other kind of resistive sensors. We are also studying ageing of this device for electrical and mechanical stress, and we plan to test more kind of conductive rubber. The application of the belt is not so tight to be oppressive so that it could be worn for long time, allowing us to plan for continuous measurement and recording.

1. Introduction

We are developing an apparatus for health monitoring, consisting in a wearable multi-sensors attached to a small board which is connected via the GPRS net to a computer in the hospital. This system would allow 24 hours logging and warning dispatching, our complete system architecture is shown elsewhere [1].

For breathing sensing we use an already known method involving a belt to sense the thorax dilatation, but we apply a new kind of belt dilatation sensor on the belt.

We sense the resistance changes of the rubber due to stress elongation, the voltage drop on the rubber is amplified (suppressing the DC component).

As much as we know the application of the conductive rubber is new in breathing detection, it is quite cheap and sensitive. We are now working on ageing behaviour of this rubber, and looking for new kind of conductive rubbers with better ageing on very long periods.

2. Breathing monitoring

In literature [2-5] it is possible to find two main methods for breathing monitoring. In the first one, the air flow is sensed while in the second one the breast dilatation is sensed.

Air flow monitoring is accurate but is very uncomfortable, since it requires tubing mouth and nose or placing sensors in mouth and in nose. This would rule out 24 hours logging. For our project we are so forced toward the breast dilatation monitoring, this may be quite less accurate, it is sensitive to arms movements but it is much more comfortable.

For breast dilatation monitoring, piezoelectric strain gauge sensor are quite problematic, since the charge generated at typical breathing frequencies (0.25Hz) are difficult to amplify. Accelerometers are not suitable, because the tiny acceleration available (about $0.02g$) compares with the gravity acceleration. But the situation is even worse since the accelerometer only sees the vertical component of the gravity, that is $g\cos\theta$ (where θ is inclination angle of the patient), that could vary largely with times comparable with respiration times according to the variations of the angle θ when patient bows.

Breast dilatation monitoring is well accomplished using a breast elastic belt, so sensing the belt stress makes it possible to sense breathing.

Aside from several stress sensor we have designed a new, very interesting conductive rubbers sensor, being it also quite cheap and easy tailored. Conductive rubbers are made mixing carbon or iron powder in the chemical reactants used to produce rubbers. They have been applied as flexible conductors and as pressure sensors, but we did not found application as dilatation sensors. Indeed conductivity of these rubbers are sensitive to stress, but among the large kind of conductive rubbers available, not all are suited for this application.

3. The conductive rubber selection

We look for conductive rubber satisfying these specifications:

- high sensitivity to the stress
- rubber should stand the stress applied to the breast belt, about 10N
- moderate conductivity, between 0.1Ωm and 10Ωm

We tested a conductive rubber coming from the CERISIE institute in Milan (Italy), but too stiff and the resistivity was not so sensitive to our range of stress.

To test the rubber we took a sample (19cm long, 3cm wide, 1mm thick) and we connected it at the ends using two couples of conductive metallic plates (1.5cm long, 6cm wide). We observed in our sample unpredictable resistance

variation with mechanical stress, while sometimes the resistance rose, sometime decreased. We suspect that this comes from contact problems due to the not so low resistivity (2.3Ωm). This material was rejected.

We test also conductive plastic foams, but again we had problems with electric contacts between foams and a metallic plate, since in this case the contact surface is much less than apparent geometric contact surface, furthermore the foam collapses slowly when compressed in the conductive plates, making contact inefficient. This material also was rejected.

We did not used any special contact pasta since we wanted to keep us away from chemical troubles and to have easy building.

We tried another sample of conductive rubber, from Xilor, whose resistivity was only $7 \cdot 10^{-5}\Omega m$, constituted by an aggregate of small conductive spheroids, about 20μm wide, see figure 1. The conductivity is controlled by the contact surface area between spheroids, this area varies according to the mechanical stress, so that resistivity is high sensitive to the mechanical stress.

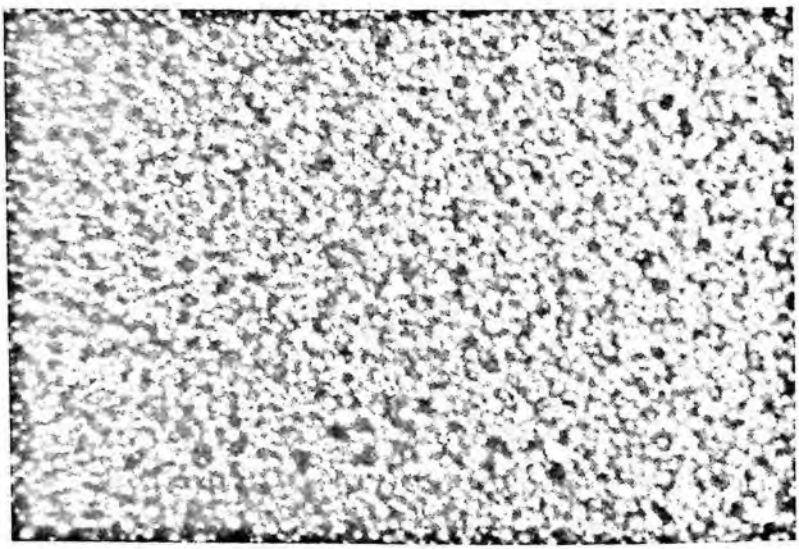

Figure 1: Microscopic view of the conductive rubber we use, on a broken side. It is clear the structure composed of microspheres of rubber.

This material did not satisfied our initial request, it is not so strong, and it has a low resistivity, but the sensibility was so high that we selected this material to develop a prototype.

We took a sample 120mm long, 20mm large and 0.3mm thick that was fit in the breast belt, at the place of a piece of belt (see figure 1 for a microscopic picture of the sample). Since the sample is not capable to stand all the belt stress, it is not feasible a full belt built only with this kind of conductive rubber.

To solve this problem, a non conductive rubber was added in a mechanical parallel to our conductive rubber.

Two couples of small iron plates where tightened to each end of the rubbers sandwich to ensure electrical connections.

4. The electronic interface

The resistance of conductive rubber, about 1Ω, was measured with the four wires method, two wires to inject a constant current, two wires to sense the voltage. We did not used the well known Weston bridge method because the sensor resistance drift due to the ageing would had required a continuous bridge balancing.

While the breathing rate ranges from about 0.1Hz to 3Hz but the breast movement spectrum has more power in the range from about 0.4Hz to 3Hz, the front end amplifier was connected to the sensor through a capacitor with a low frequency cut off at 0.4Hz, while another capacitor produces upper a cut off at 3Hz.

The dilatation signal after the front end was clear, but it is sensitive to arms movements. After the first amplification stage, signal went through more stages: a peak detection, see figure 2, a pulse shaper and a frequency to voltage converter, see figure 3 .

More detail on the rest of analogue chain are shown elsewhere, see [1].

5. Results and perspective

As shown in figure 2, the signal is clear and noiseless; it is also shown the signal from the peak detector which is well behaved.

As already said, the system has been successfully test on a wide breathing rates interval (see figure 3), but still remain the ageing problem.

Indeed the rubber resistivity raised tenfold after few hour of usage on the belt. While this could be compensated with an automatic gain control at the front end amplifier, much better would be to use the compression method.

A second problem is the sensibility to the arms movements, which could trigger false breathing pulses. This is intrinsic to the belt method, but the effect is not so frequent compared to the breathing rate.

In conclusion, our sensor has been successfully tested, the remaining problems are minor. We still are looking for other kind of conductive rubbers, cheaper or with better ageing. We plan to look for new rubbers with better mechanical properties (more stiff) better electrical properties (higher resistivity) better mechanical ageing, and cheaper.

We are also planning to implement and test another method where the breathing is sensed measuring the electrical impedance between some point of the breast, see [6].

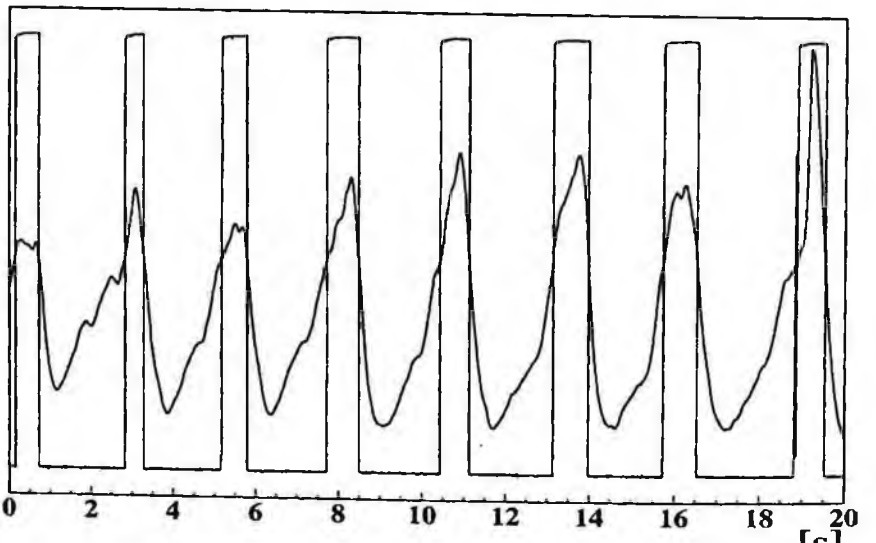

Figure 2. Sampled signals: the wavy signal is from the sensor while pulses are from peak detector.

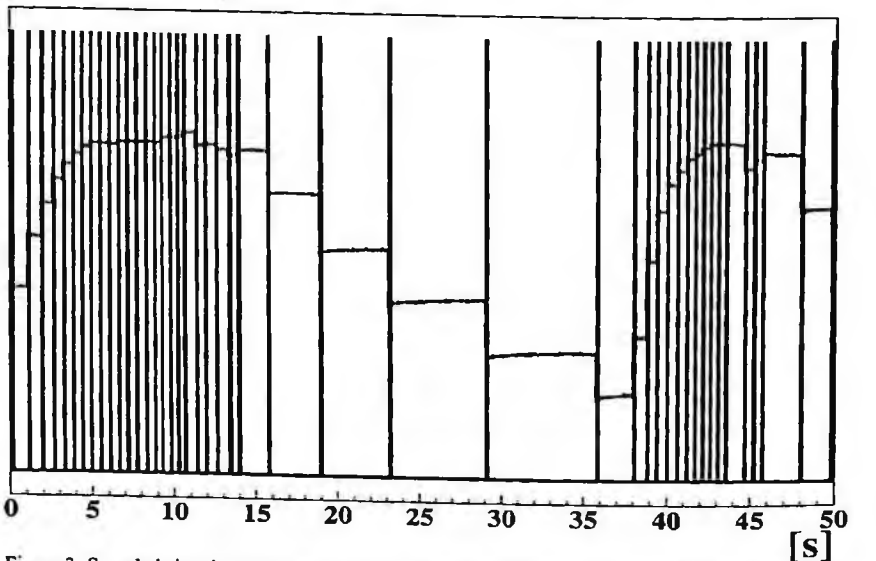

Figure 3: Sampled signals: the stepwise signal is from the S&H while pulses are from peak shaper.

Acknowledgments

We would like to thank Ing. Fausto Casa, director of CERISIE institute in Milan, for the conductive rubber sample offered for free.

References

1. G. Gelao, A. Giorgio, A.G. Perri, M. Quinto "A new dilatation sensor for the respiration rate measurement", in these proceedings
2. J. G. Webster ed., Medical instrumentation, J. Wiley (1998)
3. J. Moore ed., Zouridakis ed., Biomedical technology and devices handbook, CRC (2004)
4. F. P. Branca, Fondamenti di ingegneria clinica, Springer (2000)
5. T. Togawa, T. Tamura, P. A. Öberg, Biomedical transducers and instruments, CRC (1997)
6. J.J. Carr, J.M Brown, Introduction to biomedical equipment technology, Prentice Hall (2001)

OPTICAL-BASED PRESSURE MONITORING SYSTEM FOR ROBOT-ASSISTED SPINAL ENDOSCOPY

U. BERTOCCHI, C. STEFANINI, L. ASCARI AND P. DARIO
CRIM Lab, Scuola Superiore Sant'Anna, Pisa, Italy
E-mail: ulisse@crim.sssup.it

In this paper we present a non-contact pressure control system based on the well-known water-column principle. It is a part of a complete system for robot-assisted endoscopy of human sub-arachnoid spinal space. The sensing elements are represented by optical proximity sensors. Pressure maintaining is a fundamental task for spinal endoscopy because unacceptable pressure variations inside sub-arachnoid space may cause serious damages to the patient's vital activities. The system was tested during in-vitro experiments on an artificial mock-up of the spine and during in-vivo experiments on pigs, which proved the reliability of the system.

1. Introduction

Spinal-cord endoscopy refers to the exploration of the sub-arachnoid space, which is a narrow area around the spinal cord between two meninxes named *dura mater* and *pia mater*. It is filled with cerebrospinal fluid (CSF), a transparent liquid where very delicate structures like blood vessels and nerve roots fluctuate. The classical approach to spine surgery has in general important drawbacks; the endoscopic approach overcomes many of them; nevertheless, the endoscopic exploration of the sub-arachnoid space is still extremely challenging for the surgeon. A robotic approach to spinal endoscopy requires the design and development of a series of mechatronic devices [1], and it mainly aims to guarantee the safety of the intervention. Such a task is also accomplished by implementing supervising modules, which elaborate sensorial data and extract useful information [2], in order to prevent non-acceptable parameters configurations or dangerous catheter movements.

One of the most important parameters to be monitored is the pressure inside the explored space [3] [4]. In fact, as a time-varying quantity of liquid must be injected into navigated space through the tip of the endoscope catheter, for reducing the friction during insertion, the pressure tends to increase. Even small variations in the sub-arachnoid pressure can have serious consequences like retinal detachment. Silicon pressure sensors have been found non-optimal for our

purposes [5]. Such a kind of sensor would require proper dedicated hardware to accomplish signal amplification which usually introduces noise in measuring that affects the system accuracy. Moreover, since they must be inserted into the explored space, they should be sterilized, and it is possible only for the most expensive ones, and they should be connected by a proper wiring in order to acquire pressure values.

In conclusion, silicon-based pressure sensors seem not to be the best choice for pressure measuring in such a small and infection-sensitive environment, like sub-arachnoid space.

In this paper we describe a non-contact pressure sensor, based on the water-column principle, which doesn't need to be sterilized because it is located outside of the explored space. Moreover, it provides us with a high sensitivity to pressure variations which is needed to ensure a safe intervention. Water-column principle is one of the most employed methods in medical applications for closed-cavity pressure measuring.

2. Description of the pressure-monitoring system

2.1. *System overall organization*

A glass pipe is directly connected to the sub-arachnoid space through a flexible tube. It connects the pipe with the proximal ending of the catheter: the measure is performed close to the catheter insertion point. Changes in the pressure inside the sub-arachnoid space cause variations in the height of the liquid column in the pipe.

Pressure is monitored by checking out the level of the CSF column by using proper sensors located around the pipe. In order to maintain an optimal pressure level, the system controls a pump and a valve. The pump is employed to inject artificial CSF into the sub-arachnoid space whereas the valve is employed to adjust the amount of CSF to be extracted. In particular, the valve modulates the extracting liquid flow by closing and opening the flexible-tube connection between the sub-arachnoid space and an aspirator. The surgeon is allowed to change the intensity of liquid injection flow through a specific command in the system Graphical User Interface.

The control strategies are implemented on microcontrollers which receive sensorial information and generate proper PWM signals to modulate valve and pump activity in order to maintain optimal pressure values and to handle critical pressure conditions.

2.2. *Pressure sensor*

Artificial-CSF column level is evidenced by putting a float into the pipe. Its weight and diameter have been chosen to ensure a high sensitivity to liquid height variations and smooth movements inside the pipe. In order to localize the float position, four proximity infrared sensors are positioned around the glass pipe. They are arranged in a column array (see Figure 1). The length of the float is greater than the distance between two adjacent optical sensors, in order to get a higher sensibility and to keep the float detectable in any moment of the intervention, but also not so long to activate more than two sensors simultaneously. In our particular implementation, the length of the float is 4.7 cm, the distance between the proximity sensors 2 and 3 is 3.2 cm, whereas the distance between the sensors 1 and 2 or between the sensors 3 and 4 is 2 cm. The diameter of the pipe is 6mm.

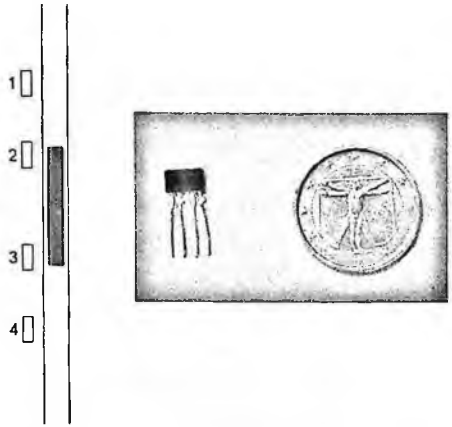

Figure 1: Pressure sensor pipe with float and proximity sensors indicated by numbers 1, 2, 3 and 4. The employed proximity sensor is shown comparing its size to a coin.

The resolution of the overall pressure sensor could be tuned by changing the distance between adjacent proximity sensors or the length of the float. In such a manner, it is possible to manufacture systems sensitive to tiny pressure variations. Such a manufacturing choice must be done by taking into account information about acceptable pressure variations but also an evaluation of the CSF-column change rate in order to get a stable system behavior. Further, by fixing the sensors array at different heights, various optimal internal pressure values to maintain can be established. That's an important feature because such a

value can change depending upon the patient. It could also be not-precisely-known before the intervention. In this case, also during the exploration, the sensors height may be easily modified, so as to obtain an on-line adjustment of the desired pressure conditions.

2.3. *Pressure maintaining strategy*

The pressure is maintained by varying the injected and extracted flows of CSF by means, respectively, of the pump and the valve depending upon what sensors are active. The tuning of the injected liquid flow is up to the surgeon and the automatic monitoring system is allowed only to stop liquid injection in some particular circumstances we will describe in the following. This design choice is due to the fact only the surgeon is completely aware of the delicate tissues in front of the catheter tip and he/she has proper knowledge to chose the better liquid-flow intensity in order to obtain a safe navigation. Differently, the modulation of liquid extraction by exploiting the valve is completely up to the monitoring system and the surgeon is not allowed to act on it.

When the two central sensors are active, the pressure conditions are considered optimal. In such a situation the system tries to keep this pressure state by tuning the valve in order to reach the optimal liquid extraction rate. The case in which the float activates only one of the central sensors is treated as the previous optimal case because the pressure variations are tiny.

The pressure variations become important when both the sensors 1 and 2 or the sensors 3 and 4 are active. When it happens for the two lower sensors, it means the pressure is decreasing and the system tries to re-establish optimal pressure conditions by stopping liquid extraction. On the other hand, when the activated sensors are the upper ones, the pressure is increasing and the system raises the extraction rate. In both the two previous cases, the surgeon sets the injected-liquid flow.

When only one of the most external sensors is active, that is sensor 1 or sensor 4, it means the pressure conditions are getting more and more dangerous and it requires an appropriate treatment. Precisely, if the lower sensor is active the liquid extraction is stopped and the surgeon can ease the re-establishment of optimal pressure conditions by modulating injected-flow rate. Alternatively, if the activated sensor is the upper one, the injection is stopped even if the surgeon has set it in a different way, and the extraction of liquid is increased in order to get optimal conditions as fast as possible. In both the previous cases the navigation is not permitted. Thus, the surgeon is not allowed to realize catheter movements. All the commands he generates on the joystick or on other human-

machine-interface buttons, for accomplishing catheter steering or backward/forward movements, are blocked by the electronics. The surgeon is allowed to navigate only after the optimal pressure level has been re-established.

Because of the high aspiration rate of the aspirator, the modulation of liquid extraction by using the valve requires a particular treatment. Such a rate cannot be appropriately modulated to be useful for our purposes only by tuning the duty cycle of the PWM signal to manage the valve. The liquid-extraction rate couldn't get small enough to extract tiny amount of artificial CSF as strongly needed to accomplish a proper pressure maintaining in such a small area. Thus, the valve PWM signal variable parameters are not only the duty-cycle value but also a number of wave periods. Such a number denotes the length of an *aspiration cycle*. Thus, the aspiration rate is modulated by varying both the duty cycle and the number of periods of the aspiration cycle. More in detail, if we suppose the aspiration cycle to accomplish a given aspiration rate is composed by N periods, the PWM signal wave would be high only in the first period for an interval whose length is specified by the duty cycle, whereas during the following N-1 periods the wave is kept down, as shown in Figure 2. In such a way we have performed a multiplicative effect of duty-cycle modulating power.

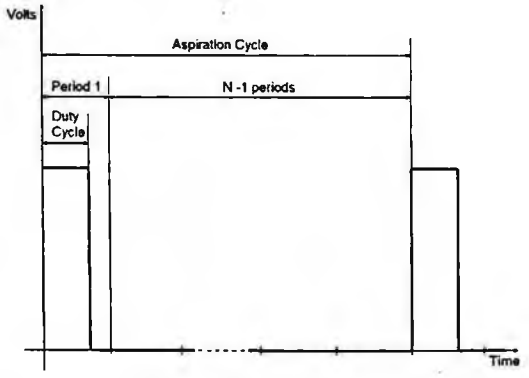

Figure 2: Aspiration Cycle, for a particular aspiration rate, and its parameters: duty cycle and number of periods

3. Tests

The sensory system was first tested during in-vitro experiments on an artificial mock-up of the spine, simulating a real endoscopic navigation. Subsequently, the system was tested on prolonged in-vivo experiment on animal (pig). Results

showed the pressure maintaining module is reliable in ensuring a stable pressure keeping. The complete system has a good sensitivity in following pressure variations and reactivity in re-establishing optimal pressure conditions when it gets sub-optimal or dangerous pressure values. For most of the intervention time the pressure was kept at the optimal level. Occasionally, it reached sub-optimal conditions which were correctly managed by the system, in such a way to re-establish optimal pressure conditions quickly. During the experiments the height at which the pipe was fixed has been changed because it was needed to adapt the sub-arachnoid internal pressure to the mutable patient conditions, and it was accomplished easily.

Acknowledgement

This work has been carried out under the european project Mi.N.O.S.C. (MicroNeuroendoscopy of Spinal Cord – contract N. QLG5-CT-2001-02150), in the framework of the "Quality of Life and Management of Living Resources" Program. The authors would like to thank the European Commission for co-funding the project.

References

1. L. Ascari, C. Stefanini, A. Menciassi, S. Sahoo, P. Rabischong and P. Dario, *A new active microendoscope for exploring the sub-arachnoid space in the spinal cord*, Proceedings of the 2003 IEEE International Conference on Robotics and Automation, Taipei, Taiwan, September 14-19, 2003.
2. L. Ascari, U. Bertocchi, C. Laschi, C. Stefanini, A. Starita and P. Dario, *A segmentation algorithm for a robotic micro-endoscope for exploration of the spinal cord*, Proceedings of the 2004 IEEE International Conference on Robotics and Automation, New Orleans, LA, April 2004.
3. K.Y. Kwan, K.V.I.S. Kaler and M.P. Mintchev, *High-pressure balloon catheter for real-time pressure monitoring in the esophagus*, IEEE 2002.
4. C. Carlsson, E. Soderqvist, L-A. Brodin, G. Kallner, J. Hultman, H.Elmqvist and S. Saha, *Initial experience with a thin single segment pressure and conductance catheter for measurement of left ventricular volume*, Proceedings of the 23rd Annual EMBS International Conference, Istanbul, Turkey, October 25-28, 2001.
5. O. Tohyama, M. Kohashi, K. Yamamoto and H. Itoh, *A fiber-optic silicon pressure sensor for ultra-thin catheters*, The 8th International Conference on solid-state sensors and actuators, and Eurosensors IX. Stockholm, Sweden, June 25-29, 1995.

OPTICAL SENSORS FOR THE CONTROL OF THE METABOLISM OF ADIPOSE TISSUE

F. BALDINI, A. GIANNETTI, A. MENCAGLIA
CNR-IFAC, Via Madonna del Piano 10, 50019 Sesto Fiorentino, Firenze, Italy

A.BIZZARRI, M. CAJLAKOVIC, C. KONRAD
Joanneum Research,Chemical Process Develop.& Control, Steyrergasse 17, 8010 Graz, Austria

One of the objective of the four year European project CLINICIP - Closed Loop Insulin Infusion in Critically Ill Patients - is the study of the metabolism of the adipose tissue in intensive care patients, by means of continuous monitoring of pH, pO_2, pCO_2. Microdialysis is the approach followed for the extraction of the sample from the subcutaneous adipose tissue; the drawn interstitial fluids flows through a microfluidic circuit formed by the CMA60 microdialysis catheter in series with a glass capillary on the internal wall of which the appropriate chemistry is immobilised. The modulation of the fluorescence lifetime is the optical working principle used for the detection of oxygen and carbon dioxide, whereas absorption modulation is the one utilised for the pH detection. On this basis, two different optoelectronic units were developed for the interrogation of the glass capillary, one for life-time measurements and the other for absorption measurements. Preliminary tests demonstrated a resolution of 0.03 pH units for pH; $\leq$ 0.55 mmHg for oxygen and $\leq$ 0.6 mmHg for carbon dioxide; and an accuracy of 0.07 pH units for pH; $\leq$ 1 mmHg for oxygen and $\leq$ 1.5 mmHg for carbon dioxide. In vitro tests with the catheter CMA60 were performed for the metabolities O_2 and pH and a recovery of about 100% and 70% respectively was measured.

1. Introduction

Metabolites such as pH, pO_2 and pCO_2 are informative indicators of the conditions of a living system and can be valuable in determining the physiologic status of critically ill patients. Bedside monitors used to measure these levels should be reliable, compact, inexpensive and fast responding. For this reason, several methods of continuous monitoring were developed during the past years. The continuous monitoring of small molecules into the interstitial fluid is a promising approach to reduce diagnostic blood loss and painful stress associated with blood sampling.
In this paper the realization of optical sensors for the monitoring of pH, pO_2, pCO_2 as metabolites of the adipose tissue is described. Microdialysis is the approach followed for the extraction of the sample from the subcutaneous adipose tissue; the drawn interstitial fluids flows through a microfluidic circuit formed by the CMA60 microdialysis catheter in series with a glass capillary on the internal wall of which the appropriate chemistry is immobilised. The modulation of the fluorescence lifetime is the optical working principle used for the detection of oxygen and carbon dioxide, whereas absorption modulation is the one utilised for the pH detection.

2. Methodology

2.1. Chemical Protocols

The sensing layer for the oxygen sensor is composed by polymerised polystyrene deposited on the glass surface, in which Platinum(II) tetrakis-pentafluorophenyl-porphyrine, PtII-TFPP, the fluorescence of which is quenched by oxygen, is entrapped.

The carbon dioxide sensor is based on the dual luminescence referencing (DLR)[1], in which two fluorophores having the same excitation wavelength and largely different decay times are combined in the sensing layer. The fluorophore characterised by the shorter lifetime is the pH-dependent indicator, 8-Hydroxypyrene-1,3,6- trisulfonate (HPTS), whereas the other one, characterised by the longer lifetime, is Ruthenium(II) tris(4,7-diphenyl-1,10-phenanthroline) ($Ru(dpp)_3^{2+}$) and is independent from the pH. HPTS was dissolved in tetraoctylammonium hydroxide (TOA-OH) and the whole cocktail was saturated with carbon dioxide. An excess amount of base (TOA-OH) was added to act as a lipophilic bicarbonate buffer system in the form of TOA^+ $HCO_3^-xH_2O$[2], together with plasticizer tributyl phosphate.

The sensing layer of the pH sensor is based on the pH indicator phenol red which is covalently bound directly to the glass surface by means of the Mannich reaction[3]. This reaction consists of the condensation of formaldehyde with the primary amines of the silane groups immobilised on the glass surfaces and the active hydrogens of the phenol red.

2.2. Optoelectronic Instrumentation

Two different optoelectronic units were developed for the interrogation of the glass capillary, one for life-time measurements and the other for absorption measurements.

The optoelectronic measuring unit for O_2 and CO_2 detection is constituted by an optoelectronic read-out module which is connected through an electric cable to the interrogating unit. The module consists of a metallic housing containing the optics and the electronic pre-amplification stage for the interrogation of 2 serially connected sensor capillaries and the Peltier elements for the temperature regulation of the sensor capillaries. For each capillary, there is a light source (a LED emitting at about 517 nm, for the O_2, and at about 470 nm for the CO_2) to excite the

luminescence signal and a detection module, which consists of a Si-photodiode, and an opportune optical filter to separate the luminescence signal from other optical signals. In Figure 1 a photo of this measurement unit is shown.

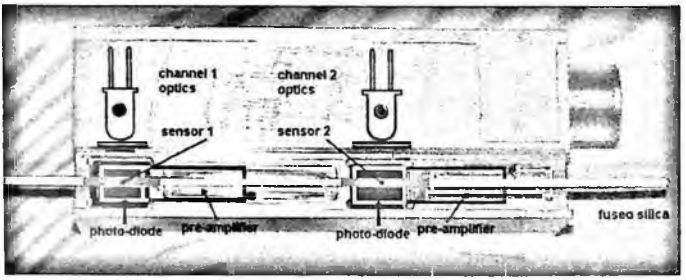

Fig. 1. Picture of the optoelectronic measurement unit for the interrogation of two sensor capillaries (sensor 1 and sensor 2 indicated in the picture) on the same line. The two capillaries are connected by means of fused silica tubing. The allocation of the optics and of the pre-amplification stages for the interrogation of the 2 sensors is also shown. The same set-up is used for the O_2 and CO_2 detection, but with the suitable optical components.

An optoelectronic unit for the interrogation of the pH sensor immobilized onto a capillary was developed. Optical fibres (core diameter: 200 μm) are used to couple the capillary with the unit. The capillary placed inside a black plastic piece having on its lateral surface precise holes for the two fibres, used to carry the light from the source to the capillary and to collect the modulated light, respectively. The optoelectronic unit makes use of a light emitting diode at 590 nm as source and a photodiode as detector. A suitable data processing allows to avoid the influence coming from source fluctuations and air micro-bubbles. The block diagram of the optoelectronic unit is shown in Figure 2.

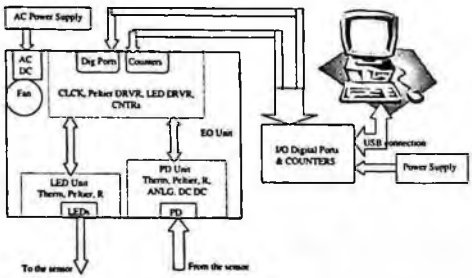

Fig. 2. Block diagram of the optoelectronic unit for the interrogation of the capillary.

2.3. Interstitial Fluid Extraction by Means of Microdialysis

The catheter CMA60 is used for the interstitial fluid extraction. The tests using this catheter were performed for oxygen and pH measurements. Figure 3 shows how the connection of the capillary to the catheter is realised: the plastic tubing of the catheter CMA60, which belong to the circuit of extraction of the interstitial fluid, is cut as short as possible, in order to reduce the exchange with O_2 and CO_2 present in the environment, and connected to the fused silica, which goes to the capillary sensor. The second plastic tubing of the catheter is used to push the carrier solution from a reservoir into the catheter.

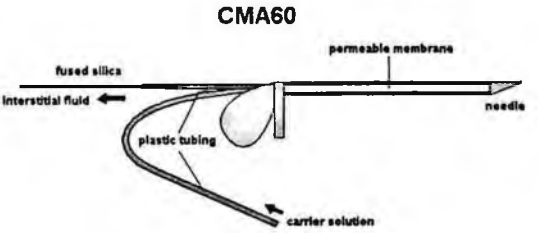

Fig. 3. Scheme of the connection to the catheter CMA60.

In an *in vitro* measurement set-up for the oxygen, the critically ill patient may be simulated by a glass vessel containing a measurement medium, such as artificial interstitial fluid, dialysed blood, a physiological solution or even simply distilled water. The glass vessel is kept at constant temperature in the physiological range 37-42°C by means of a water bath thermostat.

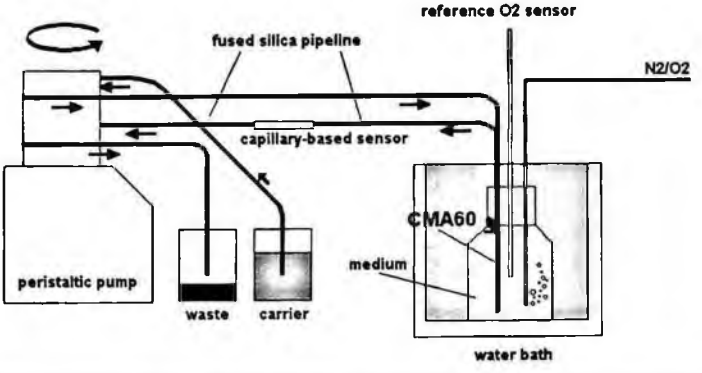

Fig. 4. Measurement set-up for the in-vitro determination of the O_2-recovery rate of a catheter CMA60.

The oxygen partial pressure in the measurement medium is set by equilibrating a mixture of pure nitrogen and oxygen in well determined concentrations into the medium. The carrier solution, ringer solution, is pumped from a reservoir in equilibrium with air by a peristaltic pump into the catheter. The dissolved oxygen in the vessel is measured by means of a reference fibre optic optochemical sensor. A scheme of the measurement set-up is shown in Figure 4.
The CMA60 catheter was also used for the pH measurements. The configuration used is the same shown in Figure 4 and the medium this time is a buffered solution. The tubing of the CMA60 was connected by means of an home made connector with a glass capillary which is then joined to the sensing capillary. The first tests were carried out using phosphate buffers as both the carrier and the sample just to show the capability of the system to measure correctly the pH. As for the oxygen sensor, the ringer solution was then used as the carrier medium.

3. Results and discussion

Laboratory tests on all the metabolite sensors were performed in order to investigate the accuracy, stability and resolution of the sensors over a period of several hours[4].
The results of the calibration procedure of O_2 and CO_2 are shown in Figure 5. Flow rate was 1 µl/min.
On the basis of the data obtained with the different concentrations of APTS used (ranging from 5% and 50%), 10% was the chosen concentration of the silane in the preparation of the capillary, being the working range of interest for intensive care applications between 6 and 8 pH units. Figure 6 shows the response curve for

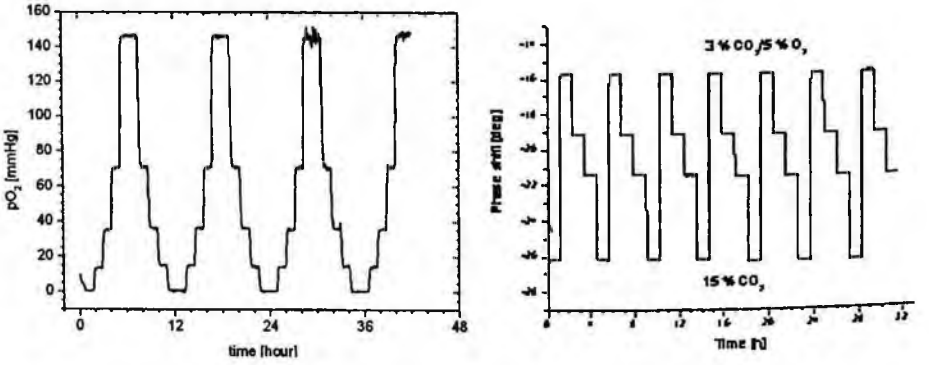

Fig. 5. Stability tests of the O_2 and CO_2 sensors. Response of sensor and reproducibility when exposed to different concentration of O_2 (on the left) and CO_2 (on the right).

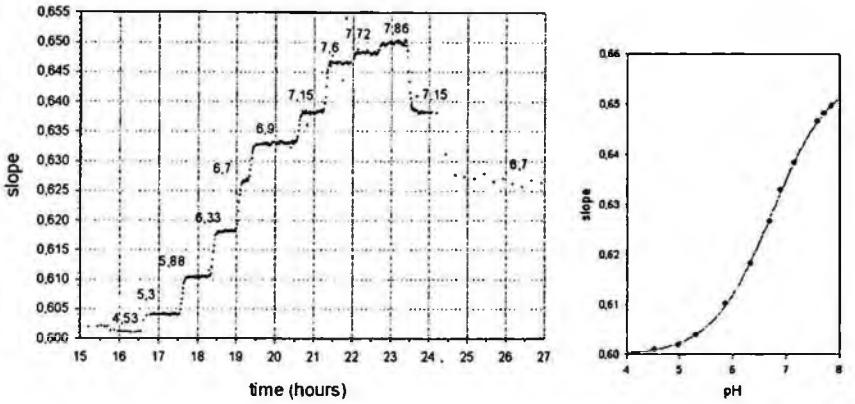

Fig. 6 Response curve of a glass capillary prepared with 10% APTS (on the left) and related calibration curve (on the right).

different pH steps and the related calibration curve.

For what concern the recovery rate of the catheter CMA60, measurements of O_2 and pH were performed. Figure 7 (on the left) shows an example of the measurements performed with capillary-based oxygen sensors at 2 µl/min flow rate and at of 37°C with the measurement set-up schematically shown in Figure 4. The pO_2 measured by the capillaries are compared together with the oxygen measurements performed directly in the glass vessel by means of a reference optical fibre sensor. By definition the ratio between the actual oxygen content in the glass vessel and the content measured in the capillary is the recovery rate of the catheter. The so calculated recovery rate in percent is almost 100%.

For the recovery rate of the pH, the same ringer solution was used as the carrier and

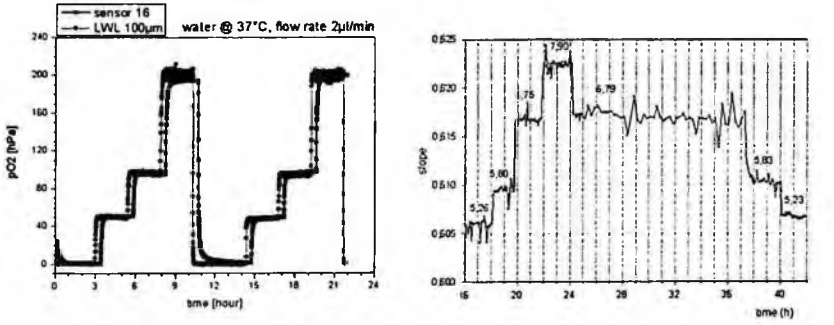

Fig. 7. Comparison between the oxygen measurement in the capillary (thick curve), by means of the sensing layer, and in the glass vessel (thin curve), by means of a reference electrode (on the left of the diagram). Response curve of the capillary sensor at different pH values (on the right of the diagram).

the CMA60 catheter was dipped in buffer solutions at different pH values. In this experiment a flow velocity of 5 microl/min was used; with this velocity it was possible to collect a reasonable amount of liquid in order to allow the measurement of the pH of the waste.
Figure 7 on the right shows the response curve of the sensor at different pH values. The recovery rate (about 70% at pH 8) was calculated on the basis of the change in the concentration of hydrogen ions.

4. Conclusions

Three capillary sensor systems for the detection of pH, pO_2 and pCO_2 were developed. Two different interrogation units were developed for the fluorescence life-time-based measurements of dissolved oxygen and carbon dioxide and for the absorption-based measurements of pH. The chosen principles provide the sensors with good repeatability and stability of calibration curves. An accuracy of 0.07 pH units, $\leq$ 1 mmHg and $\leq$ 1.5 mmHg for pH, for oxygen partial pressure and carbon dioxide partial pressure respectively was achieved. The calculated recovery rate for the oxygen sensor, using the CMA60 catheter, was almost 100%, and, although a recovery rate of 70% is obtained at pH around 8, it should be stressed the fact that this value corresponds to a change of only 0.14 pH units. The fact that the *in vivo* measurement will be carried out with a flow velocity of 1 microl/min (5 times slower than the utilised flow velocity) implies that the error in the pH measurements due to the recovery of the hydrogen ions through the CMA60 catheter can be considered negligible.
The performances of the developed sensors fulfil the requirements for their utilisation for the measurement of the interstitial fluid in intensive care patients. Next steps are related to the behaviour of the capillary sensors when exposed to biological fluids and to the first tests on animals.

References

1. Klimant, I., Huber, C., Liebsch, G., Neurauter, G., Stangelmayer, A., Wolfbeis, O.S., "Dual Lifetime Referencing (DLR) – a New Scheme for Converting Fluorescence Intensity into a Frequency-Domain or Time-Domain Information", in Valeur, B.; Brochon, J.-C. (Eds.), New Trends in Fluorescence Spectroscopy. Applications to Chemical and Life Sciences, Springer, Berlin-Heidelberg, Germany, 2001, pp. 257–274.

2. Mills A., Chang Q., McMurray N., "Equilibrium studies on novel colorimetric plastic film sensors for carbon dioxide" *Anal. Chem.*, 64, 1992, pp. 1383-1389.
3. Arend M., Westermann B., Risch N., "Modern Variants of the Mannich Reaction", *Angew. Chem. Int. Ed.*, 37, 1998: 1044-1070.
4. Baldini F., Bizzarri A., Cajlakovic M., Giannetti A., Konrad C., Mencaglia A., "Interstitial pH, pO2 and pCO2 controlled by optical sensors", Proc.SPIE 5993, *Advanced Environmental, Chemical and Biological Sensing Technologies III* (23-26 Ottobre 2005, Boston, Ma, USA), pp.599309-1 - 599309-9, 2005.

AGLAIA: A NEW, PRESSURE SENSOR-BASED ELECTRONIC MEDICAL DEVICE FOR THE ANALYSIS OF LUNG SOUNDS

AGOSTINO GIORGIO, FRANCESCO LOIACONO, ANNA GINA PERRI

Politecnico di Bari, Dipartimento di Elettronica, Laboratorio di Dispositivi Elettronici, Via E. Orabona, 4, 70125 Bari (ITALY)

The idea of the new electronic medical device we propose, named "*Aglaia*", arose in response to the growing need perceived by medicine for high-tech diagnostic aids combining such features as reliability and specifity with non-invasive techniques.
Aglaia allows the effective auscultation, the accurate processing and the detailed visualization (temporal and frequency graphs) of any lung sound. Then, it is suitable for the continuous real-time monitoring of breathing functions, resulting very useful to diagnose respiratory pathologies. It provides medical specialists with a totally non-invasive high-engineering device able to detect and analyse the widest number of data for the monitoring of the respiratory system by the simple recording and evaluation of lung sounds being a substantiated correlation between lung sounds and diseases

1. Introduction

1.1. *Auscultation and analysis of lung sounds*

Aglaia is an electronic medical device intended to provide medical specialists with a totally non-invasive high-engineering device able to detect and analyse the widest number of data for the monitoring of the respiratory system. It performs the monitoring and the analysis of respiratory health by the simple recording and evaluation of lung sounds [1, 2].

In order to give evidence of the importance of the auscultation of lung sounds as a medical practice, suffice it to remind that the objective examination of a patient always starts from the (stethoscope) "auscultation" of his/her chest.

Lung auscultation is still nowadays a widely used diagnostic method, which is accounted for by its usefulness and simplicity of execution. Indeed it is a completely non-invasive technique which provides direct information on the structure and the functioning of the respiratory system.

The quality alteration of lung sounds (i.e. variations of such characteristics as their intensity, duration or frequency) is very often directly related to respiratory disease.

1.2. *Beyond the stethoscope*

Despite its advantages stethoscope auscultation has also some well-known limitations consisting in some problems and criticality which have not been overcome yet, though many changes and improvements have been being made to attain higher performances (traditional models now coexist with a fairly wide range of electronic stethoscopes).

Nevertheless, when using a stethoscope, the recognition and differentiation of lung sounds depend on nothing else but the individual's hearing abilities, experience and skillfulness. As a result the auscultation and interpretation of sounds performed by means of this instrument have a consistent subjective component.

This accounts for the need to go beyond the stethoscope (whether electronic or not) both to process the acquired signal by means of automatic calculation devices (thereby removing subjectivity) and to perform auscultation on a larger surface by placing sensors all over the thorax simultaneously.

Thanks to its specific sensors (acoustic sensors and/or vibration sensors), which can either be applied to the body surface with a wearable elastic band or attached separately with adhesive tape, *Aglaia* allows the effective auscultation, the accurate processing and the detailed visualization of any lung sound.

Aglaia diagnoses pulmonary pathologies by a detection technique based on the correlation between lung sounds (which are previously decoded and classified) and diseases [3].

2. Main Features

Aglaia is a new technological tool specifically designed for the continuous real-time monitoring of breathing functions and therefore very useful to diagnose respiratory pathologies. It has been prototyped, as it can be seen in the picture of Figure 1

A specific management software program enables the user to process and save the acquired signals as well as to plot different graphs of them.

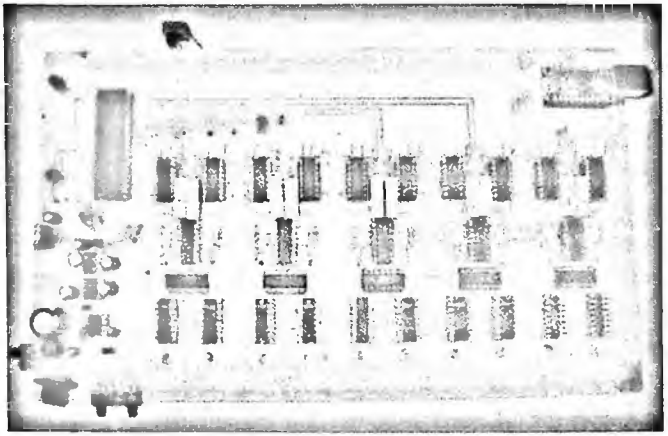

Figure 1. The prototype: a double-sided printed circuit board.

Aglaia is able to plot the graph of a signal both while recording it (real time) and after saving it (see Figure 2). The following options are available:

- temporal graph of a breathing sound;
- frequency graph of a breathing sound;
- spectrogram of a breathing sound;
- temporal graph of the airflow (optional);
- measurement of both airflow and inspiratory/expiratory volume (optional).

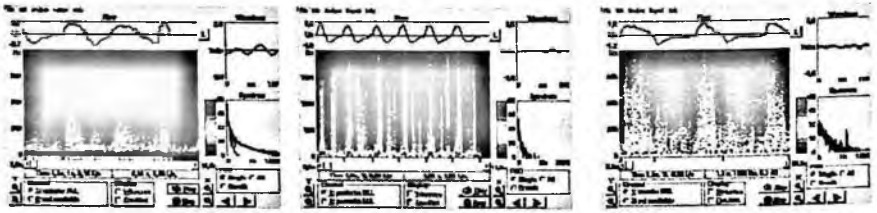

Figure 2. Graphs of some lung sounds (respectively *Normal, Crackle, Wheeze*).

Aglaia's configuration options also allow to choose the number of the channels to be displayed and those to be examined, as well as to preset a different acquiring time for each channel and an automatic detection procedure where the user is notified of pathologies by a warning message or an alarm.

Aglaia's main features:

- extreme simplicity of use;
- high miniaturization (available also with SMD components);
- USB interface ;

- microcontroller based system;
- ten on board acquisition channels;
- simultaneous acquisition;
- specific channel for the pneumotachograph (optional);
- good resolution of the acquired signals (12 bit or 16 bit);
- high immunity from noise and environmental interference assured by signal gitalization;
- expandability for new applications and future improvements (through updating of the microcontroller firmware);
- plug and play module for the sensors;
- reasonable price of the end system.

3. Conclusions and future applications

Recent research has pointed out the effectiveness of the frequency analysis of lung sounds for the diagnosis of pathologies [4].

The experiment illustrated below shows that computerized tomography (CT) results perfectly match those of a simple frequency analysis of previously recorded lung sounds.

Many studies [5] have been carried out on the frequency analysis of lung sounds and researchers have set the threshold for the detection of pulmonary pathologies at 500Hz (see Figure 3).

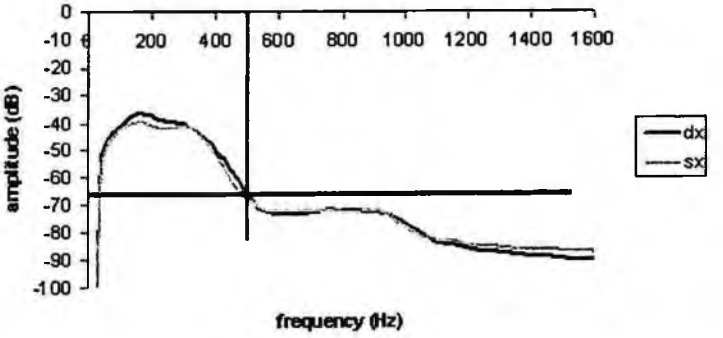

Figure 3. FFT – spectrum of a lung sound in a patient with no pulmonary pathologies.

Spectrum components over that threshold (500Hz) may be indicative of pulmonary disease.

It is widely known that in patients treated with mechanical ventilation a gradual PEEP increase (PEEP = positive end-expiratory pressure) results in a progressive re-expanding of alveoli which were previously collapsed due to a pathology.

The pictures in Figure 4 shows how a gradual PEEP increase – from 5 to 20 – has effected a gradual reduction in lung damage (marked with a grey circle), thereby leading to improvement in the patient's respiratory health.

The CT results shown in the first column perfectly match those of the frequency analysis on the right .

Moreover, there are also research projects about pulmonary acoustic imaging for the diagnosis of respiratory diseases. In fact, the respiratory sounds contain mechanical and clinical pulmonary information. Many efforts have been devoted during the past decades to analysing, processing and visualising them [6].

We can now evaluate deterministic interpolating functions to generate surface respiratory acoustic thoracic images [7].

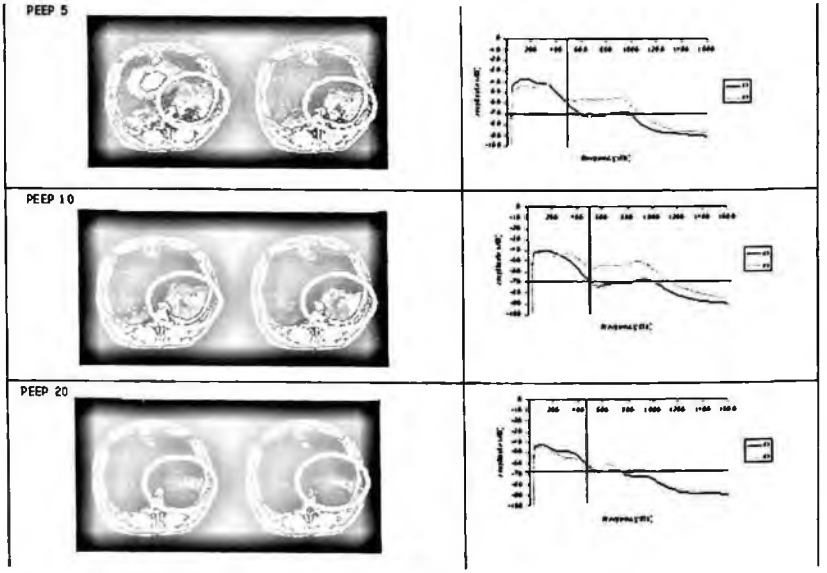

Figure 4. Correlation between CT results and spectrum analysis of lung sounds.

References

1. A.R.A. Sovijärvi, J. Vandershoot, J.E. Earis, Standardization of computerized respiratory sound analysis, *European Respiratory Review*, 2000, 10:77, p. 585.
2. J.E. Earis, B. M. G. Cheetham, Future perspectives for respiratory sound research, *European Respiratory Review*, 2000, 10:77, pp. 641-646.
3. Hans Pasterkamp, Steve S. Kraman, and George R. Wodicka, Respiratory Sounds: Advances Beyond the Stethoscop, Am. J. Respir. Crit. Care Med., Volume 156, Number 3, September 1997, 974-987.
4. Munakata M, Ukita H, Doi I, Ohtsuka Y, Masaki Y, Homma Y, Kawakami Y. Related Articles, Links Spectral and waveform characteristics of fine and coarse crackles. *Thorax*. 1991 Sep;46(9):651-7.
5. A.Vena, G. Perchiazzi, G. M. Insolera, R. Giuliani, T. Fiore, Computer analysis of acoustic respiratory signals, Modelling biomedical signals-Editors: Nardulli G. e Stramaglia S., *World Scientific Publishing*, pp. 60-66, Singapore, 2002.
6. Martin Kompis, MD, PhD, Hans Pasterkamp, MD, and George R. Wodicka, Acoustic Imaging Of The Human Chest, *Chest* 2001, 120:1309–1321.
7. S. Charleston-Villalobos, S. Cortés-Rubiano, R. González-Camarena, G. Chi-Lem, T. Aljama-Corrales, Respiratory acoustic thoracic imaging (RATHI): assesing deterministic interpolation techniques, - *Medical & Biological Engineering & Computing*, vol. 42, No. 5, pp:618-626, September 2004.

A WEARABLE, WIRELESS, LONG-TERM RECORDING ELECTROCARDIOGRAPH, IMPROVING THE NON-INVASIVE DIAGNOSIS OF CARDIAC DISEASES

ALESSANDRO CONVERTINO, AGOSTINO GIORGIO, ANNA GINA PERRI

Politecnico di Bari, Dipartimento di Elettronica, Laboratorio di Dispositivi Elettronici, Via E. Orabona, 4, 70125 Bari (ITALY)

We have designed a microcontroller-based medical device for long term recording electrocardiograph (Holter applications) allowing data from up to 12 channels to be stored, thus providing the diagnostic capabilities of the static electrocardiograph (ECG) together with the wearability and the long term registration of the cardiac activity. Thanks to its specific sensors, embedded in a kind elastic band, it is possible to place on the thorax many electrodes without reducing the movement potentials. Moreover, the elastic band is provided with a wireless module (Bluetooth) to send the data to the recorder unit. The storage support is a flash card. Therefore, the new system is miniaturised and results more comfortable than the commonly used taperecorder type portable electrocardiographs. The microcontroller permits to implement a diagnostics algorithm and/or to download real time the data by UDP channel.

1. Introduction

1.1. *State of the art*

Nowdays, the most used tape-recorder type electrocardiographs for the long term registration provide the acquisition of two or three channels thus allowing the detection of a limited number of pathologies and missing crucial details relevant to the morphology of the heart pulse and the related pathologies, given only by a static electrocardiogram (ECG) executed in the hospital or in medical centers [1 - 3]. Moreover, the sampling frequency for the analog to digital conversion of the signal, for the best known portable ECG, is typically lower than 200 Hz, thus missing important medical data carried out by the electrocardiograph signal. Finally, the most used medical devices for long term registration (Holter applications) of cardiac activity are generally so uncomfortable especially due to their dimensions.

We have designed and prototyped a new medical device for Holter applications intended to overcome the above mentioned limitations and to advance the state of the art.

In fact, the designed device presents the features/advantages listed in the following section.

1.2. *Advantages of the new system*

1. Data from up to 12 channels;
2. Sensors, embedded in a kind elastic band;
3. Possibility to place on the thorax many electrodes without reducing the movement potentials;
4. The elastic band mounting a wireless module (Bluetooth) to send the data to the recorder/storage unit;
5. The system is miniaturised and results more comfortable;
6. Implementation of a diagnostics algorithm and/or to download, in real time, the data by UDP channel

2. System architecture and prototype

The system's core is a microcontroller-based architecture. It is composed by: multiplexed internal ADC with a 12 bit resolution, 8K bytes Flash/EE program memory; 32 Programmable I/O lines, SPI and Standard UART; Normal, idle and power-down operating modes allow for flexible power management schemes suited to low power applications.

The whole system has been also prototyped. The picture in Figure 1 shows the electrocardiograph recorder/storage unit. The small dimensions are remarkable even if a further reduction is possible.

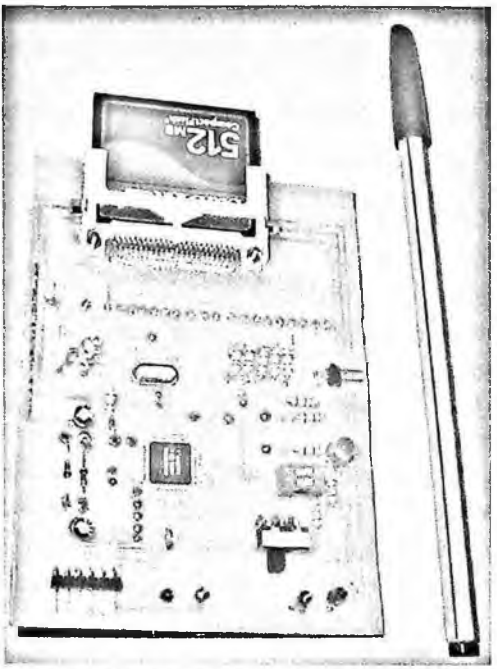

Figure 1. Picture of the prototyped new electrocardiograph receiving unit

3. Results

The management software to data-download has been properly developed by the authors, being it custom for this application.

It receives the data from the electrocardiograph and allows to store/plot them. In Figure 2 a draft of an acquisition example is shown.

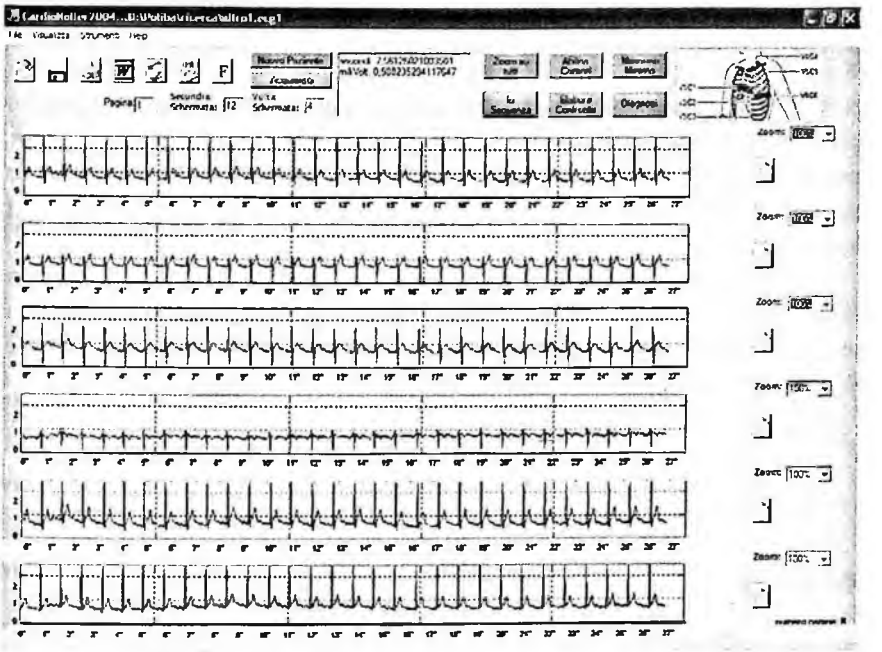

Figure 2. The main view of the management software properly developed for the new portable ECG

The management software allows to view/plot one or more channels, to make a real-time automatic analysis of the incoming signal and to perform digital filtering. In fact, in Figure 3 is plotted the Fourier Transform of the incoming signal performed by the software, useful to make a real time filtering if needed to improve the quality of the ECG. A wavelet filtering is also available. The operator has to evaluate only the frequencies to suppress, after seeing the Fourier Transform of the signal, and the software performs the signal filtering.

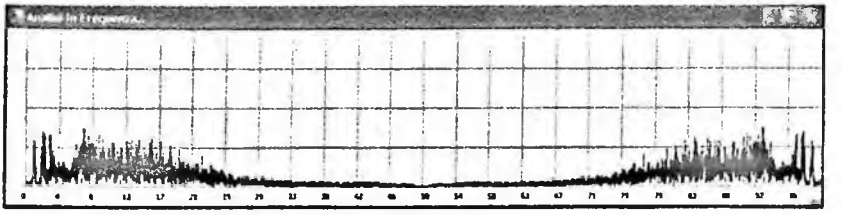

Figure 3. The Fourier Transform of the incoming ECG signal useful to perform a fast filtering if needed.

4. Conclusions and future development

We have designed and prototyped a new, long term recording electrocardiograph, intended to be very comfortable to wear and user friendly to use. The sensor band is provided with a wireless transmitter unit to reduce the problems due to the presence of cables. The management software has been also properly developed, allowing it also very important functions as digital filtering and automatic diagnosys.

As future developments we address the implementation of the compression algorithm to reduce the dimension of the stored files. Moreover, the translation on DSP/FPGA-based architecture will be done and a further reduction of the dimensions is possible in future thanks to the use of SMD components.

References

1. J.J. Carr and J.M. Brown, *Introduction to Biomedical Equipment Technology,* fourth edition, Prentice Hall (2001);
2. J.G. Webster, *Bioinstrumentation*, Jhon Wiley & Sons, Inc. (2004);
3. E. Jovanov, P. Gelabert, R. Adhami, B. Wheelock, R. Adams, *Real Time Holter Monitoring of Biomedical Signals DSP Technology and Education Conference DSPS'99*, August 4-6, 1999, Houston, Texas.

GAS SENSORS

GAS SENSITIVE LIGHT EMISSION PROPERTIER OF TIN OXIDE NANOBELTS

A. BISMUTO, S. LETTIERI, P. MADDALENA[1]

CRS Coherentia & Dipartimento di Scienze Fisiche, Università di Napoli "FedericoII", Complesso Universitario di Monte S. Angelo, Via Cintia 80126, NAPOLIi (ITALY)

G. FAGLIA, C. BARATTO, E. COMINI, G. SBERVEGLIERI

Sensor Lab – CNR-INFM Brescia University, Via Valotti 9, 25133 BRESCIA (ITALY)

L. ZANOTTI

IMEM-CNR, Parco area delle Scienze 37/A, 43010 Fontanini PARMA (ITALY)

We investigate on the light emission properties (photoluminescence) of tin oxide nanobelts systems, synthesized by thermal evaporation of oxide powders under controlled conditions. By pumping the nanobelts samples either by ultraviolet or blue light a strong light emission is obtained, whose spectrum is broad and peaked in the green region. It is observed that the photoluminescence spectrum of the samples is significantly quenched when the sample surface interacts with nitrogen dioxide, even at concentriation as low as few ppm. Therefore, we performed time-resolved photoluminescence measurements in order to determine the effect of gas interaction on the recombination time of the excited states. The results are discussed in terms of a very fast charge transfer across the nanostructure/molecule interface.

Keywords: Nanostructures, Tin oxide nanobelts, Time-resolved photoluminescence, Gas sensing.

1. Introduction

Chemical sensing based on nanostructured materials and devices has attracted enormous attention. As a matter of fact, solid-state sensors based on conventional metal oxide films suffer of some limitations: for instance, most existing metal oxide thin-film sensors work at elevated temperatures with sensing limitations around 1 ppm or even higher[1,2]. Nanowires or nanobelts made of metal oxides can deliver better performances because of their large surface-to-volume ratios. For instance, tin oxide (SnO_2) nanobelts have been demonstrated to detect 3 ppm NO_2 at room temperature[3], while detection down to 0.5 ppm has been succesfully achieved[4] by operating SnO_2 nanobelt sensors at 400°C.
Among the chemicals studied in literature, NO_2 is very important as it is one of the most dangerous air polluttants, playing a major role in the formation of ozone and acid rain.

[1] Corresponding author. E-mail: pasmad@na.infn.it, Tel. +39-81-676126

The detection of NO_2 gas is thus of great importance in both environmental protection and human health. Recent studies[5] have reported a selective reactivity of visible photoluminescence SnO_2 nanobelts on NO_2 at ppm level. In particular, it was shown that the visible photoluminescence (PL) of tin oxide nanobelts is quenched by adsorption of NO_2 in a fast and reversible way. Moreover, this response was found to be highly selective toward humidity and other polluting species such as CO and NH_3. It was suggested[5] that the adsorption of NO2 creates new non-radiative recombination paths causing the PL quenching. It is important to stress that the creation of adsoprtion-related non-radiative paths is expected to influence the nonradiative decay time of the electronic excited states.

In this work, we investigate in more detail on the effect of NO_2 adsorption on the light emission properties of SnO2 nanobelts, by performing time-resolved photoluminescence (TRPL) measurements. This technique allows the direct determination of the electronic excited states lifetimes[6] and therefore to obtain useful informations on the possible creation of nonradiative paths[7] due to NO_2 – nanostructure interaction.

2. Experimental

TRPL experiment were perfomed on semiconducting tin oxider nanobelts. The samples were prepared by thermal evaporation on allumina and silicon substrates. Inside the tubular reactor it was possible to control the flow of different gas spources. 99.9 % pure SnO powders were used as the source material, and the depositions were performed in the 800-1000 °C temperature range, obtaining belt-shaped nanostructures.

TRPL measurements were performed on a sample of SnO_2 nanobelts deposited on a silicon substrate, as bulk silicon photoluminescence efficiency is negligible compared to the tin oxide nanobelts one. The sample was photoexcited by means of the third harmonic (wavelength λ=355 nm) of the fundamental beam of a picosecond Nd:YAG laser. The pulse duration of the laser beams was 20 ps; using impinging pulse energies of about 1 mJ the PL signals coud be easily detected.

The sample was placed on a heater inside a test chamber featuring quartz window for optical measurement access. A mass flow control was connected to the test chamber, allowing the flowing of a constant flux of synthetic air (0.3 l/min) mixed with the desired amount of gaseous species. The photoluminescence emission was collected by means of a fosusing lens and was optically coupled, via multimode optical fiber, to the input slit of a monochromathor mounting a 200 lines/mm diffraction grating. The photoluminescence light diffrected by the grating was coupled to a photomultiplier tube having a fast response time (~1 ns) and connected to a digitizing oscilloscope. Taking into account the rise time of the photomultiplier and the sampling rate of the oscilloscope, we estimate an overall time resolution limit of about 2 nanoseconds. In our experiment, the sample temperature was kept at T=120°C and two sets of time-resolved phutoluminescence datas were collected. In the first set synthetic air was fluxed inside the test chamber,

while in the second set a mixture of synthetic air and NO_2 (5 ppm relative concentration) was used.

We first noticed that, when excited at 355 nm, the SnO_2 nanobelts exhibit a broad PL signal peaked in the green region. The PL emission is temperature dependent, as it increases as the temperature is lowered. In our case, we decided to operate the measurements at T=120°C as it seems to be a favourable temperature for gas sensing operation of the nanobelts[4]. Notwithstanding the fact that increasing the temperature leads to a decrease of the PL efficiency, the PL signal was still easily detectable.

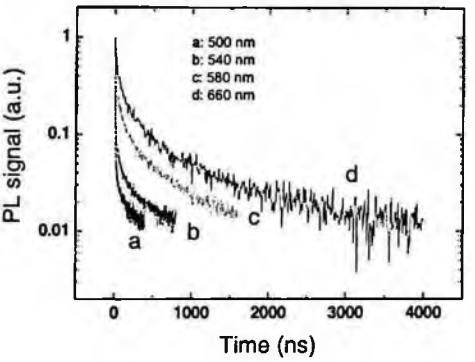

Fig. 1. Normalized TRPL curves for SmO2 nanobelts in synthetic air at different emission wavelengths.

In Fig. 1 we show, on log scale, some of the time resolved photoluminescence signals at different wavelengths for the sample exposed to synthetic air. The curves are normalized to their initial value in order to evidence the difference in decay rates. It is observed that the decay rate strongly depends on the emisison wavelength, varying from few nanoseconds to several tenths of nanoseconds going from lower wavelengths to higher wavelengths. Moreover, the decays do not follow a simple single-exponential rule, but they are more likely to follow a stretched exponential decay, as in the case of PL emission of semiconducting nanoparticles and porous silicon.

In Fig. 2 we report the results of the same measurements as in Fig. 1 but for the case of the sample interacting with the 5 ppm NO_2. Qualitative features of the decay are preserved: both the wavelength dependence of decay times and the non-exponential behaviour are not affected by the interaction with NO_2. On the other hand, the absolute values of the photoluminescence intensity at different wavelengths (e.g. the area of the time-resolved PL signals) are significantly reduced due to the NO_2 presence, confirming the results of Ref. 5.

Concerning the decay rates, our measurements show that no significant change of the decay time occurs as the NO_2 measurements are considered. This result is evidenced by Fig. 3, where an effective decay time (defined as the time in which the PL signal reaches

the 10% of its initial value) is plotted versus the emission wavelength for the two sets of measurements (air and NO_2).

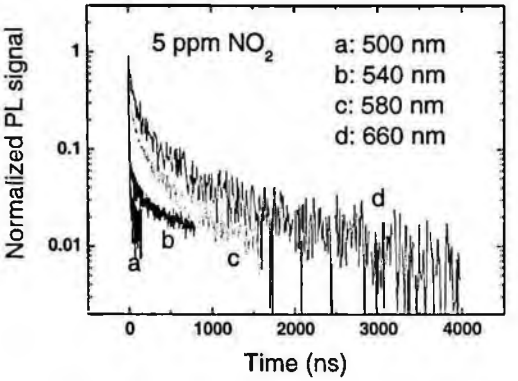

Fig. 2. Normalized TRPL curves for SmO2 nanobelts in 5 ppm NO_2 at different emission wavelengths

It can be noticed that the decay times are essentially the same, within the experimental resolution. In other worlds, the NO_2 seems to have an *extensive* effect on the electron recombinations of the system: it reduces the *total number* of radiative recombinations while not affecting qualitatively the recombinations, i.e. preserving the same decay cynetics. In order to explain such behaviour, we suggest the following argument. As we take into account the photoluminescence process in an isolated system, electrons which are optical pumped in excited states initially undergo very fast thermal relaxation. Relaxation usually requires few picoseconds or less to occur, then the relaxed population recombines following the radiative and non-radiative recombination paths wich are peculiar to a given material. Considering the time resolution of our apparatus, our TRPL experiment is able to follow the dynamics of the relaxed population but nothing can be said on the processes occurring during the relaxation of the system. As NO_2 seems to reduce the overall number of radiative recombinations but not to affect the decay rates (which are related to the intrinsic mutual interactions of electrons within the material), we suggest that during the relaxation phase a net charge transfer from the semiconductor to the gas adlayer occurs. Due to the high surface-to volume ratio of the material, a significant coverage of NO_2 molecules can occur, and therefore the total charge trapped by the gas can be a significant fraction of the photoexcited electrons. As a consequence, the number of electrons which recombines after the relaxation is reduced but no significant change of the recombination probabilities occurs.

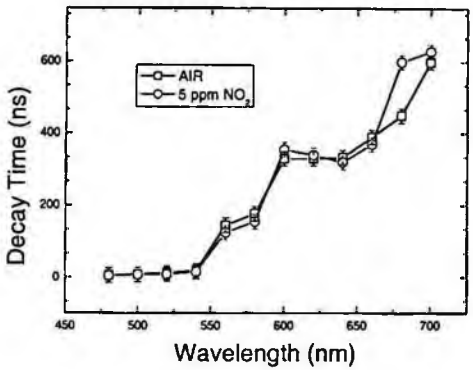

Fig. 3. Photoluminescence decay time (defined as 10% decay time) as a function of emission wavelegth for air (open squares) and 5 pmm NO_2 (open circles).

However, it is worth to pint out that the occurrence of an effective change of the faster components (sub-nanosecond) of the decay behaviour due to NO_2 adsorption is not totally ruled out by our results, taking into account the ~2 ns overall time resolution of our apparatus. Further analysis on the initial behaviour of photoluminescence decay are in progress by using a much faster experimental setup based on a streak-camera.

References

1. J. Shieh, H. Feng, M.H. Hon, H.Y. Juang, *Sens. Actuators B*, **86**, 75 (2002).
2. R. Winter, K. Scharnagl, A. Fuchs, T. Eisele, *Sens. Actuators B*, **66**, 85 (2000).
3. M. Law, H. Kind, B. Messer, F. Kim, P.D. Yang, *Angew. Chem. Int. Ed.* **41**, 2405 (2002).
4. E. Comini, G. Faglia, G. Sberveglieri, Z.W. Pan, Z.L. Wang, *Appl. Phys. Lett.* **82**, 1613 (2002).
5. G. Faglia, C. Baratto, G. Sberveglieri, M. Zha, A. Zappettini, *Appl. Phys. Lett.* **86**, 011923 (2005)
6. R.K. Ahrenkiel, *Minority-Carrier Lifetime in III-V Semiconductors*, Semiconductors and Semimetals, Vol. 39, p.71, Academic Press, New York (1993)
7. G. Amato, L. Boarino and N. Brunetto, *Thin Solid Films* **276**, 51 (1996)

HIGH TEMPERATURE DEPOSITION OF NANOSTRUCTURED WO_3 FOR GAS SENSING APPLICATIONS

A. PONZONI*, E. COMINI, M. FERRONI, G. FAGLIA, G. SBERVEGLIERI

Sensor Laboratory, INFM - Dipartimento di Chimica e Fisica per l'Ingegneria e per i Materiali, Universita' di Brescia , Via Valotti, 9 , 25133 BRESCIA , Italy

**Corresponding author. E-mail: ponzoni@tflab.ing.unibs.it*

In this paper we report on WO_3 films deposited by thermal evaporation. Layers have been characterized by means of electron microscopy techniques, revealing a microstructure suitable for gas sensing applications. Functional characterization has been carried out towards NO_2, NH_3 and CO, revealing the capability of the material to detect NO_2 concentrations lower than 100 ppb, with low cross-sensitivity towards CO and NH_3.

1. Introduction

WO_3 is a well known material for the development of solid state gas sensors for NO_2 [1 - 3] and H_2S detection [4, 5].

Beside this general feature, a wide range of properties has been reported for this material. For example, Meixner et al. report about the good performances of tungsten trioxide for NH_3 detection [1], while Prasad et al. report about its low sensitivity towards NH_3 [2].

As far as NO_2 detection is concerned, good performances are reported to occur over a wide range of temperature. Sensors featuring high response at temperature lower than 200°C have been developed by Teoh et al. [2]. The same authors report that such an high performance is maintained even decreasing the working temperature down to 36°C. Differently, Sberveglieri et al. report about a WO_3 sensor having optimal performances at 400°C [3], performances which are strongly reduced by decreasing the working temperature.

Neutron diffraction experiments carried out on powder samples [7] highlight that WO_3 undergoes reversible phase transitions after thermal treatment, allowing to establish a correspondence between temperature range and stable phase.

When WO_3 is deposited as film, deviations from such a correspondence can occur because of the substrate-film interaction for example, (see structural analysis in [1-5]).

These considerations suggest the possibility to promote the stabilization of such phases, that can not crystallize at lower temperatures, depositing WO_3 at high temperatures and to test their sensing performances.

NO_2, NH_3, and CO have been chosen as target gases. The former because of its well known high reactivity with WO_3, the second because of its different reactivity degree reported in literature as reported previously, the latter to have a more complete knowledge about interfering gases in NO_2 detection.

2. Experimental

Samples have been deposited by thermal evaporation method on 3 mm x 3 mm x 0.25 mm alumina substrates.

Before deposition, the chamber was evacuated at about 10^{-3} torr. Deposition was carried out in reactive atmosphere (O_2 pressure = 0.22 mbar) for 5 minutes, placing the substrates about 15 mm far from the source and heating them at 600°C. The source was a metallic tungsten wire (SPI Supplies Pk 10 1801), heated by Joule effect up to sublimation. A constant voltage of 4 volts was applied resulting in an electrical current of about 10 A.

The thickness of sensitive layers has been measured with a profiler to be 1.4 μm.

Samples were provided with interdigitated Pt contacts (IDC) for electrical measurements and with a Pt heater on the backside.

Gas sensing tests were carried out by flow through method in a thermostatic chamber. Certified bottles and a humidifier system have been used both to generate the reference air and gas mixtures. Sensors' responses have been monitored applying a constant voltage to the sensitive layer and measuring the electrical current by means of a picoammeter.

Transmission electron microscopy (TEM) and scanning electron microscopy (SEM) have been used to characterize the WO_3 layers.

3. Results and discussion

Thermal evaporated samples have a granular morphology. Layers are composed of particles about 10 nm in size, as shown by the SEM micrograph reported in figure 1. Such particles are grouped to form aggregates that are few hundreds of nanometers in size.

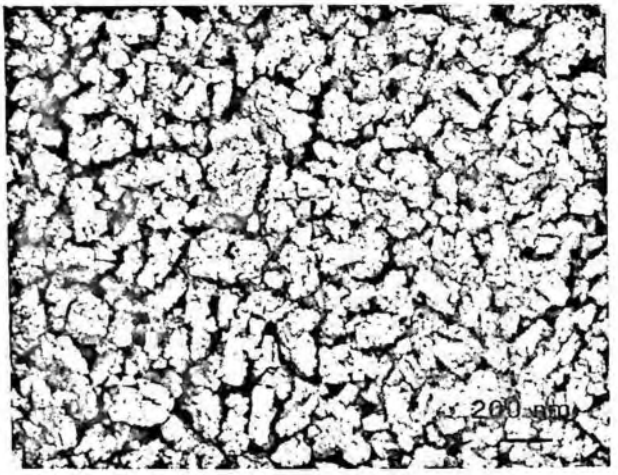

Figure 1. SEM secondary electron image of thermal evaporated WO_3 layer.

High-resolution electron microscopy (HREM) measurements revealed that samples have a non-homogeneous degree of crystallinity. The HREM micrograph reported in figure 2 shows that the crystalline grains can be clearly distinguished from amorphous regions by the presence of interference patterns, characteristic of periodic structures. The size of such particles is tens of nanometers.

Atomic interplanar distances have been determined through electron diffraction experiments. Phase identification inferred presence of a WO_3 phase with symmetry lower than cubic, such as tetragonal or monoclinic ones (presence of both phases can also be considered).

Sensing responses towards NO_2 have been observed to increase with decreasing the working temperature down to 100°C, the lower value tested for these sensors. See reference [8] for a detailed analysis of temperature influence on sensing performances. Working at 100°C, after the injection of 100 ppb of NO_2, the electrical conductivity of the film decreases of about one order of magnitude, see figure 3.

Measurements have been carried out with a relative humidity value of 30% and with a constant flux of 300 sccm.

These high performances exhibited by this material can be attributed to its microstructure. The rough morphology increases the surface area of the layer, and the nanometric size of crystalline particles strongly enhances the sensing performances, [9].

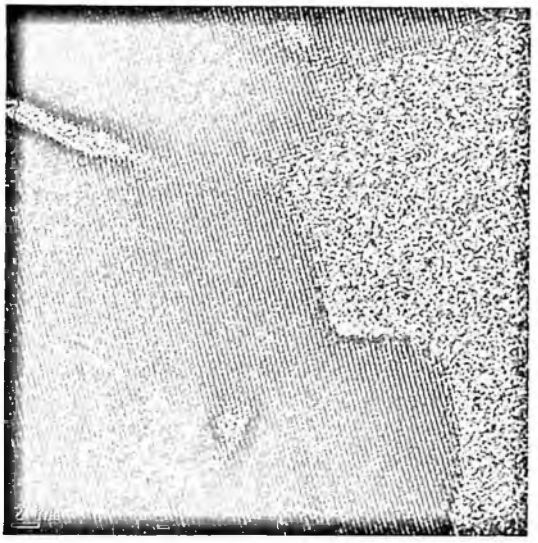

Figure 2. HREM image of thermal evaporated WO_3 layer.

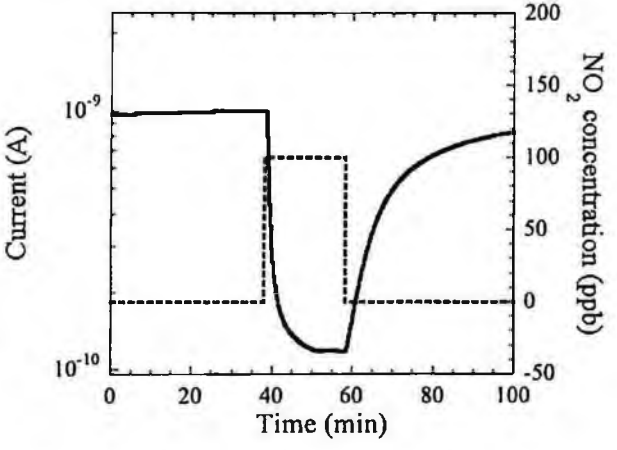

Figure 3. Response towards NO_2, 100 ppb, measured in an environment with a relative humidity value of 30% (chamber temperature is 20°C) and a total flux of 300 sccm, sensor's working temperature is 100°C.

A comparison with sensing performances exhibited by sputtered films highlights the improvement obtained by these thermal evaporated layers. For example, operating the sputtered samples at their optimal temperature of 200°C

and injecting 200 ppb of NO_2, their electrical conductivity decrease by a factor 4 [8]. This is 5 times lower than the decreasing factor of 20 observed when thermal evaporated samples, warmed at their optimal temperature (100°C) are exposed to the same gas concentration.

The achievement of these results at such a low working temperature is of particular interest for interfering effects. It is well known indeed, that metal oxide solid state gas sensors are not selective towards specific gases, but temperature can strongly enhance or reduce the responses towards different molecules.

In particular, heating the material below 150 °C, the population of chemical species like O^{2-} and O^- and on the surface layer is strongly reduced [10]. According to the reaction models proposed in [10, 11] for SnO_2, gases like CO reduce the material surface via catalytic reactions that convert carbon monoxide (CO_{gas}) in to carbon dioxide (CO_{2gas}). This occurs desorbing oxygen ions (O^-_{surf}) from the surface and releasing electrons (e^-) in the material conduction band:

$$CO_{gas} + O^-_{surf} \rightarrow CO_{2gas} + e^-$$

In the same references, surface oxidation by NO_2 molecules is modeled by interactions that do not require such ions to be present on the material surface. Thus, below 150°C, the reaction between reducing gases and WO_3 is foresee to be minimized.

Responses towards reducing gases like NH_3 and CO have been measured in the same conditions that gave best responses towards NO_2 (T=100°C, RH=30%, flux=300sccm). Low responses have been obtained. For example, after the injection of NH_3, 10 ppm, the electrical conductivity of the film increase by a factor 5, while after the injection of CO, 200 ppm, the increasing factor is less than 3.

Humidity effects have also been investigated observing responses to increase with decreasing the relative humidity (RH) value. For example, responses towards NO_2 increase of a factor 7 decreasing RH from 0 to 60%, while for NH_3, the increasing factor is 1.7.

4. Conclusions

WO_3 layers have been deposited at high temperatures (600°C) with the aim of stabilizing such phases that do not crystallize at lower temperatures.

Samples exhibit a structure with asymmetry characteristic of such high temperature phases (the cubic one is stable at room temperature).

Gas sensing tests revealed a high sensitivity towards NO_2 together with low interfering effects, at least towards CO and NH_3. Comparison with performances exhibited by sputtered samples, particularly highlight the improvements obtained by thermal evaporated films. Such performances make the material a good candidate for NO_2 monitoring both in indoor (threshold value is 1 ppm) and outdoor applications (threshold value is 50 ppb).

Acknowledgments

This work has been founded by the European Strep project "Nano-structured solid-state gas sensors with superior performance" (NANOS4) no.: 001528.

References

1. H. Meixner, J. Gerblinger, U. Lampe, M. Fleisher, *Sensors and Actuators* **B 23**, 119 (1995).
2. L.G. Teoh, Y.M. Hon, J. Shieh, W.H. Lai, M.H. Hon, *Sensors and Actuators* **B 96** 219 (2003).
3. G. Sberveglieri, L. Depero, S. Groppelli, P. Nelli, *Sensors and Actuators* **B 26-27**, 89 (1995).
4. C. Cantalini, M.Z. Atashbar, Y. Li, M.K. Ghantasala, S. Santucci, W. Wlodarski, M. Passacantando, *J. Vac. Sci. Technol.* **A 17** 1873 (1999).
5. C. Cantalini, W. Wlodarski , Y. Li, M. Passacantando, S. Santucci, E. Comini, G. Faglia, G. Sberveglieri, *Sensors and Actuators* **B 64** 182 (2000).
6. A. K. Prasad, P. I. Gouma, *Journal of Materials Science* **38**, 4347 (2003).
7. T. Vogt et al. *Journal of Solid State Chemistry* **144**, 209 (1999)
8. A. Ponzoni, E. Comini, M. Ferroni, G. Sberveglieri, *Thin Solid Films*, in press.
9. N. Yamazoe, *Sensors and Actuators* **B 5** 7 (1991).
10. P.T: Moseley, J.O.W. Norris, D.E. Williams, *Techniques and Mechanism in Gas sensing*, Adam Hilger, Bristol England (1991).
11. B. Ruhland, Th. Becker, G. Muller, *Sensors and Actuators* **B 50**, 85 (1998).

APPLICATION OF QUALITY STANDARD FOR THE REALISATION OF THICK FILM GAS SENSORS

M. BUZZOLANI*, M. BUTTURI, M.C. CAROTTA,
C. MALAGÙ, G. MARTINELLI, B. VENDEMIATI

UNIVERSITY OF FERRARA, VIA DEL PARADISO 12, 44100 FE, ITALY

Sensor and Semiconductor Laboratory of Department of Physics of Ferrara (SSL) has implemented a quality management system (ISO 9001:2000) about processes of planning, development and production of thick film gas sensors and photovoltaic cells. The management system, based on the scheme Plan, Do, Check-Act, allows the monitoring the laboratory activities to get "continual improvement". The eight principles of quality have been applied for the first time to the research activity in the University, and they turned out to be simple but powerful tools for the success of the system. Moreover, the above mentioned principles being directed toward the internal performance, not only will benefit the organization itself, but also customers and interested partners. The international standard applied to SSL is based on four major clause headings which are: manager responsibility, resource management, process management and measurement, analysis and improvement..

1. Introduction

The Project to certify the Sensor and Semiconductor Laboratory according to the Normative UNI EN ISO 9001: 2000 [1] started in 2000. The Top Management chose to improve the Quality Policy through the principles of Customer Satisfaction, Efficiency and Excellence of processes.
The International Standard, UNI EN ISO 9001:2000, represents the standard of reference to match the requirements of Quality Management Systems. This standard can be used for:

- inner scopes (to improve the internal processes of organization and the control of productive activities).
- contractual scope (to show the customers the quality of the organization of our activities).
- certification scope (to get the International Certification).

Applying a Quality Management System is a choice of the Top Management which is going to demonstrate the organization ability to supply "quality

product" to satisfy the customers needs. Application of the standard allows one to improve the products from the point of view of modernization, research and technological development through an efficient management of the processes of the organization.
The ISO 9000:2000 [2] is a generic standard in nature and intent and each organization will need to select and improve the most appropriate methods and tools from the content of this international reference. The ISO 9000:2000 identifies eight Quality Principles that can be used by the management as a framework to guide their organizations towards improved performance. These principles are:

- Customer focus
- Leadership
- Involvement of people
- Process approach
- System approach to management
- Continual improvement
- Factual approach to decision making
- Mutually beneficial supplier relationships

There are several ways of applying these quality management principles which will be implemented according to the nature of the organization, the specific needs and goals. In particular, the principles of process and system approach allow to systematically define the necessary activities to obtain a wished result. Moreover they establish clear responsibility and accountability for managing key activities. Therefore it is an issue to see the Laboratory as an ensemble of interacting processes aimed at a constant development. The continual improvement has to be the permanent objective of an organization and it will be based on the model Plan-Do-Check-Act. Consequently, it is important for any organization to proceed through the following steps:
- plan objectives
- realize processes
- measure system performance
- monitor feedback and improvement

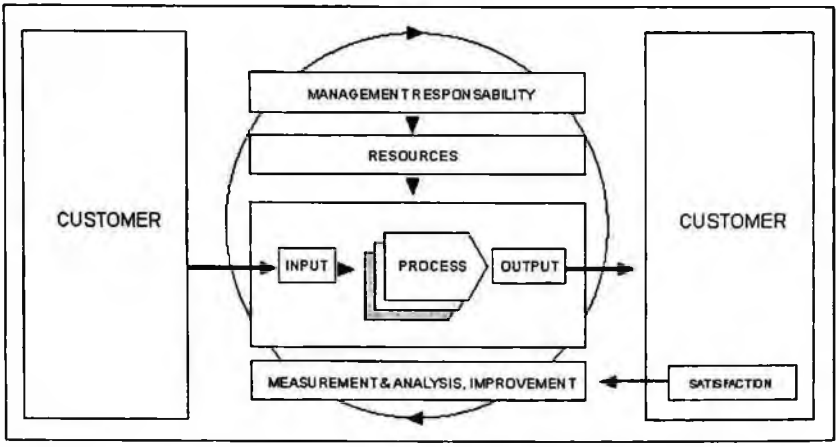

Figure 1. Example of a vertical and a horizontal loop of a management system.

2. Application

The SSL has applied the principles of the standard ISO 9001:2000 to the main processes such as management of instruments and facilities, purchasing, management of human resources etc. Particular attention has been paid to the activities of design and manufacturing of thick film gas sensors. The Top Management of the Laboratory decided to apply the ISO 9001:2000 (standard to get the certification) in 2000. Since September 2001 the SSL has certified the processes of design and manufacturing of thick film gas sensors and photovoltaic cells The main processes about planning and realization of thick film gas sensors are described in the Quality Manual (QM) [3] and in the procedures of the organization. The QM expresses the policy, the mission and the vision of the Laboratory while the procedures describe the main operational processes (both general and specific). As a consequence there are procedures that describe supporting activities (purchasing, nonconformity, management of human resources etc.) and procedures that specify peculiar processes (sensors planning, sensors development and production etc.).

The main SSL procedures are:

SYSTEM PROCEDURES	DESCRIPTION
QUALITY SYSTEM PROCEDURES AND WORK INSTRUCTIONS	How to redact the procedures and the operative instruction
PV CELLS DESIGN AND PROCESS PLANNING	How to define technical detailed lists, parameters of realization etc.
SENSORS DESIGN AND PROCESS PLANNING	How to define technical detailed lists, parameters of realization etc.
TRASH	How to treat the trash materials
INTERNAL AUDIT	How to realize internal audit (when, who, competence etc.)
PV CELLS DEVELOPMENT AND PRODUCTION	How to realize standard cells
SENSORS DEVELOPMENT AND PRODUCTION	How to realize sensors (powder preparation, thick film printing, electrical circuitry, etc.)
IN - OUT CLEEN ROOMS	How to enter and exit the clean rooms
PURCHASING	How to select suppliers, make orders etc
NONCONFORMITY	How to respond to nonconformities (taking corrective actions or preventive actions) and how to record them
QMS DATA PROCESSING	How to manage important data and quality documents and records
HUMAN RESOURCES	How to identify necessary qualifications and competences How to realize recruitment training, continual education, and development of skills

3. Conclusions

The application of International Standard ISO 9001:2000 in SSL has increased the efficiency of working and managing performances. The Standard aims at improving the ability of the organization to work in the best possible way. The goal is not to change the structure of the system to obtain a certification but to improve the internal processes to achieve excellence performances.

References

[1] ISO 9001:2000 http://www.iso.org
[2] ISO 9000:2000 http://www.iso.org
[3] QM LSS ED. 2005 – University of Ferrara, Department of Physics

OXYGEN SENSING PROPERTIES OF TiO_2 NANOPOWDERS PREPARED BY GEL COMBUSTION*

F.A. DEORSOLA, I. AMATO, B. DE BENEDETTI

Dip. Scienza dei Materiali e Ingegneria Chimica, Politecnico di Torino, Corso Duca degli Abruzzi 24, Torino, 10129, Italy

A. BONAVITA, G. MICALI, G. NERI

Dip. Chimica Industriale e Ingegneria dei Materiali, Università di Messina, Contrada di Dio, Messina, 98166, Italy

Nanostructured titanium oxide was synthesized through an innovative and low-cost process called gel combustion. The technique merges chemical gelation and combustion processes. As synthesized gel combustion TiO_2 nanopowders showed only formation of the anatase phase with a crystalline domain size of 6 nm. High temperature treatments affected largely domain size and phase composition. O_2 sensing properties at high temperature (400 – 500 °C) were evaluated on pure and Pt-doped TiO_2-based sensors.

1. Introduction

Nanostructured titanium oxide, TiO_2, has recently received great attention because of its wide range of application in several field, as pigment, photocatalysis, solar cells and gas sensing. In the field of oxygen sensing, titanium oxide, whether in anatase or rutile phase, is a promising material in order to produce low cost and small sized O_2 sensors [1].

At present, oxide nanoparticles are produced through several routes, such as co-precipitation, sol-gel and spray pyrolysis. In this work an innovative and effective synthesis process called gel combustion is presented. Then O_2 sensor devices in the thick film configuration were realized and tested with the aim to apply them as planar resistive λ-sensor in automotive applications [2].

* This work is supported by MIUR under the FIRB-SQuARE project

2. Experimental Procedures

2.1. *Synthesis and characterization*

TiO_2 synthesis was carried out starting from titanium isopropoxide $Ti[OCH_2(CH_3)_2]_4$ (Fluka), hydrogen peroxide H_2O_2 (Fluka, 35%) and isopropanol $(CH_3)_2CH_2OH$ (Aldrich, 99+%). Titanium isopropoxide was mixed with isopropanol (50/50 vol). Hydrogen peroxide was added drop by drop in the continuously stirred solution. The reaction yielded to titanium hydro-peroxide precipitates, with remarkable release of gases and temperature increase until 80°C. Isopropanol evaporation yielded to gel formation, whose structure is shown in Figure 1 according to the model of Ragai and Symons [3,4]. After drying the TiO_2–containing gel, the products obtained are ground in a mortar and the powders are treated at 250°C for 2 h.

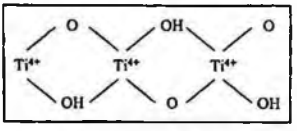

Figure 1. Structure scheme of the gel formed during reaction.

Some TiO_2 powders were also activated with platinum (1 wt%) by the Incipient Wet Impregnation (IWI) method, using tetraammineplatinum nitrate $Pt(NH_3)_4(NO_3)_2$ (Aldrich, 99,995%) as precursor.

XRD analysis was carried out on a X'Pert Philips diffractometer (range 2θ: 10÷90°, radiation Cu$K\alpha$, λ=1,54056 Å).

Morphological analysis was carried out on a Hitachi Field Emission Scanning Electron Microscope (FESEM) and a Hitachi Transmission Electron Microscope (TEM).

2.2. *Sensing tests*

Sensing tests were carried on sensor devices realized by depositing films of the TiO_2 nano-powder dispersed in water onto alumina substrates (6x3 mm^2 sized) provided with Pt interdigitated contacts (contacts space = 200 μm) and a Pt heater. The operating temperature of the sensors was in the range of 400-500°C. The measurements, expressed in terms of resistance variation during the gas target exposure, were carried out by an home made PC-interfaced apparatus, supplied with flow stream and temperature control systems, widely described in another paper presented in this book [5].

3. Results and Discussion

3.1. *Microstructural analyses*

XRD of the as prepared TiO_2 powders showed only formation of the anatase phase (Fig. 2). The heat treatment effect on the phase composition and crystalline domains size, was then investigated. All heat treatment were carried out for 2 h. It can be observed that nanopowders heat treatment affected largely domains size, calculated through the Sherrer's formula, increasing from 6 nm of as-prepared nanopowders up to 137 nm of TiO_2 treated at 900°C (Table 1). At 700°C the rutile phase peaks appeared in the XRD pattern. Treating TiO_2 nanopowders at 900°C it was possible to observe both anatase and rutile phases.

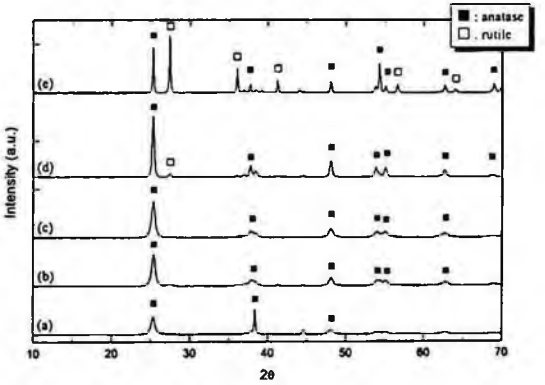

Figure 2. XRD pattern of TiO_2 powders as prepared (a) and after heat treatment at 250°C (b), 500°C (c), 700°C (d) and 900°C (e).

Table 1. Effect of heat treatment on crystalline domains size of TiO_2 nanopowders.

Heat treatment	Crystalline domains size [nm]
as-prepared	6
250°C	15
500°C	27
700°C	68
900°C	130

FESEM analysis of the TiO_2 powders treated at 250 °C showed particle size lower than 50 nm and softly agglomerated (Figure 3). The high quantity of gases released during reaction yielded to high values of specific surface area, as confirmed by BET analysis with a value of 115 m^2/g. Pt addition was found doesn't affect the structural and morphological characteristics of TiO_2 nanopowders.

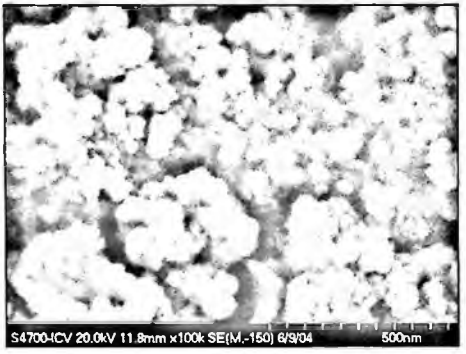

Figure 3. FESEM micrograph of TiO_2 powders treated at 250°C.

3.2. *O_2 sensing tests*

Transient oxygen tests were carried out into the range of temperature between 400 and 500 °C. As no phase transformation occurs in this temperature range, this should ensure the results reproducibility. The response to successive pulses of O_2 ranging from 2% to 20% in volume is fast and reproducible as reported in Fig. 4.

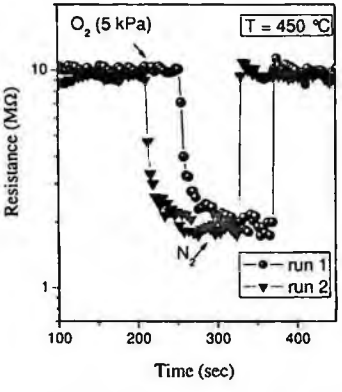

Figure 4. TiO_2 transient responses towards repeated oxygen pulses at 450°C.

The calibration curves, in the whole range of temperature investigated, are reported in Figs. 5a-b. The linearity of the sensor response is highlighted and allows us to calculate the value of the exponent m, in according to the equation:

$$\sigma \propto \frac{1}{R} \propto pO_2^{1/m}$$

The value of m calculated at 500 °C was about 3.4.
By varying the working temperature, the same slope of the calibration curves was calculated. The results obtained suggest a sensing mechanism intermediate between a surface (1/2) and bulk (1/4) mechanism [6].

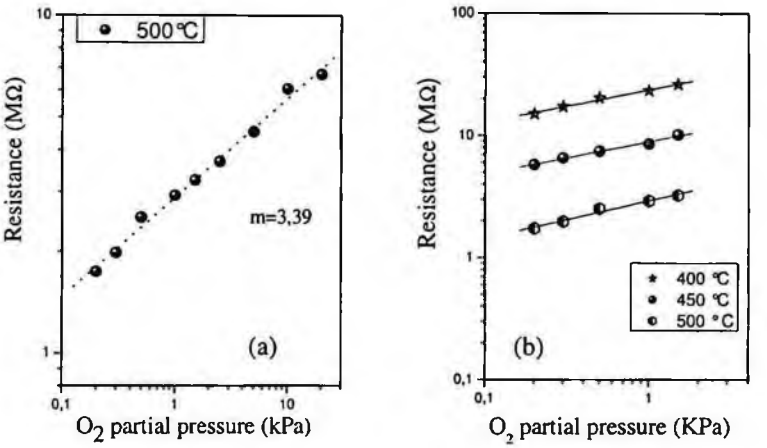

Figure 5. Calibration curves: dependence of resistance on the oxygen partial pressure at different temperature: a) 500°C; b) 400-500°C.

In Fig. 6 the resistance of TiO_2 sensors at different values of $\lambda = 1$ is reported. The fast dynamic above highlighted and the remarkable resistance change around $\lambda = 1$, make the TiO_2-based tested devices suitable for use in the O_2 monitoring for automotive applications [2].
The addition of Pt introduces a further improvement in the recovery dynamic, making it faster.
Work is in progress to investigate the sensing behaviour of these gel-combustion titanium dioxide nanopowders at higher operating temperatures and under realistic conditions of functioning.

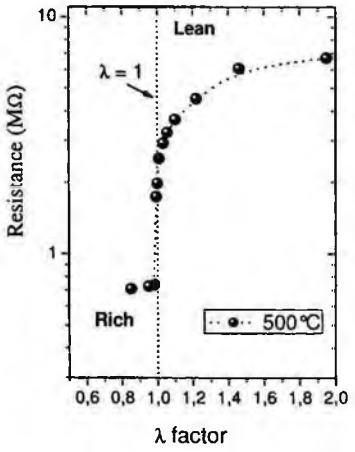

Figure 6. Resistance of the TiO_2 sensor at different λ values.

4. Conclusions

In this work nanostructured TiO_2 powders have been synthetized through gel combustion. A structural and morphological characterization of these nanoparticles, as prepared and after high temperature treatment, has been carried out. Anatase was the only phase detected up to temperature < 700 °C.
Sensing tests finalized to the application of the gel combustion synthesized TiO_2 powders as planar resistive λ-probes, have shown the promising performance of this material for the regulation of the air/fuel mixture in the exhaust steam of automotive engine.

References

1. J. W. Fergus, *J. Mater. Sci.* **38**, 4259-4270 (2003).
2. L. Francioso, D.S. Presicce, A.M. Taurino, R. Rella, P. Siciliano, A. Ficarella, *Sensors and Actuators B* **95** (2003) 66-72.
3. J. Ragai, S. I. Selim, *J. Coo. Int. Sci.* **115**, 139-146 (1986).
4. M. C. R. Symons, *Nature.* **325**, 659-660 (1987).
5. A. Bonavita, G. Neri, N. Donato, G. Pioggia, D. De Rossi, F. Di Francesco, *Sensors and Microsystems* **10** (in press)
6. R. Ramamoothy, P.K. Dutta, S.A. Akbar, *J. Mat. Sci.* **38**, 4271 (2003).

GAS SENSING APPLICATIONS OF HYBRID NANOSTRUCTURES SYNTHESIZED BY SUPERSONIC BEAMS

N. COPPEDÈ, L. AVERSA, M. NARDI, A. PALLAORO, F. SIVIERO, T. TOCCOLI, R. VERUCCHI, AND S. IANNOTTA,

IFN-CNR Istituto di Fotonica e Nanotecnologie –Via Sommarive 18, 38050 Povo di Trento – Italy

E. IACOB, V. MICHELI, M. ANDERLE

FCS – IRST , Via Sommarive 18, 38050 Povo di Trento – Italy

A.TAURINO, P.SICILIANO

IMM-CNR Istituto per la Microelettronica e Microsistemi - Via per Arnesano 73100 Lecce –Italy

An approach to the production of a new class of gas sensors consisting of nanostructured hybrid organic-inorganic thin films is proposed. It is based on the co-deposition from supersonic beams of π-conjugated organic materials and cluster-assembled metal oxides in a UHV apparatus including surface characterization methods. The unique control achievable by supersonic beams on the initial kinetic energy, momentum and state of aggregation enables the growth (SuMBE) of molecular materials with controlled properties at different length scales. On the other hand, by means of supersonic beams of clusters, nanocrystalline TiO_2 films can be grown without annealing, so that grain size and morphology can be better controlled. We show that by the co-deposition of organic molecules and titania clusters, gas sensors based on sensitized nanostructured titania can be prepared exhibiting improved and novel gas sensing properties.

1 Introduction

Gas sensing devices based on nanostructured materials have performances that strongly depend on the ability to control the active material and the interfaces at a different length scales. In particular, when dealing with metal oxides, the control on the dimension and degree of crystallinity of the nanograins is a critical issue to improve sensitivity in the gas response. The main problems with metal oxide sensors are related to the lack of selectivity and to the high temperature of operation.

The sensitization or functionalization at the mesoscale with molecular organic or bio-active species is assumed to be a very promising approach to address these problems, aiming at producing new classes of gas sensing devices. To this end we developed an approach that combines the stability of inorganic nanostructured materials like metal oxides with the flexibility and selectivity of organic molecules, realizing nanostructured hybrids. The basic idea is that supersonic beams seeded with molecules [1] and clusters [2], could be ideal to grow and tailor the properties (morphology, structure, chemical physical properties, etc.) of nanostructures in a co-deposition scheme. We show that this

is a viable and very promising approach on the basis of nanostructured TiO_2/CuPc hybrid sensors.

2 Experimental

2.1 Supersonic Beams of Organic Molecules and Clusters

Deposition of molecules by Supersonic Molecular Beam Deposition (SuMBE) [1] or Supersonic Cluster Beam Deposition (SCBD)[3] give the unique advantage of a fine control on the initial state (kinetic energy, momentum, state of aggregation) of precursors. Indeed species highly diluted in a supersonically expanding carrier gas exhibit a narrow velocity distribution, low divergence and, especially in the case of small molecules, alignment and a substantial relaxation of internal degrees of freedom [2].

The production of continuous supersonic beams of organic molecules is performed by means of a source consisting of a quartz tube in which a carrier gas (He, H_2, Ar) is seeded with species sublimated by Joule heating. The mixture then expands into vacuum through a nozzle. Kinetic energy as well as the degree of clustering can be tuned by changing the carrier gas, the nozzle diameter and the seeding parameters (source temperature, gas inlet pressure).

The deposition of clusters is performed via a Pulsed Microplasma Cluster Source (PMCS) [3] that has been developed in collaboration with the group directed by Prof. Milani at the University of Milan. Clusters are produced by quenching the plasma in a buffer gas after a discharge between two electrodes hosted in a ceramic cavity. Virtually any conducting material can be vaporized, and the contamination of the gas with chemical species can be exploited to modify the nature of the aggregates (for example oxygen is introduced in order to obtain metal oxide clusters). Control on the cluster size is attainable acting on the source operating parameters and by means of inertial aerodynamic separation effects: this is very important in order to control the structure and properties of the film, since many properties of these precursors are size-dependent.

2.2 In Situ Characterization and Co-deposition Scheme

To better understand growth and properties of the nanostructures and interfaces we developed a UHV system with suitable "in situ" characterization tools. The deposition chamber is at present equipped with two supersonic sources and an electron beam evaporator, while a Knudsen cell and a third source can be mounted, all facing the sample. Thus layer by layer growth, blending, doping and direct synthesis of nanostructures of organic, inorganic or hybrid materials can be performed. A time of flight mass spectrometer (TOF-MS), developed on purpose to characterize both supersonic beams of clusters and organic molecules

is available for beam characterization (cluster mass distribution, kinetic energy). The deposited films can be characterized at several stages of growth by means of a Jobin-Yvon ellipsometer, while the study of electronic and chemical properties of surfaces and interfaces is performed by means of Auger, X-ray and UV photoemission spectroscopy in another chamber connected via an UHV transfer system.

3 Results

3.1 Nanostructured Titania Growth and Sensitization with Organic Molecules

Very interesting results in the synthesis of nanostructured titania have been obtained using cluster beams produced by the PMCS. Particularly, the XRD, Raman and AFM characterization of films deposited at room temperature show a highly porous structure with the presence of anatase, brookite and rutile crystals with a typical size of few nm. There are indications of an existing correlation between cluster size and crystalline phase [4] so that nanocrystalline porous films can be produced without any thermal annealing process which would produce undesired grain growth and coalescence.

We experiment here the SuMBE approach for the synthesis of hybrid materials in which the properties of nanostructured titania are enhanced by functionalization with organic molecules. The key feature is the high kinetic energy (tens of eV) supplied to the molecules with respect to conventional deposition techniques, which induces ordering and enhances the chemical reactivity at the interfaces. Results obtained with organic semiconductors and oligomers point out the crucial role of kinetic energy in growing organic crystalline films with well-controlled morphologies and structures. We have achieved very promising results in the synthesis of thin films of thiophene-based oligomers [5] and pentacene [6,7]. *In situ* electron spectroscopies (UPS, XPS) performed on the interface between nanocrystalline TiO_2 and CuPc evidences how the amount of energy supplied to the species is responsible for the activation of chemical interactions between the organic and the inorganic counterpart. Fig. 1 shows the XPS spectra of the C1s core level (TiO_2/CuPc upper curve, CuPc/TiO_2 middle curve, CuPc/SiO_2/Si(100) lower curve), which gives information about the chemical state of the organic molecule. The spectrum from the CuPc/SiO_2 system well represents the typical lineshape of this organic molecule: it is characterized by the presence of three distinct features related to carbon atoms in the aromatic ring (at 284.5 eV), in the pyrrole ring (at nearly 286 eV), while the less intense structure is related to a shake-up satellite. A detailed lineshape analysis is in progress at this time, anyway it is evident that the two hybrid interfaces exhibit different chemical properties with

respect to the CuPc deposited on the SiO_2 inert surface. In the case of CuPc on titania a clear lineshape broadening is observed with indications of the presence of additional components. In the TiO_2/CuPc case appear strong modifications of lineshape: energy shift, strong line broadening as well as the appearance of new components. All together the results strongly indicate the formation of chemical bonds between the organic and inorganic materials, with a marked difference between the two interfaces studied: high KE molecules on a rigid and rough substrate for the CuPc/TiO_2 case, large metal oxide clusters on a "soft" organic film for the TiO_2/CuPc case.

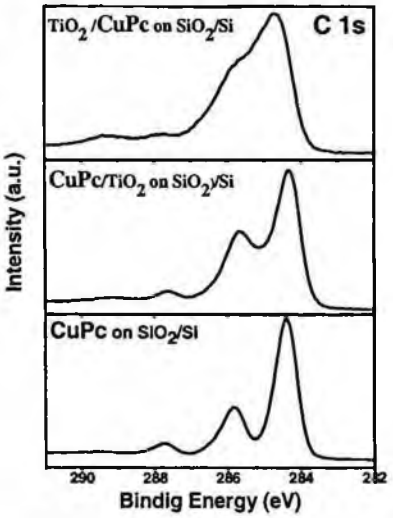

Fig. 1 – XPS spectra of the C1s core level for the TiO_2 - CuPc interfaces on SiO_2/Si(100).

3.2 Gas Sensing Applications

We previously reported on n-TiO_2 gas sensing devices produced at room temperature, showing that gas sensors based on nanocrystalline thin films produced by cluster beams, are highly performing without the need of any post-deposition thermal treatment. These sensors perform with sensitivities at the state of the art to VOCs (ethylene and methanol) [5]. The high effective area and effects related to the nanometric grain size, give to our sensors the capability of operating at temperatures well below 300°C. The lowering of operating temperature with respect to sensors produced with more standard techniques yields advantages including stability and power consumption.

Preliminary results on CuPc/TiO_2 hybrid gas sensors confirm that with the SuMBE/SCBD co-deposition approach metal oxides can be sensitized by means of organic molecules. Fig. 2 shows that under methanol exposure at low

temperature (160°C) we obtain a p-type response typical of organic materials, characterized by an undesirable baseline drift, while above 180°C a switch to a stable n-type response occurs. This is a really interesting preliminary result, since no conventional metal oxide sensor works at such a low temperature. Combining the information coming from the studies on the interfaces, e can thus say that this is a new hybrid material with new gas sensing properties, improving TiO_2-based devices from the point of view of sensitivity and operation temperature, and CuPc sensors in terms of baseline stability.

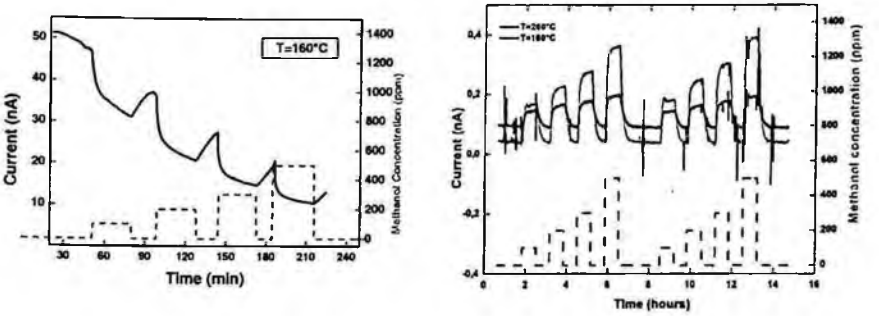

Fig. 2 – Response of a TiO2 – CuPc hybrid sensor to methanol at different temperatures and concentrations.

Aknowledgements

This work is financially supported by MIUR - FIRB Program - project SQUARE (RBNE01Y8C3_007) and FUR – Provincia Autonoma di Trento – projects RASO2 and NanoCOSHy.

References

[1] S. Iannotta and T. Toccoli, Journal of Polymer Science B 41, 2501, 2003.

[2] P. Milani and S. Iannotta, "Cluster Beam Synthesis of Nanostructured Materials", Spinger Verlag, 1999.

[3] E. Barborini, P. Piseri, P. Milani, J. Physics D: Appl. Phys. 32, L105, 1999.

[4] T. Toccoli, A. Boschetti, L. Guerini, S. Iannotta, S. Capone, P. Siciliano, A. Taurino, IEEE Sensors Journal 3, 199, 2003.

[5] S. Iannotta, T. Toccoli, F. Biasioli, A. Boschetti, M. Ferrari, Appl. Phys. Lett. 76, 1845, 2000.

[6] R.Ruiz, D.Choudhary, B. Nickel, T. Toccoli, K.C. Chang, A.C. Mayer, P. Clancy, J. M. Blakely, R. L. Headrick, S. Iannotta, and G.G. Malliaras, Chem. Mater., 16, 4497, 2004.

[7] L. Casalis, M. F. Danisman, B. Nickel, G. Bracco, T. Toccoli, S. Iannotta and G. Scoles, Physical Review Letters 90, 206101, 2003.

CHARACTERIZATION OF RF SPUTTERED InO_x / SiN_x THIN FILMS FOR GAS SENSING APPLICATIONS

A.C. FECHETE, W. WLODARSKI

School of Electrical and Computer Engineering, RMIT University
GPO Box 2476V, Melbourne, Victoria 3001, AUSTRALIA

S. KACIULIS, L. PANDOLFI

Institute for the Study of Nanostructured Materials, ISMN-CNR,
PO Box 10, 00016 Monterotondo Stazione, Rome, ITALY

Microstructural characterization of indium oxide and silicon nitride thin films has been performed in order to investigate their suitability for gas sensing applications in a layered structure employed as a Surface Acoustic Wave device. Thick silicon nitride (SiN_x) and thin InO_x films have been deposited on a lithium tantalate ($LiTaO_3$) piezoelectric substrate by using a planar RF magnetron sputtering. The deposited films were characterised by X-ray Photoelectron Spectroscopy and Atomic Force Microscopy in order to understand and to control the different parameters that affect the film gas sensing properties, such as the thickness, chemical composition and surface micro-morphology.

1. Introduction

Interest in developing gas sensors for environmental monitoring continues to grow as the emission of pollutant gases increases particularly in urban areas. This continuous development has been directed towards the investigation of different materials answering to the requirements of highly sensitive, selective and reliable gas sensors produced at low cost.

In this paper, the microstructural characterisation of the RF sputtered InO_x, SiN_x films are investigated by the X-ray Photoelectron Spectroscopy (XPS) and Atomic Force Microscopy (AFM) methods. The application of these films in a layered SAW-based sensor structure for hydrogen and ozone sensing is also presented.

InO_x, which was used as sensing layer, in its non-stoichiometric form is a semiconductor material [1,2]. Furthermore, it possesses excellent sensing properties towards oxidizing (O_3) and reducing gases (H_2) [3]. It has been shown that the sensing properties of the In_2O_3 can be correlated with the grain size distribution and the surface morphology of the deposited films [4].

The XPS analysis was used to determine the chemical composition and stoichiometry of the films and the AFM method to determine the surface micro-morphology of the InO_x films.

2. Experimental

2.1 *Sample preparation*

The SiN_x / InO_x films were deposited by a planar RF magnetron sputtering: SiN_x and (SiN_x / InO_x) layers were deposited on a one-side polished 36° rotated Y-cut X-propagating $LiTaO_3$ piezoelectric substrate (Table 1). After the deposition, the samples were annealed for three hours in air at 310 °C.

A ceramic target of Si_3N_4 with purity of 99.9 % was used to deposit 1μm thick SiN_x layers. The sputtering process was conducted for 90 minutes at a substrate temperature of 120 °C in a pure nitrogen gas atmosphere. The working pressure was 1.0×10^{-2} Torr, RF power was 140 W and the distance from the target to the substrate was 3 cm. Approximately 100 nm thick InO_x film was obtained by using 99.999 % pure In target in 90 % O_2 sputtering atmosphere at the pressure of 1.0×10^{-2} Torr. The samples were positioned at a distance of 6.5 cm from the target, the sputtering power was 80 W and the sputtering process was conducted for 20 min.

Table 1. Samples for microstructural characterization

Samples	Deposited Layers
#FB1	1μm SiN_x
#FB2	1μm SiN_x / 100 nm InO_x
#FB3	100 nm InO_x

2.2 *Characterization*

The XPS experiments were performed in a VG Escalab MkII spectrometer equipped with 5-channeltrons detection systems, an unmonochromatized Al X-ray source (K_α = 1486.6 eV) and Ar^+ ion gun, used for cyclic sample sputtering between the selected-area XPS measurements.

The surface morphology of the films was investigated by using a Digital Instruments AFM Dimension 3100. The surfaces were characterized by means of the excursion peak-valley, registered in the scanning area (Zr) of the average surface roughness (Ra), relative to a reference central plane, and a standard deviation of the z values (rms) within the given area.

2.3 *Gas sensing measurements*

The sample #FB2, consisting of the structure InO_x / SiN_x / 36° YX $LiTaO_3$, was employed in a Surface Acoustic Wave (SAW) device for gas sensing applications. Using a computer controlled multi-channel gas calibration system,

the sensor was exposed to a sequence of H_2 pulses with the concentrations in air from 0.06 % (600 ppm) up to 1 % H_2 and to different O_3 concentrations between 25 – 150 ppb in the operating temperature range of 22 – 310 °C. Certified gas bottles with balanced synthetic air were used at a constant flow rate of 0.2 l/min. Synthetic air was used to stabilize the sensor before exposure at each operating temperature. The response was recorded as a change in the operational frequency at different operating temperature. To record the oscillation frequency of the frequency counter (Fluke PM6680B), a LabView based program was developed.

3. Results and Discussion

3.1 *XPS and AFM*

The chemical compositions of the films were determined by using XPS combined with cyclic ion sputtering. On the surface, all investigated InO_x films were characterised by an In/O atomic ratio ≈ 1 (see Table 2). This elemental ratio was constant through the whole thickness of the films. The XPS spectra of In and O were the classical peaks of $In3d_{5/2}$ (444.8 eV) and O1s (530.5 eV) with binding energies, corresponding to the values for In_2O_3 in the XPS Handbook [5]. On the surface of the SiN_x layer (sample #FB1), was also present a noticeable amount of atmospheric contaminants (carbon and oxygen), however they have been removed after a short ion sputtering.

Table 2. Chemical composition of the films: atomic concentration (%) of the elements and their binding energies (eV).

Sample		In 3d5	O 1s	C 1s	Si 2p	N 1s
#FB1	Atm. %		15.3	7.4	43.8	33.5
	B.E. (eV)		532.1	284.6	101.7	397.5
#FB2	Atm. %	49.7	46.7	3.6		
	B.E. (eV)	444.8	530.4	285.0		
#FB3	Atm. %	48.2	47.3	4.5		
	B.E. (eV)	444.8	530.5	284.9		

XPS depth profile of the samples #FB2 is presented in Figure 1. This profile illustrates the uniform chemical composition of InO_x film and reveals the well-defined, neat interfaces between InO_x / SiN_x. Similar results have been obtained for the sample #FB3. The film thickness of each sample, estimated from the measurements of the sputtered crater depth, was about 120 nm and 110 nm for samples #FB2 and #FB3, respectively.

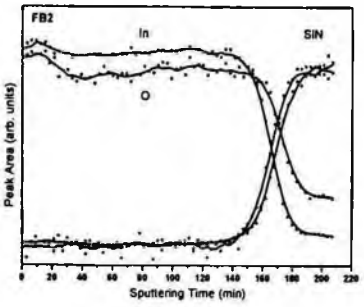

Figure 1. XPS depth profile of the sample # FB2

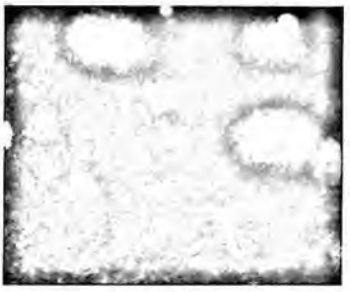

Figure 2. AFM images (2x2) μm of the sample # FB2

The AFM investigation of the InO_x film (Figure 2) revealed a nano-structured morphology with a uniform distribution of the grains with typical dimensions of 30 - 40 nm. Occasionally these grains are organised in bigger agglomerates of about 0.5 μm.

3.2 *Gas sensing*

A SAW-based sensor was fabricated, using the #FB2 sample structure of InO_x / SiN_x / 36° YX $LiTaO_3$.

Figures 3 and 4 shows the dynamic responses of the SAW sensor towards a sequence of H_2 pulses and towards different O_3 concentrations. Frequency shifts of 282 kHz for 0.25% H_2 and 338 kHz for 1% H_2 in air were recorded at the operating temperature of 215 °C. For O_3 at 190 °C, the frequency shifts of 3.7 kHz for 25 ppb and 5.1 kHz for 50 ppb were obtained.

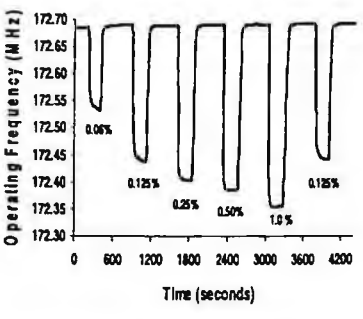

Figure 3. SAW device response to the sequence of H_2 pulses at 215 °C.

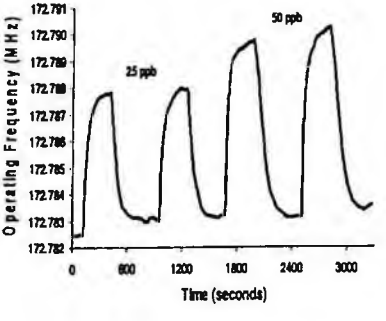

Figure 4. SAW device response to O_3 at 190 °C.

When the SAW sensor is exposed to an oxidising gas (O_3), the conductivity of the InO_x film is decreased resulting in an increase of the acoustic wave velocity. This change can be observed as an increase in the oscillation frequency. The sensitivity of InO_x films can be attributed to the oxygen vacancies in the films. By controlling the oxygen deficiency, the conductivity of InO_x films can be altered [6]. In the case of a reducing gas (H_2), a reversible chemisorption will take place. The conductivity of the InO_x layer is increased, resulting in a decrease in the acoustic wave velocity. Hence, a decrease in the oscillation frequency is observed.

The obtained results show that the sensor presents good characteristics: stable, reproducible and reversible responses to O_3 and H_2 in the operating temperature ranges of 185 – 205 °C and 165 – 310 °C, respectively.

4. Conclusions

Thin films of InO_x / SiN_x on a $LiTaO_3$ substrate have been deposited by RF magnetron sputtering and employed in a SAW gas sensor. The investigation of the chemical-physical properties of the samples revealed a good stoichiometry (In/O ≈ 1), good homogeneity of the chemical composition through the whole thickness of the films and a nano-structured surface morphology.

The application of these films in a SAW based sensor structure for H_2 and O_3 sensing produced a sensor with high magnitude, stable, reproducible and reversible responses at different operating temperatures.

The obtained results show that the RF sputtered InO_x / SiN_x films are suitable to be employed in SAW-based gas sensors for industrial applications.

References

1. G. Kiriakidis, N. Katsarakis, M. Bender, E. Gagaoudakis, V. Cimalla, Mater. Phys. Mech., **1**, 83 (2000).
2. T. Takada, K. Suzuki, M. Nakane, Sensors and Actuators B: Chemical, **13** (1993).
3. G. Korotcenkov, V. Brinzari, A. Cerneavschi, M. Ivanov, A. Cornet, J. Morante, A. Cabot, J. Arbiol, Sensors and Actuators B, **98**, 122 (2004).
4. A. Gurlo, M. Ivanovskaya, N. Bârsan, M. Schweizer-Berberich, U. Weimar, W. Göpel, A. Diéguez, Sensors and Actuators B, **44**, (1997).
5. J.F. Moulder, W.F. Stickle P.E. Sobol, K.D. Bomben. Handbook of XPS, Phys. Electronics Inc., Eden Prairie, USA (1995).
6. H. Fritzsche, B. Pashmakov, B. Claflin, Solar Energy Materials and Solar Cells, **32**, 4, (1994).

INFLUENCE OF FILLER TYPE ON SENSING PROPERTIES OF POLYMERIC COMPOSITES THIN FILMS

L. QUERCIA*, M. BOMBACE, F. LOFFREDO, G. DI FRANCIA
ENEA, Centro Ricerche Portici, 80055 Portici (NA), Italy

D. NINNO
Università di Napoli "Federico II", Dip. Scienze Fisiche, via Cinthia, 80126 Naples, Italy

Carbon black/polymer composite are very interesting materials already used to produce VOCs sensors. In this work we study the possibility to model the response of sensors quantitatively and to describe the difference between sensor obtained with same polymer matrix (poly(2-hydroxy-ethyl-methacrylate)) changing type of carbon black. We have used carbon blacks characterized by different superficial area, structure and chemical functionalization. In order to evaluate the influence of filler type on the sensitivity of the different devices prepared, we are setting up a quantitative model to obtain the responses of the sensing devices. The implemented model is a combination of a conductivity model based on the General Effective Media (GEM) and a swelling model giving information about how much the composite swells as function of vapor concentration and type.

1.1. *Introduction*

Carbon black/polymer composites are very interesting materials already used to produce vapor sensors. Sensor responses are due to vapor absorption properties of an insulating polymer whose electrical properties are modulated by a conductive "filler" [1]. In previous works we evidenced the possibility to modify the response of sensors based on same polymeric matrix using different conductive filler types [2] or fabrication process [3]. In order to evaluate the influence of filler type on the sensitivity of the different devices prepared, we are setting up a quantitative model to obtain the responses of the sensing devices. The combination of two model is needed: a) a conductivity model relating the detailed structure of the composite thin film to its resistivity, b) a thermodynamic model giving information about how much the composite swells and the conductive filler particles move from each other as function of vapor concentration and type. We have prepared composite thin films with increasing

* Corresponding autor: e-mail quercia@portici.enea.it Tel: +390817723302 Fax: +390817723344

filler volume fraction to obtain the experimental data needed to develop the conductivity model based on the General Effective Media (GEM) equation [4]. To model the swelling of the polymeric matrix in function of vapor concentration, we use literature data relative to variations of thickness of poly(2-hydroxy-ethyl-methacrylate) (PHEMA) due to swelling in presence of methanol [5].

1.2. *Experimental part*

In this work we have chosen to use two commercial carbon blacks (Black Pearls 2000 or Xc72) kindly donated by Cabot Co and a chemically modified carbon black obtained to improve the dispersion of filler in polar polymer solution [2]. The principal characteristics of fillers used to produce composites are summarized in Table 1.

The polymer/solvent solutions of different concentrations are prepared dissolving poly(2-hydroxy-ethyl-methacrylate) in ethanol. Fillers are added to solutions and the homogeneous suspensions are obtained by treatments in ultrasonic bath. Different type and amount of fillers are used to produce polymeric composites.

Table 1. Fillers used to produce thin film conductive composites.

FILLER	CB pwd	CB pel	mod-CB
Name	Cabot CB (Xc72)	Cabot CB (Black pearls 2000)	CB pel modified by chemical reaction
Preparation	Commercial sample	Commercial sample	Fenton type reaction
Morphology	powder	pellets	powder
Surface area (m^2/g)	112	1500	

Films are prepared by spinning on glass substrates. The electrical contacts consist of two fingers of silver paste (separated by a gap of 5 mm) deposited on the sensing film.

All thin film polymer composites obtained are characterized by Tencor P10 surface profiler, SEM (Leo 1530) and optical analysis (Polyvar Met, Reichert-Jung). The sensing devices responses to organic vapor are studied using a Gas Sensor Characterization System (GSCS) already described [2,3].

1.3. *Results and discussion*

The responses of sensing devices prepared with CB/PHEMA composites are compared in Figure 1. In order to rationalize experimental data we have begun to develop a theoretical model taking in count the working mechanism generally assumed for this type of sensors.

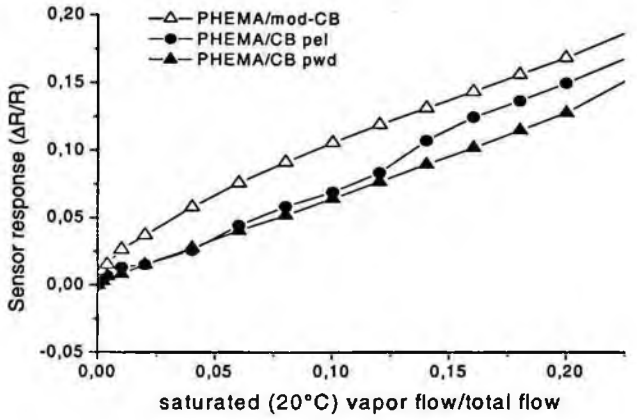

Figure 1. Responses to methanol of sensors based on PHEMA composites obtained with different CB.

In presence of organic vapor the polymeric matrix swells decreasing the volume fraction of CB. For small relative swelling $\Delta V/V << 1$ (where ΔV is the volume increase due to swelling) we have modeled the sensors responses by the equation (1).

$$\frac{\Delta R}{R} = \frac{t\phi}{(\phi - \phi_c)} \cdot \frac{\Delta V}{V} \cong t \cdot \frac{\Delta V}{V} = t \cdot aC^b \qquad (1)$$

where, ϕ is the volume fraction of CB and ϕ_c is the volume fraction at percolation threshold and t is the critical exponent as described by G.E.M. equation [4]. In our experimental conditions (always $\phi >> \phi_c$) the equation can be simplified. Moreover, we have empirically modelled the concentration-dependent swelling of polymer using a power law aC^b, with a and b being constants related to a specific composite/absorbed vapor system. The Eq. (1) is characterized from the presence of only three parameters (t, a, b) that can be estimated independently. The t parameter can be determined by the percolation curves of the specific polymer/conductive filler system while the swelling

parameters (a, b) can be determined by thickness measurements evaluating the polymer swelling in presence of the vapor of interest. In fact, assuming an isotropic swelling in the three dimensions we have:

$$\frac{\Delta V}{V} = \left(1 + \frac{\Delta T}{T}\right)^3 - 1 \qquad (2)$$

where $\frac{\Delta T}{T}$ is the relative thickness variation.

In Figure 2 we show the relative volume variations obtained using Eq. (2) and literature experimental data about PHEMA film swellings due to methanol vapors. The results of data fitting with aC^b function are summarized in Table 2. There is a good agreement between experimental data and fitting curve, confirming our choice of power-law. PHEMA films present similar values of a and b. The major differences are observed for the thin film of 55nm.

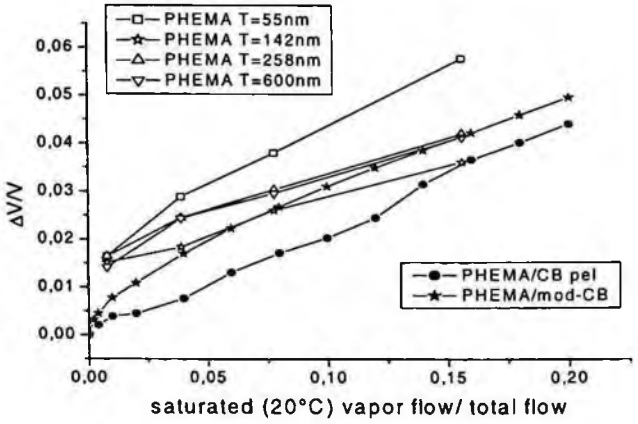

Figure 2. Variation in volume calculated with Eq. (2) for PHEMA films of different thickness (from literature [5]) and with Eq. (1) from response of Figure 1 for PHEMA/CB composites.

In Figure 2 are also reported the swelling data calculated with Eq. (1) from sensor responses of Figure 1. The t value for CB pel and mod-CB is 3.4 as estimated from our experimental percolation curves of CB pel composites. The $\Delta V/V$ values of PHEMA composites, obtained in this way, show a very good agreement with the experimental swelling data of PHEMA films. It is very interesting to note that the t parameter, calculated by percolation curve of CB pel composites, allows to obtain swelling values slightly lower than pure

polymer, as expected by filler stiffness. Moreover different *a* and *b* values for different fillers point out the influence of filler on sensing properties. *b* parameter is lower than 1 only for mod-CB suggesting different filler-polymer interactions.

Table 2 *a* and *b* parameters obtained from fitting of curves reported in Figure 2.

Sample	*a*	*b*
PHEMA/CB pel	0.24 ± 0.01	1.05 ± 0.04
PHEMA/mod-CB	0.139 ± 0.002	0.650 ± 0.008
PHEMA/CB pdw	(1.42 ± 0.05) / t	1.58 ± 0.07
PHEMA (T=55nm) [5]	0.13 ± 0.02	0.46 ± 0.05
PHEMA (T=142nm) [5]	0.06 ± 0.01	0.34 ± 0.08
PHEMA (T=258nm) [5]	0.076 ± 0.009	0.34 ± 0.04
PHEMA (T=600nm) [5]	0.080 ± 0.007	0.37 ± 0.03

1.4. *Conclusions*

Small changes in film morphology, obtained introducing different fillers in PHEMA matrix, produce sensors with different sensitivities to organic vapors.

We have tested a semi-empirical model able to quantify sensor response to vapor. In this way it is possible to discriminate between the influence of filler volume fraction on conductivity and composite swelling on the sensor responses. We compared the swelling data obtained by swelling measurements carried out on PHEMA films with swelling data estimated by our model, our experimental critical conductivity parameter *t* and responses to methanol. The swelling data obtained are, as expected, slightly lower than those relative to pure PHEMA films. The *b* parameter point out quantitative and qualitative different swelling properties for different fillers.

References

1. J. W. Hu, S. Guo Chena, M. Q. Zhangc, M. W. Li, M. Z. Rong, *Materials Letters* **58,** 3606 (2004).
2. L. Quercia, F. Loffredo, G. Di Francia, *Sensors and Actuators B* (2005) in press.
3. L. Quercia, F. Loffredo, M. Bombace, I. Nasti, G. Di Francia *Sensors and Actuators B* (2005) in press.
4. D.S. McLachlan, *Solid State Comm.* **72,** 831 (1989).

5. D. Goustouridis, K. Manolo, S. Chatzandroulis, N. Sanopoulou, I. Reptis, submitted to *Sensors and Actuators B* (2005).

COMPARISON OF HIGH TEMPERATURE MRISiC BASED GAS SENSORS WITH DIFFERENT SENSING LAYERS

A. TRINCHI, S. KANDASAMY, W. WLODARSKI

School of Electrical and Computer Engineering, RMIT University
GPO Box 2476V, Melbourne, Victoria 3001, AUSTRALIA

E. COMINI, G. SBERVEGLIERI

SENSOR, INFM
Universita` di Brescia, via valotti 9, 25133 Brescia, ITALY

Metal Reactive Insulator Silicon Carbide (MRISiC) Devices with different reactive insulator layers of Ga_2O_3, TiO_2, and WO_3 have been fabricated and their hydrogen gas sensing performance has been investigated. Responses of devices with different reactive insulator layers have been compared in terms of barrier height, operating temperature range, series resistance, time constants and turn on voltage, all of which are modified by changing the reactive insulator layer. It is shown that exposure to different gas concentrations results in changes in carrier concentration and in barrier height, which results in a change in the forward bias voltage. Voltage shifts as large as 1 V have been observed. In addition, parameters have been extracted from Current-Voltage (I-V) measurements, which have shown changes in barrier height as large as 50 meV for H_2 concentrations of 1%.

1. Introduction

Historically, Metal Oxide Semiconductor (MOS) devices have been employed in the field of gas sensing primarily for detecting reducing gases such as hydrogen. With the increasing interest in monitoring gases at elevated temperatures, Metal-Reactive Insulator-Silicon Carbide (MRISiC) devices have become the attractive evolution of the MOS gas sensor.

The reactive insulator is selected for its reactivity to the target gas, and is typically a metal oxide layer, deposited between the silicon carbide and a catalytic metal. Such devices can offer increased sensitivity, selectivity and stability[1]. These are operated as Schottky diodes, with the response being measured as the change in bias voltage at constant current. We have developed several MRISiC gas sensors. Their response to different gases was measured as the change in voltage at this constant current bias.

In this paper, we discuss how the response, barrier height, operating temperature range, series resistance, time constants and turn on voltage are all altered by changing the reactive insulator layer of the MRISiC devices. Thin films of Ga_2O_3, TiO_2, MoO_3 and WO_3, fabricated by sol-gel and r.f. sputtering,

have been investigated as reactive insulator layers. Exposure to these different gas concentrations results in a change in the carrier concentration and in the Schottky barrier height, which results in a change in the forward bias voltage.

2. Sensor Structure and Testing Procedures

Each sensor employed the nitrogen-doped (1.56×10^{18} /cm^3) n-type 6H polytype of SiC, with a thickness of 254 μm. A titanium layer (500 Å) was utilised for the ohmic contact. The catalytic metal gate was platinum (100 nm) and was selected for its catalytic behaviour towards hydrogen. All the metal layers were deposited by d.c. magnetron sputtering. The Ga_2O_3 reactive insulator layer was prepared by the sol-gel process and deposited by spin coating, with gallium isopropoxide being the starting precursor solution. The TiO_2, WO_3 and MoO_3 reactive insulator layers were deposited by r.f. sputtering. The thickness of all the reactive insulator layers was approximately 100 nm. A micro heater was placed beneath the structure to control the temperature of the device. A schematic of the sensor can be seen in Figure 1.

Figure 1: Schematic of the MRISiC sensor.

The sensors were exposed to different concentrations of hydrogen at a constant flow rate of 200 ml/minute. Further details on the fabrication and gas sensing set-up of the sensor can be found in elsewhere[2,5].

3. Results

3.1. *Gas Sensing*

The voltage shifts of the devices were recorded using a HP 33104A multi-meter. Their hydrogen responses were investigated over a temperature range of 150–650°C in an ambient of synthetic air. The gas concentration was varied from 1 to 0.25%. Figure 2 shows the largest recorded responses of the MRISiC sensors with different reactive insulator layers, at their respective operating temperatures. The sensors were biased at a constant current of 1 mA.

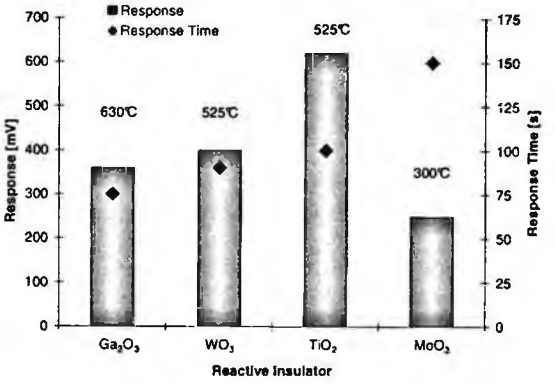

Figure 2: Response of different MRISiC devices.

For the Ga_2O_3 based device, as the operating temperature increased, the magnitude of the response increased. The largest response recorded was at an operating temperature of 630°C. On the other hand, despite having larger responses, both the WO_3 and TiO_2 based devices reached their maximum voltage shift at temperature of around 520°C. Above these temperatures, their respective responses rapidly declined. Conversely, the MoO_3 device exhibited its largest voltage shift of 250 mV at a much lower operating temperature, namely was 300°C. Such a result is attributed to the low melting point of MoO_3 (around 400°C) and hence renders this reactive insulator unstable for high temperature gas sensing applications.

Our research has shown that the response time is strongly dependent on the operating temperature. For all tests carried out, the Ga_2O_3 based devices possessed the lowest response times, around 70 seconds. Larger response times were required for the WO_3 and TiO_2 based devices and the MoO_3 sensors required more that twice the time to respond as the Ga_2O_3 based devices.

Stability is an important issue in any gas sensing application. The stability of the MRISiC sensors is strongly dependent on the reactive insulator layer. Ga_2O_3 thin films used in MRISiC devices have shown to possess uniformly distributed nano-sized grains, whose morphology is tight and compact. Conversely, The WO_3 thin films have shown to possess much larger grains, as well as homogenously distributed pores, and which are also attributable to the varying stability of the devices. Furthermore, the MoO_3 based MRISiC sensors exhibited poor baseline stability, not only as a result of the surface morphology of these films, but also from the much lower operating temperatures required.

3.2. *Electrical Characterisation*

The change in barrier height of the devices can be analysed by extrapolating information from the *I-V* characteristics. Based on the thermionic field emission conduction mechanism of Schottky diodes, for forward bias voltages greater than 3kT/q, the current through the diode can be expressed by[3]:

$$I = I_{sat} \exp(qV / nkT)$$

where k is the Boltzmann constant, n is the ideality factor, T is the temperature in Kelvin, and I_{sat} is the saturation current, which is defined as:

$$I_{sat} = SA^{**}T^2 \exp(-q\phi_b / kT)$$

where S is the cross-sectional area of the electrode at the metal/semiconductor interface (cm^2), A^{**} is the effective Richardson's constant (A/cm^2K^2) and ϕ_b is the barrier height (eV). The saturation current was obtained by extraction of the linear portion of the $\ln(I_{sat})$ vs. V plot. The *I-V* characteristics were measured using a Tektronix 571 curve tracer, from which the barrier heights of the devices were calculated. The change in barrier height of the MRISiC devices with different reactive insulators, when 1% H_2 is introduced into ambient synthetic air, is seen in Figure 3. Clearly the reactive insulator is a pertinent factor for the obtained values, and it is responsible for the difference in obtained values.

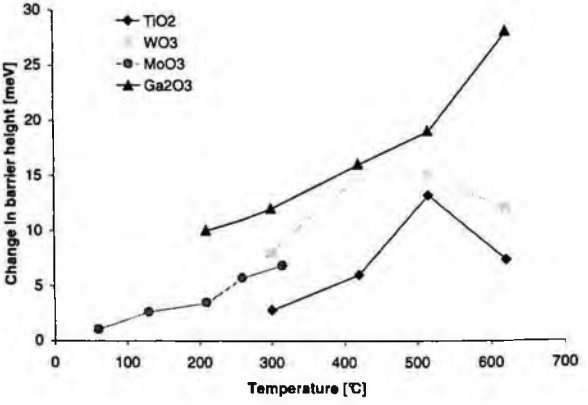

Figure 3: Change in barrier height of different MRISiC devices when 1% H_2 is introduced into ambient synthetic air.

Quite clearly, the largest change in barrier height is observed for the Ga_2O_3 based devices, despite them having lower response compared with the TiO_2 and

WO_3 based sensors. Such a factor is attributable to the much lower turn on voltage of the Ga_2O_3 based sensor as opposed the others (Figure 4). More importantly, such an observations is prominently the result of the change in the devices series resistance.

The layer introduced between the metal contact and the semiconductor, acts as a gas sensitive resistance. Applying a voltage is divided to a voltage partly over the resistance and partly over the entire device. When exposed to a gas, the change in voltage, ΔV, at a constant bias current, I_{bias}, can be described by [4]:

$$\Delta V = n\Delta\phi_B + I_{\text{bias}}\Delta R_S$$

where $\Delta\phi_B$ is the change in the Schottky barrier height and ΔR_s is the change in the series resistance of the device. If the series resistance of the device is independent of the introduced gas concentration, then the output voltage of the sensor is constant for a given current level. However, when the series resistance depends on the atmospheric gas, and the value of ΔR_s is positive, then ΔV will increase as the forward bias current increases. The voltage level is dependent on the bias current level, and the series resistance.

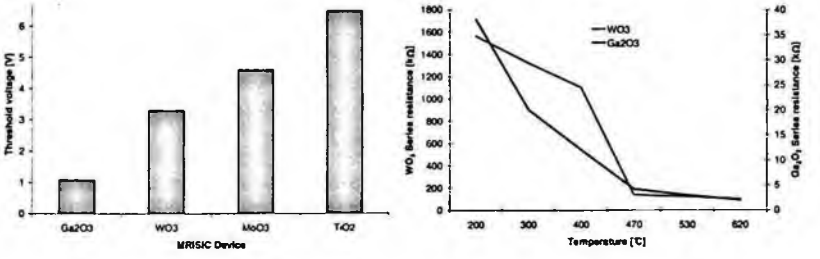

Figure 4: Threshold voltages and device series resistance for different MRISiC devices.

The reduction in the devices series resistance with increasing H_2 concentration is clearly translated to the change in shape of the *I–V* curves. As the temperature and H_2 concentration increase, the *I–V* curves increasingly resemble those of ohmic contacts, see Figure 5. The lateral shift is directly translated to the changing barrier height, and the change in slope is ascribed to the change in the series resistance. Such large changes in series resistance were not observed for MOSiC devices with SiO_2 insulating layers, and hence are largely attributed to the reactive insulator.

Series resistance is comprised of those from the reactive insulator, as well as the surface and bulk of the semiconductor. The series resistance of the device is higher in the O_2 rich ambient than that containing hydrogen, and at higher

temperatures. In fact, at 515°C, the series resistance in H_2 is reduced to 0.7 kOhms from 3 kOhms in air for the Ga_2O_3 device, as compared to 80 from 118 for the WO_3 sensors. Further information on the sensing mechanism of such devices can be found in [5].

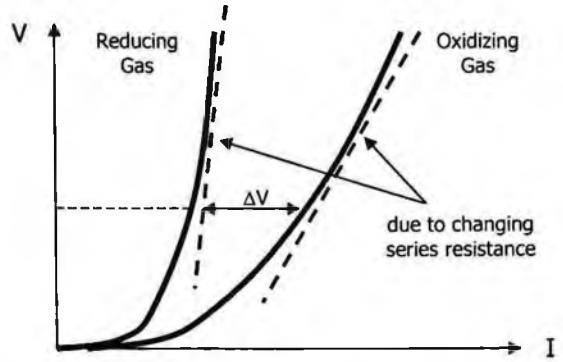

Figure 5: I-V Characteristics in different ambient atmospheres.

4. Conclusions

In this paper, we have described the gas response and some electrical models of the MRISiC based sensors with different metal oxide interfacial layers. The different response of the devices is strongly dependent on the electronic nature of the metal oxide utilised as the reactive insulator.

REFERENCES

1. G.W. Hunter, P.G. Neudeck, L.-Y. Chen, D. Knight, C. C. Liu, Q.H. Wu, in 7th International Conference on Silicon Carbide, III-Nitrides and Related Materials, Stockholm, Sweden, **2**, 1093 (1997)
2. A. Trinchi, S. Kaciulis, L. Pandolfi, M.K. Ghantasala, S. Viticoli, Y.X. Li, W. Wlodarski, E. Comini, G. Sberveglieri, *Sens. Actuators B*, **103**, 129 (2004)
3. S.M. Sze, *Physics of Semiconductor Devices* **2nd ed**, Wiley (1981)
4. S. Nakagomi, K. Okuda, Y. Kokubun, *Sens. Actuators B*, **96** 364 (2003)
5. A. Trinchi, W. Wlodarski, Y.X. Li, G. Faglia and G. Sberveglieri, *J. Phys. D*, **38**, 754 (2005)

CH_4 GAS SENSING PROPERTIES OF γ-Fe_2O_3 SEMICONDUCTOR THIN FILM BASED SENSOR

LUCA FRANCIOSO, SIMONETTA CAPONE, PIETRO SICILIANO,
INSTITUTE FOR MICROELECTRONICS AND MICROSISTEMS - CNR.
Via per Arnesano, Lecce,73100, ITALY
E-mail: simona.capone@le.imm.cnr.it

DZMITRY KOTSIKAU, MARIA IVANOVSKAYA
RESEARCH INSTITUTE FOR PHYSICAL CHEMICAL PROBLEMS OF THE BELARUSIAN STATE UNIVERSITY,
14 Leningradskaya, 220050 Minsk, Belarus.

Gas-sensitive properties of γ-Fe_2O_3 thin film, deposited on Si-substrate of new design, have been studied in this work. The layers were formed by using sol-gel derived γ-$Fe_2O_3 x n H_2O$ colloidal solution. Structural features of the films and peculiarities of iron state were obtained by employing XRD, HR-TEM, IR and Mössbauer spectroscopy. High sensitivity of the mentioned sensor to CH_4 has been established.

1. Introduction

Generally, thin film sensors based on semiconductor oxides (In_2O_3, SnO_2, Fe_2O_3) are characterised by improved performance when detecting gases of acceptor (NO_x, O_3) and donor (C_2H_5OH) nature [1]. Sensitivity of thin films to reducing gases is extremely low (CO and, particularly, CH_4). In order to improve the characteristics of thin films to flammable gases, oxide layers are commonly been doped with noble metals. It is essentially, that gas-sensitive features of Fe_2O_3 is strongly determined by its structural features like phase composition, dispersity, defectiveness, morphology etc. Shin and Park [2] successfully used γ-Fe_2O_3 as an individual layer and as a component of a multi-layer structure of ceramic sensors for detection of flammable gases. In the present work we deposited γ-Fe_2O_3 thin films by sol-gel derived γ-$Fe_2O_3 x n H_2O$ colloidal solution. The γ-Fe_2O_3 sensing layers were deposited on Si-bulk substrates equipped with Pt-interdigitated electrodes and preliminary covered with a In_2O_3 sublayer. Here, we report a study of gas-sensitive behaviour towards methane (CH_4) of deposited γ-Fe_2O_3 thin films. Detailed structural examination of the oxide layer has also been carried out.

2. Experimental

The sensitive layers were formed from the stabilised sol of Fe_2O_3 x nH_2O prepared by the Sol-Gel rout. Synthesis of the sol proceeded in a combined hydrolysis of Fe^{2+} and Fe^{3+} sulphates by aqueous ammonia, and consequent sol oxidation by oxygen flow at 100°C for 5 h. The sol was deposited onto Si-bulk substrates of new design, which were provided by IMM-CNR, Lecce. The substrates are supplied with interdigitated electrode structure on front side and Pt-heater on back side, and have size of 2x2x0.25mm^3 with an active area of approximately 1.4x1.4 mm^2. In order to provide suitable sensor conductivity, electrodes were preliminary covered with In_2O_3 sub-layer. The substrates with the deposited sensing layers were annealed at 350°C for 25 h in air. In fig.1 an image of the gas sensor device bounded on a TO-39 support is shown. Sensor response (S) was estimated as ratio I_{CH4}/I_{air}, where I_{CH4} and I_{air} are the electrical current values in CH_4 ambient and in air under constant voltage supply to the electrodes, correspondingly.

Structure of the material was studied by means of XRD, HR-TEM, DTA/TG, FT-IR and Mössbauer spectroscopy.

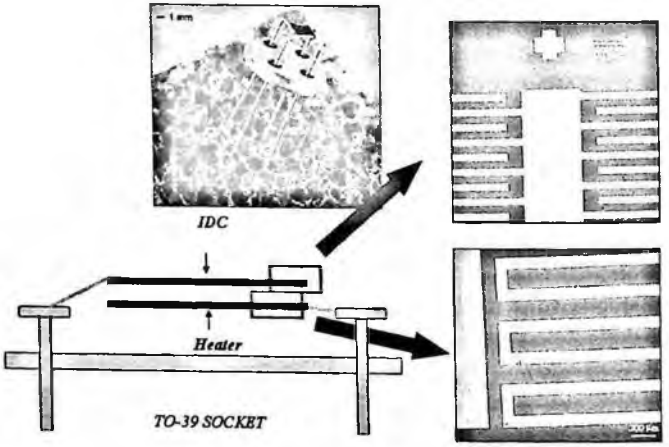

Fig.1. Image and cross section scheme of the gas sensor on 2x2 mm^2 sized Si-substrate bounded on TO-39 socket. In the inserts a magnifications of the interdigitated electrodes on the front and the Pt heater on the back of the substrate.

3. Results and Discussion

The applied conditions of Fe_2O_3 synthesis allow to obtain thin-film of γ-Fe_2O_3, which is metastable at R.T.. XRD data confirm the formation of the mentioned phase (Fig. 2). As it follows from the DTA/TG data, thus obtained γ-Fe_2O_3 remains stable up to 485°C. Annealing the sample at higher temperatures leads to its transformation into thermodynamically stable α-Fe_2O_3. However, considerable amount of γ-Fe_2O_3 preserves within the film annealed at 500°C (see Fig. 2).

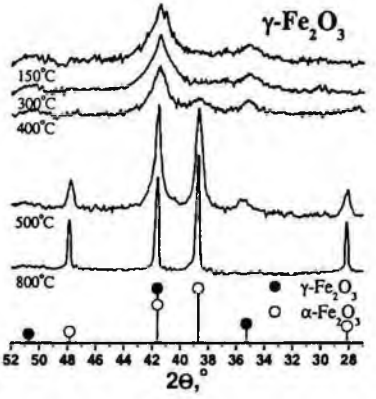

Fig. 2. XRD patterns of γ-Fe_2O_3 powder annealed at different temperatures.

According to the results of Mössbauer spectroscopy, the material heated at 300°C contains Fe^{3+} ions only; the occurrence of Fe^{2+} state was not discovered. The analysis of the parameters, which are presented in the Table 1, also confirms that γ-Fe_2O_3 phase is formed under the conditions of synthesis used. Decreased value of magnetic field (B), which is characteristic of the sol-gel derived sample, in comparison with the reference parameters for the corresponding bulk phase is explained by occurrence of very fine oxide grains.

Table 1. Parameters of ^{57}Fe Mössbauer spectra obtained from the sol-gel derived γ-Fe_2O_3 and reference data for γ -Fe_2O_3 bulk phase. Recording temperature is 300 K.

Sample	δ, mm s^{-1}	Δ, mm s^{-1}	B, T
γ-Fe_2O_3 (sol-gel)	0.34	-0.03	49.1
γ-Fe_2O_3 (bulk)	0.34	-0.05	49.8

HR-TEM characterisation gives spherical particles of size as high as 3-9 nm. The micrograph of the γ-Fe_2O_3 film, annealed at 300°C, is presented in the Fig. 3. Note, that the evident non-uniformity of the grain size distribution provides good quality of the films.

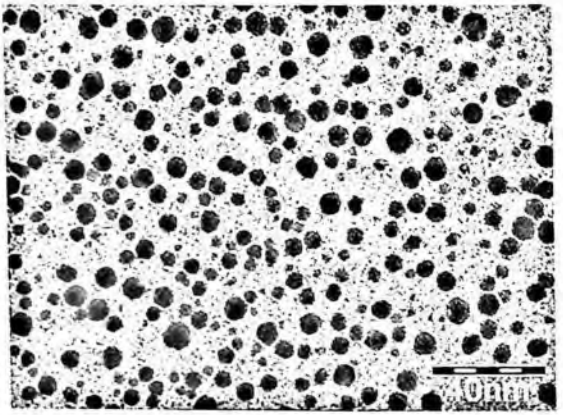

Fig. 3. HR-TEM image of γ-Fe_2O_3 film annealed at 300°C.

Gas sensing tests at different temperature and CH_4 concentration in dry air have been carried out under controlled environment. We found that the thin film sensor, based on highly dispersive γ-Fe_2O_3-In_2O_3, is characterised by high sensitivity to CH_4. Suitable sensitivity of the sensor to low CH_4 concentration (100 ppm) is reached at 350-425°C. Note, that the dynamic response profiles are well-reproducible under repeated exposition of CH_4. Initial parameters of the films recover totally after CH_4 evacuation. Optimal operating temperature, at which the sample demonstrates maximum response, fastest dynamics and linear response vs. concentration dependence, is found to be 425°C. Inverse effect to CH_4 was found at lower temperature (T=240-275°C) after a working period of higher T. In fig.4(a) and (b) the dynamic response of γ-Fe_2O_3/In_2O_3 thin film sensor to different CH_4 concentrations (4a) at high T range and at low T range (4b) is reported. Moreover, in fig. 4(c) the response vs. CH_4 concentration curves of the sensor to CH_4 at different operating temperatures is shown.

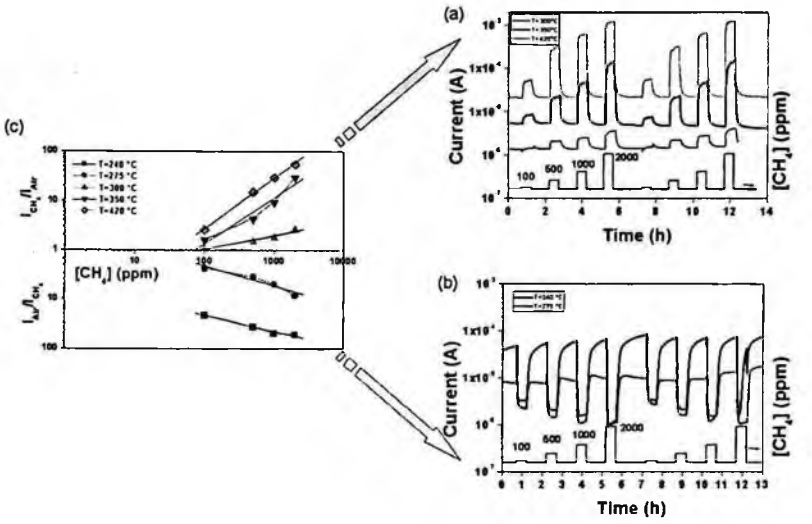

Fig. 4 (a) dynamic response of γ-Fe_2O_3/In_2O_3 thin film sensor to different CH_4 concentrations at high T range and (b) at low T range; (c) Response vs. CH_4 concentration curves at different operating temperatures.

4. Conclusions

The Sol-Gel Technique was successfully used for the preparation of good-quality thin film based on γ-Fe_2O_3 with grains of 3-9 nm in diameter. Thus obtained γ-Fe_2O_3 phase appeared to be stable with regards to γ-$Fe_2O_3 \rightarrow \alpha$-Fe2O3 phase transition up to 485°C. Good performance of metal-oxide thin film deposited on miniaturised Si-substrate covered with In_2O_3 sub-layer was achieved to CH_4 by applying highly dispersive Fe_2O_3 of adjusted structure as a sensing material.

Working is in progress in order to better understand the inverse response to CH_4 at lower T. The cross-sensitivity to other oxidizing (NO_2) and reducing gases (CO) is also in studying.

References

1. M. Ivanovskaya, D. Kotsikau, G. Faglia et al.; Sens. Actuators B, 93 (2003), pp. 422-430.
2. J-U. Shin, S-J. Park; Proc. 2nd Int. Meeting on Chemical Sensors, 1986, Bordeaux, France, pp. 123-126.

In_2O_3-SnO_2 AND SnO_2-PdO SOL-GEL THIN FILMS AS NEW GAS-SENSING MATERIALS FOR NO_2 DETECTION

LUCA FRANCIOSO, SIMONETTA CAPONE, ANGIOLA FORLEO, MAURO EPIFANI, ANTONELLA M. TAURINO, PIETRO SICILIANO
INSTITUTE FOR MICROELECTRONICS AND MICROSISTEMS - CNR.
Via per Arnesano, Lecce,73100, ITALY
E-mail: simona.capone@le.imm.cnr.it

Semiconductor sensors based on nanocrystalline SnO_2, In_2O_3 and In_2O_3-SnO_2 thin films have been investigated for detecting low concentration (2-20 ppm) of nitrogen dioxide in dry air. In this work the gas-sensitive layers were prepared by modified sol-gel methods making use of no-standard precursors and a suitable surfactant. The samples have been morphologically characterized by SEM. Good gas-sensing responses towards NO_2 have been found for all the prepared samples with improved performances for the In_2O_3-SnO_2 based sensor. The performances of the sensors have been discussed according to the surface chemical reactions between the gas phase and the semiconductor.

1. Introduction

The research of new gas-sensing materials, which can satisfy essential requisites, such as reliability, stability, selectivity, sensitivity and low cost, is one of the most important task of both academic research and industry .

Metal oxides have been traditionally used as active materials for gas sensors [1]. SnO_2 and In_2O_3 thin films have already been studied as gas sensors, their sensing properties combined in a binary oxide are not completely known. In_2O_3 shows electrophysical and chemical properties essentially different respect to SnO_2 and this different behaviour seems to considerably modify the traditional gas detection mechanism based on the mediation of surface chemisorbed oxygen species. An interaction mechanism manly based on redox reactions reversibly changing the surface composition of the metal oxide film seems to be a more realistic situation [3,4]. Pd is also a common dopant of SnO_2 with dopant concentration normally up to about 5% wt., but the possibility to reach higher concentration was not explored yet [2].

In this work, In_2O_3, SnO_2, SnO_2-PdO (1:1 molar ratio) and In_2O_3-SnO_2 (I:1 molar ratio) mixed oxides have been prepared by the sol-gel technique and deposited as thin films both on Si substrates for morphological characterization and on alumina substrates equipped with electrical contacts and Ti/Pt heater for the characterization as gas sensors. Systematic gas sensing tests towards NO_2

both in dry air (R.H.=0%) have been carried out for all the In_2O_3-SnO_2 and SnO_2-PdO mixed oxide based sensors.

2. Experimental

SnO_2, In_2O_3, SnO_2-PdO (1:1 molar ratio) and In_2O_3-SnO_2 (1:1 molar ratio) thin films have been prepared by sol-gel technique, that is a wet chemical method known to be a suitable method for the preparation of nanoscaled systems. The films were deposited by spin-coating both on silicon wafers for the structural and morphological characterization, and on pre-cut alumina wafers for the realization of the gas-sensing devices. In particular, each sensor on alumina substrate was 2 mm x 2 mm sized and provided with Pt-resistive type heater on the backside and Au-interdigitated electrodes (n=3 fingers, 160 μm spaced, 1.4 mm long and 50 μm wide) on the front side over the deposited oxide thin film.

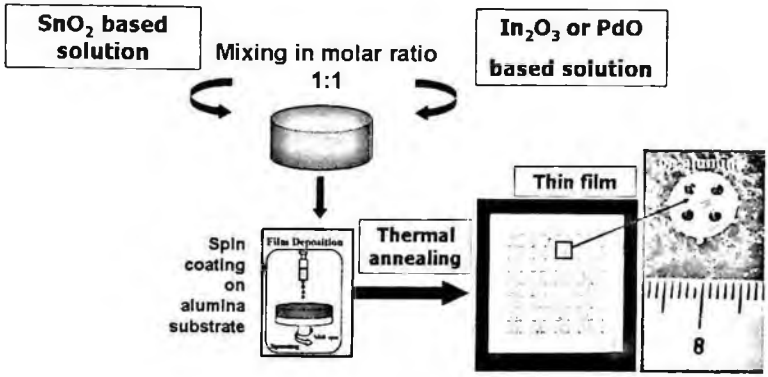

Fig. 1. Scheme of the sol-gel process for the single and mixed In_2O_3-SnO_2 and SnO_2-PdO systems.

Indium oxide sols were prepared by dissolving 1 g of $In(NO_3)_3 \cdot 5H_2O$ in 15 ml of methanol. After the dissolution of the salt, acetylacetone ($CH_3COCH_2COCH_3$, acacH) was dropped in the solution in order to chelate the In^{3+} ions, with an acacH/In molar ratio of 2. Moreover, concentrated ammonium hydroxide (30 wt% solution in water) was added to the solution, with a NH_3/In molar ratio of 2. Finally, in order to improve the adhesion on Si substrate a suitable surfactant (i.e. alkylammonium bromide) was added to the solution. As regards the SnO_2 sol, a process based on the use of Sn(II) ethylhexanoate, as Sn precursor instead of the standard and commonly used $SnCl_4$, and of the same

surfactant used in the preparation of the In_2O_3 sol) was developed. The sol for preparing In_2O_3-SnO_2 system was simply prepared by mixing in equimolar proportion the corresponding single oxide sols that were prepared with the previously described procedures. As regards the SnO_2-PdO mixed system, the solution was prepared by mixing the suitable amount of palladium acetate dissolved in acetone with a SnO_2 sol prepared with the new precursor and the surfactant. However, some problems related to the mixed SnO_2-PdO solution stability have to be mentioned. After spin coating (2000 rpm, 30 s) on alumina and Si substrates all the samples were dried at 70 °C followed by annealing at high temperature (500 °C, 1 h) into an oven in air, obtaining in such a way thin films with a thickness of about 100-140 nm. In Fig. 1 a scheme of the sol-gel process for the single and mixed oxides is shown.

The surface morphology of the oxide thin films on silicon substrates were examined by means of scanning electron microscopy (SEM-FEG Jeol 6500, operating at 10 kV). Moreover, in order to investigate the gas sensing properties of the samples, a calibration gas sensing test-bench for electrical-conductance measurements in controlled atmosphere was used.

3. Results and Discussion

SEM characterization gave evidence that both the single (SnO_2 and In_2O_3) and binary oxide (In_2O_3-SnO_2 and SnO_2-PdO) thin films are nano-scaled systems. However, the surface morphology of the In_2O_3-SnO_2 thin film sample is very different from the morphology of the corresponding single oxides. SnO_2 and In_2O_3 films showed a fine and uniform distribution of nanoclusters, whereas In_2O_3-SnO_2 film shows a non-uniform morphology with brighter and round-shaped agglomerates of nanograins on a background of dark/bright nanograin matrix. A SEM image for a In_2O_3-SnO_2 thin film on Si substrate is reported in Fig. 2a. The brighter nano-structured clusters could be attributed to the formation of Sn-rich regions with respect to the darker nanosized grains. As regards SnO_2-PdO a typical like-meander morphology appears; at higher magnification some darker clusters on a very fine and uniform nanocrystalline background is evident (Fig. 2b). However, a detailed structural analysis by TEM is necessary in order to determine the exact nature of the different dark and bright areas visible in the SEM images.

In Fig. 3 the temperature dependent response to NO_2 (5 ppm in dry air) of SnO_2, In_2O_3, SnO_2-PdO and In_2O_3-SnO_2 thin film based sensors is reported. For oxidising gases (as NO_2) the response is defined as the quotient I_{air}/I_{gas} (where I_{air} and I_{gas} are the sample electrical current under DC supply under gas exposure

and in air respectively). The maximum response of SnO_2 and In_2O_3-SnO_2 sensors to NO_2 is reached at the same temperature (~250°C), but whereas the response peak of the In_2O_3-SnO_2 sensor is narrower around the best working temperature for SnO_2, the response of the SnO_2 sensor decreases slowly at temperature higher of 250 °C. This is typical for SnO_2 films whose chemisorption mechanism of gas detection covers the whole range of operating temperature (T<450°C), while In_2O_3 based sensors generally need lower working temperatures (T<300 °C).

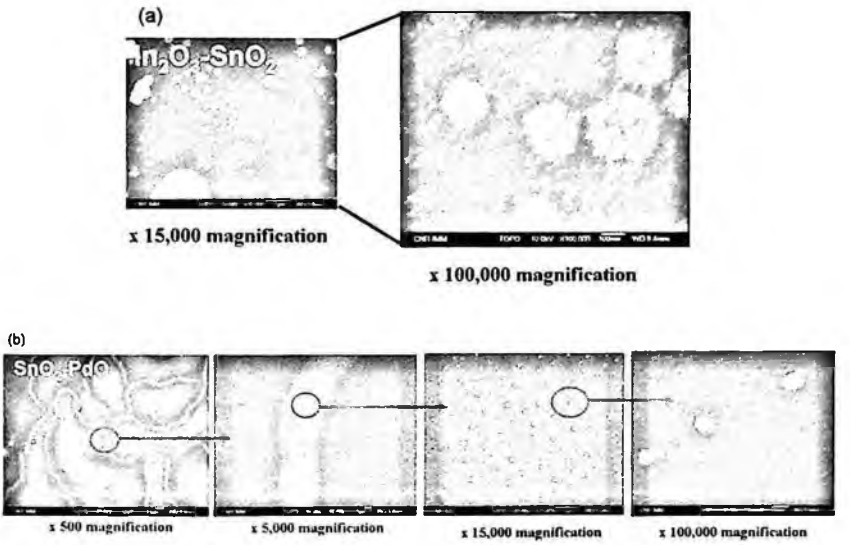

Fig. 2. SEM images at different magnification of the In_2O_3-SnO_2 (a) and SnO_2-PdO (b) films on Si-substrates.

This behaviour can be a sign of a different gas-detecting mechanism for SnO_2 and In_2O_3 based sensor. In_2O_3-SnO_2 sensor showed higher response than SnO_2 at T<250 °C, while at temperature higher than 250 °C the response value decreases and becomes comparable or lower than SnO_2. The gas response of single oxide In_2O_3 based sensor is really higher compared to both the other two sensors only at very low temperature (T~100 °C). At increasing the temperature the gas response of In_2O_3 sensor varies slowly up to T~250°C, next it decreases. SnO_2-PdO showed lower responses at T<250 °C as compared with SnO_2. Fig. 4 illustrates the transient response of In_2O_3-SnO_2 thin film based sensor to different concentration of NO_2 in dry air at T=250°C.

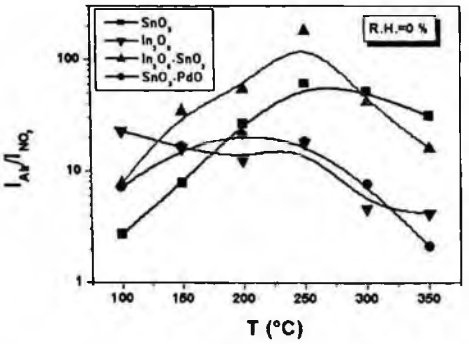

Fig. 3. Response to 5 ppm NO_2 in dry air vs. working temperature for all the sensors.

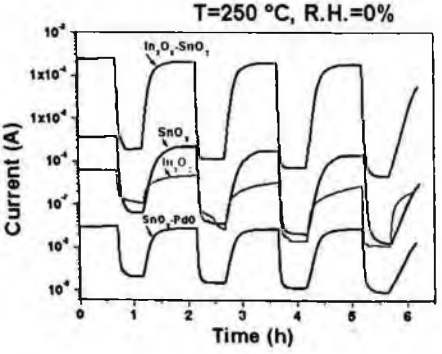

Fig. 4. dynamic response of the tested sensors at T = 250 °C and at R.H. = 0%

Some differences in gas detection mechanism between In_2O_3 and SnO_2 are schematized in Fig. 5. According to these differences, different sensing properties for In_2O_3 are expected compared to SnO_2. At low temperature, where the gas detection mechanism is dominated by a direct ionosorption of NO_2 molecules, the more basic character of In_2O_3 prevails against the less basic character of SnO_2, hence In_2O_3 showed higher responses compared to SnO_2. At increasing the temperature the higher concentration of O^-_{ads} species that lead for SnO_2 to a different interaction mediated by the adsorbed oxygen species seems to favour SnO_2 compared to In_2O_3. Nevertheless, this behaviour found in our tests may be attributed to some aging of our In_2O_3 samples or to a different microstructure or to the lower conductance. On the contrary, the In_2O_3-SnO_2 seems to add the synergic effect of good electrical conductivity properties, due to the donor-type doping of In_2O_3 by Sn, and the higher dispersivity and defectiveness of the materials due to the mixing of the two different oxide phases. Also the presence of two different metal cation ions should be a factor that imparts a more heterogeneity to the active surface of the sensor. As regards

SnO_2-PdO system, contrary to In_2O_3-SnO_2, the adding of the PdO phase to SnO_2 gave no promoting effect to the detection of NO_2. This is expected by considering the easiness of oxidation of Pd into PdO, that at the surface of the sensors bind the ambient oxygen species enjoyable for NO_2 detection on the SnO_2 phase.

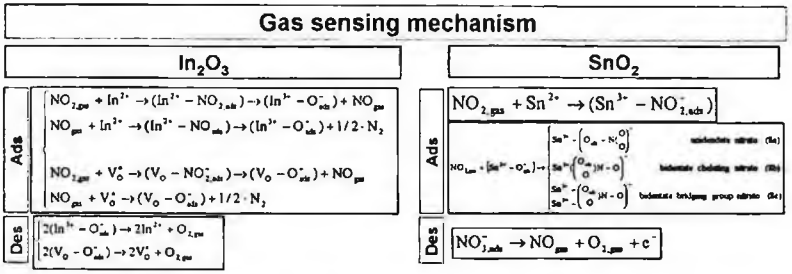

Fig. 5. Gas sensing mechanism for In_2O_3 and SnO_2 NO_2-based sensors.

4. Conclusions

All the prepared sensors showed high responses to NO_2. Some differences in the NO_2 sensing properties between the sensors were found as function of the operating temperature and the surface morphology. In general the best performances in terms of response and sensitivity were found in In_2O_3-SnO_2 based sensor. This sensor showed higher conductance than In_2O_3 and SnO_2, due a n-doping of Sn cations in In_2O_3 lattice, and higher defectiveness than single oxides. SnO_2-PdO resulted the most resistive film and, as expected, no particular advantage from the addition of the PdO phase resulted for the NO_2 detection. The NO_2-sensing of the sensors were also discussed in function of the gas/surface interaction processes and different detection mechanisms were proposed for the In_2O_3 and SnO_2 oxides.

References

1. S. Capone, P. Siciliano, in: Encyclopedia of Nanoscience and Nanotechnology, edited by H.S.Nalwa, American Scientific Publishers, 2004, Vol.3, p.769-804, ISBN:1-58883-001-2.
2. A. Cabot, A. Diéguez, A. Romano-Rodríguez, J. R. Morante, N. Bârsan, Sensors and Actuators B 79 (2001) 98-106.
3. M. Ivanovskaya, A. Gurlo, P. Bogdanov, Sensors and Actuators B 77 (2001) 264-267.
4. L. Francioso A. Forleo, S. Capone, M. Epifani, A.M. Taurino, P. Siciliano, Sensors and Actuators B, (2005) in publishing.

FLUORINATED POLYIMIDE THIN FILMS AS OPTICAL GAS SENSORS FOR VOC'S DETECTION

S.CARTURAN,* G. MAGGIONI

Università di Padova e INFN – Laboratori Nazionali di Legnaro, viale dell'Università 2, I-35020 Legnaro, Padova, Italy.

A. QUARANTA, E. NEGRO, M. TONEZZER, G. DELLA MEA

Dipartimento dei Materiali e delle Tecnologie Industriali, Università di Trento, via Mesiano 77, I-38050 Povo, Trento, Italy

INFN – Laboratori Nazionali di Legnaro, viale dell'Università 2, I-35020 Legnaro, Padova, Italy

Optical fluorescence changes of 6FDA-DAD fluorinated polyimide thin films, pure and doped with nile-red, have been monitored in presence of water, ethanol and isopropanol. The optical response depends on the species and on the concentration of the vapour, due both to the different permeation into the polymer matrix and to the hydrogen bond strength developed between the analyte molecule and the fluorophores. A lower detection limit of 500 ppm has been reached.

1. Introduction

Polymer-based matrices are currently attracting a great deal of interest in the gas sensing field [1]. Moreover, dye molecules can be dispersed or grafted into these matrices giving rise to a large number of sensing systems available for use in sensor array devices [2]. Among the different classes of polymers, aromatic polyimides exhibit improved chemical, thermal and mechanical properties [3]. Moreover, by a proper choice of the constituent monomers, their permeation [4] and optical [5] properties can be tailored in order to provide a material suitable for optical gas sensing applications. In this work, thin films of 4,4'-(hexafluoroisopropylidene) diphthalic anhydride and 2,3,5,6-tetramethyl-1,4-phenylenediamine (6FDA-DAD) transparent polyimide (see Fig. 1) have been synthesized. This kind of polyimide has been chosen since, from the literature data [4], it presents the higher permeation among the fluorinated polyimides and a good fluorescence yield owing to the formation of interchain

* E-mail: carturan@lnl.infn.it

charge transfer complexes. The changes of the fluorescence features of pure 6FDA-DAD and of 6FDA-DAD doped with the solvatochromic dye Nile-red (NR) thin films have been monitored in water, ethanol and isopropanol vapours in order to test the optical sensing capabilities of these systems to vapour organic compounds (VOCs).

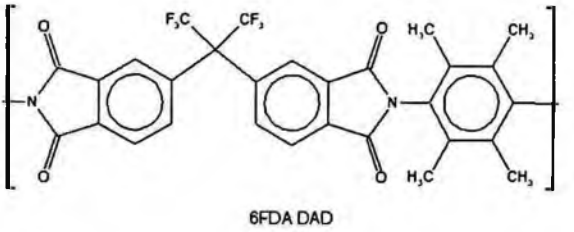

6FDA DAD

Figure 1. Chemical structure of the 6FDA-DAD polyimide.

2. Experimental

6FDA-DAD precursor monomers were polycondensed in a NMP solution and the resulting polyamic acid was chemically imidized [6]. The polyimide powders were precipitated in water and later dissolved in chloroform; the solution was spin-coated on quartz substrates and underwent a thermal treatment in vacuum at 200 °C obtaining thin films about 500 nm thick. Nile Red doping was performed by adding the dye to the chloroform solution (1.0 % weight of solid). Both full fluorescence spectra and fluorescence intensity at a fixed wavelength as a function of the time were collected with a Jasco-770 spectrofluorimeter. The samples were put into a chamber connected to the spectrofluorimeter. Two different mass flow controllers AERA FC-7800CD and AERA FC-7700CD were used to control the flow rate of pure nitrogen and of nitrogen diluted vapour. By varying the flow rates with a ROD-2M control unit connected to a PC, the samples were exposed to a fixed volume concentration of each analyte in nitrogen. Full fluorescence spectra were collected when a steady response was achieved under vapour flux and dynamic responses were recorded by exposing the sample to alternated pulses of pure nitrogen and different concentrations of vapours in nitrogen. Before the acquisition of both fluorescence spectra and dynamic response, each sample underwent a thorough conditioning procedure in order to get a stable response.

3. Results and Discussion

Undoped 6FDA-DAD exhibits a fluorescence emission band peaked at about 500 nm, whose excitation feature is placed in the UV range with the maximum at about 290 nm. In presence of the different vapours the band intensity lowers and the maximum shifts to longer wavelengths as can be observed in Fig. 2.

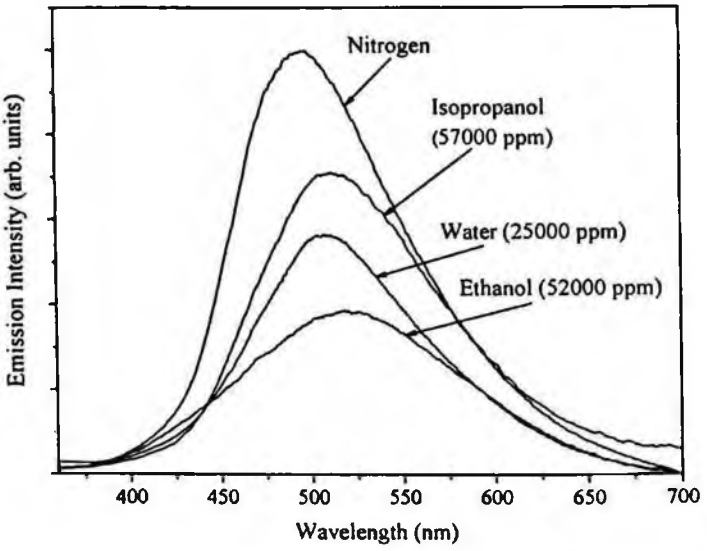

Figure 2. Intrinsic emission band (excitation wavelength 290 nm) of 6FDA-DAD during exposure to pure nitrogen, isopropanol (57000 ppm), water (25000 ppm) and ethanol (52000 ppm).

This behaviour can be related both to the cleavage of interchain CTCs, due to the steric hindrance of the vapour molecules permeating the polymer, and to the formation of hydrogen bonds which can account both for the intensity decrease and for the red-shift of the fluorescence bands [7]. The measurements in dynamic conditions (excitation wavelength at 290 nm and emission wavelength at 465 nm) evidenced a decrease of the optical signal depending on the vapour concentration. The response and recovery times are of tens of seconds, depending on the analyte species and concentration. The lowest detectable vapour concentration with this experimental apparatus is of about 500 ppm for alcohols and 1000 ppm for water. In Fig. 3 both the dynamic response to ethanol and the absolute value of the relative optical response (ROS) for the three vapours at different concentrations are shown.

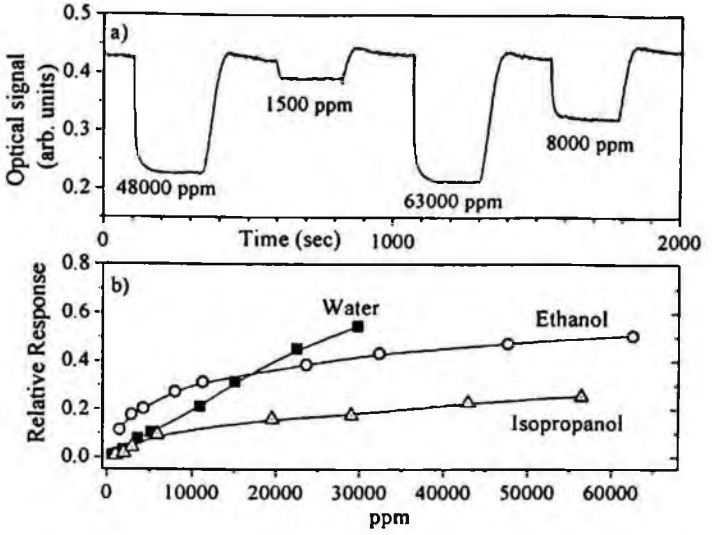

Figure 3. a) Optical response to ethanol at different vapour concentration pulses. b) Absolute value of the relative response of 6FDA-DAD intrinsic fluorescence, as a function of the analyte ppm, for water, ethanol and isopropanol. The curves are guides for the eye.

The ethanol ROS is higher at lower concentrations and saturates at higher concentrations owing to the higher permeability of 6FDA-DAD to this molecule. On the other hand, water ROS increases monotonously owing to the high hydrogen bond strength. Finally, the isopropanol ROS is lower due to a lower hydrogen bond strength developed by this molecule.

NR in 6FDA-DAD exhibits an emission band peaked at 600 nm, which shifts to longer wavelengths in presence of all the analytes and whose intensity decreases with ethanol and increases with water and isopropanol (see Fig. 4).

The NR emission changes are related both to the change of the polymer structure and to the formation of hydrogen bonds between the dye and the vapour molecules. The former effect increases the band intensity when the polymeric chains are less tightly packed around NR, whereas the latter results in a lower fluorescence intensity and in a red-shift of the emission feature. In the case of ethanol, it can be concluded that the optical response is dominated by the hydrogen bond, whereas in the other two cases the main effect can be ascribed to the polymer chain unpacking around NR probably due to the presence of competitive reversible reaction with the polymer network.

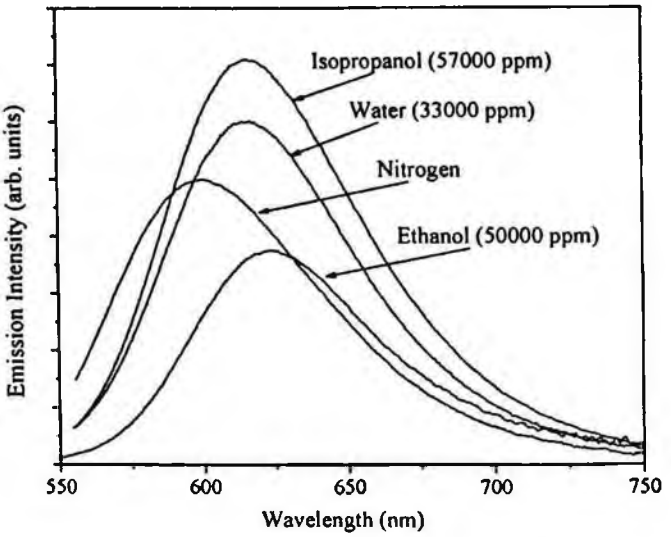

Figure 4. Emission bands (excitation wavelength 545 nm) of NR dispersed in 6FDA-DAD during exposure to pure nitrogen, isopropanol (57000 ppm), water (33000 ppm) and ethanol (50000 ppm).

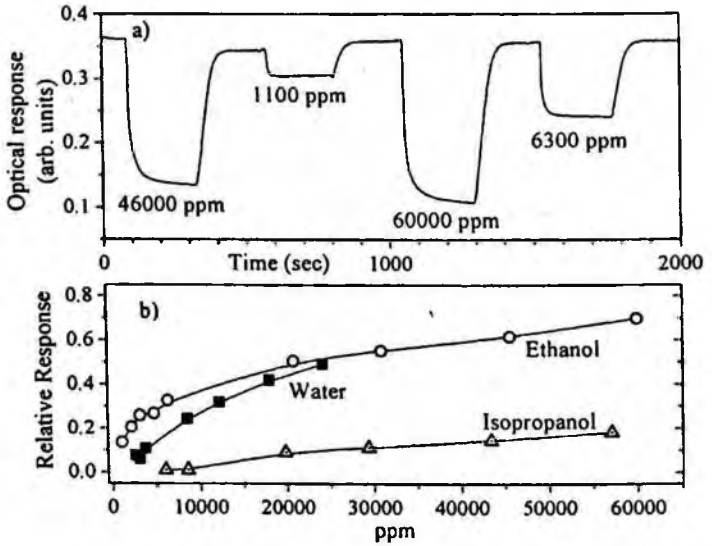

Figure 5. a) Dynamic response to ethanol of NR embedded in 6FDA-DAD. b) Absolute value of the relative response of NR embedded in 6FDA-DAD as a function of the analyte ppm for water, ethanol and isopropanol. The curves are guides for the eye.

The ROS curves behaviour (excitation at 510 nm and emission at 585 nm) resembles that of undoped 6FDA-DAD indicating the significant role played by the polymer matrix, and the values are quite similar to undoped 6FDA-DAD for the three vapours, with the exception of ethanol which exhibits higher ROS values. For all the compounds, the lower detection limit was of about 500 ppm with this instrumental apparatus.

4. Conclusions

6FDA-DAD fluorinated polyimide, both pure and doped with nile-red dye, is suitable for optical sensing of VOCs owing to fluorescence feature changes induced by the permeation of the different molecules. The response depends on the analyte species due both to the different permeability into the polymer and to the different strength of the hydrogen bond developed by the vapour molecules.

Acknowledgments

This work has been supported by the INFN DEGIMON national experiment.

References

1. B. Adhikari and S. Majumdar, *Prog. Polym. Sci.* **29**, 699 (2004).
2. D. Li, C. A. Mills and J. M. Cooper, *Sens. Actuators* **B 92**, 73 (2003).
3. *Polyimides: fundamentals and applications*, eds. Ghosh and Mittal, Marcel Dekker Inc., New York, 1996,
4. A. Y. Alentiev, K. A. Loza and Y. P. Yampolskii, *J. Membr. Sci.* **167**, 91 (2000).
5. M. Hasegawa and K. Horie, *Prog. Polym. Sci.* **26**, 259 (2001).
6 T. Takekoshi, in *Polyimides fundamentals and applications*, Eds. M.K. Ghosh, K.L. Mittal, 1996, pp. 19-21.
7. A. Cser, K. Nagy and L. Biczok, *Chem. Phys. Lett.* **360**, 473 (2002).

A COMPARISON BETWEEN OPTICAL GAS SENSING CAPABILITIES OF VACUUM EVAPORATED AND SPIN COATED TETRA PHENYL-PORPHYRIN THIN FILMS*

M. TONEZZER†, A. QUARANTA, E. NEGRO, G. DELLA MEA

Dipartimento di Ingegneria dei Materiali e Tecnologie Industriali, Università di Trento, via Mesiano 77, 38050 Povo(TN), Italy

G. MAGGIONI, S. CARTURAN

Università di Padova, c/o INFN-LNL Viale dell'Università, 2- 35020 Legnaro, Italy

In this work free (H_2TPP), cobalt (CoTPP) and iron chloride (FeTPPCl) 5,10,15,20 *meso*-tetraphenyl porphyrin thin films have been deposited by vacuum evaporation (VE) and by spin coating technique (SPIN). Chemical and morphological properties of the samples were investigated by means of FT-IR and AFM analysis. This work pointed out, through a comparison between the optical responses of VE and SPIN films exposed to acetone, ethyl alcohol and NO_2 atmospheres, a large response dependence on the deposition techniques.

1. Introduction

In the last years porphyrin thin films have gained increasing interest in gas sensing field showing to be promising materials to be employed for the fabrication of optoelectronic nose systems based on the colorimetric VOCs detection [1,2]. In order to exploit porphyrin compounds as sensing materials, the most used solution is the solid films deposition through chemical techniques (solvent casting, Langmuir-Blodgett, spin coating) [3,4].

In this work free (H_2TPP), cobalt (CoTPP) and iron chloride (FeTPPCl) 5,10,15,20 *meso*-tetraphenyl porphyrin films were prepared through spin coating (SPIN) and vacuum evaporation (VE) techniques. Their chemical and morphological properties were investigated through FT-IR and AFM analysis

* This research was financially supported by the Fifth Commission of Istituto Nazionale di Fisica Nucleare (DEGIMON project).

† Corresponding author: E-mail: tonezzer@lnl.infn.it, Ph: +39-0498068405, Fax: +39-049641925

and their optical responses toward the presence of three analytes, *i.e.* acetone, ethylic alcohol (ETOH) and nitrogen dioxide (NO_2), were compared.

2. Experimental

H_2TPP, CoTPP and FeTPPCl powders were purchased and used without further purification. These materials were vacuum evaporated (T=300°C, $P=10^{-4}$ Pa) and spin-coated (0,1% wt of porphyrin powders in chloroform at 800 rpm for 30sec; samples dried at 60 °C for 10h) onto 350-μm-thick P-doped (100) silicon wafers lapped on both faces (Atomergic Chemetals Inc.) and quartz glass slides (Heraeus Quartzglass GmbH & Co.). FT-IR spectra of the samples were recorded in the 4000-400 cm^{-1} range using a Jasco FT-IR 660 spectrometer with a resolution of 16 cm^{-1}. The surface morphology of the samples was investigated with a Danish Micro Engineering atomic force microscope mounting a DS 95-50 scanner in the tapping mode. Optical absorbance spectra were acquired utilizing an experimental apparatus in which the measure chamber, placed inside a Spectrophotometer V-570 Jasco, is connected to two mass flow controllers (AERA FC-7800CD and AERA FC-7700CD) suited to assure an accurate real-time control of the vapour concentrations into the chamber during the spectra collections. This apparatus allows to record dynamic behaviours at a fixed absorbance wavelength and complete absorbance spectra in atmospheres with different vapour concentration.

3. Results and Discussion

3.1. *Chemical and Morphological Properties*

A comparison between chemical and morphological properties of VE and SPIN films has been performed through FT-IR spectra and AFM images.

FT-IR spectra point out a high purity of the VE samples and feature the presence of retained chloroform ($CHCl_3$) in the SPIN ones, as shown by the additional peaks at 2250 cm^{-1}. FT-IR spectra of powder, VE film and SPIN film of H_2TPP are reported in Fig. 1.

AFM images highlight that VE surfaces are composed of very large and ordered needles while the SPIN ones are made up of smaller and less ordered needles and show the presence of large creaters due to chloroform evaporation. AFM images of VE and SPIN films of H_2TPP are reported in Fig. 2.

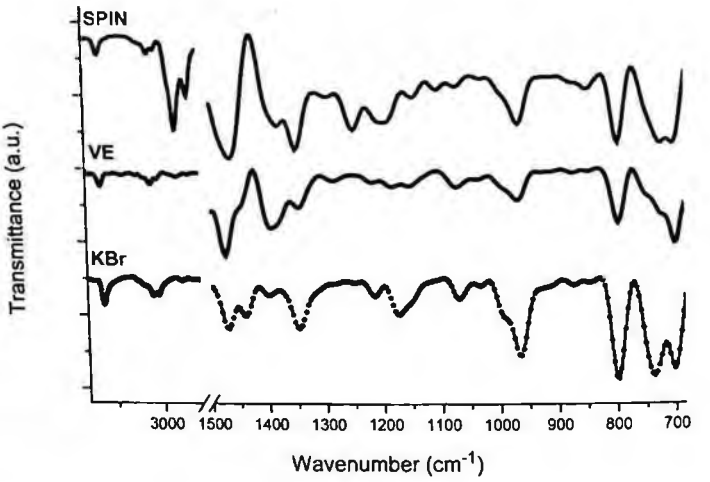

Fig.1 FT-IR spectra of powder (lower line), VE film (middle line) and SPIN film (upper line) of H_2TPP.

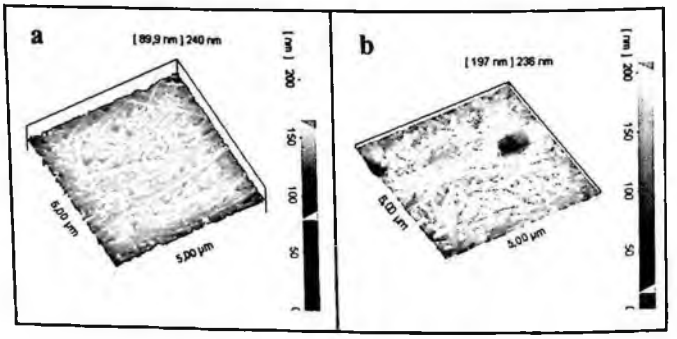

Fig.2 AFM images of VE film (a) and SPIN film (b) of H_2TPP.

3.2. *Optical responses*

An optical absorbance spectrum of all the samples was acquired in the 350-750 nm range, under a nitrogen atmosphere (A_o). Then the samples underwent a thorough conditioning procedure with exposures to saturated vapours of acetone and ETOH and to NO_2 (100 ppm in N_2) mixture: when a steady absorbance

signal was obtained, another absorbance spectrum was acquired (A_t). Conditioning procedure improves the reversibility of the samples responses upon to following analyte exposures and allows to calculate the absorbance percentual variation patterns, $\Delta A\%$, by means of the following formula:

$$\Delta A\% = [(A_t - A_o) / A_o] \times 100$$

Intensities $(\Delta A\%)_{MAX}$ and wavelengths of the maximum changes of optical absorbance are well pointed out by $\Delta A\%$ patterns. Figure 3, where are reported the $(\Delta A\%)_{MAX}$ of all the samples owing to conditioning procedure, shows higher absorbance changes for the VE samples in comparison to the SPIN ones: this different behaviour is probably due to the retained chloroform in SPIN samples, which reduces the free useful volume available for analyte molecules adsorption.

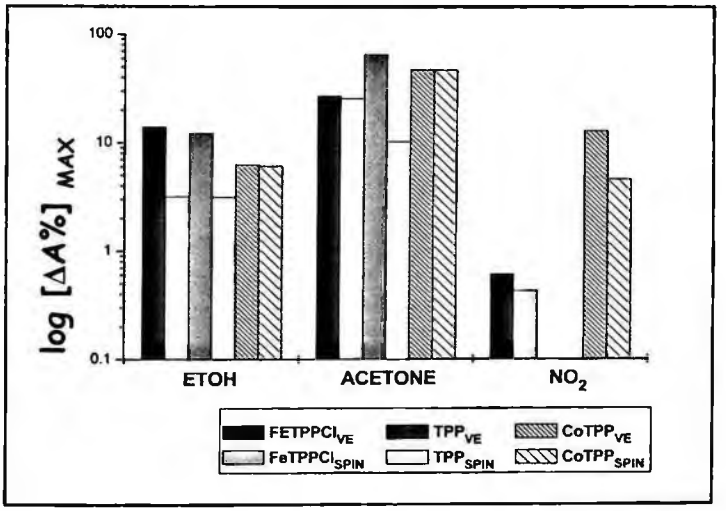

Fig.3 Maximum values of optical visible absorbance percentual variation ($\Delta A\%$) of VE and SPIN samples owing to acetone, ETOH and NO_2 conditioning procedure.

In order to analyze the sensitivity, the reversibility and the response times of the optical changes of the samples, the absorbance signal of conditioned samples, recorded at the wavelength corresponding to the maximum absorbance variation, was acquired under exposure cycles in analyte atmospheres.

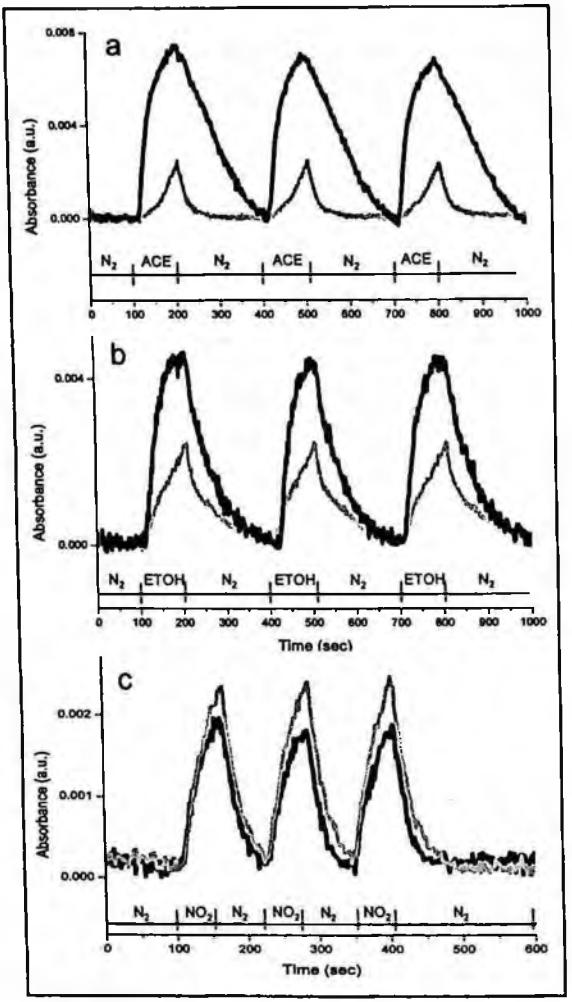

Fig. 4 Comparison of time-dependent behaviour of optical absorbance between VE and SPIN samples of FeTPPCl, TPP and CoTPP compounds upon exposure to saturated vapour of acetone (a), saturated vapour of ETOH (b) and 100 ppm NO_2 mixture (c).

The optical behaviours of VE and SPIN samples of FeTPPCl, H_2TPP and CoTPP upon to exposure cycles in saturated vapours of acetone, saturated vapours of ETOH and 100 ppm of NO_2 are reported in Fig. 4. The comparison between VE and SPIN optical responses highlights two different behaviours dependent on analyte molecule sizes: in acetone and ETOH atmospheres VE samples show highest and fastest responses, while in NO_2 atmosphere SPIN

samples show a little higher and faster responses than the VE ones. The cause of these opposite behaviours have to be searched in the chemical and morphological properties of the films: in the SPIN samples the adsorption of analyte molecules is inhibited by the presence of retained solvent and improved by the less closed surface morphology; on the contrary, in the VE samples adsorption is improved by the absence of impurities but inhibited by the very closed surface morphology. The predominance of either factor depends on the sizes of the analyte molecules.

4. Conclusions

Free (H_2TPP), cobalt (CoTPP) and iron chloride (FeTPPCl) 5,10,15,20 *meso*-tetraphenyl porphyrin thin films have been deposited by vacuum evaporation (VE) and spin coating (SPIN) methods and their chemical and morphological properties were investigated by means of FT-IR and AFM analysis. FT-IR spectra point out a great purity for the VE samples and the presence of retained solvent in the SPIN ones. AFM images highlight that VE samples are characterized by more closed and less rough surfaces than the SPIN ones. A comparison between the optical responses of VE and SPIN films exposed to acetone, ethyl alcohol and NO_2 atmospheres, investigated through conditioning procedures and exposure cycles, indicated a strong dependence on the deposition method. The conditioning procedure pointed out highest analyte-film interactions for the VE samples while exposure cycles pointed out much higher and faster responses for the VE samples in comparison to the SPIN ones under exposure to acetone and ethyl alcohol and a little higher responses for the SPIN samples under exposure to NO_2.

References

1. N.A. Rakow and K.S. Suslick, *Nature*, 406 (2000) 710.
2. O. Worsfold, C.M. Dooling, T.H. Richardson, M.O. Vysotsky, R. Tregonning, C.A. Hunter, C. Malins *Colloids and Surface A* 198-200 (2002) 859-867
3. D'Amico, C. Di Natale, R. Paolesse, A. Magagnano, A. Mantini *Sensors and Actuators B,* 65 (2000) 209-215
4. Akrajas, Muhamad Mat Salleh, Muhammad Yahaya *Sensors and Actuators B,* 85 (2002) 191-196

SIMPLIFIED MODEL FOR SnO_2 THICK FILM SENSORS RESPONSES IN CO AND OXYGEN MIXTURES

A. FORT*, M. MUGNAINI*, S. ROCCHI, M.B. SERRANO-SANTOS, V. VIGNOLI
Information Engineering Dept. – University of Siena, Via Roma, 56 Siena 53100, Italy

R. SPINICCI
Energetic Dept. – University of Florence, Via S. Marta, 3 Florence 50139, Italy

Abstract
Metal oxide gas sensors (MOXs) are widely used in olfactory electronic systems for their high sensitivity and low-cost. These sensors modify their conductivity in presence of oxidizing and reducing gases, and their performance is strictly dependent on the measurement technique adopted. In particular, it was already established by many works that a noticeable improvement in selectivity can be obtained by operating MOXs with a variable temperature. In this context, a strong interest in developing simplified models able to predict the sensor response is rising.
Keywords – Electronic nose; Metal oxide sensors; Tin oxide sensors; Carbon monoxide; Temperature modulation; Parametric model.

Introduction

Gas sensing application field relies mainly on MOXs due to their commercial availability and low cost characteristics. Nevertheless these devices show some problems because of their low selectivity and response drift. The sensing mechanism is based on the interaction of the surface vacancies and oxygen species with the reacting gases supplied to the sensor for detection. The presence either of a reducing or oxidizing gas induces a change in the sensor conductance, which can be monitored by a specific measurement system and associated with a specific reagent concentration. It is widely accepted that adsorbed oxygen ions (O_2^-, O^- and O^{2-}) have a decisive influence on the response of the semiconductor to reducing/oxidizing gases [1] - [3]. The low sensor selectivity is one of the main issue still open for this kind of sensors (in particular in this work the authors will refer to SnO_2 sensors layers) pushing the researchers to find out methods to enhance this sensor characteristic. Changing the sensor temperature during measurements, for example, allows to operate in a sequence of a non-equilibrium states whose evolution highly depends on the chemical environment. It has been already shown that, in some applications, by selecting an appropriate temperature profile, a significant improvement in terms of selectivity can be obtained [4]-[8]. In this work some simplified grey box models, derived from more complex physicochemical ones, are proposed, which

*Corresponding Author: E-mail: ada@dii.unisi.it, Ph: +390577233608

can be exploited to obtain a reliable information to guide the selection of the temperature profile.

Materials and Methods

The measurement system described in [14] used to acquire sensor responses was additionally improved through a faster and more flexible sensor temperature control system, able to individually control the temperature of each sensor with ±2°C temperature accuracy for values higher than 250°C. The temperature control system is based on a microcontroller implementing a control cycle of 100 μs, which allows to provide the wide-band temperature profiles needed for model identification.

The gas-sampling unit is a digitally controlled system providing the possibility to inject the desired gas or gas mixture into the measurement chamber, and to control the gas flow (up to 500 ml/min) by means of three mass flow controllers. The measurement chamber is kept inside an incubator for precise temperature control.

The sensors used in this study are different commercially available Taguchi screen-printed sensors TGS2620, TGS2610 and TGS2442 sensors (Figaro Inc., Japan). Both TGS2620 and TGS2442 are indicated for CO detection by the manufacturer. Charcoal filters packaged on TGS2442 sensors were removed.

Model Theory

First of all we considered the response of the sensors exposed to an oxygen mixture. A priori hypotheses are necessary to deal with the problem: first of all, it seems possible to assume that in the considered temperature range (temperatures higher than 250°C) the ionized oxygen O^- is dominant on the tin oxide surface, and that the other oxygen species can be ignored [1][3] [11]. Hence, a possible description of the chemical processes at sensor surface is:

Chemisorption: $$\tfrac{1}{2}O_2 + S \underset{k_{-1}}{\overset{k_1}{\rightleftarrows}} O-S$$

Ionization $$O-S+e^- \underset{k_{-2}}{\overset{k_2}{\rightleftarrows}} O^- - S$$

In the following N_o indicates the neutral adsorbed oxygen density [O-S] considered by the authors as the major contributor to the unoccupied surface

states, *Ns* denotes the ionized oxygen density [O-] considered as the density of occupied surface state, [S] denotes the total adsorption site density, and $[O_2]$ indicates the gas concentration. On these bases the reaction kinetics can be described by the following differential equations:

$$\frac{dN_O}{dt} = k_1([S] - N_O - N_s)[O_2]^{\frac{1}{2}} - k_{-1}N_O - \frac{dN_s}{dt} \tag{1}$$

$$\frac{dN_s}{dt} = k_2 n_s N_O - k_{-2}N_s \tag{2}$$

where k_1 and k_{-1} are the rate constants of the oxygen chemisorption, k_2 and k_{-2} are the rate constants of the oxygen ionization, and n_s is the concentration of the electrons which can reach the surface. In Eq. (2) the concentration of free electrons can be expressed as an explicit function of N_s by substituting the following relationship [11]:

$$n_S = N_D \exp\left(-\frac{q^2 N_S^2}{2k\varepsilon_r\varepsilon_0 N_D T}\right) \tag{3}$$

In the considered temperature range all donors are assumed to be ionized, hence N_D is a constant in Eq. (3) [1] [11].

To describe in this simple way the sensor response the following hypotheses were considered:

The chemisorbed oxygen is anchored to the unoccupied surface sites, whereas the physisorbed oxygen is not involved in the electron exchange process;

The chemisorption process is considered a first order reaction.

In accordance with what observed when measuring the dynamic behaviour of the examined sensors in an inert gas, where a dynamic behaviour very similar to what observed in air was highlighted, further simplification seems reasonable. In particular we considered that the variations of the adsorbed oxygen concentration are small in the interesting temperature range and observation time, and we derived the following model from Eq. (1):

$$\begin{aligned} &\frac{dN_s}{dt} = k_2 n_s N_O - k_{-2}N_s \\ &N_O = N_{ox} - N_S \end{aligned} \tag{4}$$

Where N_{ox} is the concentration of all the oxygen species on the surface, and it is considered constant during the experiments.

In addition, in presence of a reducing gas and in presence of relevant oxygen concentrations, the following reaction is the dominant process,

$$O^- - S + R \xrightarrow{k_3} RO + S + e^-$$

hence Eqs. (4) can be reshaped as follows and a new model derived accordingly:

$$\frac{dN_s}{dt} = k_2 n_s N_O - k_{-2} N_S - k_3[R] N_S \tag{5}$$

$$\frac{d[RO]}{dt} = k_3 N_S[R]\,. \tag{6}$$

This model doesn't take into account the role of humidity in the sensing mechanism, that seems to be relevant. Therefore it can be applied to dry gas mixtures after having removed the adsorbed hydroxyl groups by an appropriate heating of the sensors.

From this point on, the reaction rate constants are assumed to have the Arrhenius form:

$$k_i = k_{i0} \exp\left(\frac{-E_i}{kT}\right) \tag{7}$$

where k_{i0} is the pre-exponential factor, whose dependence on temperature is neglected in comparison with the one of the exponential factor, and E_i is the activation energy.

The sensing layer can be considered as a porous layer of large grain, hence sensors' conductance can be related to N_s by the following Eq.

$$G = G_0 \exp\left(-\frac{q^2 N_S^2}{2k\varepsilon_r \varepsilon_0 N_D T}\right) + G_C \tag{8}$$

where G_0 can be considered as a constant. Defining N_s' as in Eq. (9), and substituting in (8) a new expression for G can be found in (10):

$$N_s'^2 = \frac{q^2}{2\varepsilon_r \varepsilon_0 N_D k} N_s^2 \tag{9}$$

$$G = G'_0 T^{-\frac{3}{2}} \exp\left(-\frac{N_S^{2\prime}}{T}\right) + G_C \tag{10}$$

where G_c is an additive constant contribution used to take into account drift (as suggested by [11]). An additional step can be performed dividing the constant value of G_0 from the temperature and indicating the new term as G_0' again shown in Eq. (10).

Assuming that the chemisorption is a slow process compared with the ionisation one, the following Eq. (11), obtained from Eq. (4) with the addition of the term for the reducing gas, can be formulated:

$$\frac{dN_s'}{dt} = \exp\left(\frac{-N_s'^2}{T}\right) A'' \exp\left(\frac{-\lambda_1''}{T}\right) - C'' \exp\left(\frac{-\lambda_1''}{T}\right) \exp\left(\frac{-N_s'^2}{T}\right) N_s' - B \exp\left(\frac{-\lambda_2}{T}\right) N_s' - D \exp\left(\frac{-\lambda_4}{T}\right) N_s' \tag{11}$$

where: $A'' = N_{ox} N_D k_{20} \frac{q}{\sqrt{2\varepsilon_r \varepsilon_0 N_D k}}$, $B = k_{-20}$, $\lambda''_1 = \frac{E_2}{k}$, $C'' = N_D k_{20}$,

$D = k_{30}[R]$, $\lambda_2 = \frac{E_{-2}}{k}$; $\lambda_4 = \frac{E_3}{k}$.

This model allows the user to predict sensor response using a limited parameters set. Nevertheless such parameters (present in there), need to be correctly identified. To cover this aspect an experimental campaign has been conducted.

Experiments

The model parameters were estimated by solving a nonlinear least squares (nonlinear data-fitting) problem within Matlab environment (*'lsqnonlin'* function). Initial values for the searched parameters were obtained from values found in literature [11]. Measurements were performed while the sensors temperature was modulated with various shapes. All the used temperature profiles start with a 300*s* pulse at high temperature (about 450°C) to lead the sensor response to a steady state independently from the starting conditions. This allows to avoid the estimation of the initial condition for N_s', whatever the considered model. The model in Eq. (11) requires the estimation of 5-parameters only (A'',B,C'',λ_1'',λ_2) in oxygen as shown in figure 2b). In presence of a reducing gas two, extra parameters have to be estimated (D and λ_4). All the parameters included G'_0 and G_c in Eq. (10) can be determined by a unique estimation routine minimizing the fitting error between the estimated and the measured conductance. Nevertheless, in this work we estimated the two parameters G'_0 and G_c by an independent pre-processing step. This allows to reduce the number of unknown parameters, and to obtain a more robust optimization problem. The model was validated by means of measurements

performed in dry synthetic air (21% O_2 + 79% N_2, purity 99.999%), synthetic air and CO (200 and 400 ppm) and Nitrogen. The dynamic responses of the model to air and 200ppm CO mixtures are shown in figure 1a) and 1b) while in figure 2a) the steady state conductance of the studied sensors in dry air as a function of temperature is reported.

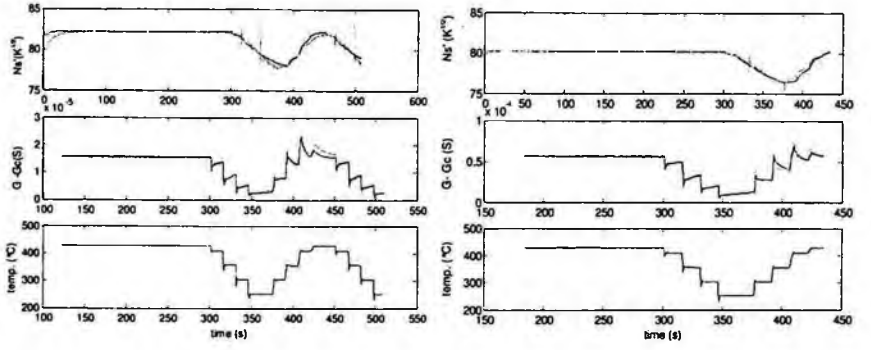

a) b)

Figure 1. TGS2620 and TGS2610 sensor responses for model in Eq. (11), respectively. Upper plots: N's. Middle plots: conductance. Light-gray lines represent the measured quantities, while dark-gray lines represent the simulated ones. Lower plots: temperature profile (used in the calibration phase): a) experiment in synthetic air; r.m.s. fitting error = 7%; b) experiment in synthetic air and 200 ppm CO (v/v), r.m.s. fitting error = 7%.

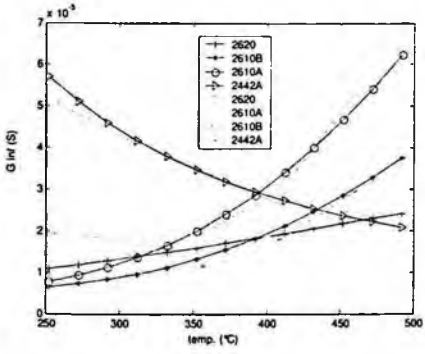

Sensor	5-parameter Model - AIR						
	A'' ($K^{1/2}$/s)	B (1/s)	C'' (1/s)	λ_1'' (K)	λ_2 (K)	r.m.s. Err. (%) Cal	r.m.s. Err. (%) Val.
TGS2620	50390	2.051	4.714	1315	4066	7.2	10
TGS2610A	27610	28.39	3.250	880.0	6117	8.1	11
TGS2610B	19720	28.39	3.250	880.0	6117	8.0	8.7
TGS2442A	42510	0.2200	14.46	3022	1975	5.2	10
TGS2442B	41590	0.5833	15.91	3309	2675	9.0	15

a) b)

Figure 2. a) Steady state conductance of the studied sensors in dry air as a function of temperature, evaluated using the 5-parameter model of Eq. (11). Dark gray: simulated data; light gray: measured data. b) Model parameter for synthetic air environment.

Conclusions

In this paper a simple gray-box model for predicting tin-oxide films' behaviour is proposed, discussed, and validated in different experimental conditions and with different commercial sensors. In detail, even if highly simplified, this model gave satisfactory results when used for measurements performed with fast temperature variations, both in air and in mixtures of air and low concentrations of CO. The 5-parameter model predicts the sensor behaviour in the studied temperature range with acceptable r.m.s. errors (usually < 10% also in model validation). Further evidences from the proposed results are that, among the Figaro Inc. commercial sensors used for this study, the TGS26XX are more stable and repeatable after a reasonably long heating pre-treatment while the TGS2442s show a more marked medium term time-variability.

References

[1] N.Barsan, U.Weimar, "Conduction model of metal Oxide Gas sensor", Jour. Of Electroceramics, vol. 7, pp.143-167, 2001,.

[2] J.F. McAleer et al., J. Chem. Soc., Faraday Trans., vol. 83, pp.1323-1346, 1987.

[3] N. Bârsan, U. Weimar, "Understanding the fundamental principles of metal oxide based gas sensors; the example of CO sensing with SnO_2 sensors in presence of humidity", *Jour. Of Physics: Condensed Matter*, vol. 15, pp. 813-839, 2003.

[4] M. Schweizer-Berberich M. Zdraleka, U. Weimar, W. Gopel, T. Viard, D. Martinez, A. Seube, A. Peyre-Lavigne, "Pulsed mode of operation and artificial neural network evaluation for improving the CO selectivity of SnO2 gas sensors", *Sensors and Actuators B: Chemical*, Vol. 65 (1)-3, pp. 91-93, 2000.

[5] A. Fort, M. Gregorkiewitz, N. Machetti, S. Rocchi, B. Serrano, L. Tondi, N. Ulivieri, V. Vignoli, G. Faglia and E. Comini R.E., "Selectivity enhancement of SnO_2 sensors by means of operating temperature modulation", *Thin Solid Films*, Vol. 418 (1), pp. 2-8, 1 October 2002.

[6] R.E. Cavicchi, J.S. Suehle, K.G. Kreider, M. Gaitana, P. Chaparala, "Optimized temperature-pulse sequences for the enhancement of chemically specific response patterns from micro-hotplate gas sensors", *Sens. Actuators B*, vol.33, pp. 142-146, 1996.

[7] A. Heilig, N. Barsan, U. Weimar, M. Schweizer-Berberich, J.W. Gardner, "Gas identification by modulating temperatures of SnO2-based thick film sensors", *Sensors and Actuators B: Chemical*, vol.43, pp.45–51, 1997.

[8] A. Burresi, A. Fort, S. Rocchi, B. Serrano, N. Ulivieri and V. Vignoli, "Temperature Profile Investigation of SnO_2 Sensors for CO Detection Enhancement", *IEEE Transactions on Instrumentation and Measurement*, vol. 54(1), pp. 79 – 86, February 2005.

[9] T. A. Kunt, T. J. McAvoy, R. E. Cavicchi, S. Semancik.,"Optimization of temperature programmed sensing for gas identification using micro-hotplate sensors", *Sensors and Actuators B: Chemical*, Vol. 53, pp. 24-43, 1998.

[10] V. Brynzary, G. Korotchenkov, S. Dmitriev, "Simulation of thin film gas sensors kinetics", *Sensors and Actuators B: Chemical*, Vol. 61, pp. 143-153, 1999.

[11] J. Ding, T. J. McAvoy, R. E. Cavicchi and S. Semancik, "Surface state trapping models for SnO2-based microhotplate sensors", *Sensors and Actuators B: Chemical*, Vol. 77 (3), pp. 597-613, July 2001.

[12] R. Ionescu, E. Llobet, S. Al-Khalifa, J.W. Gardner, X. Vilanova, J. Brezmes, X. Correig, "Response model for thermally modulated tin oxide-based microhotplate gas sensors", *Sensors and Actuators B: Chemical*, Vol. 95, pp. 203–211, 2003.

[13] W. Schmid, N. Bârsan and U. Weimar, "Sensing of hydrocarbons and CO in low oxygen conditions with tin dioxide sensors: possible conversion paths", *Sensors and Actuators B: Chemical*, Vol. 103(1-2), pp. 362-368, September 2004.

[14] Fort, A.; Machetti, N.; Rocchi, S.; Serrano Santos, M.B.; Tondi, L.; Ulivieri, N.; Vignoli, V.; Sberveglieri, G.; "Tin oxide gas sensing: comparison among different measurement techniques for gas mixture classification", IEEE Transactions on Instrumentation and Measurement, vol. 52(3) , pp. 921 – 926, June 2003.

ENHANCEMENT OF SENSOR PERFORMANCE BY USING METAL OXIDE NANOCRYSTALS

G. NERI, A. BONAVITA, G. RIZZO, S. GALVAGNO
DEPT. OF INDUSTRIAL CHEMISTRY AND MATERIALS ENGINEERING, UNIVERSITY OF MESSINA,
Contrada Papardo Salita Sperone, 31, 98166 Messina, Italy
E-mail: neri@ingegneria.unime.it

N. PINNA, M. NIEDERBERGER
MAX-PLANK-INSTITUTE OF COLLOIDS AND INTERFACES, POSTDAM, GERMANY

S. CAPONE, P. SICILIANO
INSTITUTE FOR MICROELECTRONICS AND MICROSISTEMS - CNR.
Via per Arnesano, Lecce,73100, ITALY
E-mail: simona.capone@le.imm.cnr.it

A new non-aqueous sol-gel process has been implemented for the preparation of SnO_2- and In_2O_3-nanostructured oxides. Thick films of these nanopowders were tested in the monitoring of trace level of both oxidizing and reducing gas. These devices have shown enhanced performances respect to conventional sensors with linearity in a wide range of concentration, lower operating temperature and fast dynamic.

1. Introduction

The increasing attention on industrial health and safety, environmental monitoring and process control is the driving force for a further improvement of the gas sensing devices performance. One of the most promising approach for the next generation of high performance gas sensors is the development of nanostructured sensing materials. Indeed, as grain size decrease, the gas sensitivity is drastically enhanced, particularly when nanocrystallite size is smaller than twice of the space-charge layer thickness [1].

To prepare such nanostructured materials, the sol-gel technique is widely used because it offers the possibility to control particle size and homogeneity at nanometer level. In order to improve the crystallinity of very small particles, we proposed an alternative route to the classical aqueous sol-gel method [2]. SnO2, In_2O_3, Nb_2O_5 and perovskite nanopowders have been synthesized by this approach [3-5].

Gas sensors have been realized by printing the as-synthesized nanopowders on the surface of a ceramic substrate. The as-prepared gas sensor were tested for detection both oxidizing (NO_2) and reducing gas (CO and CH_4).

2. Experimental

The preparation of nanopowders of pure and mixed tin-indium metal oxides (SnO_2, In_2O_3, $Sn_{1-y}In_yO_x$) follows a reaction mechanism involving an aprotic condensation reaction based on an unusual ether elimination step [2]. The reaction scheme is reported in Fig. 1.

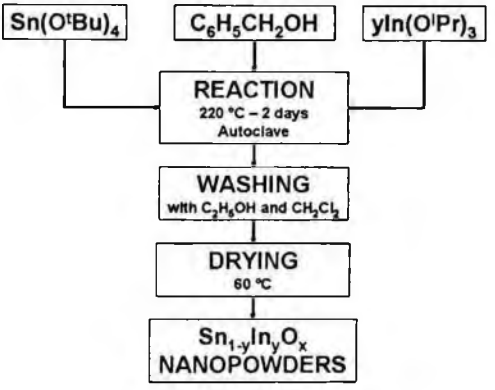

Fig. 1. Reaction scheme

Both single SnO_2 and In_2O_3 and mixed oxides $Sn_{0.95}In_{0.05}O_x$ (2b) and $Sn_{0.90}In_{0.10}O_x$ (2c) powders have been thus prepared. They have been characterized by HRTEM and XRD. For transmission electron microscopy (TEM) studies, one or more drops of the solution of the nanoparticles dispersed in ethanol were deposited on the amorphous carbon film. A Philips CM200 FEG microscope, 200 kV, equipped with a field emission gun was used. The coefficient of spherical aberration was Cs=1.35 mm. X-ray pow-der diffraction (XRD) patterns of all samples were meas-ured in reflection mode (CuKα radiation) on a Bruker D8 diffractometer equipped with a scintillation counter. Variable temperature XRD experiments were carried out using an in-situ cell attached to the diffractometer. on sensors realized by de-positing thin films (thickness around 1 μm) of the nano-powders dispersed in water onto alumina substrates (3x3 mm^2). On the front side, the substrates provide gold

interdigitated contacts. On the backside, there is a Pt heater. The sensors were bounded as suspended devices onto TO-8 supports and introduced in a teflon test chamber for the sensing tests with CO, CH_4 and NO_2 in controlled atmosphere.

3. Results and Discussion

A detailed HRTEM and XRD characterization of the metal oxide nanocrystals has shown that they exhibit nanometer grain sizes and are well crystallized even at such small size.

The XRD pattern of the pure SnO_2 (reported in Figure 2a) displays four broad peaks due to the very small crystallite size, relative to. the tetragonal cassiterite phase. Calculation from the Debye scattering equation for spherical, monodisperse particles with a diameter of 2.2 nm (dotted line). The mixed oxides $Sn_{0.95}In_{0.05}O_x$ (2b) and $Sn_{0.90}In_{0.10}O_x$ (2c), exhibit a similar XRD pattern like the pure SnO_2 and the broad reflections are characteristic for particle sizes around 2.2 nm. In_2O_3 nanoparticles (2d) shows sharp peaks corresponding to the In_2O_3 cubic structure. The sharpness of the peaks points to a much larger particle size ($\cong$ 20 nm) compared to SnO_2.

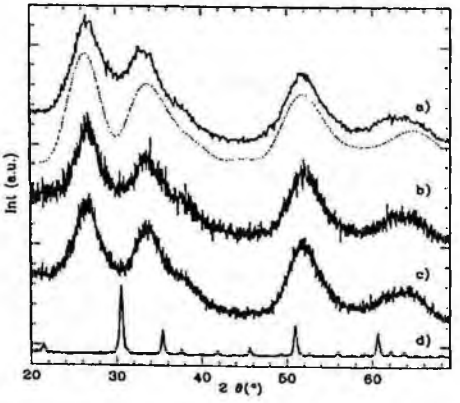

Fig. 2. XRD spectra of the samples: a) SnO_2; b) $Sn_{0.95}In_{0.05}O_x$; c) $Sn_{0.90}In_{0.10}O_x$; d) In_2O_3.

TEM analysis showed that SnO_2 and SnO_2-In_2O_3 mixed oxide particles are characterized by an average size of 2-2.5 nm. In_2O_3 nanoparticles with a cube-like shape have an average size of 20 nm. In agreement with the XRD measurements, the nanoparticles present well-defined lattice fringes in the high-resolution TEM investigations, pointing out that they are highly crystalline. As

an example, Fig. 3 shows the TEM and HRTEM results for some SnO_2 and In_2O_3 samples.

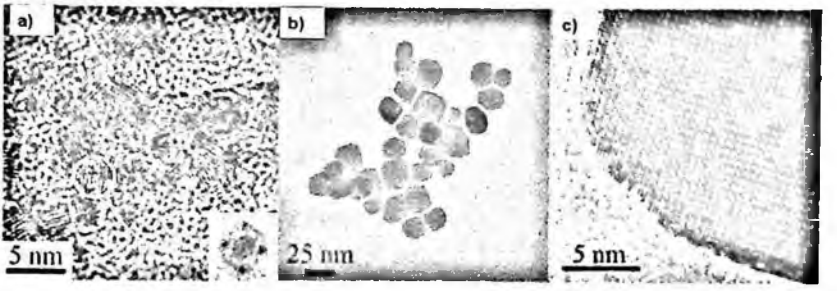

Fig. 3. (a) HRTEM of 2.5 nm SnO_2 nanoparticles and power spectrum of one of them showing monocrystallinity; (b) TEM of 20 nm cube-like In_2O_3 nanoparticles; (c) HRTEM of a part of a In_2O_3 nanocube showing high crystallinity.

The sensing properties of In_2O_3-and SnO_2-based sensors were evaluated as gas sensor by exposing them to NO_2 (2÷20 ppm), CH_4 (100÷2000 ppm) and CO (5÷100 ppm) at R.H.=0%. Tests were made at different temperatures in order to find the optimum operating temperature for each gas. SnO_2 and $Sn_{0.95}In_{0.05}O_x$ and $Sn_{0.90}In_{0.10}O_x$ sensors resulted highly resistive maybe due to the extremely small particle size of the sensing layers. In_2O_3 gas sensor resulted highly selective for NO_2, showing higher responses to NO_2 compared to SnO_2 and very low responses to CO and CH_4. On the contrary, SnO_2-based sensors showed higher responses to CO or CH_4 compared to In_2O_3. The temperature detection range for NO_2 is lower (100÷300 °C) in comparison to CO and CH_4 (300÷550 °C). See Fig. 4.

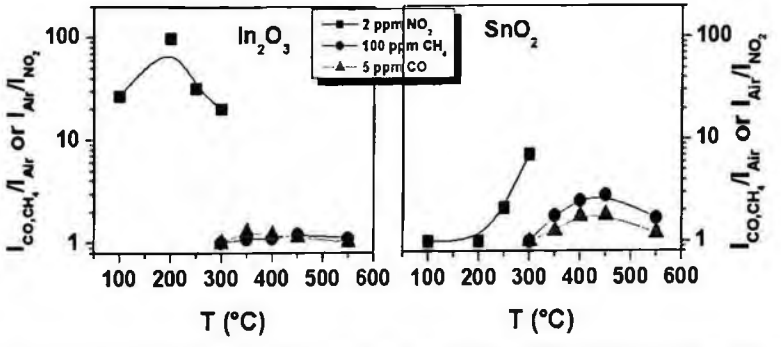

Fig. 4. Response curves for In_2O_3 and SnO_2 based sensors for 2 ppm NO_2, 100 ppm CH_4 and 5 ppm CO.

In Fig. 5 the dynamic responses to the target gases are reported.

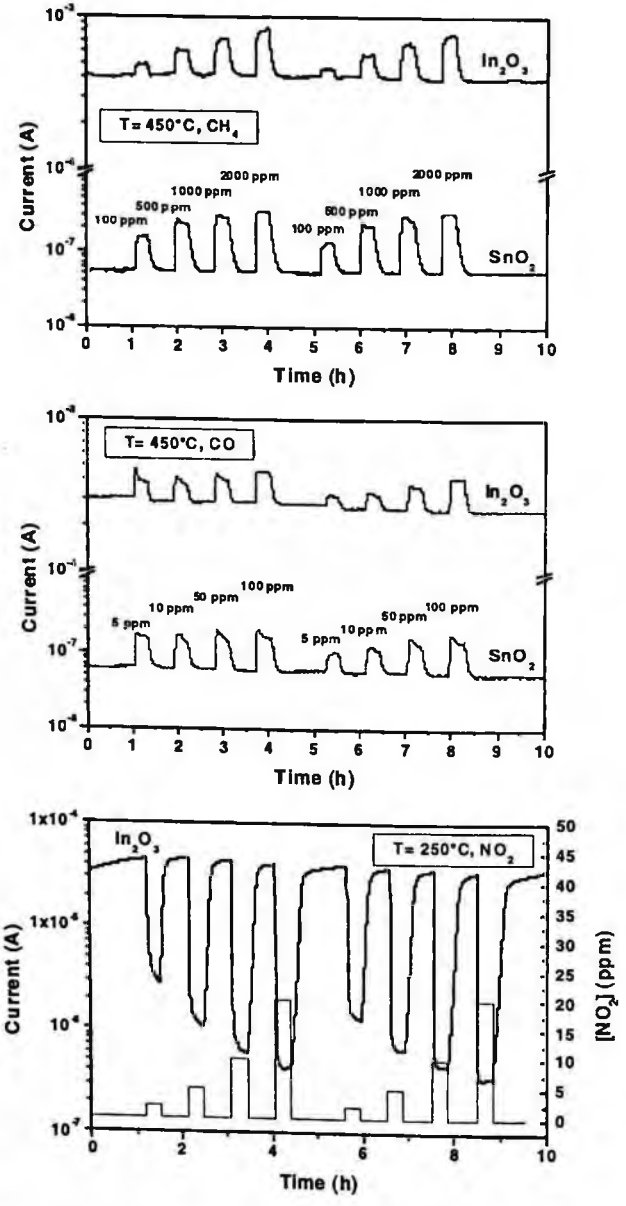

Fig. 5. Dynamic responses of SnO_2 and In_2O_3 sensors to different gases.

4. Conclusions

SnO_2 and In_2O_3 nanoparticles prepared by a novel, nonaqueous sol-gel synthesis showed superior performances when compared to conventional sensing materials which make them promising materials as sensing layer in gas sensor devices.

Research is actually in progress in order to achieve better performances by: 1) an improved control of the sensing layers morphology; 2) grain size selection; 3) metal doping.

References

1. Y. Shimizu, M. Egashira, MRS Bull. 6 (1999), pp.18-24.
2. M. Niederberger, N. Pinna, J. Polleux, M. Antonietti, Angew. Chem. Int. Ed., 43, (2004), pp.2270-2273.
3. N. Pinna, M. Antonietti, M. Niederberger, Colloids Surf., A 250, (2004), pp. 211-213
4. N. Pinna, A. Bonavita, G. Neri, S. Capone, P. Siciliano, M. Niederberger, Proceedings 3th IEEE Sensors Conference, Vienna (2004).
5. N. Pinna, G. Neri, M. Antonietti, M. Niederberger, Angew. Chem. Int. Ed., 43, (2004) pp. 4345-4349

EXPERIMENTAL SET-UP FOR THE EVALUTION OF GAS SENSORS PERFORMANCE

A. BONAVITA, G. MICALI, G. NERI

Dipartimento di Chimica Industriale ed Ingegneria dei Materiali, Università degli Studi di Messina
98166 Messina, Italy

N. DONATO

Dipartimento di Fisica della Materia e Tecnologie Fisiche Avanzate, Università degli Studi di Messina
98166 Messina, Italy

G. PIOGGIA, D. DE ROSSI

Centro Interdipartimentale di Ricerca "E. Piaggio" - Facoltà di Ingegneria - Università di Pisa

F. DI FRANCESCO

Istituto di Fisiologia Clinica - Consiglio Nazionale delle Ricerche- Pisa

Semiconductor gas sensors are widely used due to high sensitivity to many chemicals and low costs, that make them interesting for applications in many different fields. In this paper a system for a complete evaluation of gas sensor response is described. An array of mass flow controllers and a radially symmetric stainless steel measurement chamber allowed to expose the sensors to controlled gas mixtures. The measurement chamber was designed to obtain an homogeneous flow without significant recirculating zones or stagnant volumes and to guarantee all sensors to be exposed at any time in the same conditions. A dedicated sensor holder avoided the need of microbonding procedures and allowed an easy mounting and a stable electrical contact with the sensor tracks and the platinum resistor embedded into the sensor support. The temperature of each sensor was independently controlled in the range 30 - 700 °C thanks to a PID control loop. The determination of the resistance-temperature calibration curves allowed to use the platinum resistors also as temperature sensors. The experimental set-up was fully automated by a dedicated software developed in Labview 7 environment. The gas sensors performance have been evaluated by this integrated experimental set-up in a fast, easy and complete way.

1. Introduction

Semiconductor gas sensors are widely used due to high sensitivity to many chemicals and low costs, that make them interesting for applications in many different fields. The development of systems that allow to characterize the response of many sensors in the same time and at different temperature conditions is of great importance [1]. By this way is possible to achieve useful information about different sensing materials exposed at the same gas mixture in the same time; of course it is possible to expose the same materials at different operating conditions. These systems are fundamental for the optimization of the sensing material, the sensor configuration and operating conditions.

2. System Description

A system for a dynamic analysis of volatile compounds equipped with chemical sensors is composed of sampling system which, by means of a carrier gas, conveys the sample under test to the exposure chamber where the sample interacts with the array of sensors and the chemical-physical concentration signals are converted into electric signals as output. Responses of the sensors are thus acquired, amplified and digitalized by the acquisition system. Some features are derived from these signals, for example rise time, peak values and/or steady state.
The shape of the signal depends on four main factors, i.e. the properties of the:

- sample (chemical composition, concentration)
- active substrate (porosity and physical structure, kinetics of interaction between the sample and the active material)
- substrate that supports the active material (thermal conductivity)
- sampling system (environmental conditions such as the relative humidity, temperature and pressure; carrier gas, spread of the sample inside the active material, flow profile)

To ensure the maximum reproducibility of the measurements, the sampling device should be designed to control and optimize all the factors that contribute to generating the signal, irrespectively of the specific type of the sample. In particular, the chamber must be designed in order to optimize the sensors signals in terms of stability, repeatability as well as amplitude and response time.

3. Measurement Chamber Development and Realization

The measurement chamber is designed to expose the sensors to the mixtures generated by the sampling system. In summary, critical design points for an exposure chamber are:

- sensor arrangement with reference to the incident flow: an inadequate arrangement of sensors can lead to different exposure conditions among sensors;
- geometry: sharp variations cause recirculating zones;
- dead volumes: these extend the response time of the system and can cause an uneven distribution of flow rate.

To expose an array of sensors to a chemical mixture in optimal conditions, the chamber must allow all the sensors to be simultaneously exposed under the same conditions and make it possible to accurately reproduce the shape of the input concentration signal at each sensor position. Moreover, it must be designed to obtain the same concentration profile in repeated measurements and short analyte concentration rise/fall times, to avoid memory effects and sample dilution, and to use only a small amount of sample.

These features were obtained by correctly setting the size of the airways and creating homogeneous flow conditions with low velocity gradients (without any recirculating or stagnant volumes) by means of a radially symmetric geometry for the chamber with a dedicated flow splitter. Figure 1 shows the rendering of the components of the chamber.

All the components in the chamber are in stainless steel so as to limit any adsorption of the chemical compounds and to allow for easy cleaning. The chamber consists of a body that has six radial holes into which six connectors can be inserted, a flow splitter and a cap. In the upper part of the flow splitter a fitting allows the flow to leave the chamber. The flow splitter shares out and conveys the same flow quantity for each sensor. The flow splitter and the cap are connected to the body axially via three screws. The cap also has a fitting in the lower part which allows the flow to leave the chamber. The body is equipped with a series of grooves where a coil of the hydraulic circuit of a thermostatic bath can be inserted. If less than six sensors need to be exposed, it is possible to use closed connectors; this ensures that the flow conditions remain the same. On the other hand, if more than six sensors need to be exposed, a suitable number of chambers can be used in parallel and/or in series, so that each chamber undergoes the same flow rate.

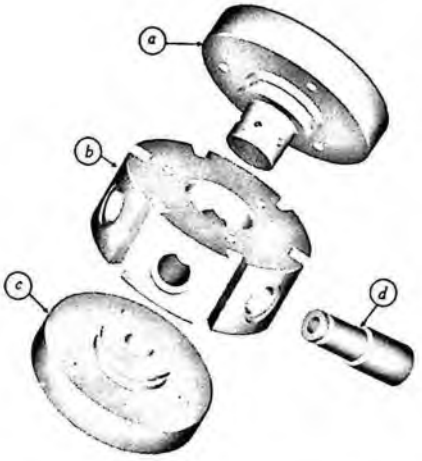

Figure 1. Rendering of the components of the measurement chamber; a) flow splitter; b) body; c) cap; d) connector.

4. Sensor Configuration and Connector

The sensor devices were prepared by deposition of the sensing layer on an alumina substrate with a dual configuration; on a side there is an interdigitated platinum contact that allows us to characterize the sensing material, on the opposite side there is a platinum heater that allows to set and control the operating temperature (Figure 2).

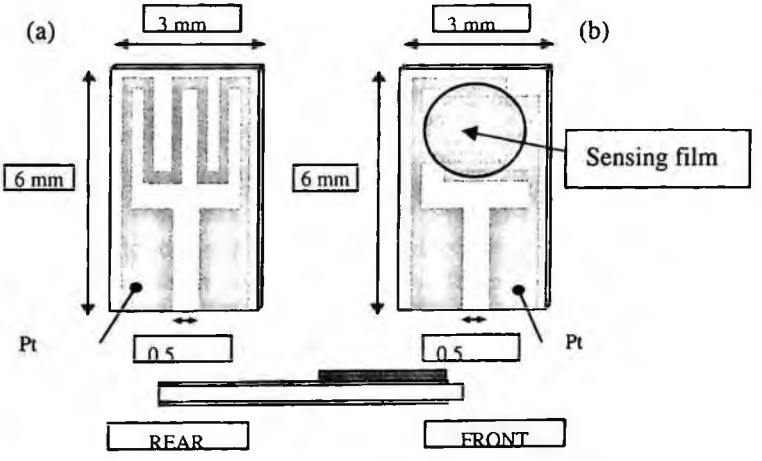

Figure 2. Substrate configuration; a) heater; b) interdigitated.

The upper part of the connector has a holder that support the sensor and carries out the contacts with the substrate. It is realized in Macor®, which is an easily workable non-porous ceramic with excellent mechanical and thermal properties (1000°C temperature limit). The sliding contacts of the holder, taken from commercially available PLCC sockets, ensure an easy assembly and avoid the need for any micro-bonding procedures. The electrical contacts have been found to be extremely stable. The contacts from the holder meet in a standard electric connector which facilitates the connection with the electronic section for acquisition and control. Once the holder has been mounted and the contacts with the electric connector made, the connector is filled, via a lateral hole, with an elastomer which guarantees the sailing. Figure 3 shows a schematic view and a picture of the holder. The chamber was optimized to hold substrates of the type shown in the Figure 2, however, while retaining its characteristics, it is possible to adapt the system for other types of sensors by making simple changes to the holder and to the connector.

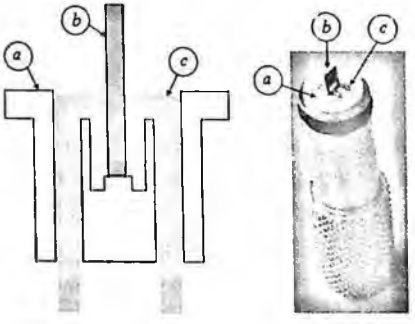

Figure 3. Holder; a) holder; b) substrate; c) contact.

5. Temperature Control

The temperature of each sensor was independently controlled in the range 30 - 700 °C. This control is based upon a PID feedback monitoring and controlling of the power supplied and sensed by two Agilent 3632 supplies. By this way the platinum heater works like temperature sensor and actuator. In Figure 4 the power vs. temperature characterization is reported, by a third order polynomial fitting we are able to apply this behavior to a digital control developed with National Labview tool.

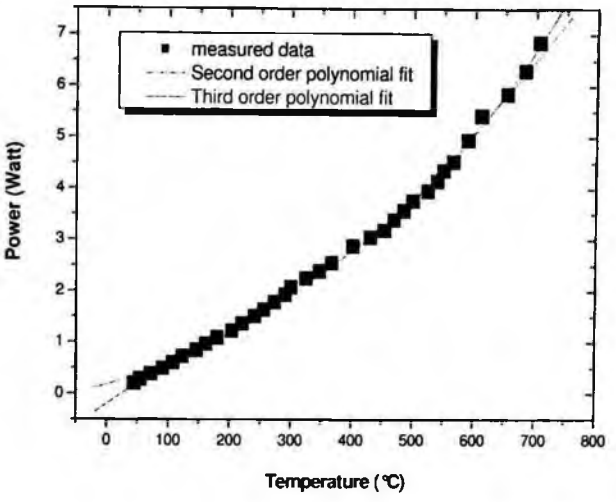

Figure 4. Power vs. temperature characterization of the sensor/heater.

6. Data Aquisition

The control routine is part of the software developed for monitoring all the process variables (gas fluxes and mixing, mass-flow signal, etc) and characterizing sensors. By this software we are able to record all the variables in the process of characterization. An Agilent 34970 allows us to measure resistance dc values up to six sensors in the same time, and a Stanford Research Lock In SR830 is used for impedance Spectroscopy (frequency range 1mH-100 KHz).

Data obtained in the characterization of oxygen sensors at low and high temperature, by using the system here described, are reported in two papers reported in this book [2,3].

References

1. Di Francesco F., Falcitelli M., Marano L., Pioggia G., Sensors Actuators B, in press.
2. Bonavita A. , Neri G, Micali G., Galvagno S. Pinna N. Niederberger M., *Sensors and Microsystems* **10** (in press).
3. Deorsola F.A., Amato I., De Benedetti B., Bonavita A., Micali G., Neri G., *Sensors and Microsystems* **10** (in press).

DEPENDENCE OF THE RESPONSE OF SnO_2 BASED THICK FILM GAS SENSORS ON HUMIDITY

A. GIBERTI, M.C. CAROTTA, V. GUIDI, C. MALAGÙ, L. MILANO, M. PIGA, AND G. MARTINELLI

University of Ferrara and INFM,via del Paradiso 12, 44100 FE, Italy

The conductance in air of thick-film gas sensors operating via flow trough tecnique strongly depends on the flux. In this work we demonstrate that the major effect of the flow rate is a change in humidity, because the thermal effect on the sensor is negligible. A mathematical model based on heat exchange and direct measurements of the resistance of the heater confirms this hypothesis and humidity compensation gave very good results.

1. Introduction

Sensors capable of substituting analytical methods not only have to measure traces of gases in the atmosphere, with sensitivity and selectivity comparable to those of the conventional devices, but also have to be highly repetitive and reliable [1]. As a consequence, to validate the sensors response, high repeatability of working conditions has to be attained; this task implies a careful co-ordination of all the different processes involved, such as the powder synthesis, structural characterization, deposition of sensing layers, realization of the optimal substrates, and electronic control. Among these, standardization of a testing procedure such as the flow through technique is of paramount importance for a reproducible data processing. Aim of this work is the implementation of an analytical method that predicts the effect of the carrier flow rate on the calibration curves of the sensors.

2. Experimental

A set of 8 SnO_2 thick-film gas sensors was prepared with the method described in our previous work [2]. All the steps of deposition and realisation of the sensors were controlled in order to obtain the highest repeatability. The 8 sensors operated at 350 °C inside the test chamber. A flow chamber with variable volume in the range of 150 to 600 cc was used in order to estimate the relationship between flux and volume in the modification of the sensors response (see Figure 1). The position of the 8 sensors inside the chamber allows the

maximum homogeneity of working conditions. The chamber is equipped with 5 temperature sensors near the gas sensors and with a humidity sensor. The temperature and humidity stabilization are attained thanks to a climatic chamber.

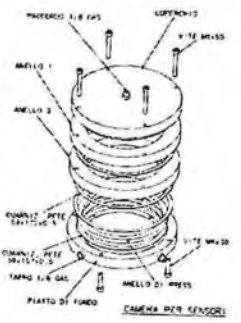

Figure 1. Test chamber with variable volume. The sensors are placed symmetrically, and the flux enters the chamber trough a series of nozzles placed symmetrically.

3. Resuts and Discussion

In order to investigate the dependence of the sensor's response on the flux, a series of steps of dry air, from 100 to 500 sccm (*standard cm³/min*) was superimposed on the set of sensors, and their response decreased when increasing the flow rate (see Figure2).

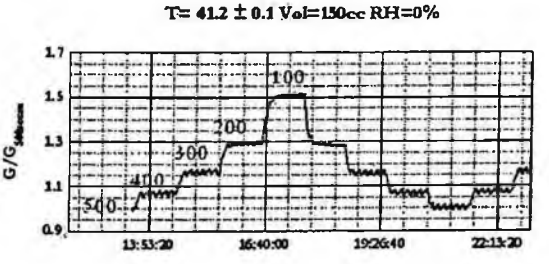

Figure 2. Sensor average conductance versus time under 5 steps of flow rate in dry air. The response is normalized to that of 500 cm^3/min.

This behavior can be explained in two ways:

- an enhancement of the thermal dissipation of the sensor;
- a change of the humidity.

To understand what happens in terms of heat dissipation, a mathematical model describing the thermal exchange has been developed, providing the temperature in the various parts of the system (2nd column of Table 1 is an example). The

model consists of 4 coupled equations for the film, the TO8 support, the air within the chamber and the chamber itself. These equations are simply heat exchange ones, and take into account irradiation, convenction and conduction terms [3]. The variation in the resistance of the sensor heater due to a change of some hundreds of sccm is of the order $10^{-2}\ \Omega$, corresponding to about $1°C$. The latter can hardly modify the sensor's response, because the term of forced convection due to the flow rate is negligibile [3]. This observation was validated by several measurements of the resistance of the heater (see Table 1).

Table 1. Some theoretical and experimental values about the temperatures versus flow rate. (From left to right): Heat exchange model prediction of the temperature of the heater, measured temperatures of the support (TO8), air within the TO8, and chamber, for 2 extreme flow rates. The variation is of the order of 10^{-1} degree.

Φ(sccm)	$T_{H\ predicted}$ (°C)	T_H (°C)	T_{extTO8} (°C)	T_{intTO8} (°C)	$T_{chamber}$ (°C)
100	449	446.3	89.4	197.9	20.1
700	448.7	445.8	88.9	197.5	19.7

Consequently, the primary effect of a flow rate variation is a change of humidity. What is the reason? The lower the flow rate the lower the overpressure in the chamber with respect to athmospheric pressure, and humidity enters from the outside (with very long stabilization time if the pipes and joints are of good quality). In the limit of zero flow and infinite time, the humidity in the test chamber equals the humidity in the external environment. To prove this, a conductance measurement after a sudden change of flow rate (from 700 to 100 sccm) was performed, as one can see in Figure 3. It can be noticed that after the flow variation, the partial pressure of water vapor slowly increased, reaching a steady state after about 24 hours, and the sensor's response followed the humidity trend.

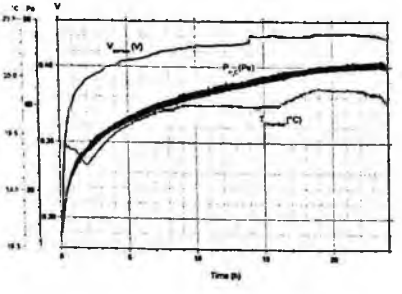

Figure 3. A sudden change in the flow rate, from 700 to 100 sccm results in a slow increase in the partial pressure of water.

Thus, in order to achieve equality between on-field and laboratory measurements, the unique way is to have a good control of the partial pressure of water vapor. This can be achived with the algorithm for the humidity compensation, as shown in a previous work [4]. Indeed, a calibration surface, namely sensor's conductance as a function of target gas and humidity, described by the following mathematical function

$$G = G_{dry\,air} + a\, p_{gas}^{\alpha} + b\, p_{H_2O}^{\beta} + c\, p_{gas}^{\alpha}\, p_{H_2O}^{\beta} \qquad (1)$$

can compensate the humidity effect on sensor's response, avoiding discepancies between laboratory measurements and on-field measurements. Figure 4 shows an example of a CO calibration surface for a SnO_2:Pd sensor. As can be seen in Fig.5, the sensor response in a typical urban situation is in good agreement with the conventional analysers if we apply the described compensation, while the discepancies are very large without it. The chosen period was between winter and spring, with a strong increase of humidity at the end of February, which raised the sensor signal with respect to the real CO concentration. By applying the compensation (1) to the on-field data, the agreement with conventional analysers is very satisfactory. This alghoritm was recently impemented in a chip for the direct real-time on-field compensation and works very well.

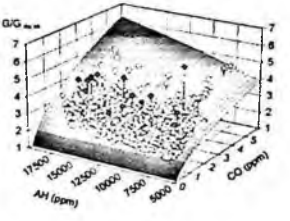

Figure 4. Example of a CO calibration surface for an SnO_2:Pd sensor.

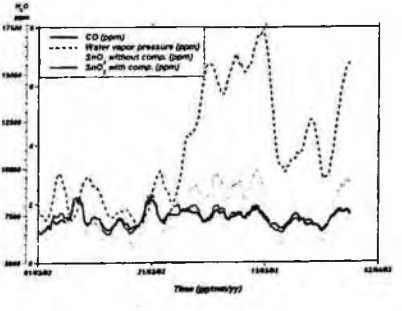

Figure 5. Compensated and non-compensated on-field responses for a SnO_2:Pd sensor. The period was about 2 months, during spring, with a strong change of humidity at the end of February.

4. Conclusions

The dependence of the conductance on the humidity was determined. In particular, the discrepacies between on-field and laboratory data are due to the effect of the flow rate on test chamber humidity, in form of water vapor partial pressure. It turned out that the thermal effect on the sensor is negligible. An algorithm for the compensation of humidity was proposed and succesfully tested on environmental data.

References

1. M.C. Carotta, G. Martinelli, L. Crema, C. Malagù, M.Merli, G. Ghiotti and E. Traversa, *Sensors and Actuators B,* **76**, 336 (2001).
2. A. Chiorino, G. Ghiotti, F. Prinetto, M.C. Carotta, D. Gnani, G. Martinelli, *Sensors and Actuators B,* **58**, 338 (1999).
3. C. Malagù, M.C. Carotta, A. Giberti, V. Guidi, L. Milano, M. Piga, and G. Martinelli, *Proceedings of Eurosensors XVIII,* September 13-15, 2004 Italy, Rome, p.630.
4. M.C. Carotta, A. Giberti, V. Guidi, C. Malagù, G. Martinelli, M. Piga, B. Vendemiati, *Sensors and Actuators B,* **103**, 272 (2004).

CO-PRECIPITATION SYNTHESIS OF $Sn_{1-X}Ti_XO_2$ SOLID SOLUTIONS FOR SENSING OF REDUCING GASES

B. VENDEMIATI*, M. BLO, M. C. CAROTTA, V. GUIDI,
C. MALAGÙ, G. MARTINELLI, A. ZANNI
INFM and Physics Department, University of Ferrara, Via del Paradiso 12
44100 Ferrara,Italy
**corresponding author: vendemiati@fe.infn.it*
G. KEPPEL
INFM and Legnaro National Laboratory, Via Università 2
35020 Legnaro (PD), Italy

A novel co-precipitation route for preparing pure Tin-Titanium solid solutions has been developed. Special emphasis focused on $Sn_{1-x}Ti_xO_2$ systems with x = 0.3, 0.5 and 0.7 for investigating the influence of composition, microstructure and morphology on gas sensitivity. Nano-grained powders have been obtained for each stoichiometry and have been characterized by DTA/TG, XRD, microanalysis and SEM techniques. We deposited the $Sn_{1-x}Ti_xO_2$ powders as thick films, which were comparatively tested vs. reducing gases. Preliminary studies stated that each layer exhibits an higher response respect to SnO_2 and TiO_2 reference layers, when tested in the same working conditions (100 ppm of CO, 300-400 °C working temperature). In particular, for 7:3 Tin-Titanium ratio the magnitude of the response attained at 300 °C was S = 25.

1. Introduction

Single transition-metal oxides are one of the most extensively studied class of solids, because of their wide range of technological applications in the field of photocatalysis, optics, photovoltaics and gas sensing [1]. In recent years, great attention deals with mixed transition-metal oxides and solid solutions is associated with the expectation of better physical and chemical properties with respect to the two single-oxide counterparts. In particular, solid solutions are characterized by a non-random distribution of the metals in the inorganic network [2], thus they exhibit unique properties.

SnO_2 and TiO_2 oxides are traditional n-type semiconductors, and a lot of papers [3,4] report on their important role in the gas-sensing field. Indeed, they are the fundamental components in most of the commercial chemoresistive gas sensors for H_2, CH_4 and CO detection, operating within a moderate range of temperature (300-400 °C). SnO_2 sensor's characteristics concern mainly about high sensitivity though they exhibit poor selectivity and chemical degradation at high temperature and low partial pressure of oxygen, which correspond to a fluctuation of the electrical properties upon prolonged exposure in reducing gas atmosphere [5]. On the other hand, TiO_2 is characterized by a remarkable

resistance to reduction at high temperature in reducing atmosphere and its response is less affected by humidity than for SnO_2 [3, 4].

This work focuses on the sol-gel synthesis of Sn-Ti solid-solutions with different stoichiometry, in order to merge the chemical and physical properties of SnO_2 and TiO_2, and their use as thick-film gas sensors for the detection of reducing gases. Stoichiometry should strongly affect the structure and morphology of the powders, thus their grain size and porosity, whose role is of primary importance in gas response.

2. Experimental

The sol-gel process is a well known soft-chemistry technique for preparing nanometric powders. The synthesis of solid solutions (and simple oxide) via sol-gel is easily achieved by choosing suitable precursors and tuning the working conditions (media, concentrations, temperature and pH). In the literature, there are several studies concerning Sn-Ti oxides [6], however to our knowledge, no report about synthesis performed starting from both metallorganic precursors, exists. The advantage of this route is the complete absence of anions in the wet-precursor, which eventually reduces the number of washing stages and contaminations of the final powders.

Sn-Ti oxides, $Sn_{1-x}Ti_xO_2$ ($0.3 \leq x \leq 0.7$), were prepared from stoichiometric solutions of the correspondent metal-alkoxides. A diluted acid solution was used to hydrolyse the metallorganic molecules. The resulting colloids were washed, peptized and dried. All amorphous precursors were subjected to thermogravimetric analysis (TG-DTA) and subsequently calcined at different temperatures, from 550 to 1050 °C in air for 2h. The resultant powders were characterised by means XRD, SEM and microanalysis.

The DTA graphs of the precursors show sharp peaks nearby 120 °C, accompanied by a fast weight loss. They are attributed to the decomposition of the residual by-products. The conversion of the precursors into the respective solid solution occurs slowly, together with a weight loss of 8 % in the region between 200 and 420 °C. The structural rearrangements lead to stable solid solutions up to 550 °C.

The influence of temperature over the phase evolution and cristallinity of the oxides was investigated by XRD powder diffraction performed at room temperature. The $Sn_{1-x}Ti_xO_2$ (annealed at 550, 650, 850 or 1050 °C for 2) diffraction patterns indicate that the samples are rutile-like single-phase solid solutions, independently on the stoichiometry, and show no band attributed to either SnO_2 or TiO_2 single oxides. As the annealing temperature increases, the diffraction peaks of the oxides (labelled as ST30 $x = 0.3$, ST50 $x = 0.5$ and ST70

x = 0.7) become more intense and sharp, which correspond to a better cristallinity. $Sn_{1-x}Ti_xO_2$ proved to suffer phase decomposition under annealing [2], which is although necessary to stabilize the powders for gas-sensing purpose. The single phase stability is unambiguously and reproducibly determined up to 850 °C for almost all powders, while phase separation was observed only for the Ti-rich sample (x = 0.7) when calcined at 1050°C. The results are in good agreement with the literature [2, 6].

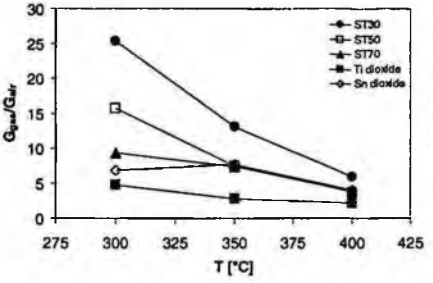

Figure 1 Responses of STx layers vs. 100 ppm of CO in dry air. ST30 behaves as the most responsive material, over the entire range of temperatures, respect to traditional SnO_2 and TiO_2 layers.

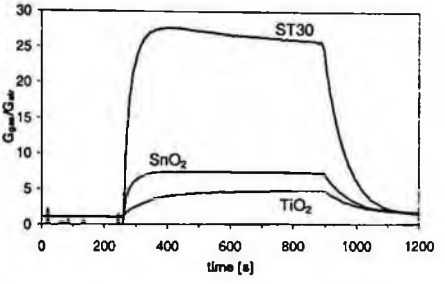

Figure 2 Difference between the amplitude of ST30 and standard layers responses. ST30 showed to be as fast as SnO_2 together with a better recovery time.

Sn-rich (x=0.3) and Sn-Ti equimolar powders (x=0.5) showed a sub-structure with grain dimension ranging in the nanometric scale for any annealing temperature. SEM micrographs of the aggregates highlighted an even distribution of nanometric grains both at the surface and in the bulk, and the powders morphology was found to be strongly affected by stoichiometry. The $Sn_{0.3}Ti_{0.7}O_2$ solid solution consists of spherical micrometrics agglomerates with revealed an inner sub-structure, which is strengthened at higher temperature of calcination, though accompanied by negligible coalescence.

Stoichiometry imparted during the synthesis proved to be consistent with the *metal-to-metal* ratio determined in the final solutions by microanalysis: ST30 =29.0, ST50=50.9, ST70=73.3 (% atoms of Ti, annealing at 650 °C for 2h).

CO detection of the STx sensors in dry air as carrier and in the temperature range of 300-400 °C has been preliminary studied. The responses of the layers (n-type behaviour) toward the tested gas, is defined as G_{gas}/G_{air} where G_{gas} and G_{air} are the conductance in CO-rich atmosphere and dry air respectively. All the responses were comparatively tested toward those of pure TiO_2 and SnO_2 layers (see Fig. 1), at the same working conditions (100 ppm of CO). Ti- and Sn-reference materials have been previously synthesised by sol-gel technique in our

laboratory. Since the phase and grain size of all solid solutions are very similar, the gas-response is expected to depend solely on the stoichiometry and working temperature. Remarkable sensitivity to CO has been demonstrated for ST30 ceramics at 300 °C. The $Sn_{0.7}Ti_{0.3}O_2$ oxide showed to be the most responsive over the whole temperature range (see Fig.2).

3. Conclusions

$Sn_{1-x}Ti_xO_2$ solid solutions have been prepared by co-precipitation then deposited by screen-printing as thick films. The influence of the *Sn to Ti* ratio proved to be relevant over gas response toward 100 ppm of CO, when compared with pure SnO_2 and TiO_2 layers. In particular 30% atoms structured in SnO_2 network yielded the highest response (G_{gas}/G_{air} = 25). Future plans address a systematic study about the response vs. other reducing gases as well as about selectivity toward gas mixtures.

References

1. M. M. Oliveira, D. C. Schnitzler, A. J. G. Zarbin, Chem. Mater. (2003), 15, 1903-1909
2. S.K. Kulshreshtha, R. Sasikala, V. Sudarsan, J. Mater. Chem., (2001), 11, 930-935
3. E. Traversa, M. L. Di Vona, S. Licoccia, M. Sacerdoti, M. C. Carotta, L. Crema, G. Martinelli, J. Sol-Gel Sci. Tec., 22, 167-179, 2001
4. G. Martinelli, M. C. Carotta, Sens. Actuat. B, 23, (1995), 157-161
5. M. Radwoka *et al.*, Sens. and Actuat. B, 47, (1998), 194-204
6. L.B. Kong *et al.*, J. Alloy Comp., 336, (2002), 315-319

ELECTRICAL CHARACTERIZATION OF PORPHYRIN THIN FILM TOWARDS HUMIDITY CONCENTRATION

S. PANTALEI[1], E. ZAMPETTI[1], E. SGRECCIA[1], E. MARTINELLI[1], L. SANDRO[1], J. MIO BERTOLO[2], A. BEARZOTTI[2], A. MACAGNANO[2], R. PAOLESSE[2,3], C. DI NATALE[1,3]

1. *Department of Electronic Engineering, Univeristy of Rome Tor Vergata Via del politecnico 1, 00133 Roma, Italy*
2. CNR-IMM, via del Fosso del Cavaliere 110, 00133 Roma, Italy
3. *Department of Chemical Science and Technology, University of Rome Tor Vergata, via della Ricerca Scientifica, 00133 Roma; Italy*

In this work, the conductivity behaviour of a porphyrin was studied. The effect of electrode nature and film thickness was also considered together with the exposure to dry and wet air. Results shows that porphyrin is intrinsically insulator but the conductance of thin films deposited on metallic electrodes can largely increase when exposed to humid air.

1. Introduction

In the last years, porphyrins have been studied and utilized as sensors materials for their properties as a chemically interactive material. Their sensitivity properties was exploited in many applications among which: medical, food and environmental applications [1,2].

Beside their sensing properties porphyrins were also investigated for their optical and electrical characteristics. From this point of view it is rather known that many organic materials and porphyrins in particular, in certain conditions may show a semiconductor conductivity behaviour. On the other hand, electrical properties may also depend on environmental conditions. Indeed, for some materials, that in vacuum conditions are electrical insulators, the interaction with water molecules may induce a semiconductor character [3,4,5].

In this paper we considered a porphyrin known to be semiconductor of p type, H_2-TPP, and measured the electrical properties in presence of variable relative humidity conditions [6].

2. Experimental

In order to measure the conductivity of porphyrin it was deposited over an insulator substrate where a couple of interdigitated electrodes were previously evaporated on silicon oxide wafers. The structure was made by 50 pairs of fingers, with width and interfinger distance of 20 μm each.

This studied porphyrin was H_2TPP. The electrical behaviour of molecule was studied in the past putting in evidence its semiconductor character. In particular H_2TPP was found to behave as a p-type material.

The deposition of organic films were perfomed using two different techniques: evaporation and spray casting. As shown in figure 1 this technique give rise to a polycrystalline and inhomogeneous large structure. The films were deposited with the same thickness. The versatility of spray casting was exploited depositing films of different thicknesses giving the opportunity to consider the film thickness as a further variable.

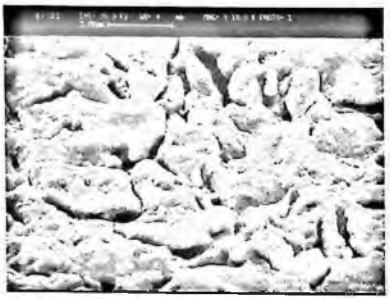

Figure 1- SEM photography of H_2TPP deposited by spray casting

As known from semiconductor technology, the interaction between the semiconductor and the metallic electrodes plays an important role in defining the overall properties of devices. To investigate the effect of organic-metal junction the following metals was used as electrodes: gold, chromium, aluminum, and titanium.

Electrical conductance properties was evaluated measuring the I-V characteristics exposing the sensor to a nitrogen atmosphere with a low relative humidity content of about 4%. I-V curves were measured applying voltage in the range -5V, + 5V. The applied voltage was slowly varied (10 mV each 5 seconds) to minimize capacitive effects.

Different relative humidity conditions were simply provided diluting the saturated water vapor (at ambient temperature and pressure) with nitrogen by means of proper mass-flow controllers. The response to relative humidity was measured biasing the sample with constant voltage.

3. Results and discussion

Figure 1 shows the I/V curves, measured in nitrogen atmosphere, of H_2TPP layers contacted by the four different metal electrodes. The curves deviate from the expected behaviour and show a strong hysteresis probably due to an accumulation of charges during the voltage inversion. In all cases the metal-porphyrin-metal structures exhibit very high resistances in the range 300 GΩ – 2.5 TΩ. In any case about one order of magnitude of variation is observed between the four cases. In particular, it is worth to remark that in the case of gold electrodes the highest conductivity has been achieved.

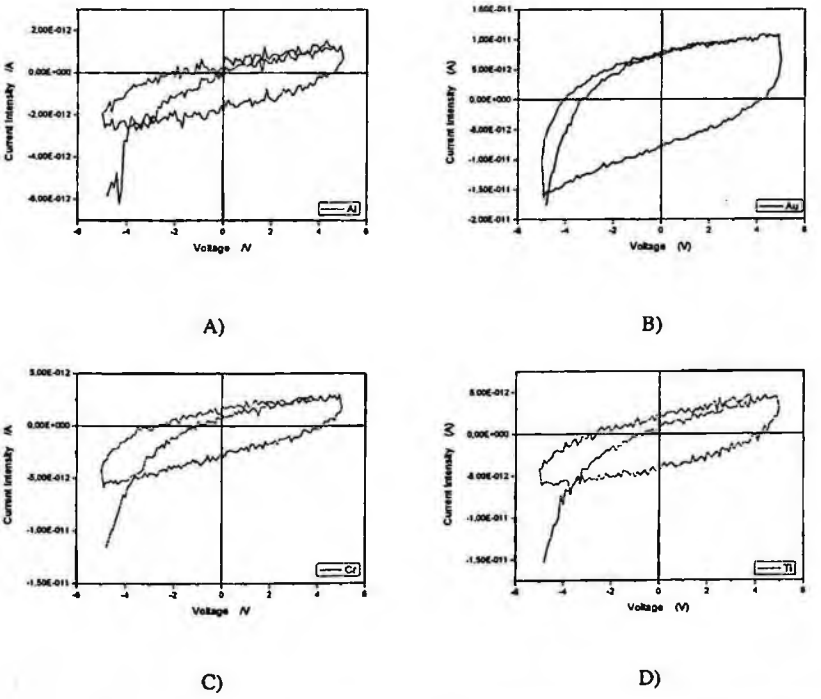

Figure 2 I-V curves of H_2TPP deposited on substrates with four different metal electrodes: A) Aluminum B) Gold C) Chromium D) Titanium.
Measures was performed at RH = 4% and T = 26 °C. Values of resistance are between 300 GΩ and 2.5 TΩ approximately.

Figure 3 shows the current versus repeated cycles of relative humidity. As in figure 2, curves related to the four metallic electrodes are shown. Relative humidity was continuously varied from 4% to 95% and back. The cycle was repeated at least twice. During measurements samples were biased the constant voltage of 1 V.

Curves show the typical saturation behaviour during the relative humidity increasing part of the cycle. An hysteresis appears during the decreasing part of the cycle.

A large resistance variation, about 5 orders of magnitude, was observed. It is also important to note that sensor conductivity does not change at low relative humidity. This behaviour suggests that absorbed water does not act a simple dopant but that some concurrent conduction mechanism, involving absorbed water molecules, may take place inside the material justifying the large conductance shift. A drift of the resistance value is also observed between successive relative humidity cycle.

The influence of film thickness is also shown in figure 3. For each film a basic deposition is compared with a film with a thickness of either 2/3 or 3/4 of the basic film. Response changes with film thickness, in particular at high relative humidity levels. Nonetheless, thickness plays a minor role in defining the sensor sensitivity to water vapor. This result is different from that observed coupling porphyrins to mass transducers like thickness shear mode resonators where sensor sensitivity is more largely dependent on the sensing layer thickness [7].

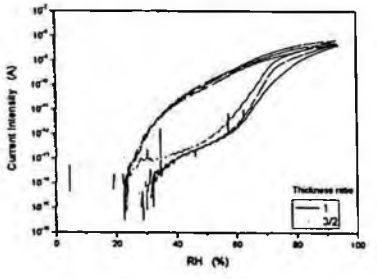

A)

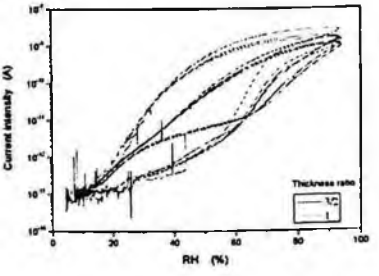

B)

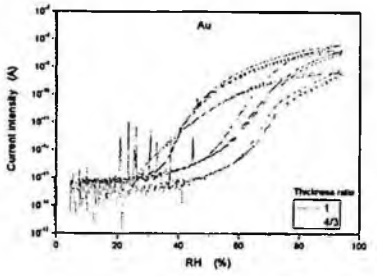

C)

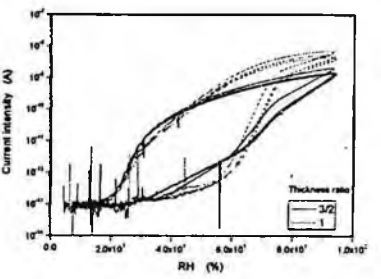

D)

Figure 3 – figures show the current versus relative humidity of four H_2TPP deposited on substrate with different electrodes (A: aluminum; B: titanium; C: gold; D: chromium). consecutive cycles of exposure from 4% to 95% and back of relative humidity in nitrogen are shown. in each subfigure behaviour related to two different molecular layer thicknesses are shown.

Conclusions

Measurements demonstrated that although in literature porphyrins are described with a semiconductor character, their behaviour largely depends on the nature of the metallic contacts. In some cases, as shown in this paper, the metallic contact can completely hide the semiconductor properties.

Results shown in this paper also confirmed the expected relationship between electric properties and environmental properties. In particular, very large conductance variations were observed exposing the material to wet air with a variation of about five orders of magnitude between dry and moistened air. the nature of this variation has still to be investigate also if the threshold effect observed at low relative humidity values suggests that a parallel conduction mechanism involving water is activated rather than a modification of intrinsic porphyrin electronics levels.

References

1. C. Di Natale, A. Macagnano, G. Repole, G. Saggio, A. D'Amico, R. Paolesse, T. Boschi, Materials Science and Engineering C 5 (1998) 208-215
2. C. Di Natale, G. Pennazza, A. Macagnano, E. Martinelli, R. Paolesse, A. D'Amico, Sensors and Actuators B 91 (2003) 169-174
3. B.J. Stanbery, M. Gouterman, R.M. Burgess, J. Phys. Chem. 89 (1985) 4950

4. K. Yamashita, Y. Harima, T. Matsubayashi, J. Phys. Chem. 93 (1989) 5311-5315
5. Y. Harima, K. Yamashita, H. Hishii, K. Seki, Thin Solid Films 366 (2000) 237-248
6. J. Mio Bertolo, A. Bearzotti, P. Falcaro, E. Traversa, P. Innocenzi, Sensor Letters 1 (2004) 64-70
7. J.A.J. Brunink, C. Di Natale, F. Bungaro, F. Davide, A. D'Amico, R. Paolesse, T. Boschi, M. Faccio, G. Ferri; Analytica Chimica Acta 325 (1996) 53-64

SOL-GEL TiO_2 COMBUSTION SENSOR: ON-BOARD EXPERIMENTALS AND COMPARISON WITH COMMERCIAL LAMBDA PROBE

L. FRANCIOSO, D.S. PRESICCE, M. EPIFANI, P. SICILIANO

IMM – CNR, Section of Lecce
Monteroni Street, CNR Area
73100 Lecce, ITALY
E-mail: luca.francioso@le.imm.cnr.it

The aim of this work is to carry out a performance comparison between a commercial Bosch Lambda probe and a sol-gel TiO_2 thin film deposited an alumina substrates. Actually, zirconia based lambda probes are a well-established technology in the field of combustion control in fuel injection engines. An experimental bench was realized in order to perform contemporary data acquisition of a Bosch lambda probe Mod. LSF 4.2 and a TiO_2 thin film sensors. The signals of both sensors is acquired with an electrometer with scanner card on real gasoline engine. Fast response time is observed from TiO_2 sol-gel sensor, while best results were obtained from first experimental data on Pt doped devices, that outline response time comparable with commercial probe.

1. Introduction

Studies about controllability of combustion for gasoline or diesel engines and the reduction of emissions by catalytic converters have been carried out to meet the emission standards [1-5]. However the need of the reduction of emissions level has led to the improvement in different fields and in particular on sensor systems that measure exhaust gas. The verification of long term stability of emission control systems is an important tool for controlling pollutants. In this paper we carried out tests to the aim to compare the performance of a commercial Bosch lambda probe LSF 4.2 and a sol-gel TiO_2 thin film sensor on alumina substrate. The commercial lambda probe are actually based on a potentiometric cell of zirconium oxide, that performs a voltage output related to oxygen partial pressure difference between atmospheric environment and exhaust gases [6]. Actually slow thermal activation and expensive production process are disadvantages of this probe, introduced however in most fuel injection systems.

We evaluate response of a sol-gel TiO_2 gas sensors as exhaust gas probes in severe conditions, like exhaust gas of internal combustion engine. The

production process of this sensor, and particularly thin film deposition can be carried out on a entire wafer of alumina and with a single batch process obtaining 255 sensors for wafer, 2x2 mm^2 with same facilities of silicon technology. Active film deposition technology widely used for synthesis of different sensitive films is sol-gel [7], a cheap chemical method, actually implemented in our labs in a CMOS compatible process of fabrication. This is an important advantage of this technique concerning low cost production and batch process potential.

2. Experimental

Pure TiO_2 sols were prepared in a glove-box with <1 ppm H_2O. Titanium butoxide (2.13 ml) was dissolved in 10 ml of butanol and chelated with 0.64 ml of acetylacetone. After 30 minutes since the addition of acetylacetone, 0.45 ml of water were added dropwise, obtaining a yellow, clear sol; for the preparation of Pt doped TiO2 sols, to a pure sol prepared as above Pt (II) bis-acetylacetonate was added after dissolution in tetrahydrofuran.

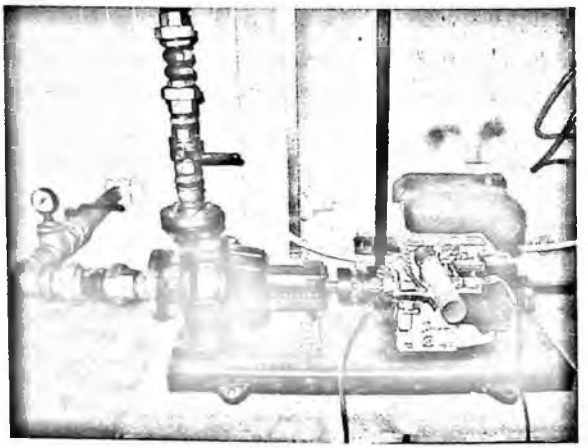

Fig. 1. Spark ignition engine test bench

The amount of the Pt precursor was such to get a Pt/Ti atomic ratio of 0.05. Thin films were deposited from the previous sols by spin-coating onto alumina

substrates in low-moisture atmosphere (about 30% RH), then heat-treating the films at 500°C in a tubular oven. Two layers were deposited of each material.
An experimental bench was realized in order to perform contemporary data acquisition of a Bosch lambda probe Mod. LSF 4.2 [8] and our thin film sensors. The internal combustion engine of 220 cm^3 of displacement was mounted on bench with a modified pipe supplied with two 18 mm threaded holes for probe and sensors insertion into pipe (Fig. 1). Figure 2 shows a detail of the brass adapter realized with electrical feedthroughs to perform sensor heating and signal acquisition ; an electrometer with scanner card permits to switch from sensor to lambda probe in 0.1 seconds and acquire voltage signal from commercial probe and DC current from thin film sensor.

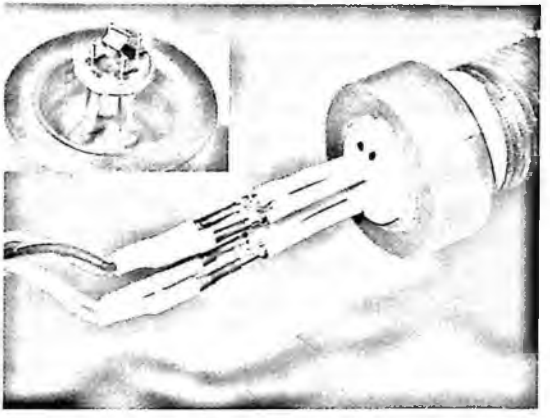

Fig. 2. Engine brass adapter for sensor

The initial warm-up time for sensor is two minutes after warm-up time of engine (10 minutes), under exhaust flow and contemporary heating performed by platinum heater embedded on alumina die; temperature of gas from engine ranges from 250 to 270 °C, measured with a K-type thermocouple, readed also from the scanner card of electrometer, in order to discriminate sensor drift related to modified exhausts temperature.In any case small temperature variations related to different regimes of engine had not effect on baseline signal of sensor, also during rich-lean large current shift.
About signal of lambda probe, the common zirconia based electrochemical cells are characterized by a voltage between two terminals of cell that satisfy the

Nernst's law [9]. After preliminary test to investigate optimal working temperature, a film temperature set between 520 °C and 800 °C was adopted for active film of TiO_2, with electrical contact bias of 3.00 Volts. The first experimental protocol test set the acquisition runs on costant rotation of engine with acquisition frequency of 10 Hz, alternatively for both transducers.
Measurements protocol was defined in order to have 10 minutes of warm-up time after engine ignition while sensor's heater was supplied after this warm-up for 2 minute before acquisition, engine rotation was regulated to 3000 rpm and acquisition of both sensors started. Acquisition frequency was the same of previous tests, with 15 minutes of total acquisiton time for each temperature.

3. Results and discussion

Thin film sensor showed a good response in correlation with the Bosch probe, and short response time can be outpointed. A manual regulation of air/fuel ratio during engine run permits to obtain rapid changes of mixture composition, as revealed by Bosch probe with large shift from 0.9 Volts to 0.1 Volts [9].
An interesting feature is that, despite well-know long response time of semiconductor gas sensors [10], we obtain interesting time of response. tThe response of the sensor calculated as ratio of sensor current between two measured points, is better than one order of magnitude from rich to lean mixture. New investigation run was carried out to verify performance of undoped titania thin film versus operative temperature Graphs show the dinamic response of sensor to different temperatures and with different values of lambda ratio. Temperatures range was from 520 to 800 °C. Moreover previous experiments of gas sensing in titania film showed useful response time above 500 °C for automotive applications[11], so only experimental data of temperature between 630 and 800 °C were analyzed and elaborated.
In Fig. 3 the thin film trasducers shows a good overlapping with commercial probe signal, so a strong effect of film's bulk conduction is supposable. On the contrary, at temperature below 800°C the sensitivity of sensor towards oxygen concentrations decreases while sensitivity towards other species like NO_x and CO increases [12].

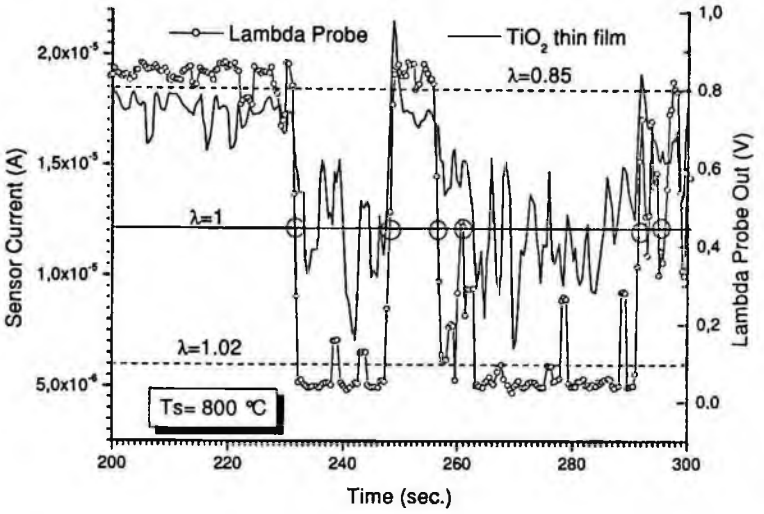

Fig. 3: Dynamic response of pure TiO_2 sensor and Bosch probe at 800 °C to exhausts

At lower temperature, behaviour of thin film sensor is similar to higher temperatures (800 °C), but slower response time can be observed at lower temperature, around about 500 °C; film response is nevertheless coherent to n-type semiconductor conductivity both in reach and lean regimes. In fact the response of two trasducers can be overlapped again, with a good response at extreme lambda value, where commercial lambda probe saturates around 0.85 Volts corresponding to $\lambda = 0.7$, while TiO_2 sensor permits to gain useful informations also at this stechiometric conditions. About the response time at 800 °C thin film sensor seems to supply a good performance in terms of response time and repeatibility of behaviours during entire acquisition; response time at 90% of saturation currents ranges from 0.6 to 1 seconds for commercial probe, while our device show time between 1.5 and 2.0 seconds. Nevertheless an investigation about capabilities of thin film sensor to perform correct discriminations of different lambda value overall complete acquisition run was carried out.

In order to define the protocol that permits to extract current value of TiO_2 in correspondance of differents lambda value, three differents values of lambda were selected, respectively $\lambda = 0.85$, $\lambda = 1.00$ and $\lambda = 1.02$. From official Bosch datasheet [9], corresponding value of probe output voltage were chosen as described in Table 1. Since the acquisition of probe signal showed a lot of spikes related to unhomogeneity of flue gas into exhaust pipe and high flow regimes, a preliminary median filter with 5-value window was applied to raw lambda voltage values acquired from electrometer. This 5-value window median filter elaboration apported by Matlab code [13], permits to remove single spikes from commercial probe acquired data and reduce false data extraction from thin film sensor data population. Filtered value of Bosch probe voltage was elaborated with conditional relation visibile in Table 1; when probe output ranges from 425 to 475 mV, for each point that verifies this condition, corresponding value of titania sensor was extracted and collected as corresponding to $\lambda = 1.00$, in similar manner for 75-125 mV range for $\lambda = 1.02$ and 775-825 mV range for $\lambda = 0.85$. All this experimental points without further elaboration this different values collected from sensor are plotted in Fig. 4.

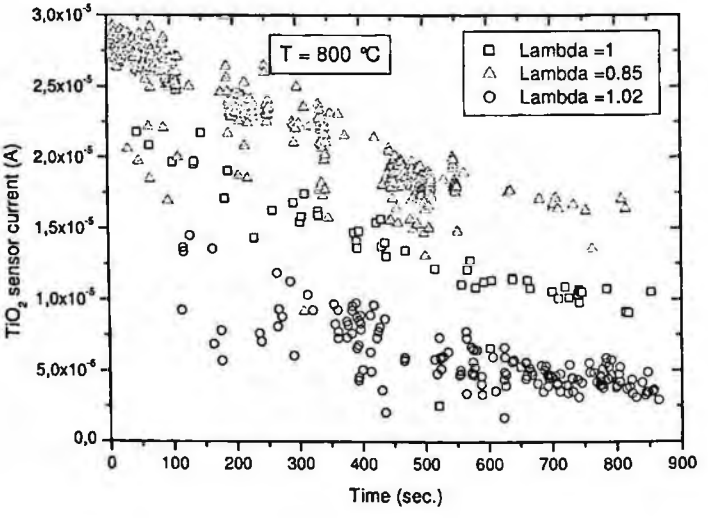

Fig. 4. Pure TiO_2 sensor experimental data collected at different lambda values at 800 °C

If sensor exhibits good separation properties, experimental data will arrange on three horizontal straight lines, corresponding to different saturation current of sensor for different lambda ratio. Discrimination properties become considerable at 800 °C for pure titania film, with clear discrimination of lambda values, while a little drift is visible for first period of acquisition run. This type of data extraction don't require high computational power, and an ON/OFF output from a cheap integrated window comparator like an operational amplifier like LM322 [14] can be easily obtained, once defined threshold value of current from rich to lean mixture. Work is in progress to verifying electrical contacts degradation and morphological behaviour, since old gold metalization implemented for electrical contacts [15], was now upgraded to platinum metal.

3 Conclusions

A direct comparison of performances between a commercial Bosch lambda probe and a novel sol-gel thin film TiO_2 sensor was evaluated. The test bench realized permits to acquire with intervals of 0.1 seconds the signal of both sensors and temperature. A good response is observed between different combustion regimes of rich and lean mixture, but the attactive feature is the fast response time of about 1 second from from rich mistures ($\lambda < 0.8$) to lean mixtures ($\lambda > 1.2$) and from lean to rich. The best response time were recorded for Pt doped (0.05 Pt/Pd atomic ratio) sensitive materials at 630 °C and pure titania at 800 °C. A 5-value windows median filter software elaboration via Matlab code was performed to reduce spikes from raw acquired data of Bosch probe. Conditional extracted experimental data of TiO_2 sensor were plotted vs time and at higher temperature for pure titania a good discrimination between differents values of lambda was highlighted. Also a good discrimination performance was obtained from Pt doped film at lower temperature, together with fast response time around 1.0 seconds at 90% of saturation current. At the moment, work is in progress to verify response repeatibility and ageing of electrical contacts and long term stability of active film.

References

1. S. Shundoh, N. Komori and K. Tsujimura, "NOx Reduction from Diesel Combustion Using Pilot Injection with Pressure Fuel Injection", SAE paper 920461.
2. T. Inoue, S. Matsushita, K. Nakanishi and H. Okano, "Toyota lean combustion system the third generation system", SAE paper 930873.
3. N. Uchida, Y. Daisho, T. Saito and H. Sugano, "Combined effects of EGR andSupercharging on Diesel Combustion and Emissions", SAE paper 930601.
4. M. Konno, T. Chikahisa, T. Murayama and M. Iwamoto, "Catalytic Reduction of NOx in Actual Diesel Engine Exhaust", SAE paper 920091.
5. G. Muramatsu, A. Abe, M. Furuyama and K. Yoshida "Catalytic reduction of NOx in Diesel Exhaust", SAE paper 930135
6. Kaidantzis, P. , Rasmussen P.,"Robust, self-calibrating lambda feedback for SI engines" SAE Paper 930860
7. S. Capone, M. Epifani, F. Quaranta, P. Siciliano, L. Vasanelli, "Application of a semiconductor sol–gel sensor array to the discrimination of pollutant in air", Thin Solid Films 391 (2) (2001) 314-319
8. Bosch LSF 4.2 Original equipment information, Robert Bosch Gmbh
9. J. Lee, B. Kim, K. Lee, K. Han "A new catalyst monitoring sensor for gasoline engine using YSZ-Al_2O_3 as solid elecrolyte and gas diffusion barrier", Sensors and Actuators, B 59 (1999) 9-15
10. D.E. Williams, Conduction and gas response of semiconductor gas sensors" P.T. Moseley, B.C. Tofield (Eds.), Solid State Gas Sensors, Adam Hilger, Bristol, 1987, pp. 71–123.
11. Sheng J., Yoshida N., Karasawa J., Fukami T. Platinum doped titania film oxygen sensor integrated with temperature compensating thermistor, Sensors and Actuators B 41 (1997), pp1331-136
12. Menil F., Coillard V., Lucat C. Critical review of nitrogen monoxide sensors for exhaust gases of lean burn engines, Sensors and Actuators B: 67 (2000), pp. 1–23
13. Matlab Software, Mathworks Official Web Page and User's Manual
14. LM 322 Operational Ampplifier Application Notes, National Semiconductor
15. Francioso L., Presicce D.S., Taurino A.M., Rella R., Siciliano P. and Ficarella A. Automotive application of sol – gel TiO_2 thin film – based sensor for lambda measurement. Sensors and Actuators B 95 (2003), pp. 66-72

EXPLOITING GAS-SENSING PROPERTIES OF LANGMUIR-BLODGETT/SCHAEFFER FILMS BY REFLECTANCE ANISOTROPY SPECTROSCOPY

M. RUSSO[†], R. PAOLESSE

Department of Science and Chemical Technology, Università Tor Vergata, via Ricerca Scientifica 1 00133, Rome, Italy

G. BUSSETTI, C. GOLETTI, P. CHIARADIA

Department of Physics and Unità INFM, Università Tor Vergata, via Ricerca Scientifica 1 00133, Rome, Italy

C. DI NATALE, A. D'AMICO

Department of Electronic Engineering, Università Tor Vergata, via del Politecnico 1 00133, Rome, Italy

L. VALLI

Department of Innovation Engineering, Università di Lecce, via Monteroni 73100, Lecce, Italy

By reflectance anisotropy spectroscopy we have measured significant changes in the optical spectrum of Langmuir-Blodgett (LB) and Langmuir-Schaeffer (LS) porphyrin films, induced by vapour organic compounds (ethanol and propanol). Variations of the optical signal have been mainly detected in the Soret band region of the molecule, namely at 2.84 and 2.88 eV, with an evident dependence upon the different cycles of exposure/purging.

This result has a twofold implication: on one side it helps to comprehend the origin of the thickness dependence of RAS spectra measured at LB and LS layers; on the other, it opens an intriguing possibility towards the development of a sensitive optical gas-sensor.

[†] reference author e-mail: michele.russo@uniroma2.it.

1. Introduction

In the last decades engineering research has devoted its attention to the development and characterization of new gas-sensors, based on organic compounds as porphyrins, phtalocyanine, etc. [1].
Some organic deposition techniques, like Langmuir-Blodgett (LB) and Langmuir-Schaeffer (LS) methods [2], are now well established in thickness control and reliability. Moreover porphyrins, known for their particular properties in some basic processes of life, with respect to other organic molecules can be easily synthesised and deposited on different substrates by LB or LS deposition. As a result, by growing thin layers of porphyrins on an oscillating quartz, a prototype of organic sensor has been carried out [3].
A deep spectroscopic investigation of the interactions between porphyrin layers and organic vapours, although important for further developments in sensor devices, is still lacking. In this respect, optical probes are a suitable choice since they can be used in different experimental environments without producing any contamination of organic films. In particular, reflectance anisotropy spectroscopy (RAS) has been recently applied to characterize LB and LS films, showing an excellent sensitivity in monitoring very low optical changes with respect to traditional absorbance data [4].
In this communication we present the first RAS measurements acquired during the exposure of a free base porphyrin LB layer film to vapour organic compound (V.O.C). V.O.C. influences the intensity and line-shape of RAS signal in the Soret band region. Following the spectral intensity change, we are able to monitor the influence of ethanol and propanol on organic layers in concentration as low as 10^2 ppm. These results open the possibility of achieving a new optical gas-sensor prototype [5].

2. Experimental

2.1. *Chemical description*

5,10,15,20-tetrakis-[4-(1-Heptyloxy)phenyl]-porphyrin (H_2THOPP) was synthesized from 4-Heptyloxybenzaldehyde and pyrrole following the Adler method [6] and deposited onto oxidised Si(001) substrates. LB and LS film depositions were carried out using a KS5000 System 3 apparatus. 1:4 molar mixture of H_2THOPP and arachidic acid was dissolved in chlorophorm. Barrier pressure and dipping speed were respectively 25mN/m (LB) and 10mm/min (LS).

Two samples were prepared: i) 30ML thick with LB technique; ii) 12ML thick with LS technique. Samples are inserted in a little plastic chamber with inlet and outlet gates for V.O.C.. A home-made glass window allows the optical access to the sample. The ethanol and propanol concentration has been varied by two flux-meters from 10^2ppm up to $2x10^4$ppm (saturate vapours).

2.2. *RAS apparatus*

In RAS one measures, in normal incidence, the difference of the sample reflectivity for light polarized alternatively -with frequency ν_0- along two perpendicular directions (*a* and *b*). Usually, *a* and *b* coincide with well-defined symmetry directions of the sample. Differently from metals and semiconductors, for organic systems the identification of such directions is not straightforward, since in this case they cannot be gathered from the superstructure yielded by growth.

In RAS the ratio between the difference of the sample reflectivity (ΔR) and the average reflectivity (R) is measured as a function of photon wavelength:

$$\frac{\Delta R}{R} = 2\frac{R_a - R_b}{R_a + R_b} \tag{1}$$

where R_i (i=*a*,*b*) is the square modulus of the Fresnel complex coefficients for reflection (r_i) of polarization *i*.

The RAS signal is measured at the frequency ν_0 (about 100kHz) by a lock-in amplifier, as discussed elsewhere [4,7]. All the spectra have been recorded in the photon wavelength range 200÷800nm (1.5÷5.5eV). The samples have been always kept at room temperature. The linearly polarised electric field of light (along *a* and *b*) were aligned with the edges of the rectangular substrate. This experimental configuration has been chosen measuring the dependence of RAS spectra upon the azimuthal rotation by an angle ϕ around the axis perpendicular to the substrate and looking for the maximum signal amplitude (ϕ_0).

In particular, we have monitored the optical signal variation in a reduced energy range (around the Soret band region, 2.84-2.88eV), during the exposure of porphyrins to V.O.C. at different concentrations. Finally, in the same range, we have followed by RAS also the effect of purging due to pure nitrogen introduced in the chamber. In this condition the anisotropy signal comes back to the initial value it had before the layer was exposed to V.O.C., in consequence of the reversible interaction process between layer and gas.

3. Results

In Fig.1 we report the RAS spectrum of a H_2THOPP 30ML thick LB layer. The main positive peak coincides with the Soret band (λ=431nm, 2.88eV) of the molecule, while the negative peak at 437nm (2.83eV) is a peculiar spectroscopic feature of RAS spectrum, not seen in UV-Vis absorbance data. The four structures at lower photon energies (known as Q bands) are related to meta-stable transitions of the free-base porphyrin.

The Soret band region of this sample appears to be particularly affected by exposure to saturate vapours of ethanol. In particular, the positive peak increases its anisotropy by some RAS units (Fig.2-i), while the negative peak decreases its absolute value by some tens of RAS units (Fig.2-ii). In both cases, the sample was exposed to V.O.C. ($2x10^4$ppm) for 2.5 minutes. The full recovery of the original level, after exposure to N_2, takes just few seconds.

RAS spectrum of 12ML of H_2THOPP (LS deposition) is reported in Fig.3. The broad structure at high energy (400nm, 3.1eV) results from two terms: a known optical contribution of H-aggregate molecules [8] and an optical transition of molecule (415nm, 2.99eV). The minimum at 441nm (2.8eV) is related to J-aggregate molecules [8]. The huge oscillation around 465nm is not visible in UV-Vis absorbance spectra.

Finally in Fig.4 we show the signal variation for the LS sample, measured during exposure/purging cycles to different concentrations of V.O.C. ($5x10^2$, 10^3, $5x10^3$ppm).

4. Discussion

In a recent theoretical work [9], the oscillating behaviour of the RAS signal in the Soret band region, generally observed on LB and LS samples after a certain critical coverage value [4], is explained in terms of dipole interactions between the ordered porphyrin molecules adsorbed onto the substrate. *A* and *B* structures (see Fig.1) have the same explanation in ref. 9, with a consequent equivalence in their line-shape and layer-thickness evolution. On the contrary, in this experiment samples show clearly different trends for *A* and *B*, when exposed to organic vapours. *A* increases its anisotropy intensity of few RAS units, while *B* decreases the absolute signal value. Moreover, we note that the LS sample displays an anisotropic structure in a spectral region (455÷471nm) where no optical transitions are expected for the molecule. We believe that a further theoretical examination on the puzzling RAS signal origin is therefore necessary.

From reported spectra (Fig.2), we estimate a RAS sensitivity to V.O.C. in the order of 10^2ppm. To confirm this value, we exposed the 12ML film to propanol

vapours of increasing V.O.C. concentration. As reported in Fig.4 the RAS signal has a reproducible behaviour during exposure/purging cycles. The porphyrin layer response to the gas takes few seconds: this result and the sharp intensity variation in the RAS spectrum allow a fast optical detection of organic vapours. For low percentage of organic vapours, spectral changes seems to be proportional to the concentration of the gas.

In summary, we have monitored by reflectance anisotropy spectroscopy the effect of V.O.C. to porphyrin layers. The collected data reveal the capabilities of RAS as a powerful tool in fast detection of small concentration of organic vapours and allow us to project an original optical gas-sensor prototype.

5. Figures

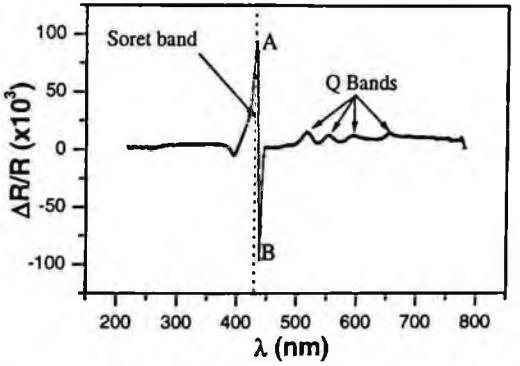

Figure 1. Ras spectrum of a LB film of 30ML H_2THOPP. The dot line indicates the spectral position of the Soret band, as taken from UV-Vis spectra. *A* labels the main peak, coincident with the Soret band of the molecule, while *B* indicates the negative peak (see text).

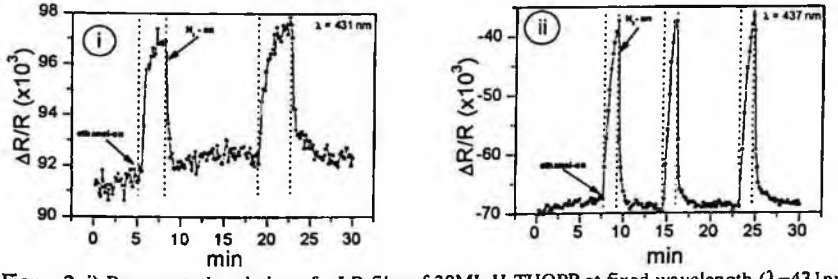

Figure 2. i) Ras spectral variation of a LB film of 30ML H_2THOPP at fixed wavelength (λ=431nm, 2.88eV), during exposure to ethanol saturate vapours ($2x10^4$ppm). The dot lines alternatively indicate the exposure of the sample to the vapours (ethanol-on) and the purging of the LB film (N_2-on). ii) RAS monitoring of the LB sample at fixed wavelength (λ=437nm, 2.83eV), during periodic cycles of exposure/purging to ethanol.

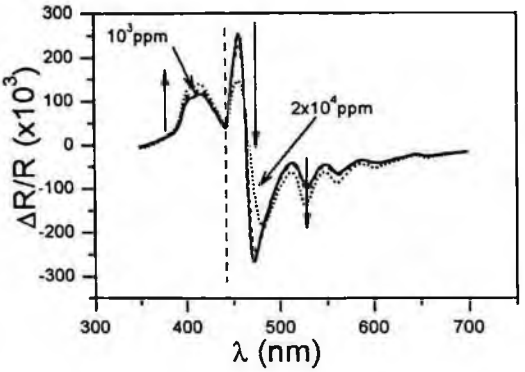

Figure 3. RAS signal of a H_2THOPP 12ML thick layer (LS deposition). The dashed line indicates the Soret band spectral position in traditional UV-Vis absorbance spectra. The bold arrows specify the sum of RAS signal variations, during exposure of the sample to saturate propanol vapours.

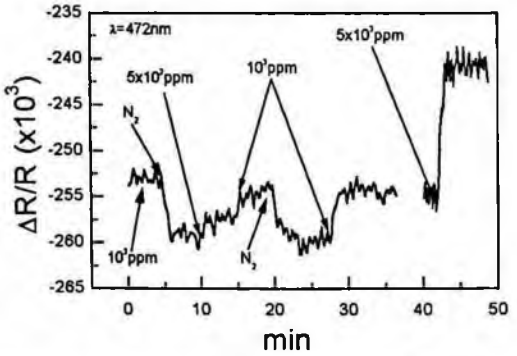

Figure 4. Exposure/purging cycles of propanol on a H_2THOPP 12ML thick layer (LS deposition). The RAS signal appears to be proportional to different concentrations of vapours.

References

1. J. Spadavecchia, G. Ciccarella, R. Rella, *Sensors and Actuators* **B106** 212–220 (2005) and references therein.
2. R. H. Tredgold, *Rep. Prog. Phys.* 50 1609-1656 (1987).
3. R. Paolesse, C. Di Natale, A. Macagnano, F. Davide, T. Boschi, A . D'Amico, *Sensors and Actuators* **B47** 70-76 (1998).

4. C. Goletti, G. Bussetti, P. Chiaradia, A. Sassella, A. Borghesi, *Organic Electronics* **5(1-3)** 73-81 (2004) and references therein.
5. M. Giordano, M. Russo, A. Cusano, A. Cutolo, G. Mensitieri, L. Nicolais, *Appl. Phys. Lett.* **85** 5349-5351 (2004).
6. A. D. Adler, F. R. Longo, J. D. Finarelli, J. Goldmacher, J. Assour, L. Karsakoff, *J. Org. Chem.* **32** 476 (1967).
7. A. Salvati, P. Chiaradia, *Appl. Opt.* **39** 5820 (2000).
8. M. Kasha, H. R. Rawls, *Pure Appl. Chem.* **11** 371 (1965).
9. N. Arzate, B. S. Mendoza, R. A. Vàzquez-Nava, *J. Phys. Condens. Matter* **16** S4259-S4278 (2004).

OPTICAL FIBER AND ACOUSTIC SENSORS BASED ON SINGLE WALLED CARBON NANOTUBES FOR CHEMICAL DETECTION OF ORGANIC VAPORS

M. CONSALES, S. CAMPOPIANO, A. CUSANO, A. CUTOLO
Optoelectronic Division, Engineering Department, University of Sannio, Benevento, Italy

M. PENZA , G. CASSANO , P. AVERSA , L. CAPODIECI
ENEA, C.R. Brindisi, Materials and New Technologies Unit, Brindisi, Italy

M. GIORDANO
Institute of Composite Biomedical Materials, National Research Council, Napoli, Italy

Carbon nanotubes are fascinating new functional nanomaterials with remarkable electrical, optical, structural and mechanical properties [1]. The sensing properties of Langmuir-Blodgett (LB) films consisting of tangled single-walled carbon nanotubes (SWCNTs) used as sensitive nanomaterials for volatile organic compounds detection have been investigated by using Quartz Crystal Microbalance (QCM) 10 MHz AT-cut quartz resonators and standard Silica Optical Fiber (SOF) based on light reflectometry at a wavelength of 1310 nm [2,3]. The proposed detection techniques are focused on two key parameters in the gas sensing applications as mass change and complex refractive index change induced by gas molecules adsorption. High sensitivity to ethanol and ethylacetate vapors with concentration in the range 10-500 ppm, very fast responses and sub-ppm limits of detection have been observed for both sensors.

1. Introduction

Carbon nanotube research is probably the most active research field in carbon science at the present time. The experimental identification in 1991 of multi-wall carbon nanotubes [4] first attracted attention to the field, further stimulated by the experimental discovery of the simpler and more fundamental single-wall carbon nanotubes in 1993 [5,6]. The fundamental carbon nanotube can be thought as being formed by folding a graphene sheet to give a seamless cylinder. SWCNTs exhibit nanosized morphology, a high specific surface area (100-1800 m^2/g) and a peculiar hollow structure, making them excellent nanomaterials for highly sensitive gas adsorption at room temperature.

In this work, the sensing properties of such nanomaterial for Volatile Organic Compounds (VOCs) detection have been demonstrated by using SOF sensors based on light reflectometry at a wavelength of 1310 nm and acoustic sensors based on QCM 10 MHz AT-cut quartz resonators. Both transducers incorporate thin films of SWCNTs deposited by means of the Langmuir-Blodgett (LB) deposition technique, allowing the fabrication of defect-free, molecularly ordered ultra-thin films with controlled thickness and orientation. The optical

and acoustic sensors, based on two different transducing principles such as complex dielectric constant change and mass change, respectively, provide high sensitivity, very low limits of VOCs detection and fast response, at room temperature. The simultaneous detection of targeted VOCs by using transducers with different principles of operation, coated by the same sensitive nanomaterial, could be very useful to enhance the features extraction of multicomponent mixtures in vapor discrimination and chemical recognition applications.

2. Principles and methods

The key point of the proposed SOF sensors is that the complex dielectric function of the sensitive overlayer and thus the fiber–film interface reflectance change upon exposure to target analytes due to their molecules adsorption into the film. The power reflected by the sensitive overlayer, normalized to the power emitted by the source, is the SOF sensor output, continuously monitored by means of a proper interrogation system [2,3], as shown in Fig. 1a.

The main principle of a QCM sensor is that a mass added or removed from a vibrating body changes its resonant frequency. Upon exposures, the analyte molecules are adsorbed by the sensitive overlayer deposited onto the QCM device, causing its mass loading and, in turn, changes in the fundamental oscillation frequency, taken as the sensor output.

The molecular engineering Langmuir-Blodgett deposition technique is a way of making ultra-thin organic films with a precise control over the architecture of the films at the molecular level. This means that films can be designed to offer certain desirable properties tailored to suit the application required. For this reason this technique has been chosen to deposit multilayers of SWCNTs onto both SOFs tip and QCMs substrate, appropriately buffered by a CdA buffer multilayer in order to enhance the adhesion of carbon nanotubes.

The deposition process of both the CdA buffer material onto the bare optical fiber and of the SWCNTs multilayer onto the CdA have been real-time monitored by means of the experimental setup reported in Fig. 1a. The normalized reflectance changes during the deposition of 20 monolayers of CdA onto the bare fiber and 10 monolayers of SWCNTs onto the CdA buffer (see Fig.1b) show that, in the case of the CdA deposition, an increasing of the CdA film thickness induces a decreasing of the optical reflectance, while in the case of SWCNTs deposition the reflectance increases with the film thickness, except for the deposition of the first two monolayers. It is worth to note, however, that different expressions rule the relationship between reflectance and sensing overlayers features.

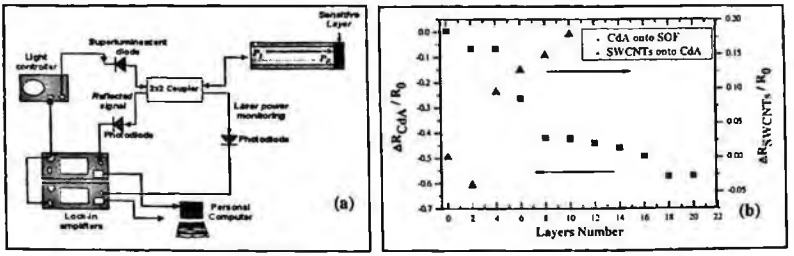

Fig. 1: a) Schematic view of the optical fiber sensors interrogation system; b) Normalized reflectance changes during the deposition of 20 Mon. of CdA onto SOF and of 10 Mon. of SWCNTs onto CdA.

As matter of fact, in the case of CdA thin film the reflectance can be expressed according to the following expressions:

$$R_{CdA} = \left| \frac{r_{12} + r_{23} \cdot e^{i \cdot \beta 2}}{1 + r_{12} r_{23} \cdot e^{i \cdot \beta 2}} \right|^2 \qquad \text{(Eq. 1)}$$

with

$$r_{12} = \frac{\sqrt{\varepsilon_f} - \sqrt{\tilde{\varepsilon}_{CdA}}}{\sqrt{\varepsilon_f} + \sqrt{\tilde{\varepsilon}_{CdA}}}; \; r_{23} = \frac{\sqrt{\tilde{\varepsilon}_{CdA}} - \sqrt{\varepsilon_{ext}}}{\sqrt{\tilde{\varepsilon}_{CdA}} + \sqrt{\varepsilon_{ext}}}; \; \beta_2 = \frac{2\pi \cdot \left(2\sqrt{\tilde{\varepsilon}_{CdA}} \cdot d_{CdA} \right)}{\lambda} \qquad \text{(Eq. 2)}$$

where ε_f and ε_{ext} are the optical fiber and external medium dielectric functions, λ is the optical wavelength, $\tilde{\varepsilon}_{CdA}$ and d_{CdA} represent the complex dielectric function and the thickness of the CdA layer, respectively. For the deposition of SWCNTs, instead, the reflectance can be written as follows:

$$R_{SWCNTs} = \left| \frac{r_{12} + r_{23}^{*} \cdot e^{i \cdot \beta_2} + r_{34} \cdot e^{i(\beta_2 + \beta_3)} + r_{12} r_{23}^{*} r_{34} \cdot e^{i \cdot \beta_3}}{1 + r_{12} r_{23}^{*} \cdot e^{i \cdot \beta_2} + r_{12} r_{34} \cdot e^{i(\beta_2 + \beta_3)} + r_{23}^{*} r_{34} \cdot e^{i \cdot \beta_3}} \right|^2 \qquad \text{(Eq. 3)}$$

with

$$r^{*}_{23} = \frac{\sqrt{\tilde{\varepsilon}_{CdA}} - \sqrt{\tilde{\varepsilon}_{NTs}}}{\sqrt{\tilde{\varepsilon}_{CdA}} + \sqrt{\tilde{\varepsilon}_{NTs}}}; r_{34} = \frac{\sqrt{\tilde{\varepsilon}_{NTs}} - \sqrt{\varepsilon_{ext}}}{\sqrt{\tilde{\varepsilon}_{NTs}} + \sqrt{\varepsilon_{ext}}}; \beta_3 = \frac{2\pi \cdot \left(2\sqrt{\tilde{\varepsilon}_{NTs}} \cdot d_{NTs} \right)}{\lambda} \qquad \text{(Eq. 4)}$$

where r_{12} and β_2 are provided by the expressions used for the CdA film, $\tilde{\varepsilon}_{NTs}$ and d_{NTs} are the complex dielectric function and the thickness of the SWCNTs sensing overlayer, respectively.

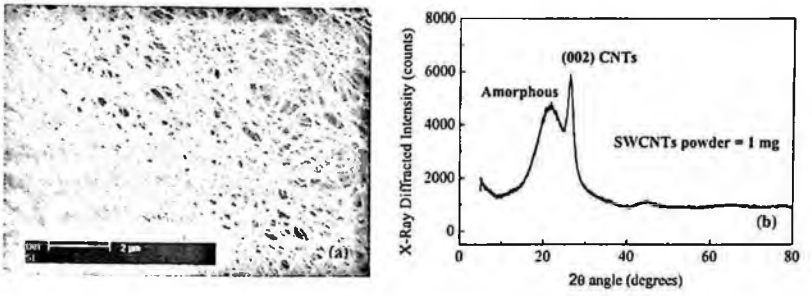

Fig. 2: (a) SEM image of SWCNTs bundles and (b) XRD spectrum of SWCNTs powders.

The fabricated sensors have been characterized by means of SEM measurements (Fig. 2a), showing that SWCNTs films are organized in bundles with individual nanotubes arranged in a dense net, and by X-ray diffraction measurements (Fig. 2b) on pristine SWCNTs powders from which a monolayer spacing of about 2.0 nm has been estimated for SWCNTs. The thickness of a cadmium arachidate (CdA) monolayer is of 2.8 nm.

3. Experimental results

The optical and acoustic chemical sensors have been located in the same test chamber (1000 ml) for simultaneous exposures to ethanol and ethylacetate vapors. The results obtained for SOF and QCM sensors coated by 2 monolayers of SWCNTs onto 20 monolayers of CdA are reported in Fig 3.

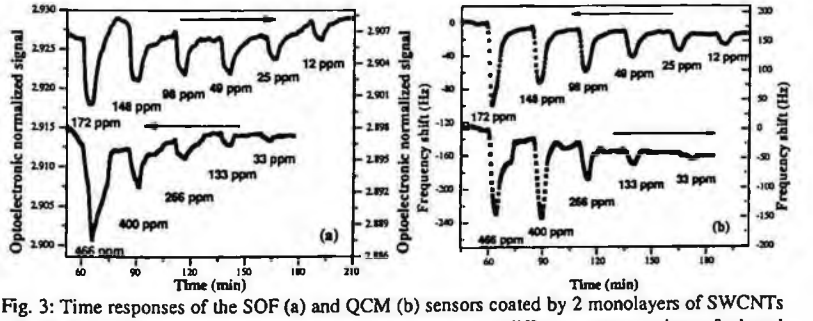

Fig. 3: Time responses of the SOF (a) and QCM (b) sensors coated by 2 monolayers of SWCNTs onto 20 monolayers of CdA, exposed, at room temperature, to different concentrations of ethanol (upper curves) and ethylacetate (lower curves).

Although a weak drift can be observed in the time responses due to thermal change inside the test chamber, high sensitivity, quite good recovery and very low limits of VOCs detection have been registered for both sensors. The sensitivities to ethanol and ethylacetate of the SOF sensor, expressed as normalized signal changes over concentration unit, have been measured, for low concentrations, as $5.7 \cdot 10^{-5}$ ppm^{-1} and 7.7 10^{-6} ppm^{-1}, respectively. In the case of the QCM sensor, the sensitivity is expressed as frequency shift over concentration unit and has been measured as 0.51 Hz/ppm and 0.34 Hz/ppm, respectively. Fig. 4 reports the transient response of the SOF and QCM sensors coated by 6 monolayers of SWCNTs onto 20 monolayers of CdA, exposed to decreasing concentration of ethanol, at room temperature. As can be seen, differently from the QCM, the SOF sensor response increases upon exposures. This effect can be attributed to the fact that the film reflectance, and thus the SOF sensor sensitivity, is a quasi-periodic function of the film thickness. For this reason upon exposures, the sensor response can else increase or decrease depending on the thickness of the sensitive layers deposited onto the fiber end. This means also that by appropriately choosing the SWCNTs film thickness it is possible to efficiently tailor the sensors sensitivity and the sign of response for the specific sensing applications.

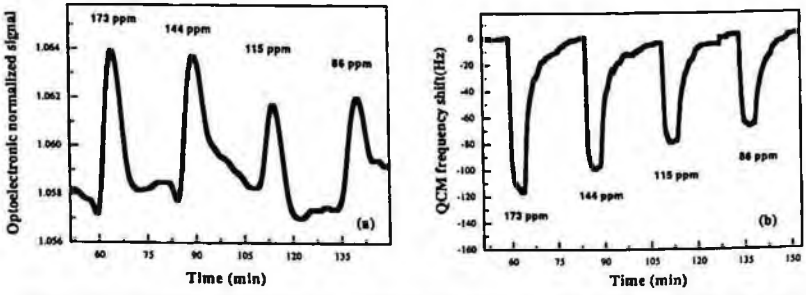

Fig. 4: Time responses of the (a) SOF and (b) QCM sensors coated by 6 Mon. of SWCNTs onto 20 Mon. of CdA, exposed, at room temperature, to decreasing concentrations of ethanol.

4. Conclusions

In summary, the sensing performances of SOF optical and QCM acoustic sensors incorporating carbon nanotubes as highly sensitive coatings for VOCs detection, at room temperature, have been investigated. SWCNTs films have been transferred onto SOFs and QCMs sensors surfaces, buffered by a linker-multilayer of CdA, using the molecular engineering LB deposition technique. The SOF sensors coating process has been real-time monitored during the

deposition of both the CdA onto the bare fiber and the SWCNTs onto the CdA buffer material. The fabricated sensors have been characterized by means of X-ray diffraction and SEM measurements, and exposed simultaneously to ethanol and ethylacetate individual vapors in a concentration range of about 10-500 ppm by using a proper designed test chamber. The sensors based on SWCNTs provide high sensitivity, very low limits of VOCs detection and fast response, at room temperature. Differently from acoustic sensors, opposite behavior of the output signal can be obtained by using SOF sensors with a proper choice of the overlayer thickness, giving the possibility to tailor the sensors sensitivity for the specific sensing applications.

Acknowledgments

The authors wish to thank M. A. Tagliente for X-ray diffraction measurements.

References

1. M. S. Dresselhaus, G. Dresselhaus, Ph. Avouris, Carbon Nanotubes-Synthesis, Structure, Properties and Applications, Springer, Berlin (2001).
2. M. Penza, G. Cassano, P. Aversa, F. Antolini, A. Cusano, A. Cutolo, M. Giordano, L. Nicolais, *Appl. Phys. Lett.*, **85**, 2379 (2004).
3. M. Penza, G. Cassano, P. Aversa, F. Antolini, A. Cusano, M. Consales, M. Giordano, L. Nicolais, *Sens. Actuators B*, (2005). In press.
4. S. Iijima, *Nature* (London) **354**, 56 (1991).
5. S. Iijima and T. Ichihashi, *Nature* (London) **363**, 603 (1993).
6. D. S. Bethune, C. H. Kiang, M. S. de Vries, G. Gorman, R. Savoy, J. Vazquez, R. Beyers, *Nature* (London) **363**, 605 (1993).

CHEMICAL SENSORS BASED ON LONG PERIOD GRATINGS COATED WITH SYNDIOTACTIC POLYSTIRENE

P. PILLA, A. IADICICCO, L. CONTESSA, S. CAMPOPIANO, A. CUSANO, A. CUTOLO

Optoelectronic Division, Engineering Department, University of Sannio, Benevento - Italy

M. GIORDANO

Institute of Composite Biomedical Materials, National Research Council – Napoli – Italy

In this work, a coated Long Period grating based novel fiber optic sensor able to measure the concentration of organic analytes, in aqueous environment is presented. Syndiotactic polystyrene was used as sensitive polymeric layer due to its high sorption properties towards chlorinated and aromatic compounds. In particular, a thin semi-crystalline syndiotactic polystyrene film with crystalline nanoporous δ form was deposited along the sensing element by using dip-coating technique. Chemical detection has been carried out by measuring the wavelength shift and the amplitude change in the attenuation bands of the long period grating due to analytes sorption. Experimental results demonstrate the capability of the proposed sensor to detect very low concentrations (sub ppm) of chloroform in water. Finally the reversibility of the chloroform absorption is successfully investigated.

1. Introduction

A topic of great interest in the field of the chemical detection is the development of environmental microsensors highly selective to target chemicals. The combination of suitable sensitive materials and sensing techniques is the key point for the design of microsensors based detectors.

The intrinsic and high refractive index sensitivity of LPGs has been used to form refractive index sensors or chemical concentration sensors [1,2]. Long Period Gratings (LPG's) are photoinduced fiber devices which couple light from the core of a singlemode optical fiber into the fiber cladding at discrete wavelengths, producing one or more attenuation bands in the fiber transmission. The transmitted spectra are sensitive to the local environment as temperature, strain, bend radius and to the refractive index of the medium surrounding the fiber (SRI) [3]. It is attractive to consider the prospect of depositing overlay of

specific sensitive materials that exhibit changes in their refractive index in response to chemical sorption [4,5]. In this work, the integration of LPGs with thin films of Syndiotactic Polystyrene (sPS) was proposed for high sensitive chemical sensors [6]. To the aim to show the excellent performance of the proposed sensor, variations in the attenuation bands related to different cladding order modes have investigated in terms of wavelength shift and amplitude changes to detect chloroform in water in the range of few ppm.

2. Principle of operation

An LPG is an ultraviolet (UV)-induced modulation of the fiber core refractive index, with period between 100–500 μm and length of 2-4 cm. The LPG acts to couple light from the propagating core mode to co-propagating cladding modes. As direct consequence, the transmission spectrum consists in a series of attenuation bands centred at resonant wavelengths given by:

$$\lambda_{res} = (n_{eff} - n_{clm})\Lambda$$

where n_{eff} is the effective refractive index of the core mode, n_{clm} the effective refractive index of the mth radial cladding mode and Λ is the grating pitch. The effective refractive index of the mth radial cladding mode and thus λ_{res} is strongly sensitive to surrounding refractive index (n_{sur}). In addition, the higher sensitivity is shown by the higher order modes, and occurs at refractive indices approaching that of the cladding [3]. Although it is possible to enhance the sensitivity of an LPG by manipulating the fiber parameters [7], however, it is not possible to provide chemical selectivity with a bare LPG.

In this work, in order to obtain a species-specific chemical sensor, an LPG, coated with a thin film of syndiotactic polystyrene, is presented. The δ form of sPS exhibits high sorption capability due to its nanoporous crystalline structure which presents a regularly spaced array of nanocavities of well defined size and shape where low molecular weight substances can be hosted. In particular, the sorption in the crystalline domain would induce an increase in the material density leading to an increase in the refractive index[4,5]. Moreover, the sPS, which refractive index is higher than the cladding one can operate in water environments. In these conditions, the exposition of the sPS coated LPG would induce a consequent modification of the cladding modes distributions leading to a wavelength shift of the attenuation bands combined with amplitude changes.

3. Sensor Fabrication

The dip-coating method was used to deposit the δ form sPS layer on a standard 30mm long LPG, with period of 340μm. The optoelectronic set-up comprises a

broadband superluminescent diode (2mW) and an optical spectrum analyzer for transmitted spectrum monitoring with a resolution of 0.05 nm. A properly holder was designed in order to fix the fiber without changing its tensional and bending state, as shows in fig. 1. It comprises two complementary moulds of Teflon, forming a 50mm long test chamber. The temperature was held constant at 20°C. The bare LPG was characterized in terms of wavelength shift and amplitude changes of the attenuation band centered around 1300 nm as function

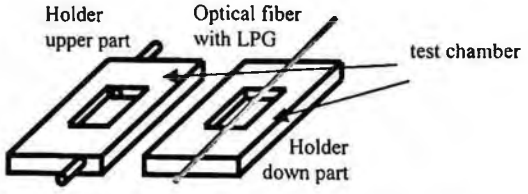

Fig. 1. Schematic diagram of the sample holder (not in scale).

of the external refractive index showing a sensitivity of -5.06nm and 3.59dB referred to the distilled water as surrounding refractive index, respectively.
With the aim to obtain a thin film, a sPS chloroform solution (2%b.w.) is used. In particular, the test chamber is filled up with sPS solution and then it is emptied out in about 3 seconds.
After the deposition the transmission spectrum of the attenuation band centered around 1300nm, showed a blue wavelength shift of 2.45nm with air as external medium. Since the sPS film refractive index is 1.5781 [5], this effect is probably due to a layer thickness less than 250nm, in agreement with Tatam et al. [8].

4. Experimental results and discussion

Chloroform was used as analyte to test the performances of the opto-electronic sensor for chemical detection. Measurements consisted in recording the transmitted spectra of the sensing grating as the sorption of the analyte in the nanocavities promotes an increasing of the polymer layer refractive index. The spectra were recorded every 40 seconds and a centroid analysis allowed computing the central wavelength of the attenuation band. The sensitivities and the response time are related to the overlay thickness and the order of the investigated cladding mode coupling. In particular, thinner is the thickness faster would be the sensor response, while a higher sensitivity can be achieved by a properly chosen of the grating features. To this aim the attenuation band related to two cladding modes and for different thickness overlay are investigated.

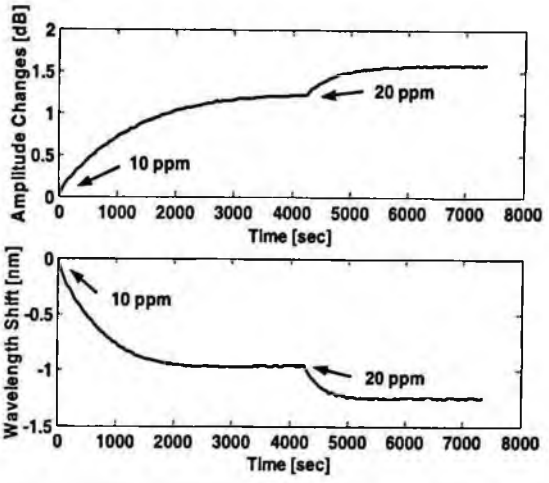

Fig. 2. Time response of the sensor, referred to attenuation band centered around 1300nm.

The holder, with the sPS coated LPG, was connected with a thermostated beaker (20°C), containing initially 1 liter of pure distilled water. In this way, the holder was filled up of pure water. Analyte (chloroform) was then added by successive steps of 10ppm (μl/l). The solutions were always magnetically stirred in order to ensure the maximum dispersion of the analyte in water and then added to the holder with the sensor. Chloroform sorption induces an increase in the overlay refractive index leading to higher effective refractive index for the coupled cladding mode. As direct consequence, two effects are evident: a blue wavelength shift, according with eq. (1), and a decrease of the peak transmission loss due to a lower coupling coefficient produced by a diminution of the cladding mode intensity within the core layer. Fig. 2a and 2b show the time responses of the sensor in terms of amplitude changes and wavelength blue shift during the addition of chloroform, respectively. When the chloroform is added, the equilibrium response of the sensor progressively decreases. The 10ppm and 20ppm chloroform concentrations induce a wavelength shift of -0.96nm and −1.26nm, respectively, and amplitude changes of 1.20dB and 1.57dB, respectively. This is probably related to the combination of the non linear behavior of the effective refractive index of the coupled cladding mode on the overlay refractive index with the non linear relationship between adsorbed mass of chloroform and its concentration in the liquid phase. Non linear sorption equilibrium was, in fact, reported in literature for sorption in the vapor phase [5]. Moreover, the difference in wavelength shifts time response between the 10ppm and 20ppm chloroform concentrations is probably due to the reached

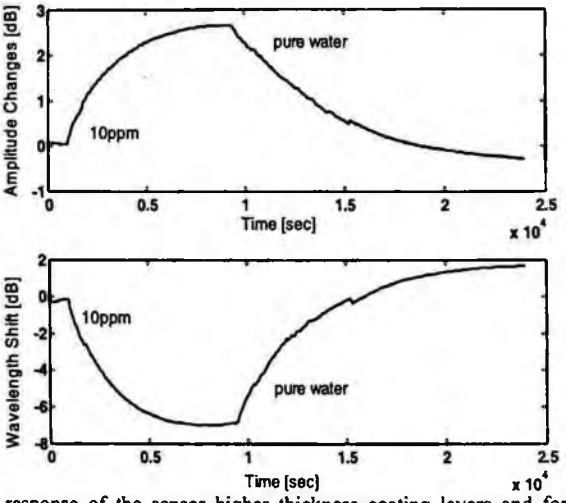

Fig. 3 Time response of the sensor higher thickness coating layers and for higher order cladding mode.

saturation of the nano-cavities in the crystalline phase. Sensitivities of -0.130nm/ppm and 0.163dB/ppm in terms of wavelength shift and amplitude changes, respectively, were observed, in the range 0-10ppm. With the resolution provided by the optical spectrum analyzer, sub-ppm detection of chloroform in water is possible with the proposed sensor

Higher sensitivity was also observed for higher thickness coating layers and for higher order cladding mode demonstrating the excellent performance of the proposed configuration, as shown in fig. 3. Here the amplitude changes and wavelength shift related to the attenuation band around 1550nm is observed. The 10ppm chloroform concentrations induce a wavelength shift of -7.0nm and amplitude changes of 2.64dB. In this case the sPS debsorption in pure water, showing the excellent performance of the proposed sensors, is observed.

5. Conclusions

In this work, a chemical fiber optic sensor, based on Long Period Fiber Gratings coated with syndiotactic polystyrene thin film, able to detect few ppm of chloroform in water is presented. The sPS exhibits high sorption capacity and an improved selectivity towards low molecular weight substances. The thin film of δ phase sPS was cast by dip-coating around a standard LPG. Wavelength shifts and amplitude changes have been observed in the attenuation band of the coated LPG due to the addition of few ppm of chloroform in water. Sensitivities of -

0.130nm/ppm and 0.163dB/ppm, in terms of wavelength shift and amplitude changes in the range 0-10ppm have been obtained by monitoring the attenuation band related to the 3rd cladding mode. Higher sensitivities have been obtained monitoring the attenuation band associated to a higher order mode, as a higher thickness coating layers is dipped. Finally, to prove the excellent performance of the proposed sensor the desorption capability of the sPS coated LPG is successfully investigated. Experimental results demonstrated the capability of the proposed sensor, at low concentration levels, to perform sub-ppm detection of chloroform in water. Sensitivity and response time can be significantly improved by a proper choice of the sensing grating features and the layer thickness.

References

1. X. Shu, L. Zhang, I. Bennion, "Sensitivity characteristics of long period fiber gratings," J. Lightwave Technol., vol. 20, pp. 255–266, Feb. 2002.
2. R.Falciai, A.G.Mignani, A.Vannini, "Long period gratings as solution concentration sensors", Sensors Actuators B 74 74–7, 2001.
3. V.Bhatia, "Applications of long-period gratings to single and multi-parameter sensing", Opt. Express 4,457–66,1999.
4. M.Giordano, M.Russo, A.Cusano, G.Mensitieri, G.Guerra "Syndiotactic Polystyrene Thin Film as Sensitive Layer for an Optoelectronic Chemical Sensing Device", Sensors and Actuators B (in press)
5. M.Giordano, M.Russo, A.Cusano, A.Cutolo, G.Mensitieri, L.Nicolais, "Optical sensor based on ultrathin films of δ-form syndiotactic polystyrene for fast and high resolution detection of chloroform", Applied Physics Letters, Vol 85, pp. 5349-5351, 11-2004.
6. P.Pilla, A.Iadicicco, L.Contessa, S.Campopiano, A.Cutolo, M.Giordano, A.Cusano, "Optical Chemo-Sensor based on Long Period Gratings coated with δ form Syndiotactic Polystyrene", IEEE Photon. Technology Letters, August 2005 (in press.).
7. I. Del Villar, I.R. Matias, F.J. Arregui and P. Lalanne, "Optimization of sensitivity in Long Period Fiber Gratings with overlay deposition", Opt. Exp., Vol. 13, No.1, 56-69, 2005.
8. S.W.James, N.D.Rees, G.J.Ashwell, R.P.Tatam, "Optical fibre long period gratings with Langmuir Blodgett thin film overlays", Opt. Lett. 9 686–8, 2002.

A NEW POROUS SILICON BASED SENSOR FOR SO_2

ANNA CASTALDO

Enea, UTS MAT-NANO, Portici Research Center
Portici (Na), Italy, 80055, Via Vecchio Macello

GIROLAMO DI FRANCIA

Enea, UTS MAT-NANO, Portici Research Center
Portici (Na), Italy, 80055, Via Vecchio Macello

LUIGI QUERCIA

Enea, UTS MAT-NANO, Portici Research Center
Portici (Na),Italy, 80055, Via Vecchio Macello

This study identifies an n-type porous silicon material that responds in a rapid and reversible manner to sulphur dioxide at room temperature, by an high quenching of its photoluminescence (PL), even at concentrations in the range of hundreds of ppb. PL quenching behaviour of this material has been investigated in nitrogen and in air, operating mechanism discussed, at the purpose of utilizing it for the fabrication of a stable device, that could satisfy the severe environmental requirements imposed by current laws.

1.1. Introduction

Worldwide, sulphur oxides and in particular, sulphur dioxide (SO_2) are emitted by both man-made and natural sources of combustion. Erupting volcanoes and decaying organic matter are two examples of natural sources which release sulphur oxides. Commercial combustion in industrialized regions is the largest single source of sulphur oxides pollution locally.

Acidic deposition, or acid rain as it is commonly known, occurs when chemically laden emissions react in the atmosphere with water, oxygen and oxidants to form various acidic compounds. These compounds then fall to the earth in either a dry form (as gas and particles) or wet form (as rain, fog, or snow). The acid rain causes surface water acidification and damages trees. High concentrations degrade visibility and pose a risk to public health. High levels of

SO_2 have proved to cause or aggravate various types of lung disorders [1]. In addition, acid rain accelerates the decay of building materials and paints.

In Italy the D.M. 2.04.2002 n.60 establishes that SO_2 concentration limits are: 350 μg/ m^3 (134 ppb) for 1 hour and 125 μg/ m^3 (47 ppb) for 24 hours. Commercial sensors (in particular electrochemical) are not useful because they operate generally in the range 0-10 ppm with a low resolution (400 ppb at least). At this moment only expensive techniques are utilized in environmental stations to monitor this pollutant. It would be very desirable to discover a sensible, low resolution, cheap, solid state sensor working at room temperature.

The feasibility of a SO_2 solid state sensor using porous silicon was initially proposed by T. Kelly, J.K.M. Chun and A. Bocarsly [2], who observed that oxide-coated porous silicon p-type photoluminescence is slightly quenched by gas phase SO_2 (1,2 % at 650 nm in argon atmosphere) and proposed a mechanism to explain such quenching. In particular they speculated on the increase of Pb_1 defects at the interface porous silicon-silicon oxide, as responsible for the response to SO_2. Therefore, they attributed to iodine molecule, a photoluminescence quenching on the porous silicon based on a similar mechanism [3]. Clearly, a major problem with using oxide coated porous silicon is the oxide layer itself. Over the time the oxide layer grows to a point where the luminescent silicon is no longer sensitive to the quenching effects of SO_2 , and the sensor in few weeks fails [4].

Herein, we report on a very specific, reversible, strong interaction between n-type porous silicon and sulfur dioxide at room temperature, in nitrogen and in air. This interaction could be used for the realization of a sensor device, since, as we show in the following, its PL quenching is ten-fold higher than the sensor proposed by Bocarsly and the lifetime is twenty-fold higher.

1.2. Experimental

Single-crystal <100> phosphorus-doped n-type silicon wafers with 1 Ω·cm resistivity, 525 micron thick, have been used for the current study. Before anodization a 1500 Å thick ITO back contact has been deposited on substrates by e-beam evaporation. Porous silicon samples 70 μm thick have been fabricated by electrochemical etching, using a solution of HF: H_2O: 2-Propanol (35:40:25 wt %), at a constant current density of 40 mA/cm^2, under the light of a 300W Hg lamp positioned at 15 cm from the sample. The etching time was 14 minutes. After the etching, samples have been rinsed in pentane, dried using N_2 and oxidized spontaneously in air for 6 week. PL quenching measurements were performed in a pressure chamber equipped with mass flow controllers. Through a quartz window, PL was excited by He-Cd Laser radiation (441 nm). Emission spectra have been collected and recorded by a CCD spectrometer. The gas-bottle of SO_2 used for this study has a concentration of 10 ppm in air.

1.3. Results and Discussion

The obtained porous silicon has a photoluminescence emission between 500 and 800 nm with maximum around 650 nm.

We characterize its sensing properties with respect to SO_2 by the following experiments. The first consists in keeping the sample in nitrogen flow, exposing it to 10 ppm SO_2 in air for 3 minutes and monitoring the photoluminescence behaviour. Dynamic response in nitrogen to the pollutant gas is reported in Fig 1. In presence of SO_2 we observe a very high quenching of photoluminescence, that reaches its maximum value (25-35% at 642 nm) in 7 minutes. When SO_2 source is removed and the material exposed again to the nitrogen flow, quickly recovers and the sample becomes available for new responses. In other terms, the sensor in N_2 atmosphere is reversible.

The exact entity of the quenching depends on substrate photo-oxidation. In particular it is noticeable that laser light in presence of air (carrier of the SO_2) oxides porous silicon in an irreversible manner. Sensing properties, as it is known, lays to the presence of some superficial oxide. If we consider exposition to the light time equal to the measurement time (< 1min) the light will not have much effect on the first response, while it will acquire progressively importance for the successive exposures.

Moreover, in nitrogen atmosphere we verify sensibility of our material. The minimal concentration that we can monitor with our apparatus is 1/10 of the nominal concentration of our gas bottle, i.e. 100 ppb. By exposure to 100 ppb of SO_2 we observe a 4% PL quenching.

On the basis of previous considerations with respect to the photo-oxidation process, the behaviour in air of our material is supposed to be more complex. Laser light photo-oxidizes the material in air and this influences SO_2 sensing behaviour. It is interesting to note that response to the gas is definite and different with respect to the PL quenching in air, where under the laser light, PL intensity decreases with a predictable kinetic up to the PL stabilization. It is possible to perform the measurement before and after the stabilization. Before the stabilization exposure to the SO_2 determines a PL quenching which is the sum of that foreseen in the air plus the definite amount lied to the gas.

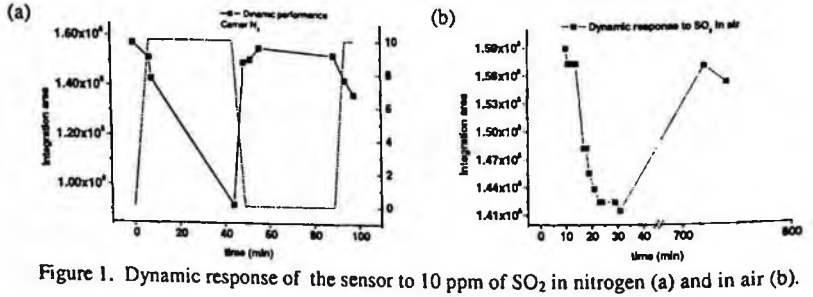

Figure 1. Dynamic response of the sensor to 10 ppm of SO_2 in nitrogen (a) and in air (b).

We think that the PL quenching due to the air and the interaction with SO_2 operate independently, likely at different sites of the surface.

In air, under laser illumination, porous silicon photoluminescence declines by a slow and irreversible photo-oxidation process. In such condition exposure to SO_2 causes a quenching simultaneous and competitive with respect to the photo-oxidation At the aim of characterizing the performances in air of our sensitive material we stabilized photo-oxidation (it is possible in approximately 3 hours) and then exposed it to SO_2.In Figure 1b it is reported the evolution of a system stabilized in air and then exposed to 10 ppm of the pollutant gas. Photoluminescence quenching is now between 15% and 20 %. Restoring in air seems possible, although it is quite slow as it requires a few hours.

In order to understand the operating mechanism of the sensor we have made a simple chemiresistor device, based on the same porous silicon material, contacted with a gold film deposited above its surface and with ITO on the back and we have measured electric current after exposure to SO_2. It is observed a rapid decrease of the electrical current in the porous silicon n-type, in correspondence of the exposure to the pollutant gas (see Figure 2).

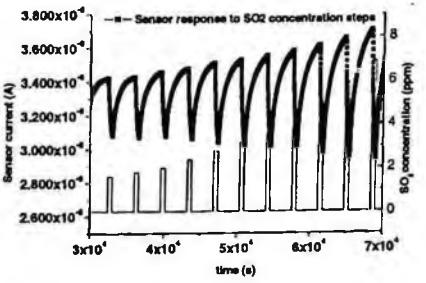

Figure 2. Electrical current of the chemiresistor exposed to SO_2.

As for as the operating mechanism is concerned we believe that the electrical current decrease can be lied to an electronic transfer from porous silicon to sulphur dioxide. In Figure 3 we report FT-IR spectra recorded before (solid line in Fig 3), and after (dash line in Fig 3) exposure to iodine of our sample and after restoring of their photoluminescence by flowing with nitrogen (dot line in Fig.3). It is known by the literature that SO_2 and iodine induce a similar PL quenching on the oxidized porous silicon samples p-type [5] and we have experimentally verified that exposure of our material to iodine determines a reversible PL quenching. IR-spectra show a general trend of high absorbance and an unusual increase in the 3300-3600 cm^{-1} and 1600-1800 cm^{-1} regions. In the same regions nitrogen flow restoring produces shape modifications of the bands. In particular maximum absorbance of 3300 band shifts to slower wave-number and at 1400 cm^{-1} appears a new band. These experiments seems to

confirm that exposure to SO_2 cause an increase of Pb_1 paramagnetic defects to the interface between porous silicon and porous silicon oxide, with concomitant enhancement of unpaired electrons (increase of system absorbance), variation of Si-O-Si bonds (1400 cm^{-1} band), formation of transitory OH-bonds. There is probably a transfer of electrons from PS to d-orbitals of sulphur dioxide, with concomitant other Pb_1 creation. As a result electrical current decreases and there is a general trend of higher absorbance.

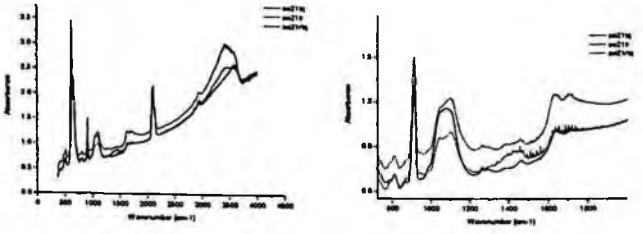

Figure 3. IR Spectra are reported before (solid line) and after (dash line) exposure to iodine and after restoring with nitrogen (dot line).

At this stage of knowledge there are no further evidence supporting a different sensing mechanism. Despite the mechanism proposed by Bocarsly is not exhaustive and does not explain photo-oxidative behaviour, it still represents a good basis for the comprehension of the interaction between our porous silicon and sulphur dioxide.

1.4. Conclusions

In this work has been obtained an n-type porous silicon sensitive material, that responds rapidly and reversibly to SO_2 in N_2, with a surprising 35% PL quenching at 10 ppm and a good sensitivity (100 ppb). The same response has been obtained in air, but the reversibility is lower than in N_2. We have been studying the operating mechanism, at the purpose of fabricating a device based on the excellent sensing properties of our substrate with respect to the pollutant gas.

References

1. R. Scheslinger, Ch. **26**: "Toxicology of sulphur oxides" in Holgate S.T. et al (ed), Air pollution and health, London: Academic Press (1999).
2. M.T. Kelly, J.K.M Chun, A. B. Bocarsly, *Nature,* **382,** 214 (1996).
3. M.T. Kelly, A. B. Bocarsly, *Chem. Mater.*, **9,** 1659 (1997).
4. M.T. Kelly, A. B. Bocarsly, *Coordination Chemistry Reviews* **171,** 245 (1998).
5. *Ibidem*

LOW TEMPERATURE OXYGEN SENSORS BASED ON NANOSTRUCTURED MATERIALS

A. BONAVITA, G. NERI, G. MICALI, G. RIZZO, S. GALVAGNO
Dept. of Industrial Chemistry and Materials Engineering, University of Messina, Italy

N. PINNA, M. NIEDERBERGER
Max-Plank-Institute of Colloids and Interfaces, Postdam, Germany

In this paper a study on In_2O_3-based oxygen sensors operating at low temperature is reported. The accurate control of the morphology and grain size, achieved by applying a new non aqueous sol-gel modified route, allowed us to obtain oxygen resistive sensors with enhanced sensitivity at low temperature. The effects of operating temperature and Pt doping on the sensor response and the sensing mechanism were evaluated.

1. Introduction

Oxygen sensors have their main applications in the control of combustion process. These devices (lambda-probes) are used in the control of air-to-fuel ratio for improving the engine efficiency. However λ-sensors, for environmental and functional reasons, work only at high temperature.
Oxygen monitoring under mild conditions has applications in the medical field, food processing and waste management industries.
So far, very few n-type metal oxide have been reported as oxygen sensors at low temperature (< 300 °C) and moreover the sensitivity of these devices is very low. In literature is reported a nanosized p-type oxide ($SrTiO_3$) as possible candidate for low temperature oxygen sensing [1-2]. $SrTiO_3$ has a perovskite structure and gives an appreciable oxygen response at 40 °C. However, it presents a low conductance and this reduces the capability of reading the baseline signal by using conventional instrumentation and makes the oxygen measurement acquisition very noisy.
In the present work we focus our attention on In_2O_3 as a sensing material for O_2 at low temperature. In_2O_3 is a n-type, low resistive oxide promising for gas sensing application [3-5].

Since the application of nanostructured materials in the gas sensing field is a way for the optimization of the devices performance in term of sensitivity and response time [6-8], we have opportunely sized the In_2O_3 in the nanometer scale by using a new synthesis method through a non-aqueous chemical route. Addition of Pt into the In_2O_3 sensing material to promote the O_2 response has been also evaluated.

2. Experimental

Nanopowders of In_2O_3 were synthesized by a sol-gel modified route useful for the preparation of nanometric crystalline particles of different oxides [9]. Indium isopropoxide $In(O^iPr)_3$ was used as precursor. It was mixed to benzyl alcohol, put into a glovebox and maintained in autoclave for two days at 220 °C. The In_2O_3 powders obtained in this way were finally calcinated at 400 °C.

The microstructural characterization was carried out by a powder diffractometer Bruker D8 for XRD measurements and by a Philips CM200 FEG microscope for TEM analysis.

Pt/In_2O_3 powders were also prepared by impregnation of the indium oxide nanopowders with an aqueous solution of H_2PtCl_6. The noble metal loading was 1 wt %.

Sensors were fabricated by mixing the nanopowders with water to create a paste which was successively painted onto rectangular alumina substrates supplied with Pt interdigitated electrodes and heaters, and treated at 350 °C to stabilize the film texture.

Gas sensing test was carried out by using an home made computer assisted apparatus and reading the resistance variation of the realized devices in dry flow of nitrogen containing different concentrations of oxygen, ranging from 2.5 to 20% in volume. The working temperature during the measurements was varied from ambient (~25 °C) up to 350 °C.

3. Results and discussion

3.1. *Microstructural characterization*

The In_2O_3 powders analyzed by XRD have shown high crystallinity and the characteristic diffraction peaks of the cubic phase. Their size, evaluated by the Scherrer equation, are around 20 nm. These data have been confirmed by a detailed HRTEM analyses, as elsewhere reported [10].

3.2. *Sensing tests*

Before the sensing tests, In_2O_3 sensors were activated at 350 °C in air, then returned at room temperature and stabilized in dry nitrogen since the signal baseline reached a stable value. Then the dynamic of the response was evaluated at different temperature up to 350 °C.

Pure In_2O_3-based sensors give a measurable response to O_2 at near room temperature but the dynamic of the response is too low. To promote both the sensitivity and response time tests were carried at higher temperature. Figure 1 reports the dynamic response, registered at 80°C, to successive pulses of oxygen ranging from 2.5-20% in dry N_2. The calibration curve shows in this range of concentration a good linearity.

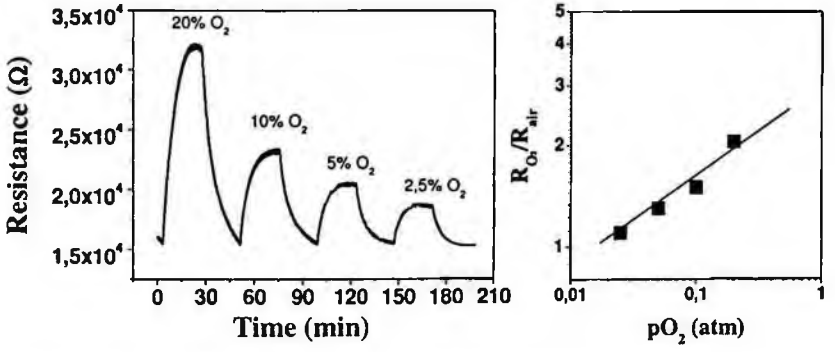

Figure 1. Dynamic of the response of the In_2O_3 sensor at 80 °C and relative calibration curve.

As expected temperature promotes the response to oxygen with a maximum around 250 °C. A significant difference in the response behavior can be noted observing the shape changes in the response curves. Three ranges of temperature are easily identifiable as reported in figure 2: a) low (<100 °C); middle (100-200 °C); high (250-350°C).

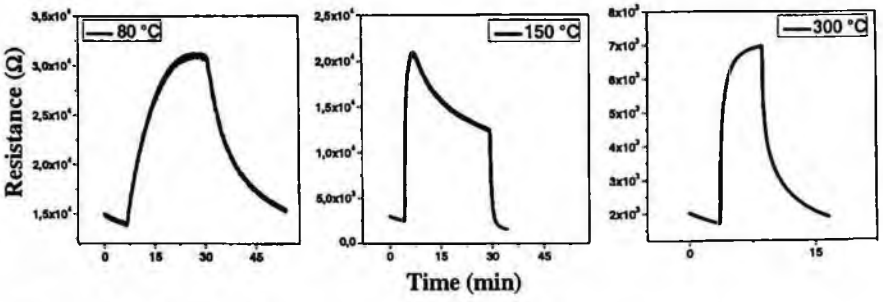

Figure 2. Characteristic response shapes during exposure to 20% of O_2.

This effect was attributed to the change of the sensing mechanism by increasing the temperature from surface to bulk–interaction. By expressing the response of an oxygen sensor in the usual form [11-12]:

$$\sigma \propto \frac{1}{R} \propto pO_2^{1/m}$$

where σ is the conductance and pO_2 the partial pressure of oxygen in the gas stream, and plotting the calibration curve as a log-log plot of conductance *vs.* pO_2, we can calculate the m parameter value, as reported in Figure 3.

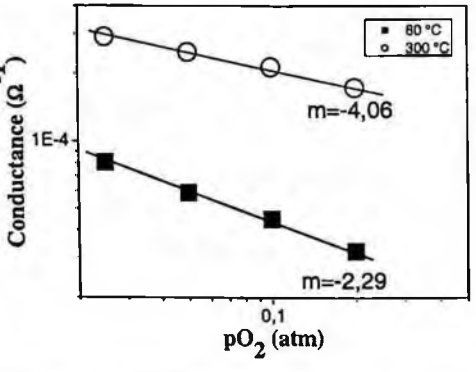

Figure 3. Conductace vs. pO_2 plot of the undoped sample at different temperature.

The slope 1/m, at all the temperature investigated, is negative, confirming the n-type behavior of In_2O_3. Moreover the slope absolute value, |1/m| at low temperature is near to ½, while at 300 °C it is about ¼, corresponding to surface and bulk sensing mechanisms, respectively [13].

3.3. *Pt-doping effects*

The addition of Pt to indium oxide was found to strongly increase the response to O_2 in the whole range of temperature investigated. Figure 4a show the beneficial effect of Pt-doping on the O_2 response at different temperatures.

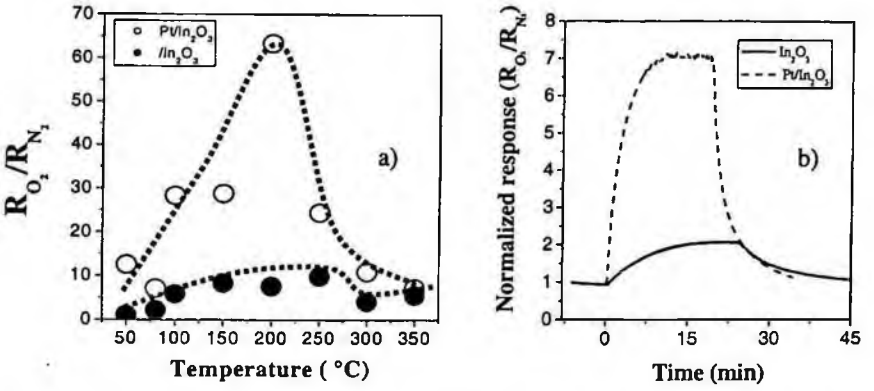

Figure 4. Pt-doping effects on the response to 20 % of O_2: a) at different temperatures; b) transient response at 80 °C.

The slope, 1/m, of the calibration curves calculated for the Pt-doped samples is the same as for the undoped samples, suggesting that the noble metal does not modify the sensing mechanism.

Further considerations on the Pt-effect may be made on the response dynamics, observing the response and recovery times successively to pulsed exposure to 20% of O_2 for the pure and doped samples at the temperature of 80 °C (Fig. 4b). The presence of Pt reduces the response and the recovery times making the sensing dynamics faster.

The oxygen activation in this range of temperatures well explains the above reported phenomena with an effect of Pt on the adsorption and exchange of the atmospheric O_2 on the sensing layer, considering the well known effects of Pt on the O_2 dissociation [14]. These dissociated O^- species can diffuse easiest in the bulk, improving the characteristics of sensitivity and dynamics of the Pt-doped sensors.

4. Conclusions

Semiconductor based O_2 sensors operating at low temperature have been successfully realized by using In_2O_3 nanostructured powders. The response mechanism and Pt-doping effects on the indium oxide response were evaluated. The addition of Pt enhances the response to O_2 of In_2O_3 powders and decreases the response and recovery time. It acts by providing a greater number of oxygen chemisorption sites and favoring the kinetic of exchange of gaseous O_2 with adsorbed oxygen species on the In_2O_3, without modifying the sensing mechanism.

References

1. Y. Hu, O.K. Tan, W. Cao, W. Zhu, *Ceram. Int.* **30**, 1819 (2004).
2. Y. Hu, O.K. Tan, J.S. Pan, X. Yao, W Zhu, *J. Phys. Chem. B.* **108**, 11214 (2004).
3. G. Korotcenkov , A. Cerneavschi, V. Brinzari, A. Vasiliev, M. Ivanov, A. Cornet, J. Morante, A. Cabot, J. Arbiol, *Sens. Actuators B* **99**, 297 (2004).
4. A. Gurlo, N. Barsan, M. Ivanovskaya, U. Weimar, W. Gopel, *Sens. Actuators B* **47**, 92 (1998).
5. H. Yamaura,T. Jinkawa, J. Tamaki, N. Miura, N. Yamazoe, K. Moriya, *Sens. Actuators B* **35-36**, 325 (1995).
6. G. Zhang, M. Liu, *Sens. Actuators B* **69**, 144 (2000).
7. A. Rothschild, Y. Komem, *J. Electroceram.* **13**, 697 (2004).
8. A. Gurlo, M. Ivanovskaya, N. Bârsan, M. Schweizer-Berberich, U. Weimar, W Göpel, A. Diéguez, *Sens. Actuators B* **44**, 327 (1997).
9. M. Niederberger, N. Pinna, J. Polleux, M. Antonietti, *Angew. Chem.* **116**, 2320 (2004); *Angew. Chem. Int. Ed.* **43**, 2270 (2004).
10. N. Pinna, G. Neri, M. Antonietti, M. Niederberger, *Angew. Chem. Int. Ed.* **43**, 4345 (2004).
11. R. Ramamoothy, P.K. Dutta, S.A. Akbar, *J. Mat. Sci.* **38**, 4271 (2003).
12. J. W. Fergus, *J. Mat. Sci.* **38**, 4259 (2003).
13. Y. Xu, X. Zhou, O. Toft Sorensen, *Sens. Actuators B* **65**, 2 (2000).
14. Ž. Šljivančanin, B. Hammer, *Surf. Sci.* **515**, 235 (2002).

EFFECTS OF THE RH ON MELAMINIC LAMINATES AND POLYMERIZED LINSEED OIL FILM-SURFACE ELECTRICAL CONDUCTIVITY

LUCREZIA PALUMMO† GIULIO AIELLI, RINALDO SANTONICO

Physic Department, Rome University "Tor Vergata" Via della Ricerca Scientifica 1, 00133 Rome Italy

JOHNNY MIO BERTOLO, ANDREA BEARZOTTI

IMM-CNR "Area di Ricerca di Roma Tor Vergata" Via del Fosso del Cavaliere 100, 00133 Rome Italy

RPC (Resistive Plate Chambers) are used as trigger detectors of the muon system in LHC experiments (ATLAS, CMS and ALICE). These detectors are made of phenolich-melaminic laminate electrodes, coated with a polymerized linseed oil film delimiting the gaseous sensitive volume. Our purpose is to understand the relative humidity (r.h.) influence on the conduction mechanisms in these electrodes. We present here the results of amperometric measurements on sample kept at fixed temperature 22° C on r.h. ranging within 10 and 90 % in cyclic way.

1. Introduction

The purpose of the present paper is to study the humidity effects on the electrodes of a planar gaseous detector which is known in the particle physics as Resistive Plate Chamber (RPC).[1,2,3]

RPCs are made of 2 parallel electrode plates which define a gaseous gap of 2 mm. When the gas is ionized an electrical discharge is generated by the uniform field of about 5 kV/mm acting inside the gap. The electrode plates are made of thermoset polymer laminates 2 mm thick, with a phenolic core sandwiched between two melaminic superficial layers. In order to reduce the detector noise the electrode plate surfaces faced to the gas are coated with a polymerized linseed oil layer about 1 micron thick. Phenolich and melaminic laminates

† *CORRESPONDING AUTHOR:*
E-mail: lucrezia.palummo@roma2.infn.it, Ph: 06-49934572, 06-2023644 Fax: 06-49934061.

exhibit a moderate bulk electrical conductivity which is sufficient to feed the electrical discharges in the gas.
For the LHC applications these electrodes are required to conduct a stable current of the order 100 $\mu A \cdot m^{-2}$ during about 10 years operation. For such large current densities we have observed a gradual resistivity increase for long working times. We have show that this ageing phenomenon[4]. can be reduced or eliminated when the plates operate in a humidified environment (r.h. > 40%).
This paper is dedicated to study the interaction of the electrode surfaces with water vapor. For this purpose we monitored the surface conductivity of a number of small size phenolic melaminic laminates both oil coated and uncoated, that were kept under well defined r.h. conditions. This investigation in addition of giving information on the water ad/absorption mechanisms has also the merit of focusing on a parameter like the plate surface resistivity which is a potential unwanted effect r.h. increase.

2. Experimental Setup

The test was carried out with a cylindrical stainless steel cell of 40 cm^3 volume flushed with nitrogen of the wanted r.h. Both temperature and r.h. were measured by proper sensors located inside the cell.
Samples of 1x1cm^2 were introduced in the cell. The surface conductivity was monitored insider an area delimited by two thin electrode fingers 10 mm long and 4 mm spaced. Relative humidity (r.h.) inside the cell was regulated with a two channels MKS mass flow meters which mixed the a stream of dry and wet N_2. Mass flow meters operated at a constant total flow rate of 200 standard cm^3/min. The electrical response of the resistive-type samples to r.h. variations were tested.
The resistance values were measured using the standard two probe method and recording the current vs volt (I/V) at fixed r.h. or the electrical response towards r.h. variations, at constant applied voltage (5 Volt, T=22 °C).

3. Results and Discussion

The I/V characteristic (Fig.1), performed at r.h. ≈ 9 % on sample coated (a) with linseed oil, showed a typical linear behavior in the range between (-10 – +10) Volt without a noticeable hysteresis. Measurements at r.h. ≈ 90 %, (-5 – +5) Volt were also performed to highlight the electrical conductivity modification induced by a r.h. near to the dew point.

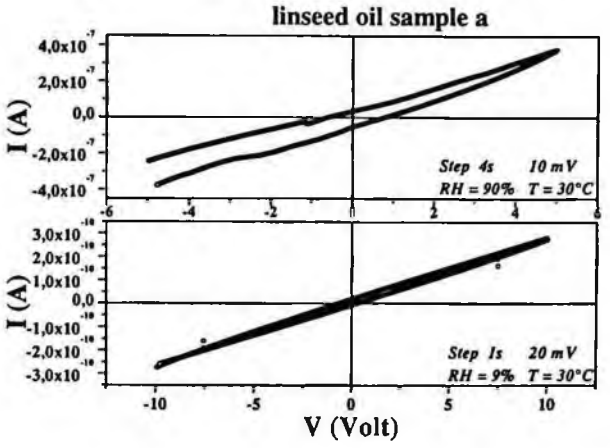

Figure 1. I/V characteristic coated sample (a) recorded at r.h = 9% , applied voltage –10, +10 Volts, step delay 1 s and at r.h = 90, applied voltage –5, +5 Volts, step delay 4 s.

In order to obtain a more complete information, we also performed resistive measurements by scanning the r.h. at fixed applied voltage.

Cycles amperometric (Fig. 2) varying within 10 and 90 % r.h., with applied voltage 5 Volt and time step ts = 300 s, on three linseed oil coated sample and three uncoated sample for comparison were recorded.

The response curves (Fig. 2) show a large change of current intensity, which point out a significant interaction of polymeric surface with the water vapor. A current intensity increase with relative humidity has been found for all samples. Stronger effects have been registered for bakelite laminates coated with linseed oil film as showed in figure 2.

Different exposure times between 2 – 20 hours to relative humidity don't affect the behavior of electrical response. The effect of the duration times of each r.h. step is shown in fig. 3 and fig. 4 for uncoated and coated samples.

For the uncoated sample with linseed oil two time step were tested, ts = 300 s (corresponding to a full cycle with about 7 hours lasting) and ts = 600 s (about 14 hours). Both cycles very similar, showing, a knee due to a faster current increase for r.h. values above 70 %.

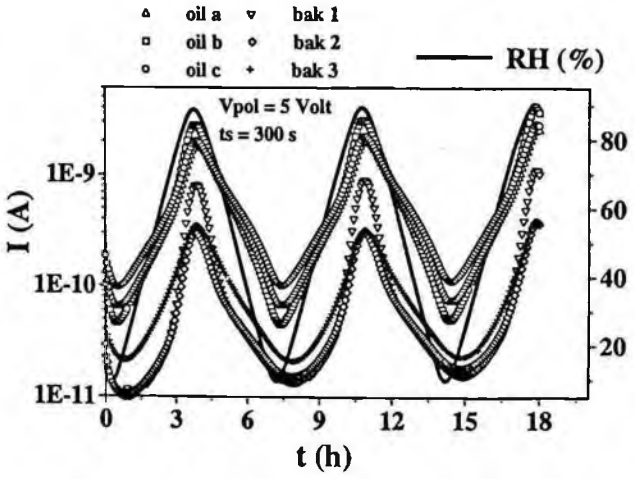

Figure 2. Electrical response towards r.h. variation of tree oil coated and tree uncoated samples (5 Volt, time step ts = 300 s).

For the coated sample with linseed oil (Fig. 4) four time steps were tested, ts = 90 s ts = 300 s, ts = 600 s, ts = 900 s corresponding a full cycle of 2h, 7h, 14h or 20 hours respectively.

Even in this case the surface interaction with water vapor seems to be weakly influenced by the exposure times. For a r.h. change from 10% to 90% we observed a a current increase in the range of $10^{-11} - 10^{-9}$ A for uncoated samples and a range of $10^{-10} - 10^{-8}$ A for the coated samples.

The variation is almost two orders of magnitude in both cases, the conductivity of the oil coated samples being about a factor of 5 higher with respect to the non coated samples.

Moreover the peaks of current at the maximum r.h. are all sharp and in phase with the r.h. (black line in fig. 2) both for coated and uncoated samples. On the contrary the deeps of current at the minimum r.h. are also sharp and in phase for the oiled samples but look much wider and some 50 min delayed with respect to the r.h. for the non oiled samples.

Samples have shown a different responses to r.h. variation suggesting a different ad/absorption mechanism.

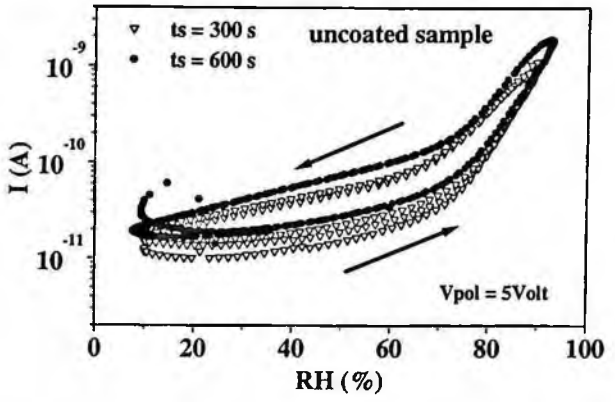

Figure 3. Electrical response towards r.h. variation uncoated sample with two different time step ts = 300s, ts = 600 s (5 Volt).

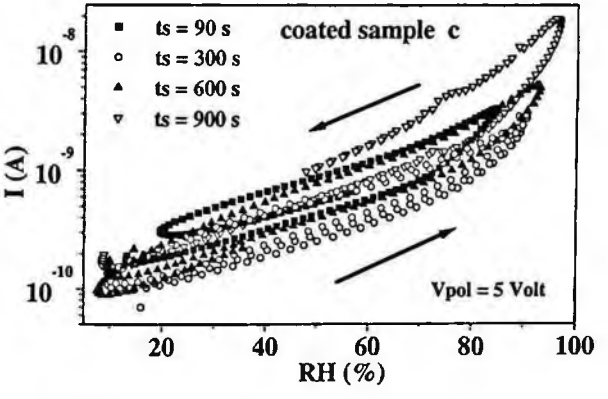

Figure 4. Electrical response towards r.h. variation coated sample c with four different time step ts = 90s, ts = 300 s, ts = 600 s, ts = 900 s (5 Volt).

The material exhibits good reversibility properties. Moreover consecutive measurements have shown the absence of memory effects, caused by irreversible or temporary modifications on this scale of times.

4. Conclusions

We have shown that the phenolic melaminic laminates with both oil coated and uncoated surfaces have a significant interaction with water vapor. In particular our data indicate that

a) this interaction is stronger for the linseed oil coating than for the natural melaminic surface of the laminate
b) the response to r.h. changes is faster in the of the oil coated samples
c) the desorption time is similar to the absorption time for the oiled sample and substantially longer for the non oiled samples
d) non oiled samples show a significant slope change around 70% r.h. in the plot of I vs r.h. This change is weaker for the oiled samples. This observation suggests that the water penetration in the bulk is more important for the non oiled samples.

References

[1] R. Santonico, R. Cardarelli, Nucl. Instr. And Meth.187 (1981) 377.
[2] M. De Vincenzi, G. Hull, S. M: Mari,, G. Pellizzoni, Nucl. Instr. Meth.508 (2003) 94.
[3] G. Aielli et al., Nucl. Instr. And Meth.518 (2003) 335.
[4] G. Aielli et al., Nucl. Instr. And Meth.533 (2004) 86.

Pd- AND Ca-DOPED IRON OXIDE FOR ETHANOL VAPOR SENSING

C. BARATTO, G. FAGLIA, G. SBERVEGLIERI
INFM & Dept of Chemistry and Physics, University of Brescia, Via Valotti 9, Italy

G. NERI, G. RIZZO, A. BONAVITA
Dept. of Industrial Chemistry and Materials Engineering, Univ. of Messina, Contrada di Dio, 98122 Messina, Italy

Ca- and Pd-doped iron oxide thin films have been prepared by a liquid-phase deposition method (LPD) starting from aqueous solutions of the precursors. Aim of this work is to investigate the role of Ca and Pd in modifying the sensing properties of Fe_2O_3 thin films for ethanol vapor sensing. Thin films sensing properties were investigated at constant relative humidity (50%) varying the sensor working temperature in the range 200-400°C. The response to some interferent gases like NO_2, CO, NH_3 was also studied. Ca doping was found an effective way to enhance the sensor response and also to increase the selectivity to ethanol. Pd doping improves the recovery times but decreases the selectivity to ethanol enhancing the CO response.

1. Introduction

The monitoring of alcohol vapors by means of miniaturized devices can be useful for the prevention of road accident caused by guide in state of drunkness. Indeed, these small gas sensors can be easily integrated in the cellular telephones or in AQS of the cars, as recently proposed [1].
MOS devices respond to many of the specific and stringent technical characteristics of the safety sector. Moreover, an opportune tailoring of the sensing layer with the use of catalysts and/or promoters may improve the unsolved question about the lack of selectivity [2-3].
In our previous works we investigated the effects of the addition of CeO_2, a basic additive, to film of Fe_2O_3 for the monitoring of different alcohols [4-5].

In this work we extend the investigation to the addition of another basic promoter, Ca, and a catalytic modifier, Pd, in order to promote the ethanol sensing characteristics of iron oxide films.

2. Experimental

The sensor devices have been realized in the thin film configuration by depositing sensing layers of different compositions (see Table 1) on alumina substrates (3x3 mm^2) supplied with gold electrodes and Pt heater by LPD (Liquid Phase Deposition), as described in detail elsewhere [6]. The starting precursors were $Fe(NO_3)_3$, $Ca(NO_3)_2$ and $PdCl_2$, dissolved in water to give solutions 0.01M and mixed in the opportune volumetric ratios. Thin films obtained in this way were successively calcined at 400 °C.

Table 1. Sensors codes and compositions.

CODE	Sensing element composition (moles %)		
	Fe	Ca	Pd
Fe100	100	-	-
FeCa05	95	5	-
FeCa10	90	10	-
Pd02-FeCa05	93.1	4.9	2
Pd05-FeCa05	90.25	4.75	5

The electrical response of the thin films was studied by monitoring the change in conductivity when gas traces were fed into the test chamber. Since the device was biased at constant voltage (1 V) the change in conductivity was revealed by a variation of the current flowing through the device. The working temperature was varied between 200 and 400 °C.

All measurements were performed by keeping the test chamber at constant relative humidity (RH=50%) measured at 20°C. The gas carrier (synthetic air) and tested gases, ethanol, CO, NO_2 and NH_3 come from certified bottles. Details of the mixing systems principle can be found elsewhere [7]. The concentration of the examined species are: ethanol (100-500 ppm), CO (100-500 ppm), NO_2 0.2-0.7 ppm) and NH_3 (25 ppm). Total flow was kept constant at 300 *sccm*.

3. Results and Discussions

Preliminary electrical measurements were addressed to the study of the variations of the electrical conductance of the Fe_2O_3-based thin films as a function of the operating temperature. Iron oxide, as all the metal oxide semiconductor, is sensitive to oxygen and other gases and/or vapors in the atmosphere. It changes its conductivity due to surface and/or bulk interaction between the gases adsorbed and activated on its surface and the lattice ionic

species, and to the operating temperature which modulates the fundamental adsorption-desorption processes on the active surface of the sensing layer.

The undoped iron oxide film has an n-type behavior. Therefore, in consequence to the interaction with ethanol (a reducing vapor), the electrical resistance decreases. However, it present , in air, an high resistance. At 200°C the baseline resistance was too high to obtain affordable measurement with a picoammeter. The baseline resistance of the thin films is of about 10 GΩ at 300°C and decrease to about 1 GΩ at 400°C. As expected, the presence of Ca increases the resistance and, due to this effect, there is an obvious difficulty in the signal reading on the Ca-doped films with higher Ca loading.

In the range of temperature investigated, on all the samples, a high response towards ethanol was observed. Moreover, the relative response towards CO and NO_2 is one order of magnitude lower than that towards ethanol. Figure 1 reports the dynamic responses (a) and calibration curves (b) at 300°C of FeCa05 and Pd05-FeCa05 sensors towards ethanol, compared to the undoped Fe100 sample. Data are expressed in relative scale, showing I/I_0 ratios, where I is the value of current flowing thought the device in the presence of the target gas and I_0 is the baseline value of the current on the sensor in the reference wet air.

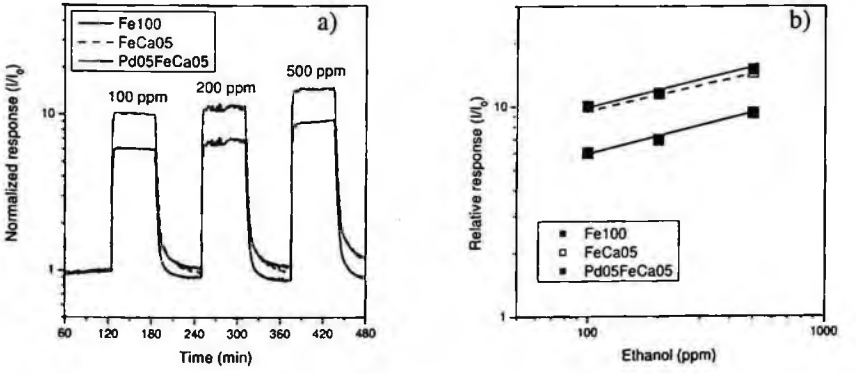

Figure 1. Dynamic responses (a) and calibration curves (b) to different concentrations of ethanol of the Fe100, FeCa05 and Pd05-FeCa05 sensors at 300 °C.

These results evinced moreover that the sensors dynamic is fast: the response and recovery times are lower than 100 and 200 sec respectively, for all samples. At this temperature, the addition of Pd, although doesn't affects the sensitivity, makes the recovery time faster (Figure 2).

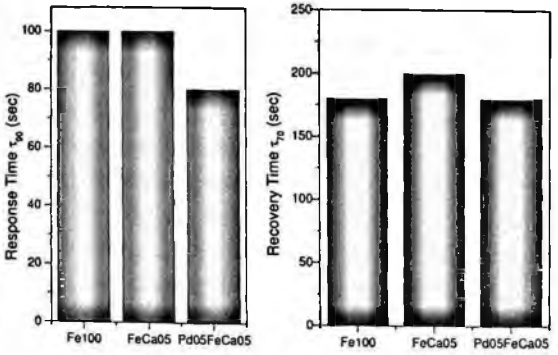

Figure 2. Comparisons of the response and recovery times of the Fe100, FeCa05 and Pd05-FeCa05 samples at 300 °C.

Figure 3 shows the response dynamics (a) and calibration curves (b) at 400 °C

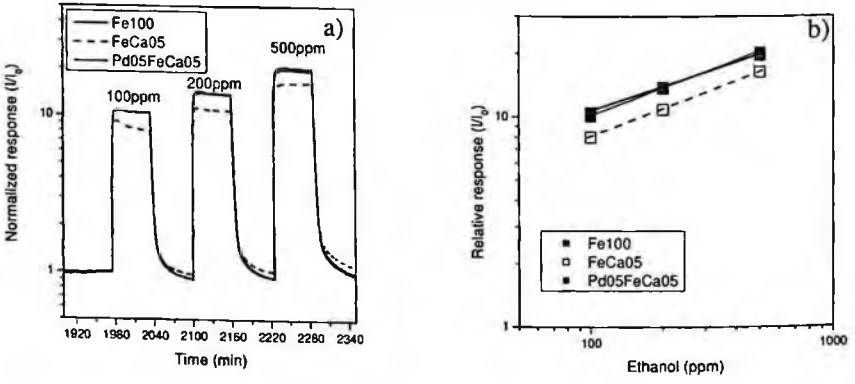

Figure 3. Dynamic responses(a) and calibration curves (b) to different concentrations of ethanol of the Fe100, FeCa05 and Pd05-FeCa05 sensors at 400 °C.

At the temperature of 400 °C Ca addition is ineffective in the promoting the ethanol response, as better shown in figure 4, where the relative response to 100 ppm of ethanol is reported *vs.* the Ca loading.

It can be noted as Ca promotes the response to ethanol at 300 °C, while this effect is reversed at 400°C. The same behavior was also reported on Fe_2O_3 thin films doped with Ce [4-5]. On the basis of the characterization data reported in those previous works, we can attribute the increase of response observed on the Ca-doped iron oxide films at 300°C, to an increasing of the number of basic sites with the promoter loading. Basic sites promote the activity in the oxidation

of ethanol and address the selectivity towards the dehydrogenation route rather than the dehydration step. These combination of factors increases the response. However, as the temperature increases the adsorption of CH_3CH_2OH molecules on the Ca basic sites, and their successive reaction with oxygen species, become too fast and then limited only on the upper part of the sensing film. This causes the impossibility to the adsorbed species to reach the bulk and, then, the change of the electrical resistance cannot be revealed.
A detailed microstructural analysis is actually in progress on these samples with the aim to better understand these phenomena.

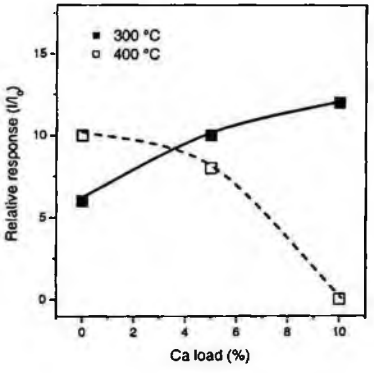

Figure 4. Relative response to 100ppm of ethanol vs. Ca loading at different temperature.

4. Conclusions

In this wok the effects of Ca and Pd doping on Fe_2O_3 response to ethanol were evaluated. At low temperature (300 °C), Ca was found as an effective promoter increasing the sensitivity to ethanol and decreasing that of some common interferent gases. The basic nature of this promoter was invocated to explain the results reported.
Pd addition results in a promotion of the response and recovery times but it decreases the selectivity to ethanol , increasing the response towards CO.

References

1. H. Jyh-Jier, Y.K. Fang, K.H. Wu, W.T Hsieh, C.H. Chen, G.S. Chen, M.S. Ju, L. Jing-Jenn, *Sensors and Actuators B* **50**, 227 (1998).
2. T. Jinkawa, G. Sakai, J. Tamaki, N. Miura, N. Yamazoe, *Journal of Molecular Catalysis A: Chemical*, **155**, 193 (2000).

3. P. Ivanov, E. Llobet, X. Vilanova, J. Brezmes, J. Hubalek, X. Correig, *Sensors and Actuators B* **99**, 201 (2001).
4. G. Neri, A. Bonavita, G. Rizzo, S. Galvagno, S. Capone, P. Siciliano, *Sensors and Actuators B* (in press).
5. G. Neri, A. Bonavita, G. Rizzo, S. Galvagno S. Capone, P. Siciliano, *Sensors and Actuators B* (in press).
6. G. Neri, A. Bonavita, S. Galvagno, N. Donato, C. Pace, J. *Mat. Science: Materials in Electronics* **13**, 561 (2002).
7. H. Endres, H. Jander, W. Göttler, *Sensors and Actuators B* **23**, 163 (1995).

CVD-DIAMOND/PD THERMOCOUPLE FOR GAS SENSING

A. BALDUCCI*, M. MARINELLI, E. MILANI, M.E. MORGADA, G. PUCELLA, G. RODRIGUEZ, A. TUCCIARONE, G. VERONA-RINATI

Dipartimento di Ingegneria Meccanica, Università di Tor Vergata via del Politecnico 1, Roma, Italy

A. D'AMICO, C. DI NATALE

IMM-Sezione di Roma, CNR via Fosso del Cavaliere 100, Roma Italia

The operation of sensors in environments characterized by high temperature, high pressure, chemical activity or nuclear radiation is increasing their relevance in several engineering applications. Thus, the development of sensors based on materials suitable for operation in harsh environment is desirable. The outstanding physical and chemical properties of Chemical Vapor Deposition diamond could then be profitably exploited in the realization of electronic devices that could work when commercial sensor fail. To this purpose, a thermochemical sensor was designed using p-type CVD-diamond films and Palladium. The sensor was tested for different temperature drops, showing values of the thermoelectric power as high as 350 μV/°C with good stability. The catalytic properties of thin palladium films allow the thermocouple to be used for gas detection. As an example the hydrogen content, within a hydrogen-nitrogen gas mixture, was measured by means of the change occurred in the Seebeck output voltage, showed by the thermocouple, at constant values of the temperature drop. The sensor response was measured for hydrogen contents varying between 0.5 % and 2 %.

1. Introduction

The design of low-cost and low-maintenance hydrogen sensors has become a forthcoming research field due to the recent diffusion of hydrogen for several industrial and commercial applications. The advent of fuel cell powered vehicles or the increase in scientific space missions using hydrogen as main propellant has increased the need for both the leakage detection in order to avoid explosions and the exhaust mixture monitoring to control the energy production process [1-4].

The use of catalytic metals i.e. palladium or platinum, for the realization of gas sensors, represents a suitable solution because of the simple detection

* Corresponding author: Antonio Balducci *antobald@libero.it*

mechanism. Since the hydrogen chemisorption on the metal surface modifies its physical properties [5], the operation of a standard sensor can be easily converted into that of a gas sensitive device introducing a catalytic metal electrode. Several works report about the possible use of palladium films for hydrogen detection exploiting the change of electronic [6] as well as mechanical [1], optical [3] and physical properties [7] of the existing devices. Nevertheless, the increasing relevance of applications characterized by harsh environment operation showed the limits of commercially available sensors, thus enhancing the research for proper materials [8]. Among them diamond has been considered one of the most promising one because of its excellent physical properties [9, 10].

In this work a hydrogen sensitive device was developed taking advantage of the high sensitivity to temperature of a chemical vapor deposition (CVD) diamond-based thermocouple. In particular, the sensor has been designed building a metal-semiconductor-metal structure and the gas sensing capability was achieved using a thin palladium film as one of the electrodes of the temperature sensor. The characterization of the diamond-based sensor has been accomplished in two-steps. The first step consisted in the evaluation of the thermoelectric properties of the boron doped diamond film for different operation conditions. The gas sensing properties have been then assessed exposing the prototype to different hydrogen concentrations while a constant temperature drop was kept across the diamond film. The gas sensitivity is indeed carried out by a change in the sensor response due to the modification of the built-in potential at the diamond-Pd junction resulting from the hydrogen adsorption. The diamond thermocouple has been easily converted into a hydrogen sensitive device only by using a catalytic metal as contact electrode.

2. Experimental

Diamond films were grown by plasma enhanced chemical vapour deposition in two successive steps on p-type silicon substrates. Firstly, a 50 μm film of intrinsic diamond has been grown. A 1% CH_4-H_2 mixture at a temperature of 750 °C has been used as gas feed within a tubular reactor, while a 2.45 GHz microwave generator has been used to create the plasma. Then, a 13 μm boron doped diamond growth using CH_3OH+B_2O_3 vapor addition. The intrinsic diamond film ensures insulation between the p-type silicon wafer and the. The sensor prototype has been built depositing a 120 nm gold contact on one end of the sample by electron beam deposition and a palladium contact of the same thickness was deposited on the other end.

An appropriate characterization setup was built to test the sensor in steady state temperature conditions and under gas exposition. Two 12x12 mm^2 Peltier cells have been mounted on the top of a water cooled copper block used to keep the temperature of one face of the cells at a constant temperature. On the other faces of the cells two 2 mm thick copper block have been glued and used to fix the sensor and two Class A Pt100 thermistors. Temperature values were monitored and transferred to a PC by means of digital multimeters. Computer control ensures a feedback action on heaters in order to stabilize both reference and test temperature. The test equipment was placed in a properly designed vacuum chamber allowing an appropriate control of gas flow and discharge.

3. Results and Discussion

The thermoelectric properties of the diamond-based thermocouple have been evaluated for three different prototype characterized by decreasing values of the doping level. In order to measure the sensor response for increasing temperature drops applied between the tips of the samples, the temperature value of one tip has been kept constant (reference temperature) at 273 K, while the other one has been varied in the 275-320 K range.

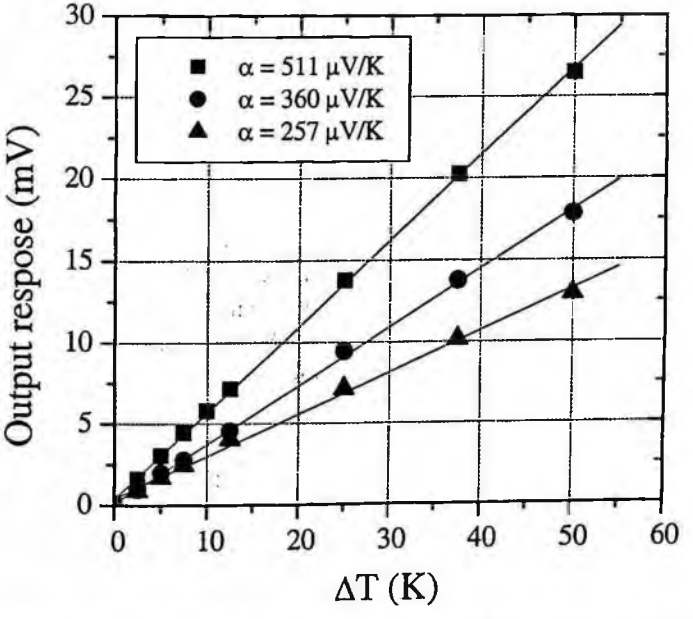

Figure 1. E.m.f. of CVD diamond based thermocouple as a function of temperature for three samples of different electrical resistivity.

The results are shown in Fig.1 for all the three samples. Since a linear increase of the output signal is shown in all cases, the Seebeck coefficient α can be easily calculated from the slope of the

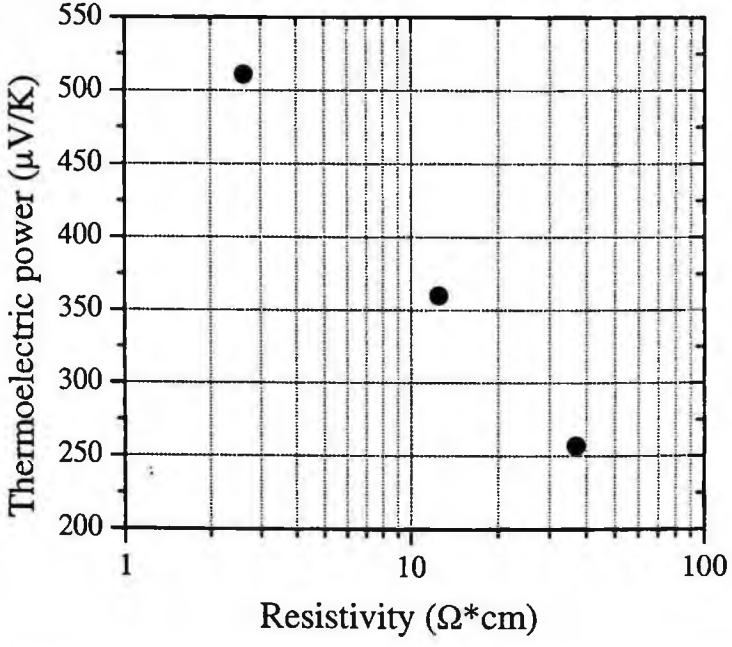

Figure 2 Seebeck coefficient of the three samples calculated from the slope of the response curve obtained for increasing temperature drops.

output response as a function of the temperature drop and results in 511, 360 and 257 μV/K. In Fig.2 the thermopower values of the three samples have been plotted as a function of their electrical resistivity. The highest value of the Seebeck coefficient is observed in the highly doped sample while the thermopower decreases with increasing resistivity. The positive sign of the output signal as a function of the applied temperature drop confirms the p-type conduction mechanism due to boron acceptors. Moreover, the thermoelectric potential always results much higher than that shown by metals respect to semiconducting materials, thus allowing an accurate temperature measurement even when a single thermocouple instead of a multiple element thermopile is used as sensitive element. As previously discussed, the gas sensing capability is

due to the presence of a catalytic metal film that reacts to the hydrogen exposition modifying its physical properties. In this case, the palladium film modifies its Fermi energy level, thus inducing a change in total Seebeck potential measured across the thermocouple. The change in thermoelectric response depends on atmospheric hydrogen content. In particular, the increase in the sensor response for 0.5, 1 and 2 % hydrogen percentage content in pure nitrogen respectively is shown in Figure 3. These results corresponds to the lowest B-doped diamond sample and have been obtained fixing a temperature drop of about 2 K. The device has shown good stability and repeatability, but no additional information on the characteristic rise and fall times can be estimated due to the unknown mixing time between nitrogen and hydrogen within the test chamber.

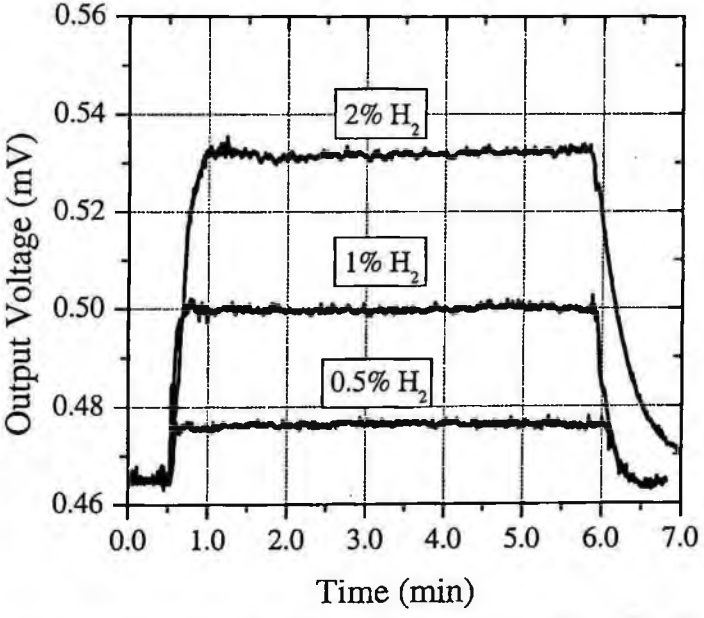

Figure 3 Response of the sample to 0.5, 1 and 2 % hydrogen exposition at $\Delta T = 2°C$.

4. Conclusions

A thin film thermocouple for gas sensing application has been built using boron doped CVD-diamond and palladium. The thermoelectric response has been measured for different temperature drops, showing thermoelectric power

dependes on doping level. In particular, a higher Seebeck coefficient has been measured as doping level increases.

The catalytic properties of the palladium film allow the hydrogen detection due to the change in the diamond/Pd junction potential as a consequence of the gas exposition. Three different hydrogen concentrations in nitrogen have been used to test the gas sensing properties of the diamond based device, showing a quite linear increase in the sensor response with increasing gas concentrations.

Work is in progress in order to evaluate the capability of the boron-doped diamond-based device for the measurement of hydrogen concentration much lower than 1 %, relevant for environmental sensing, and to increase the device sensitivity by the realization of diamond based thermopiles.

References

1. D.R. Baselt, B. Fruhberger, E. Klaassen, S. Cemalovic, C.L. Britton Jr., S.V. Patel, T.E. Mlsna, D. McCorkle, B. Warmack. Sens. Actuators B 88 (2003) 120–131
2. K. Scharnagl, M. Eriksson, A. Karthigeyan, M. Burgmair, M. Zimmer, I. Eisele. Sens. Actuators B 78 (2001) 138–143
3. Massood Tabib-Azar, Boonsong Sutapun, Rose Petrick, Alex Kazemi. Sens. Actuators B 56 (1999) 158–163
4. R.S. Glass (Ed.), Sensor needs and requirements for proton-exchange membrane fuel cell systems and direct-injection engines, in: US Office of Transportation Technologies (OTT) Workshop Report, 25– 26 January, 2000.
5. F.C. Thompkins, Chemisorption of gases on metals, Academic Press, New York, 1978.
6. I. Lundström, M.S. Shivaraman, C. Svensson, L. Lundkvist. Appl. Phys. Lett. 26 (1975) 55.
7. C.A. Papadopoulos, D.S. Vlachos, J.N. Avaritsiotis. Sens. Actuators B 34 (1996) 527-527
8. Fahrner W.L. R. Job, M. Werner. Microsyst Technol 7 (2001) 138-144
9. Kohn E., Gluche P., Adamschik M. Diam Rel Mater 8 (1999) 934-940
10. Nebel C.E. Semicond Sci Technol 18 (2003) S1-S11
11. Osamu Yamashita. J Appl Phys 95 (2004) 178-183
12. R. Horiuchi, K. Okano, N. Rupesinghe, M. Chhowalla, G.A.J. Amaratunga. Phys. Stat. Sol. (a) 193 (2002) 457–461

PALLADIUM THIN FILM THERMOPILES AS HYDROGEN SENSOR

L. SANDRO, A. BEARZOTTI

Institute for Microelectronic and Microsystems - Sensor and Microsystem Group
CNR – Research Area Tor Vergata – Via Fosso del Cavaliere, 100
00133 Rome, Italy - tel. +39-06-49934572

The aim of this research is to study and fabricate a high sensitive [1] sensor for hydrogen detection, based on palladium. For this purpose, the thermoelectric power of some metals was used, for the fabbrication of varieties of thin film thermopiles with a number of junctions from 20 to 140. Each device was constructed by usign Pd and another suitable metal, such as Cu and Al. We have used the two most rilevant features of Palladium: its capability to adsorbe hydrogen and the consequential change of its thermoelectric power. We have caracterized the response of these devices in function of the temperature difference ΔT present between the hot and cold junction. Afterwards we have studied the translation of the response curve when the device under test was exposed to a specific hydrogen concentration.

1. Introduction

There is a great and growing interest in the development of catalytic materials which are suitable for incorporation onto microfabricated chemical sensor devices. The principal problem is that many kinds of catalyst system are not easy to be integrated into MEMS device, and sometimes these do not adhere well to the Si-based structures and sensors.

Hydrogen is a very important gas, so that it has been increasingly recognized as a clean energy resource, or a new fuel gas. This gas has the advantage to be free from the problems associated with greenhouse warming. There are many branch of actual tecnologies in wich hydrogen has a first order rule: hydrogen is a principal propellent for aerospace; it is a fundamental gas for fuel-cells; it is present in many chemical reaction, especially in industrial steps (in which its concentration is a fundamental parameter in many kinds of chemical reactions).

In every application the concentration knowledge is a fundamental aspect; hydrogen gas leaks easily from gas lines and systems, and is one of the explosive gases. Therefore the hydrogen detection is an important problem.

From the viewpoint of the sensors implementation in hydrogen energy systems, new hydrogen gas sensors should be small, cheap, easy to be implanted on

integrated circuits, and should work with extremely small power consumption. From the viewpoint of the electrical and chemical properties, new hydrogen gas sensors should be fabricated with high reliability, excellent selectivity, small humidity dependence, full reversibility and long time stability. The aim of this research is to design and fabricate a high sensitivity sensor for hydrogen gas detection based on Pd as a catalitic material.

2. Sensor Principles

In norder to set this hydrogen sensor, two different physical principles are used: the capabilty of Palladium (one of the two metals) to adsorbe hydrogen and its consequent thermoelectric power variation. For this purpose, we have fabricated thin film thermopiles (a series thermocouples connected togheter) on Si/SiO_2 substrate. By these thin film thermopiles our purpose was to increase the sensitivity of our device. In fact the *emf* generated from n thermocouples connected in serie is a sum of the *emf* generated from every single thermocouple; at the same time our porpouse was to have a very small sensitive area. For the thermopile fabrication, it's necessary to choose the materials and this choice depends on metal ATP ([1]). The thermoelements of the thermopiles are Palladium and Copper. The Palladium acts as a membrane sensitive to hydrogen due to its cathalitic property. To obtain a good signal level it is preferible to use a second metal with an opposite ATP sign; we have chosen Copper because it respond to this requisite. We have studied and characterized the response of these devices vs temperature difference, i.e. ΔT; afterwards we have studied the response curve shift when the device under test is exposed to a specific hydrogen concentration, under the condition of ΔT constant.

3. Theory

In a thermopile, when the temperature difference between reference and measure junctions is constant, the *Vout* (*emf*) generated from the Seeback effect is constant. The generated *emf* (E_{AB}) is an integral of the difference from the parameters definited as *Absolute Thermoelectric Power* ([2]), and indicated with S, i.e.:

---

[1] ATP is *Absolute Thermoelectric Power*, i.e. a parameter related to thermoelectric properties.

[2] It's important to discern from ATP, which caracterize a single metal, and *Seeback Coefficient*, which caracterize a signal out from a thermocouple with this metal and platinum.

$$\frac{dE_{AB}}{dT} = S_A - S_B \quad \rightarrow \quad E_{AB} = \int_{T_1}^{T_2} (S_A - S_B)\, dT = .. \tag{1}$$

The parameter S is related to the reversible rate of entropy change in the narrow band structure and characterizes a single metal. Often is not possible to find a graphical rappresentation of ATP for a single element; nevertheless, a generic model, that can be considered the best approximation of the real ATP function, is a sum of increasing power of T with decreasing coefficients c_n (S is the ATP and x is a generic metal):

$$S_X(t) = c_0 + c_1 \cdot T + c_2 \cdot T^2 + c_3 \cdot T^3 + c_4 \cdot T^4 + ...c_n \cdot T^n = \tag{2}$$

$$= S_X = \sum_{n=0}^{\infty} c_n T^n \quad \text{with} \quad |c_n| \rightarrow 0 \quad \text{for } n \Rightarrow \infty$$

Coefficients of T power for every metal are not all known; in literature these coefficients are avaible for standard thermocouples that have specified *emf-temperature* relation (type B, type E, type J,.....).

The ideal behaviour of ATP is totally indipendent from the variable T, i.e. $S_X = c_0$ with $c_n \cdot T^n$ negligible for $n \geq 1$; in this case the generated *emf* (E_{AB}) is linear with applied ΔT , i.e.:

$$E_{AB} = E_0 + C_{Dif} \cdot (T_2 - T_1) \Rightarrow C_{Dif} \cdot (\Delta T) \tag{3}$$

with the integration constant E_0 egual to 0.

Considering a real situation, if the ΔT range is not too large, approximately <100 °C, it's possible to assume a linear dipendence from *ATP* to T , i.e.:

$$S_A = m_A T + C_A; \;\; S_B = m_B T + C_B; \Rightarrow \frac{dE_{AB}}{dT} = S_A - S_B = C_{Dif} + (m_A - m_B) \cdot T \tag{4}$$

where m_A and m_B are angular coefficients and C_{Dif} is a difference between C_B e C_A. The *emf-temperature* relation became in this case:

$$E_{AB} = \int_{T_1}^{T_2} (S_A - S_B)\, dT = \int_{T_1}^{T_2} \left[(m_A - m_B) \cdot T + C_{Dif} \right] dT = ... \tag{5}$$

After some mathematical rearranging, it's possible to find as follows ([3]):

$$E_{AB} = \frac{1}{2}(m_A - m_B) \cdot \Delta T^2 + \left(C_{Dif} + (m_A - m_B) \cdot T_1\right) \cdot \Delta T \quad \text{for } |\Delta T| <\approx 100°C \tag{6}$$

The *emf* generated can be expressed by:

$$V_{OUT} = E_{AB} = \frac{1}{2} C^* \cdot \Delta T^2 + \left(C + C^* \cdot T_1\right) \cdot \Delta T \tag{7}$$

[3] It's possible to achieve an equivalent relation with T2 as parmeter; we have to choice two indipendent variables from three parameters.

with: $C^*=m_A-m_B$ and $C=C_{Dif}$.
If we have an H_2 concentration in the measuring enviroment, we have to consider an other term (an additive *emf*, V_{H2}) that takes into account the ATP variation of the Palladium:

$$V_{OUT} = E_{AB} = \frac{1}{2}C^* \cdot \Delta T^2 + \left(C + C^* \cdot T_1\right) \cdot \Delta T + V_{H_2}(\Delta T) \qquad (8)$$

Note that the V_{H2} is function of ΔT; i.e. $V_{H2} = 0$ if $\Delta T=0$.
There are several aspects to analize in this equation.

- we can calculate coefficients C and C*, but equation (8) is valid only around the temperature at which the ATP is reported; ATP reported at related T are available in literature.
- the relation between ΔT and generated *emf* is a second order polinomial without note term.
- this parabolic curve is function of T_1; if ΔT is maintained constant, the generated *Vout* is a linear function of T_1; this means that the *Vout* with the same ΔT is different for different T_1 values. Temperature T_1 determines a shift of the parabolic *emf* function along y axis.

4. Measurements

We have designed and implemented a specific measuring system to make a accurate measurements; on the left of fig.1 is reported the associated scheme, and on the right of fig.1 is reported a detail of heater and cooler.

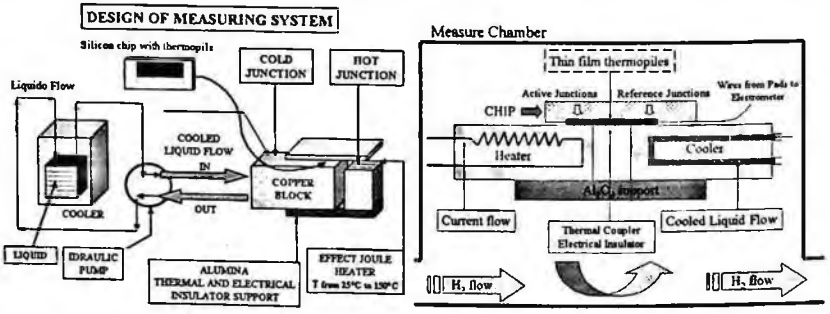

Figure 1. a scheme of our measuring system (left) and mechanic contacts from chip to heater and cooler (right).

We have used a kantal wire controlled with a power supply to heat the first junction; to cool the second junction we have forced a liquid to flow trought a block of brass. This liquid was maintained at low temperatures, -20°C at minimum. With this apparatus we have been able to maintain the hot and cold junction at a temperature difference ranging form 10°C to 150°C.

5. Calibration Curves

From thermopiles with different layout and number of thermocouples we have acquired data values in presence of O_2 or H_2 (diluted in N_2) at specific concentration. From our measurement system we have token the generated *emf* and temperatures T_1 and T_2; we have used these parameters to determine coefficients C and C*. Note that in order to solve equation (8) we need to know T_1 and T_2 because they are indipendent variables. If the difference between T_1 and T_2, i.e. ΔT, is small, we can semplify our model negletting the second order term to calculate coefficients C and C*; from (7) and (8) we can write:

$$V_{OUT} = (C + C^* \cdot T_1) \cdot \Delta T = K(T_1) \cdot \Delta T \qquad (9)$$

$$V_{OUT} = (C + C^* \cdot T_1) \cdot \Delta T + V_{H_2} = K(T_1) \cdot \Delta T + V_{H_2}(\Delta T) \qquad (10)$$

With this approximation we have a linear relation from *emf* and ΔT; the relation coefficient K is related to T_1; V_{H_2} is function of ΔT, i.e. $V_{H_2} = 0$ if $\Delta T = 0$.

Our esperimental results satisfies this approximation; in fig.2 it's shown that the lower curve, *thermopile emf*, can be considered proportional to the higher curve, *ΔT values*; on the right side of the figure (see filled arrow) it's shown that when the ΔT is constant, but T_1 changes, the *emf* value changes (we know proportionally to T_1).

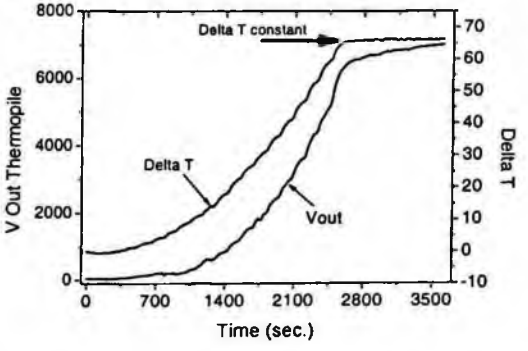

Figure 2: thermopile *emf* and ΔT; for small ΔT, *emf* can be considered proportionally to ΔT; when ΔT becames constant, *emf* is subjecto to a derive of T_1 (and therefore of T_2).

We have made measurements with the system in stationary conditions, i.e. with the temperature difference between T_1 and T_2 constant.
From eq. (9) it's possible to write:

$$V_{OUT} = C \cdot \Delta T + C^* \cdot T_1 \cdot \Delta T + V_{H_2} \qquad (11)$$

Our signal in presence of H_2 is a sum of three contributes, related to T_1, ΔT and H_2 concentration; in other words we have a combination of linear therms.

By supposing that relation between *emf* and ΔT is eq. 9, we have calculated the coefficints C and C* from two points of a single measured curve in stationary conditions; then we have used a linear properties to separe these single contributes. That is we have calculated a working point for each measurement, and then we have determined a response level to a specific H_2 concentration.

6. Results and Conclusion

We have reported and analized the behaviour of thin film thermopiles made with Pd in presence of hydrogen; relative calibration curves, with and without H_2, are showed. For each measured *emf* it's possible to construct a second order curve, but it's necessary to know that relative coefficients of this behaviuor are only valid around the measurement point.

Note that a single *emf* curve is calculated starting from a defined ΔT and T_1; sometimes T_1 is different in different measurements. Therefore, these points that we have reported can be considered to belong at the same curve, that is supposed linear in our case, only if a change of T_1 is negligible, that is supposing T_1 constant for every measurement.

We have found that in our thermopiles the ATP value is smaller than the aspected ATP; the difference is not negligible. A measured value of the ATP of a thermocouples with 25 micron fingers is shown in fig. 5.

A difference from our measured values and literature reference values is related to some different causes. A first problem is the thermal coupling, wich is insufficient due to wiring connecting problems. A second problem is an imperfect cristallografic structure of thin film metals, Pd and Cu in our case; we suppose that some parameters related to the cristalline structure [1] can be influenced. Last problem is the high thermal conducibility of silicon substrate.

Our device can detect hydrogen at concentration of 1%; at lower concentration, the signal variation is too low.

In presence of H_2 the generated *emf* shifts to a lower level; we have made measurements for different types of thermopiles.

In fig. 4 we have reported five measurement points of *emf* generated from a thermopile with 20 junctions of 50 micron fingers in presence of O_2; lower we have reported five measure points of the same thermopile in presence of 1% of H_2; we have two parallel curves. Note that with the first four points we have an *emf* that can be considered a linear function of ΔT. If the ΔT is increased, the absolute level of *emf* variation increases; but we have showed that the percentage variation decreases.

At present we are working on new design geometries of the thermopiles in order to remove the presence of connecting wires responsable of the low thermal coupling with heat and cols sources; we are also considering to change the type of substrate, choosing a low thermal conductivity material; on the silicon substrate there is a too high thermal flow.

Our project is to increase about of one order of magnitude the response level of our thermopiles.

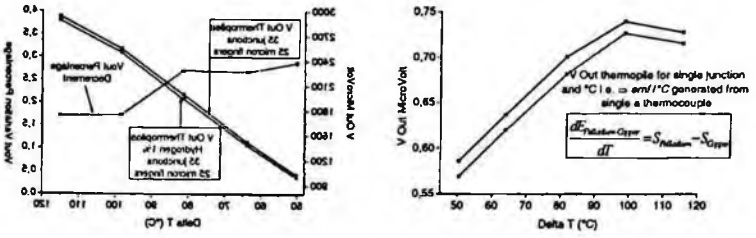

Figure 4: on the left side are reported 5 measurement points of emf generated generated from a thermopile with 35 junctions of 25 micron fingers in presence of O_2 and 1% of H_2; on right side relative ATP are showed.

References

1. Robert R. Heikes, Roland W. Ure, Thermoelectricity: scienze and engineering; John Wiley & sons, Inc.
2. D. K. C. MacDonald Thermoelectricity: an introduction to the principles. Intersciences Publishiers.
3. Alain Giani *, Asmail Al Bayaz, Abdel Boulouz, Fre´de´rique Pascal-Delannoy,Alain Foucaran, Andre´ Boyer. Thermoelectric microsensor for pressure and gas concentration measurement.
   Materials Science and Engineering B95 (2002) 268_/274
4. A. D'Amico, E. Verona, C. Caliendo, M. Baciocchi, A. Bearzotti, M. Gentili, A. Lucchesini. Cu/Pd thin-film Thermopile as a Temperature and hydrogen Sensor; Sensor and Actuators, A21-A23 (1990) 631-635.
5. *S.U.Jen*,C.C.Yu,C.H.Liu,G.Y.LeeY. Piezoresistance and electrical resistivity of Pd, Au,and Cu films*
6. *E. Broitman, P. Alonso, R Zimmerman, Deviation from Matthiessen's rule in continuous metals*
7. *A. D'Amico, C. Di Natale, A Contribution on some basic definitions of sensors properties*
8. *Hydrogen in Metals; Edited by G. Alefeld and J. Volkl*

CHEMICAL SENSOR BASED ON THIN FILM BULK ACOUSTIC WAVE RESONATOR (TFBAR)

M. BENETTI, D. CANNATÀ, F. DI PIETRANTONIO, E.VERONA

Istituto di Acustica "O.M. Corbino", CNR, Via del Fosso del Cavaliere 100, Rome, I-00133, Italy

V. FOGLIETTI

Istituto di Fotonica e Nanotecnologie, CNR, Via Cineto Romano, 42, 00156 Rome, Italy

A. MACAGNANO

Istituto per la Microelettronica e Microsistemi (Rome section), CNR, Via del Fosso del Cavaliere 100, 00133 Rome, Italy

A novel electro-acoustic chemical sensor based on thin film bulk acoustic resonators (TFBAR) is presented. The use of TFBAR resonators, in the GHz range of frequencies, can widely improve the sensitivity of the well known quartz crystal micro-balance (QCM), whose operation frequencies (a few tens of MHz), limits their use to those applications where the detection of pollutants in concentrations of a few or less ppm is not essential. The TFBAR structure is implemented on (001) silicon substrates, an anisotropic chemical etching from the back side of the Si wafer is used to obtain the Si_3N_4 or SiO_2 - AlN resonating membrane. The devices result robust in construction and miniaturized in size; the technologies involved in their fabrication are fully compatible with those of the Si integrated circuits. The performances of the sensors have been tested using thermal evaporated thin layer of Co-tetra-phenyl-porphyrin, deposited on the etched side of the membrane. Time response upon different cycles of CO and Ethanol adsorption and de-sorption are reported together with the sensors calibration curves. Time stability, repeatability and sensitivity have been tested and reported.

1. Introduction

Bulk and surface acoustic wave devices are largely used in many application areas such as mobile telephones, satellite services or as sensing devices. Sensors based on electro-acoustic transduction are a powerful tool to measure physical parameters, such as force, acceleration, pressure, electric and magnetic fields, potentials, etc., or chemical and biochemical values, such as gas, vapour or ion concentrations in both gaseous and liquid environments.

Chemical/biochemical sensitivity is typically obtained by coating a proper chemically interactive material (CIM) on the acoustically active region of the devices. Adsorption and desorption of the analyte by the CIM, give rise to changes in its mass, which are detected as shifts in the resonant frequency. For this reason these devices are also called *micro-gravimetric* sensors.

The performances of the well known quartz crystal microbalance (QCM), whose operation frequency is limited to a few tens of MHz, are largely improved by the use of TFBAR structures, whose operation frequencies is extended to the GHz range. In fact, limiting our attention to the *micro-gravimetric* sensors, it is possible to assume that the response to added mass, in terms of absolute frequency changes, increases with the square of the operating frequency [1].

In this paper we present a chemical sensor based on a TFBAR structure using a thin film of Co-tetra-phenyl-porphyrin as chemically interactive material. Sensor tests have been performed by exposing the device to different cycles of ethanol and CO adsorption and desorption, at different concentrations, in nitrogen. Time stability, repeatability and sensitivity have been tested and reported. The device design, based on Mason's equivalent circuit analysis is reported together with the technological fabrication steps.

TFBAR sensors are robust in construction and miniaturized in size; the technologies involved in their fabrication are fully compatible with those of the Si integrated circuits, so that a monolithic integration of arrays of TFBAR sensors with the oscillator amplifiers and electronic conditioning circuits is possible.

2. Simulation

The resonant frequency, as well as the electric impedance behaviour vs. frequency of the TFBAR has been evaluated on the basis of Mason's equivalent circuit [2].

The equivalent circuit for the complete resonator structure, consisting of the membrane (Si_3N_4 or SiO_2) and a piezoelectric AlN layer with two aluminium electrodes apart, is shown in figure 1.

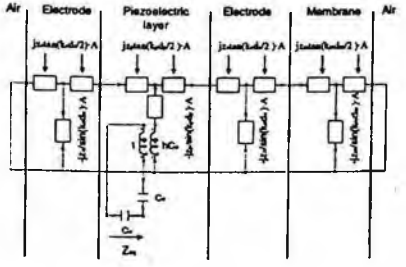

Figure 1. Equivalent Mason's circuit for a TFBAR.

Table II. Fundamental resonant frequencies obtained from simulations.

AlN thickness (μm)	Fundamental resonant frequency (GHz)	
	SiO_2	Si_3N_4
4	0.89	1.01
2	1.03	1.32
1	1.16	1.57

The resonant frequencies are evaluated by calculating Z_{eq} vs. ω, once the geometry of the structure and the properties of each material are known. The fundamental resonant frequency, as evaluated using Mason's equivalent circuit, for different thicknesses of the piezoelectric AlN layer and at a constant thickness of the Si_3N_4 or SiO_2 membrane (1μm) and Al electrodes (100 nm) is reported in Table II.

3. TFBAR Device Structure

The experimental TFBAR prototypes have been implemented on (001) silicon substrates covered on both sides with a layer, 1 μm thick, of CVD Si_3N_4. The structure of the resonator is schematized in figure 2 (a).

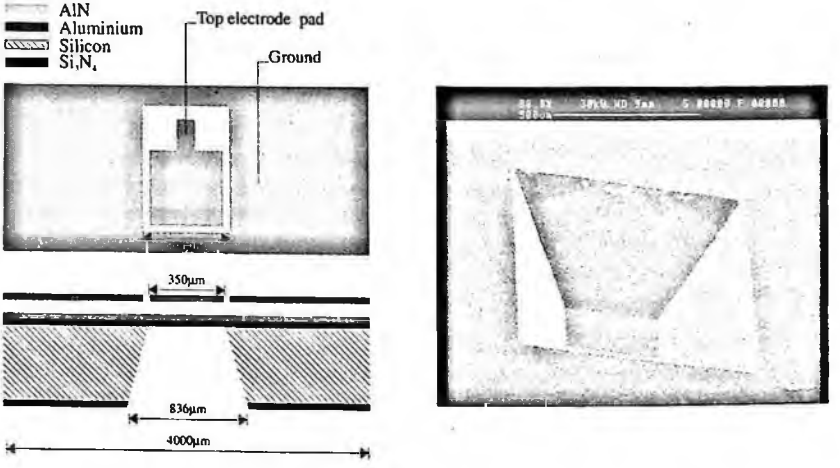

Figure 2. Structure of the experimental TFBARs (a) and SEM photography of the etched silicon region and membrane (b).

The first technological step for the device fabrication consists in opening windows on the Si_3N_4 layer for Si etching, on one side of the substrate, using photolitographic techniques and reactive ion etching (RIE) in CHF_3/O_2 plasma. The opposite side of the wafer is then coated with an Al film, 100 nm thick (ground electrode) and with the piezoelectric AlN layer, deposited by rf sputtering [3,4]. The second Al electrode is finally deposited and defined according to the geometry shown figure 2, by lift-off technique. An accurate two side mask alignment procedure is required. Anisotropic etching of Si is performed using a KOH solution, at 80 °C, in a special jig designed in order to protect the side of the Si wafer containing the resonators; the Si_3N_4 layer acts as stop etching [5]. The final step of the process consists in dicing the 105 devices

fabricated at the same time on the wafer in each run. Figure 2 (b) is a SEM photography of the back side of the Si wafer containing the etched region and membrane.

The soldering pad for the top electrode is out of the membrane region in order to avoid any possible breakdown during the ultrasonic wire bonding process. In order to avoid window opening process through the AlN film, the ground contact is directly connected to the top Al metal film, being its potential almost the same as that of the ground electrode, thanks to the large ratio between the resonator electric capacity and that between ground electrode and ground pad.

4. Experimental

Sensing material thin films were deposited onto the surface of membrane by sublimating porphyrins (synthesized according literature [6]) under vacuum in a silica glass crucible heated at about 220°C by a tungsten filament (High Vacuum Deposition Device INFICON XTM/2). The deposition rate was estimated to be about 0.2 A/sec by a 6 MHz (AT-cut) quartz microbalance.

The prediction of the expected affinity of a certain metalloporphyrin for a specific gas can be explained by means of Pearson's principle: hard acid exhibit a preference for hard bases. In these experiments, the choice of CoTPP (Co-tetra-phenyl-porphyrin) is due to the peculiarity of this molecule to exhibit a pronounced affinity for either oxygen- or nitrogen-donating sites. A good sensitivity is presumed after physico-chemical interactions between the ordered film of porphyrin and good electron donors as Carbon Monoxide end Ethanol, involving, the latter one, H-bonds too.

To allow the gas adsorption by the CIM, the TFBAR device was mounted on the edge of a microstrip, leaving the membrane free to oscillate. The measurements chamber with the device is shown in figure 3. This system allowed a reliable test of the resonator before and after Co-TPP coating, under the same conditions.

Figure 3. Measurements chamber and TFBAR device.

The S11 parameter of the TFBAR, measured in both magnitude and phase formats using an HP8753A Network Analyzer, is reported in figure 4 before (continuous line) and after (dot line) the deposition of 36 nm thick Co-TPP film. The frequency shift in the resonance peak (10.5 MHz) is in accordance with that evaluated using the Sauerbrey-Lostis approximation.

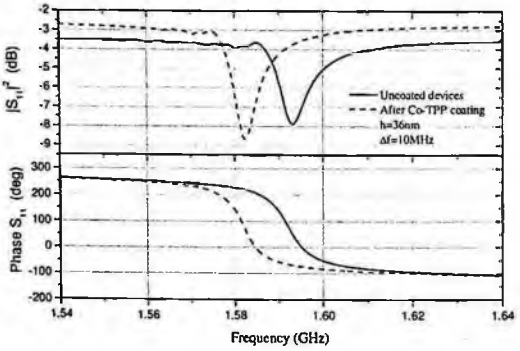

Figure 4. Frequency response before (continuous line) and after (dot line) Co-TPP coating.

Measurements upon cycles of ethanol and CO adsorption/desorption have been performed by exposing the membrane to different ethanol or CO concentrations in N_2 or to pure N_2 (desorption) at a constant flow rate of 250sccm. The TFBAR sensor response was detected using the Network Analyzer, tracking the frequency of the resonance peak that correspond to the inflexion point of the phase curve.

The time curve for the concentration of 1905 ppm of ethanol, reported in figure 5, shows that the response is fast and repeatable. The response curve obtained by exposing the sensor to different ethanol and CO concentrations is reported in figure 6.

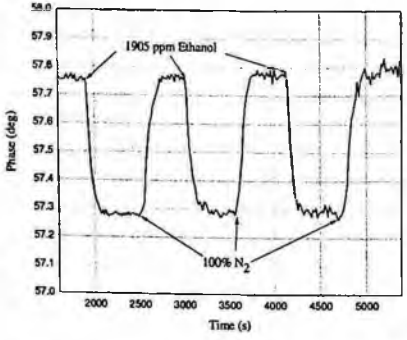

Figure 5. Time response to 1905 ppm of ethanol.

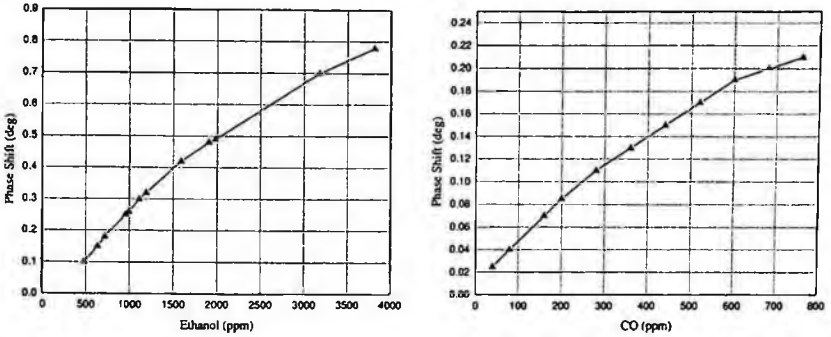

Figure 6. Response curve to ethanol (a) and CO (b).

5. Conclusion

In conclusion a micro-gravimetric sensor, based on the use of a TFBAR, has been implemented and tested. The device is similar in operation to the quartz micro-balance, extending its operation frequency from a few tens of MHz to the GHz range. The increased operation frequency give rise to larger sensor signals, which is a condition for improved sensitivity devices.

Preliminary experiments, performed using a Co-TPP chemical interactive membrane (CIM), have demonstrated promising performances in the operation of the new device.

References

1. G. Sauerbrey, Verwendung von Schwingquarzen zur Wägung dunner Schichten und zur Mikrowägung, Z. Phys. **155,** 206 (1955).
2. D. Royer, E. Dieulesaint, Elastic Waves in Solids, Vol II, Springer-Verlag (Berlin Heidelberg 2000) pp 10 - 15.
3. M.A. Dubois, P. Muralt Properties of aluminum nitride thin films for piezoelectic transducers and microwave filter applications, Appl. Phys. Lett., **74**, 3032 (1999).
4. H.P. Loebl, M. Klee, C. Metzmacher, W. Brand, R. Milsom, P. Lok, Piezoelectric thin AlN films for bulk acoustic wave (BAW) resonators, Mat. Chem and Phys., **79**, 143 (2003).
5. M.A. Dubois, P. Muralt, V. P. Plessky, BAW resonators based on aluminium nitride thin films ,IEEE Ultrasonic Symposium Proceedings, **Vol. 2**, pp 9078 (1999).
6. K.M. Kadish, K.M. Smith. R. Guilards (Eds), The porphyrin handbook, Academic Press, New York, 2000.

SINGLE-WALLED CARBON NANOTUBES NANOCOMPOSITE MICROACOUSTIC SENSORS FOR DETECTION OF ORGANIC VAPORS

M. PENZA, M. A. TAGLIENTE, G. CASSANO, P. AVERSA AND L. CAPODIECI

ENEA, Materials and New Technologies Unit
C.R. Brindisi, SS.7, Appia, km 714 - 72100 Brindisi, Italy
E-mail: michele.penza@brindisi.enea.it

We have developed highly sensitive microacoustic vapor sensors based on surface acoustic waves (SAWs) ST-,X quartz 433 MHz two-port resonator oscillators. A nanocomposite film of single-walled carbon nanotubes (SWCNTs) embedded in a cadmium arachidate (CdA) amphiphilic organic matrix was prepared by Langmuir-Blodgett technique with a different SWCNTs weight filler-content onto SAW transducers as sensing interface for vapor detection, at room temperature. The structural properties and surface morphology of the nanocomposite have been examined by X-ray diffraction and scanning electron microscopy, respectively. The sensing properties of SWCNTs nanocomposite LB films have been also investigated by using Quartz Crystal Microbalance (QCM) 10 MHz AT-cut quartz resonators. The measured acoustic sensing characteristics indicate that the sensitivity to polar and non-polar tested organic molecules (ethanol, ethylacetate, toluene) of the SWCNTs/CdA nanocomposite increases with the content of SWCNTs embedded in the nanocomposite with a linearity in the frequency change response and a very low sub-ppm limit of detection. Pattern recognition based on ANNs has been successfully applied for VOCs recognition using SAW and QCM sensors coated with 27.5 and 75.0 wt.% SWCNTs nanocomposite.

1. Introduction

The carbon nanotubes are nanomaterials with interesting electronic, chemical, optical, mechanical, thermal properties[1]. A single-walled carbon nanotube (SWCNT) can be visualized as a graphene sheet rolled up into a long cylinder consisting of an one-dimensional tubular wire with only surface-arranged carbon atoms. In the contrast, the multi-walled carbon nanotubes are concentric SWCNTs with total greater diameter. Due to their peculiar hollow structure, nanosized morphology (diameter 1-10 nm) and high surface area (500-1500 m^2/g), the carbon nanotubes are ideal candidates for highly sensitive gas adsorption, hence they are strongly attractive as gas sensor nanomaterials. In recent years, the carbon nanotubes have been studied and used as advanced functional materials to fabricate innovative gas sensors[2-7] demonstrating that CNTs are promising sensing nanomaterials for molecular sensors.

An interesting application of the carbon nanotubes may be the embedding of controlled quantity of nanotubes inside the host-matrix of a foreign material for

the synthesis of a nanocomposite with tailored amount of nanotube-filler content. Nanocomposites of SWCNTs incorporated in different material-matrixes are of considerable interest for the development of nanomaterials with increased properties for gas sensing applications. The development of processing techniques for carbon nanotubes is crucial for gas sensing applications to achieve a better control over the arrangement and aggregation of SWCNTs films onto sensing device. The Langmuir-Blodgett (LB) process is a promising method for depositing defect-free, molecularly ordered ultra-thin films with controlled thickness and orientation. This technique allows fine surface modifications in a multilayered film of carbon nanotubes with a highly controlled manipulation to implement molecularly self-organizing nanomaterials in well-defined structures.
Microacoustic sensors have been used as platform transducers: a surface acoustic wave (SAW) two-port resonator 433 MHz oscillator based on ST,X-quartz substrate and a quartz crystal microbalance (QCM) vibrating at 10 MHz based on AT-cut quartz substrate. The simultaneous detection utilizing both chemical microacoustic sensors based on nanocomposite of SWCNTs permits a successful ANNs-based pattern recognition for discriminating VOCs under test.
In this work, SAW and QCM microacoustic gas sensors using LB nanocomposite films of SWCNTs embedded in CdA host-matrix for chemical VOCs detection, at room temperature, have been characterized including a pattern recognition study based on artificial neural networks (ANNs) for sensed VOCs discrimination.

2. Experimental

Commercially available SAW 433.92 MHz two-port resonators (R2632, Siemens) are used as passive acoustic elements. The two-port resonators (4.0 mm x 1.0 mm x 0.5 mm) are mounted on 3-pin round TO-39 package-case. The metal pattern of interdigital transducers (IDTs) and half-wavelength-wide acoustic reflectors for the resonators was made by 0.15 μm thick Al with a IDTs period of 7 μm. The high Q (> 2500) and low insertion loss (< 15 dB) make these devices stable when inserted in an oscillator circuit with frequency output.
A conventional 10 MHz QCM has been used consisting of a circularly shaped AT-cut quartz crystal with a diameter of 10 mm and a thickness of 0.1 mm. The Al electrodes deposited on both sides of the quartz were 0.10 μm thick and 4 mm in diameter. The active area for deposition of coating was 12.5 mm^2. The noise of the uncoated 10 MHz QCM sensor was 0.5 Hz in 10 min. The resonant frequency of the QCM-based oscillator was the sensor output.
The deposition of the LB films was carried out using a Langmuir trough (KSV 5000). The Y-type LB cadmium arachidate (CdA) was used as host-matrix

material due to its molecular structure, suitability for LB process and knowledge of LB deposition know-how[7]. The thickness of CdA monolayer was 2.8 nm. The single-walled carbon nanotubes pristine material (purchased from CNI, USA) was used as-bought without any purification treatment. The diameter of a single SWCNT was in the range 1-4 nm with a gaussian distribution centred on about 2 nm. LB nanocomposite of SWCNTs incorporated in a CdA host-matrix was prepared with a weight-filler content of 27.5 and 75.0 wt.%. A solution (0.734 mg/ml) of arachidic acid in chloroform and a separate solution (0.202 or 0.551 mg/ml) of single-walled carbon nanotubes in chloroform were prepared for 27.5 and 75.0 wt.% nanocomposite, respectively. A volume of 400 µl was taken from each solution to form a mixed solution with a total volume of 800 µl. This mixed solution was accurately dispersed and stirred in an ultrasonic bath for 1h. Then, only a volume of 200 µl was used for LB composite film deposition. This solution of 200 µl was spread onto a subphase constituted by deionized water (18MΩ) with 10^{-4}M $CdCl_2$. The subphase pH was 6.0 and the temperature was 19°C. The monolayer of nanocomposite was compressed with a barrier rate of 15 mm/min up to a surface pressure of 27 mN/m. The dipping rate was of 14 mm/min. The transfer ratio of the monolayer from subphase to hydrophobic surface of a sensor was 0.6 to 0.7. A nanocomposite of 2 and 10 monolayers of SWCNTs embedded in a CdA matrix was prepared onto SAW and QCM sensors, respectively.

The 433 MHz SAW and 10 MHz QCM sensors properly coated by SWCNTs nanocomposite and, alternatively coated by CdA multilayer only, have been located in a test cell (1000 ml volume) for VOCs exposure measurements. Dry air was used as reference gas and carrier gas to transport the individual VOCs of ethanol (1-180 ppm), ethylacetate (1-500 ppm) and toluene (1-150 ppm) with different concentrations in the test cell containing the sensors. The total flow rate per exposure was kept constant at 1000 ml/min. The VOCs vapors were generated by the bubbling method with a thermostated flask containing the liquid analyte. The experiments were conducted at room temperature. The output frequency of the SAW and QCM acoustic sensors was measured by a frequency counter (Agilent 53132A) with multiplexed read-out.

3. Results and Discussion

Figure 1 shows a typical X-ray diffraction spectrum of as-bought HiPco SWCNTs powder pristine material. The pattern exhibits a well defined graphite-like (002) diffraction peak at $2\theta = 26.5°$ and a broad band centred at lower $2\theta = 22°$ from amorphous carbon or nonnanotube carbon material. A FE-SEM image of SWCNTs-in-CdA 27.5 wt.% LB nanocomposite film is reported in Figure 2. The SWCNTs appear coated by the CdA host-matrix and randomly distributed in tangled nets of nanotubular chains and densely aggregated mats.

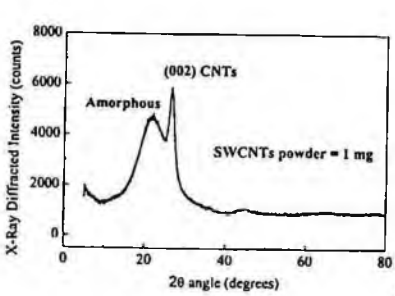

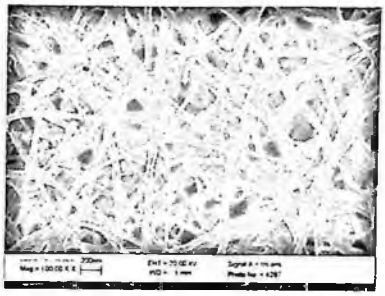

(1) (2)

Figure 1. XRD pattern of HiPco SWCNTs pristine material.

Figure 2. FE-SEM images of SWCNTs-in-CdA 27.5 wt.% nanocomposite LB film.

Figure 3 shows a typical time response of a SAW 433 MHz oscillating sensor coated by 2 LB monolayers of SWCNTs-in-CdA 75 wt.% nanocomposite and exposed, at room temperature, to 5-minute pulses of ethanol. The SAW frequency response decreases upon vapor exposure due to mass loading of vapor adsorbed into composite. Figure 4 shows a comparison of the SAW frequency shift measured using nanocoatings of 2 LB monolayers with different SWCNTs weight-filler content and exposed, at room temperature, to ethanol. A linear dependence of the SAW response has been observed for each tested nanocomposite with a sensitivity, intended as slope of the calibration curve, increasing with the content of SWCNTs in the composite from 20.05 to 131.84 Hz/ppm for CdA host-matrix and 75.0 wt.% nanocomposite, respectively. These results demonstrate that the SWCNTs are highly vapor adsorbent materials. The high sensitivity impacts on very low sub-ppm limit of detection (LODs) measured as 0.16 ppm for ethanol using a 75.0 wt.% composite sensor. Usually, the LOD improves with the increasing content of SWCNTs in the composite.

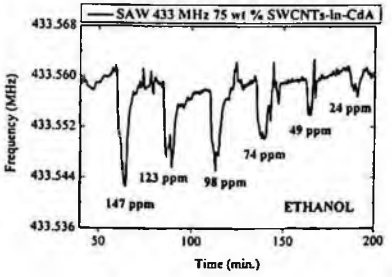

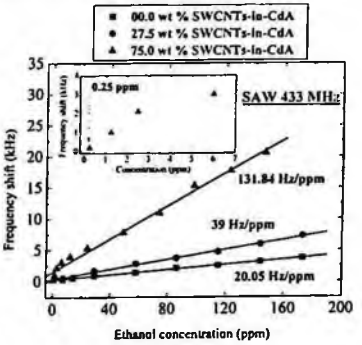

(3) (4)

Figure 3. Transient response of SAW 433 MHz 2-monolayer 75 wt. % SWCNTs-in-CdA LB nanocomposite sensor to 5-minute pulses of ethanol, at room temperature.

Figure 4. Calibration curves to ethanol of SAW 433 MHz sensor coated by 2-monolayer LB nanocomposite with different SWCNTs weight-filler content, at room temperature.

Figure 5 shows a typical transient response of a QCM 10 MHz sensor both-side coated by a 10-monolayer thick SWCNTs-in-CdA 75 wt.% LB nanocomposite, exposed, at room temperature, to 5-minute pulses of ethylacetate. The mass loading of the vapor molecules adsorbed into nanomaterial causes a decrease in the resonant frequency. Also, the vapor sensitivity of the nanocomposite improves with the content of SWCNTs in the composite nanomaterial, as illustrated in the Figure 6. The ethylacetate sensitivity of the 75 wt.% SWCNTs nanocomposite is about two-times higher than unembedded CdA host-matrix. This enhanced sensitivity can be attributed to high surface area of SWCNTs.

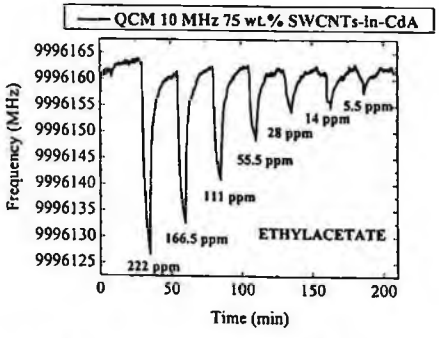

(5)

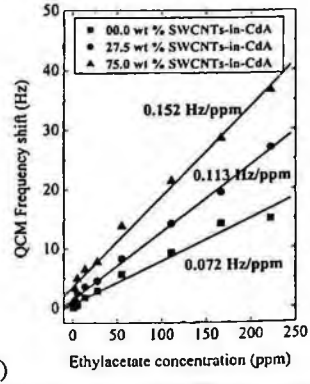

(6)

Figure 5. Transient response of QCM 10 MHz 10-monolayer 75 wt. % SWCNTs-in-CdA LB nanocomposite sensor to 5-minute pulses of ethylacetate, at room temperature.

Figure 6. Calibration curves to ethylacetate of QCM 10 MHz sensor coated by 10-monolayer LB nanocomposite with different SWCNTs weight-filler, at room temperature.

In order to discriminate three VOCs tested of ethanol, ethylacetate and toluene, a ANNs simulator (see Figure 7) has been implemented using the autoscaled responses of 4 acoustic sensors: 2 SAW and 2 QCM devices coated with 27.5 and 75.0 wt.% LB nanocomposite. The thickness of nanocomposite for SAW and QCM sensors is 2 and 10 LB monolayers, respectively.

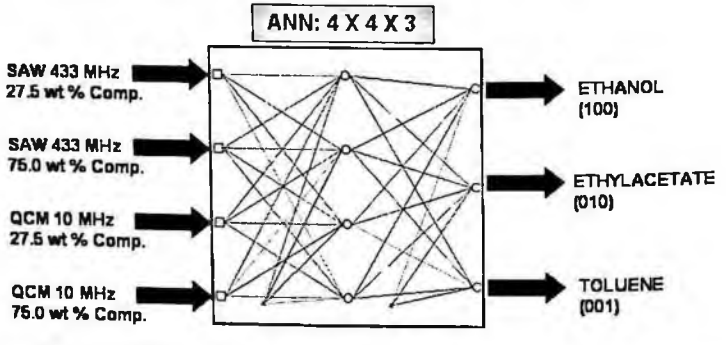

Figure 7. Artificial Neural Network used for discriminating three VOCs under test.

The neural network has been trained by *back-propagation* algorithm. The membership classes of the analytes in the network has been coded by *one-of-many* encoding. The network has been validated by *leave-one-out* method. The total available dataset was constituted by 23 patterns. The overall ANN performance of VOCs recognition has been evaluated by using the confusion matrix. The results achieved indicate that ethanol and ethylacetate have been correctly 100% predicted and toluene only for 86% over total cases with a very good total accuracy of 95%. The ANN robustness and the prediction rate can be enhanced by a more numerous patterns dataset.

4. Conclusions

We have characterized SAW 433 MHz and QCM 10 MHz microacoustic sensors based on single-walled carbon nanotubes nanocomposite for VOCs detection, at room temperature. The results suggest that it is possible to use the LB SWCNTs/CdA nanocomposite to measure polar and nonpolar organic vapors concentration down to sub-ppm level range, at room temperature. Hence, the SAW sensors coated by the nanocomposite of SWCNTs embedded in the CdA organic host-matrix appear to serve as an excellent chemical nanosensor with high sensitivity, reversibility, linearity and very low limit of detection, at room temperature. The positive effects of the different SWCNTs-filler weight content in the nanocomposite on the SAW and QCM vapor sensitivity for various organic solvents examined have been clearly measured. The integration of nanostructured materials as SWCNTs-based nanocomposite and hybrid sensing systems based on different transducing principles can enhance the VOCs recognition performance by pattern recognition based on ANNs for chemical analysis. The results obtained show that this is a successful attempt of combining various acoustic multisensors for VOCs recognition.

Acknowledgments. This work was financially supported by ENEA under project ProTeMa. The authors wish to thank E. Serra for the FE-SEM observations.

References

1. H. Dai, *Acc. Chem. Res.* **35**, 1035 (2002).
2. J. Kong et al., *Science* **287**, 622 (2000).
3. S. Chopra et al., *Appl. Phys. Lett.* **83**, 2280 (2003).
4. M. Penza et al., *Sens. Actuators B* **100**, 47 (2004).
5. M. Penza et al., *Appl. Phys. Lett.* **85**, 2379 (2004).
6. Y.M. Wong et al., *Sens. Actuators B* **93**, 327 (2003).
7. M. Penza et al., *Proc. IEEE Sensors 2004*, 403 (2004).

LIQUID PHASE CHEMICAL SENSORS

AMMONIA DETECTION IN WATER WITH A TIN DIOXIDE BASED OPTICAL SENSOR

M. PISCO, M. CONSALES, P. CAPOLUONGO, S. CAMPOPIANO, A. CUSANO, A.CUTOLO

Optoelectronic Division-Department of Engineering, University of Sannio, Benevento,82100, Italy

R. VITER

Department of Experimental Physics, Odessa National University, Odessa, Ukraine

M. GIORDANO

Institute for Composite and Biomedical Materials, CNR, Napoli, Italy

Experimental results on the capability of a Metal Oxides (MOXs) based optical sensor to perform ammonia detection in water, at room temperature, are presented. Electro-spray pyrolisis technique has been used to deposit the SnO_2 films on the distal end of standard Silica Optical Fibers (SOFs). Single wavelength reflectance measurements have been carried out to test the sensing performances for ammonia detection in water. High sensitivity to the target analyte with fast time response and good desorption properties in the minutes range has been demonstrated.

1. INTRODUCTION

In the last years, the use of optical fiber sensors has expanded rapidly. The use of an optical sensing mechanism offers several advantages like the immunity to electromagnetic interference and the dual functionality to serve as transducers and sensing data transportation systems. A lot of different types of resistive tin dioxide sensors were performed for detecting hydrogen, carbon monoxide, methane, ammonia, nitrogen oxides and different organic solvents [1]. These sensors work on the principle of resistance change under gas adsorption on their surfaces. Because of their operating principle, they have never been used in liquid environment. Furthermore, the gas sensitivity of MOX based sensors usually reaches for maximum at high temperatures (250-450°C). By adding catalytic dopants the operating temperature can be decreased even tough the heater consumption power remains high [2]. In this paper, tin dioxide thin films have been integrated with optical fiber technology in order to develop a new class of optoelectronic sensors able to work in water for ppm detection of ammonia, at room temperature. The sensing probe has been fabricated by

coating the distal end of a single mode SOF with a film of tin dioxide. Electrostatic spray pyrolisis technique has been used for MOX films deposition [3]. Its process parameters can be appropriately adapted in order to obtain films with different thickness and surface structure. Spectral characterization of the obtained sensing probes has been carried out in the range 1520-1620nm. Single-wavelength (1550nm) film reflectance measurements have been carried out to test the sensing performances of the realized sensors. Experimental results on the capability to perform ammonia detection with ppm resolution at room temperature are here presented.

2. Sensor fabrication and characterization

The sensor has been fabricated by depositing, with the electrostatic spray pyrolisis technique, a tin dioxide layer on the distal end of a single mode SOF. The deposition process parameters, like the metal chloride concentration, the solution volume and the substrate temperature, have been changed in order to tailor the structural properties of the film such as crystalline size, thickness and porosity. The MOX layer growths due to the thermal transformation of metal chloride to metal oxide as a consequence of the interaction with water vapor according to the following reaction [4]:

$$SnCl_4 + 2H_2O \rightarrow SnO_2 + 4HCl \qquad (1)$$

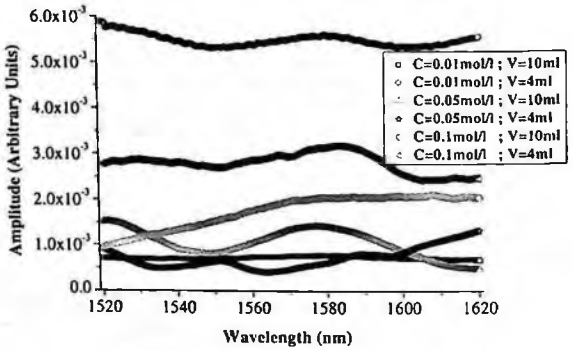

Figure 1: Reflectance spectra of the tin dioxide films.

In particular, for SnO_2 films fabrication two different volumes (4 and 10 ml) of an ethanol solution of $SnCl_4 \cdot 5H_2O$ with three different concentrations (0.01, 0.05 and 0.1 mol/l) have been prepared.

The reflectance of the films fabricated has been measured in the wavelength range 1520-1620nm by using a tuneable laser and an optical spectrum analyzer at constant temperature (20°C). The obtained spectra are shown in fig. 1. As can be seen, different deposition parameters lead to different reflectance spectra, demonstrating the optical and geometric features dependency of the fabricated films on the solution volume and $SnCl_4$ concentration.

3. Experimentals

The optical fiber based sensing system configuration [5] is reported in fig. 2. Reflectance measurements have been performed by lighting the optical fiber with a superluminescent diode (40 nm bandwidth) operating at a wavelength of 1550nm. To enhance the system performances, synchronous detection has been implemented: the light source has been externally amplitude modulated at 200Hz and the sensor outputs have been recovered by using two lock-in amplifiers. The normalized optoelectronic sensor output, V, consists of the ratio between the reflected signal from the sensing probe and the one corresponding to the source. The temperature has been constantly monitored by a fiber Bragg grating interrogation system [6] working at 1310nm. The sensor output sensitivity to temperature changes has been measured for the films under test demonstrating that a few degree temperature variation cannot affect the sensor output significantly. In this configuration any change of the system output signal can be attributed only to changes in the film reflectance. The sensor operating principle relies on the measurement of the light intensity reflected by the fiber-sensitive layer interface. The reflectance at the fiber end interface can be expressed as function of the optical and geometric features according to:

$$R = f\left(n_{eff}, \lambda, \varepsilon, d, n_{ext}\right) \tag{2}$$

where n_{eff} is the effective refractive index of the guided mode, λ is the optical wavelength, d is the film thickness, n_{ext} is the external medium refractive index and $\varepsilon = \varepsilon_1 + j\varepsilon_2$ is the complex dielectric function of the SnO_2 film.

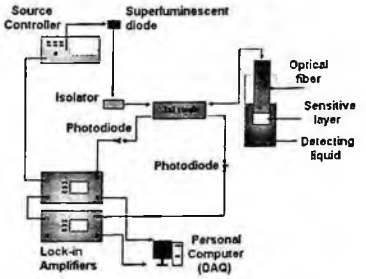

Figure 2: Schematic view of the optical fiber based sensing system.

Any effect able to modify the real or the imaginary part of the film dielectric function would modify the film reflectance according to the following equation:

$$\Delta R = \frac{\partial R}{\partial \varepsilon_1}\Delta\varepsilon_1 + \frac{\partial R}{\partial \varepsilon_2}\Delta\varepsilon_2 \tag{3}$$

4. Results

In order to evaluate the MOX based optical sensor response to ppm concentrations of ammonia, several insertions in the test baker of an ammonia aqueous solution (20.5% in wt.) have been performed. The NH_4OH quantity present in the aqueous solution for each insertion has been calculated to be approximately 4 ppm. For low concentrations of ammonia, the water refractive index changes can be neglected in respect to the variations in the dielectric function of the film due to the analyte sorption. Fig. 3 shows the optical response of the tin dioxide based sensor, fabricated by using a $SnCl_4$ concentration of 0.1 mol/l and a solution volume of 10 ml, to three steps of 4ppm ammonia concentrations. Response times lower than four minutes and a

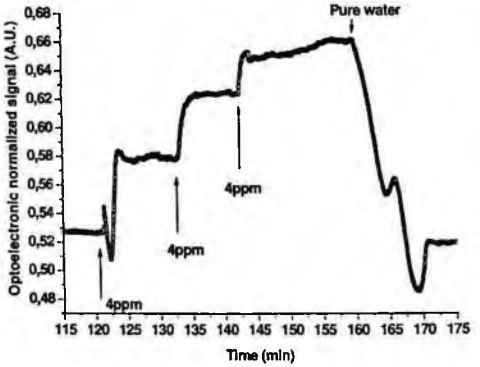

Fig. 3 Time response of the sensor.

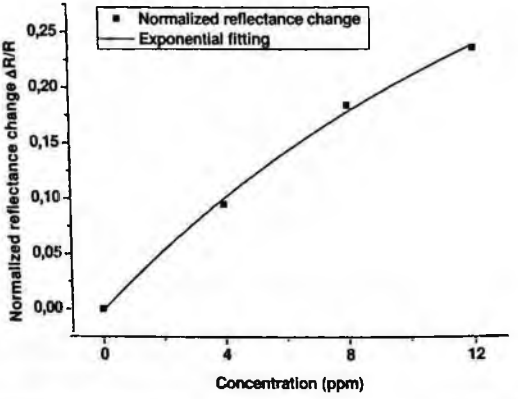

Fig.4 Normalized reflectance changes versus concentration unit.

recovery time, for an overall ammonia concentration of 12ppm, lower than fifteen minutes have been observed. In fig. 4 the calibration curve is reported in terms of relative reflectance changes. A non-linear dependency of the

optoelectronic normalized signal on the ammonia concentration has been revealed demonstrating an increase of approximately 26% for an overall ammonia concentration of 12ppm. Considering the minimum detectable normalized signal, a limit of detection as low as sub-ppm level has been obtained.

5. Conclusions

In summary, a novel SnO_2 based optical sensor for in water ammonia detection at room temperature has been demonstrated. The combination of the excellent sensing properties of MOX films with the potentiality of the optical fiber technology was proposed to develop a novel class of sensors able to work in water and at room temperature. Tin dioxide films have been successfully deposited onto the distal end of single-mode SOFs by means of the electrostatic spray pyrolisis deposition technique. The fabricated sensors have been employed in a reflectometric system involving single wavelength reflectance measurements in order to test the sensing performances. Here, experimental results are reported on the sensor capability to detect ppm ammonia concentrations in water at room temperature. Fast time response in the minutes range and sub ppm resolution was demonstrated.

References

1. D.D.Lee, D.S.Lee, Environmental gas sensors, IEEE Sensors Journal, Vol. 1, No 3, 2001,pp.214-224
2. M. C. Horrillo, A. Serventi, D. Rickerby and J. Gutierrez, "Influence of tin oxide microstructure on the sensitivity to reductor gases", Sensors and Actuators, B 58 (1999) 474-477
3. El Hadj Aldaphe Diagne, M. Lumbreras, "Elaboration and characterization of tin oxide - lanthanum oxide mixed layers prepared by electrostatic spray pyrolisis technique", Sensors and Actuators, B 78 (2001) 98-105
4. G. S. Korotchenkov, S. V. Dmitriev and V. I. Brynzari, "Processes development for low cost and low power consuming SnO2 thin film gas sensors (TFGS)", Sensors and Act. B: Chemical Vol. 54, Is. 3, pp 202-209
5. A. Cusano, A. Cutolo, M. Giordano, and L. Nicolais, "Optoelectronic refractive index measurements: application to smart processing," IEEE Sensors J., vol. 3, pp. 781-787, December 2003.
6. A. Cusano, G. Breglio, M. Giordano, L. Nicolais, A. Cutolo, "Dynamic strain measurements by fibre Bragg grating sensor", IEEE/ASME Trans. mechatronics, 9, 1, Mar 2004

ON-LINE FULLY AUTOMATED MEASUREMENT OF CR(VI) CONCENTRATION IN WATER BY A FIBER OPTIC PROBE AND A LOW COST SPECTROPHOTOMETER

GIULIO D'EMILIA(*), EMANUELA NATALE
Department of Ingegneria Meccanica, Energetica e Gestionale (DIMEG)
(*) Corr. Author, tel. +39 0862 434324, fax +39 0862 434303,
e-mail: demilia@ing.univaq.it
University of L'Aquila, Italy

A measurement system conjugating the flow-injection technique in an automatic system and a low cost spectrometer as the photo-detecting device has been set in order to evaluate the concentration of Chromium (VI) in water. Light absorption spectra of the complex Chromium (VI) – Diphenylcarbazide, carried into the measuring cell, were analysed to detect the effect of interfering quantities and substances by also operating with suitable data processing techniques, like neural network. The aim of this work is to check the feasibility of this approach, for on-line and distributed measurements. Aspects concerning instrumentation system and operating steps are analysed in order to evaluate uncertainty causes and their effects on the whole uncertainty of the methodology, taking into account requirements of method reproducibility and standardization.

1. Introduction

The measurement of pollution deriving from Chromium (VI), in particular in water, often requires distributed monitoring systems. In fact, in many areas industrial processes producing Chromium pollution in waste water (leather tanning industry, galvanic, wood and typographic industries...) are realized by little and diffused production sites so that a very diffused map of pollution sources should be taken into account in environmental monitoring.

In previous papers [1] [2] [3] a research work has been described aiming to set a simple and low cost automatic measuring apparatus for on line measurement of Cr(VI) concentration in water, which is able to be controlled by a PC and to be inserted in an integrated environmental control multi-sensor network. Measuring section is a miniaturized fiber optic probe, whose working principle is light absorption of the complex Chromium (VI) – Diphenylcarbazide, carried into the measuring cell by a flow-injection (FIA) technique. Automatic operating procedure and configuration were set, taking into account not only measurement procedure requirements, but also reduction of measurement uncertainty depending on interfering quantities of different type, fluid dynamic, optical, environmental, taking into account "in situ" measuring conditions.

FIA appear as a very used and accepted investigation tool in many applications of environmental interest, regarding both concentration evaluation of emissions in industrial effluents and process control of manufacturing continuous processes, due to its capability of allowing automated and high sampling rate analysis. Further advantages of FIA, which are well know too, could be summarized: suitable cost, reduced sample and reagent consumption and feasibility of procedures to be implemented. Very large amount of references can be found [4], [5].

The above mentioned characteristics have suggested to improve and to enlarge the field of application of this analysis approach, by using more sophisticated instrumentation and data processing techniques, like, for instance, spectrophotometry and neural network data analysis [1], [6], [7], [8].

This trend, if allows to remarkably enlarge the field of application of FIA and makes it powerful, on the other hand requires that attention should be paid to theoretical and experimental aspects concerning the reproducibility of measurements, useful for

validation and standardization of this technique, in order to set procedures which are widely acceptable and comparable as for results.
Taking in mind these considerations, a systematic effort aiming to evaluate the different uncertainty causes of measurements and to prevent errors could be very useful, both in the design activity of new instrumentation and in the operation of the existent instruments.
Therefore, analysis of causes of uncertainty in measurements could be very useful, with reference to many aspects, of operating type, like the temperature of fluids and components, the flow rate in ducts and in measuring probe, the sample volume effects, or connected to environmental problems, like interfering substances, or, finally, depending on data processing techniques, ...
Taking into account the above considerations, uncertainty analysis will be studied with reference to an application concerning a measuring method for Chromium (VI) concentration in water, by means of an automated measuring section, operating according to a FIA method; spectral absorbance measurements are carried out by means of a fiber optic low cost spectrometer, with possibility of acquiring a time sequence of spectra. Its working principle is light absorption of the complex Chromium (VI) – Diphenylcarbazide, with the final aim of setting up a simple and low cost automatic measuring apparatus for on line measurement of Cr(VI) concentration in water, which is able to be controlled by a PC and to be inserted in an integrated environmental control multi-sensor network.
Specific aspects of the methodology will be described in this paper, aiming to integrate, in prospective, in a quite simple, economic and efficacious way spectral measurements during a flow injection diagram and advanced data processing techniques based on neural networks.

2. The methodology and the test bench

The whole measuring chain is shown in figure 1. Typical experimental configuration for FIA analysis has been used; previous work has allowed to set the best operating conditions as for flow rate, geometry of flow cell, stability during time of operation [3].

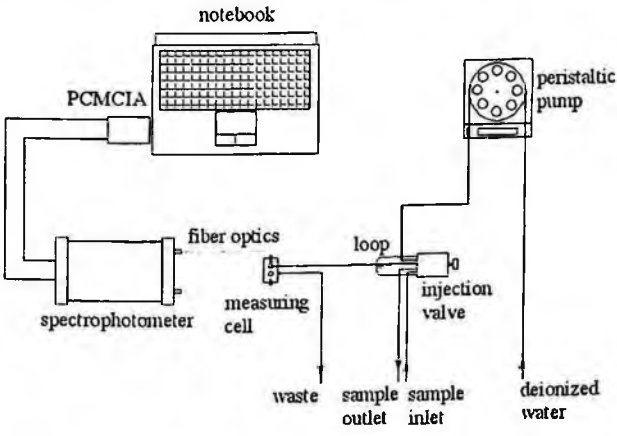

Figure 1. FIA based measuring system; a spectrophotometer is used for absorption spectra analysis.

In a miniaturized flow cell, absorption spectra are obtained by means of a low cost fiber optic spectrophotometer operating in the VIS wavelength range 400 to 700 nm; the flow cell, with miniaturized optics (GRIN focusing and receiving lenses) [1], is automatically feed with the sample to be analysed and a temporal sequence of spectra can be obtained, during the whole flow injection duration. All phases of the measurement procedure can be operated automatically, also with reference to a real field application.
Time interval between next spectra has been set to 0.4 s. A short sampling interval is useful for accurate time positioning of the maximum of FIA time absorption diagram.

3. Experimental results

In order to evaluate both uncertainty contributions and method sensitivity, tests have been carried out using water solutions as samples with a concentration of Cr (VI) in the range 0 to 500 µg/l.
If a specific wavelength is examined, as in figure 2, typical time diagram of a flow injection analysis can be obtained; it is to be noticed that for complex Chromium (VI) – Diphenylcarbazide the peak of absorbivity is at λ = 540 nm and can be done very high, being in the order of 232*102 l/(mol*cm). This value can be calculated from the diagram of figure 3.
In previous papers [1] [2] [3] has been showed that analysing the absorbance around the peak at 540 nm with a photodetector and in static conditions, that is filling directly the measurement cell with chromium solution, the absorbivity results to be in the order of 307*102 l/(mol*cm).
The reduced absorbivity value of FIA technique to respect the static analysis is due to diluition phenomena in the flow injection phase, that reduce the absorbance value.
Experimental repeatability of measurements results to be in the order of σrep= ± 8 µg/l.
All values refer to the peak absorbance at a wavelength of 540 nm.

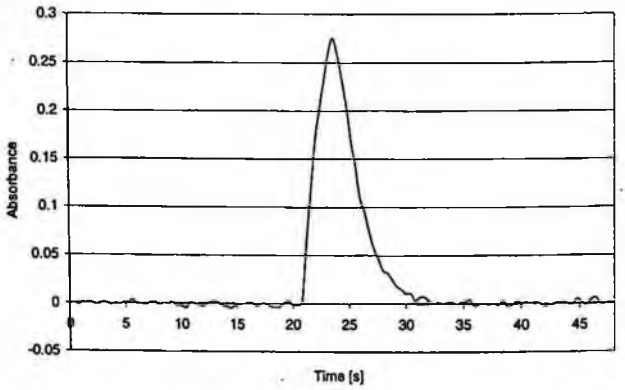

Figure 2. Time absorbance behaviour at: λ =540 nm, for a Chromium(VI) sample with a concentration of: (400 + 1)µg/l.

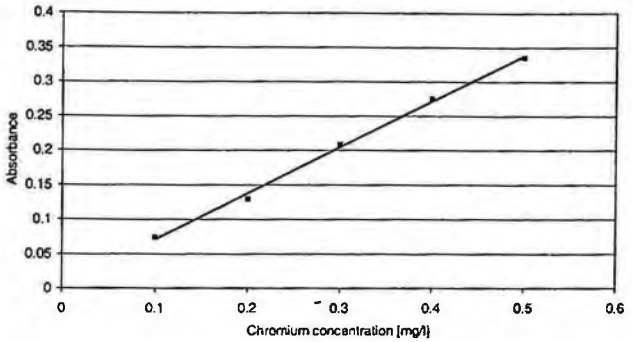

Figure 3. Peak absorbance diagram at 540 nm for Cr(VI) solutions.

Uncertainty of Cr (VI) in the used samples is $\sigma st = \pm 1$ µg/l. Linearity standard deviation, as computed from linear regression analysis, has been estimated to be $\sigma l = \pm 8$ µg/l.
If repeatability, linearity and standard contribution are taken into account a global standard uncertainty of $\sigma wh = \pm 12$ µg/l, could be estimated.
Spectral data for different Cr(VI) concentrations have been depicted in figure 4, with reference to the time instant corresponding to the peak absorbance, and have been analysed by means of a linear neural network.
Preliminary results show equivalent information with respect single wavelength analysis if the concentration of pure Chromium(VI) as to be measured. Spectral analysis by neural network approach will be used in the continuation of the research for identification of interfering substances.

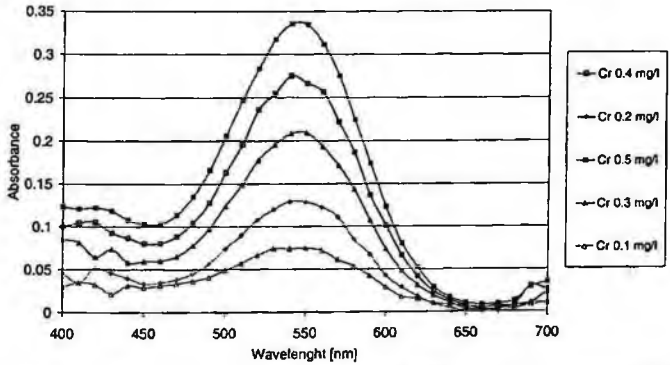

Figure 4. Peak absorbance spectra for solutions with different concentrations of Cr(VI).

4. Conclusion

An experimental procedure based on the flow-injection technique and a low cost spectrometer as photo-detecting device, has been set with the aim of reducing the whole uncertainty of Chromium (VI) concentration in water measurements.
A low cost spectrophotometer operating in the VIS wavelength range 400 to 700 nm was used for cost reduction, which, anyway, allowed to get a time resolved sequence of absorbance spectra at the time sampling of 0.4 s.

Chromium solutions in water in the range 0-500 µg/l have been analysed by this modified flow injection method, whose working principle is light absorption of the complex Chromium(VI) – Diphenylcarbazide. The specific wavelength of 540 nm has been examined, and at this frequency has been detected the absorbance time diagram peak; in this way an absorbivity of 232*102 l/(mol*cm) has been obtained.
If repeatability, linearity and standard contribution are taken into account, a global standard uncertainty of σwh= ± 12 µg/l has been estimated for this method. Preliminary results with a neural network method to analyse whole absorbance spectra encourage to pursuit this approach, in order to preventing effect due to interfering substances.

References

[1] D'Emilia G., " Fiber Optic Probe for Continous Measurement of Chromium(VI) Concentration ", Sensors and MicroSystem, Proceedings of the 5th Italian Conference extended to Mediterranean Countries, 12-16 Febbraio 2000, Lecce, Italy, pp. 404-408, World Scientific Publication, Singapore.
[2] D'Emilia G., Natale E., "Design and set up of an automatic device for on-line measurement of Cr(VI) concentration in water, based on a fiber optic probe", International Workshop on "New Developments on Sensors for Environmental Control", ENVSENS 2002, S. Cesarea Terme, Lecce, 27-29 Maggio 2002, pp. 179-184, World Scientific Publication, Singapore.
[3] D'Emilia G., Natale E., "On-line fully automated measurement of Cr(VI) concentration in water by a fiber optic probe: measurement accuracy improvement and evaluation", SPIE Paper 5459 – 39, PHOTONICS EUROPE, Strasburgo, Francia, 26-30 Aprile 2004.
[4] Ruzicka J. " Flow injection analysis: from test tube to integrated micro-conducts", Analytical Chemistry, vol. 55, 1993, pp. 1040-1053.
[5] Ruzicka J., Hansen E. H., " Flow injection analysis – Where are we heading?", Trends in Analytical Chemistry, vol. 17, no. 2, 1998, pp. 69-73.
[6] Ruisanchez I., Lozano J., Larrechi M.S.,Rius F.X., Zupan J., "On-line automated analitica signal diagnosis in sequential injection analysis systems using artificial neural networks", Analytica Chimica Acta 348 (1997) 113-127.
[7] Wang H., Zhou Y., Zhao Y., Li Q., Xingguo Chen X., Hu Z., "Optimization of on-line microwave flow injection analysis system by artificial neural networks for the determination of ruthenium", Analytica Chimica Acta 429 (2001) 207–213.
[8] Li-Xian Sun, Mahipal Reddy A., Matsuda N., Takatsu A.,Kato K., Tatsuhiro Okada T., "Simultaneous determination of methylene blue and new methylene blue by slab optical waveguide spectroscopy and artificial neural networks", Analytica Chimica Acta 487 (2003) 109–116.

NEW VOLTAMMETRIC METHOD FOR CHECKING TOTAL ANTIOXIDANT CAPACITY OF VEGETAL EXTRACTS

LUIGI CAMPANELLA, ELISABETTA MARTINI, GUIDO RITA, MAURO TOMASSETTI

Department of Chemistry, University of Rome "La Sapienza", P.le A. Moro 5, 00185 Rome, Italy.

Abstract

Some of the vegetal matrixes that are more common and more frequently described in the literature for their high antioxidant activity, such as green tea, black tea, rosemary and coffee, were selected. Methanol, acetone and aqueous dry extracts were prepared from each of these vegetal matrixes, using for extraction solvents considered to be complementary in processes for the extraction of antioxidant substances present in the vegetal matrixes. For the three extracts obtained from each matrix the antioxidant capacity was determined using a new electrochemical method based on the measurement of the anodic area of a cyclic voltammogram.

1. Introduction

The oxygen-free radicals are part of the large family of reactive oxygen species (ROS); that is, they comprise a species with a strong oxidizing tendency both of a radical nature, i.e. the superoxide radical and a non radical nature i.e. hydrogen peroxide. ROS owing to their strong reactivity, can cause damage to all molecules of the body [1]. For this reason, in recent years, growing efforts have been made in the fields of pharmaceuticals and foodstuffs to study socalled antioxidants, especially those of natural origin. For some years now our group has been engaged in measuring "in vitro" the antioxidant capacity of the active pharmaceutical principles contained in natural substances, especially those of vegetal origin [2, 3]. In the present research, unlike preceding work in which only homogenates and centrifugates of aqueous solutions of different plants, both fresh and dry, were investigated, a determination was made of the antioxidant capacity of dry methanol, acetone or aqueous extracts of several common vegetal matrixes that are frequently cited in literature for their very high antioxidant activity (green tea, black tea, rosemary, coffee). The antioxidant capacity of the extracts produced from these five matrixes was determined using an electrochemical method based on measuring the anodic area of a cyclic voltammogram [4]. The results obtained for the respective extracts were then compared in order to discover the best solvent to use for extraction from the point of view of total extract quantity and total antioxidant

capacity. Furthermore a determination was performed also on infusions made using the same vegetals.

2. Experimental

2.1. Samples analysed

In the present work several matrices of common vegetals were analysed; the total antioxidant capacity of dry extract of each sample was evaluated, specifically: Green Tea, Black tea, Rosemary and Coffee.

2.2. Obtaining and testing the dry extracts and infusions

All the vegetal matrixes were tested in the solid state: tea leaves, rosemary needles, ground coffee beans. For this reason solid/liquid extractions were required. Water, acetone and methanol were selected as extracting solvents, that is, the three solvents most frequently used for this purpose according to the literature [5]. The extract was obtained using 1 g of the different matrixes which, after being ground up and placed in the different solvents. In the case of methanol and acetone extracts the extraction was performed using a Soxhlet, refluxing for four hours; the total volume of extracting solvent was 25 mL. In the case of aqueous extract the sample was placed in a round-bottomed flask with 25 mL of solvent and maintained in reflux ebullition for 1 h. After extraction the mixture was centrifuged for 10 min at 3000 rpm. The supernatant was evaporated to dryness by Rotavapor (in the case of acetone and methanol), or by heating with a vacuum pump (in the case of water). In the voltammetric analysis the dry extract obtained from 1g of substance was placed in the measuring cell and dissolved in 20 mL of working solution. As well as the measurement of the antioxidant capacity of the dry extracts of vegetal substances tested by us, the same matrixes were used to obtain also aqueous infusions. The method followed to obtain the infusion was varied as the matrix analysed varied. For equal weights (1g of substance) infusions were prepared from the following vegetal substances: green tea and black tea. The infusions of these vegetal substances were prepared from 1 g of substance, placed in 100 mL of distilled water, at 95 °C and left to stand for 5 minutes. The coffee, on the other hand, was obtained using a classical moka machine. For the infusions of green tea, black tea and coffee, the measurement of antioxidant capacity using the voltammetric method was carried out on 1 ml of infusion obtained using the above-mentioned procedures. For rosemary, on the other hand, in view of the type of solid matrix, 1 g of needles were weighed out and placed in a 5%,

methanol solution for 3 days: the antioxidant capacity was then measured using 1 mL of the infusion obtained.

3. Method

3.1. Cyclic voltammetry measurements

All measures of antioxidant capacity were performed using a method based on cyclic voltammetry, which has recently been investigated in our laboratory [6], using an AMEL polarograph (mod.433). The tests were run in a voltammetric cell using three electrodes: a glassy carbon electrode as indicator electrode, a platinum electrode as counter electrode and a calomel electrode as reference electrode. The measuring cell, which was connected to a nitrogen bubble, contained the working solution with a supporting electrolyte ($NaClO_4$ $0.1 molL^{-1}$) and the analyte; between the working electrode and the reference electrode a variable potential difference was applied as a triangular waveform, obtaining the corresponding response in current. The tests were run in "inverse scanning" mode starting from more negative potentials (-0.3 V) in the direction of more positive potentials (+1.3 V); the scanning direction was then inverted, returning the potential to its initial value. The voltammogram, recorded at a scanning rate of 400 mV/s and with a bottom of scale of 40 μA, displayed a cathodic reduction curve and an anodic oxidation curve that were generally highly asymmetric. At the end of the analysis, the area below the anodic curve of the voltammogram was taken into consideration (see fig.1). The method was based on the correlation between this anodic area and the total antioxidant capacity of the sample. The anodic area represents the reductive, and therefore antioxidant, capacity of the test substance; the anodic curve actually depends on the substance's electron donating capacity and therefore, in a context in which free radicals are present, on the capacity to act as a radical scavenger. The results may be expressed as (mg) equivalents of vitamin C, the reference standard, through simple proportion between the anodic area of the standard and that of the sample. Ascorbic acid was selected as reference in the calculation of antioxidant capacity owing to the excellent reproducibility of the anodic curve (see Table 1) of its voltammogram and also because it is an antioxidant compounds that is relatively widespread in nature and in diets.

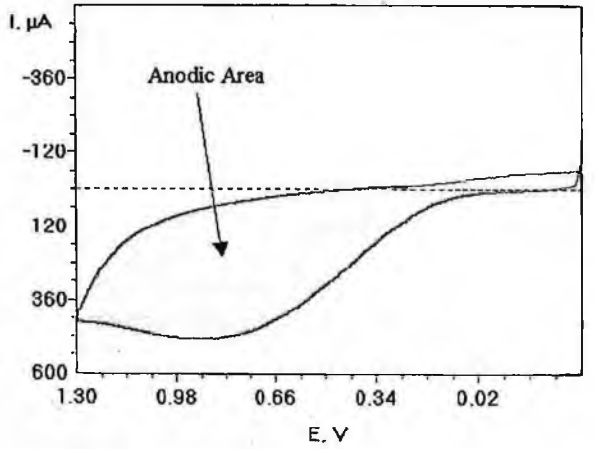

Figure 1: cyclic voltammogram of a vegetal infusion of green tea showing the anodic area, the size of which is proportional to the antioxidant capacity of the sample.

Table 1: Equation of calibration curve obtained with increasing Ascorbic Acid concentrations.

Linear range for Ascorbic Acid	0.5-2.0x 10^{-3} mol L^{-1}
Equation of calibration curve	y = 4.46x + 0.55
r^2	0.99865
Precision of measurement (RSD%)	≤ 5

4. Results and Discussion

In table 2 the mg of substance extracted using the respective solvents from 1g of the original matrix, and in table 3 the total antioxidant capacity of each of these extracts, expressed as mg of ascorbic acid equivalent.

Table 2: comparison of results obtained for the samples analysed, mg of dry extract obtained using different extraction solvents from 1g of sample.

SAMPLE	Methanolic dry extract (mg)	Acetonic dry extract (mg)	Aqueous dry extract (mg)
Coffee	310.0	190.0	350.0
Green tea	410.0	470.0	340.0
Black tea	300.0	380.0	270.0
Rosemary	370.0	180.0	50.0

Table 3: comparison of results obtained for the samples analysed, total antioxidant capacity of dry extract obtained using different extraction solvents.

SAMPLE	Methanolic dry extract (*)	Acetonic dry extract (*)	Aqueous dry extract (*)
Coffee	492.4	156.8	726.5
Green tea	962.6	506.0	908.5
Black tea	809.1	373.1	760.3
Rosemary	672.0	678.7	606.6

* Total antioxidant capacity (as mg equivalent of ascorbic acid).

From the results obtained (tables 2 and 3), the best extraction solvents were sometimes found to be water, sometimes acetone and sometimes methanol. On the other hand, methanol extracts and aqueous extracts are those that generally display greater total antioxidant capacity. Furthermore, extraction with water is much faster and cheaper and any solvent residues in the extracts do not entail any toxicity for the human organism. Aqueous extracts are therefore of great interest to the pharmaceuticals and food industry. Also methanol is an excellent extracting solvent and indeed can dissolve many classes of antioxidant compounds very well [7]. The acetone extraction of antioxidant substances contained in vegetal matrixes is the one that was found to be least effective in two cases out of four. Moreover, acetone extracts are those with the lowest total antioxidant activity. For these extracts it is also impossible to hypothesize any application in the food sector in view of the toxic effects of acetone on human body. However, it cannot be ruled out that acetone extracts can be used in the pharmaceuticals field after complete drying. Lastly, fig. 4, shows the antioxidant capacity in mg of ascorbic acid equivalent determined using the voltammetric method on 1 mL of infusion, obtained for each of the vegetal matrixes considered after performing the various pre-treatments described in section 2.2. Clearly, in this case, the values obtained are strongly affected also by the lack of homogeneity in the pre-treatments by which the infusions have been obtained.

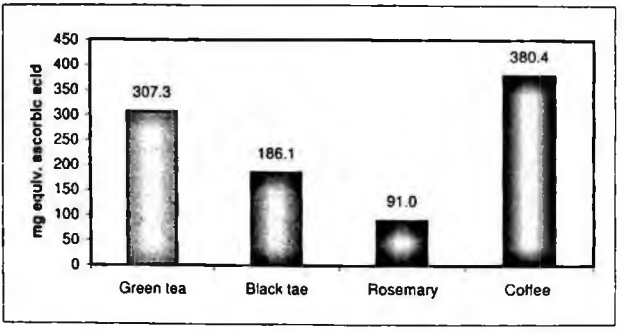

Figure 4: antioxidant capacity values referring to vegetal substances in the form of infusions.

5. Conclusions

It was found that, although the aqueous and methanol solvents did not always extract the greatest percentage by weight of dry product, they were certainly those that extracted the greatest quantity of antioxidant product percentage wise. It must also be pointed out that the voltammometric method used made it possible, without any pretreatment, to measure the antioxidant capacity of all the extracts and infusions of the different vegetal matrixes tested.

References

1. A. Romay, J. Armesto, D. Remirez, R. Gonzales, N. Ledon, I. Garcia; *Inflamm. Res.*, 47 (1998), pp 36-41.
2. Musa Özcan; *Grasas y Aceitas*, 50 (5) (1999), 355-358.
3. L. Campanella, A. Bonanni, G. Favero, M. Tomassetti; *Anal. Bioanal. Chem.*, 375 (2003), 1011-1016.
4. S. Chevion, M.A. Roberts, M. Chevion; Free Rad. Biol. Med., 28 (2000), 860-870.
5. L. Tavani, A. Pregnolato, C. La Vecchia, E. Negri, R. Talamini, S. Franceschi; *Int. J. Cancer*, 73 (1997), 193-196
6. L. Campanella, A. Bonanni, D. Bellantoni, M. Tomassetti; *Journal of Pharm. Biomed. Anal.* 35 (2004), pp 303-320.
7. K. G Lee, A. E. Mitchell, T. Shibamoto; *J. Agric. Food Chem.*, 48 (2000), 4817-4820.

NEW STRATEGIES TO ASSEMBLE SELECTIVE AND SENSITIVE SENSORS FOR DETECTION OF NITRITES

VANESSA BIAGIOTTI, FEDERICA VALENTINI, DANILA MOSCONE, GIUSEPPE PALLESCHI
Chemistry Department, Tor Vergata University , via della Ricerca Scientifica 1, 00133 Rome,(Italy)

ANTONELLA CURULLI
Institute of Nanostructured Materials (ISMN) CNR, Division II, via del Castro Laurenziano 7, 00161 Rome (Italy)

MIHAELA BADEA
Biotechnology Department, Institute for Chemical Research, University of Bucharest, Bucharest, Romania

Platinum electrodes modified with electropolymerised film were assembled for rapid amperometric detection of nitrites. Parameters such as the permeability of the fims to nitrites, interference effects and film morphology were studied. The new nitrite sensor was fully characterized by Flow Injection Analysis (FIA).

1. Introduction

In recent years, there has been a growing concern about the role of the nitrite ion as an important precursors in the formation of N-nitrosamines, many of which have been shown to be carcinogens[1]. The occurrence of nitrite salts in the environment and their use for food preservation is widespread[2]; therefore it is important that sensitive and accurate methods be available for the determination of nitrite ion. Numerous papers have been published on the determination of nitrite. Among them, spectrophotometry and ion-chromatography are mainly used. Electrochemical methods offer useful alternatives since they allow faster, cheaper and safer analysis[3]. Accordingly, it is well known that nitrite is oxidized at platinum, glassy carbon (GC), gold, diamond, and transition metal oxides electrodes[4]. However, the application of these electrodes is limited because several species may poison the electrode surfaces and decrease the electrode sensitivity and accuracy. Therefore, a new and elegant approach for these analytical purposes, implies the use of chemically modified electrodes (CMEs) which have been developed to decrease the overpotential for nitrite oxidation. In this work, we modify platinum electrodes by electropolymerised films. For this purpose non-conventional conducting polymers, such as: poly(1,2-;1,4-

diaminobenzene), poly(1,8-diaminonaphtalene) and o-anisidine, had been electrochemically synthesised and characterised.

2. Experimental

2.1 Reagents and solutions

1,2-Diaminobenzene (1,2-DAB), 1,4-diaminobenzene (1,4-DAB), $NaNO_2$ were from Sigma Chemical Co., St. Louis, MO. 1,8-Diaminonaphtalene (1,8-DAN), o-anisidine and Phenol were from Fluka, Buchs, Switzerland. ; CH_3COOH, NaH_2PO_4, CH_3COONa, HCl, H_2SO_4, Na_2SO_3, NaOH, Ascorbic Acid were from Carlo Erba, Milano, Italy ; Pt foils 0.025 mm thick were from Sigma Aldrich; Al_2O_3 0.3 and 0.05 μm were from Buehler, Evanston, IL.
All solutions were prepared with distilled water.

2.2 Apparatus

Voltammetric studies were carried out using an Autolab potentiostat PGSTAT-10 with GPES 3 software. For amperometric measurement we used a 641-VA Detector (Metrohm, Switzerland) and currents were recorded using a Linseis L6512 recorder (Linseis, Selb, Germany). A combined auxiliary/reference electrode (Pt- Ag/AgCl/ 3 M KCl) model 805/CPG/12 was used. For FIA apparatus we used a wall-jet cell (Model 656) from Metrohom, Herisau, Switzerland, assembled with platinum working electrode (3 mm diameter), platinum counter electrode and Ag/AgCl reference electrode. The peristaltic pump Minipuls 3 (Gilson, France), the PTFE connection tubes (i.d. 0.5 mm) from Supelco (Bellofonte, CA) and a six-way injection valve (Model 5020) with a closed loop of 250 μl (Rheodyne, USA) were used.

2.3 Procedure

2.3.1 Electrode polishing

The platinum electrode surfaces were polished with alumina powder of particle sizes of 0.3 and 0.05 μM before use. After rinsing with distilled water, the electrodes were pre-treated by potential cycling in 0.5 mol/l H_2SO_4 from 0 to +1.0 V (vs SCE) at a scan rate of 20 mV/s until no changes were observed in the cyclic voltammograms (at least 20 cycles).

2.3.2 Electropolymerisation

1,2-DAB, 1,4-DAB, 1,8-DAN and o-anisidine were electropolimerised on the electrode surface by cyclic voltammetry. All the monomers, except the diaminonaphtalene isomers were used at a concentration of 5 mM and dissolved in 0.1 M phosphate buffer solution at pH 6.5. The substituted naphthalene derivative was electropolymerised in 3 M HCl because of his higher hydrophobicity. The potential was continuosly cycled (10 cycles) from 0 to + 0.8 V except for 1,8-DAN when the potential was cycled from – 0.15 to + 1.3 V. The scan rate was 2 mV/s. The electrodes were stored dried when not in use.

3. Results and discussion

Since the potential of nitrite oxidation is high, many other electroactive species can be oxidised and thus interfere with the nitrite analysis. In order to avoid these interferences we covered the electrode surface with electropolymerised films. We selected three interferences wich can be oxidased at our applied potential: ascorbic acid (AA) wich is the classic interferent in nitrite determination, phenol (PhOH) which can be present in polluted waters and solfite (SO_3^{2-}) which is a little anion comparable to nitrite.
Film's permeability to target analyte and interferences was evaluated in cyclic voltammetry. We compare peak current relative to each one at a concentration of 40 mM in 0.1 M acetate buffer pH 4.

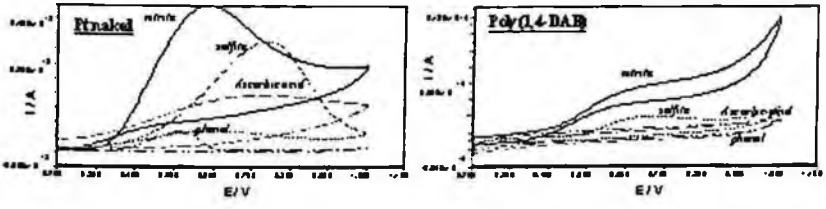

The permeability (P%) was defined as follows:

$$P\% = (I_{film}/I_{bare})*100$$

Where I_{bare} was the peak current when the electrode is naked and I_{film} was the peak current when the electrode is covered by electropolymerised film.
Then we evaluate the ratio $P\%_{nitrite}/P\%_{interferences}$ and we reported the results in following table:

	P_{NO2}/P_{AA}	$P_{NO2}/P_{SO3\,2-}$	P_{NO2}/P_{PhOH}
1,2-DAB	2.0	0.16	0.35
1,4-DAB	4.9	17.5	0.74
1,8-DAN	1.3	0.38	0.021
o-anisidine	13.7	0.83	0.14

Better results in terms of selectivity was obtained with poly(1,4-DAB).
For this reason electrodes modified with this polymer were putted in a FIA system to evaluate analytical parameters:

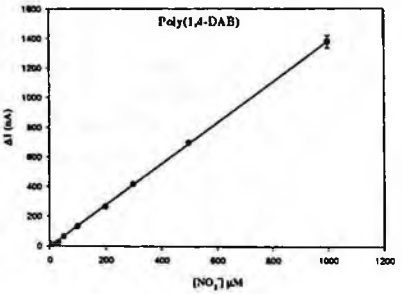

linear range: 10-1000 μ M
linear regression:
Y/(nA) = 1.10x/ (μ M)
LOD: 1.82 μ M
response time: 12 ± 1 s

The obtained LOD was lower than nitrite concentration law limit for drinking water in Italy (2μM).

Polymers were also observed at FE-SEM in order to verify morphology. Images of poly (1,4-DAB) show clearly the typical globular structure of polymeric films obtained by cyclic voltammetry using platinum foil as working electrode.

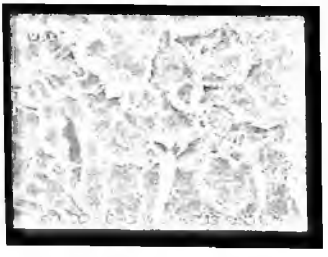

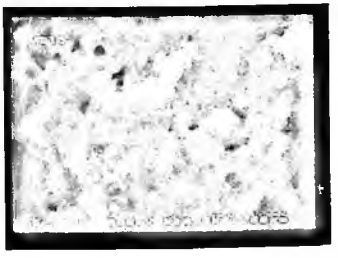

Acknowledgments

The authors wish to thank the FIRB project for financial support.

REFERENCES

1. Hall, et al., Med. Toxycol., 1 (1986), 470-471;
2. P.F. Swann, Proc. R. Soc. Med. 70 (1977) 113;
3. M. Badea, et al, J. of Electroanalytical Chemistry, 509 (2001), 66-72
4. R. Guidelli, F. Pergolo, G. Raspi, Anal. Chem., 44 (1972), 745

GOLD-BASED SCREEN-PRINTED SENSOR FOR DETECTION OF ARSENIC

SERENA LASCHI[1], ILARIA PALCHETTI, MARCO MASCINI

Università degli Studi di Firenze, Dipartimento di Chimica, Polo Scientifico via della Lastruccia 3, 50019, Sesto Fiorentino, Firenze, Italy.

Abstract

Screen-printed sensors are interesting devices for disposable, cheap and reliable analysis of heavy metals in connection with stripping analysis.
In this paper, we describe a novel gold-based screen-printed sensor which avoids the toxicity and the environmental contamination associated with mercury based sensor. The sensor consist of a screen-printed three electrode cell: a gold working electrode, a silver pseudo-reference electrode and a graphite counter electrode. It is used in combination with Square Wave Anodic Stripping Voltammetry (SWASV), using a portable electrochemical instrument.

The developed sensor was applied to arsenic detection. The optimised analytical parameters allows the convenient monitoring of micromolar and sub-micromolar concentrations of As(III) following short deposition time. Preliminary results on environmental samples analysis are illustrated.

1. Introduction

Stripping analysis is a powerful tool for measuring heavy metals in environmental, clinical and industrial samples [1]. For these applications mercury-based electrodes have been traditionally employed in order to obtain high reproducibility and sensitivity. However, the growing interest in decentralised analysis, coupled with environmental issues, requires new approaches involving mercury-free electrochemical sensors.

Gold electrodes of different forms (solid as well as gold-film electrodes) have been used to detect heavy metals [2]: however, with a reusable sensor, there are problems of electrode surface fouling, which is one of the main drawbacks of electrochemical sensors. Among other techniques, screen-printing technology is a particularly attractive technique for the mass production of cheap and disposable sensors [3].

The present paper describes the application of a gold-based screen printed sensor to As(III) detection by using SWASV as electrochemical technique. The method utilises electrolytic deposition of arsenic onto a gold film and its subsequent reoxidation by performing a voltammetric scan against more positive potential values:

[1] *Corresponding author. Fax: (+39)-055-4573397. E-mail:serena.laschi@unifi.it*

Accumulation step: $As(III) + 3e^- \rightarrow As$

Stripping step: $As \rightarrow As(III) + 3e^-$

Thereafter, SWASV measurement is performed by using the optimised conditions.

2. Screen Printed Electrode

The electrochemical cells were planar three electrode strips, based on a gold working electrode, a carbon counter electrode and a silver pseudo-reference electrode (Figure 1).

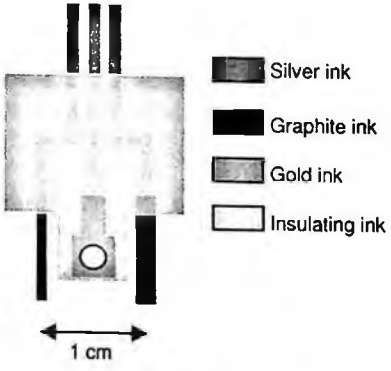

Fig. 1: Scheme of a screen-printed gold sensor

The electrodes were screen-printed in house using a DEK 248 screen-printing machine (DEK, Weymouth, UK).

Silver-based (Electrodag PF-410) and graphite-based (Electrodag 423 SS) polymeric inks were obtained from Acheson Italiana (Milan, Italy); the gold-based ink (R-464 (DPM-78)) was obtained from Ercon Inc. (MA, USA) and the insulating ink (Vinylfast 36–100) from Argon Italiana (Lodi, Italy). A polyester flexible film (Autostat CT5), obtained from Autotype (Milan, Italy), was used as the printing substrate. The silver ink was printed to obtain the conductive tracks and the silver pseudo-reference electrode. The carbon and gold inks were then printed to obtain the auxiliary and working electrodes, respectively. After each step, silver, carbon and gold inks were cured at 120° C for 10 min. The insulating ink was finally used to define the working electrode surface (Ø= 3 mm). A curing period of 20 min at 70° C was applied.

All the experiments were carried out using a PalmSens portable electrochemical analyser (Palmsens BV, Houten, The Netherlands).

Square wave voltammetry conditions were: conditioning step (E_{cond}): +0.7 V for 30 s, deposition step (E_{dep}): -0.5 V for 180 s, equilibration time (t_{eq}): 15 s. Stripping analysis: scan range: from -0.5 to +0.7 V, pulse amplitude (E_{amp}): 28 mV, step potential (E_{step}): 3 mV, frequency *(f)*: 15 Hz. The medium used was HCl 2 M.

3. Analytical procedure

Medium concentration and accumulation time were experimentally optimised.

SWASV cycles of As(III) 100 µg/L were performed in solutions containing various HCl concentrations. The heights of the obtained peaks were then plotted against the HCl concentration obtaining the graph reported in figure 2:

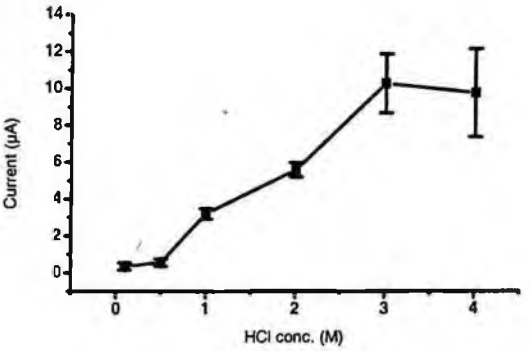

Fig. 2: Optimisation of HCl concentration. SWASV on As(III) 100 µg/L

As it can be seen, a high response with good reproducibility is obtained with a concentration of HCl 2 M; with acid concentrations higher than 2 M a higher response was observed, but the reproducibility was very poor.

Accumulation time also influences the sensor performance. To investigate this effect, As(III) 100 µg/L was detected by SWASV cycles using different accumulation times: in this case, peak currents increase until a value of 180 s; for times higher than it, the height of the peak decreases, whereas the reproducibility of the measure is reduced (%RSD higher than 15%). This is probably due to the formation of a layer of As^0 which insulate the electrode surface. For this reason, an accumulation time of 180 s was used.

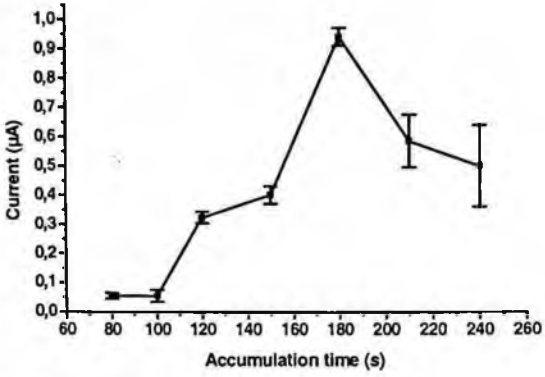

Fig. 3: Optimisation of the accumulation time. SWASV on As(III) 100 µg/L

4. Calibration curve for As(III)

Figures 4a and 4b show respectively SWASV voltammograms and the corresponding calibration curve obtained for As(III) in the range 0-300 µg/L, using the optimised conditions.

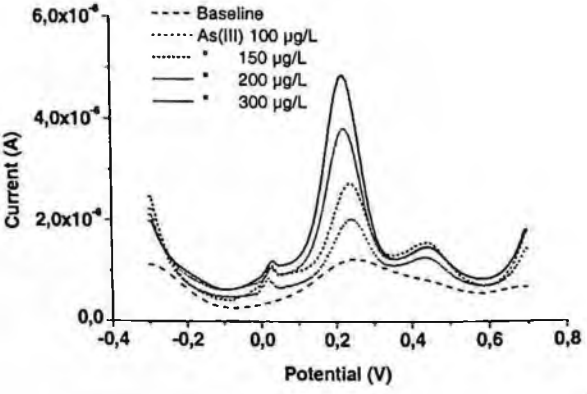

a)

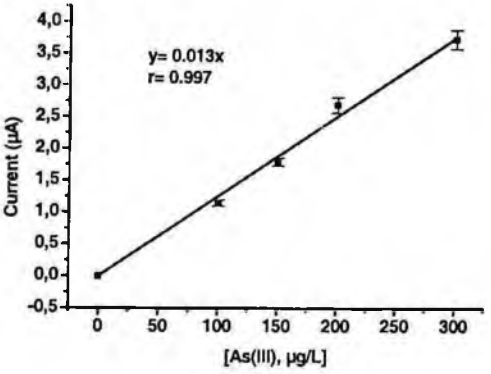

b)

Fig. 4: ASV voltammograms **A)** and related calibration curve **B)** obtained for As(III) in the concentration range 0-300 μg/L.

A linear response was observed in the investigated range (r=0.997), coupled with a good reproducibility; a %RSD of 4% was calculated on the slope of the curve obtained in triplicate. The theoretical detection limit of the method, calculated as three times the standard deviation of the blank divided by the slope of the curve, was of 12 μg/L, whereas not less of 80 μg/L was experimentally detectable.

5. Conclusions

The proposed gold-based screen-printed electrodes are suitable electrochemical devices for As(III) detection. The reported data indicate that the proposed gold-based sensor holds great promise for decentralised testing for As(III) using a "mercury free" sensing surface.

References

[1] Ashley K., Electroanalytical applications in occupational and environmental health, Electroanalysis, (1994), 6, 805–820.
[2] Brainina Kh. and Neyman E., Electroanalytical Stripping Methods, John Wiley & Sons, Inc., New York, 1993, pp. 49-65.
[3] I. Palchetti, S. Laschi, M. Mascini, Miniaturised stripping-based carbon modified sensor for in field analysis of heavy metals, Analytica Chimica Acta, 530, (2005), 61-67.

FURTHER INVESTIGATION ON ISEs FOR CATIONIC SURFACTANT ANALYSIS

LUIGI CAMPANELLA, FRANCESCO CAVALLARI, ELISABETTA MARTINI, MAURO TOMASSETTI

Department of Chemistry, University of Rome "La Sapienza", P.le A. Moro 5, 00185 Rome Italy

Abstract

A polymeric membrane ion-selective electrode (ISE) has been constructed to be used to determine quaternary ammonium salts contained in detergents for industrial use. The sensor we developed is based on PVC, as base polymer, and dibutylphthalate as plasticizer. The polymeric membrane thus obtained also contains a dodecyltrimethylammonium reineckate (DDTMAR) as cationic exchanger, which gives the membrane its characteristics of selectivity. For the electrochemical characterization of the ISE a standard dodecyltrimethylammonium bromide (DDTMABr) solution was used.

1. Introduction

Frequently one considers that the use of the surfactants consists only in domestic or industrial cleanliness; on the contrary their versatility is wide and their utilization turns to very different fields. Really are interested in the surfactants the textile industry, the pharmaceutical industry, the metallurgical industry, the oil industry, the industries of polymers and paints, the tanning and paper industries, the mineral industry and so on. Surfactants are also used for the study of the electrostatic interactions in solution and the behaviour of the colloidal systems; they are also employed in biological researches as a model of simplified membrane microenvironment study. Object of this research was to set up, owing to our previous researches in this sector [1,2], a method of analysis for the determination of several cationic surfactants in commercial products, used commonly to clean of industrial silos containing mineral oils, or for their action as biocids.

2. Methods

Preparation of the exchanger: The dodecyltrimethylammonium reineckate (DDTMAR) was prepared by mixing 100 mL of dodecyltrimethylammonium bromide, $5x10^{-3}$ molL^{-1}, with 100 mL of a solution of Reinecke salt, $5x10^{-3}$ molL^{-1}. The dodecyltrimethylammonium reineckate precipitate obtained was filtered, washed twice in distilled water and finally dried at room temperature for 12 h. Ultimately this dried exchanger was collected on a filter paper, placed on a Petri dish and stored in an dessicator until used.

Preparation of the membrane: The polymeric membrane of the ISE was obtained by means of the following operations: 165 mg of PVC (as basic polymer) were dissolved in 3 mL of THF, stirred using a magnetic bar in a 25 mL glass stoppered Erlenmeyer flask; after 1-2 hours (when completely dissolved) 8.25 mg (5% by weight) of DDTMAR exchanger was added; after the solution had become homogeneous, 330 mg of dibutylphthalate (DBP) was added as plasticizer; after stirring for about 1 hour, the solution was allowed to evaporate in a Petri dish (5.5 cm in diameter) for two days until a completely dry membrane was obtained. The disk was then stored in a dessicator, protected by Parafilm.

Preparation of the internal solution: a 10^{-2} molL^{-1} in DDTMABr and 10^{-1}molL^{-1} in KCl internal solution was prepared. To this end the appropriate quantities of KCl and DDTMABr were weighed out, placed in a 50 mL graduated flask and made up to volume with distilled water.

Preparation of the binder and application to the membrane: the adhesive was prepared by dissolving a small quantity of PVC in cyclohexanone. This adhesive was then used to attach the membrane to a small tube, also made of PVC. After gluing, in order to guarantee a homogeneous pressure that would favour lasting adherence a circular Al sheet, 2.5 cm in diameter, was positioned on top of the glued membrane so as to form a base to support the weight of a 50mL beaker filled with water balanced on the aluminium disk. By means of its weight, the beaker made the adherence of the membrane uniform. The whole assembly was allowed to stand in this position overnight.

Potentiometric measure: The ISE device and the calomel reference electrode were coupled to the potentiometer. Both were then immersed in a 50 mL beaker containing 10 mL of distilled water at room temperature and under stirring (using a magnetic bar). In this way the following electrochemical cell was constructed:

Ag / AgCl, KCl 10^{-1} molL^{-1}, DDTMABr, 10^{-2} molL^{-1}/Exchanger membrane /Aqueous solution /Hg_2Cl_2, KCl_{sat} / Hg

3. Results and Discussion

1st Measuring procedure: A 3% solution p/v, that is, (10^{-1} molL^{-1}) as dodecyltrimethylammonium bromide standard (DDTMABr) was prepared. The electrode was conditioned in distilled water for (12 - 15) minutes, until a stable value was obtained for the potential; additions were therefore made of aliquots (from 10 to 300 μL) of the DDTMABr solution and the potential differences obtained were recorded. Subsequent tests were carried out, repeated using the same electrode. The slopes and the correlation coefficients of the calibration straight lines thus obtained are shown in table 1.

The calibration straight line thus obtained is displayed in figure 1. The ISE response time was found to be very rapid, in the order of 15-20 s; the regression straight line shows a Nernstian slope over a wide linearity range and a very satisfactory correlation coefficient.

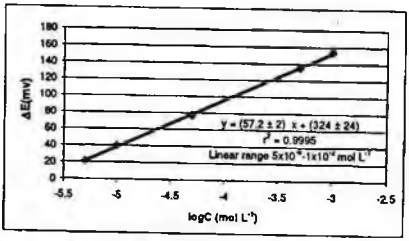

Fig.1: Trend of calibration straight line obtained for individual additions of standard solution of DDTMABr, i.e. using the 2nd measuring procedure.

4. Analysis of commercial sample

By means the calibration straight line shown in figure 1, obtained using the DDTMABr standard and the 2nd measuring procedure, four commercial samples have been analysed; the results are shown in table 2. As may be observed in this table, the alkyldimethylbenzylammonium chloride (ADMBACl) contained in the sample 1 and the didecyldimethylammonium chloride (DDDMACl) contained in the sample 3 seem to present extremely high concentration values compared with the values of the concentrations usually contained in the commercial samples, while the alkyltrimethylammonium chloride (ATMACl) contained in the sample 2, and hexadecyltrimethylammonium chloride (EDTMACl) contained in the sample 4, which possess very similar molecular structures. present very similar concentration values, lower than those of the sample 2 and 4, although still rather high taking account of the relevant values in the literature [3, 4]. In order to elucidate several anomalies occurring in these results, a series of tests was run also to determine the following:

–Any positive interference due to the phenyl and benzyl group in the case of the commercial product containing alkyldimethylbenzylammonium chloride. For this purpose, the possibility of modifying the Nernstian slope of the instrument response was investigated by analyzing the standard DDTMABr in aqueous solution containing benzoic or phenylacetic acid at different concentrations in order to verify the sensor response trend under somewhat similar conditions to those in which sample 1 is measured. However, on the basis of the results obtained, no actual correlation is found between benzoic or phenylacetic acid concentration in the solution and exchange membrane response. –The influence of the steric hindrance of the quaternary ammonium salt of the product tested; this was evaluated using tetrabutylammonium iodide, a molecule that contains no unduly long methylene chains but has a substantial steric hindrance. It has

Tab. 1: Analytical data referring to successive calibration straight lines, between 3×10^{-5} and 1×10^{-2} mol L^{-1}.

Straight line, n°	Slope (ΔmV/ΔlogC) (C=molL^{-1})	r^2
1.	54.1	0.9999
2.	56.2	0.9991
3.	48.6	0.9997
4.	50.8	0.9991
5.	51.4	0.9997
6.	52.5	0.9996
7.	49.4	0.9992

This 1st procedure, based on successive additions of DDTMABr to the aqueous solution, proved not to be wholly applicable to quantitative measures, under the operating conditions described. The results obtained actually show that the sensor membrane retains a "memory" of the DDTMABr concentrations previously used and, although with highly diluted additions, the successive calibrations produce straight line intervals that are shifted towards higher concentrations (with a decrease in slope, see Table 1), which would cause appreciable dosage errors. It is as though the exchange capacity of the membrane is partially inhibited. On the other hand, its exchange capacity represents the fundamental principle of the analytical mechanism in obtaining the electrochemical signal. A different approach it was therefore used which implied the use of a different operating procedure.

2nd Measuring procedure: Taking into account the results obtained using the 1st procedure, it was decided to consider only the potential values obtainable after the first addition; to this end, the potential measured when the electrode is immersed in 10 mL of distilled water, is allowed to stabilize; a small aliquot (of the order of several tens of μL) of the standard solution of DDTMABr is added and the corresponding potential measured after the addition. A subsequent analogous measure is then made after washing the cell and allowing the electrode to stabilize in 10 mL of distilled water. The results of the potential variations obtained using this second procedure are shown in table 2.

Tab.2: Results of concentration calculated for all four commercial samples tested using DDTMABr as reference standard

Samples	Concentration (mol L^{-1})
Sample 1 containing ADMBACl	56.6 ± 6
Sample 2 containing ATMACl	5.9 ± 0.8
Sample 3 containing DDDMACl	141 ± 12
Sample 4containing EDTMACl	5.6 ± 0.5

been shown that, in such a case, interaction with the membrane is reduced; in particular, accessibility to the exchanger contained in the membrane is partly impaired. Indeed, analyzing the tetrabutylammonium iodide solution of known concentration (0.01 $molL^{-1}$), a concentration of 8.66 x 10^{-4} $molL^{-1}$ was found, i.e. less than the effective concentration which is two orders of magnitude higher, thus an indication of the reduced exchange capacity of the membrane it was evidenced.

–The sensor response to standard solutions of different standard quaternary ammonium salts is all the better the closer the standard molecular structure is to the structure of the product contained in the commercial sample tested. For this purpose calibration straight lines were constructed using quaternary ammonium salts as similar as possible to the analyte to be determined (Tab. 3).

Tab.3: Comparison between the molecular structure of DDTMABr, used as standard in the preceding tests, and the structure of (BDTDACl and EDTMABr) the new standards used.

Standard solution	Standard structure
Dodecyltrimethylammonium bromide (DDTMABr)	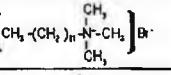
Benzyldimethyltetradecylammonium bromide chloride (BDTDACl)	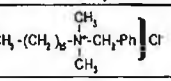
Esadecyltrimethylammonium bromide (EDTMABr)	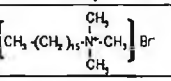

The results, set out in Tables 4 and 5, clearly indicate the need when performing quantitative determinations to use reference standards as similar as possible to the analytes to be determined. The results, set out in table 5, are certainly more reliable than those previously reported in Tab. 2 and confirm the need to use standards with a structure as close as possible to that of the analyte to analyse in quantitative determinations. It was thus possible to obtain a sufficiently reliable determination of the commercial products 2 and 4 using reference standards as similar as possible to the ammonium salts contained in them. Measurement of sample 1 nevertheless entrained several difficulties as its determination apparently caused a degree of "wear" of the membrane. Nevertheless, this dosage, using the benzyldimethyltetradecylammonium chloride standard solution, allowed easily reproducible data to be obtained. On the other hand, in the case of sample 3, it was not possible to find standards very similar to the analyte contained in it, i.e. ammonium salts with a double long alkyl chain, which at the same time were sufficiently soluble in water at ambient temperature. This objective limit has so far not been overcome.

Tab.4: Analytical data referring to the respective calibration curves obtained using new standards that are more similar in their structure to the cationic surfactants contained in the commercial samples tested.

Standard solution utilised	Slope (ΔmV/logC) (C=molL^{-1})	Linear range (mol L^{-1})	r^2
BDTDACl	54.9 ± 0.5	5 x 10^{-6} - 1 x 10^{-3}	0.9995
EDTMABr	53.5 ± 0.9	5 x 10^{-6} - 1 x 10^{-3}	0.9996

Tab.5: Concentrations of the three commercial samples obtained using the new standards illustrated in tab.3.

Samples and standard used	Concentration found (mol L^{-1})
Sample 1 using BDTDACl	0.058 ± 0.003
Sample 2 using EDTMABr	0.042 ± 0.001
Sample 4 using EDTMABr	0.039 ± 0.002

5. Conclusion

An ISE has been constructed that can be used for the quantitative determination of quaternary ammonium salts in commercial compounds. It is used to analyse commercial samples containing cationic surfactants, leading to satisfactory analytical results in the case of samples containing alkyldimethylbenzylammonium chloride, or hexadecyltrimethylammonium chloride, or alkyltrimethylammonium chloride. Quantitative determination proved to be more problematic in the sample containing didecylmethylammonium chloride because of the impossibility of obtaining a standard quaternary ammonium salt with 2 long-chain alkyl groups and at the same time that was sufficiently soluble in water at ambient temperature. It has been shown that it is necessary to take into account the steric hindrance of the cationic centers of the surfactants analysed as well as the interaction between the latter and the membrane exchanger and that, therefore, for quantitative determinations, e.g. of dialkyldimethylammonium salts, it is necessary to use a standard that is structurally similar to that of the analyte to be determined in order to optimize the membrane exchange conditions.

References

1. L. Campanella, L. Aiello, C. Colapicchioni, M. Tomassetti; Analusis, 1996, 24: 387-391.
2. L. Campanella, L. Aiello, C. Colapicchioni, M. Tomassetti; Analytical Letters, 1997, 30 (9): 1611-1629.
3. M. Sak-Bosnar, Z. Grabaric, B.S. Grabaric; Food Technol. Biotecnol., 2004, 42(3): 197-206.
4. C. Gavach, P. Seta; Analytical Chimica Acta, 1970, 50: 407-412.

CHEMICAL SENSOR ARRAYS

DEVELOPMENT OF GAS SENSOR ARRAY WITH LINEAR TEMPERATURE GRADIENT FOR WINE QUALITY MONITORING

A. ADAMI, L. LORENZELLI*, V. GUARNIERI,
ITC-irst, via Sommarive, 18,
38050 Povo(TN), Italy

L. FRANCIOSO, A. TAURINO, P. SICILIANO
CNR-IMM Sezione di Lecce, Via per Arnesano,
73100 Lecce, Italy

G. AGNUSDEI
Consorzio OPTEL, Cittadella della Ricerca, SS.7 Km 7,300
72100 Brindisi Italy

In this work, we describe the design implementation, validated by experimental results, of an innovative gas sensor array for wine quality monitoring. The main innovation of this integrated array deals with the simultaneous outputs of 8 different signals coming from a WO_3 thin film structure heated in a linear temperature gradient mode, allowing an overall evaluation of gas sensing properties of the material in a 100°C-wide window. Preliminary tests of gas sensing showed good responses to the target analytes for the specific application (1-heptanol, 3-methyl butanol, benzaldehyde and ethyl-hexanoate).

1. Introduction

Monitoring and determining the constituents of a sample gas typically involves collecting samples and analyzing them in a gas chromatograph-mass spectrometer (GCMS) of significant size and cost. Nevertheless, many applications need smaller, more portable, cheaper, and even disposable sensor-based systems. However the selectivity of an individual sensor remains as a problem to be solved. Several approaches, including the study of new sensitive layers [1], advanced sensor array architectures for electronic noses [2, 3] and the gas identification by modulating the metal oxide temperature [4] have been adopted to increase the sensor selectivity.

In this work, we describe the device implementation by means of analytical models and Finite Elements (FE) analysis, validated by experimental results, of an innovative gas sensor array for wine quality monitoring.

The device consists of a semiconductor oxide sensitive layer patterned on a thin film suspended membrane with Polysilicon micro-heaters and temperature sensors designed for providing and monitoring a linear temperature gradient on active area. Data collected from the eight elements of the array can be analysed with pattern recognition analytical tools and principal component analysis in order to enhance the sensor selectivity. The target analytes selected for device testing are 1-heptanol, 3-methyl butanol, benzaldehyde and ethyl-hexanoate, according to a preliminary analysis of wine quality using chromatographic and mass spectroscopy methods.

2. Device implementation

The device has been implemented on a thin Silicon oxide and nitride multilayer membrane, allowing low power consumption, proper temperature control and a fast heating because of low thermal mass and heat dissipation of dielectric suspended structures. Device heating is provided by poly-Si heaters embedded in the membrane, while thermometers allow temperature monitoring. The electrical contacts for the eight element sensor array have been implemented on the active area with Platinum interdigitated wires, providing high temperature stability. The multilayer membrane structure has been balanced considering residual stress and thermal expansion of deposed films. The main mechanical aspect to consider in structure definition is the overall stress on membrane section, which must be slightly tensile to prevent structure buckling and failure. The defined film sequence and material properties are shown in Table 1.

Since preliminarily WO_3 has been chosen as gas sensing layer, the target working temperature has been set to the 250-350°C range, reported in the literature as a suitable temperature range for this material [5].

Name	Thickness [nm]	Resistance/sq [Ω/sq]	Stress [MPa]
Structural layers			+tensile -compr.
Silicon 15 wafers	489.5 ± 1.6*	12-24**	
Field oxide	297 ± 3,3		-344 ± 2
Nitride	142,3 ± 7.1		+1270 ± 190
LTO	317 ± 3,1		30.2 ± 0.3
Poly-sllicon P	435 ± 4,1	47 ± 1	-313 ±25
Poly-silicon B	435 ± 4,1	83.7 ± 0.6	-313 ±25
TEOS+BPSG+TEOS	471,03 ±6		-38 ± 14
Platinum	50,1 ± 1,2%	6.56 ± 0,74%	
Evaporated Cr/Au	10,5/200,4	0.1486 ± 1,81%	+155 ± 5

Table 1: Membrane structure and layer properties

2.1. *Thermal-electrical FE simulations*

In order to match the target properties of the device and to optimize the power consumption performances, simulations of array electro-thermal behaviour have been performed using the ISE-Solidis simulation software including the dependence on temperature of poly-silicon resistance and air thermal conductivity. The extracted design parameters regarded the membrane dimension, strictly related to the power consumption, and the definition of the heater geometry to obtain the correct temperature range and the linear temperature profile on the sensor array.

Heat dissipation in small devices can be modelled at low temperature using the heat transfer equation for conduction mode in the surrounding air layers, while convection mode can be neglected. Furthermore the radiative dissipation affects the behaviour at high temperatures [6]. Simulation results are shown in Figure 1B, where temperature profiles and power consumption are summarized and compared with experimental data. The temperature profile is linear over a wide range of bias conditions, increasing the temperature gradient for increasing power consumption.

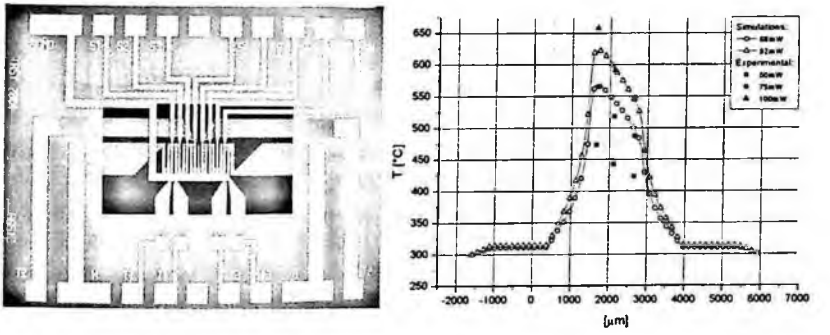

Figure 1: A) Photograph of single heater array B) Temperature profiles on array, simulations and experimental results.

2.2. *Design*

According to the simulation results, the meander heater wires spacing and width have been tuned in order to provide the heat density needed to compensate the larger heat dissipation from lateral elements and then to set the target temperature profile on the array.

Platinum interdigitated contacts for the metal oxide layer connections have been implemented on the 1140µm x 500µm active area. According to the thermo-electrical simulation results, four different layouts have been implemented and two different membrane dimensions (3500µm x 3000µm and

3500μm x 2000μm) with two different heater configurations have been adopted. In the "standard" configuration (Figure 1A) a single heater provides the temperature gradient, while in the three-heater configuration the heater sections can be biased separately, allowing a wider choice of operating conditions of the gas sensor array. In both the configurations the heater is wider (1340μm x 600μm) then sensitive region, to provide better temperature uniformity on sensors. Since the metal oxide resistivity is strongly affected by temperature variations, thermometers have been implemented in the structures for monitoring working conditions of the metal oxide layer.

3. Fabrication

The membrane is a SiO_2 - Si_3N_4 multilayer of about 1 μm thickness and 3500 μm x 3000 μm in size. The membrane backside opening has been performed by means of a TMAH bulk etching technique. The sensor electrodes have been realized in Platinum by lift-off. Active layer implemented in this array is WO_3 deposited via reactive sputtering RF on suspended membrane, starting from a pure 99,99 % 4" target of tungsten oxide in Ar/O2 atmosphere.

4. Array sensitivity and PCA results

The characterisation of sensitive layers has been performed using 1-heptanole (1ppm), ethyl esanoate (1-2-5-10 ppm), 3-methylbutanole (1-2-5-10 ppm) and benzaldehyde (1-5 ppm) with a constant total gas flow of 100 sccm, and working temperature in the range of 300÷400°C.

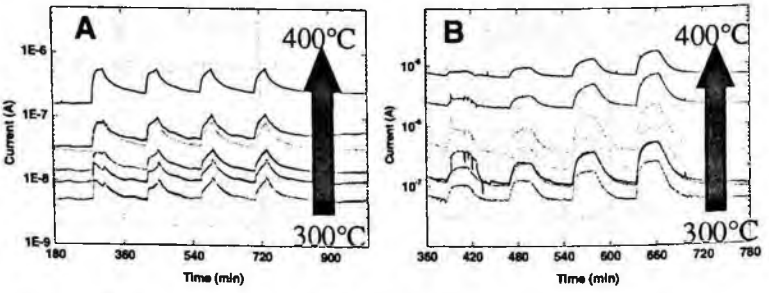

Figure 2: Dynamic responses of WO_3-based sensor array to: (A) 1-heptanole (four injection 1ppm) and (B) 3-methylbutanole (1-2-5-10 ppm).

Figure 2 shows an example of dynamic response of the sensor array to analytes. The different resistances of array elements in inert environment confirm the gradient of temperature set by the micro-hotplate structure. Array elements show

different dynamic responses to analytes in relation to different working temperature, validating the device implementation. Moreover the reproducibility
of sensor responses can be observed in Figure 2 (a) where result of repeated injection of 1 ppm of 1-heptanole into the measurement chamber is shown.

In order to test the discrimination capability of the system, preliminary Principal Component Analysis (PCA) has been performed on described data. PCA score plot (Figure 3) shows a good discrimination of 3-methylbutanole and 1-heptanole, while further analysis are required in order to optimise ethyl esanoate versus benzaldehyde identification.

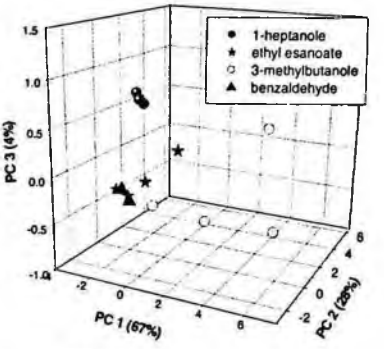

Figure 3: PCA 3D score plot of the analysed samples.

5. Conclusions

In this paper we presented an innovative approach for monitoring wine aromatic compounds by using a microhotplate-based silicon gas sensor arrays with linear temperature gradient. In particular, the possibility to use such microsystem for the detection of 1-heptanole, 3-methylbutanole, ethyl-esanoate and benzaldehyde wine has been demonstrated for concentrations ranging from 1 ppm to 10 ppm. Future works will be devoted to validate the system in operating condition with particular emphasis to test specific wine sample.

Acknowledgements

This work has been funded by the "Programma Operativo Nazionale "Ricerca, Sviluppo ed Alta Formazione" - MINICONTAL Project.

References

1. S. Zarcomb, J.R. Stretter, *Sensors and Actuators*, **6**, 225-243, (1984).
2. H.V. Shurmer, J.W. Gardener, P. Corcoran, *Sensors and Actuators B*, **1**, 256-260, (1990).
3. J. W Gardner, *Sensors and Actuators B*, **4**, 109-115, (1991).
4. J.F. Currie et al., *Sensors and Actuators B*, **59**, 235–241, (1999).
5. S. Capone, A. Forleo, L. Francioso, R. Rella, P. Siciliano, J. Spadavecchia, D. S. Presicce, A. M. Taurino - *Journal of Optoelectronics and Advanced Materials* Vol. 5, No. 5, 2003, p. 1335 - 1348
6. A. Pike, J. W. Gardner, *Sensors and Actuators B* 45, 19-26, (1997).

A MULTILAYER APPROACH TO SENSOR FUSION FOR SMALL MATRICES OF THIN FILM GAS SENSORS

SAVERIO DE VITO[†],GIROLAMO DI FRANCIA, FAUSTA LOFFREDO, ETTORE MASSERA, LUIGI QUERCIA

ENEA UTS MAT, C.R. Portici, Via Vecchio Macello
80055 Portici, Naples, Italy

Sensor Fusion by means of different architectural approaches has shown to be a powerful tool for the analysis of data produced by arrays of chemical sensors. In this work, we focus our attention on two sensor fusion architectures based on Multilayer perceptrons, applied to a small matrix (4–elements) of chemiresistors based on thin film polymer composites, in order to obtain significative enhancement in both gas estimation precision and sensor dynamic behavior (speed).

1. Introduction

During last decade, Back Propagation Networks (BPN) have often been used for analyzing chemical sensors outputs in different scenarios. Application scenarios includes mixture classification [1],[2],[3] and concentration estimation both steady state [4] and continuous [5],[6]. In continuous gas concentration estimation, responsiveness is a primary goal, especially when dealing with toxic compounds. Unfortunately, thin film gas sensors, operating at room temperature and so very suitable for portable applications, do not show optimal performance as regards to speed of response. We expect that a tapped delay BPN based sensor fusion architecture, can boost both responsiveness and precision of a small matrix of thin film gas sensors. Furthermore, in different application context, the use of multilayer fusion architecture has shown its ability to improve context awareness [7] producing, for example, information on reliability of the fusion outputs. In this work, we compare a multilayer fusion architecture with a single BPN approach working on novel 4-elements matrix of carbon black/Poly(methyl-methacrylate) based chemiresistors. Sensing devices are

[†] Corresponding author. Tel.: +39 081 772 3364; fax: +39 081 772 3344;
e-mail: *saverio.devito@portici.enea.it*

actually picked up from a 8x8 matrix prepared by spinning the above mentioned dispersion on a 4x4 cm^2 allumina substrate. In this way, it is possible to realize multiple small devices (5x5 mm^2 area), obtained by the same PMMA/Carbon black composite but differing in the filler/polymer volume ratio [8]. The ratio is expected to be reduced continuously moving along the diagonal of 4x4 cm^2 allumina substrate from the central to the peripheral device.

2. Experimental

The first proposed fusion scheme, is a two-layer tapped-delay BPN analyzing 10 homogeneously spaced samples (last 9 plus the current one) for each of the four selected sensors. The hidden layer is built up by 10 sigmoidal neurons. Finally, a single linear function neuron is used in order to provide an estimation of current gas concentration.

The second proposed architecture, is based on a Multiple Expert Systems approach with a primary layer equipped with four tapped-delay BPN applied to, and trained for, the output of single chemiresistors. The next fusion layer is equipped with a combiner, implementing a simple combining scheme. The scheme is applied to the output of the four virtual sensors and provides the final estimation of current gas concentration. The combination scheme rejects the worst performing sensor selecting it by means of a mean value centered cluster approach. The systems then output the overall estimation based on the mean value of the remaining virtual sensors outputs. MSE allow also to evaluate the confidence level of the final output. Like the first architecture network, tapped delay length has been chosen to be 10.

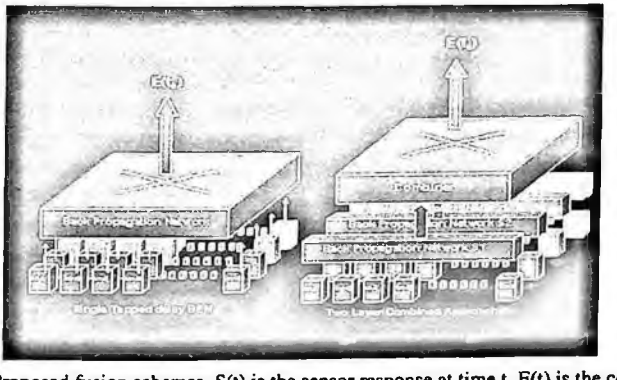

Figure 1: Proposed fusion schemes. S(t) is the sensor response at time t, E(t) is the concentration value estimated by the two alternative fusion systems at time t.

All the Back Propagation Networks have been trained using Levenberg-Marquardt optimization scheme with a [50% Training, 25% Validation, 25% Test] dataset partition. Early stopping is, in fact, been used to avoid over-fitting problems [9][10]. The dataset has been built by collecting sensor responses to acetone vapours (ranging from 0.2% to 80% of its vapour pressure at 20°C) during 40 complete exposure cycles. Sensor responses have been characterized using a Gas Sensor Characterization System.

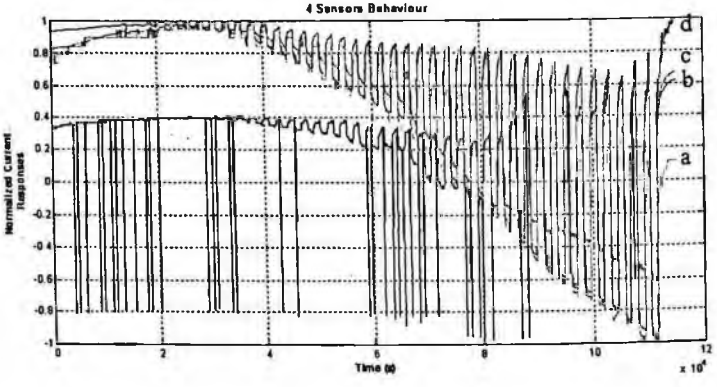

Figure 2: Sensor responses to the 40 acetone vapors exposure cycles. Note the instable behavior of sensor d.

3. Results

Each of the proposed architecture has shown good performance in terms of speed and precision (view fig. 3,4). Network outputs, seems, in fact, to respond very quickly (1-2 samples corresponding to 30-60secs) also to rapid concentration variations.

The approaches have also shown to be very robust considering the overall quality of the input data (view fig 2). Sensors responses at low P/P0 (% of vapor pressure), hence during early characterization phases, was in fact affected (wobbling) by the incomplete evaporation of a solvent used for preliminary set up. Furthermore, one of the selected sensors, has shown severe electrical problems causing several uncorrelated resistivity spikes in its response (view fig. 2). Estimation

Table 1: MSE Performances (Test Set)	
Single 10TD BPN	4.15×10^{-4}
Multilayer Approach	7.88×10^{-4}

precision performance of the two approaches has been evaluated using MSE (Mean Square Error) during multiple runs and best results are shown in table 1.

As shown in table 1, results obtained by the two architectures are actually comparable but the single layer architecture seems to show a slightly better estimation performance. This appears to be due to the very small number of sensors used, and probably to the sub optimal sensor selection scheme. The multilayer approach, conversely, offers a simpler reliability indicator of the output P/P0 estimation that makes it more appealing for the integration in a more complex fusion scheme.

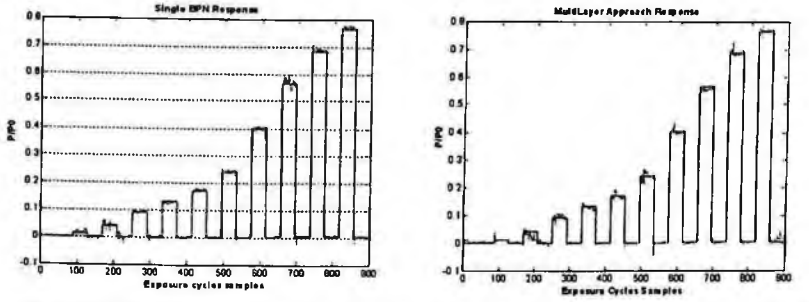

Figure 3: Overall architectures responses to 10 acetone vapor exposure cycles (test set), with respect to ground truth (black).

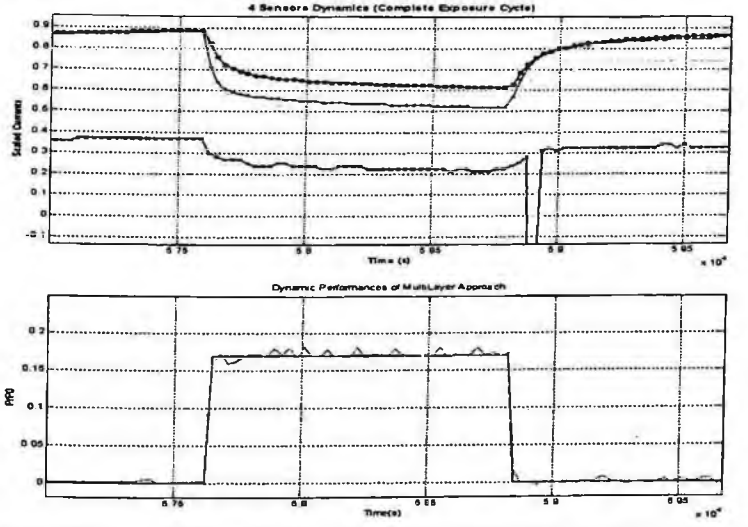

Figure 4: Details of combined architecture dynamic behavior during a complete exposure cycle compared to single sensors. Speed of response is greatly enhanced, and precision shows very good performance, despite of electrical instability shown by sensor d (x-ed).

4. Conclusions

It is possible to obtain significative performance enhancement applying a multilayer fusion scheme to small matrices of thin film polymer composite based gas sensors, so to obtain a single composite virtual sensor. Both dynamic and steady state performance are positively affected by the proposed approach, that has revealed to be very robust to sensor responses variation. The approach seems also to be suitable for application to pre-commercial prototypes, since BPNs on-chip implementation are commercially available, so that BPN based sensor fusion architecture can be easily integrated on portable devices. Future works will be focused on testing the proposed architectures with a hybrid sensors array operating at room temperature for concentration estimation in a complex gas mixture scenario.

References

1. H. Nanto *et al.*, "Identification of aromas from wine using quartz-resonator gas sensors in conjunction with neural-network analysis", Sens. Act. B 24-25 (1995), 794-796
2. D. Lee *et al.* , "Explosive gas recognition system using thick film sensor array and neural network", Sens. Act. B 71 (2000), 90-98
3. T. Roppel. *et al.*, "Design of a Low-Power, Portable Sensor System Using Embedded Neural Networks and Hardware Pre-processing", IJCNN'99, Washington, D.C., 1999
4. H. Sundgren *et al.*, "Artificial neural Networks and gas sensors array: quantification of individual components in a gas mixture", Meas. Sci.Technol. 2 (1991) 464-469
5. M. Pardo *et al.*, "A time delay neural network for estimation of gas concentrations in a mixture", Sens. Act. B 65 (2000) 267-269
6. D. Rebiere *et al.*, " Improvement of Surface acoustic wave gas sensor response time using neural-network pattern recognition", Sens. And Act. B 24-25 (1995) 777-778
7. R.C. Luo *et al.*, "Multisensor Fusion and Integration: Approaches, Applications, and Future Research Directions", IEEE Sens. Journ., Vol.2, No.2, April 2002 107-119
8. L. Quercia *et al.*: "Effects of thin polymer composite preparation on vapor sensing devices characteristics" , Sens. and Act. B, in press.
9. M. Pardo, G. Sberveglieri, "Remarks on the Use of MultiLayer Perceptrons for the Analysis ofChemical Sensor Array Data, IEEE Sensors Journal, Vol. 4, No.3, June 2004. 355-363
10. M.T. Hagan and M. Menhaj, "training feedforward networks with the marquardt algorithm", IEEE Trans. Neural Networks, pp. 989-993, Oct. 1994

DETECTION OF FUNGAL CONTAMINATION OF CEREAL GRAIN SAMPLES BY AN ELECTRONIC NOSE *

R. PAOLESSE,[1,3]* S. NARDIS,[1] A. ALIMELLI,[1] E. MARTINELLI,[2] C. DI NATALE,[2,3] A. D'AMICO,[2,3] M. G. D'EGIDIO,[4] G. AURELI,[4] M. EPIFANI,[4] A. RICELLI,[5] C. FANELLI[5]

1. *Department of Chemical Science and Technologies, University of Rome "Tor Vergata", via della Ricerca Scientifica, 00133 Roma; Italy*
2. *Department of Electronic Engineering, University of Rome "Tor Vergata", via di Tor Vergata 110, 00133 Roma; Italy*
3. *IMM-CNR, via del Fosso del Cavaliere, 00133 Roma; Italy*
4. *C.R.A- Istituto Sperimentale per la Cerealicoltura, 00191 Roma, (Italy).*
5. *Università degli Studi di Roma "La Sapienza", Dipartimento di Biologia Vegetale, 00165 Roma, (Italy)*

Fungal growth on cereal grains is one of the main concerns in the storage of raw materials for food industry: because it reduces their nutritional value and due to he risk associted with the probable production of toxic metabolites (mycotoxins). Therefore, attempts are coming out for early detection and quantification of the fungal contamination degree. The aim of this work was to study the possibility of the application of electronic nose for detecting the volatile compounds, produced by the fungi metabolism, in the samples headspace.
The LibraNose showed promising performances in the discrimination between non infected samples and samples infected with two different species of fungi (*P. chrysogenum* and *F. verticillioides*).

1. Introduction

Contamination of food and feeds by spoilage or pathogenic microorganism can make many of them no more edible or affect their taste by the production of undesirable flavours. In some cases the activity of these microorganisms can lead to the formation of toxic substances, hazardous to human and animal health.

In the past, control of food safety has been carried out by testing both raw and processed samples without any control of the processing.[1] Recently, instead, the Hazard Analysis Critical Control Point (HACCP)[1,2] system have been applied to identify the steps where hazards could occur within the processing, in order to perform and implement monitoring procedures.

The subsequent cultural detection methodology, which consists in growing the microorganisms on selective media, is time consuming, since it requires several days from isolation to identification, and expensive.[1]

* This work is supported by MIUR-FIRB (project # RBNE01KZZM_001)

Then the development of faster and low cost detection methods, will reduce both the health risks and the economical losses, compared to the actually commercially available methods.[3-6]

A new methodology has been proposed based on the detection and characterization of the volatiles and odors (alcohols, ketones, aldehydes, esters, carboxylic acids, lactones, terpenes, sulphur and nitrogen compounds)[7, 8] produced during the microorganisms metabolism depending on substrate temperature, pH, oxygen concentration, age of culture and microbial specie.[9, 10]

The study of volatile patterns has been useful to detect the early stages of grain spoilage and to distinguish between the presence of toxigenic and non-toxigenic strains of fungi.[11-13]

Flavors are generally constituted by a large number of components perceived by the human olfactory system as integrated response, without separating the individual components.[14] From this point of view the Electronic Nose approach parallels the biological sense of smell.[14] In such a device, a group of low selective chemical sensors works as olfactory receptors producing a time-dependant electrical signal in response to an odor. This technology has already proven to be useful for the early detection of fungal and bacterial activity in samples of good and poor quality grain.[15]

In the present work we have employed the LibraNose system to analyse volatile chemical patterns related to the contamination of wheat seeds by *P. chrysogenum* or *F. verticillioides*, at different water activities, with the aim to improve rapid methodologies for the detection of food spoilage micro-organisms.

2. Experimental

2.1. *Samples*

Soft wheat seeds (cv Pandas) were supplied by "Istituto Sperimentale per la Cerealicoltura". Experiments have been performed on sterilized and not sterilized cereal grain samples (50 g), sealed in vials with inlet and outlet, at controlled temperature (30 °C) and at different water activity (blank, 0.80, 0.90, 0.95 aw). Fungal inocula on the seed samples were performed using *Penicillium chrysogenum* (Thom) and *Fusarium verticillioides Saccardo* (Nirenberg), from the collection of the Department of Plant Biology, University of Rome "La Sapienza". Microscopic observation has been performed to investigate the fungal genera and their relative abundance on the assayed seeds.

Measurements have been carried out using a LibraNose[16] made up of an array of eight thickness shear mode resonators (20 MHz) coated with seven different films of metal complexes (Mn, Fe, Cu, Ni, Sn, Ru and Co) and a free-base Tetrakis(4-butyloxyphenyl) porphyrin (H2TBPP).[17]

2.2. *Grain sample measurements*

Three different experiments have been conducted. The first protocol consisted in analysing the headspace for five days after the vials closure. The flux was re-injected into the vials by a closed circuit, in order to minimize the variation of headspace composition after each measurement. On the basis of the results obtained, we performed a second experiment using grain samples stored at two different water activities (0.85 and 0.95) and inoculated respectively with *Penicillium chrysogenum* and *Fusarium verticillioides*. Blank samples for the two different water activity and not moistened blanks were also analysed. In the third experiment, the seed samples were sterilized before the inoculums to avoid accidental fungal contamination and the headspace evolution was measured.

3. Results and Discussion

The grain headspace has been measured leading, by data analysis technique, to the discrimination of each sample for each day of measurement: the evolution of different samples follows complicated patterns, probably due to a non-linear variation of the chemical composition of the headspaces.

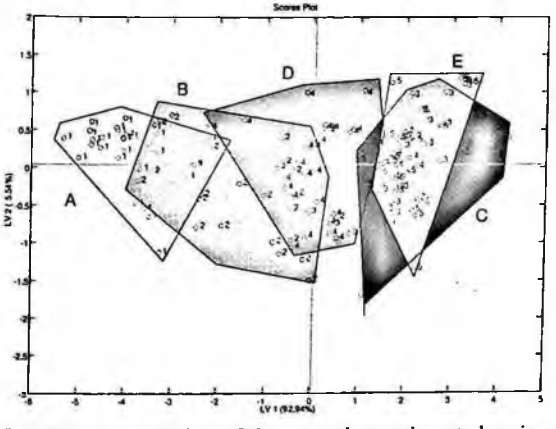

Figure 1. PLS-DA representation of the second experiment showing the classification of the five grain samples.

In the second experiment, the regression model is aimed at discriminating among the five different grain samples: blank-not moistened (A), blank at two different water activity values (B at 0.85 aw and C at 0.95 aw), samples inoculated with *Penicillium chrysogenum* (D at 0.85 aw) and with *Fusarium verticillioides* (E at 0.95 aw). The scores plot of the first two latent variables of this PLS-DA model shows a partial overlapping of the classes at the same water activity (Figure 1).

The same remark can be done observing Table 1, which shows the confusion matrix of the model described above.

Table 1.Confusion matrix of the second experiment model.

	A	B	C	D	E
A	29	0	0	0	0
B	7	10	1	8	0
C	0	0	12	3	15
D	1	0	0	28	0
E	0	1	6	0	23

Samples with inoculated fungi are well discriminated (classes D and E), while bigger errors occur for the samples of the classes B and C, misclassified respectively as D and E. These two couples of classes, B-D and C-E, are characterized by the same water activity.

The explanation for the low discrimination obtained for inoculated and blank samples was found in the presence of *Penicillium* (at 0.85 and 0.90 aw) and *Fusarium* (at 0.95 aw) species also in the blank batches, as confirmed by the mycological analysis.

Then the overlap observed in the analysis of these samples is due to the presence of the same fungi species at the same water activity, resulting in a similar chemical compositions of the related headspaces.

In the third experiment, the seed samples were previously sterilized by autoclaving to avoid contamination, then inoculated with *P. chrysogenum* or *F. verticillioides* to study the performance of the LibraNose in the discrimination of the two fungal species. In this case a better discrimination among the classes has been obtained, with a classification rate of 85.3%. The recognition rate for all

the classes was higher than 71%, while for the second experiment, for classes B and C, was lower than 45%.

These results confirm that the discrimination among the different samples depends on the volatile chemical pattern produced by the fungi metabolism.

4. Conclusions

The results obtained from these studies demonstrated the ability of the LibraNose to follow, for at least five days, the variation of grain sample headspaces due to the fungal contamination at different water activity (Experiment 1). More over our device was able to discriminate between two fungi species: *P. chrysogenum* and *F. Verticillioides.* The analysis with the electronic nose also demonstrated that not sterilized blank samples develop fungi contamination, due to the mycoflora naturally present on seeds, depending on the water activity (Experiment 2) and may not be distinguished from artificially contaminated ones. Mycological analysis confirmed the electronic nose result. These features make LibraNose a promising device for rapid and non-invasive detection of fungal contamination of grain seeds.

References

1. M E. de Boer, R.R. Beumer, International Journal of Food Microbiology 50, 119-130 (1999).
2. Jay J.M. 1996. Modern Food microbiology 5th ed. New York: Chapman and Hall.
3. Ingianni A.,Floris M., Palomba P., Madeddu M.A., Quartuccio M. & Pompei R. 2001. Rapid detection of Listeria monocytogenes in foods by a combination of PCR and DNA probe. Molecular and Cellular Probes 15: 275-280
4. Girardin H. 1997. Detection of filamentous fungi in foods. Science Des Aliments 17:3-19.
5. Deisingh A. 2003. Biosensors for microbial detection. Microbiologists 4(2):30-33.
6. Grow A.E., Wood L.L., Claycomb J.L., & Thompson P.A. 2003. New biochip technology for label-free detection of pathogens and their toxins. Journal of Microbiological Methods 53:221-233.
7. Pasanen, A.L., Lappalainen, S., Pasanen, P. Volatile organic metabolites associated with some toxic fungi and their mycotoxins. Analyst. 1996, 121, 1949-1953.

8. Hodgins D. & Simmonds D. 1995. The electronic NOSE and its application to the manufacture of food products. Journal of Automatic Chemistry 17: 179-185.
9. Borjesson, T.; Stollman, U.; Schnürer, J. Volatile metabolites produced by six fungal species compared with other indicators of fungal growth on cereal grain. Appl. Environ. Microbiol. 1992, 58 (8), 2599-2605.
10. Olsson, J.; Borjesson, T.; Lundstedt, T; Schnürer, J. Detection and quantification of ochratoxin A and deoxynivalenol in barley grains by GC-MS and electronic nose. Int. J.Food Microbiol. 2002, 72, 203-214.
11. Keshri, G.; Magan, N. Detection and differentiation between mycotoxigenic and non-mycotoxigenic strains of two Fusarium spp. using volatile production profiles and hydrolytic enzymes. J. Appl. Microbiol. 2000, 89 (5), 825-833.
12. Cowell D. & Ratcliffe N. 1997. The detection of micro-organisms in foodstuffs by the use of vapour sensors. Measurements and Control 30:39-42.
13. Larsen, T.O.; Frisvad, J.C. Characterization of volatile metabolites from 47 Penicillium taxa. Mycol. Res. 1995a, 99(10), 1153-1166.
14. Craven M.A., Gardner J.W., & Bartlett P.N. 1996. Electronic noses-development and future prospects. Trends in Analytical Chemistry 15: 486-493.
15. Magan N., Keshri G., Needham R. and Sneath R. (2003) Use of electronic nose technology for the early detection of spoilage moulds in cereal products. In Advances in Stored Product Protection, pp.139-143. Edited by P.Credland, M. Armitage C.H. Bell & P-M- Colgan CABI International.
16. D'Amico, A.; Di Natale, C.; Macagnano, A.; Davide, F.; Mantini, A.; Tarizzo, E., Paolesse, R.; Boschi, T. Technology and tools for mimicking olfaction: status of the Rome "Tor Vergata" electronic nose Biosensors and Bioelectronics. 1998, 13, 711.
17. Di Natale, C.; Paolesse, R.; Macagnano, A.; Nardis, S.; Martinelli, E.; Dalcanale, E.; Costa, M. and D'Amico, A. Sensitivity-selectivity balance in mass sensors: the case of metalloporphyrins J. Mater. Chem., 2004, 14, 1281.

DETECTION OF FUSARIUM POAE CONTAMINATED WHEAT BY ELECTRONIC NOSE

D.S. PRESICCE, A. FORLEO, L. FRANCIOSO, A.M. TAURINO, P.SICILIANO
CNR-IMM Section of Lecce, Monteroni street
Lecce 73100, Italy

B. LADDOMADA, A. LOGRIECO, A. VISCONTI
CNR-ISPA, Section of Lecce, Monteroni street
Lecce 73100, Italy

Odorous contaminant in wheat have been detected using a conducting metal oxide semiconductor gas sensor array. Cereal grains contaminated by toxigenic fungi and relative mycotoxins can be detected and quantified using complex extraction procedures and analytical techniques. We studied the wheat odour, the presence of non-grain volatile metabolites due to Fusarium poae contamination for the determination of wheat quality classification by SPME-GC/MS and by electronic nose in order to compare analytical tecnique and sensor array tecnique.

1. Introduction

There is significant interest in methods for the early detection of quality changes in cereal grains. The development of Electronic Nose (EN) technology in recent years has stimulated interest in the use of characteristic volatiles and odours as a rapid, early indication of deterioration in grain quality [1]. Traditionally, toxigenic fungi and relative mycotoxins contamination of cereal grains can be detected and quantified using complex extraction procedures and analytical techniques. Normally, the grain odour, i.e. the presence of non-grain volatile metabolites, is used for quality classification of grain [2]. Thus it is very important to detect fungal deterioration in stored wheat at an early stage. This would facilitate and improve existing management of wheat stores. It would also allow remedial measures to be more effectively implemented, allowing significant losses and grain downgrading to be avoided.

We have investigated the possibility of using volatile metabolites produced by Fusarium poae toxigenic strains as indicators of fungal deterioration and possible occurrence of mycotoxins in wheat. In this work an Electronic Nose, a sensors array based on In2O3 and pure and Pd-, Rh-doped SnO2 sol-gel thin films [3], was used for the discrimination of different wheat samples.Tests were carried out on inoculated wheat samples and no contaminated samples during the time.

Classical analytical technique like Headspace-Solid Phase Micro Extraction \ Gas Chromatography \ Mass Spectrometry (HS-SPME\GC\MS) analysis was performed to relate results with the sensor array responses.

Principal Component Analysis (PCA) was applied to sensor array responses and GC/MS data in order to assess the capability of the electronic nose to detect and classify different samples with the GC data.

2. Experimental

The fungal strain used first in the present study was Fusarium poae ITEM 3258. The strain was obtained from the culture collection of the Institute of Sciences of Food Production and reported to produce trichothecenes [4,5].

5 g of durum wheat (Triticum durum, var. dicoccoides) with 45% of distilled water were autoclaved at 120°C for 20 min and then were inoculated with the fungal strain. The vials were then sealed and held at 23°C at dark. Controls were treated in the same way, except that they were not inoculated.

Headspace analysis were carried out (in triplicate trials) at the same day of inoculation (TO) and after 1, 2, 5 and 7 days (T1, T2, T5 and T7) by either Electronic Nose (Fig. 1) and HS-SPME\GC\MS. The aim of this work was to establish the time of maximum development of volatile compounds.

Analysis of wheat headspace were carried out with dry air-nitrogen baseline and by means of a deviation of nitrogen flow through the vials.

The wheat samples were at 23°C while the sensors working temperature was 300°C. The sampling was performed for 15 min while the recovery time was 30 min.

Wheat samples were analysed for the qualitative determination of volatile compounds by SHS - SPME/GC/MS. SPME 50µm CAR (Carboxen) -PDMS (polydimethylsiloxane) fibres were used and exposed to wheat sample in 20 ml gastight vials at 21°C. After this, fibre was desorbed in a split/splitless injector,

equipped with deactivated SPME glass inserts, and analyses were carried out on a 30m x 250 μm ID x 0.25 μm HP INNOVAX polyetilenglicole column. A GC system HP 6890 Series, Agilent Technologies, was coupled with HP 5973 mass selective detector, Agilent Technologies. Injection was split 5:1 with 5 min relay time. GC conditions were: 40°C for 5 min, 150°C at 4°C/min, then 250°C at 15°C/min; injector temperature was 250°C, helium flow was 1ml/min. Transfer line was held at 260°C. Spectra were produced in the electron impact mode at 70 eV. Compounds were identified by comparison with NIST reference spectra. Mass range was 30-350 amu, solvent delay time was 4 min, threshold 150 and scan rate 4,45 scan/sec.

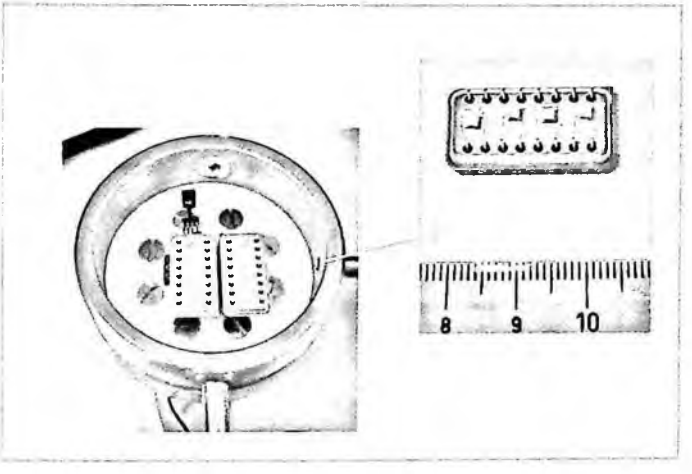

Figure 1. Test chamber for headspace E-Nose measurements.

Some volatile compounds have been determined by GC/MS analysis, highlighting the occurrence of contamination or not. This behaviour is clearly shown in PCA score plot where there is a sharp separation of clusters (Fig 2).

PCA score plots show a good agreement between EN (Fig. 3) and GC data and a clear trend could be find in the case of contaminated samples.

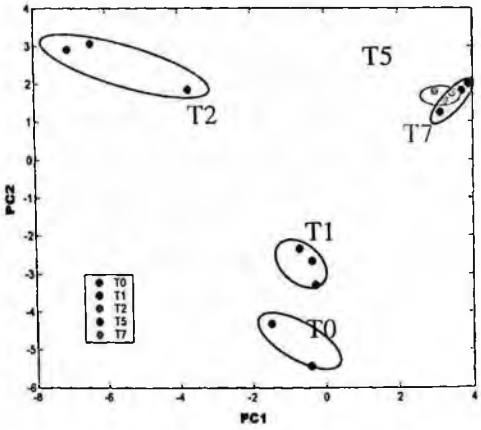

Figure 2. PCA score plot of SPME- GC/MS analysis of contaminated samples during the time.

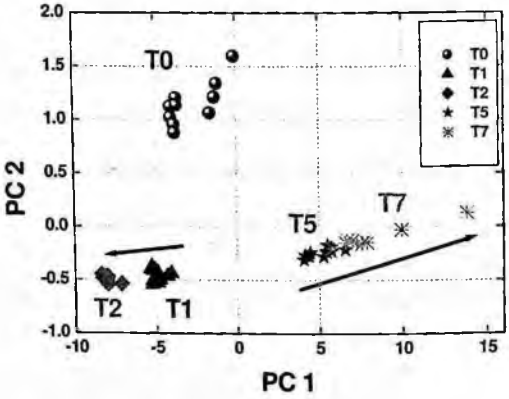

Figure 3. PCA score plot of EN analysis of contaminated samples during the time.

3. Conclusions

It has been developed a new analytical method for the determination of volatile compounds in wheat by SPME-GC/MS. An array of sensors has been set for the same aim. It has been shown that both tecniques allow to discriminate inoculated and control sample during 7 days. Most differences have been highlighted after 1-2 days from the inoculation. This could be due to the maximum growth of Fusarium poae ITEM 3258.

After 5-7 days the volatile compounds profile/array was different from the previous samplings. At this stage the wheat substrate was completely colonized and visibly deteriorated.

Study is in progress for other species of toxigenic fungi (Fusarium graminearum, F. avenaceum, Aspergillus flavus, A. ochraceus, Penicillium verrucosum) in order to verify the capability of the EN to discriminate different strain of fungi through the production of volatile secondary metabolites and to demonstrate the variation of the metabolic pathway due to the contamination of grain.

References

1. N. Magan, P. Evans, *Journal of Stored Products Research*, **36** (2000), pp 319-340.
2. J. Olsson, T. B□rjesson, T. Lundstedt, J. Schn□rer, *International Journal of Food Microbiology*, **72** (2002), pp 203–214.
3. A.M. Taurino, D. Balzarano, A. Basso, S. Capone, C. Distante, D. Dello Monaco, M. Epifani, L. Ferrara, G. Maglione, R. Rella, P. Siciliano, *Sensors and Actuators B*, **95** (2003) pp 123-131.
4. Thrane, U., A. Adler, P.-E. Clasen, F. Galvano, W. Langseth, H. Lew, A. Logrieco, K.F. Nielsen, A. Ritieni. *International Journal of Food Microbioliology*, **95** (2004), pp 257-266.
5. http://www.ispa.cnr.it/Collection.

POLYPYRROLE-DERIVATES NANO-GRAVIMETRIC SENSORS FOR THE LIBRA NOSE APPLICATION TO THE ESSENTIAL OIL DISCRIMINATION.

A. Scarpa[#], C. Deidda[*], D. Del Turco[#], L. Fachechi[#], S. Bernardi [#], S. Mazzola[#]

*# Technobiochip s.c.a.r.l. Via Carrara 12/a 04100 Latina Italy. Phone: +39 0773 632643 Fax: +39 0773 631009, * Chemistry Engineering Dept. Cagliari Italy.*

a.scarpa@tecnobiochip.com

Abstract:

Novels series of nano-gravimetric sensors are obtain from the deposition of new polypyrrole-derivates compound, on the oscillating quartz surface. In fact these polymers are used to modify the surface of the transductor with some functional chemical groups with affinity for a great class of volatile organic and inorganic compounds. In this article, a test that proves the chemical affinity of polypyrrole derivates sensors to a series of essential oils is reported.

Introduction.

At the beginning of the nineteen eighties, Persaud et. al (1982), wrote the first paper about the electronic nose following the idea of a receptor – nervous system scheme. Using a sensors array based on metal oxide, this instrument was able to developed a digital finger of an odor [1].
Since then the Electronic Nose system has attracted the attention of many researcher for possible industrial applications[2, 3, 4]. Thanks to its versatility it is possible to detect and measure chemical compounds in gas phase. It is clearly important in most areas of modern life, including industrial process control, health and safety monitoring and environmental monitoring. Seven 20 MHz resonant quartzes coated with a series of polymer opportunely modified via an easy polymerization *in situ*. The sensors obtained are applied in a electronic nose system (Libra-nose) developed by Technobiochip for the determination of gas compound analytes. The functionality of the sensor is based on the mass variation (Δm) of the quartz surface, due to a direct interaction between sensor and the analyte. As a consequence it is possible to observe a frequency variation Δf of the quartz fundamental oscillation frequency f_0, as explained by the Sauerbrey's law [5](eq.1). Where A is the area of the sensitive layer and C_f the mass sensitivity constant.

$$\Delta f = -\frac{C_f f_0^2}{A}\Delta m$$

Eq.1: Sauerbrey's law.

1. Experimental.

1.1 Materials. reagents and analytes.

The quartz crystal used as mass transductor, with fundamental oscillation frequency of 20 MHz. are AT- cut with gold surface purchased by Nuova Mistral. All reagents were purchased by Aldrich. The essential oil used as analyte were produce by GRICAR Milan Italy.
The electronic nose used to test a set of eight sensors was the Libra Nose 2.1developed by Technobiochip. It is a compact, easy-to-use instrument which has been thought to perform reversible measurements and to distinguish different odors classified on a qualitative basis. This instrument uses a set of piezoelectric transducers placed in a measuring chamber. Each piezoelectric transducer covered by a molecular layer acts as a sensor. In this way the instrument can be promptly reused after a short cycle of cleaning using nitrogen or filtered air. The instrument is formed by a thermostatic measuring chamber, where the seven sensors are positioned, a pump with adjustable flow rate and an electro valve which is possible to control via software (Fig.1).

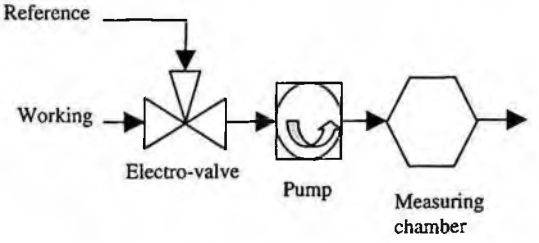

Fig. 1: scheme of the functioning of Libra-Nose.

To carry out the Principal Component Analysis (PCA) the "*NasoStat Analisi Statistica Dati per Libra Nose*" by SIGEDA Milan Italy was used.

1.2 Experimental section.

Before the polymerization, the quartzes are cleaned with a mix ammonia hydroxide – hydrogen peroxide 1:1 Vol. solution. After the first cycle the quartzes are washed with ultra pure water and dried under nitrogen flux. Equimolar pyrrole and aldehyde solution are deposited on the quartz surfaces, and then they are put in a sature BF_3 environment acting as catalyst [6, 7, 8] (Fig. 2).

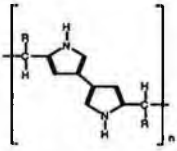

Fig. 2 Chemical formula of polypyrrole-derivates.

Seven aldehydes were selected to obtain an array of sensors with different functional group surface, and as an effect there are different interactions between analytes and polymer.

Aldehydes	Polymers.
Phenanthren-9-aldehyde	Poly[2-(-9phenanthrylmethyl)]-1H-pyrrole
Trans-cinnamaldehyde	Poly{2-[2-(2E)-3-phenylprop-2-enyl]-1H-pyrrole}
Ferrocene carboxialdehyde	Poly[ferrocene]-1H-pyrrole
Benzaldehyde	Poly2-(benzil)-1H-pyrrole
Anisaldehyde	Poly[2-4(methoxybenzil)]-1H-pyrrole
3-Hydroxy,4-Methoxibenzoaldehyde	Poly[2etoxy-5-(1H-pyrrol-2-ylmethyl)]phenol
Thiophene-2-carboxaldehyde	Poly[2-(thien-2-ylmethyl)]-1H-pyrrole

2µl of sample are put in a glass container close with volume of 0.5L with a micropipette. Once the essential pure oil was completely evaporate it was possible to start the series of acquisition. The set of quartz modified with the different polymers was tested with three pure essential oil: Lavender, Eucalyptus, Rosemary, and a mix of Lavender Eucalyptus 1-1 V/V. To avoid that the results could be effected by the sensor's derive, the tests were carried out in a random order. During the tests the flow was kept constant at 0.3 L./min, the measuring chamber's temperature was 303 °K. The cleaning phase of the sensors with technical air was set to 7 min. and the acquisition time was 5 min.

3 Results and discussion.

From fig.3 it is possible to see typical sensors signals of the quartzes microbalance transducer coated with Polypyrrole-derivates as a function of number acquisition for several essential oil. 1,5,8) lavender essential oil. 2,4) eucalyptus essential oil. 6,9) rosemary essential oil. 3,7) lavender +eucalyptus essential oil. It is evident that the sensors signals are completely reversible, which proves the weak bond between the analyte and the sensors matrix. In fact the sensor's signal after the acquisition time, recovers in a few minutes the initial frequency.

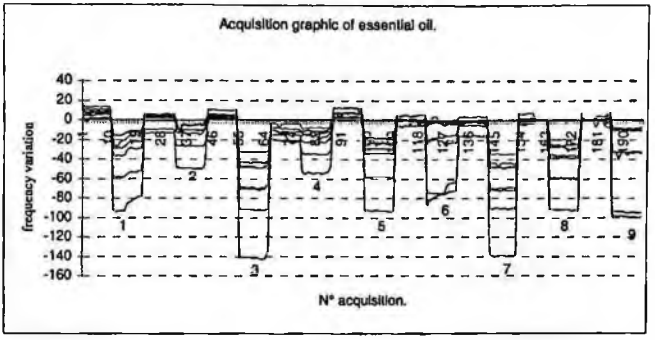

Fig.3 Typical sensors signals of the quartzes microbalance transducer coated with poly-pyrrole derivates.

The data obtained from the acquisitions in Fig. 3 have been treated with a Principal Component Analysis (PCA) see Fig. 4.

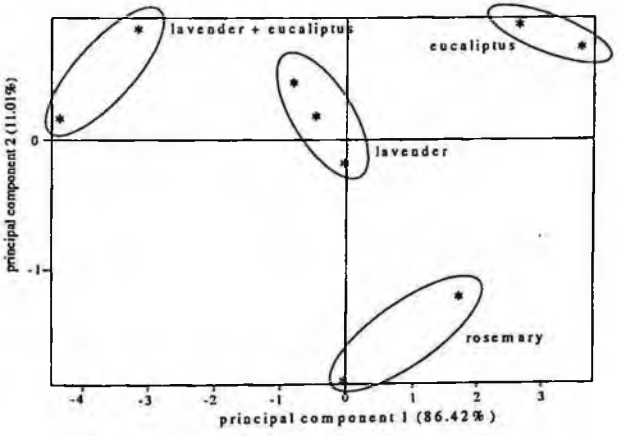

Fig. 4 Principal Component Analysis of different essential oils

From the data obtained with the PCA, see fig. 4, it results that the selected and tested nano-gravimetric sensors are able to discriminate the different essential oils and the lavender-eucalyptus mix. The first and the second principal component are sufficient at a 97.5% level to explain the variant.

5 Conclusions.

From acquisitions and Principal Component Analysis (see above) we can say that this series of analyzed polymers made by Technobiochip have the capacity to adsorb organic molecules in gaseous phase. These molecules present some advantages if confronted with traditional receptor molecules: an easy synthesis, they are more resistant because the polymer shows a strong bond with surface of gold electrode (this bond was not studied yet). Besides, the array of selected polypyrrole-derivate sensors show to have an high capacity to discriminate different kind of essential oils.

References.

[1] K.C. Persuad, G.Todd, Analysis of discrimination mechanisms in the mammalian olfactory system using a model nose, Nature 299 (1982)352.

[2] Di Natale C., Olafsdottir G., Einarssson S., Martinelli E., Paolesse R., D'Amico A. (2001). *Comparison and integration of different electronic noses for freshness evaluation of cod-fish fillets.* Sens. Actuators B. 77, p. 572–578.

[3] Feast S. (2001). *Potential application of electronic nose in cereals.* Cereal Food World 46 (4), p. 159–161.

[4] Mielle P. (1996). *Electronic noses: towards the objective instrumental characterization of food aroma.* Trends Food Sci. Technol. 7 (12), p. 432–439.

[5] G.Sauerbrey, *Use of vibrating quartz for thin film weighing and micro weighing,* Z.Phys., 155 (159) 206-222.

[6] Alder, A. D.; Longo, F. R.; Kampus, F.; Kim, J. *J. Inorg. Nucl. Chem.* 1970, *32*, 2443.

[7] Alder, A. D.; Longo, F. R.; Finarelli, J. D.; Goldmacher, J.;Assou, J.; Korsakokoff, L. *J. Org. Chem.* 1976, *32*, 476.

[8] Alder, A. D.; Longo, F. R.; Vardi, V. *Inorg. Synth.* 1976, *16*, 213.

APPLICATION OF AN ARTIFICIAL OLFACTORY SYSTEM TO CHARACTERISATION OF OLIVE OILS

A. BANTI*, N. MINNAJA*, E. COLLE**, E. DAL CANALE**, L. SCARSELLI°, A. TESSA°, L. SENSI°°

*Società tra i Poli Scientifici e Tecnologici della Toscana Occidentale srl – Navacchio
**Dipartimento di Chimica Organica e Industriale - Università di Parma
°Agenzia Regionale per la Protezione Ambientale della Toscana - Lucca
°°Industria Sistemi Elettronici Srl - Migliarino Pisano

Abstract

A novel artificial olfactory system has been tested in order to investigate its capability of certifying extra-virgin olive oils in terms of flavour characteristics, with the eventual goal of determining their geographic origin. The results, obtained for many tens of samples coming from Tuscany, are encouraging: the system is able to detect the main defects, and its output can be correlated satisfactorily with the assessments of a panel about the organoleptic features, with the province origin and with the majority cultivar. Such results allow establishing a road map toward a protocol for the application of the system as complementary o alternative to panel tests.

1. Objective and Scope

This research started as a project funded by the Italian Ministry of Research. The aim was to provide an integrated system containing an electronic nose and able to characterise different types of extra-virgin olive oils in terms of defects and organoleptic features, in order to provide in short time reliable information to producers and to consumers, and possibly to appoint a quality label.

A first output of the project is the novel artificial olfactory system *ISE NOSE 2000*, designed by SOATEC Srl and manufactured by Ingegneria dei Sistemi Elettronici Srl, based on metal oxide sensors available off the shelf, and on commercial software for multivariate analysis.

Discriminant function analysis (DFA) has been used to check the capability of the system in assigning oil samples to pre-defined classes, as province of origin, main cultivar, level of defect (artificially introduced in measured dilution), main organoleptic features.

2. Description of the Equipment and of Data Processing

The ISE NOSE 2000 Artificial Olfactory System consists in the following parts:

- a data acquisition and signal conditioning unit, containing the sensor chamber, an air flow regulator and an injection valve;
- a 15 position sampling unit, where each position consists in a vial where a small oil volume is in equilibrium with clean air, and from which the regulated air flow forwards the sample head spaces to the sensor chamber;
- a PC acting as control and data processing unit, which is the interface with the operator and hosts the dedicated software.

To ensure reproducibility, the vials are kept at the steady temperature of 30±1°C by a thermostatic bath, and the humidity of transport gas is also controlled (20%).

The sensor chamber hosts 12 thick layer commercial gas sensors (Figaro – Japan), consisting in metal oxide thick layers whose electrical resistance is affected by reducing gases, and in addition two sensors for humidity and temperature. A controlled air flow coming from a chromatographic air generator is continuously maintained on the sensors, to ensure them a constant oxygen feed. When just clean humidified air is present, each sensor exhibits a steady-state electrical resistance (base line). The base line has to be recovered after each measurement; 15 s after that, the injection valve switches the air flow through the vial holding the oil sample to be analyzed. The transport gas, containing now the volatile compounds of the head space, is convoyed to the sensor chamber for 15 s; the volatile compounds act as reducing agents, introducing oxygen vacancies into the sensor matrix, and therefore inducing a decrease of the electrical resistance. Right after the injection, the sensors are exposed again to pure chromatographic air for 530 s, till the reducing effect disappears, the base line is recovered, and the system is ready for a new measure cycle. In each cycle, the resistances of all sensors are monitored and recorded *vs.* time for the first 200 s, yielding a "fingerprint" if the oil under test.

The equipment allows measuring 45 samples per 8 hr shift, taking into account also the time needed to replace the 15 vials when all loaded samples have been tested.

The "fingerprint" of each sample is reduced to a set of 36 numerical data, namely the modules of the first 3 Fourier components of functions resistance *vs.* time for each of the 12 sensors. Accordingly, every sample is represented by one point in a 36-dimensional hyperspace.

These data may be processed taking advantage of standard multivariate analysis techniques. For instance, clusters of points representing oils with some common feature may be defined as a training set; when a new oil sample is

submitted to the system, it is assigned to one of these clusters through discriminant function analysis (DFA).

3. Experimental Data

3.1 Evaluation of Defects

A first extensive test of the system has been performed at the University of Parma, Dep.t of Organic and Industrial Chemistry, and has been reported elsewhere (F. Camurati, G. Cristofanilli, M. Bonadonna, E. Colle, E. Dalcanale, "Riconoscimento dei difetti negli oli vergini di oliva: confronto fra panel test e sistemi olfattivi artificiali", *Riv. Ital. Sostanze Grasse, 79*, 65-70 (2003)). The training set consisted in two clusters, one of extra-virgin oil samples and the other of defected oils according to the judgement of a qualified panel.

In this study, the extra-virgin oils for the training set have been selected again according to the assessment of a panel; the defected oils, instead, have been obtained by blending the same oils with standard single defects, as defined by the COI committee. This allowed the definition of a sensitivity scale, because blending was done by addition of controlled quantities of the selected single defects ("vinegary", "rancid" and "fusty"). The analysis has been performed at the ARPAT Lucca facility for food quality control. A typical example is given in Figure 1, in which the coordinate (for sake of clarity it is replicated as x and y) has been selected by DFA, and the defect is "vinegary". Figure 2 exhibits 3 clusters, corresponding to extra-virgin oil, oil with addition of "rancid" defect, oil with addition of "fusty" defect, respectively.

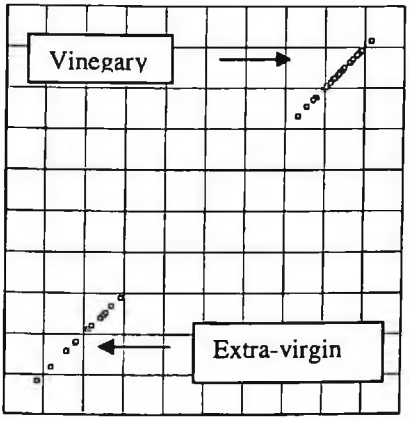

Figure 1 - Extra-virgin *vs.*"vinegary" oil.

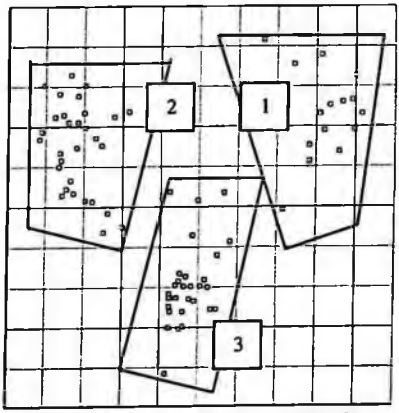

Figure 2 – Extra-virgin (1) *vs.* "rancid" (2) and "fusty" (3) oil.

3.2 Assessment of Quality Parameters

Several extra-virgin olive oils selected from different Tuscanian provinces and different cultivars have been tested in the new facility *Polo Tecnologico del Gusto* of Società tra i Poli Scientifici e Tecnologici della Toscana Occidentale. The aim was to detect the differences among them, and then try to correlate them due either to the predominant cultivar, to the origin, and to the organoleptic features assessed by a qualified panel.

3.2.1 Cultivar

Figure 3 shows the results on 16 samples, all produced in a small area of the Pisa province: one cluster is made up by single cultivar oils ("Frantoio"), while all blended oils are collected in the second one.

3.2.2 Origin

20 different samples coming from 8 provinces of Tuscany have been tested. The system has recognised the 8 different clusters.

3.2.3 Organoleptic features

The same 20 samples have been submitted to a qualified panel, which gave ranking for three main taste features, namely "fruity", "bitter" and "spicy". The system is able to distinguish between 2 clusters for each organoleptic feature, namely higher and lower than average.

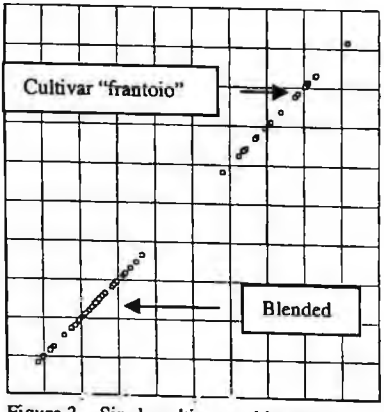

Figure 3 – Single cultivar *vs.* blended oil

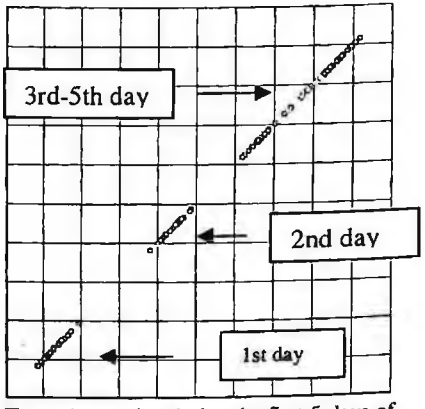

Figure 4 – Ageing during the first 5 days of operation

3.3 Critical Issues

The main concern for large scale adoption of electronic nose is the stability of the sensors, which is both long term (drift) and short term (lack of reproducibility).

The first precaution taken is an ageing of the whole system before beginning a set of measurements: the results are considered valid and recorded only after some days of exposure to working conditions. This approach means that the system is not suitable for spot measurements: it has to work continuously for the whole time in which data have to be collected.

The day-by-day drift is clearly shown in Figure 4, where the clusters represent results taken for the same set of samples in subsequent days of the first week after initial ageing; the trend to reduction is clearly seen, even for the "worst" DFA coordinate; on the other hand, the main features are not affected at the time scale of some weeks. The easiest solution is to establish again the training set when needed; if the intended application for the system is the certification of oil quality, a protocol has to establish the time of validity of a selected training set; according to the present experience, one month seems to be a reasonable length of time.

For the short term stability, a repetition of the measurements is an effective guarantee of the stability of the mean value; as a matter of fact, all data presented here are results of repeated measures (typically 6) on the same samples, and the so-called "outliers" are just a few and may also be easily discarded, if preferred so (as a matter of fact, no outlier has been discarded in all plots shown in this paper). On the other hand, the outcomes of the single panellists in a panel test are scattered (so that a figure for "robustness" is always attached to the median, taken as the best result), and much more than the results of the electronic nose.

As for data processing, the simple DFA approach is not able to assess the likelihood of a very simple and naive statement like "this sample belongs to this pre-defined cluster". This is a limitation of to-day's release of the apparatus: the available techniques of multivariate calibration will overcome this limitation.

4. Results and Conclusions

The set of obtained results is very encouraging for promoting an extensive adoption of an electronic nose for validation of olive oil, as a valuable tool complementary to the panel test, and will be presented soon to the regional agency for innovation in agriculture and to associations of oil producers. Scales for defects and for organoleptic features may be established, and periodically

validated through comparison with qualified panels; this would allow a steady maintenance of the training set.

This opens the way to two stimulating perspectives:

1) for practical applications: a protocol can be established for the use of an electronic nose as a step in the qualification procedures of an extra-virgin olive oil (DOP or IGP);
2) from a theoretical point-of-view: at least in the case of olive oil, a metrics of the olfactory sensations can be tentatively proposed and perhaps established later, after a more comprehensive investigation.

The mission of *Polo Tecnologico del Gusto* will include a service for quality assessment of olive oils, which will be supported by dedicated enhanced software.

OPTICAL SENSOR ARRAY FOR MULTI-GAS SENSING

A.G. MIGNANI, A.A. MENCAGLIA, L. CIACCHERI
CNR-IFAC, Via Panciatichi, 64 – 50127 Firenze (Italy)

R. RELLA, J. SPADAVECCHIA
CNR-IMM, Sezione di Lecce, Via Arnesano – 73100 Lecce (Italy)

R. PAOLESSE, C. DI NATALE, A. D'AMICO
Università di Roma 'Tor Vergata' e CNR-IMM, Sezione di Roma, Via Fosso del Cavaliere, 100 – 00133 Roma (Italy)

The monitoring of gases and vapors of industrial and environmental interest was addressed using guided wave technologies. Hybrid optical devices making use of fiber optics and microoptics were used as an optical platform, on which to deposit gas or vapor-sensitive innovative materials. These materials, based on metal-coordinated porphyrins, phthalocyanines and their blends, were functionalized so as to offer their dielectric constants reversibly modulated by the interaction with analytes. The optical platform fitted to an electro-optical scanner, allowed the sensitive materials to be spectrally interrogated in the whole or in selected bands of the visible spectral range, so as to achieve a gas- or vapor-modulated absorption spectroscopy signal.
The optical sensors were exposed to CO, SO_2, NO_2 and NH_3 in the 25-100 ppm range. The overall sensor response was processed by means of chemometric methodologies. The experiments aimed to emulate an artificial olfactory perception as far as these toxic gases/vapors were concerned. The sensor-array demonstrated an excellent capability of discriminating the gases/vapors types and their concentrations.

Introduction

This work is addressed to the monitoring of gases and vapors of interest for industrial and environmental applications by means of the same array of optical sensors. Innovative nanomaterials, based on metal-substituted porphyrins, phthalocyanines, and their blends have been made and used as optochemical sensors for the monitoring of CO, SO_2, NO_2 and NH_3. These optochemical sensors change the color, and, consequently, the absorption spectrum when exposed to gases and vapors.

A novel fiber-optic-based spectroscopic platform, consisting of a microoptic scanner for the spectral interrogation of the sensor array has been implemented. The spectroscopic platform, fitted with the sensor array, demonstrated an ability to achieve an olfactory perception of the experimented gases and vapors.

The working principle

Metal-substituted porphyrins and phthalocyanines are highly sensitive to a wide range of volatile compounds [1-10]. They change the absorption spectrum and,

consequently, the color when exposed to many types of vapors, although they are lacking in high selectivity.

As the sensitivity and selectivity of porphyrins and phthalocyanines are greatly influenced by the coordinated metal, an array of blends of metalloporphyrin- and metallophthalocyanin-based materials made of different metals was made, and their overall response to gases and vapors was processed by means of chemometric methodologies, in order to achieve an olfactory perception.

In practice, an olfactory pattern was achieved by means of the color pattern of chromophore-array, which was detected by means of a spectrometric-based device.

The spectroscopic platform

A novel spectroscopic platform was implemented to experiment the same sensor array for the monitoring of different gases and vapors. A diagram of the platform is shown in Figure 1. The vapors were guided by means of a nitrogen flux inside a flow cell containing the sensors. A micro-optic scanner fitted inside the flow cell was used for spectral interrogation of the sensors while exposing them to the different concentrations and types of the analytes [11]. The sensors were prepared from water-ethanol metalloporphyrin and metallophthalocyanin solutions and blends that were sprayed on glass disks.

The scanner consisted of a revolving platform with 16 slots powered by a step motor: in one slot, a glass disk was positioned as a reference for signal normalization, while the optochemical sensors were positioned in the remaining fifteen slots. Two optical fibers, connected to an optical fiber spectrophotometer, were fitted to the flow cell in a fixed position so that they could perform transmission measurements of all the sensors while the revolving platform rotated.

The spectrophotometer used for the spectral interrogation of the sensor array was a custom-made device operating in the 400-700 nm spectral range, with a resolution of 10 nm [12]. LabView software was used to manage all measurements, to set the spectrophotometer parameters, to operate the step motor, and to store the spectral data. A view of the spectroscopic platform is shown in Figure 2.

The experimental results

The sensor array was exposed to different concentrations of CO, NO_2, NH_3 e SO_2 in the 25-100 ppm range, by fluxing nitrogen between the exposures.

As an example, Figure 3 shows the sensor array response to CO at 100 ppm, while Figure 4 shows the response of a single sensor to all experimented gases at all considered concentrations.

The results of multivariate data processing by means of Principal Component Analysis of the full set of spectral responses is given in the 3D map of Figure 5,

while Figure 6 shows the decision boundaries which were obtained by means of the KNN method [13, 14].

The discrimination of the sensor array was very good and the olfactory sensitivity to the different concentrations of each gas was also clearly measurable.

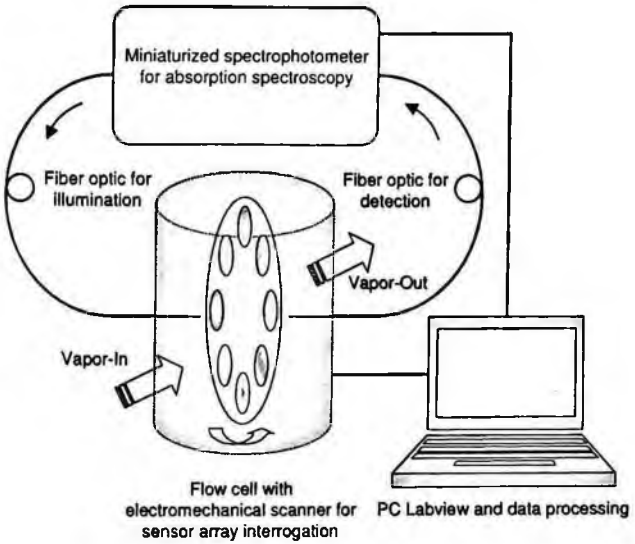

Figure 1. Diagram of the spectroscopic platform for sensor array interrogation.

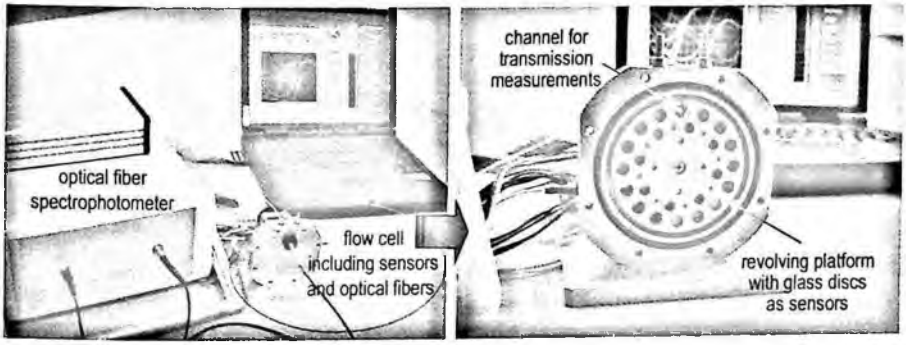

Figure 2. Practical implementation of the spectroscopic platform.

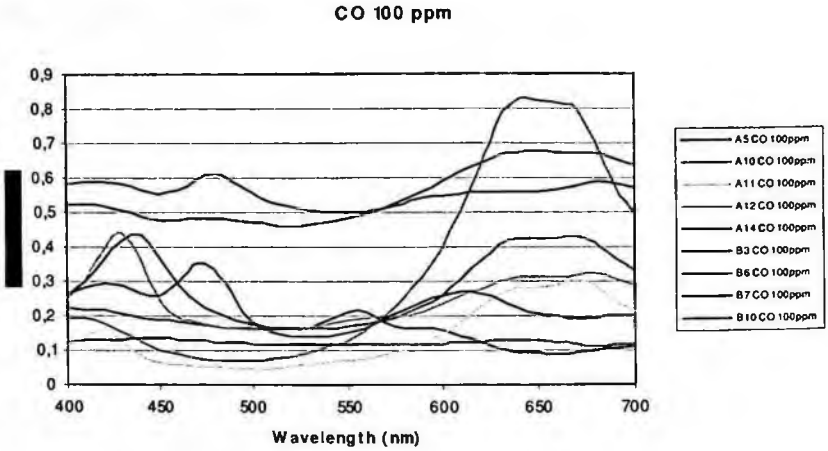

Figure 3. A typical response of the sensor array to CO at 100 ppm.

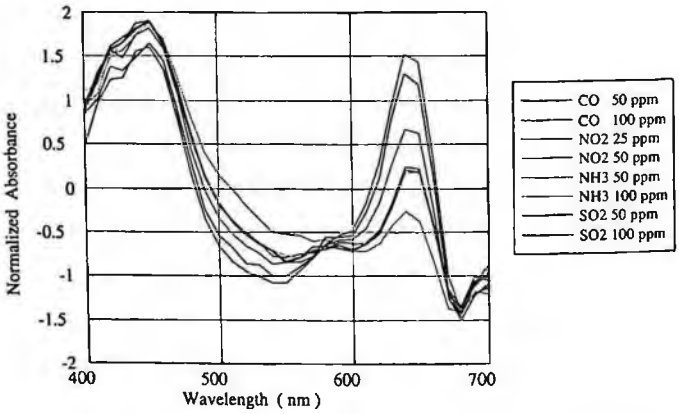

Figure 4. A typical response of one sensor of the array to the full set of experimented gases/vapors and concentrations.

Perspectives

An array of optochemical sensors made of metalloporphyrin- and metallophthalocyanin-based materials and their blends was used to detect different types of vapors and gases of interest for industrial and environmental applications. A good gas/vapor discrimination as well as the perception of various concentration was demonstrated.

The microoptic device used for sensor interrogation can be easily miniaturized. The sensors can be spayed on a grid-based glass slide and equipped with an array of microlenses so as to provide coupling to a microoptic illumination/detection device.

In practice, a microoptic chip can be achieved, solar-cell powered, which can be fitted to a badge or in every application needing a stand-alone device.

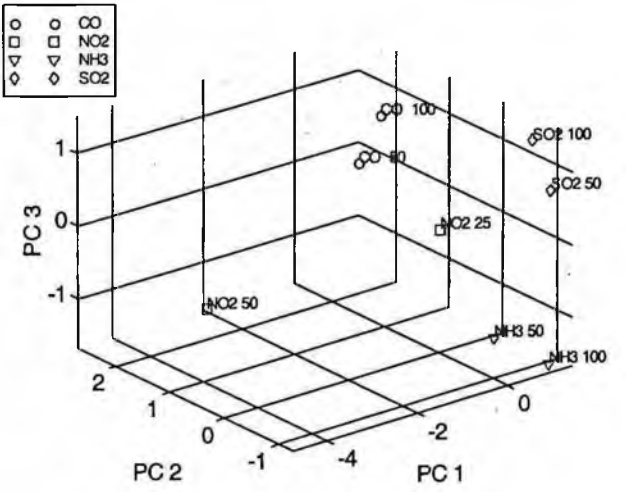

Figure 5. Sensor array response to the different concentrations of gases/vapors.

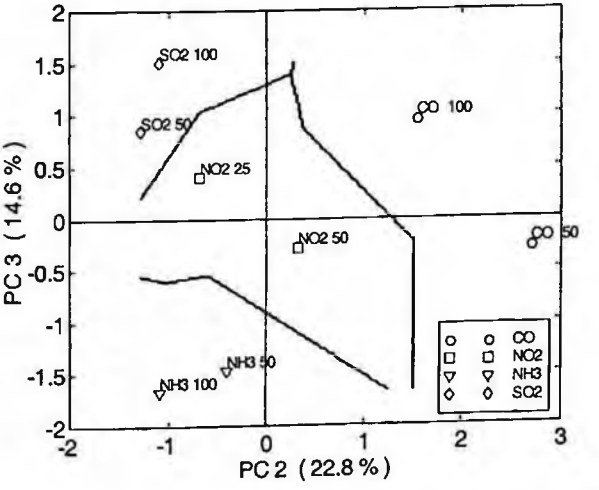

Figure 6. Decision boundaries for the sensitivity to the different gases/vapors.

Acknowledgments

Projects MIUR-FIRB 'Biosens' and MIUR-FISR 'SAIA-ARGO' are acknowledged for partial financial support. The authors are grateful to Mr. Franco Cosi and Mr. Flavio Casino for the technical assistance, and to Mr. Daniele Tirelli for the mechanical designs.

References

1. D. Dolphin, Ed., '*The Porphyrins*', vol. III, Academic Press, New York, 1978.
2. R. Paolesse, C. Di Natale, V. Campo Dall'Orto, A. Macagnano, A. Angelaccio, N. Motta, A. Sgarlata, J. Hurst, I. Rezzano, M. Mascini, A. D'Amico, 'Porphyrin thin films coated quartz crystal microbalances prepared by electropolymerization technique', *Thin Solid Films*, **354**, 1999, pp. 245-250.
3. T.C. Pearce, S.S. Schiffman, H.T. Nagle, J. W. Gardner, Eds.,'*Handbook of Machine Olfaction: Electronic Nose Technology*', Wiley, 2003.
4. C. Di Natale, R. Paolesse, A. Macagnano, S. Nardis, E. Martinelli, E. Dalcanale, M. Costa and A. D'Amico, 'Sensitivity-selectivity balance in mass sensors: the case of metalloporphyrins', *Journal of Material Chemistry*, **14**, 2004, pp.1281-1287.
5. S. Capone, R. Rella, P. Siciliano, L. Vasanelli, L. Valli, L. Troisi, 'On the characterization and gas sensing properties of Cu(tetra)alkylamino-carbonyl phthalocyanine LB films', *Thin Solid Films*, **327-329**, 1998, pp. 465-468.
6. R. Rella, J. Spadavecchia, G. Ciccarella, P. Siciliano, G. Vasapollo, L. Valli, 'Optochemical vapour detection using spin coated thin films of metal substituted phthalocyanines', *Sens. Act. B*, **89**, 2003, pp. 86-91.
7. J. Spadavecchia, G. Ciccarella, S. Capone, P. Siciliano, R. Rella, 'Metallophthalocyanines thin films in array configuration for electronic optical nose applications', *Sens. Act. B*, **96**, 2003, pp. 489-497.
8. C. Di Natale, D. Salimbeni, R. Paolesse, A. Macagnano, A. D'Amico, 'Porphyrins-based opto-electronic nose for volatile compounds detection', *Sensors and Actuators B*, **65**, 2000, pp. 220-226.
9. N.A. Rakow, K.S. Suslick, 'A colorimetric sensor array for odour visualization', *Nature*, **406**, 2000, pp. 710-713.
10. J. Spadavecchia, G. Ciccarella, T. Stomeo, R. Rella, S. Capone, P. Siciliano, 'Variation in the optical sensing responses toward vapors of a porphyrin-phthalocyanine hybrid thin film', *Chemistry of Materials*, **16**, 2004, pp. 2083-2090.
11. R. Paolesse, C. Di Natale, A. Macagnano, S. Nardis, A. D'Amico, A.A. Mencaglia, P. Bizzarri, A.G. Mignani, 'Toward an artificial olfactory perception: a fiber-optic spectroscopic platform for interrogating an array of optochemical sensors', Proc. *16th Optical Fiber Sensors Conference*, Technical Digest ISBN-4-89114-036-4, K. Hotate, H. Nagai Eds., 2003, pp. 742-745.
12. A.G. Mignani and A.A. Mencaglia, 'Direct and chemically mediated absorption spectroscopy using optical fiber instrumentation', *IEEE Sens. J.*, **2**, 2002, pp. 52-57.
13. I.A. Cove, J.W. McNicol, 'The use of principal component in the analysis of the near infrared spectra', *App. Spectr.*, **39**, 1985, pp. 257-266.
14. T.M. Cover, P.E. Hart, 'Nearest neighbor pattern classification', *IEEE Trans.Information Theory*, 13, 1967, pp. 21-27.

ANALYSIS OF ITALIAN WHITE WINES BY A PORPHYRIN BASED 'ELECTRONIC TONGUE' SYSTEM

GIORGIO MARIA VERRELLI

Department of Chemical Sciences and Technologies, University of Rome "Tor Vergata", Via della Ricerca Scientifica 00133 Rome, Italy

LARISA LVOVA

Department of Chemical Sciences and Technologies, University of Rome "Tor Vergata", Via della Ricerca Scientifica 00133 Rome, Italy

ROBERTO PAOLESSE

Department of Chemical Sciences and Technologies, University of Rome "Tor Vergata", Via della Ricerca Scientifica 00133 Rome, Italy

CORRADO DI NATALE

Department of Electronic Engineering, University of Rome "Tor Vergata", Via del Politecnico 1 00133 Rome, Italy

ARNALDO D'AMICO

Department of Electronic Engineering, University of Rome, "Tor Vergata", Via del Politecnico 1 00133 Rome, Italy

Tasting systems based on array of cross-sensitive sensors are one of the most promising ways of performing rapid and low-cost analysis for foodstuff quality control. In literature many applications of Electronic tongue devices can be found for the characterization of different kinds of red wines, while the number of similar experiments concerning white wines is smaller. In the present study the electro-chemical properties of PVC-based solid contact sensors doped with different metallo-porphyrins have been evaluated, and their application in Electronic tongue system for the classification of Italian "Verdicchio" white wines is reported.

1. Introduction

In the last few years, an increasing need to monitor and control different chemical environments has been observed; for this reason, atmosphere in closed rooms, air quality in urban areas, flavor of foods or beverages, medical applications on revealing some important pathologies, etc. have become the centre of many researchers attentions [1]. An advantageous solution to measure complex chemical environments, characterized by the simultaneous presence of several compounds has been demonstrated to be the integration of chemical sensors, which allow fast and low cost analysis, in arrays [2,3].

In literature, porphyrin based chemical sensors have been widely reported for the study of different red wines [4,5], while the application of these kind of sensors for the study of white wines samples are not so diffused.

In this study an Electronic Tongue [6,7] composed of different porphyrin based cross-sensitive sensors, has been applied to the study of different samples of Italian white wines, of 'Verdicchio D.O.C.' quality, allowing both qualitative both quantitative results.

2. Experimental

2.1. *Reagents*

Metal complexes of porphyrins were synthesized following literature methods [8].

Poly(vinyl chloride) (PVC), plasticizers [*o*-nitrophenyl octyl ether (*o*-NPOE), bys(2-ethylexyl) sebacate (DOS) and tris(2-ethylexyl) phosphate (TOP)], and ionic additives [potassium tetrakis(4-chlorophenyl) borate (TpClPBK) and tetra-dodecylammonium chloride (TDACl)] were used as received from Fluka.

Buffer solutions were prepared with Tris[hydroxymethyl]aminomethane (Trizma Base or TRIS) and 2-(N-Morpholino)ethanesulforic acid (MES), purchased from Sigma.

Tetrahydrofurane (THF) used to dissolve membranes was from Fluka.

All aqueous solutions were prepared with salts of the highest purity available from Fluka.

2.2. *Wine samples*

Different samples were analyzed in this experiment. All samples of Italian white wines were of quality 'Verdicchio'. They were commercial samples available in local markets and they are listed in table 3.

Potentiometric properties shown by sensors and their characteristics of cross-sensitivity have been studied, and an array of highly cross-selective membranes has been chosen and applied for the study of 7 different samples of white wines.

Data analysis was performed with different techniques, which allowed the evaluation of both qualitative both quantitative considerations. For the quantitative analysis we decided to monitor some peculiar parameters of white wines [9], to look for a good correlation model by regression methods. Parameters which we decided to study are listed in table 4.

2.3. *Potentiometric properties of membranes and measures*

Potentiometric properties of the membranes, measured versus a standard calomel reference electrode, were evaluated measuring the response in solutions containing different ions in a concentration range from 10^{-5}M to 10^{-1}M. These measures were conducted using a buffer solution, because of the strong influence of pH on sensors performances. After preliminary studies, we decided to study the sensors responses using as buffer solution a 0.01M solution of MES; the pH value was then adjusted to the value of 5.5 by NaOH.

Wine samples were measured immediately after opening the bottle, to avoid alterations in the composition of wine because of the contact with air. Measures were about 7 minutes long and the potentiometric data obtained by the sensors, were collected by an home-made PC equipped with high-impedance input analog-to-digital converter.

The samples were analyzed in a random order [to avoid 'memory effects' on the responses of the sensors] and between each measure a conditioning solution, called *artificial wine*, was used to restore the membrane characteristics. At the end of each measure, sensors were soaked with a 0.01M solution of NaCl.

The membranes were deposited on the electrode surface by casting. The solution has been prepared dissolving the mixture of poly(vinyl-chloride), plasticizer and membrane active component (M.A.C.) by an appropriate amount of THF.

3. Results and Discussion

The set of membranes studied in this work is reported in Table 1:

Table 1: Membranes composition of the Electronic Tongue (R=-O-$(CH_2)_6$-CH_3)

Membrane	Matrix	Plasticizer	Ionophore	Ionic Additive
1	PVC 33wt%	DOS 66wt%	H_2TPP 1wt%	-
2	PVC 33wt%	o-NPOE 66wt%	Co(III)TPPBr 1wt%	-
3	PVC 33wt%	DOS 65.6wt%	Co(II)TPP-R 1wt%	TpClPBK 0.4wt%
4	PVC 33wt%	TOP 67%	-	-
5	PVC 33wt%	-	-	TDACl 40mol%
6	PVC 33wt%	DOS	Pt(II)TPP	TDACl 40mol%
7	PVC 33wt%	o-NPOE 66wt%	Pt(IV)TPPCl$_2$	-
8	PVC 33wt%	o-NPOE 66wt%	Pt(IV)TPPCl$_2$	TDACl 40mol%

We first studied the potentiometric properties of these membranes, measuring the response in solutions containing different ions, in a concentration range from 10^{-5}M to 10^{-1}M, by varying this value every 100 sec.

Influence of solution pH was also evaluated by studying the responses of sensors in a solution called *universal buffer*, prepared by dissolving in distilled water citric acid (concentration $6.7*10^{-3}$M), boric acid ($11.4*10^{-3}$M) and NaH_2PO_4 (10^{-2}M); the starting pH value of 2.5 has then been increased until the value of 11 by additions of NaOH 1M.

The responses are reported in Table 2:

Table 2: Slopes of the sensors responses (millivolts per decay)

Mb	NaCl	NaBr	$NaNO_3$	$NaNO_2$	Na_2SO_4	pH
1	+11±6	+13±1	+10±2	-1±2	+6±4	-25±0
2	+13±3	+14±1	+13±1	-31±3	+9±1	-37±1
3	-10±6	-12±6	-12±3	-21±3	-6±7	-10±5
4	+37±10	+45±3	+32±1	+30±2	+40±6	-9±2
5	-35±1	-46±2	-40±7	-53±4	-2±3	-18±3
6	-49±0	-58±3	-53±3	-7±11	1±4	-9
7	-40±1	-48±6	-41±4	-19±9	1±0	-8
8	-35±3	-46±3	-43±1	-42±1	6±5	-34

The array of PVC-based membranes shown in Table 2 has been applied for quantitative and qualitative analysis of different samples of Italian white wines of quality Verdicchio; all samples were chosen between the commercial ones, available in markets, and were analyzed in 3 consecutive days, and keep stored at 4°C.

The analyzed samples are shown in Table 3:

Table 3: List of samples analysed by array composed of 8 non-specific sensors

Sample	Cantina
1	"Caldirola"
2	"Casal dei Cavalieri"
3	"Fazi Battaglia"
4	"Piersanti"
5	"Moncaro"
6	"San Sisto"
7	"Sant'Ignazio"

According to [9], we decided to study some peculiar parameters, which can well characterize the white wines, to evaluate quantitative analysis. All studied parameters are listed in Table 4:

Table 4: List of some wine parameters obtained by independent chemical analysis

Sample	ost1	2	3	4	5	6	7
Alcohol	11.72	12.65	12.20	12.31	12.19	13.01	12.95
Volatile acidity	0.27	0.34	0.31	0.27	0.22	0.46	0.40
SO_2	90	80	96	90	77	93	61
L-Malic acid	1.05	0.31	1.70	0.86	1.06	0.36	0.26
L-Lactic Acid	0.18	1.82	0.80	0.53	0.16	0.87	1.13
Total	21.6	8.81	9.24	8.91	8.12	9.67	6.53
polyphenols	4.76	5.74	6.92	6.48	6.70	6.62	4.98

Using PCA, we could not reach good results in samples discrimination, with a percentage of correct classification lower than 70%, while better results have been obtained by processing data by PLS. In Figure 1 the PLS score plot can be seen:

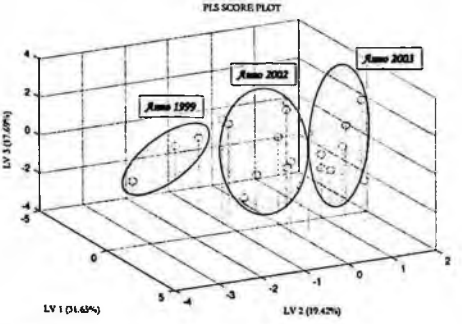

Figure 1: PLS Score Plot of first 3 latent variables

Score plot represented in Figure 1 was obtained by plotting the first 3 latent variables of the PLS model, by using as input matrix, potentials from all sensors (8 working electrodes and pH glass electrode) and a total variance of 68.76% is represented. All measures were very reproducible during the whole period of measures and well defined clusters can be seen; we could easy distinguish 3 big clusters corresponding to the different ages of the wines (1999, 2002 and 2003).

We also tried to evaluate quantitative considerations on analyzed samples. Not for all studied parameters we were able to reach good results; good results were obtained, e.g., for Total SO_2 (Figure 2) and Polyphenols (Figure 3).

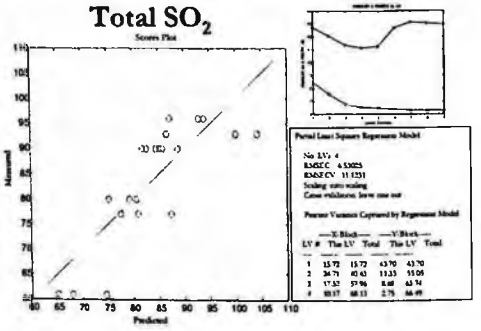

Figure 2: Measured vs Predicted graph, RSMECV and RSEMC and mathematical model characteristics for Total SO_2

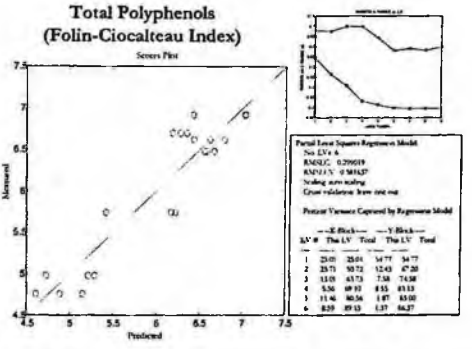

Figure 3: Measured vs Predicted graph, RSMECV and RSEMC and mathematical model characteristics for Total Polyphenols (Folin-Ciocalteau Index)

In Figures 2 and 3 we report the predicted vs measured graph obtained by using, respectively, 4 and 6 latent variables, the characteristics of the mathematical model created by Matlab and the RMSEC and RMSECV graph.

Because of the small number of measures we decided to perform data treatment by *leave-one-out* cross-validation technique. As can be seen in figures 2 and 3, the model was able to correctly predict the value of all the samples for these parameters.

4. Conclusions

The Electronic Tongue device, composed of 8 highly cross-sensitive sensors, was able to clearly distinguish 7 different samples of Italian white wine (Verdicchio quality). Data analysis performed on measured samples, showed a good reproducibility and stability of the measures.

The system was able to well define 3 big clusters of samples, corresponding to the different age of the wines (produced in 1999, 2002 and 2003 respectively). The system was also able to give quantitative informations about some of the measured parameters which characterize the total quality of wines, e.g. SO_2 and Total Polyphenols.

References

1. W. Gopel, K.D. Schierbaum in Sensors, Vol. 2, (Eds.: W. Gopel, T.A. Jones, M. Kleitz, J. Lundstrom, T. Seiyama, Wiley-VCH, Weinheim (1991)

2. S. Zaromb, J.R. Stetter, Sens. Actuators 6 (1984) 225

3. W.P. Carey, B.R. Kowalski, Anal. Chem. 58 (1986) 3077.

4. A. Legin, A. Rudnitskaya, Y. Vlasov, C. Di Natale, E. Mazzone, A. D'Amico, Electroanalysis 11. (1999) 814.

5. A. Legin, A. Rudnitskaya, L. Lvova, Y. Vlasov, C. Di Natale, A. D'Amico, Anal. Chim. Acta 484 (2003) 33–44.

6. Y.G. Vlasov, A.V. Legin, A.M. Rudnitskaya, A. D'Amico, C. Di Natale, Sens. Actuators B 65 (2000) 235.

7. Winquist, S. Holmin, C. Krantz-Rülcker, P. Wide, I. Lundström, Anal. Chim. Acta 406 (2000) 147.

8. R.Paolesse, The porphyrin Handbook Academic, New York, 2000, 1

9. M.A. Amerine, C.S. Ough, Wine and Must Analysis, Wiley, New York, 1974.

MICROFABRICATION AND MICROSYSTEMS

SIMULATION AND MODELING OF THE EFFECT OF TEMPERATURE ON MEMS RESONATORS

A. MOLFESE*†, A. NANNINI*, D. PACI*†, F. PIERI*

*Dipartimento di Ingegneria dell'Informazione, Università di Pisa
†IEIIT - Sezione di Pisa, CNR
Via Caruso, 56122 Pisa, Italy

The influence of axial stress (typically originated by temperature difference) on the resonance frequency of three different types of flexural MEMS resonators, fabricated in a thick polysilicon technology, is investigated. Both clamped-clamped and a free-free resonators are considered, with a higher quality factor expected in the latter because of reduced mechanical losses in the anchors. Nominal resonance frequencies of the devices are between 10 MHz and 50 MHz. FEM simulations are performed and discussed, and their results compared, where possible, with theoretical models.

1. Introduction

MEMS resonators have been proposed as fundamental components for RF filters, mixers and oscillators [1]. Because of their very high quality factors [2][3] (in the range of 10.000 or above) low phase noise, and thus very high short-term frequency stability, is expected in MEMS-based electronic oscillators. However, if they are to be used as frequency references, high long-term and temperature stabilities are mandatory [4][5][6]. Also, their sensitivity to fluctuations of the fabrication process parameters is of great importance in the same respect. Specifically, the residual stress acting on the beam, which mainly depends on the deposition conditions of the material which constitutes the resonator, is expected to influence the resonance frequency of nominally identical resonators, either from different chips or from the same chip.

In this paper three different two-port flexural resonators with lateral driving and sensing are considered: a classic clamped-clamped beam [7] (type CC1), a free-free beam with matched flexural support beams [6], resonating on the first resonance mode (type FF1), and a free-free resonator with matched flexural support beams, resonating on the third resonance mode (type FF3). This last device is similar to the one presented in [8], but in that case the matched supports were torsional rods. The structure of the three types of devices is sketched in fig. 1. In the paper, FEM simulations performed with FEMLAB® on

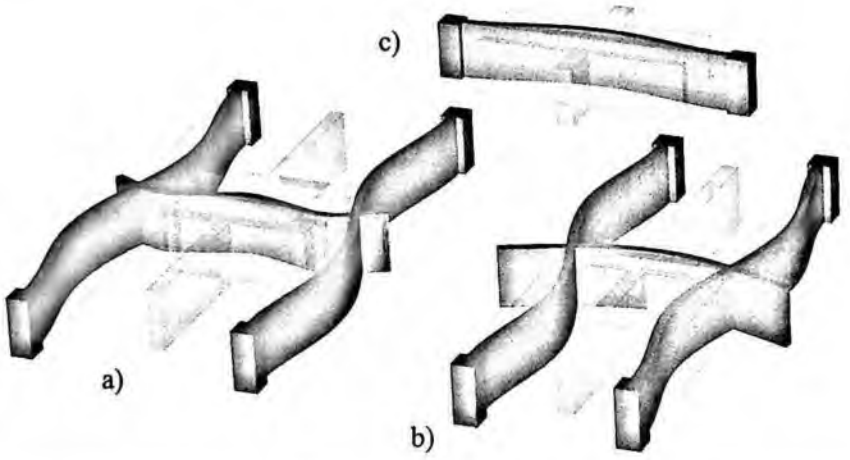

Figure 1. Schematic view of the fabricated resonators: a) free-free resonator, third mode; b) free-free resonator, first mode; c) clamped-clamped resonator, first mode. Deflected shapes are solid, shapes at rest and input/output electrodes are shaded.

the three geometries are presented, with emphasis on the aforementioned effects (temperature and residual stress) on the resonance frequencies. A theoretical analysis of the expected behavior of the CC1 resonator is presented. Closed form analytical expression for the frequency shift is derived and compared with the simulation results.

2. Fabrication and Design

The resonators were fabricated by using the THELMA MEMS technology, developed at STMicroelectronics. To maximize the electromechanical coupling between the electrodes and the resonator, the gap between them must be kept as small as possible [9]. To overcome the resolution limit of the process, the electrodes were mounted on electrostatic micro-motors to drive them closer to the beam [7].

The CC resonator is obtained simply by clamping the ends of the beam to the substrate. The free-free condition, instead, is obtained [6] by suspending the resonating beam by two doubly clamped support beams, joined to the main beam in two points which correspond to the nodes of the free-free mode which has to be excited. The length of the supporting beams is designed so that they resonate on their second clamped-clamped mode at the same frequency of the main beam. As a consequence, at least ideally, they do not exert any bending moment on the

main beam. This approach is valid both for FF1 and FF3 resonators, provided that the driving and sensing electrodes are properly positioned along the beam. They were placed to maximize the electro-mechanical coupling coefficient for the desired mode shape, which is proportional to the mode-shape integral on the electrodes length [9]; a possible geometry for a FF3 resonator is shown in Fig. 4, where the electrodes and the deflected shape are also represented.

3. Analytical modeling of the axial stress for clamped beams

The analytical derivation of the resonance frequencies for axially loaded clamped-clamped beams has been already carried out in [10]. Our approach is slightly different and leads to a closed form for the resonance frequencies. The effect of temperature and/or residual stress on CC1 resonators can be modeled by supposing a uniform stress parallel to the beam axis, and by including its effect on the equation of motion of the beam. The total compressive axial stress σ_{eq} can be caused by the fabrication residual stress σ_R, by the temperature difference between the beam and the substrate, and by the difference between their respective thermal expansion coefficients. Its expression can be written

$$\sigma_{eq} = \sigma_R + E\left[\alpha_m \Delta T + \left(T_m - T_{ref}\right)\Delta\alpha\right] \tag{1}$$

where α_m is the mean value of the thermal expansion coefficients of the resonator and substrate, and $\Delta\alpha$ their difference; T_m is the mean temperature of the resonator and the substrate, ΔT is their difference and T_{ref} a reference temperature; E is the Young's modulus of the material. To obtain the resonance frequencies of a clamped-clamped beam, the Euler-Bernoulli equation for a beam with rectangular section under axial load has to be solved. The resonance frequencies of the structure are given by:

$$f_n = \frac{1}{2\pi}\left(\frac{\lambda_n}{L}\right)^2 \sqrt{\frac{E}{12\rho}}W \tag{2}$$

where ρ is the volumetric mass density of the resonator, and W and L are the width and the length of the resonator, respectively; λ_n is the n^{th} solution of the eigenvalue equation [10]:

$$1 - \cos\left(\lambda_{1n}\right)\cosh\left(\lambda_{2n}\right) = \frac{\lambda_{1n}^2 - \lambda_{2n}^2}{2\lambda_{1n}\lambda_{2n}}\sin\left(\lambda_{1n}\right)\sinh\left(\lambda_{2n}\right) \tag{3}$$

with

$$\lambda_{1n}=\frac{1}{\sqrt{2}}\sqrt{\sqrt{4\lambda_n^4+\left(\frac{12\sigma_{eq}L^2}{EW^2}\right)^2}+\frac{12\sigma_{eq}L^2}{EW^2}},\quad \lambda_{2n}=\frac{1}{\sqrt{2}}\sqrt{\sqrt{4\lambda_n^4+\left(\frac{12\sigma_{eq}L^2}{EW^2}\right)^2}-\frac{12\sigma_{eq}L^2}{EW^2}}$$

If the axial load is small enough, it is possible to obtain, after straightforward algebraic manipulation, an expression for the n^{th} resonance frequency f_n:

$$f_n=f_n^0\left[1-\frac{3}{\pi W f_n^0}\frac{G(\lambda_n^0)}{\sqrt{12E\rho}}\sigma_{eq}\right] \tag{4}$$

where f_n^0 is the n^{th} resonance frequency of the unstressed structure, λ_n^0 the eigenvalue of the unstressed beam, and $G(\lambda_n^0)$ is a function only of the eigenvalue λ_n^0 and of the mode-shape of the unstressed structure:

$$G(\lambda_n^0)=\frac{\lambda_n^0\left(\cosh\lambda_n^0\sin\lambda_n^0+\cos\lambda_n^0\sinh\lambda_n^0\right)-2\sinh\lambda_n^0\sin\lambda_n^0}{\lambda_n^0\left(\cosh\lambda_n^0\sin\lambda_n^0-\cos\lambda_n^0\sinh\lambda_n^0\right)} \tag{5}$$

$G(\lambda_n^0)$ increases with n and it is nearly 1 for $n>5$. The *stability* of f_n descends at once from Eq. (4). For example, its value with respect to the temperature difference ΔT between resonator and substrate is:

$$S=\frac{1}{f_n^0}\frac{\partial f_n}{\partial\Delta T}=-\frac{3\alpha_m}{\pi W f_n^0}G(\lambda_0^n)\sqrt{\frac{E}{12\rho}}. \tag{6}$$

4. FEM simulation and discussion

Finite element simulations of the dependence of the resonance frequency on the temperature were performed. The analyses were focused on the effect of the axial stress caused by the temperature and neglected other temperature effects, like Young's modulus changes, which however are quite simple to model, at least for little temperature changes [5]. All the analyses were executed in FEMLAB®.

In Fig. 2 a comparison between the analytical model of Eq. (4) and simulations for a CC1 resonator is shown. The error on the resonance frequency (Fig. 2, left), although small, increases for increasing beam thickness, an effect which is not accounted for by the analytical model. The stability (Fig 2, right) is affected by the beam thickness. Once the resonance frequency is specified, the latter graph gives interesting suggestions for the design of CC resonators: specifically, thicker beams are expected to be less sensitive to temperature, because their behavior is less affected by axial loads.

The situation for FF1 and FF3 resonators is complicated by the presence of

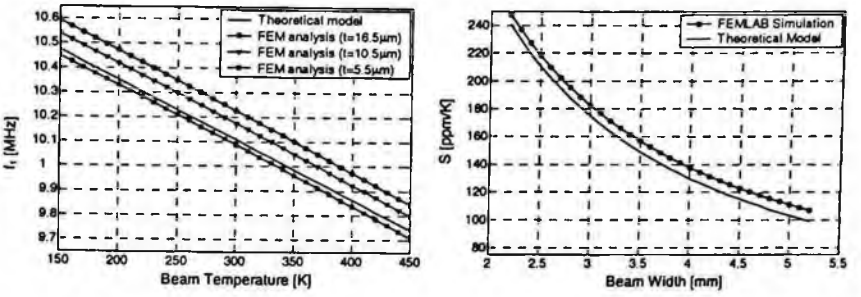

Figure 2. Behavior of clamped-clamped beams. On the left, simulated and theoretical resonance frequency for different beam temperatures and thicknesses On the right, simulated and theoretical stability for different beam widths (Nominal resonance is at 10 MHz at every width). The substrate temperature is 300 K, the thermal expansion coefficient is α_m = 4.5 ppm/K.

the supports, which are CC beams (resonating on their second mode) themselves. A comparison between the simulation results for the three resonator types is shown in Fig. 3. The resonance frequency was simulated for three devices with the same nominal resonance frequency (10 MHz) at 300 K, and the same width (2.2 μm). The average thermal expansion coefficient used was α_m = 4.5ppm/K. The worst performance (worst stability) is that of a free-free resonator, namely the FF1 type. FF3 has the best performance, while the CC1 type performs between the two. It is interesting that a higher order FF mode is more stable that a lower order one: this is just the opposite of the behavior predicted by Eq. (6) for CC modes.

An interpretation of the results for FF resonators is not straightforward: in particular, while the main beam in these two cases can be supposed to be axially unloaded (it can easily expand, discharging any axial stress), the frequency shift cannot be ascribed (at least not completely) to the frequency shift of the supports. This has been verified by separate simulations, which show that CC2 (clamped-clamped second mode) beams of the appropriate length show a much better stability when on their own, i.e. when not connected with the main beam.

Acknowledgments

STMicroelectronics fabricated the resonators at their Cornaredo (Milan) plant, in the framework of the joint University of Pisa-STMicroelectronics Microsystems R&D center.

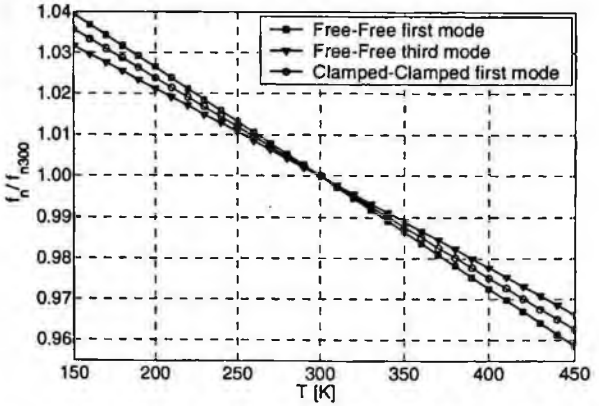

Figure 3. Simulated dependence of the resonance frequency (normalized at 300 K) for the three kinds of devices. The sensitivity values are 269 ppm/K, 244 ppm/K, and 218 ppm/K for the FF1, CC1, and FF3 resonator, respectively.

References

1. C. T.-C. Nguyen, *Silicon Monolithic Integrated Circuits in RF Systems*, Ann Arbor (USA), Sep. 12-14 2001, 23.
2. T. Mattila, J. Kiihamäki, T. Lamminmäki, O. Jaakkola, P. Rantakari, A. Oja, H. Seppä, H. Kattelus and I. Tittonen, *Sens. Actuators A* **101**, 1 (2002).
3. S. Lee, M. U. Demirci, C. T.-C. Nguyen, *11th Int. Conf. on Solid-State Sensors & Actuators (Transducers '01)*, Munich (Germany), Jun. 10-14 2001, 1094.
4. M. Koskenvuori, T. Mattila, A. Häärä, J. Kiihamäki, I. Tittonen, A. Oja and H. Seppä, *Sens. Actuators A* **115**, 23 (2004).
5. Wan-Thai Hsu; J. R. Clark, Nguyen, C.T.-C., *IEEE Electron Devices Meeting (IEDM 2000)*, Hong Kong (PRC), Dec. 10-13 2000, 399.
6. W.-T. Hsu, J. R. Clark, C. T.-C. Nguyen, *11th Int. Conf. on Solid-State Sensors & Actuators (Transducers'01)*, Munich (Germany), Jun. 10-14 2001, 1110.
7. D. Galayko, A. Kaiser, B. Legrand, D. Collard, L. Buchaillot, C. Combi, *IEEE Int. Conf. on Micro Electro Mechanical Systems (MEMS2002)*, Las Vegas (USA), Jan. 20-24 2002, 665.
8. M. U. Demirci, C. T.-C. Nguyen, *IEEE Int. Frequency Control Symposium and PDA Exhibition*, Tampa (USA), May 4-8 2003, 810.
9. H. A. C. Tilmans, *J. Micromech. Microeng.* **7**, 285 (1997).
10. H. A. C. Tilmans, M. Elwenspoek, J. H. J. Fluitman, *Sens. Actuators A* **30**, 35 (1992).

SUSPENDED CONNECTION ARRAY FOR ULTRA LOW TEMPERATURE APPLICATIONS

B.MARGESIN, A. BAGOLINI

Microsistems Division, ITC-IRST, via Sommarive 18
38100 Trento, Italy

A silicon MEMS based component is projected and fabricated, that allows for minimum heat conductivity, while providing electrical connection on many channels by adopting an array of suspended superconducting metal lines, for ultra low temperature applications in the order of hundreds of microkelvin. The device is designed with L-Edit™ software and is fabricated at ITC-IRST microelectronics facility. The process has three mask levels and is divided into two splittings: one splitting is based on SU8 as polymer underlayer, the other uses polyimide. Bulk micromachining by anisotropic wet etching is used to create a cavity underneath the metal lines, and the dielectric layers underneath the lines are then dry etched leaving them suspended. The components are fabricated and technology issues related to the processing are investigated: self aligning of the polymer to the metal layer is examined to evaluate the undercut during plasma etching, and final release of the structure by silicon oxide removal is studied.

1. Introduction

Ultra low temperature applications in the order of hundreds of microkelvin require to thermally insulate the sensors from the rest. At such temperatures leading power lines to the sensor and extracting signals can become critical because of the thermal input that comes together with electrical connections. Minimizing the physical connection becomes crucial, therefore a silicon MEMS based component is ideal, as it allows for minimum heat conductivity thanks to the reduced dimension of the wires. Electrical connection on many channels is possible by adopting an array of suspended superconducting metal lines with a section of 20 by 1 μm each. The metal is supported by a polymer layer that is self aligned to it, and has a thickness of about 4μm: this layer is required to provide robustness to the device. The silicon substrate and the dielectric layers under the metal lines can be removed by bulk micromachining and dry etching, generating a cavity in the chip, that is crossed by the metal lines. The frame is mounted as a bridge between the sensors and the electronics, then the short edges are removed by cleaving them along the line of a trench fabricated on the back side during bulk micromachining (see figure 1).

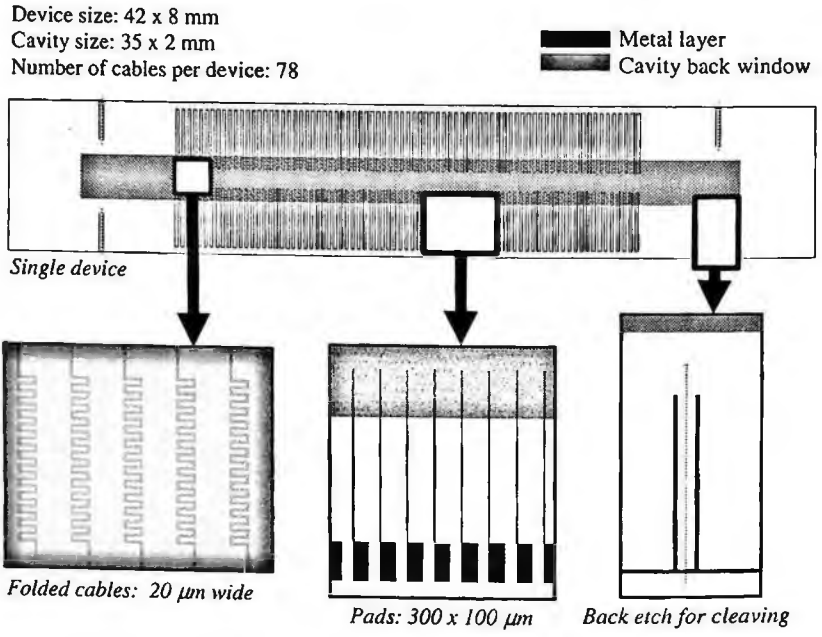

Fig. 1: layout of the device

2. Processing

Fabrication is based on standard 4" single crystal (100) silicon wafers, and is performed at ITC-IRST fabrication facilities. The process steps are depicted in figure 2. The process has two mask levels, one for the metal and one for the etching cavity on the back side. Processing begins with the deposition of the masking multilayer, made by low pressure chemical vapor deposition of TEOS and silicon nitride (a). The back mask is then patterned and etched (b). On the front side, the polymer is deposited by spin coating and aluminum is deposited on it by RF sputtering (b). The metal is patterned by dry etching, and then used as a mask for the self alignment of the polymer underneath it, by dry etching in oxygen plasma (c).

The front side of the wafer is then covered with a spin-on varnish to protect it during anisotropic etching (c). Bulk anisotropic etching is performed using a 25% TMAH solution (d). The silicon is completely removed, leaving a dielectric membrane with the metal lines on it. Then the dielectric layers are removed from under the lines to release them (e) by dry etching from the back side of the wafer.

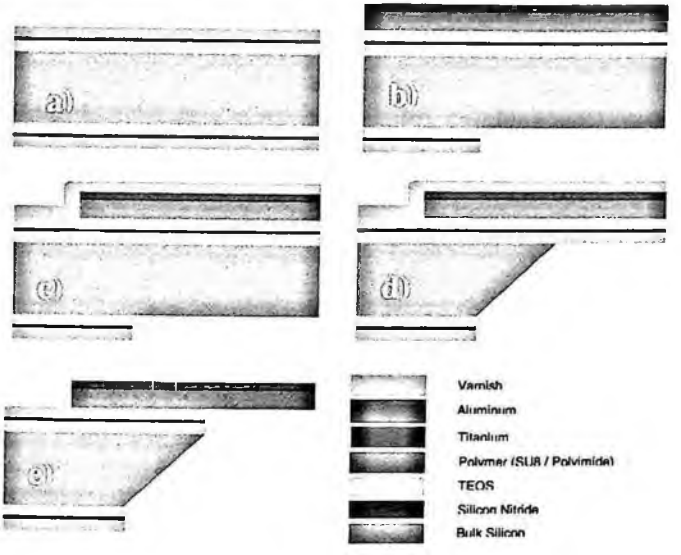

Fig. 2: schematic of the process steps.

Due to the dimension of the membranes that are released during anisotropic etching, the step becomes critical as the membrane can break under the pressure of the solution or because of the stress induced by the thermal mismatch between room temperature and reactor temperature (90°C) during processing. To strengthen the membrane and to protect the front side in case of a leakage due to breaking, a varnish is used, that remains undamaged in TMAH solution for about 10 minutes.

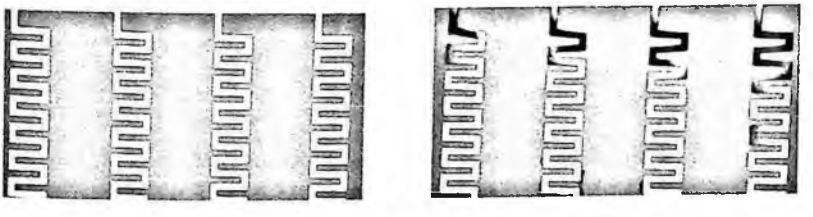

Fig.3: metal lines with polyimide underneath (a) and partly suspended due to lolyimide underetch (b)

Though SU8 has a high resistance to TMAH solution and is therefore preferable when bulk micromachining has to be made, problems arise using SU8 as a polymer under the metal, since a 4 μm thick layer it is not so easily removable in plasma. To ease the process we therefore adopted polyimide.

Also critical is the self aligning of the polyimide under the metal layer: due to non uniform dry etching, some parts of the metal can be completely released from the substrate because of excessive underetching (see figure 3).

The final release of the metal lines by dry etching of the dielectric membrane requires a long etching time to fully remove residuals hanging from the edge of the cavity (figure 4).

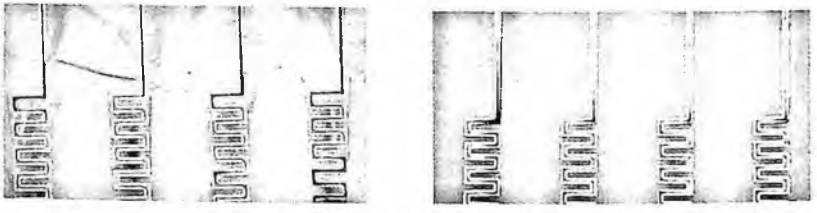

Fig.4: partly (a) and fully (b) re moved dielectric membrane under the metal lines

3. Conclusions

A suspended connection array has been designed and fabricated by means of microelectronics and micromechanics processing, to provide an electrical connection together with very low thermal conduction for ultra low temperature experiments. The fabrication has been analyzed and optimized to obtain a process sequence. The use of polyimide is preferable to SU8 as it is easier to remove by dry etching. The etching time has to be controlled to avoid excessive underetch and consequent release of the metal layer. A set of devices has been fully processed and a photograph of the finished device is reported in figure 5.

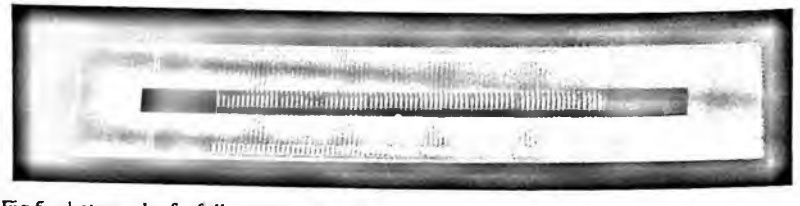

Fig.5: photograph of a fully processed wafer.

MODELLING AND DESIGN OF A MICROCANTILEVER-BASED SENSOR MODULE FOR CHROMATOGRAPHIC SYSTEMS

ANDREA ADAMI, MASSIMILIANO DECARLI, LEANDRO LORENZELLI*

ITC-irst, Microsystems Division, via Sommarive 18
38050 Povo(TN), Italy

Microcantilevers are MEMS-structures suitable for chemical sensing. Sensitivity to specific analytes can be achieved by coating the beam surface with proper chemically sensitive films. This work presents the development of a microcantilever-based sensor array for agro-food applications. Modelling, design and fabrication process are presented.

1. Introduction

Microcantilevers are MEMS-structures suitable for chemical sensing; sensitivity to specific analytes can be achieved by coating the beam surface with proper chemically sensitive films. Analyte adsorption onto the surface affects both resonance frequency and beam bending, leading to different read-out approach which can be also combined [1, 2].

This work presents the development of silicon microcantilever-based sensor arrays designed for integration in a chromatographic system for food quality monitoring applications.

The selected detection method for analyte adsorption is the resonant frequency shift; beam bending is monitored using integrated piezoresistors. In order to optimize the resonant properties and the read-out performances of the structure the investigation of the electro-mechanical behaviour of the system has been implemented by both finite element analysis, performed with ANSYS™ software, and analytical models.

Since the cantilever sensitivity is inversely proportional to the beam thickness, the fabrication process has been implemented for two different technologies using standard bulk micromachining and SOI techniques, where the first has been implemented for preliminary tests on functionalisation and system integration, and the SOI process, which allows a better reproducibility of beam thickness, is intended for the final devices.

2. Device modelling and design

2.1. *Analytical modelling*

Analytical modelling has been performed using relationships that can be found in literature. Resonance has been evaluated by means of the mass-spring simplified model, where beam bending stiffness has been calculated using the laminate theory, in order to consider the multilayer structure of the beam, and mass has been corrected for rectangular beam geometry [3]. The beam damping has been taken into account to evaluate the resonance quality factor, using the drag resistance in gas of an equivalent sphere with radius equal to the beam width, which is a suitable model for approximated resonance evaluation [4].

Table 1. Dimensions and resonance frequency of implemented beams.

L [μm]	W [μm]	t [μm]	w_0 [kHz]	Q
500	106	10	53	495
1000	106	10	13	248
150	50	2	112	83
300	50	2	38	42

The analytical results have been used to define the beam geometry in order to obtain the proper resonance frequency for actuation system, which is a commercial piezoelectric device suitable for frequency up to 200 kHz. Dimensions chosen for device implementation are summarized in Table 1. "Ideal" stress distribution related to the actuation has been calculated for preliminary design further refined using the finite elements analysis.

2.2. *Finite elements analysis*

Finite element (FE) analysis have been implemented in order to evaluate the "non-ideal" stresses at the beam root and to optimize the geometry and the position of piezoresistive read-out. (Figure 1)

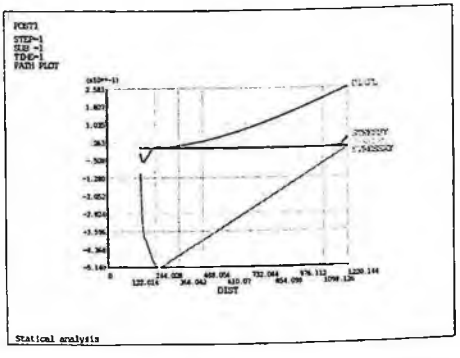

Figure 1. Stress distribution and vertical displacement on beam axis.

Furthermore the effects on resonance and on stress distribution of geometric tolerance due to fabrication process have been evaluated by means of static and

modal FE analysis. In particular the effect of under-etch during back-side etching has been simulated, resulting in a shift of the design beam resonant frequency.

2.3. *Array design*

The preliminary four beam arrays have been designed according to the modelling results, using the previously described geometries and a Wheatstone bridge configuration for piezoresistors to increase the read-out response.

According to the application preliminary study, a four-bridge array has been considered a configuration suitable for the device. An example of implemented array is shown in Figure 2.

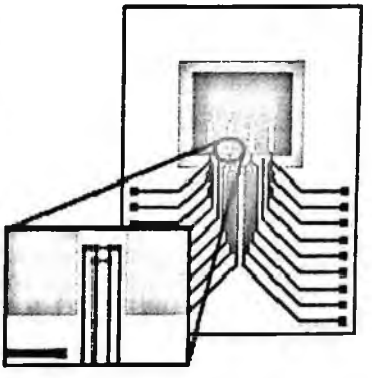

Figure 2. Layout of a test cantilever array. In the inset a detail of the beam root (in white) showing the Wheatstone bridge configuration and the bulk contact.

3. Fabrication process

3.1. *Preliminary process*

The starting material is a 4-inch, 500 um thick, 10 Ohm-cm, n-type, (100) oriented, double side polished silicon wafer. The piezoresistors are implemented through a BF_2 implantation, with a dose of 10^{14} at cm^{-2}, and energy of 80 keV, in order to have, after a proper activation step (20 minutes, 975 °C), a junction depth of 360 nm with a simulated sheet resistance of 1275 Ω/sq. The substrate contact is done with a phosphorus implantation, having a dose of 3 x 10^{15} and energy of 80 keV. The metal lines are a sputtered multilayer of Titanium/Titanium Nitride/Aluminium 1%Silicon alloy/Titanium. The 3-dimensional microcantilever structures are obtained through an appropriate sequence of back and front-side silicon anisotropic wet etchings, with TMAH 25 wt% as etchant. The final beam thickness for this preliminary test structures is about 10 μm.

3.2. *SOI fabrication process*

The final devices have been implemented using SOI (Silicon On Insulators) wafers, having the following specifications: 2 μm of silicon device layer, 500 nm of buried oxide layer and 500 μm of silicon handle layer.

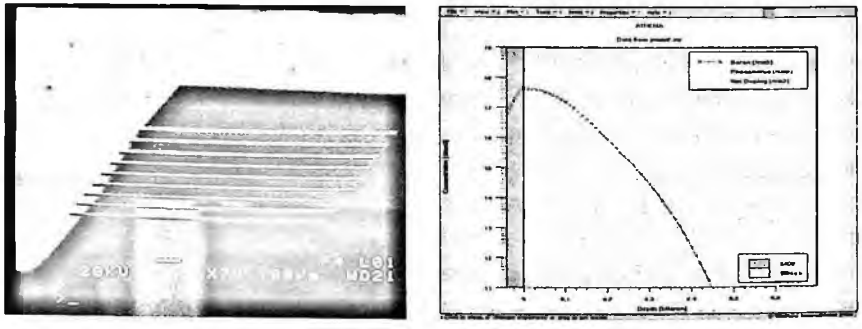

Figure 3. A) SEM photograph of a dummy beam array. B) Simulation of piezoresistor doping profile for the SOI fabrication process (Athena Silvaco™ simulation software).

A key-point to optimize the device sensitivity is the definition of the fabrication parameters for the piezoresistors implantation, in order to obtain a very shallow p-doped layer. Results of ATHENA (Silvaco™ software) implant simulation are shown in Figure 3B. Finally the implant conditions for piezoresistors have been a dose of 5 x 10^{12} at cm^{-2}, and energy 80 keV, using BF2. According to the process step simulations a junction depth of 288 nm and a sheet resistance of 7383 Ω/sq can be obtained. These conditions are targeted to the sensitivity optimisation of p-type Si resistors, which can be obtained at low carrier concentrations [5]. Nevertheless, since the piezoresistivity coefficient depends on temperature for low net doping, a splitting using a higher implant dose (5 x 10^{14} at cm^{-2}) has been also implemented in order to increase the measurement stability. Also for this process the metal lines are a sputtered multilayer of Titanium/Titanium Nitride/Aluminium 1% Silicon/Titanium. The beam structures are obtained through a first silicon bulk micromachining step, performed with TMAH 25 wt% aqueous solution on the back of the wafer and a subsequent front-side silicon dry etching (SF_6/O_2 plasma). The last fabrication step is the buried oxide removal, done through a dry etching performed on the back of the wafer, in order to release the silicon microcantilevers.

4. Conclusions

The development of a microcantilever array for food quality monitoring has been presented, showing the approach followed for device modelling and design. Furthermore the fabrication process outline and the optimization of the critical steps of a bulk micromachining techniques and SOI techniques have been described.

Acknowledgments

This work has been partially funded by the "Food Safety and Quality Monitoring with Microsystems" IP-GOODFOOD EU Project and the National Project FIRB-MIUR "Development of multifunctional microsystems for applications in clinical diagnostics and food analysis.

References

1. T. Thundat, R. J. Warmack, G. Y. Chen, D. P. Allison, *Appl. Phys Lett.* **1994**, *64*, 2894-2903.
2. J. R. Barnes, R. J. Stephenson, M. E. Welland, C. Gerber, J. K. Gimzewski, *Nature* **1994**, *372*, 79.
3. G. Y. Chen, T. Thundat, E. A. Wachter and R. J. Warmack, *J. Applied Physics* **1995**, 77, 3618-3622.
4. G Chen, R Warmack, T Thundat et al., *Rev. Sci. Instrum.* **1994** 65 (8), 2532-2537.
5. B. Kloeck, *Sensors*, Vol. 7, 146-172.

TOWARDS THE PLASTIC ISFET: A FLEXIBLE, ORGANIC, ION SENSITIVE FIELD EFFECT TRANSISTOR

ILEANA MANUNZA, ANDREA LOI
INFM-University of Cagliari Department of Electric and Electronic Engineering, piazza d'Armi
09123 Cagliari, Italy

ANNALISA BONFIGLIO
INFM-University of Cagliari Department of Electric and Electronic Engineering, piazza d'Armi
09123 Cagliari, Italy
INFM-S3 "nanoStructures and bioSystems at Surfaces", Modena, Italy

We have fabricated the first example of flexible field effect device for chemical detection based on an organic field effect transistor (OFET) made by pentacene films grown on flexible plastic structures. The ion sensitivity is achieved by employing a thin Mylar™ foil as gate dielectric. The active layer is vacuum-sublimed on one side of the foil, pre-patterned with bottom-contact Au source and drain electrodes. The opposite side of the insulating film is in contact with an electrolytic solution that together with a reference electrode forms an ionic gate. A sensitivity of the device to the pH of the electrolyte solution has been observed. Thanks to the flexibility of the substrate and the low cost of the employed technology, this device opens the way for the production of flexible chemical sensors that can be employed in a variety of innovative applications.

1. Introduction

Organic materials, based on conjugated organic small molecules and polymers, have paved the way, in the last decade, for the production of devices on large-area, low-cost, plastic substrates[1]. So far, great progress has been made in the field of optoelectronic devices, like Organic Light-Emitting Diodes (OLEDs)[2] and for switching functions by means of Organic Field Effect Transistors (OFETs)[3].

Organic semiconductors offer several advantages due to easy processing, good compatibility with a wide variety of substrates including flexible plastics, and great opportunities in terms of structural modifications. Furthermore, thin films of organic semiconductors are mechanically robust and flexible, and this characteristic offers new possibilities for non-planar flexible electronics. Until now, only few examples of organic semiconductor based field effect sensors

have been presented and none of them is fully capable of exploiting the favourable mechanical properties of organic semiconductors. Recently, a fully flexible structure for field effect devices has been produced[4]. The main advantage of this structure is that it is assembled starting from a flexible insulating film, but without any substrate. Thanks to this feature, it is possible to expose the gate side of film to an external medium; this is normally impossible for structures assembled on a substrate. In this way, it is in principle possible to realize with a fully flexible structure a function similar to that of a silicon based Ion Sensitive Field Effect Transistor[5] (ISFET). Ion sensitivity in silicon based FETs results from the presence on the surface of the insulating layer of specific sites for H+ ions in the electrolytic solution[6]. Starting from this principle, several examples of (bio)sensors have been developed, based on the possibility of functionalizing the surface of the insulating layer with molecular layers with specific binding properties for the (bio)molecules dissolved in the medium to monitor[7]. Something similar can be envisaged also for organic field effect sensors, that, compared to silicon structures, have several advantages, as the low cost of the technology and the possibility to achieve mechanically flexible structures. Nevertheless, the mobility of organic semiconductors is still low, even if it seems realistic to obtain in a few years devices working at relatively low voltages, comparable with the performances of devices made from amorphous silicon[8,9]. Ion Sensitive Organic FETs (ISOFETs) fabricated on plastic substrates could open the way to the fabrication of flexible devices for solution monitoring and for a number of innovative applications (as, for example, smart food packages) that are not possible at present for silicon based devices.

2. Methods and Materials

A 900 nm-thick Mylar™ sheet (Du Pont), adapted to a plastic frame, works as insulator and, at the same time, as a free-standing surface for device assembling. The Mylar™ sheet has a dielectric constant close to that of silicon dioxide (3.3)and a dielectric rigidity of 10^5 V/cm that allows to apply a gate bias sufficiently high to induce a field-effect in the organic semiconductor

Bottom-contact Au source and drain electrodes have been patterned on one side of the dielectric using a standard photolithographic technique whilst the opposite side of the Mylar film is exposed to the electrolytic solution where an Ag/AgCl reference electrode is immersed. Gold source and drain electrodes with W/L = 250 (W and L are the channel width and length, respectively), with L = 25 μm, have been used. Prior to organic deposition, the substrate has been

cleaned with acetone, washed with deionized water, and dried with a Nitrogen flux. Pentacene (Sigma Aldrich) has been used as received. Pentacene films with a nominal thickness of 50 nm have been grown by vacuum-sublimation at a nominal deposition flux of about 1 Å/s.

Measurements of drain-source current (Ids) versus drain-source and gate-source voltages have been carried out at room temperature in air, by means of a HP 4155 Semiconductor Parameter Analyzer.

In order to avoid ageing effects, all measurements have been performed immediately after pentacene deposition.

The basic structure of the device[10] is shown in Figure 1

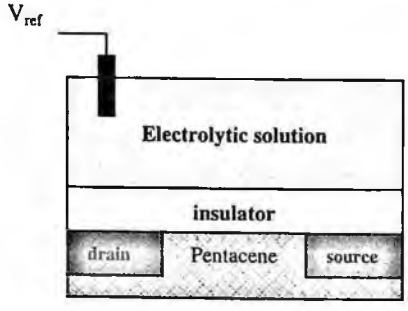

Figure 1. Basic structure of the device

3. Results and discussion

The device has the typical behaviour of organic p-type field effect transistors, working in accumulation mode, with increasing negative values of Ids with increasing negative Vds values and with a clear field effect induced by the Vgs voltage. Figure 2 shows the output characteristic of the device This curve has been registered in presence of an electrolytic solution with a pH of 7 after the reference electrode has been left to stabilize in the same solution for about half a hour. This procedure has been done with the aim of obtaining more stable measurements. As can be seen, $|Ids,sat|$ increases with the increase of $|Vgs|$ similarly to OFETs with a metallic gate. Namely, as can be seen from Figure 3 that shows I_{ds} versus time at different pH values (taken by leaving a 30 minutes hold time after every pH variation; curves are taken at Vds = -90 V, Vgs = -50 V), there is a decrease of the current with basic solutions and an increase with acid solutions that clearly indicate that there is a modulation of the charge at the interface between the insulating layer and the solution.

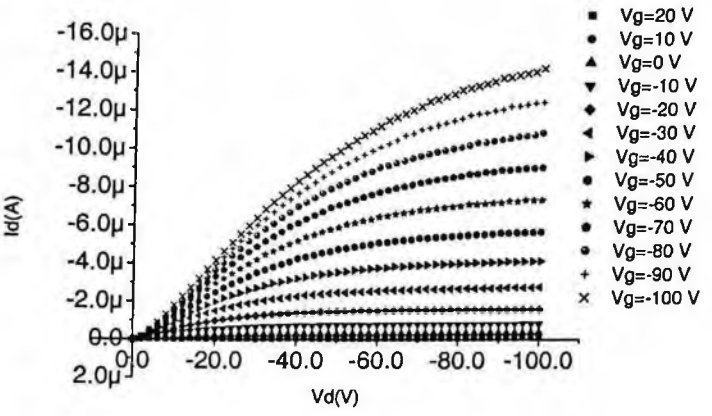

Figure 2.Output characteristic of a device recorded at pH=7

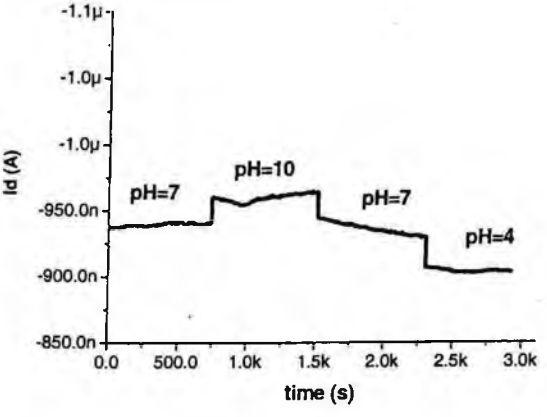

Figure 3. I_{ds} versus time at different pH values(Vds = -90 V, Vgs = -50 V)

When negative charge density is increased in the bulk (and as a consequence, at the insulator/solution interface), as for basic solutions, holes accumulate in the channel in higher density than in the case of neutral or acid solutions. As a consequence, the (negative) current recorded with fixed values of Vds and Vgs is higher. Conversely, in the case of acid solutions, the positive charge accumulated at the insulator/solution interface causes a decrease of the hole density in the channel and a (negative) lower value of Ids.

The dependence of the transistor current on the pH value of the solution must be related to a variation of the threshold voltage of the device due to a charge variation at the solution-insulator interface that can be explained in the frame of the Gouy-Chapman-Stern theory[6] for the behavior of an interface between a solid surface and an electrolytic solution.

According to this theory, an insulator exposed to an aqueous solution interacts with H+ ions and causes a redistribution of the charge in the solution. When the structure formed by the insulator and the electrolytic solution is completed by a semiconductor layer located at the opposite side of the insulator, as in the case of MOSFET and OFET structures, the charge variation at the insulator/solution interface capacitively induces a redistribution of charge in the semiconductor. In field effect devices, this variation is directly detectable through the variation of the threshold voltage of the device. This working principle is valid both for MOSFETs and OFETs, as already demonstrated by C. Bartic et al.[11], with the obvious differences due to the specific features of organic semiconductor based devices (as low current and high operating voltages).

4. Conclusions

In conclusion, for the first time ion sensitive field effect transistors have been produced on fully flexible plastic films. The devices are based on pentacene films grown on bottom-contact Au-patterned on 900 nm-thick Mylar™ gate dielectric. The electrical characteristics indicate that the device behaves as a typical p-channel transistor working in accumulation mode. Output current is modulated by the pH value of an electrolytic solution put in contact with the insulating layer. Taking advantage of the full mechanical flexibility of the insulating sheet, smart electronic films with sensing properties can be produced with this technique. At present, sensitivity to the presence of ions in the solution has been achieved without any treatment of the insulating layer. Work is in progress for obtaining properties of chemical selectivity by a proper functionalization of the insulating layer.

References

1. S. R. Forrest, Nature **428**, 911 (2004).
2. T. Tsujimura, SID 2003 Technical Digest Vol.XXXIV, Book 1,6 (2003).
3. C. Dimitrakopoulos, P. R. L. Malenfant, Adv. Mater. **14**, 99 (2002).
4. A. Bonfiglio, F. Mameli, and O. Sanna, Appl. Phys. Lett. **82**, 3550 (2003).
5. P. Bergveld, Sensors and Actuators B 88 1-20 2003.
6. M. Grattarola and G. Massobrio "Bioelectronics Handbook: MOSFETs, Biosensors, Neurons" Mc Graw Hill, 1999.
7 P. Bergveld and A. Sibbald, Analytical and Biomedical Applications of ISFETs (Elsevier, Amsterdam, 1988).
8. Y. Kato, S. Iba, R. Teramoto, T. Sekitani, T. Someya, H. Kawaguki, T. Sakurai, Appl. Phys. Lett., **84**, 3789 (2004).

9. H. Klauk, M. Halik, U. Zschieschang, G. Schmid, W. Radlik, W. Weber, J. of Appl. Phys., **92**, 5259 (2002).
10. A. Loi, I. Manunza and A.Bonfiglio, Appl Phys. Lett. **86**,.103512 (2005)
11. C. Bartic, A. Campitelli, S. Borghs, Appl. Phys. Lett. **82**, 475 (2003).

DESIGN AND FABRICATION OF A SILICON MICRO-ALCOHOLOMETER

VITTORIO GUARNIERI, MASSIMILIANO DECARLI, MARIO ZEN
ITC-Irst, Via Sommarive 18, Povo (Tn) 38050 Italy

GIOVANNI SONCINI
Dept. Of Information and Communication Technologies, via Sommarive, 14, 38050 Povo (TN), Italy

This paper reports the development of a new MEMS device based on an innovative principle of measurement of the alcoholic strength. The new procedure takes advantage of many properties of the hydro-alcoholic solutions. The working principle of this new Silicon micromachined alcoholometer is the measurement of the evaporation energy of a droplet of solution dispensed by a tiny capillary. A microhotplate based on dielectric thin membrane has been designed in order to heat and measure the temperature of the droplets of hydro-alcoholic solution. The major advantages expected from microalcoholometer device are: small dimensions, low cost, low power of consumption, on-line measurement, small quantities of solution needed (<10 mg), good accuracy and resolution, and wide range of measurement. Future work will develop a dedicated read-out electronic and the design of the acquisition system set up in order to manage automatically the experimental measurements. The results of this work brought to the application for a European patent.

1. Introduction

The alcoholometer system relates to a process and equipment for determining the alcoholic strength (alcohol concentration by volume) of an alcoholic beverage and water/alcohol solutions in general. The system is formed by an equipment with a capillary dispenser, a MEMS sensor and a read-out electronic.

1.1. *Innovative principle*

In the hydro-alcoholic solutions the physical properties such as the density, the boiling point, the specific heat, the surface tension and at least hypothetically, the latent heat of evaporation, are decreasing monotonous functions of the alcohol concentration [1]. The measurement method presented

in this work is based on the synergic interaction between all these properties. In order to determine the alcoholic strength of water/alcohol solution, according to the new measurement method, a capillary conduit having a predetermined diameter, such as the needle of a syringe, is used and operatively placed in a vertical position. The weight "mg" of the drops falling from the capillary, is linked to the surface tension γ through Tate's law. One drop is placed and deposited on a heating device, which is activated in a controlled manner so as to carry on the heating of the drop until it completely or partially evaporates.

The total energy or heat necessary to evaporate one drop of liquid corresponds to the sum of the heat required to heat from ambient temperature to the boiling point, and the heat required to complete disappearance of the drop, as indicated in the following formula (1):

$$Q_{TOT} = 2 \pi r_c \gamma (C_p \Delta T + \Delta H_E)/g \qquad (1)$$

Where r_c is the radius of the capillary, Cp is the heat capacity, ΔT is given by the difference between the boiling point T_b and the room temperature T_r and ΔH_E is the latent heat of evaporation.

During this heating and evaporation of the solution the change in temperature over time is detected. Measuring the total energy necessary to carry on complete or partial evaporation of the solution is indicative of the concentration of alcohol by volume in the solution under investigation through a calibration curve which has previously been determined by experiment.

1.2. *Equipment*

The system that permits to validate the process described above is essentially based on a heating resistor connected to a power supply. A thermistor acting as an electrical temperature sensor is associated with the heating resistor. In order to implement the electrical device, the heating resistor and the thermistor are fabricated on a Silicon substrate using Platinum thin film. These Pt resistors are embedded on a thin dielectric membrane to give low power consumption and a fast response in temperature changes.

A capillary, also the needle of a syringe, dispense the drop precisely in the center of the active surface of a microheater.

2. Layout

The sensor layout has been designed with the L-Edit™ Tanner Tools™ software. The layout process has 3 mask layers; we splitted the layout in 4 parts

in order to test 4 different conditions, in particular relating to membrane dimensions and the heating element.

Figure 1a) shows a device with a central Platinum resistor with meander shape (width 40 um, length 6600 um) acting as a temperature sensing element.

This resistor is positioned in the centre of a membrane, opened from the back side of the wafer with dimensions from 2728x2728 um^2 to 4900x4900 um^2, and covers a total area of 800x800 um^2. Other three Platinum resistors (width 40 um, length 6600 um) are positioned on the Silicon bulk in order to measure the substrate temperature.

The microheater has different geometrical dimensions keeping the same total square number allowing the same electrical resistance for different splittings. Figure 1b) shows a similar layout using as heater and temperature sensing element a Gold shaped resistor.

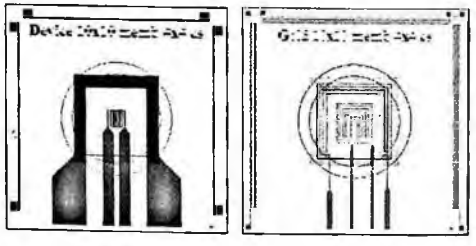

Figure 1a) Layout Platinum device 1b) Layout Gold device

3. Fabrication process

The starting material for alcoholometer fabrication is (100) 4-inch, p-type Silicon wafer, CZ double polished with a resistivity of 16÷24 Ωcm. The membrane structure has been realized onto the substrate by a 500-nm-thick layer of Silicon oxide grown by thermal wet oxidation; followed by a 150-nm-thick stoichiometric Si_3N_4 film deposited by LPCVD (Low Pressure Chemical Vapour Deposition). A further insulating multilayer (500-nm undoped TEOS oxide) is deposited. A backside lithography opens the etching windows trough the back multilayer films by dry plasma etch.

An evaporation of Cr/Pt with 5/50 nm respectively, is deposited on the front trough a negative photoresist etched with a lift off technique. An evaporation of Cr/Au with 5/150 nm respectively, is deposited on the front for the pad contacts and the gold splitting [2].

Silicon has been then removed from the backside by tetramethyl ammonium hydroxide (TMAH) wet anisotropic etching leaving a thin diaphragm [3]. The

cross section of the sensor fabrication technology is schematized in Figure 2 and the fabricated device photos are shown in Figure 3.

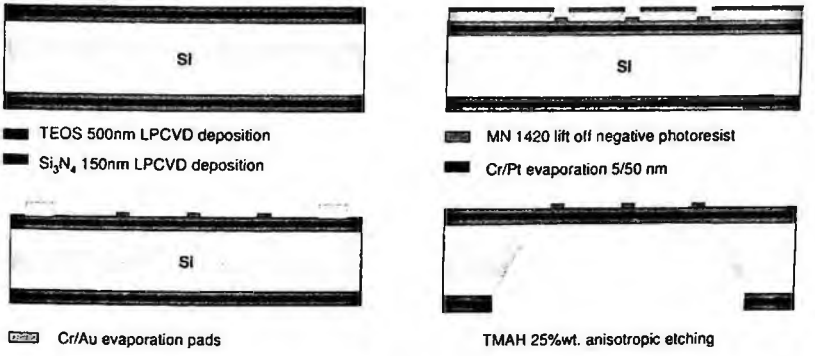

Figure 2 Layout of the fabrication process flow

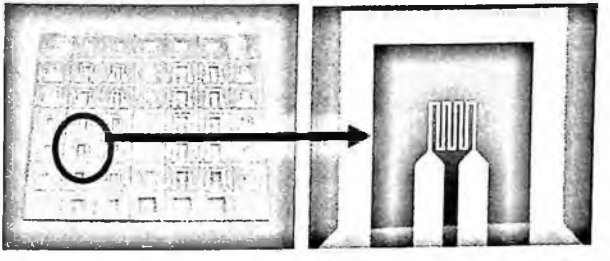

Figure 3 Photographs of the fabricated devices

4. Electronic

4.1. *Read-out*

The read-out electronic is basically made of two parts: the heater driving system and the thermistor reading system. The first is dedicated to detect the voltage drop across the membrane thermistor that is correlated with the change in resistance due to temperature variation during drop evaporation. In addition an amplification stage is needed to properly detect the signal. A second part controls the heater placed on the bulk silicon around the membrane. The circuit is made of an operational amplifier that compares two input voltages; one is fixed and the second is variable due to the change in resistance of the heater resistor caused by the temperature of the drop. When there is no drop the circuit gives a certain amount of power to the heater resistance connected in Wheatstone bridge with other three fixed resistors. When the drop falls on the membrane the

values of the resistance and therefore of the voltage drop across the heater change and the circuit reacts giving much power to the Wheatstone bridge through the Darlington transistor. This is useful in order to minimize the power consumption giving power to the system only when the drop is present on the chip.

5. Experimental results

5.1. *Packaging*

A dedicated package has been designed in order to permit both the electrical connections to the resistors and to hold the drop during the evaporation. Microheater and resistors are controlled with a dedicated electronic and the data are acquired with LabVIEW™ software.

5.2. *TCR (Temperature Coefficient of Resistance)*

The microalcholometer silicon chip has been mounted in a Dual In Line (DIL) ceramic package in order to evaluate the temperature characteristics of the Platinum and Gold resistors. The testing has been performed with a thermostated oven (WATLOW™ with P.I.D. controller). The values of the resistances have been monitored with a FLUKE™ 8840A multimeter with temperatures ranging from 22°C to 100°C. In the temperature range of the measurements Pt as long as Au resistors shows a good linear response with TCR (Temperature Coefficient of Resistance) values of 1824 ppm/°C for Platinum and 1940 ppm/°C for Gold.

5.3. *Characterization of the devices*

A preliminary characterization of the Platinum device has been done without the dedicated read-out electronic. A voltage supplier (GW™ GPC-3030) has been connected with the heater resistor with a bias voltage of 6 V, corresponding to a power consumption of 375 mW. A DC current source (KEITHLEY™ 6221) supplied the membrane thermometer resistance and the bulk thermometer resistance connected in series with 10 μA. A 12-bit acquisition board (NATIONAL INSTRUMENTS™ AT MIO-16L-9) has been used to read out the voltage drop across these resistors and interfaced with a PC running a LabView™ software (NATIONAL INSTRUMENTS™). This software application converts the voltage drop in temperature, by means of the Pt TCR value and calculates the integral area underneath the evaporation curve. Results are shown on the chart of Figure 4, where the x axis represents the alcoholic strength of the samples and the y axis shows the integral value of the

corresponding evaporation curves. The chart demonstrates the dependency of the integral value from the alcoholic strength in the range of 20 to 76 %Vol.

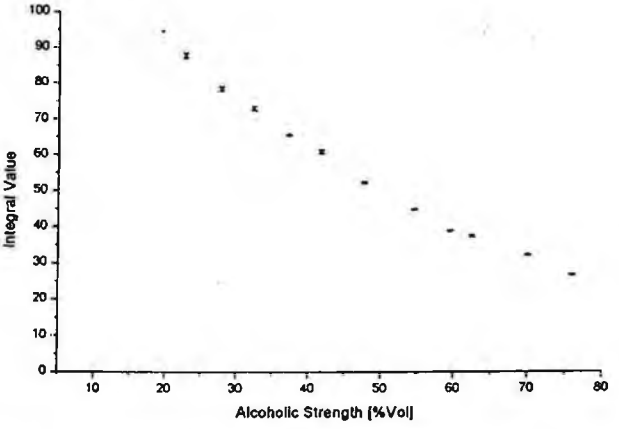

Figure 4 Chart of the evaporation integral of a droplet versus alcoholic degree.

6. Conclusions

The design, realization and testing of a new micro-alcoholometer has been reported, demonstrating the validity of an innovative principle of measurement. Results show the feasibility of a new device that can substitute old measurement systems in wine and spirit production.

Acknowledgments

We would like to thank Ing. Michele Corrà and 3TEC Company for the design and realization of a custom read-out electronic.

References

1. J. S. Rowlinson, *Liquids and Liquid Mixtures, Butter-worths,* London, (1969).
2. V. Guarnieri et al., *Low power Silicon microheaters on a thin dielectric membrane with thick film sensing layer for gas sensor applications.* MMN 2000, pp. 254–258.
3. S. Brida et al., *Characterization of Silicon anisotropic TMAH etch for bulk micromachining*, AISEM 1998, Castromarina (Le) (1998)

A MICROCHAMBER FOR LAB-ON-CHIP APPLICATIONS BASED ON SILICON-GLASS ANODIC BONDING

LUCA DE STEFANO*, LUCIA ROTIROTI, K. MALECKI AND IVO RENDINA

Institute for Microelectronics and Microsystems, Department of Naples, National Council of Research, Via P. Castellino 111, 80131 Naples, Italy

F. G. DELLA CORTE, LUIGI MORETTI

"Mediterranea" University of Reggio Calabria, Località Feo di Vito, 89060 Reggio Calabria, Italy

In this communication, the compatibility of porous silicon and anodic bonding (AB) technologies for the realization of sensing micro components in lab-on-chip applications has been demonstrated. The two techniques have been combined for the fabrication of a chemical sensor, in view of its miniaturization and integration with a smart micro-dosage system. For this application a very quick and low temperature AB process is essential in order to prevent pores filling with thermal oxides.

Keywords: Porous silicon, anodic bonding, microchamber, lab-on-chip.

1. Introduction

The recent interest for the integration of micro-electro-mechanical systems (MEMS) and micro-total-analysis systems (μTAS) is promoting silicon-glass anodic bonding (AB) as one of the most promising techniques in this field [1-4]. This technique easily allows the encapsulation and sealing on silicon chips of three-dimensional microfluidic structures, such as channels, chambers, cavities and other complex gas and liquid routes [5]. Additionally, glass transparency at optical wavelengths enables simple, but highly accurate, alignment of pre-patterned or structured glass and silicon wafers. The transmission features can also be exploited for optical addressing and probing.

Porous silicon (PSi) is widely exploited as a sacrificial material in micromachining technology, and as a buffer layer in the realization of microsensors and microsystems due to its very low thermal and electrical conductivity. Anyway, the main interest in PSi is related to its sponge-like nanostructure (specific surfaces up to 500 m^2 cm^{-3}) which makes it a smart

* Author to whom correspondence should be addressed: luca.destefano@na.imm.cnr.it

transducer material able to effectively interact with several chemicals and biological molecules. In fact, on exposure at chemical substances, several physical quantities, such as refractive index, photoluminescence, and electrical conductivity, change drastically. In particular, in the last years, a lot of experimental work has been reported concerning its use as optical sensors in chemical and biological sensing [6-8]. In environmental monitoring, optical read-out techniques are of particular interest mainly because they do not require electric contacts that may cause explosions or fire in dangerous environment, they are not affected by electromagnetic interference, and, moreover, allow wireless remote interrogation. Also in these kinds of applications, the exploitation of PSi seems to be very promising. As a matter of fact, the possibilities of modulating the PSi porosity, as well as the good control of the interface between layers of different porosity, permit to fabricate not only single-layer optical interferometers but also multi-layer structures with high optical contrast such as high reflectivity Bragg reflectors, optical waveguides and high quality Fabry-Perot filters. We recently proposed PSi optical sensors with monolayer as well as multilayer structure. They are based on the refractive index change induced in different ways by chemicals (such as hydrocarbons, flammable substances, pesticides, etc.) and biological species (DNA and enzymes) [9-13]. In the case of chemical substances in the vapour or liquid phase, the phenomenon of capillary condensation occurs in the nanometric pores, causing an increase of the average refractive index of PSi microcavity structure, and therefore a marked red-shift of its reflectivity spectrum. The detection of biological species is based on the refractive index change induced by their covalent bonding on the porous surface. The technique requires the preventive functionalization of the silicon surface with probing macromolecules (typically, single strand DNA or protein).

Through the association of these two technologies, AB and PSi, new chemo-biological sensors can be fabricated, promising integrability with electronics and high sensitivity.

In this work, the compatibility of porous silicon and anodic bonding technologies for the realization of sensing micro-components in lab-on-chip applications has been demonstrated. The two techniques have been combined for the fabrication of a bio-chemical sensor, in view of its miniaturization and integration with a smart micro-dosage system.

1.1 *Devices design and fabrication*

We have designed and fabricated a sensor device constituted by PSi, as the transducer material, and glass, as cover material: the analysis chamber is dug into the crystalline silicon. The schematic of this sensing device is shown in Figure 1.

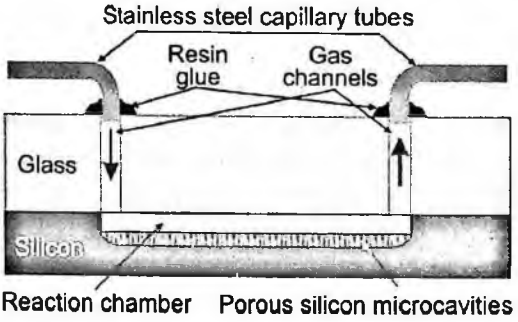

Figure 1: Schematic of the hybrid device. Components are not on scale.

The micro chamber used in the device was produced by a two-step electrochemical etching of a <100> silicon wafer, p+ type, with a resistivity of 8-12 mΩ/cm, using an HF/EtOH (50:50) solution. The first step, performed by applying a current density of 400 mA/cm^2 for about 300 s, creates a thick sacrificial layer of high porosity PSi. A short current density peak of 800 mA/cm^2 has been applied to lift up this layer which has been completely removed by NaOH (0.5 M) solution. The result is an empty 180 μm deep chamber into the silicon substrate. The depth of the chamber has been measured by a profilometer (TENCOR P-15). Since the diameter of the porous silicon area is about 1 cm, the total volume of the analysis chamber is about 14.1 μl. By using a fresh etching HF/EtOH (50:50) solution in the same electrochemical cell, a second etch step (400 mA/cm^2 for 3.2 s) produces, on the bottom of the chamber, a porous silicon layer of approximately 5 μm thickness. Each step can be performed without moving the chip from the electrochemical cell, reducing handling and alignment problems. At the end of the whole process the chip was moved from the back of the cell, rinsed with deionised water and ethanol, and then dried with a nitrogen stream.

A Borofloat 33 type glass, 1 mm thick, has been chosen as a chip cover, and silicon and glass elements have been polished before the bonding process. A

standard wet cleaning process based on Acetone, Potassium Dichromate (K_2Cr2O_7) and Isopropanol has been adopted for smoothing the contact angle and activating the surface. A further treatment in H_2O_2 was performed for both silicon and glass wafers for hydrophilic surface formation.

In order to apply gas or liquid substances, inlet and outlet channels have been mechanically drilled in the top glass wafer, on the opposite sides of the porous region. The general-view of the real device is shown in Figure 2.

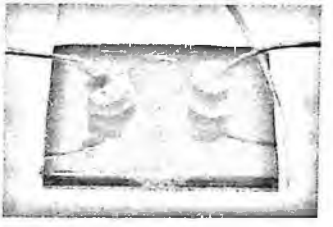

Figure 2: Real view of the integrated porous silicon based optical sensor.

2. Experimental and results

For this specific application, a very short-time AB process is essential, moreover performed at low temperatures, in order to prevent pore filling with thermal oxides which could affect the sensitivity of the sensor: the lower the porosity, the lower is the change in the average refractive index of the structure and the consequent shift in the reflectivity spectrum. We have therefore characterized the silicon-glass AB process for various temperatures, applied voltages, glass wafer thickness, and electrode type. In the case of planar electrode, satisfactory strength and bond quality was obtained at temperatures as low as 200 °C, at voltages of 2500V, with process times lower than 2 minutes (see Figure 3).

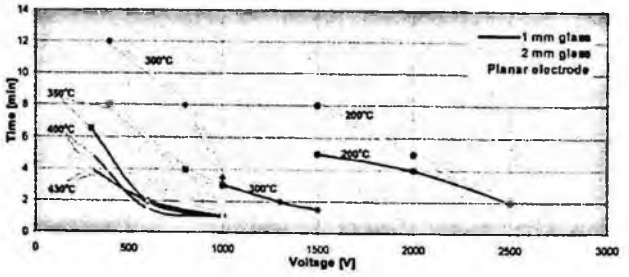

Figure 3: Time characteristics of AB versus voltage, with temperature and glass thickness as parameters, for planar electrode.

The porous silicon transducer was exposed to acetone vapours (non-saturated atmosphere) and liquid to test sensor features: the measured shifts of reflectivity spectrum are reported in Figure 4 together with the experimental set-up for optical signal detection.

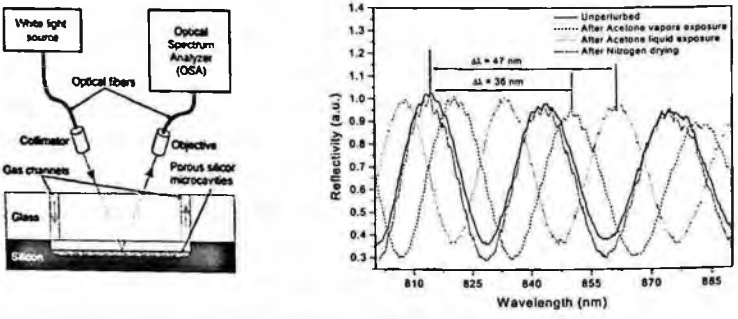

Figure 4: Experimental set-up and reflectivity spectra of the PSi monolayer after the exposure to vapour and liquid acetone.

A white light impinges, through an optical fiber and a collimator, on the PSi layer and the output is collected by an objective and coupled into a multimode fiber. The signal is sent to an optical spectrum analyser (Ando, Mod. AQ-6315B) and measured with a 0.2 nm resolution. Vapours and liquid is injected in the microchip by syringes. The fluidic in the micro lab-on-chip is very easy.

Before anodic bonding procedure, reflectivity spectrum shifted 60 nm, in case of liquid exposure, with respect to the unperturbed position. Using the micro chamber, we obtained a 47 nm shift in presence of liquid acetone. This result shows that the anodic bonding process does not prevent the effective operation of the microsensor, even thought a lowering of the sensitivity is registered. After drying the micro volume by nitrogen stream, the reflectivity spectrum recovers its starting position, so that the sensing mechanism is completely reversible.

3. Conclusion

The sensing device realised in this work has features and advantages, from a micro-opto-mechanical point of view. The technological solutions adopted can be mixed to reach best performances and flexibility. In this work we have demonstrated the complete compatibility between two technologies of great appeal in the realisation of micro-total-analysis systems: anodic bonding and porous silicon. The microsensor configuration has been designed and fabricated.

A first sensing test using vapour and liquid Acetone confirmed the feasibility and good features of the device proposed.

Acknowledgment

This work has been supported by Marie Currie Fellowship of the European Community programme "Technologies for micro-opto-mechanical systems" under contract number contract n. HPMD-CT-2001-00104, and by PON-MIUR n. 156 "Sviluppo di tecnologie innovative per la società dell'informazione: optoelettronica, nanoelettronica e sensoristica".

References

1. Cozma, B. Puers, "Characterisation of the electrostatic bonding of silicon and Pyrex glasses", J. Micromech. Microeng. 5, pp 98-102, 1995.
2. J.Wei, H.Xie, M.L.Nai, C.K.Wong, L.C.Lee, "Low temperature wafer anodic bonding", J. Micromech. Microeng. 13, pp 217–222, 2003.
3. Hannenborg, M. Nese, H. Jakobsen, R. Holm, "Silicon-to-thin film anodic bonding", J. Micromech. Microeng. 2, pp 117-121, 1992.

4. T. Rogers, J. Kowal, "Selection of glass, anodic bonding conditions and material compatibility for silicon-glass capacitive sensors", Sensors and Actuators A46/47, pp. 113-120, 1995.
5. Ljibisa Ristic, Sensors Technology and Devices, pp. 207, 1994.
6. P. A. Snow, E. K. Squire, P. St. J. Russel, and L. T. Canaham, J. Appl. Phys. 86, 1781 (1999).
7. T. M. Benson, H. F. Arrand, P. Sewell, D. Niemeyer, A. Loni, R. J. Bozeat, M. Kruger, R. Arens-Fischer, M. Thoenissen, and H. Luth, Mat. Sci. Eng. B 69-70, 92-99 (1999).
8. V. Mulloni and L. Pavesi, Appl. Phys. Lett. 76, 2523 (2000).
9. L. De Stefano, I. Rendina, L. Moretti, A.M. Rossi, S. Tundo, "Smart optical sensors for chemical substances based on porous silicon technology", Applied Optics, 43/1, 167-172, 2004.
10. L. De Stefano, I. Rendina, L. Moretti, A.M. Rossi, "Quantitative optical sensing in two-component mixtures using porous silicon microcavities", Phys. Stat. Sol. (a) 201, No. 5, 1011–1016 (2004).
11. L. De Stefano, I. Rendina, L. Moretti, A.M. Rossi, A. Lamberti, P. Arcari, O. Longo, M. Rocchia, "Optical sensors for vapors, liquids, and biological molecules based on porous silicon technology", IEEE Transaction on Nanotechnology 3, N. 1, 49-54, (2004).
12. L. De Stefano, I. Rendina, L. Moretti, A.M. Rossi, "Time-resolved sensing of chemical species in porous silicon optical microcavity", Sensor and Actuators B, 100, 168-172, 2004.
13. L. Rotiroti, L. De Stefano, L. Moretti, A. Piccolo, I. Rendina, A. M. Rossi, "Optical micro-sensors for pesticides identification based on porous silicon technology", in press on Biosensors and Bioelectronics, available on line.

DIELECTROPHORETIC SAMPLE HANDLING DEVICE FOR MICRO TOTAL ANALYSIS SYSTEMS

M. CATTANEO, E. GALEAZZI, U. MASTROMATTEO, M. PALMIERI, S. SASSOLINI, M. SCURATI
STMicroelectronics - via Tolomeo, 1 - 20010 Cornaredo, Italy
G. GRADL, T. MULLER, T. SCHNELLE
Evotec Technologies GmbH c/o humboldt Universitat zu Berlin Institut furBiologie Invalidenstr. 42 - D-10115 Berlin

In order to include in a silicon Lab On Chip the functional block for sample preparation, it has been developed a device based on dielectrophoresis (DEP) able to sort, isolate and burst target cells from clinically relevant samples. Although the physics may appear complex, the technology needed to accomplish DEP is straightforward and relatively inexpensive.
Because the DEP force is proportional to two independent terms, it is possible to exploit this versatility applying appropriate electrical signals to the electrodes and so optimize each application in accordance to the dielectric characteristic of the particles. The developed device has been designed for the separation of white blood cells in a diluted row blood sample and then lead these cells in an electroporation section to perform lysis for the genetic information extraction.

1. Introduction

1.1. *Dielectorphoresis force*

It is well known that a spatially nonuniform electric field exerts a net force on the field-induced dipole of a particle. This force is independent from the charge of the particle, but only depends from the induced dipole and the gradient of the applied electric field. The dielectrophoretic force may be positive or negative.
The following conditions determine the DEP application range:

1- The electric field has to be nonuniform;
2- AC or DC electric fields are both suitable;
3- Positive DEP is obtained when $\varepsilon_m < \varepsilon_p$ where ε_m is the medium permittivity and ε_p the particle permittivity;
4- Negative DEP is obtained when $\varepsilon_p < \varepsilon_m$;
5- The particle size can range from 1 to 1000 μm.

Using AC fields is preferred because of charging reduction of electrodes and biological cells, moreover using high frequencies fields the impact on the cell physiology is much lower.
Another important parameter influencing the DEP force is the conductivity of the particle σ_p and medium σ_m. Because both the conductivity and the permittivity are frequency depending, it is possible to obtain positive or negative DEP force just varying the frequency of the electric driving signals.

In the figure 1 it is possible to see the variation of the dielectrophoretic force as a function of the electric field frequency and of the medium conductivity.

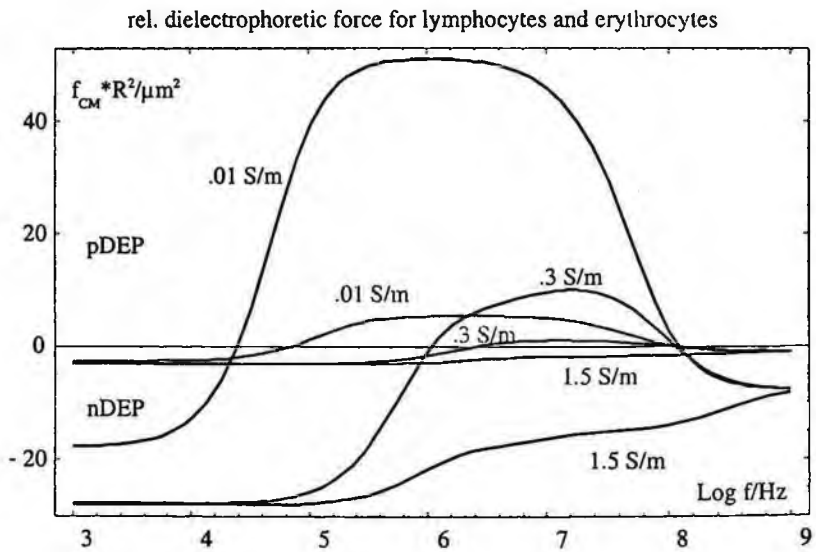

Figure 1. Dielectrophoretic force versus electric field frequency.

1.2. *DEP for blood cells separation*

Cell and particle sorting is easily achieved by DEP when the composition or cell sizes are clearly distinct. This is the case for lymphocytes and erythrocytes in the blood. In order to set up a test device for the mentioned separation, a microfluidic chamber has been designed where several electrodes configuration are integrated using the technology developed for silicon MEMS.

The microfluidic chamber has been made using a silicon wafer with platinum electrodes bonded to a glass wafers with patterned ITO transparent metal electrodes. A patterned polymeric material has been used for the spacers and the glass had holes for the inlet and outlet of the biologic fluid.

In the figure 2 is possible to see a schematic cross section of the chamber and also a top view for one of the separation DEP barriers. As it is showed in the sketched top view the DEP barrier acts only for the white blood cells, while the red ones can follow the flow without any deviation. In this way it is possible to have channel regions with a very high white cell concentration.

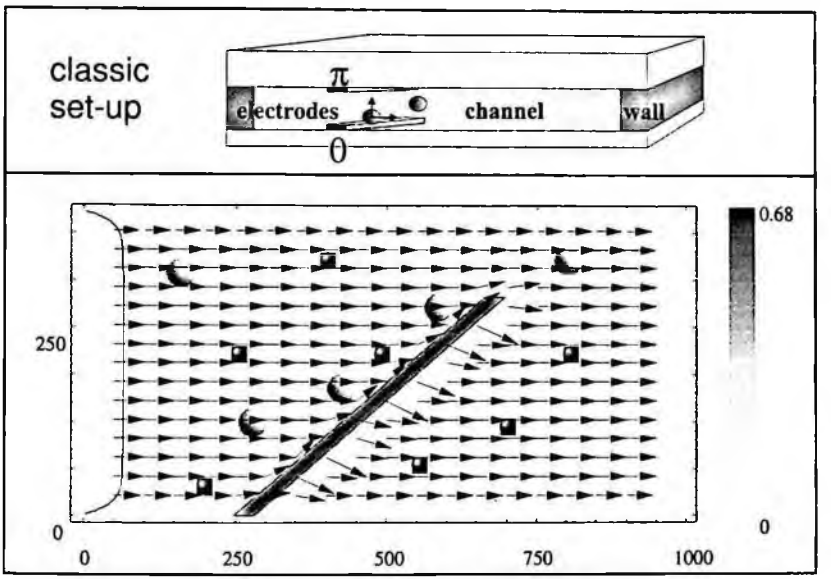

Figure 2 Schematic view of the DEP chamber

1.3. *Genetic information extraction*

In order to exploit the advantages offered by DEP for the sample preparation in a biologic protocol in a Lab On a Chip, once the separation or cell sorting has increased nucleated cell concentration in a dedicated microfluidic channel, to proceed directly with an electrical cell lysis to extract the material containing the genetic information from the nucleus.

The figure 3 shows the layout of the lysis region made using the same layers of the dielctrophoresis. On the left of the picture it is possible to see the a specific electrodes configuration to drive the cells into a double planar electrodes gap where electroporation of the cell membrane occurs.

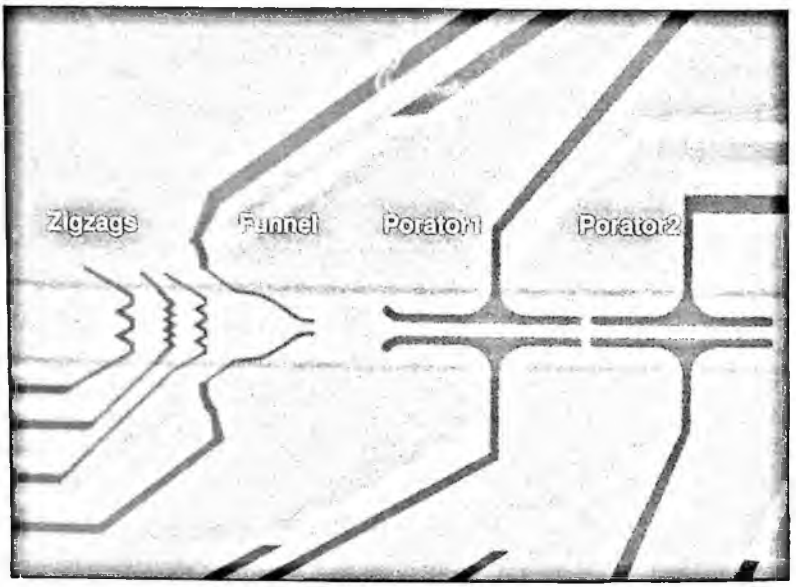

Figure 3. Lysis layout configuration

1.4 Conclusions

A silicon Lab On a Chip for detection of PCR products has already been developed in STMicroelectronics labs. The possibility to integrate on these kind of chips the fluidic function able to sort and burst target cells from clinically relevant samples, will allow rapid and automatic molecular assays. What we have described is one of the possible approaches to accomplish key processing steps. To create a complete system for applications in molecular diagnostics it will be necessary to combine several enabling technologies like DEP, PCR and hybridization detection in a sequential flow-through fashion.

References

1. *Proceedings of the IEEE, special issue on: Biomedical Applications for MEMSand Microfluidics*; volume 92, number 1; January 2004
2. Y. Ghallab an W. Badwy, IEEE Circuits and Systems, Vol 4, N. 3 (2004), pp 5-15

HIGH ASPECT RATIO SiO_2 MICRONEEDLE ARRAY FABRICATION

G. BARILLARO*, S. CIUCCI, A. DILIGENTI, G. PENNELLI
Dipartimento di Ingegneria dell'Informazione: Elettronica,Informatica, Telecomunicazioni
Via G. Caruso, 56122 Pisa, Italy
**E-mail: g.barillaro@ing.unipi.it*

A two-mask low cost technology for the fabrication of arrays of hollow, high aspect ratio silicon dioxide microneedles is presented. The process is based on the following technological steps: photo-electrochemical etching of silicon to etch a deep regular macropore array; wet thermal oxidation of macropores to produce silicon dioxide microchannels; silicon wet etching to release the microchannels and obtain the microneedles. Advantages and drawbacks of this approach are discussed on the basis of obtained experimental results.

1. Introduction

Microfabrication technology is a very powerful tool for fabricating sensors, actuators and passive structures for automotive (i.e. accelerometers, gyroscope), optic (i.e. photonic crystals), space (i.e. field emitter array) applications, etc.
Recently, the application of microfabrication technologies to the biomedical field has risen a great interest because of the possibility of development of new diagnostic and therapeutic tools. As a matter of fact, devices to sense, stimulate and deliver drugs to biological systems, i.e. micropumps, tissue scaffold, and stents, have been fabricated so far [1]. One of the most critical components of such systems are microchannels and hollow microneedles, that provide pathways for fluids flow and the necessary complement for integrated microfluidic components [2]. However, techniques employed for the fabrication of such components are usually quite complex [3, 4].
Recently, photo-electrochemical etching of silicon has been proposed as a simple approach for fabrication of silicon dioxide microneedles [5]. Photoelectro-chemical etching of silicon in HF-based electrolytes is a well known technique for etching deep regular macropore arrays in *n*-type silicon substrates. By pre-patterning the surface with defect sites it is possible to determine where macropores will grow [6, 7].
In this work we present a two mask process for the fabrication of hollow, high aspect ratio silicon dioxide microneedles array by employing a low cost

technology. The process basically exploits: 1) the silicon photo-electrochemical etching to etch a deep regular macropore array; 2) a wet thermal oxidation of macropores to produce silicon dioxide microchannels; 3) a silicon wet etching to release a part of the microchannels and obtain the microneedles. Advantages and drawbacks of this approach are discussed on the basis of obtained experimental results.

2. Fabrication process

The microneedles fabrication process consists of technological steps reported in fig. 1. The starting material was a *n*-type silicon wafer with resistivity of 2.2–4 Ω·cm, thickness of 550 μm, ⟨100⟩ orientated, single-side polished. A thermal dry oxidation (1h at 1050 °C) was performed in order to grow a silicon dioxide layer, about 100 nm thick. A regular pattern of square holes, with a diameter of 2 μm and pitch of 4 μm, was defined in the oxide layer by using a standard lithographic step (first mask) and a wet etching. A KOH etching step was then used to transfer the pattern to the silicon, producing in this way an array of notches which was used as a seed for pore growth (Fig. 1a).
Photo-electrochemical etching in a HF-based solution was then performed for controlled macropore formation (Fig.1b). The macropores etching rate was of the order of 2 μm/min, so that macropores with a depth of over 200 μm were grown in 2 hours. Silicon dioxide microchannels were then produced by a

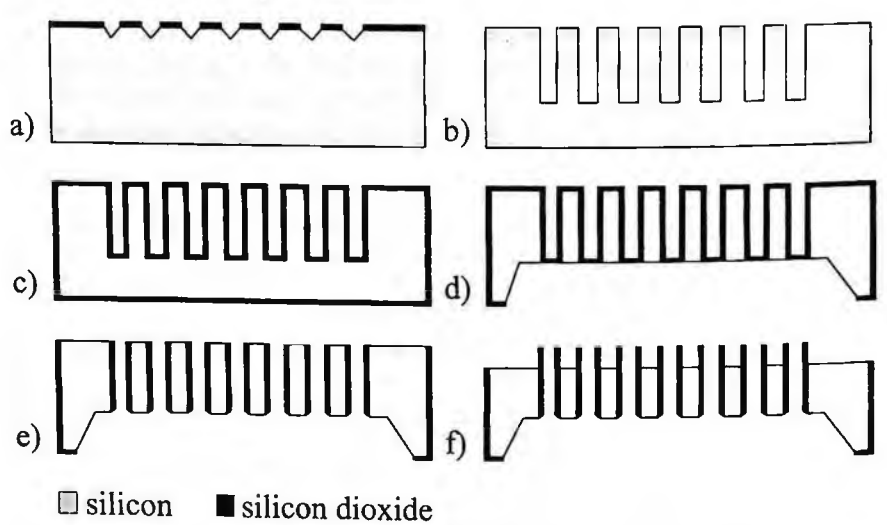

Figure 1. Silicon dioxide microneedles array fabrication process: technological steps (not to scale).

second oxidation of the sample (2.5h wet oxidation at 1050 °C, resulting in a 1 μm thick oxide layer) (Fig. 1c). A square window was opened on the back oxide layer of the sample by means of a standard lithographic step (second mask) and a wet etching. A KOH (20% weight) etching step was then used to remove bulk silicon from the back–side in order to discover the bottom of oxidized microchannels (2h at 70 °C) (Fig. 1 d). The next step was the back opening of oxide microchannels by wet etching in order to obtain hollow microchannels. A mechanical polishing procedure on the front-side of the sample was then used to expose the silicon surface (Fig. 1e). The last step of the process was a KOH silicon etching on the front side of the sample in order to release a part of microchannels and obtain the microneedles (Fig. 1f). The time required for the whole process is of few hours.

3. Experimental results and discussion

The key role on the silicon dioxide microneedles fabrication process is played by the photo-electrochemical etching of silicon in HF-based electrolytes for deep, ordered macropores formation.

Photo-electrochemical etching of a *n*-type silicon substrate in HF solutions can be controlled to produce highly regular macropore array [6, 7] as well as silicon microstructures [8]. Electrochemical etching of silicon in HF electrolytes is activated by holes. For *n*-type substrates holes can be generated by illuminating the back surface of the wafer. Under anodization biasing conditions, generated holes move toward the front-side silicon surface, which is in contact with the electrolyte, and are collected at the surface defects where they react giving rise to the dissolution of silicon. Surface defects therefore act as seeding points for silicon dissolution. By pre-patterning the wafer surface with defect sites, for example by means of a standard lithographic step, it is possible to decide where the silicon etching takes place. The resulting structure depends on the pre-patterned geometry as well as on the etching parameters, such as etching current and voltage, etching time, temperature, electrolyte composition, etc. By controlling these parameters it is possible to fabricate silicon macropores and microstructures as deep as the wafer thickness, with high lateral (parallel to the wafer surface) and vertical (perpendicular to the wafer surface) uniformity.

Figure 2 shows SEM pictures of three different stages of silicon dioxide microneedles fabrication process: 1) after the photo-electrochemical etching step (fig. 2a, 2b); 2) after the wet oxidation step (fig.2c, 2d); and 3) after the microneedles have been released for a 30 μm length (fig. 2e, 2f).

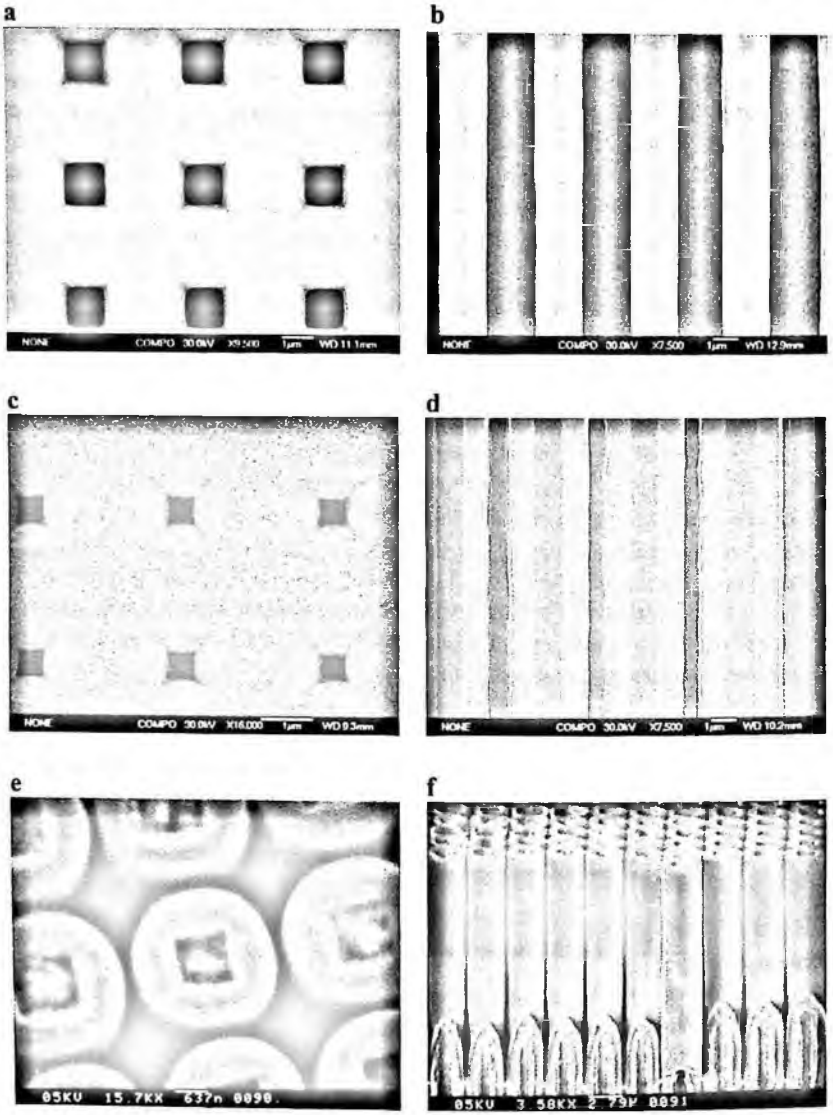

Figure 2. Different stages of the microneedles fabrication process: 1) top view (a) and section (b) of the sample after the photo-electrochemical step; 2) top view (c) and section (d) of the sample after the wet thermal oxidation step; 3) top view (e) and section (f) of the sample after the last step (release of the microneedles).

While typical approaches for microneedles fabrication rely on radically different techniques, with respect to the one presented here, to produce silicon [3] or metallic [4] needles, the use of silicon dioxide is a great improvement in terms of biocompatibility. Moreover, with the proposed technology, high lateral and vertical uniformity of the samples is achieved at every process step (top and cross-sectional view); most design variables are easily controlled: the pitch of microneedles is defined by the first lithographic step, while the channel diameter is controlled by the anodization current density and by the second oxidation step; finally, the microneedle length depends on the last KOH etching step.
The main drawback of this approach, related to the photo-electrochemical etching, is the dependence of the size and pitch of macropores on the resistivity of the silicon substrate, which is a constraint for the maximum diameter and pitch of the needles. However, this constraint can be relaxed by selecting a suitable substrate resistivity and initial lithographic pattern [7].

4. Conclusions

In this paper the viability of hollow, high-aspect ratio silicon dioxide microneedles fabrication by using a two mask process has been demonstrated. The process is based on: 1) the photo-electrochemical etching process to etch a deep regular macropore array; 2) a wet thermal oxidation of macropores to produce silicon dioxide microchannels; 3) a silicon wet etching to release a part of the microchannels and obtain the microneedles. The proposed process enables the fabrication of silicon dioxide microneedles using a low cost technology for biomedical applications.

References

1. S. L. Tao, Tejal A. Desai, Advanced Drug Delivery Reviews, 55, pp. 315-328 (2003).
2. M. R. Prausnitz, Advanced Drug Delivery Reviews, 56, pp. 581-587 (2004).
3. E. V. Mukerjee, S. D. Collins, R. R. Isseroff, R. L. Smith, *Sens. Actuators A*, 114, pp. 267-275 (2004).
4. S.P. Davis, B.J. Landis, Z.H. Adams, M.G. Allen, M.R. Prausnitz, J. of Biomechanics, 37, pp. 1155-1163 (2004).
5. S. Rajaraman and H.T. Henderson, Sens. Actuators *B*, 105, pp. 443-448 (2005).
6. V. Lehmann, J. Electrochem. Soc., 137, pp. 653-658 (1990).
7. G. Barillaro, A. Nannini, F. Pieri, J. Electro-chem. Soc., 149, pp. C180-C185 (2002).

8. G. Barillaro, A. Nannini, M. Piotto, Sens. Actuators A, 102 (1-2), 195-201 (2002)

A MICROELECTRODE ARRAY FABRICATION TECHNOLOGY FOR ELECTROPHYSIOLOGICAL MEASUREMENTS

CRISTIAN COLLINI[†]
ITC-irst Microsystems Division,
Via Sommarive 18, Povo 38050, Trento, Italy.

LEANDRO LORENZELLI, ALESSANDRO FAES,
FLAVIO GIACOMOZZI, BENNO MARGESIN
ITC-irst Microsystems Division,
Via Sommarive 18, Povo 38050, Trento, Italy.

SERGIO MARTINOIA

DIBE, University of Genova, Via all' Opera Pia 11A – 16145 Genova – Italy

In this work we present the microfabrication process for micro-electrode arrays (MEAs) designed for monitoring the electrophysiological behavior of neuron networks.

The developed devices mainly consist of planar multi-electrodes and three-dimensional structures for cell guided growth and networking.

Starting from a quartz wafer (double polished optical prime grade material, flame fused quartz, thickness 0.5 mm) the proposed fabrication process implements a Ti/TiN/Al/TiN low resistance multilayer for all the wires and electrical connections. All the exposed surfaces of the microelectrodes are realized in an Au/Cr (150nm/5nm) double layer: the thin Chromium layer is used in order to promote gold adhesion. The three-dimensional structures have been realized by means of a SU-8 negative resist. From a technological point of view, this research focused on obtaining i.) metal wires and electrodes with low resistivity and ii.) very thick SU-8 structures with improved performance in terms of adhesion. In order to implement well defined areas, connected by means of micro-channels, the development of reproducible procedure for SU-8 thick films deposition has been considered a central issue of this fabrication process.

[†] *Tel.: +39 0461 314 497, E-mail : ccollini@itc.it*

1. Microelectrode Array Design.

Quartz based miniaturized electrode arrays have been designed and fabricated. The microsystem basically consists of a microelectrode array and three-dimensional structures for cell guided growth and networking. Different MEAs layout configurations have been design and manufactured to test the technology; figure 1 shows the layout of the two types of microelectrode arrays that have been realized.

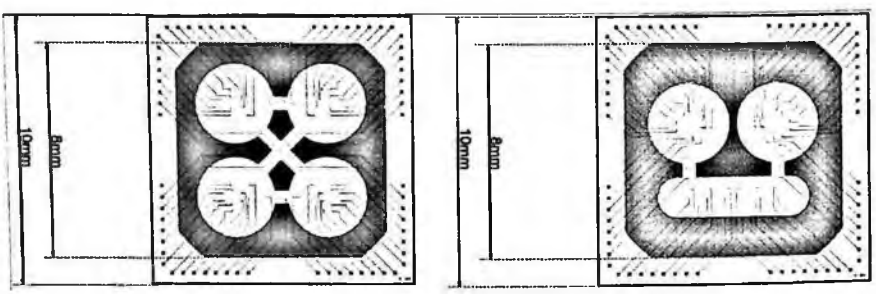

Figure.1 Layout of Micro-electrode array.

2. Fabrication Process

The main process steps of the fabrication sequence are shown in figure 2.

a. Substrate: 500 µm thick quartz wafer (double side polished, optical prime grade).
b. A Ti/TiN/Al/TiN multilayer is deposited by sputtering.
c. This multilayer is patterned by photolithography and plasma dry etching to form the electrodes, lines and the contact pin zone.
d. A layer of Si_3N_4 (200nm) is then deposited by PECVD in order to insulate the metal lines.
e. Contacts are opened through the Si_3N_4 layer by plasma dry etching.
f. Evaporation of Cr and Au is carried out (5 nm and 150 nm, respectively).
g. The Chromium and Gold layers are patterned by wet etching.
h. A very thick double layer of SU-8 negative photoresist is deposited by spin coating.
i. The thick SU-8 layer is patterned by wet-etching.

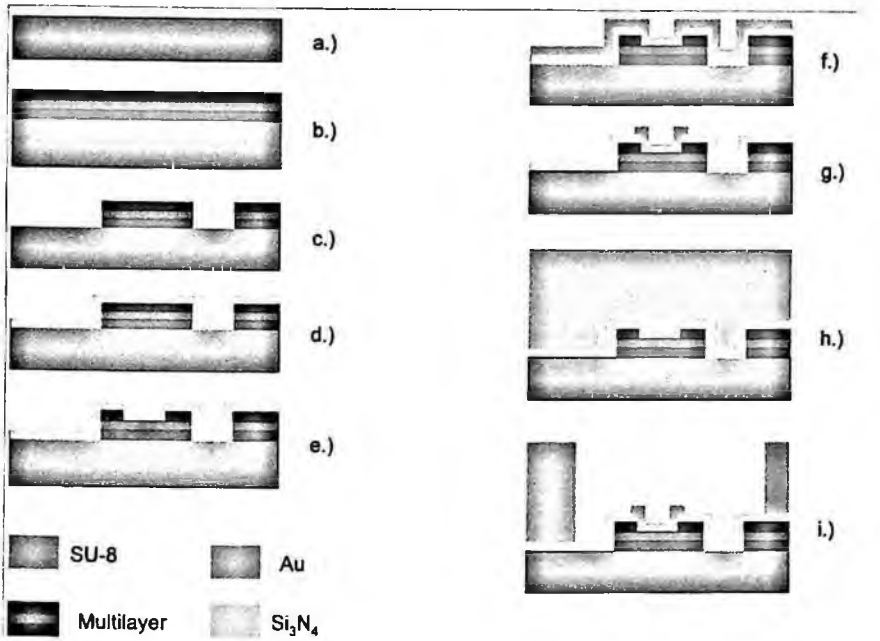

Figure 2: Fabrication process outline

3. Morphological and structural testing

Electric characterization and SEM characterization of electrodes have been performed (see figure 3). The three-dimensional polymeric structures have been manufactured by using two layers of negative photoresist with different viscosity (SU-8 2015 and SU-8 2100) and with a thickness of 16 μm and 200 μm, respectively.

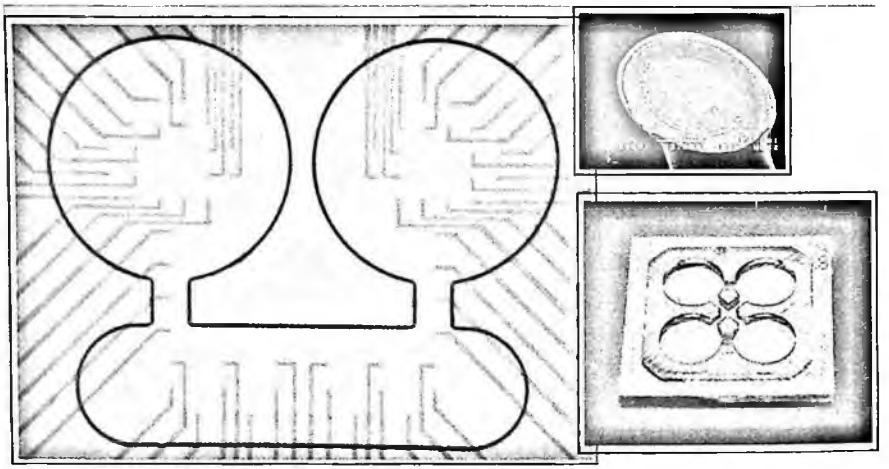

Figure. 3 Microelectrode array: the inset shows a SEM image of a Microelectrode

The exposed area of the microelectrodes is 7500 μm^2, the thickness and the diameter of the SU-8 tubs are 250 μm and 3 mm, respectively.

4. Devices packaging

A customized package has been designed and developed, in order to provide electrical connections. Figure 4 shows the final devices mount on the printed circuit board (PCB), including a glass ring glued on the top of the PCB. **Ayanda Biosystems** (PSE Parc Scientifique, Swiss Federal Institute of Technology campus in Lausanne, Switzerland) developed a similar approach in the past.

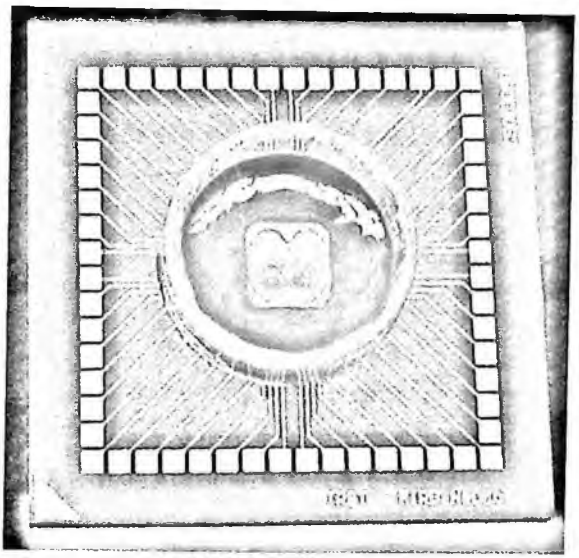

Figure 4: Final device in the packaging structure

5. Acknowledgments

This work has been partially funded by MIUR FIRB Project "*Development of multifunctional microsystems for applications in clinical diagnostics and food analysis*" and MIUR FIRB project "*In-vitro neuronal networks chronically coupled to microtransducer arrays and interacting with an artificial body: a new powerful tool to study brain – machine interface and in-vitro brain plasticity* "..

References

1. Lorenz, M. Despont, P. Vettiger, P. Renaud H., "Fabrication of photoplastic high-aspect ratio microparts and micromolds using SU8 UV resist" , Microsystem Technologies, 4, pp.143-146, (1998)
2. Martinoia, et. al., "Development of ISFET array-based microsystems for bioelectrochemical measurements of cell populations", Biosensors & Bioelectronics, 16 1043–1050, (2001)
3. M. O. Heuschkel, "Fabrication of multi-electrode array devices for electrophysiological monitoring of in-vitro cell/tissue cultures", Hartung-Gorre Verlag, Konstanz, Germany, Series in Microsystems Vol. 13, pp. 188, (2001).

RADIOFREQUENCY TRANSIENT BEHAVIOUR OF OHMIC RF-MEMS SWITCHES.

J. IANNACCI, L. DEL TIN, M. BELLEI, R. GADDI, A. GNUDI
Centro di Ricerca E. De Castro (ARCES), Università di Bologna
Viale Risorgimento, 2, 40136 Bologna, Italy
E-mail: jiannacci@deis.unibo.it

B. MARGESIN, F. GIACOMOZZI
ITC-irst, Divisione Miscrosistemi, Via Sommarive, 16, 38050 Povo (TN), Italy

In this paper the transient behaviour of ohmic RF-MEMS switches will be investigated by both experimental and simulation means. The devices are based on a suspended gold membrane and vertical electrostatic transduction, with gold ohmic contacts along the RF signal path. Dynamic RF measurements are performed by using a power detector to monitor opening and closing transitions of both series and shunt switches. Compact models of the fabricated devices are also implemented in Cadence® through a developed MEMS model library based on modified nodal analysis. Pull-in voltage, actuation and release transition time have been observed and compared, achieving a better understanding of squeeze-film damping effect.

1. Introduction

RF-MEMS switches have emerged in recent years as a potential alternative to solid state devices for improving reconfigurability in multi-standard wireless systems [1] [2]. However, their reliability and dynamic behaviour characterization, such as transient switching times, still require further evaluation and development efforts. Moreover, since the application of MEMS technology to RF circuits is relatively recent, further availability of both suitable simulation tools and test structures to provide experimental measurements is required.

The present work shows the results of dynamic measurements performed on RF-MEMS ohmic shunt switches designed and fabricated in ITC-irst RF-MEMS technology [3], describing their dynamic RF behaviour through a suitable measurements setup.

Moreover, the simulation of the switch structure behaviour has been ac-

complished by means of a suitable interconnection of elementary component models (e.g. Euler flexible beam and suspended electrostatic rigid plate) included in a MEMS library implemented by the Authors in Cadence® SpectreHDL® language [4].

2. The RF-MEMS Ohmic Shunt Switch Structure

The technology process utilized for the fabrication of the switches is based on an electrodeposited suspended gold membrane layer, one high resistivity poly silicon layer for the actuation electrodes and a Al-Ti-TiN multilayer for the RF-signal path. The ohmic switches have two electrically separated electrodes underneath the suspended plate surface, one for the RF-signal and one for applying the control voltage [1]. The shunt and series switches differ only for the topology of the RF-signal electrodes. Input and output RF ports are physically connected by the signal fingers in the shunt switch, while they are isolated in the series switch. In both cases, dummy poly bricks are placed underneath the signal electrodes, which are therefore the only contact area towards the collapsed plate, while actuation electrodes always remain untouched.

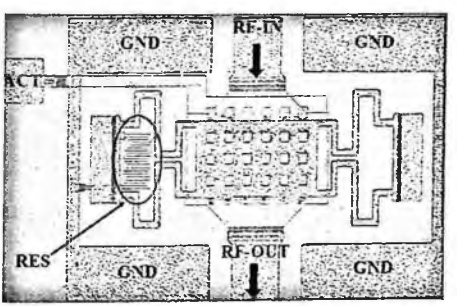

Figure 1. The Ohmic-Series switch.

3. Dynamic measurement setup

A suitable setup has been arranged to perform on-wafer dynamic measurements of the switch RF behaviour. An RF signal with constant power and a frequency of 2GHz is fed at the switch input port, while the output port is connected to a Schottky-diode based power detector, obtaining a voltage response that is proportional to the RF signal amplitude. The actuation

voltage is obtained by an arbitrary waveform generator whose signal is amplified in order to go beyond the pull-in voltage. An oscilloscope is utilized to monitor both the actuation voltage and the power detector output voltage, and its trigger is synchronized to the arbitrary waveform generator. All the instruments are connected to a PC via GPIB bus and controlled within a developed LabView virtual instrument.

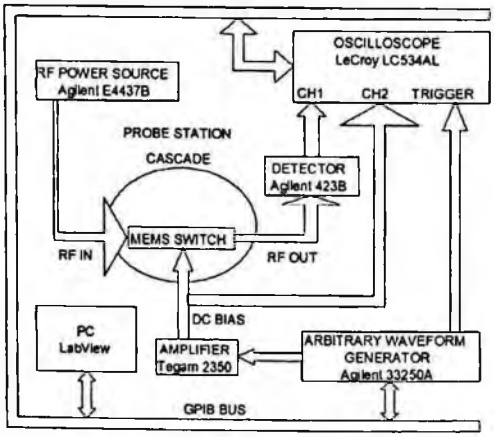

Figure 2. Dynamic measurements setup.

4. Measurements, simulations and discussion

Measurement data of a series ohmic switch was compared with simulations to better understand qualitative switching behaviour. A bias voltage pulse was applied to the switch with a period of 1ms, peak value 50V, rise and fall times 200ns, delay 100μs and pulse width 500μs. Figure 3-m1 shows the bias voltage driving the switch actuation, while Fig. 3-m2 shows the corresponding behaviour of the RF power at the output port. The relationship between the applied RF signal and the voltage showed by the oscilloscope has been obtained by applying several RF power values to a short transmission line with negligible losses, and reading the corresponding output voltages. By keeping the power values in the linear region of the power detector, the coefficient to convert the output voltage to the corresponding output power value has been calculated.

On the other hand, Fig. 3-s1 represents the simulated behaviour of the switch resistance, assumed to be 1MΩ when the switch is not actuated and

1Ω as the plate contact to the signal electrode is established. Finally the Fig. 3-s2 is referred to the mechanical displacement (simulated), of the suspended plate along the z-direction. Actuation voltages up to 50V, three times higher than the static pull-in value of 15V, have been necessary to achieve repeatable RF transient behaviour.

Actuation transitions show switching time around 50μs and transition times around 10μs while the release transitions are one order of magnitude faster, leading to both switching and transition times around 1μs. It is noticeable that the mechanical oscillations of the switch during the release time, shown in the Fig. 3-s2, do not seem to affect the total transmitted power (Fig. 3-m2). This is due to the contribution of the switch coupling capacitance to ground, which is small at this operating frequency (2GHz) compared to the down-state resistance. This affects the switching time as well because a small upward movement of the plate from the collapsed position is sufficient to have an abrupt transition of the RF output power, while the actuation time is larger due to the squeeze-film damping effect.

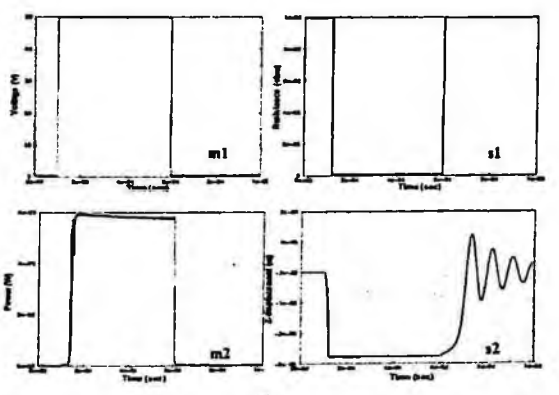

Figure 3. Comparisons between measurements (m1 and m2) and simulations (s1 and s2) of the switch dynamic behaviour.

To highlight the influence of the squeeze-film damping on the dynamic behaviour of the switch, transient simulations with different values of the air viscosity coefficient have been performed. Fig. 4 shows how this variation affects both actuation and release switching dynamics. More in details, by increasing the viscosity coefficient the actuation time becomes larger such as the release transition. However, the instant of the detachment at the beginning of the release transition is not affected.

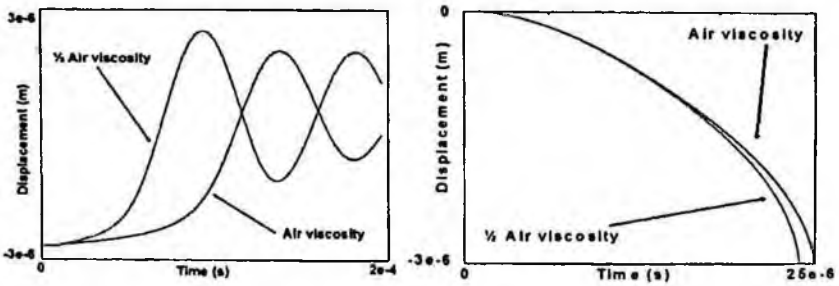

Figure 4. Release (left) and actuation (right) transitions with air viscosity coefficient (blue mark), and half of the air viscosity coefficient (red mark).

5. Conclusions

In this work the transient behaviour of an ohmic RF-MEMS switch, based on suspended gold membrane and vertical electrostatic transduction, was investigated by means of both experimental measurements and simulations. A suitable setup to perform the dynamic RF test measurements has been arranged, while the simulations in Cadence were based on a MEMS model library developed by the Authors and implemented in HDL language [4]. By comparing measured and simulated data it has been possible to notice that mechanical oscillations during the release transition cannot be observed in the measured RF output power at frequencies around 2GHz. Moreover, parametric transient simulations showed that the the squeeze-film damping mainly affects the actuation switching time.

References

1. R. Gaddi, M. Bellei, A. Gnudi, B. Margesin, F. Giacomozzi, *"Interdigitated Low-Loss Ohmic RF-MEMS Switches"*, Proceedings of NSTI-Nanotech 2004, (2004), Vol. 2, 327-330.
2. E. R. Brown, *"RF-MEMS Switches for Reconfigurable Integrated Circuit"*, IEEE, Transaction on Microwave Theory and Techniques, Vol. 46, NO. 11, Nov. 1998.
3. F. Giacomozzi, et Al., *"Electromechanical Aspects in the Optimization of the Transmission Characteristics of Series Ohmic RF-Switches 5th Workshop on MEMS for millimeterwave Communications"*, (MEMSWAVE2004), Uppsala, Sweden, 30th June - 2nd July 2004, pp. C25-C28.
4. R. Gaddi, J. Iannacci, *"Hierarchical Multidomain MEMS Simulation within an IC-Design Framework"*, Proceedings of 8th Italian Conference Sensor and Microsystems (AISEM 2003), (2003), World Scientific, 461-466.

A MICROMACHINED INERTIAL ACCELEROMETER FOR AVIONICS

A. BAGOLINI, B.MARGESIN, A. FAES
Microsistems Division, ITC-IRST, via Sommarive 18
38100 Trento, Italy

SOUMEN DAS
Microelectronics Laboratory, Indian Institute of Technology,
Kharagpur - 721302,India

The design and fabrication process of a micromachined piezoresistive accelerometer based on an inertial proofmass is proposed. The sensor is addressed to aeronautical applications, that require a resonant frequency higher than 100 Hz and high damping. FEM simulations are carried out to verify the compliance of this structure with the given specifications, and an analysis of the fabrication process is presented. The readout circuit is based on Wheatstone bridge, and is designed to minimize the off axis acceleration signal [1,2]. The structure consists of a silicon made rectangular proof mass that is supported by four arms at the four edges, with piezoresistors located at both ends of each support. The fabrication of the structure is based on bulk micromechanics, by wet anisotropic etching of both sides of the silicon wafer in TMAH solution. The proof mass has convex corners that require corner compensation structures. Gold electroplating is used to deposit an additional thick layer on top of the mass.

1. Introduction

Accelerometers are essential parts of the navigation system for most advanced vehicles. Aeronautical applications require a resonant frequency higher than 100 Hz and high damping, in order to avoid interferences from the vibrations of the aircraft. For this purpose, inertial accelerometers can be compliant, adopting the structure depicted in figure 1: the mechanical part consists of a proofmass that is suspended to the structure by four arms (b) and will impose a bending of the supports when the sensor is accelerated [1]. The bending is transduced into a variation of electrical resistance by piezoresistors located at each end of the supports. The resistors are arranged into a wheatstone bridge, so to produce an electrical signal proportional to the acceleration. This sensor has a major drawback in the fact that its mechanical structure is not selective to the axis of the acceleration, having all 6 degrees of freedom active. By placing the resistors

along the axis of the supports, we can make them sensitive to the Z axis bending only. Nevertheless this bending can be generated by three different accelerations, as shown in figure 2.

By adopting a dedicated circuit layout (fig.3) the signal generated by both the Y and X axis rotation can be minimized and neglected [2]. This makes the sensor sensitive to the Z axis acceleration only.

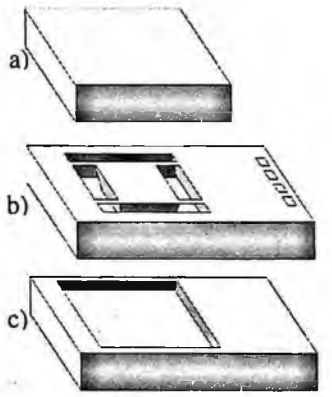

Fig.1: schematic of the three parts of the accelerometer, the top and bottom covers (a,c) and the device die (b)

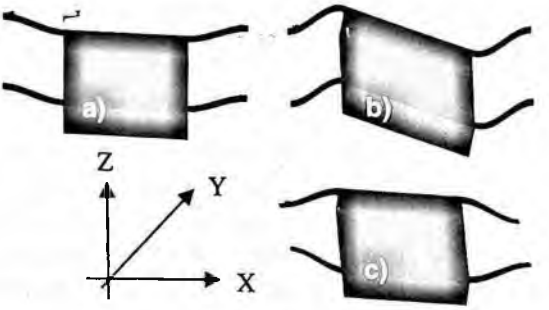

Fig.2: different accelerations that induce a bending of the supports. Acceleration along the Z axis (a), rotation on the Y and X axis (b,c).

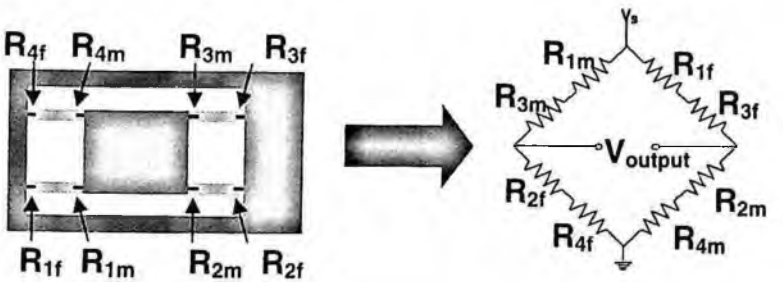

Fig.3: schematic of the position of the piezoresistors on the supports (left) and the wheatstone bridge the circuit (right)

2. Simulation

The behavior of the device under acceleration has been simulated by Ansys™ FEM tool, to dimension the proofmass and the supports. Static analysis of the stress due to the displacement of the proofmass has been performed: the resistors regions have to be subject to a maximum stress of 20MPa, that allows for a sensitivity of about 1V/g with this circuit configuration. Frequency analysis of the device is also made to ensure that the resonant frequency is higher than 100Hz. Simulation output is reported in figures 4 and 5.

The sensor is dimensioned to obtain a maximum proofmass displacement of 6um along the Z axis, for an acceleration of 5g. To reduce the dimension of the proofmass a gold layer is put on top of it: the layer increases the proofmass weight without increasing its area.

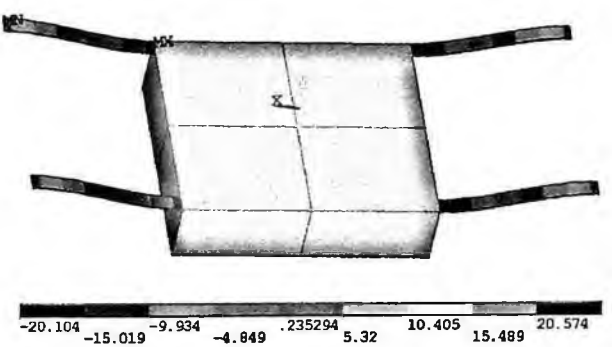

Fig. 4: stress distribution under a peak acceleration of 5g. The scale is in GPa.

3. Layout design

The layout is drawn using LEdit™ software. The main dimensions of the device are as reported in table 1.

Table 1: dimensions of the device.

Part	X (μm)	Y (μm)	Z (μm)
Proof mass	2500	2500	500
supports	1200	180	10
Gold layer	2850	2850	15
Die	11360	6120	6120

The circuit design is made to reduce to the minimum the crossing of metal lines (fig.5). On each support two substrate contacts are designed, in the proximity of

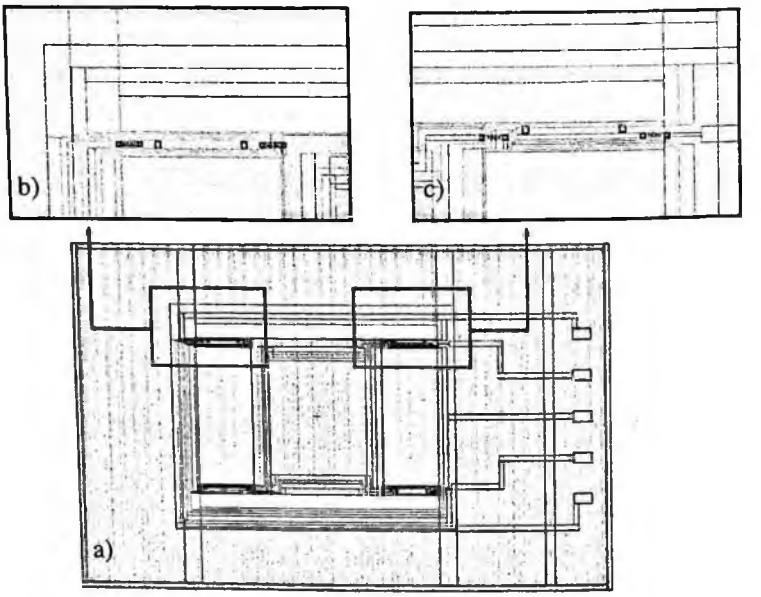

Fig.5: layout of the device (a), and details of the supports (b,c)

the resistors, so to polarize the substrate to avoid losses. The electrical signal is led to four pads located at the right of the chip: the pads are designed to remain outside the top cover, so to allow the bonding to the package pads.

4. Fabrication process

The accelerometer is fabricated on standard 4-inch (100) single crystal silicon wafers. The whole process is summarized in figure 6. The first part of the fabrication is the planar process, the second is the micromachining. Processing begins with the growth of a thermal silicon oxide, followed by the definition of the resistors area, and a p-ion implantation to create the piezoresistors.

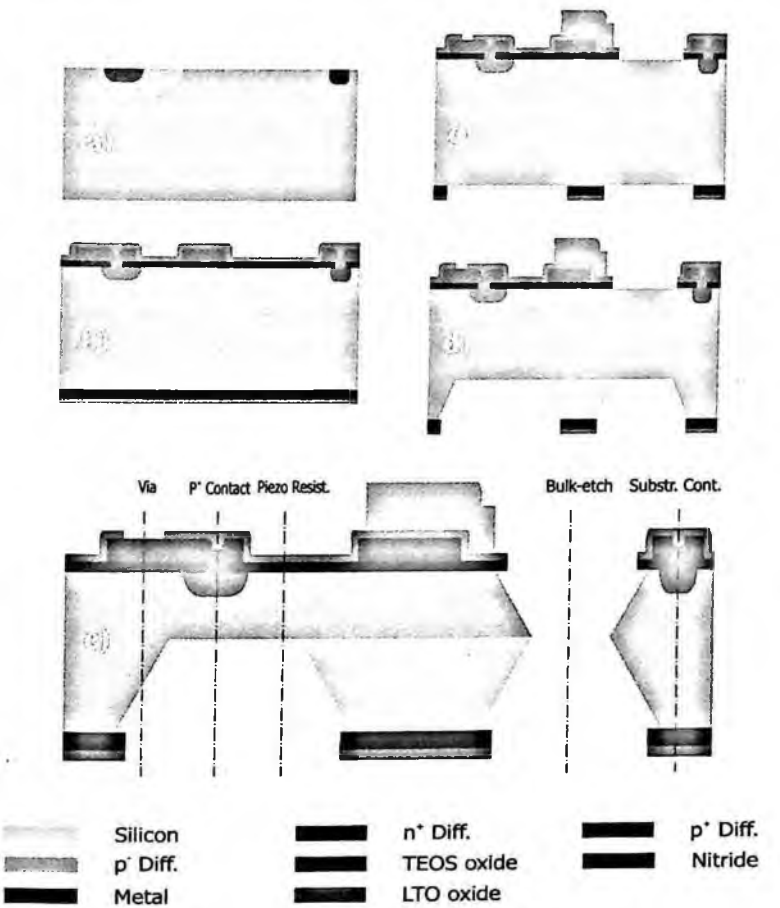

Fig.6: schematic of the fabrication process.

The screen oxide is removed and n-ion implantation is performed (a) to create the substrate contact. TEOS oxide and Si_3N_4 are deposited on the back of the wafer to create the back mask for the bulk etching (b). Aluminum metal is deposited and patterned on the front side, and an LTO oxide film is used as insulator (b). The dielectric layers are patterned to open vias and etching windows on the front and back side (c). A chromium-gold seedlayer is deposited by PVD on the front side for electroplating, then a photoresist is deposited and patterned to open the areas on top of the proofmass. A gold layer is then electroplated on the proof mass (c). The planar process is finished, and bulk micromachining begins: anisotropic etching of the back side is performed by TMAH (d). Final release of the structure is done in a proper solution of TMAH, silicic acid and ammonium sulfate, to preserve the Aluminum layer (e).

5. Conclusions

A MEMS inertial accelerometer for aero-motive applications is proposed, with chip dimensions of 5x11x1.5 mm. Layout is based on FEM analysis. Fabrication technology consists of two parts: (1) IC processing with implanted piezoresistors and metal lines; (2) structure release by bulk micromachining form both the back and front side of the wafer.

References

1. S. Terry, "A miniature silicon accelerometer with build in damping", IEEE Technical Digest, Workshop on solid state Sensors and Actuators, 114-116, 1998.
2. S. Das, K. Biswas, D.K. Maurya and S. Kal, technology Development for bulk micromachined accelerometer, Proc. IWPSD-2003, International conference, IIT Madras, India, December (2003).

MICRO-INTEGRATED DOUBLE AXIS PLANAR FLUXGATE

Andrea Baschirotto

Dept. of Innovation Engineering, University of Lecce, 73100 Lecce – Italy

Enrico Dallago, Piero Malcovati, Marco Marchesi, Giuseppe Venchi

Power Electronics Laboratory, Department of Electrical Engineering, University of Pavia, 27100 Pavia – Italy

Abstract *– In this paper a double axis micro-integrated Fluxgate magnetic sensor is presented. The device was designed using a PCB dual axis sensor previously realized as a starting point. In the PCB version the experimental results exhibit excellent agreement with the simulations performed using a tool based on the finite element method Using the same design approach a version of the double axis Fluxgate structure to be realized in IC technology is here proposed. The accurate study of the magnetic field distribution allows a 75% area saving for the IC version with respect to a direct scaling of the PCB version. Imposing an external magnetic field of about 60 μT, the simulated differential output voltage of the micro-integrated Fluxgate sensor achieves a peak value of 1 mV with 5 mA sinusoidal excitation current peak at 100 kHz.*

Keywords *– Planar Fluxgate; Amorphous Magnetic Core; Magnetic Sensors;*

INTRODUCTION

In the realization of planar fluxgate magnetic sensors [1] the main technologies used are the Printed Circuit Board technology [2-4] and the integrated process [5]. The choice in favour of PCB technology derives primarily from its reduced cost and efficient fabrication, due above all to the very thin commercially available ferromagnetic material used for the core. On the other hand, the low power consumption and small dimensions are indeed the fundamental requirements for a magnetic field sensor to be embedded in portable devices. Therefore a micro-integrated version is mandatory for these applications. In this last case a study to foresee the characteristics of the micro-integrated sensor can be very useful.

In this paper, starting with both the simulation results obtained by using the Flux3D® [6] FEM tools and the experimental results for the PCB version of a planar fluxgate, an evaluation of a micro-integrated version of the same planar fluxgate will be presented.

SENSOR STRUCTURE

The schematic of the PCB structure realized for the double axis Fluxgate is shown in Fig. 1. It consists of an excitation coil and four sensing coils. The actual implementation is shown in the photo of Fig. 2. The planar excitation coil is characterized by 30 μm thickness, 30 turns and 400 μm pitch. The current in

the excitation coil should be enough to saturate the ferromagnetic material glued over the PCB (see Fig. 2). This material is shaped as a cross in order to make the device sensitive to the two components of a magnetic field coplanar with the PCB. For each component of the magnetic field the output voltage is obtained from two sensing coils placed in differential configuration, having 17 μm thickness, 21 turns and 400 μm pitch. The excitation and sensing coils are realized on two different metal layers of the multilayer PCB structure, at a distance of 50 μm from each other. The total device size is 57.3 mm x 58.1 mm. The ferromagnetic material core is the amorphous alloy Vitrovac 6025 [7]. This material was chosen because of its extremely high relative permeability ($\mu r = 105$) and low losses. Its saturation magnetic induction is 0.55 T.

SIMULATION MODEL

The main issue in the setup of the model was to create a good mesh after taking into account the geometrical configuration of the ferromagnetic material, which is a cross sheet with dimensions of about 37700 μm x 3400 μm x 25 μm on the diagonal (Fig. 2). The critical dimension is the thickness of only 25 μm, which leads to a large number of elements in the mesh (285985 volume elements). The minimum peak value of the excitation current that guarantees the saturation of the ferromagnetic material was then evaluated. Using different magnetostatic analyses we verified that a peak current of about 600 mA is necessary to saturate the Vitrovac, as shown in Fig. 3. After this, the transient response of the device was investigated considering the geometrical model proposed in Fig. 1 with a 10 kHz, 600 mA peak amplitude sinusoidal excitation current together with a field of 20 μT coplanar to the PCB and parallel to the ferromagnetic material. The results of this transient magnetic simulation, for one axis of sensitivity, are shown in Fig. 4, that reports also the comparison with the experimental result.

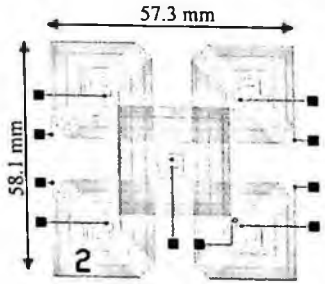

Fig. 1 Schematic of the PCB double axis Fluxgate realized

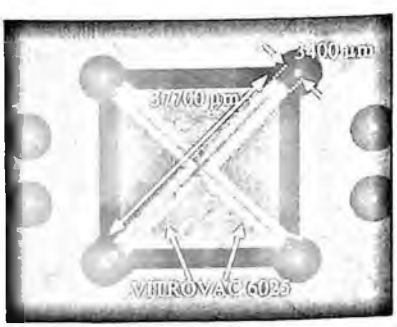

Fig. 2 Photograph of the double axis planar Fluxgate proposed

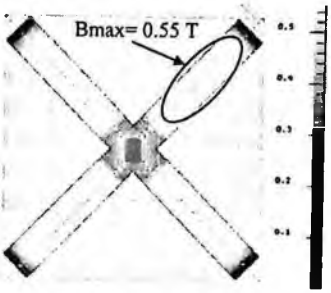

Fig. 3 Simulated magnetic induction

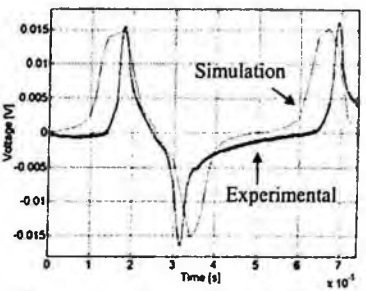

Fig. 4 Comparison between the simulation and experimental result

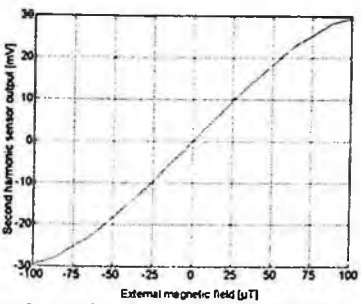

Fig. 5 Transfer characteristic of the PCB Fluxgate obtained with a spectrum analyzer

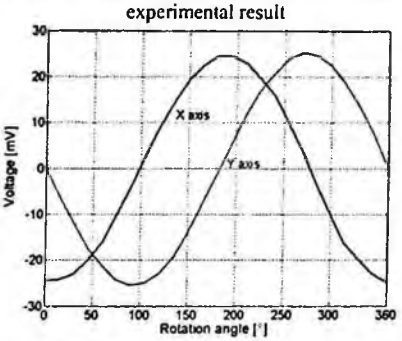

Fig. 6 Angle response for the two measurement axes (X and Y).

EXPERIMENTAL RESULTS

Imposing an external magnetic field with a pair of Helmholtz coils, the differential output voltage of the PCB structure has been evaluated. The comparison between the simulation and experimental results, shown in Fig. 4, gives an error of about 10 % on the amplitude of the output voltage. This error is extremely low in consideration of the simulation conditions adopted to reduce the computation time.

To characterize the PCB structure, the external magnetic field has been varied in the range of $\pm 100\,\mu T$. The differential output voltage from the pick-up coils was analyzed with a 3562A Hewlett Packard Dynamic Signal Analyzer to extract the value of the 2nd order harmonic (at double the frequency of the excitation signal). This voltage is plotted in Fig. 5 against the external magnetic field. The sensor shows a linearity error of about 2.6% full scale in the range of $\pm 60\,\mu T$ with a sensitivity of 0.37 mV/μT.

To evaluate the possibility of using the sensor as a 2D-vector magnetic field detector a suitable read-out circuit has been realized. Different analyses have been realized as reported in [4]. The voltage output of the sensor measured while rotating it in a horizontal plane is shown in Fig. 6. The angle error was smaller than 6° and included signal non-linearity, hysteresis and noise.

INTEGRATED MICRO STRUCTURE

Using the experience with the PCB prototype an IC version of the double axis Fluxgate sensor for low power applications requiring small dimension has been analyzed with the FEM simulator. The design features have been assumed in agreement with the IC realization of the coils in a 0.5 μm CMOS technology with a post processing for the deposition of the ferromagnetic material. The model created in Flux3D is shown in
Fig. 7: it consists of an excitation coil and four sensing coils, of which only two are visualized in figure. The planar excitation coil is characterized by 5.5 μm thickness, 95 turns and 9 μm pitch (5 μm width and 4 μm spacing). The total area for the excitation coil is (1760 x 1760) μm^2.
In order to optimize the device area occupation a number of magnetostatic analyses were performed varying the area of the sensing coil. The simulations showed that the component of magnetic induction associated with the ferromagnetic material perpendicular to the plane of the sensing coil is concentrated in a small area under each of the outer end of the core branches. Therefore the sensing coils were centered in these areas and their size was reduced to the minimum possible. This gives a 75% area saving with respect to the direct scaling of the PCB prototype, without any performance loss. The geometrical parameters of the sensing coils based on the used technology are: 1 μm thickness, 1.3 μm width and 1.6 μm spacing. The total area for the sensing coils, consisting of 75 turns, is 450 x 450 μm^2.
The Vitrovac 6025 has been introduced in the simulation in cross shape with the dimensions of 2513 μm x 113 μm on the diagonal (Fig. 7). The minimum thickness for the ferromagnetic material that can be saturated with a peak current of about 5 mA (in order to limit the power consumption) was investigated. Using different magnetostatic analysis we established that the complete saturation condition is obtained with a thickness of 1 μm.

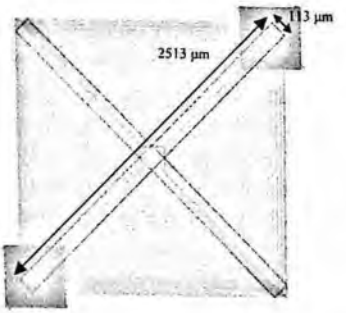

Fig. 7 Simulation model of the integrated version of the PCB structure.

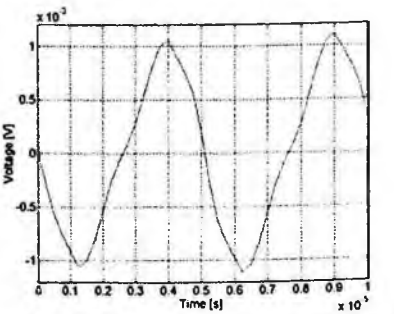

Fig. 8 Differential output voltage simulated with Flux3D

A transient time analysis was performed considering the geometrical model proposed in Fig. 7 with a 100 kHz, 5 mA peak amplitude sinusoidal excitation

current together with a 60 μT magnetic field coplanar to the micro-integrated structure and parallel to the ferromagnetic material. The results of this transient magnetic simulation, for one axis of sensitivity, are shown in Fig. 8. The output voltage obtained has an amplitude of about 1 mV, sufficiently large to be processed by the readout circuit.

CONCLUSIONS

A PCB double axis Fluxgate magnetic sensor has been realized and analyzed with a software tool based on the finite element method. The simulations showed a good agreement with the experimental results, therefore the same software has been used to evaluate the performance of a micro-integrated version of the double axis Fluxgate, which is presently under fabrication. The simulation results predict that the micro-integrated sensor will have enough sensitivity for sensing the Earth's magnetic field, with a power consumption two orders of magnitude lower than the PCB version.

ACKNOWLEDGMENTS

The authors would like to thank STMicroelectronics, Cornaredo Italy, for technological support, Cedrat, Grenoble France, for allowing our use of their FEM simulator and Vacuumschmelze, Hanau Germany, for Vitrovac® samples.

References

[1] Pavel Ripka, "Magnetic Sensors and magnetometers", Artech House Boston, London (2001).

[2] A. Baschirotto, E. Dallago, P. Malcovati, M. Marchesi, G. Venchi "Fluxgate magnetic sensor in PCB technology", Proceeding of Instrumentation and Measurement Technology Conference (IMTC-2004), Como 2004, Vol.2 pp. 808-812.

[3] P. Kejik, L. Chiesi, B. Janossy, R. D. Popovic, "A new compact 2D planar fluxgate sensor with amorphous metal core" Sensors and Actuators 81 (2000) 180 – 183.

[4] A. Baschirotto, E. Dallago, P. Malcovati, M. Marchesi, G. Venchi, "Precise vector-2D magnetic field sensor system for electronic compass", Proceeding of IEEE Sensors 2004, Wien 24 – 27 October 2004, pp. 1028-1031.

[5] S.O. Choi, S. Kawahito, Y. Matsumoto, M. Ishida, Y. Tadokoro, "An integrated micro fluxgate magnetic sensor" Sensors and Actuators A 55 (1996) pp. 121 – 126.

[6] CEDRAT: Flux3D® User's guide, Cedrat Meylan France (2002) www.cedrat.com

[7] Vacuumschmelze Hanau Germany, Amorphous metals VITROVAC www.vacuumschmelze.de

Si-BASED LIQUID SEPARATION MICROSYSTEMS FOR AGROFOOD APPLICATION

A. BENVENUTO, L. LORENZELLI*, V. GUARNIERI AND M. ZEN
ITC-irst, Microsystems Division, via Sommarive 18, 38050 Povo(TN), Italy

In this work a Si-based liquid separation microsystem for phenolic compounds detection in wine is presented. The main modules of the chip are *i.*) a Si-micromachined separation column with inlet and outlet for fluidic connections, *ii.*) a three-electrode amperometric sensor and *iii.)* a Pt microheater. Analytical calculations and finite element analysis have been performed to optimize microcolumn design. Preliminary test structures have been developed by implementing a microfabrication technological process. A system approach has been followed in the chip design in order to optimize the final packaging.

1. Introduction

During the last years, quality and safety in the agro-food field have acquired more and more importance and remarkable interest has been placed in the development of reliable, sensitive, hand-held and low cost instruments for liquid separation. The miniaturization of separation modules by means of silicon-based microfabrication technologies introduces multiple advantages, such as the rapidity of separation, since reduced dimensions imply faster separation process, and the possibility to carry out on-line measurements by means of easy to use and low cost devices [1-2].

This paper reports the design and simulation results of a Si-based liquid separation microsystem consisting of *i.*) Si-micromachined separation columns, *ii.*) three-electrode amperometric sensors and iii.) Pt microheaters.

The design of microcolumns geometrical characteristics has been defined in order to optimize column separation efficiency. Finite element analysis of the structure has been performed by using ANSYS tools and the results have been compared with the analytical calculations.

The three-electrode amperometric sensors consist of two Pt electrodes (working and counter) and an Ag/AgCl electrode (reference).

In order to operate at 40 °C (typical working temperature of liquid separation systems) Pt heaters have been designed on the back of the column.

Preliminary test structures have been developed by implementing a microfabrication technological process, which mainly consists of Silicon anisotropic etching with TMAH solution, room temperature deep reactive ion etching (DRIE) and anodic bonding.

2. Microcolumn design

2.1. *Analytical Calculations*

The analytical microcolumn geometrical parameters have been investigated for open-tubular columns, with the aim of optimizing the column efficiency that is expressed as number of theoretical plates (N = L/HETP, L= column length, HETP = height equivalent of a theoretical plate). HETP can be expressed according to the van Deemter equation as function of mobile phase linear velocity (u), as described in Eq. 1. The minimum of the van Deemter curve represents the ideal flow velocity where maximum column efficiency is obtained.

$$HETP = \frac{2D_m}{u} + 4\frac{(\frac{z}{2})^2(1+11k+\frac{51}{2}k^2)}{105D_m(1+k^2)}u \qquad (1)$$

The Eq. 1 has been solved for different channel depths (z), by considering as mobile phase a mixture of methanol and water with viscosity η = 1 mPas and diffusion coefficient $D_m = 10^{-9}$ m^2/s; the partition coefficient has been chosen as k < 10. The results obtained are summarized in Table 1, where the retention time has also been calculated. Different values of the column width have been considered and corresponding flow rates (Q) have been calculated by assuming z = 20 μm, as schematized in Table 2.

Table 1. u, HETP and retention time for different channel depths.

	u [mm/s]	HETP [μm]	t [min]
z = 10 μm	0.299	13.3	6
z = 15 μm	0.199	20	8
z= 20 μm	0.149	26.7	11
z =25 μm	0.119	33.4	14

Table 2. Flow rates (Q) for different channel widths.

Width [μm]	100	150	200	250
Q [nl/min]	17.9	26.9	35.8	44.8

According to the results obtained and technological constraints, the microcolumn has been designed with the following geometrical characteristics: channel length=10 cm, channel depth = 20 μm, channel width = 100 μm, ducts spacing = 50 μm. Inlet and outlet dimensions have been calculated in order to fit with column section after the etching; the inlet and outlet section is 767 μm x 767 μm.

2.2. *Simulations*

Finite element analysis of a simplified structure with L = 1.5 cm has been performed by means of ANSYS tools. In order to have a constant flow rate and u = 0.149 mm/s in the channel, it is necessary to apply u_{in} = 0.0005 mm/s at the inlet. A laminar flow has been supposed; the results obtained for mobile phase flow at inlet/outlet are represented in Figure 1. Figure 2 shows the vector plot of the flow velocity in the channel. The results obtained from ANSYS simulations fit with results of analytical calculations.

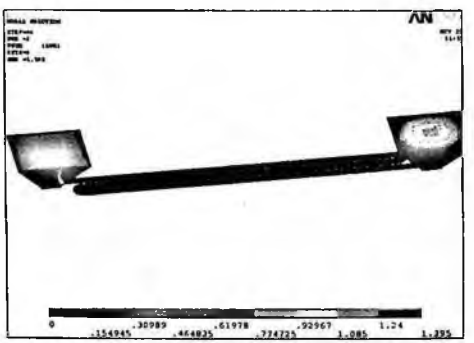

Figure 1. ANSYS nodal solution of velocity [μm/s] at inlet/outlet.

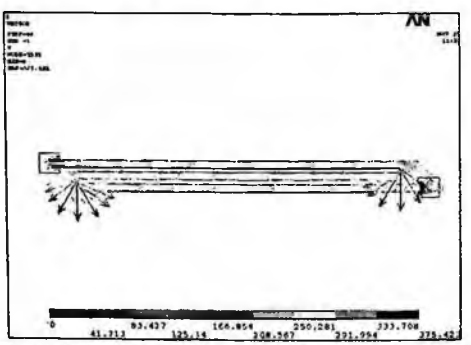

Figure 2. Vector plot of the velocity [μm/s] in the channel

3. Microsystem design

Different layouts of the system have been studied: i.) one inlet for each column with outlet at the end of the column; ii.) a common inlet for the two column with outlet at the end of the column; iii.) outlet in the centre of the column. Figure 3 shows a system layout.

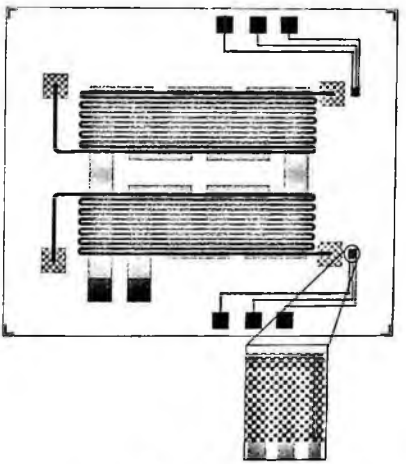

Figure 3. System layout

The three-electrode amperometric sensors consist of two Pt electrodes (working and counter) and an Ag/AgCl electrode (reference). The distance of the sensor from the outlet has been chosen at 200 μm; according to the results obtained from analytical calculations and simulations, the velocity at outlet is about 1 μm/s, therefore the time for reaching the working electrode is about 3 min. Different electrodes geometries have been designed in order to experimentally choose the best one.

In order to operate at 40 °C (typical working temperature of liquid separation systems) a Pt heater has been designed on the back of the column. The geometrical characteristics of the heater have been calculated by considering a dissipated power P = 100 mW (for structures with outlet at the end of the column) or P = 30 mW (for structures with outlet in the centre of the column) and a bias voltage V = 5V.

4. Technological process

A fabrication process for the microsystem has been set up. The column fabrication steps at a glance are:

1. Deposition of TEOS/Nitride/LTO (500 nm/100 nm/300 nm) by LPCVD as passivation layers on a <100>, n-type silicon wafer.
2. Definition of the column spiral configuration on silicon wafers by room temperature Deep Reactive Ion Etching (DRIE).
3. Sealing of the column to a Pyrex wafer by anodic bonding.
4. Deposition and pattern of Pt by lift-off on the wafer back side for on chip microelectrodes and heater.
5. Deposition of Si_3N_4 by PECVD for electrodes and heater passivation.
6. Realisation of inlets/outlet (~480-μm-deep holes) on the wafer back side by TMAH (4:1, T=90 °C) wet chemical etching.
7. Ag/AgCl electrochemical deposition for the reference electrode.

Preliminary microcolumn test structures have been developed. A package including tubing for flow forcing through the electrodes has been designed.

Conclusions

The design and simulation of a Si-based microsystem for liquid handling and separation have been presented. A technological process has been set up and microcolumn test structures have been fabricated. Future work will be addressed to appropriate functionalisation of the column for phenolic compounds in wine detection.

Acknowledgments

This work has been partially funded by the European Integrated Project "GoodFood -Safety and Quality Monitoring with Microsystems" (508774-IP), by the Province Autonomous of Trento Post-Doc Project "MICROM - Silicon-based microsystems for agro-food chromatographic analysis" and by the European CRAFT Project "MINICGSENS - Miniaturised Gas Chromatographic Analysis System Based on Micromachined silicon and Metal Oxide Semiconductors (EU/CRAFT-1999-71468).

References

1. P. G. Vahey, S. Park, et al. *Talanta*, **51**, 1205 (2000)
2. M. M. Mc Enery, A. Tan, J. Alderman, J. Patterson, S. C. O'Mathuna and J. D. Glennon, *Analyst* **125**, 25 (2000).

OPTICAL SENSORS

CH_4 INFRARED SENSOR SYSTEM INCLUDING A MICROHEATER AND A THERMOPILE

A. CATINI, A. ORSINI, A. D'AMICO, C. DI NATALE
University of Rome "Tor Vergata", Via del Politecnico 1, 00133 – Rome – Italy

C. CORSI
CREO, Alenia, L'Aquila – Italy

A.TIBUZZI, M. DECARLI, G. SONCINI
University of Trento, 38050 Povo (TN) – Italy

V. GUARNIERI
ITC-IRST, Via Sommarive 16, 38050 Povo (TN) – Italy

This paper describes an electro-optical sensor system used for the detection of methane with a low limit resolution of about 500 ppm. An integrated micro-heater has been used as infrared source, a commercial thermopile as infrared sensor and a 12 bit acquisition board to process data.

1. Introduction

Methane (CH_4) gas is colourless, odourless and lighter than air and it is the most common saturated hydrocarbon present in the atmosphere. It is the principal product of organic decay in swamps and marshes, the gas being delivered by the action of bacteria. Methane is a greenhouse gas and the primary gas in Kyoto protocol; in fact, methane has an explosive characteristic and an asphyxiating effect. Large increases in methane concentration have been observed since the pre-industrial period (a 150% increase, from 750 to 1750 ppb). Methane detection may take advantage of the absorption of infrared energy by methane gas molecules at their characteristic absorption band[a]; the absorption is proportional to the concentration according to Lambert-Beer law:

[a]Peak absorption wavelength: $\lambda \approx 3.31 \mu m$.

$$I = I_0 e^{-\alpha(\lambda)lC}$$

where I is the intensity of the infrared output radiation, I_0 is the intensity of the infrared input radiation, C is the gas concentration, l is the length of the optical path and $\alpha(\lambda)$ is the absorption coefficient of the gas.

We have developed an electro-optical system able to generate infrared radiation, to detect the part of the infrared radiation absorbed by methane and to process data (amplifier, filter, digital data acquisition). In this paper we present the system, the experimental testing and its results.

2. System

Our sensor system (figure below) comprises a micro-heater (used as an infrared source), a copper chamber (required to direct the radiation toward the detector), two sapphire windows (which close the chamber with a negligible absorption of infrared radiation), an optical filter and a thermopile (infrared detector).

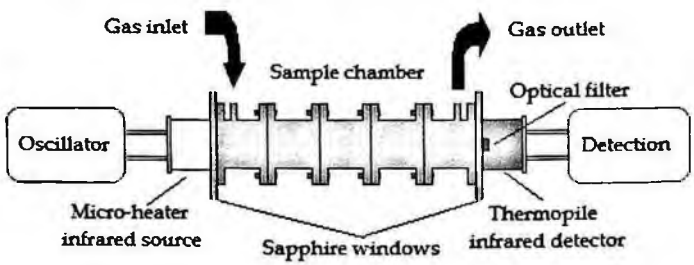

Applying an appropriate voltage on the micro-heater, a current flows through it and increases its temperature (Joule effect). In this manner the micro-heater can emit radiation (like a black body) according to Planck law:

$$R_\lambda = \frac{2\pi c_0^2 h}{\lambda^5 \left(e^{\frac{hc_0}{\lambda kT}} - 1 \right)}$$

where R_λ is the spectral emittance per unit area, λ is the wavelength, T is the absolute temperature, c_0 is the light velocity, h is the Planck constant and k is the Boltzmann constant.

The voltage applied to the micro-heater has been modulated at 11 Hz to avoid possible noise from other infrared sources.

A thermopile, consisting of twenty single Copper-Constantane thermocouples, has been used as infrared detector. This type of thermopile offers good response at λ=3.31 μm and at room temperature. An optical filter has been placed in front of the thermopile with a peak of trasmittance at 3.31 μm and a pass-band of 0.15 μm to ensure the best selectivity to the sensor system.

3. Experimental Testing

The response of the sensor system has been tested by varying the length of the chamber (from 3.0 cm to 9.0 cm) and fluxing several different quantities of CH_4 and N_2 as carrier into the chamber. A mass flow controller has been employed to mix the two gases and reach the desired CH_4 concentration.

The output signal (amplified and filtered) has been acquired by an acquisition board (ADC 12 bit).

As shown in figure below, in presence of CH_4 the output signal V_{fin} (i.e. the output voltage of the thermopile filtered and amplified) is lower than V_{in} (the output signal in absence of CH_4).

The ratio V_{in}/V_{fin} is related to the CH_4 concentration in the chamber.

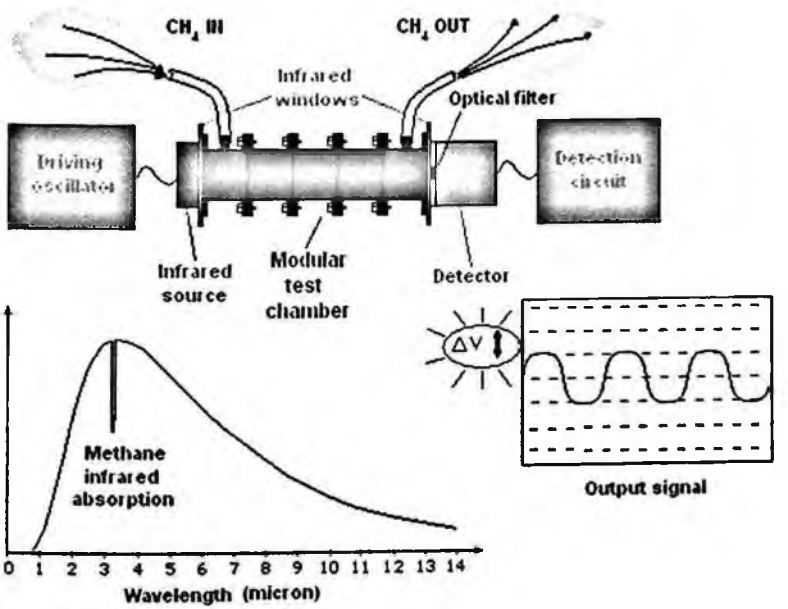

4. Results and discussion

As shown in figure below, the longer the chamber (optical path), the better the results for the same CH_4 concentration (Lambert-Beer law).

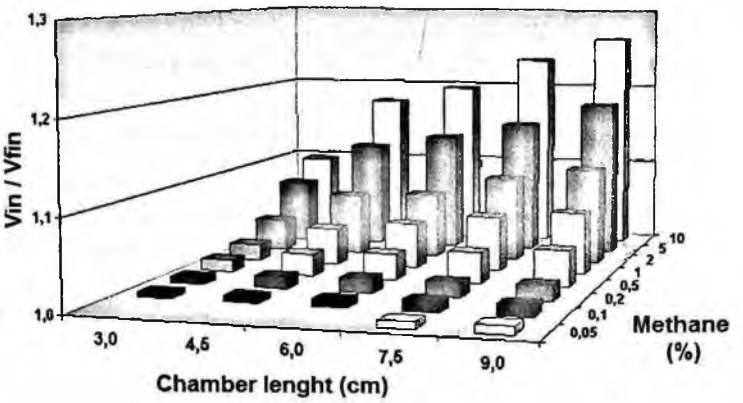

When the length of the chamber is 9 cm the sensor is able to detect 500 ppm of CH_4. The length of the chamber could be reduced (in order to obtain also better results) using multi-reflection structure; in fact, this system increases the optical path reducing the physical one.

5. Conclusions

In this paper we have shown an electro-optical sensor system able to detect methane with a limit of detection of 500 ppm. At the moment we are designing a multi-reflection structure to improve results and to reduce the overall dimension of the sensor system.

Furthermore we are testing the possibility to integrate more than one thermopile in this sensor system in order to allow the detection at the same time of different gases (CH_4, CO_2, CO etc.) which have different absorption bands.

References

1. Kruse, McGlauchlin, and McQuistan, **"Elements of infrared technology: generation, trasmission, and detection"** John Wiley & sons, New York.
2. R.J. Keyes, **"Optical and Infrared Detectors"** R.J. Keyes, New York.

OPTIMIZATION OF PLANAR WAVEGUIDES FOR FLUORESCENCE BASED BIOSENSORS

ROMEO BERNINI
IREA- CNR, Via Diocleziano 328, 80124 Napoli, Italy

N. CENNAMO, A. MINARDO, L. ZENI
Dipartimento di Ingegneria dell'Informazione, Seconda Università di Napoli, via Roma, 29, 81031 Aversa (CE), Italy

Optimization of planar waveguides for fluorescence biosensing is presented in this work. In particular, we show that optical (refractive index) and geometrical parameters have a strong influence on the efficiency of excitation and collection of fluorescent signals. Numerical analyses showed that a single-mode slab waveguide, operating at its fundamental TM mode and near its cut-off point, results in an efficient fluorescence excitation when employed as evanescent wave biosensor. A high refractive index contrast is demonstrated to be the key parameter for an efficient fluorescence collection. Other geometries, alternative to the classical slab waveguide, may result in an improvement of the fluorescence excitation and collection efficiencies.

1. Introduction

In optical waveguides, light confinement is usually based on total internal reflection (TIR). When TIR occurs, a small portion of the reflected light penetrates through the interface and propagates parallel to the surface in the plane of incidence creating an electromagnetic field in the cover medium. Evanescent field can be employed in a planar optical waveguide in both absorption and fluorescence sensors. In fluorescence-based biosensors, the evanescent field is employed for the excitation of fluorophores residing in the immediate region near the interface. For both kind of sensors, it is necessary to understand the role of the surrounding absorbing and/or fluorescent medium on the sensor efficiency. In particular, it is useful to define a single parameter, which quantifies the efficiency of evanescent field-based sensors, independently of the particular waveguide geometry adopted for the sensor. We define this parameter as the ratio between the change in the absorption coefficient of the waveguide guided mode (α), and the change in the absorption coefficient of the cover medium where the biological probe is present (α_c). For a particular bound mode in which the unperturbed propagation constant β_0 is real, the absorption coefficient α produced by $\delta\varepsilon_c$ is:

$$\alpha = \mathrm{Im}\{\beta\} \cong (2\beta_0)^{-1}\,\mathrm{Im}\{\delta(\beta^2)\} \tag{1}$$

where the calculation of $\delta(\beta^2)$ is carried out by employing a first-order perturbation approach (for TE and TM mode) [1].

Bulk absorption can be regarded as the absorption of a plane wave and is given by:

$$\alpha_c = \frac{K_0 * \mathrm{Im}(\delta\varepsilon_c)}{2 * n_c * \varepsilon_0} \tag{2}$$

n_c being the unperturbed refractive index of the cover medium. Note that this efficiency is useful both for absorbance-based and fluorescence-based sensors. In fact, for these sensors the emitted power of fluorescence radiation is proportional to the total power absorbed by the fluorophores [2], which in turn depends on the absorption coefficient of the waveguide mode. Hence, for a fixed fluorophores concentration in the cover medium (i.e. for a fixed absorption coefficient of the cover medium), fluorescence emitted power depends on the waveguide efficiency parameter considered in our analysis.

In this paper, we analyze how planar waveguides can be efficiently used for excitation and collection of fluorescence by evanescent waves. We report a numerical analysis for optimization of fluorescence excitation/detection in different waveguide geometries. In particular, we present a comparative analysis between slot waveguides and slab waveguides, because in the case considered in this work, the commonly used buffered clad slab waveguides have always shown (varying both thickness and refractive index of the buffer layer) a lower efficiency.

2. Fluorescence excitation efficiency for Slab and slot waveguides

We start our discussion considering a mono-dimensional slab waveguide. Unless otherwise specified, we will consider throughout the paper a guiding layer with refractive index $n_H = 2$, a substrate with refractive index $n_s = 1.44$, and a cladding medium (where the biological probe is present) with refractive index $n_c = 1.33$. By numerically solving the slab waveguide characteristic equation, we determine the electric and magnetic fields associated to the fundamental TE and TM mode, which are employed for the evaluation of the quantities expressed in eqs. (1-2). Calculations are performed by setting the excitation wavelength to 633 nm, while varying the core width w_H. Results are shown in Figure 1, which refers to the first three TE modes and the first three TM modes. Numerical results suggest that the maximum efficiency is achieved by employing the fundamental TM mode.

In principle, we could imagine a multimode waveguide, so that the overall efficiency will be a weighted average of the efficiency of the single excited modes, in dependence of the power distribution among the different modes.

However, this solution may result in a lack of repeatability of the sensor response, because it depends on the actual distribution of the optical power among the excited guided modes. Hence, a single-mode waveguide is generally preferred, so that the efficiency of the sensor will remain the same.

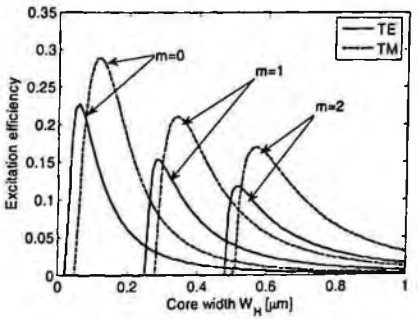

Figure 1. Excitation efficiency for a slab waveguide evanescent field-based sensor

Recently, a novel waveguide geometry, named slot waveguide, has been proposed for light guiding in nanometer-sized structures [3]. Such a waveguide is constituted by two slab waveguides, placed at a distance (a fraction of the wavelength), such that they couple each other. Such structure is able to confine the optical field in the low-refractive-index nanometer-wide slot region. This behaviour is observed only for the normal component (E_x), this latter being the principal electric field component in the TM mode. Hence, only the fundamental TM mode will be considered in our analysis, as the TE mode exhibits a much lower slot effect. We calculated the maximum achievable efficiency of the TM mode, for each fixed slot thickness, while varying the core width. Results are shown in Figure 2.

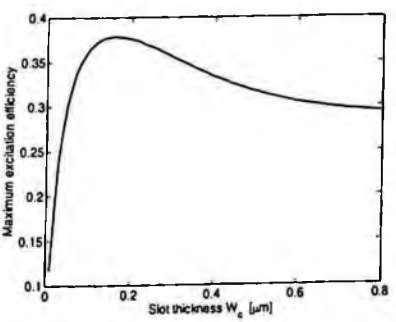

Figure 2. Maximum excitation efficiency for the TM mode of the slot waveguide, as a function of the slot thickness Wc

It is useful to analyze the possible improvement in fluorescence excitation efficiency which can be achieved by using a slot geometry instead of a slab

geometry. To this aim, we compared the sensitivity of the two geometries, with respect to the fundamental TM mode. Results are shown in Figure 3, where the quantity on the x-axis is the width of the single slab (for a slab geometry) or the width of the two slabs forming the slot geometry. For the slot waveguide case, we considered a distance between the two coupled slab waveguides (slot thickness) equal to Wc = 160 nm, as this value has been demonstrated to guarantee the maximum sensitivity for the fundamental TM mode. It can be seen that an increase on the maximum efficiency as high as 36% can be achieved by using the slot geometry.

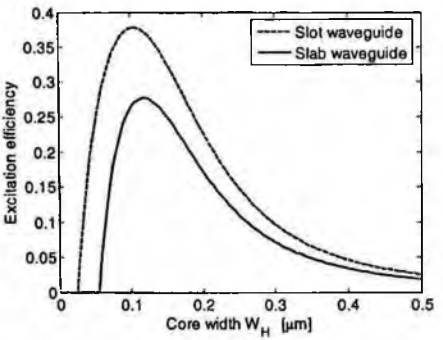

Figure 3. Comparison between fundamental TM mode for slab and slot waveguides as a function of the core width WH

3. Fluorescent collection efficiency for slab and slot waveguides

The collection efficiency of the radiation emitted by sources located within the evanescent field of waveguide structures has been studied in different papers [4, 5]. Collection efficiency by means of a light guiding structure can be calculated by summing over the collection efficiency of each mode (TE or TM) supported by the waveguide. By modelling the fluorophores as elementary isotropic dipoles, the collection efficiency of each single mode can be evaluated as the ratio between the integral of the squared electric field, related to the mode of interest, over the region occupied by the fluorophores, and the total power carried by the mode itself [4], that is:

$$(collection\,efficiency)_{\nu} = \frac{\int_{V} S\left|\vec{E}_{\nu}\right|^{2}}{P_{0}} \tag{3}$$

where S indicates the source strength. The volume integral extends over the region occupied by the fluorophores. The subscript ν refers to the modal index. The wavelength for fluorescence collection analysis is set to 690 nm. Numerical results show that the fluorescence collection efficiency of multimode waveguides is not much influenced by the core width, both in slab and slot geometries.

Therefore, we have considered the influence of the refractive index difference between the core layer and the active layer, this latter being the layer where the fluorophores are present. We set the waveguide core width to 3 μm, whereas the refractive index of the core (guiding) layer is varied from 1.45 to 3. Refractive index of the active layer is still set to $n_c = 1.33$ while for the substrate $n_s = 1.44$. Results are shown in Figure 4, which clearly indicates that a high-index core layer should be chosen for better collection efficiency. It is also apparent that, for the considered range of core layer refractive index, collection efficiency of the slot waveguides is superior to the efficiency exhibited by the slab waveguide.

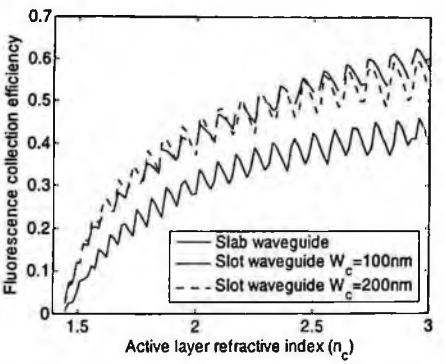

Figure 4. Fluorescence collection efficiency as a function of the guiding layer refractive index

Conclusions

We presented some numerical results showing that a high-refractive-index slab waveguide can efficiently be employed as evanescent-wave-based fluorescence sensor. In particular, we studied the influence of geometry, refractive indexes, and electric field polarization on the sensor efficiency. We showed how the use of slot waveguides can further improve the efficiency of such a sensor.

References

[1] W. H. Weber, S. L. McCarthy, and G. W. Ford, Applied Optics, Vol. 13, no. 4, pp. 715-716 (1974).
[2] H. P. Lehr, A. Brandenburg, G. Sulz, Sensors and Actuators B, Vol. 92, pp. 303-314 (2003).
[3] Q. Fu, V. R. Almeida, R. R. Panepucci, and M. Lipson, Optics Letters, Vol. 29, no. 14, pp. 1626-1628 (2004).
[4] D. Marcuse, IEEE J. Ligthwave Technology, Vol. 6, pp. 1273-1279 (1988).
[5] R. Srivastava, C. Bao, C. Gomez-Reino, Sensors and Actuators A, vol. 51, pp. 165-171 (1996).

SILICON RESONANT CAVITY ENHANCED PHOTODETECTOR AT 1.55 μm

M. CASALINO[1], L. SIRLETO[1], L. MORETTI[1], D. PANZERA[1], S. LIBERTINO[2], I. RENDINA[1]

Consiglio Nazionale delle Ricerche (CNR)
Istituto per la Microelettronica e Microsistemi (IMM)
[1] Sezione di Napoli -Via P. Castellino 111, 80131 Napoli (Italia)
[2] Sezione di Catania- Stradale Primosole 50, 95121 CATANIA (Italia)

Silicon optical receivers, operating at the optical communication wavelengths in the 1.3-1.55 μm range, have attracted much research effort. Unfortunately, the performance of the devices proposed in literature are poor because this wavelength range is beyond the absorption edge of silicon. In order to extend the maximum detectable wavelength, the most common approach, in the realization of Si-based detectors, is the use of silicon-germanium layers on silicon, anyway, requiring processes non compatible with standard CMOS technology. In this paper, with the aim to extend the operation of silicon-based photo-detectors up to the 1.3-1.55 μm range, an alternative approach is investigated: we propose the design of a resonant cavity enhanced Schottky photodetector based on the internal photoemission effect. The device fabrication is completely compatible with standard silicon technology.

1. Introduction

High performance photodetectors operating at the wavelength of 1.55 micron are required for ultrafast photodetection in optical communication, measurement and sampling systems. The photodetector performance is measured by the bandwidth-efficiency product. For conventional vertically illuminated photodetectors, quantum efficiency and bandwidth have inverse dependencies on the photoabsorption layer thickness. This limit is overcome by edge-coupled and waveguides configurations. The disadvantages of these classes of devices are a more complex fabrication and integration, along with more difficult light coupling [1].

Resonant-cavity-enhanced (RCE) photodetectors offer the best performance in order to overcome the limitation of conventional photodetectors. The enhancement in η in RCE photodetectors, defined as the probability that a single photon incident on the device generates an electron hole pair which contributes to the detector current, is obtained by placing the active strucuture inside a Fabry-Perot resonat microcavity. The enhancement of the optical field in a Fabry-Perot resonator allows the use of thin absorbing layers, which minimizes the transit time of the photogenerated carriers without hampering the

quantum efficiency. RCE devices benefit from the wavelength selectivity and the large increase of the resonant optical field introduced by the cavity [2].
RCE photodetector research has mainly concentrated on using p-i-n type photodiodes (PD's) [3,4], whereas there have been only a few reports on *RCE Schottky PD's* [5,6,7]. In top-illuminated RCE Schottky PD's, a Schottky contact can also function as the top reflector of the resonant cavity. Optical losses in the metal contact limit the quantum efficiency. Effort to increase the device responsivity has been pursued by utilizing semi-transparent Sckottky contacts. The RCE detection scheme is particularly attractive for Schottky type photodetector, since it allows the fabrication of high performance photoreceivers by means of the relatively simple structures and fabrication processes.
Traditionally, the operation of conventional and RCE photodetectors are based on the semiconductor interband transition effect. Such devices give an electrical signal when the photon energy is greater than the semiconductor band-gap. In silicon (Si), this corresponds to a cutoff wavelength of about 1.1 μm, which is not in the 1.3-1.55 μm fiber optic communication wavelenght range. A possible alternative is the use of silicon-germanium, but the growth of this compound on silicon is still a challenge in terms of cost and complexity [8,9]. The exploitation of the *internal emission effect* over the metal-semiconductor Schottky barrier may offer a solution. In fact, depending on the height of the metal-semiconductor barrier, the cut-off wavelength can be shifted at wavelength well beyond 1.6 μm [10,11].
Si photodetectors have already found wide acceptance for visible light (0.400-0.700 μm) applications, because of their near perfect efficiency at these wavelengths. Regarding near IR wavelengths for data communications applications, Si could offer the potential of low fabrication cost and direct integration with complementary metal-oxide-semiconductor (CMOS) circuits. In this paper, the design of a RCE Si Schottky photodiode operating at 1.55 μm, and based on the internal photoemission effect, is proposed. The advantage is that the design is completely compatible with ULSI silicon technology.

2. Device Design

The proposed device is a *RCE metal Schottky* photodetector illuminated from the metal side, based on internal photoemission effect, and operating at 1.55 micron. The resonant cavity has a Fabry-Perot vertical-to-the-surface structure. It is formed using a buried reflector and a mirror top interface. The buried reflector is formed by alternating layers of different refractive indices. The semiconductor part of the Schottky junction is a $\lambda/2$-silicon-layer. A protection coating layer deposited on the semitransparent Schottky metal functions as the top reflector of the resonant cavity (Fig.1).

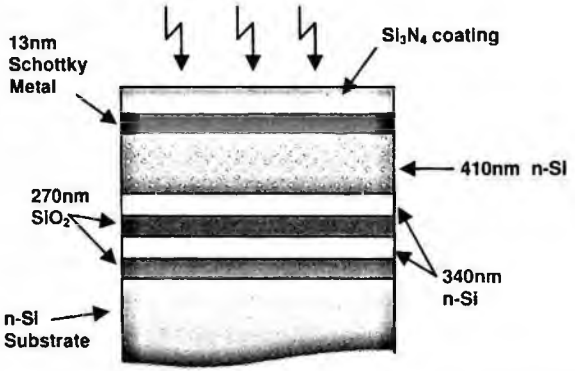

Figure 1: Schematic cross section of our RCE Schottky photodetector.

The quantum efficiency of a *RCE metal Schottky* photodetector, based on internal photoemission effect can be obtained by the following formulas [12]:

$$\eta = A_T F_e P_E \tag{1}$$

A_T is the absorptance in the schottky metal layer calculated using Transfer Matrix Method [13] as we showed in a our last work[14].

$$A_T = \left\{ \left(n_{Si_3N_4} \left| \frac{M_{A_{11}}}{M_{TOT_{11}}} \right|^2 + n_{Si} \left| \frac{M_{B_{21}}}{M_{TOT_{11}}} \right|^2 \right) - \left(n_{Si_3N_4} \left| \frac{M_{A_{21}}}{M_{TOT_{11}}} \right|^2 + n_{Si} \left| \frac{M_{B_{11}}}{M_{TOT_{11}}} \right|^2 \right) \right\} \tag{2}$$

where $M_{TOTi,j}$ are the elements of the matrix M of the whole system, $M_{Ai,j}$ are the elements of the matrix calculated from interface between protection coating and metal to the final plane, while $M_{Bi,j}$ are the elements of the matrix calculated from interface between metal and n-Si layer to the final plane.

F_E is the fraction of the absorbed photons which produce photoelectrons with the appropriate energy and momenta before scattering to contribute to the photocurrent is obtained in the case in wich energy photon is close to potential barrier ($h\nu \approx \Phi_B$)[15].

$$F_e = \frac{N_B}{N_A} = \frac{\left[(h\nu - \phi_B)^2 + (kT\pi)^2 / 3 \right]}{8kTE_F \log\left[1 + e^{\frac{h\nu - \phi_B}{kT}} \right]} \tag{3}$$

where E_F is metal Fermi level.

P_e is the accumulated probability that the electrons will have sufficient normal kinetic energy to overcome potential barrier[12].

$$P_E \cong \left[1-\exp\left(-\frac{d}{L_e}\right)\right]^{\frac{1}{2}} \quad (4)$$

where d is metal thickness and L_e is metal mean free path.

3. Numerical Results

In our design we propose a DBR centered at 1.55μm. The DBR could be formed by alternate layers of Si and SiO_2 having refractive index 3.45 and 1.45, and thickness of 340nm and 270nm, respectively. The DBR has a high reflectivity (≈0.9) over a broad range of wavelengths (Fig. 2):

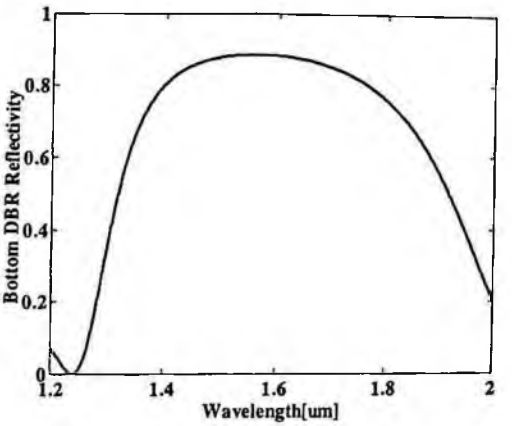

Figure 2: Variation of bottom mirror reflectivity with wavelenght.

The top reflector of the resonant cavity can be formed by an protection coating layer deposited on semitransparent Schottky contact. Choice of elements plays an important role in the technological development of a Schottky contact, in fact, for a given metal–semiconductor system, the Schottky barrier height can be varied changing the metal, the semiconductor doping profile or the crystallographic orientation.

In our design, in order to satisfy the relation $h\nu \cong \phi_B$ at the wavelength of 1.55 μm, we choose gold as the Schottky metal (E_F=5.3eV). In particular the optimum value of Au thickness was calculated to be 13nm, in the case we consider a real part of the complex refractive index 0.174 and extinction coefficients 9.96. Finally, a Si_3N_4 layer, having refractive index 2.0, can be

deposited on top of the gold layer for passivation and protection purposes. The optimum value of efficiency is mainteined for a Si_3N_4 thikness of 350nm.
The thickness of the n-Si-layer between the two mirrors, calculated in order to fulfill constructive interference condition, is 410 nm.

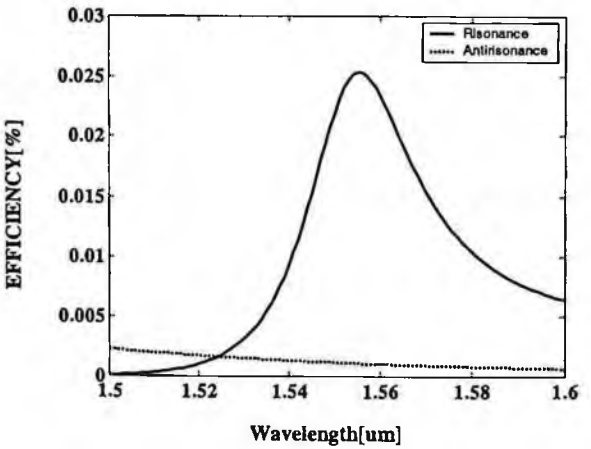

Figure 3: Calculated quantum efficiency versus the wavelength.

In Fig. 3, in order to prove the efficiency enhancement due to the cavity effect, we report the quantum efficiency calculated for resonance and antiresonance conditions, as a function of the incident wavelength. It is evident that the presence of the microcavity, operating in resonance condition produces an enhancement of the efficiency of about one order of magnitude.

4. Conclusions

In this paper, the design of a Si resonant cavity enhanced Schottky photodetector, based on the internal photoemission effect, and operating at 1.55 micron is reported. Using Au-Si as Schottky barrier a 0.026% quantum efficiency has been obtained, this prove that the enhancement due to the presence of cavity has a significant effect. This preliminary theoretical result is encouraging for future investigations. Work is in progress in order to realise and charactise the proposed devices.

5. References

[1]H. Zimmermann. Silicon Photo-Receivers, in Silicon Photonics, Topics Appl. Physics, (2004), 94, pp. 239-268 [and reference therein].
[2] M. S. Unlu and S. Strite, Appl. Phys. Rev., 1995, vol.78, N. 2, pp.607-639.

[3]I. Kimukin, N. Biyikli, B. Butun, O. Aytur, M. S. Unlu and E. Ozbay, IEEE Photonic Technology Letters, (2002), vol. 14, N. 3, pp. 366-368.

[4] E. Ozbay, I. Kimukin, N. Biyikli, O. Aytur, M. Gokkava, G. Ulu, S. M. Unlu, R. P. Mirin, K. A. Bertness and D. H. Christensen. Appl. Phys. Lett., (1999), vol. 74, N. 8, pp. 1072-1074

[5] M. Gokkavas, B. M. Onat, E. Ozbay, E. P. Alta, E. P. Ata, J. Xu, E. Towe, M. S. Unlu, IEEE Journal of Quantum Electronics, (1999), vol. 35, N. 2, pp.208-215

[6]J. A. Jervase, H. Bourdoucen, IEEE Transactions on Electron Devices, vol 47, N.6, 2000, pp.1158

[7] I. Kimukin, E. Ozbay, N. Biyikli, T. Kartaloglu, O. Aytur, S. Unlu, G. Tuttle, Applied physics Letters, 2000, vo.77, N.24, pp.3890-3892.

[8] S. Famà, L. Colace, G. Masini and G. Assanto, Applied Physics Letters, (2002), vol. 81, N.4, pp.586-588

[9] O. I. Dosunmu, D. D. Cannon, M. K. Emsley, L. C. Kimerling and M. S. Unlu, IEEE Photonic Technology Letters, (2005), vol. 17, N. 1, pp.175-177.

[10] E. Y. Chan, H. C. Card, M. C. Teich, IEEE Journal of Quantum Electronics, vol. QE-16, N. 3, 1980, pp373-381

[11] E.H. Rhoderick and R. H. Williams, Metal-Semiconductor Contacts, Clarendon Press-Oxford-1988

[12] V. E. Vickers, Applied Optics, vol. 10, No.), 1971, 2190-2192

[13] M. A. Muriel, A. Carballar. IEEE Photonics technology letters, (1997), vol. 9, N. 7, pp.955-957.

[14] M. Casalino, L. Sirleto, L. Moretti, D. Panzera, S. Libertino, I. Rendina, "Silicon resonant cavity enhanced photodetectors at 1.55 um," SPIE, (2005), N. 5840-81.

[15] R. H. Fowler, Physical Review, 1931, vol. 38, pp.45-56.

SENSING IN POROUS SILICON BY RAMAN SCATTERING

M. A. FERRARA[1], L. SIRLETO[1], L. MORETTI[1], I. RENDINA[1], A.M. ROSSI[2], E. SANTAMATO[3]

[1]*Istituto per la Microelettronica e Microsistemi- CNR*
Via P. Castellino 111 - 80131 Napoli (Italy)
[2]*Istituto Elettrotecnico Nazionale "G. Ferraris", Strada delle Cacce 91, Torino, Italy*
[3]*Dipartimento di Scienze Fisiche Università "Federico II"*
Via Cinthia Monte Sant'Angelo I-80126 Napoli (Italy)

ABSTRACT

In this paper, we present experimental results concerning sensing of vapours and liquids in porous silicon by spontaneous Raman scattering. Raman spectra are measured in backscattering configuration using a diode laser at 404 nm. The adsorption of chemical species induces a compressive strain in the porous silicon due to the action of the molecular forces, as a consequences a reversible blue-shift of the Raman spectra of the cavity has been observed.

1. Introduction

POROUS SILICON (PS) is a material of great interest for the study of adsorption phenomena. PS has a sponge-like structures with a specific area of the order of 200 ÷ 500 m^2 cm^{-3}, so there is a very effective interaction with several substances; therefore it can be used as sensor for detection of vapours and liquids [1]. Moreover PS is a low-cost material and CMOS compatible.

Raman spectroscopy allows the determination of the fingerprint of the species present and it is structurally specific[2]. Moreover, Raman scattering can be used to measure strain induced in substrate, in fact compressive stress will result in an increase of the Raman frequency shift, while tensile stress results in a decrease [3].

Fluid-solid interfacial phenomena are always the subject of much interest. Adsorption and wetting phenomena are due to the action of molecular interactions between a fluid and the adsorbent, which is usually considered to be rigid. In the adsorption phenomena the adsorbent also experiences the action of the molecular forces, and some substrate deformation must exist, as indeed revealed by numerous observation of adsorption strains. Measurements of adsorption strains in porous silicon are of great interest, because it is a unique example of a

crystalline porous material having the structural properties of a nearly perfect crystal. Measures in PS of strains induced by vapours adsorption have been already reported by X-ray diffraction[4]. On this line of argument, in this paper, we investigate adsorption strains in porous silicon but using Raman spectroscopy. We prove that when the PS structure is exposed to saturated vapor of pentane, a reversible blue shift of the Raman spectra is observed.

2. Spontaneous Raman Scattering and Adsorption strains

In order to obtain spontaneous Raman scattering, a beam of light has to illuminate a material (solid, liquid or gas). Measuring the spectra of the scattered light, two weak sidebands are observed beyond to the strong signal corresponding to the frequency of the incident light. The Raman bands arise from changes in the polarization density in a crystal or molecule during vibrations. The difference of frequency among such components and the input source depends on the characteristics of diffusing means. These two sidebands are called Stokes component, shifted down by increments equal to vibrational frequencies of the material irradiated, and anti-Stokes component, shifted to frequencies equal to the sum of the incident wave frequency and the vibrational frequencies. The Stokes component is typically orders of magnitude more intense than the anti-Stokes component and usually dominate in measuraments [5]. In Raman scattering both energy and momentum are conserved. Since the induced polarization for Stokes and anti-Stokes scattering differ only in their frequencies and wavevectors, we will restrict ourselves to Stokes scattering.

The spontaneous scattering efficiency is given by the percentage of scattered radiation per unit of solid angle per unit length

$$S = S_0 \sum_{j=1,2,3} | e_S \cdot \Re \cdot e_i |^2 , \qquad S_0 = \frac{k_0^4}{32\pi^2 n} V \chi_R^2 \tag{1}$$

where $\Re$ is the Raman tensor, e_i, e_S are the polarizations of the incident and scattered radiation respectively, k_0 is the Stokes wavevector, n is the refraction index, and V is the scattering volume. Symmetry of the medium is imposed because the scattered radiation vanishes for certain choice of the polarization e_i, e_S. These so called Raman selection rules are very useful for determining the symmetry of Raman-active phonons.

The peak position of Stokes component can be calculated using a quantitative model described in Refs [6,7], it mainly depends on the

number of atoms included in a cluster, while the width of the spectra depends on the shape of crystallites.

When PS is exposed to vapour, capillary condensation in the silicon pores have been observed [8]. When the vapour is stable in a large volume, the liquid phase can condense in a confined volume, and is then separated from the vapour phase by a concave spherical meniscus [4]. The maximum capillary stress ΔP occurs when the meniscus enter the pores and it is given in first approximation by the Laplace equation

$$\Delta P = 2\gamma_S / r \tag{2}$$

where γ_S is surface tension of the liquid and r is the pore radius. In this situation, inside the pore, there is a negative pressure in the liquid leading to a contraction of the adsorbent. The isotropic strain ε is given by

$$\varepsilon = -\Delta P / 3K = -2\gamma_S / 3Kr \tag{3}$$

where K is the bulk modulus of a macroscopic sample.

3. Experimental results

In this experiment we use a porous silicon microcavity (PSM) obtained by electro-chemical eching on p^+ type (ρ=8-12mΩ cm) standard silicon wafer. In order to realise a cavity a $\lambda/2$-thick defect has to be placed in between two distribuited Bragg reflectors (DBRs). The DBR structures are made alternating high and low porosities layers with 57 and 79% porosity, respectively. The total PSM thickness is 5 micron. In p^+ type silicon wafer, the pores have an anisotropic cylindrical structure of about 10 nm diameter, with axis parallel to the (001) direction.

Shown in figure 1 is the experimental setup used to measure Raman spectra in backscattering configuration. The pump is a diode laser operating at 404 nm; the output from the laser is splitted into two orthogonal lineary polarised components by a Polarizing cube Beam Splitter (PBS). In our configuration P-polarised light is transmitted and acts as a Raman pump, while S-polarised light is reflected. The P-polarised beam is reflected by the mirror (M) and, crossing a microscope objective lens (L_1= 5X), impinges onto the sample. The microscope objective lens is also useful in order to collect the signal obtained by the sum of reflected beam and backscattered Raman signal. The collected

signal, impinging on the PBS, is splitted in two lineary polarised beams. The reflected signal, collected in fiber optics by a microscope objective (L_2= 20X), is sent to an Optical Spectrum Analizer (OSA) for analysis. The measures are carried out at room temperature.

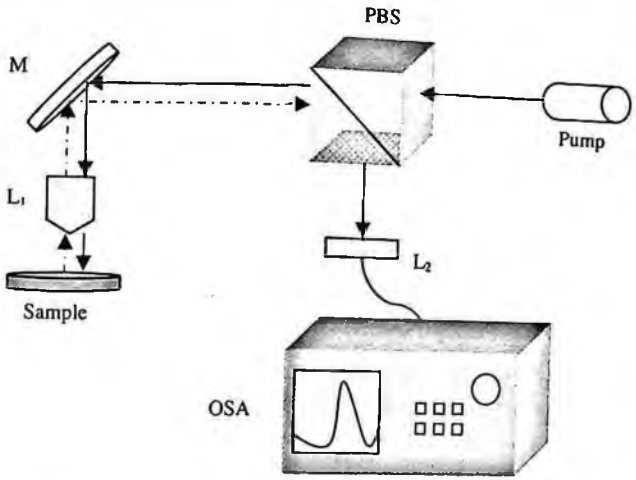

Figure 1 : Experimental setup for measurement of spontaneous Raman scattering. Pump: Diode laser at 404 nm; PBS: Polarising Beam Splitter; M: Mirror; L_1 and L_2 microscope objective lens; OSA: Optical Spectrum Analyser.

The selection rule previously discussed are satisfied by our experimental setup. The experiment has been carried out in an "out-of-resonance configuration", both for exitation and Raman radiations, and using a low power laser radiation (about 10mW). Moreover, we note that all spectra are obteined by normalization of the measured reflected signals with respect to the laser signal. Finally, the location of the Raman peaks are obtained fitting the experimental results by a Lorentzian curve.

The first step was the measure of the normalised Raman spectra in unperturbed porous silicon microcavity. The results are shown in figure 2. The measured peak is at about 413.6 nm, this result is in agreement with the shift, with respect to the pump wavelength, due to the optical phonon frequency in porous silicon (corresponding at 15.7 THz red-shifted) [5].

Afterwards, with the aim of study the influence of the chemical species infiltration in PS, a small amount of volatile liquids were added to the vial containing the PSM. The vapors saturated rapidly the vial atmosphere, after that the acquisition of spectra were carried out.

The experimental Raman spectra for pentane is shown in fig. 3. Fitting the experimental results with a Lorentzian profile, the Raman peak is obtained at about 409.1 nm. So, we measure a shift of Raman spectra with respect to the unperturbed case of about 4 nm for pentane. We note that the Raman shift is reversible.

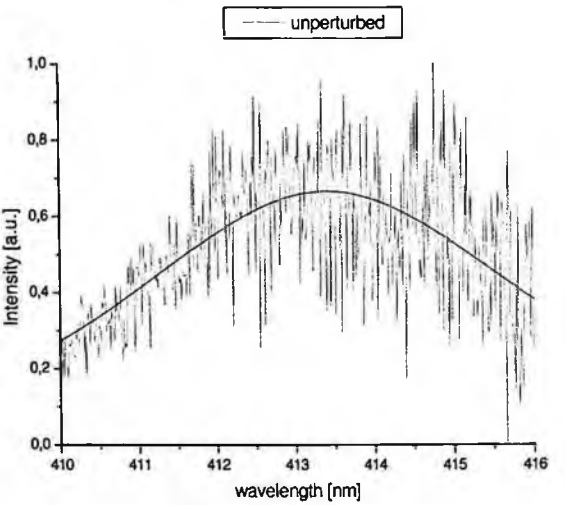

Figure 2: Spontaneous Raman spectra in porous silicon microcavity

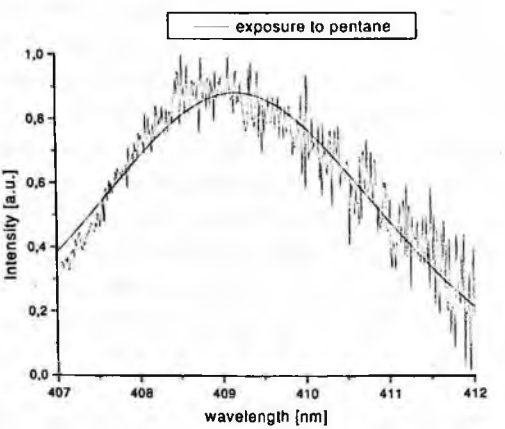

Figure 3: Spontaneous Raman spectra in porous silicon microcavity exposed to air saturated with vapour of pentane

4. Conclusions

In this paper, the influence on Raman spectra in porous silicon, due to liquids infiltrated in its pores, has been investigated. The experimental results prove that pentane infiltrated in the porous silicon structure induces strains and therefore a reversible blue shift of the Raman spectra of about 4 nm is observed. We believe that these measures could open the way to a new family of chemical sensors.

References

[1] P.A. Snow, E.K. Squire, P.St.J. Russel, L.T. Canham, "Vapor sensing using the optical properties of porous silicon Bragg mirrors", *J. Appl. Phys.* 86 (1999) 1781

[2] R.G.W. Brown, "Optical fibre sensing using light scattering techniques", *J. Phys. E:Sci.* Instum. 20 (1987) 1312-1320.

[3] I. De Wolf. *Spectroscopy Europe* 15/2 (2003)

[4] G. Dolino, D. Bellet, and C. Faivre, "Adsorption strains in porous silicon", *Physical Review B*, vol. 54, No. 24, 1996.

[5] P.Y. Yu, M. Cardona, "Fundamentals of semiconductors – Physics and materials properties"

[6] H. Ritcher, Z.P. Wang and L. Ley, "The one phonon Raman spectrum in microcrystalline silicon", *Solid State Communications*, 39 (1981), 625-629.

[7] I.H. Campbell and P.M. Fauchet, "The effects of microcrystal size and shape on the phonon Raman spectra of crystalline semiconductors", *Solid State Communications*, 58 (1986), 739-741.

[8] A.V. Neimark, P.I. Ravikovitch, Micro. Meso. Mat. 44-45 (2001) 697-707

MICRO-STRUCTURED FIBER BRAGG GRATINGS FOR REFRACTIVE INDEX MEASUREMENTS

A. IADICICCO, S. CAMPOPIANO, A. CUTOLO, A. CUSANO
Optoelectronic Division, Engineering Department, University of Sannio, Benevento, Italy

M. GIORDANO
Institute for Composite and Biomedical Materials, CNR, Napoli, Italy

A novel method based on micro-structured fiber Bragg gratings, for high-resolution refractive index measurement, is presented. The in-fiber structure relies on a partial and localized etching of the cladding layer along a standard grating. The main spectral changes of the structured grating are the increasing of the stop-band and the formation of a defect state inside the stop-band. The etching induces strong sensitivity of the reflected spectrum to the surrounding refractive index. Experimental results reveal the possibility to carry out low cost refractive index measurements by monitoring the reflected power using a narrow bandwidth interrogation. Resolution of $4 \cdot 10^{-5}$ for refractive index around 1.41 is obtained.

1. Introduction

In literature, Fiber Bragg Gratings (FBGs) have been widely used as strain and temperature sensors. Their unique characteristics and performances allow practical measurements not obtainable with conventional sensing techniques. Based on this line of argument, the possibility to employ this class of sensor for chemical and environmental applications should be advisable. Recently, the use of uniformly thinned FBGs (ThFBG) for high resolution refractive index measurements have been demonstrated [1-2] allowing significant advantages with respect to long period grating based refractometers or Fabry-Perot configurations, in terms of interrogation system required and multiplexing capability [3-4].

In this work, with the aim to develop low cost sensors for environment monitoring applications, a new structure as in fiber refractometer is presented. The proposed device consists in a standard gratings with the cladding layer removed on a small and well defined region within the grating. The main effect of the localized perturbation results in the formation of a narrow allowed band, or defect state, inside the grating stop-band [5]. Moreover, the etching induces

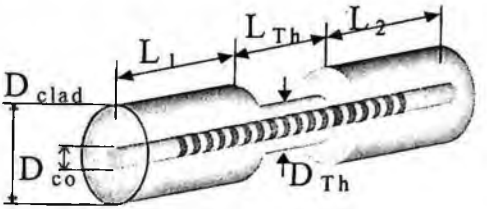

Fig. 1 Schematic diagram of the structure (not in scale).

strong sensitivity of the reflected spectrum to the surrounding refractive index. Experimental results reveal the possibility to carry out low cost refractive index measurements by monitoring the reflected power using a narrow bandwidth interrogation. Resolution of 4·10-5 for refractive index around 1.41 is obtained [6].

2. Structure and Analysis

The investigated structure consists in a standard grating with a partial or total stripping of the cladding layer with radial symmetry as shown in fig. 1. In order to outline the dependence of the spectral behavior on the n_{out} and the perturbation features, the multi-layer approach method [2], in combination with the three-layer fiber model [2], is used. Here the numerical analyses are referred to the standard Corning SMF-28 optical fiber parameters: numerical aperture 0.14, refractive index difference 0.36%, cladding and core diameter, D_{clad}=125μm and D_{co}=8.2μm, respectively. The grating parameters are: pitch of 0.531μm, amplitude of the core refractive index modulations of the $\Delta n=5\cdot10^{-4}$ and length L_B=4mm.

The spectral responses for three different values of n_{out} are shown in fig. 2. Reflectivity spectra were obtained considering a central etching along the grating ($L_1=L_2$) and a perturbation length of L_{Th}=500μm. The reported investigation is referred to the case of completely removed cladding (full etching, $D_{Th}=D_{co}$). As observable, the perturbation along the grating leads to strong changes in the reflected spectrum: a band-gap is induced in the stop-band structure of the grating, similarly to the effect observed in phase shift gratings (PSGs). The principle of operation relies on the optical beating between the spectra of the unperturbed grating regions modulated by the phase shift induced by the perturbation. The stop-band of the new device increases due to the diminution of the length associated to the two lateral grating regions according to the FBG standard rules. In particular, the destructive interference of the

optical signals reflected from the two lateral gratings leads to the formation of allowed state or defect state inside the band-gap according to the Fabry-Perot effect [5-6]. The spectral position of the defect state inside the stop-band is related to the phase delay introduced by the etching region and so strongly dependent on the n_{out}. As the n_{out} changes, a consequent modification of the effective refractive index in the thinned region and thus of the phase delay occurs leading to a wavelength shift of the defect state. Based on the reported analysis and with the aim to develop refractive index sensor, a novel configuration involving structured FBGs is proposed. Intensity measurements based on narrowband interrogation system at fixed wavelength seems to be the suitable demodulation strategy to develop low cost and extremely high sensitive in fiber sensor.

3. Experimental Results

The cladding reduction is obtained by wet chemical etching using an aqueous hydrofluoric acid (HF) solution at 24% [5-6]. A commercial 8mm long FBG demonstrating a peak reflectance of 95%, a central wavelength of 1549.74nm and a bandwidth (FWHM) of 0.46nm, was selected. A properly protective mask was obtained by using an epoxy resin, leading to about 700μm long etched region. The holder for the etching is realized with two plastic tubes arranged on Teflon support. The space between the two tubes corresponds to the etching region, which can be controlled with a resolution of 100μm. The fiber

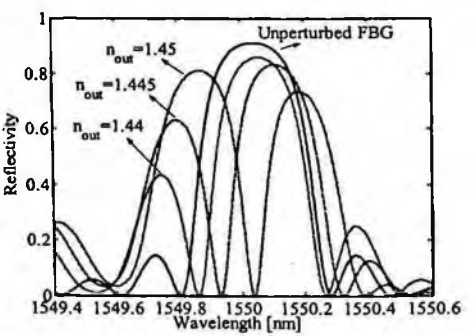

Fig. 2 Spectral responses of the micro-structured grating for different surrounding refractive index in case of full etching and L_{Th}=500μm;

with the grating is arranged inside the tubes, which are then filled up with epoxy resin to protect the fiber. Finally a test tube with dual functionalities pipes is arranged on the holder for the etching step. After an etching time of about 221 minutes at room temperature (20°C) a 10.5μm etched diameter, measured by

using microscopic analysis, is obtained. Fig. 3a shows the spectral response of the micro-structured grating for two different values of n_{out}. According to theoretical analysis, wavelength shift of the defect state is achieved as n_{out} changes. It's worth to note the formation of a small lobe out of the investigated band, at approx. 1546.9nm for n_{out}=1.414 and at about 1548.3 for n_{out}=1.449. This is due to the secondary effect of the etched region, which represents a grating with reduced length (L_{Th}) and with an effective refractive index lower than the unperturbed regions one due to the effect of the surrounding refractive index [5,6].

Based on the obtained results a successive experimental step has been carried out by using narrowband interrogation and direct reflectometric

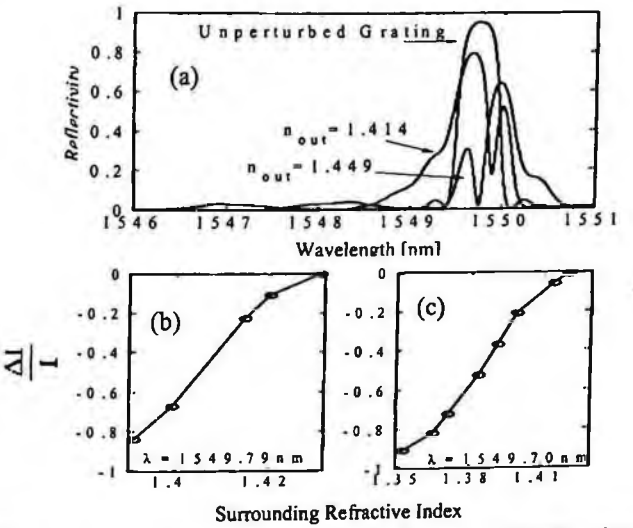

Fig. 3 Experimental responses of the micro-structured grating: (a) Reflected spectrum for different the surrounding refractive index; (b) and (c) Reflectivity at λ=1549.79nm and at λ=1549.70nm, respectively versus the surrounding refractive index.

interrogation. The optoelectronic setup for refractive index measurements comprises a 3mW laser source tunable in the range 1520-1620nm with a step-resolution of 1pm, a directional 3dB 2x2 coupler to collect the reflected signal from the sensor head and to provide an additional channel for power monitoring. Fig. 3b and c show the relative change in the normalized output signals obtained by the ratio between the reflected signals from the structure and the signal devoted to power monitoring for two operating wavelengths 1549.79nm and 1549.70nm, respectively. In the investigated refractive index ranges 1.391-1.420 and 1.364-1.40, the normalized signals change of about 75%

and 60%, respectively, leading to refractive index resolutions of $4 \cdot 10^{-5}$ and $6 \cdot 10^{-5}$ by using detection units able to resolve 0.1% intensity changes. It's worth to note that the proposed configuration has been realized with low cost fabrication stages, and exhibits performances in terms of resolution adequate to be used in practical application of environment monitoring.

4. Conclusions

In this work, a novel in fiber refractometer employing micro-structured FBGs has been demonstrated. The investigated device consists in a standard gratings with the cladding layer removed on a small and well defined region within the grating. The main effect of the localized perturbation is the formation of defect states within the stop-band spectrum of the structure, strongly dependent on the surrounding refractive index. A prototype of the proposed device was realized by wet chemical etching, in HF solution, by using a proper masking procedure. Narrowband interrogation and intensity-based measurements were used as efficient method to provide low cost and very accurate measurements. Experimental results, for the 10.5μm partially etched FBG, show resolutions of $4 \cdot 10^{-5}$ and $6 \cdot 10^{-5}$ for n_{out} around 1.41 and 1.38, respectively, by using a detection units able to resolve 0.1% intensity changes.

References

1. A. Iadicicco, A. Cusano, A. Cutolo, R. Bernini, M. Giordano, "Thinned Fiber Bragg Gratings as High Sensitivity Refractive Index Sensor", IEEE Photonics Technology Letters, Vol. 16, No. 4, April 2004.
2. A. Iadicicco, A. Cusano, S. Campopiano, A. Cutolo, M. Giordano, "Thinned Fiber Bragg Gratings as Refractive Index Sensors", IEEE Sensors Journal (in press).
3. H.J. Patrick, A.D. Kersey, F. Bucholtz, "Analysis of the Response of Long Period Fiber Gratings to External Index of Refraction", Journal of Lightwave Technology, vol. 16, no. 9, 1998.
4. M. Giordano, M. Russo, A. Cusano, A. Cutolo, G. Mensitieri, L. Nicolais, "Sensor Based On Ultra Thin Film of δ-Form Syndiotactic Polystyrene for Fast and High Resolution Volatile Organic Compounds Detection", Applied Physics Letters, 85, 22, 5349-5351, 2004.
5. A. Iadicicco, S. Campopiano, A. Cutolo, M. Giordano, A. Cusano, "Micro-Structured Fiber Bragg Gratings: Analysis and Fabrication", IEE Electronic Letters, Issue 8, 14 April 2005.
6. A. Iadicicco, S. Campopiano, A. Cutolo, M. Giordano, A. Cusano, "Refractive Index Sensor Based on Micro-Structured Fiber Bragg Grating", IEEE Photonics Technology Letters, Vol. 17, No. 6, June 2005.

CMOS ELECTRO-OPTICAL MIXER FOR RANGE FINDERS

L. PANCHERI*, G.-F. DALLA BETTA
DIT, Università di Trento, Via Sommarive 14, I-38050 Povo di Trento, Italy

M . SCANDIUZZO, F. DE NISI, D. STOPPA, L. GONZO, A. SIMONI
ITC-irst, via Sommarive 18, I-38050 Povo di Trento, Italy

We report on a novel CMOS photon mixing sensor aimed at distance measurements, which can be fabricated in a standard CMOS technology. This device can be organized in array structures to realize range-finding integrated imagers. The measurement exploits the time of flight technique: the modulated light travels to a target and is back-scattered onto the detector. The distance is proportional to the phase shift between incident and reflected light. The photon mixing sensor, based on two interdigitated n-well diffusions on a p substrate, has been integrated together with dedicated read-out electronics, in a 500 μm x 25 μm pixel. The operation principle is based on the modulation of the space-charge region width by the applied voltage. A 128-pixel linear array has been designed in 0.35-μm, 3.3-V CMOS technology (4 metal, 2 poly). An electro-optical characterization of dedicated test structures has been carried out.

1. Introduction

In the past few years a number of different solutions has been proposed in order to obtain a 3D range-finding camera, based on the Indirect Time of Flight technique. The various approaches have employed photogate photon mixing devices[1,2], metal-semiconductor-metal diodes[3] or simple photodiodes[4]. While designs based on photodiodes are feasible in a standard CMOS technology, the other solutions require more expensive dedicated technologies.

We have already reported on a range finding test-chip fabricated in a 0.35 µm, 3.3V CMOS technology[5]: owing to an innovative fully differential approach in the design of the active pixel, the sensor provides a distance-map between 2m and 9m with a precision better than 5% and an accuracy of about 1%. In order to further improve the performance of our 3D camera, a photon mixing device should be employed in place of a simple photodiode. To this

* Corresponding Author: E-mail: lucio.pancheri@dit.unitn.it, Ph: +390461883920, Fax: +390461882093

purpose, an alternative structure can be used, that is presented in this paper. A read-out channel has been designed for this device and a test-chip, containing some test structures and a 128-pixel linear array, has been fabricated in a 0.35-μm CMOS technology.

The device operation is presented in section 2, together with numerical simulation results. The pixel operation is explained in section 3. Experimental results obtained on test structures fabricated in a 0.35 μm CMOS technology are presented in section 4.

2. Device operation

The proposed photon mixing sensor is based on two closely-spaced p-n junctions, and can be fabricated in a standard CMOS technology. A schematic layout and a cross section of the test structure are shown in Fig. 1. The device is composed of two interdigitated n-well diffusions on a p-substrate. The operation principle is based on the modulation of the space-charge region width by the applied voltage. Thus, the responsivity of the two fingers can be varied as a function of the applied bias voltage.

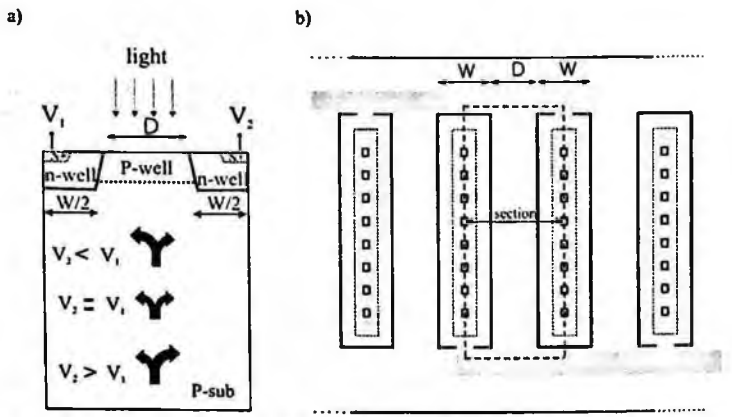

Figure 1. (a) Schematic cross-section and (b) layout of the proposed photon mixing sensor

The behavior of the sensor has been investigated by using physical device simulations performed with DESSIS[6], solving the drift-diffusion formulation of the semiconductor transport equations. The simulation domain is the same as shown in Fig. 1(a). Both technological and geometrical parameters adopted in the simulations are typical of a 0.35 μm CMOS process and could be tuned from previous projects.

The most important sensor parameter, related to the phase shift, is the demodulation contrast χ, defined as the ratio between the difference and the sum of the currents at the two electrodes.

The demodulation contrast as a function of frequency has been calculated from ac simulations, and is shown in Fig. 2 for λ = 860 nm with different inter-finger spacing D. It can be seen that the contrast decreases with D as well as with frequency. A series of test structures with n-well width $2W$ = 1.7 μm and inter-finger distance D varying from 1 to 3 μm with a step of 0.5 μm have been designed in order to validate the simulation results.

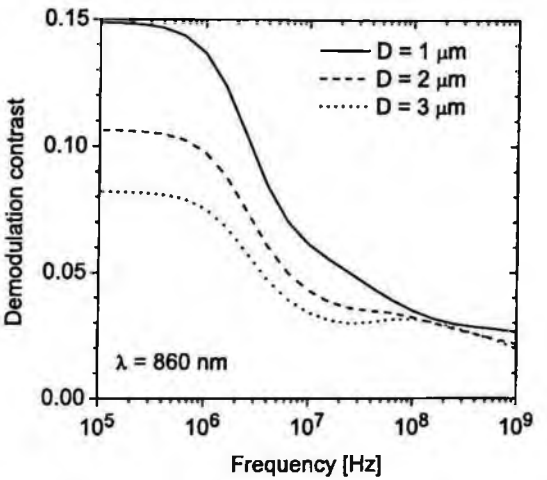

Figure 2. Simulated frequency dependence of the demodulation contrast for different inter-finger spacing

3. Read-out channel

The very good linearity between responsivity and applied voltage difference makes the photon mixing sensor suitable for operation with modulated incident light. A read-out channel has been designed in order to extract the phase shift information at the pixel level.

A block diagram of the proposed pixel is shown in Figure 3. A scene is illuminated with a modulated light source. The voltage at the two electrodes is modulated at the same frequency, one in phase with the laser and the other with a 180° phase shift. The photo-generated currents are low-pass filtered and integrated. The difference between the two photocurrents contains information about the phase shift between the modulation voltage and the backscattered light intensity. From this information the distance between the pixel and the scene can be reconstructed.

The photon mixing sensor has been integrated, together with dedicated read-out electronics, in a 500 μm x 25 μm pixel. A 128-pixel linear array has been designed and fabricated in a 0.35-μm CMOS technology.

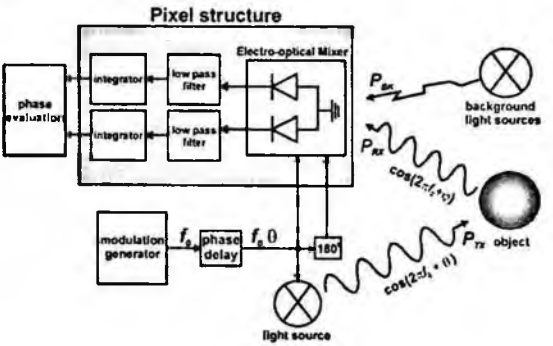

Figure 3. Block diagram of the proposed pixel

4. Experimental results

The I-V characteristics of one of the test structures are shown in Figure 4, and exhibit an excellent linearity as predicted by device simulations. The measured demodulation contrast as a function of the inter-finger spacing is shown in Figure 5. The device has been illuminated with a wavelength of 860 nm and χ has been calculated for a voltage difference $\Delta V = 1$ V between the electrodes.

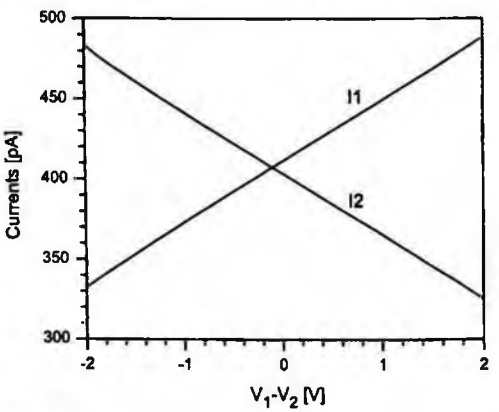

Figure 4. Measured I-V characteristics of the photon mixing sensor illuminated with a 860 nm light

From spectral responsivity measurements performed on the two electrodes biased at different voltages, χ has been calculated as a function of light wavelength. The demodulation contrast increases with the wavelength from 3%

to 4% for D = 2.5 μm, while it remains almost constant with a value of 9% for D = 1.5 μm. The observed values, particularly at the smallest D, are encouraging in view of the application, although it should be stressed that a dynamic demodulation contrast measurement is necessary to our purpose.

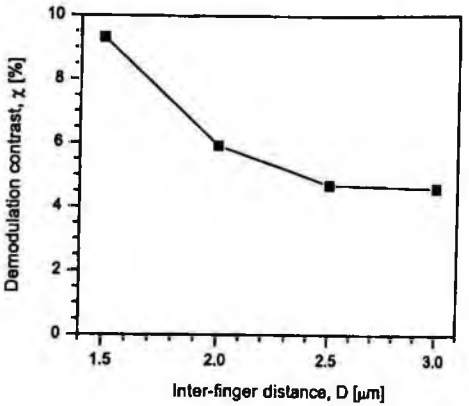

Figure 5. Measured demodulation contrast as a function of inter-finger distance D, with DV=1V and l = 860 nm

5. Conclusions

The design of an innovative CMOS demodulating pixel architecture has been presented. The pixel is based on an photon mixing sensor consisting of inter-digitated n-well diffusions on a CMOS p substrate, exploiting the modulation of the space charge region width by the applied voltage. The system is conceived for distance measurements according to a continuous wave phase modulation time of flight technique. Preliminary experimental results confirm the suitability of the proposed device as a photocurrent mixer.

References

1. R. Lange, P. Seitz, *IEEE Journal of Quantum Electronics*, 37, 390 (2001).
2. R. Schwarte, Z. Xu, H. Heinol, J. Olk, R. Klein, B. Buxbaum, H. Fisher, and J. Schulte, *Laser'97*, Munich, (1997).
3. P. Gulden, D. Becker, M. Vossiek, *IEEE Sensors Journal*, 4, 612 (2004).
4. Jeremias, W. Brockherde, G. Doemens, B. Hosticka, L. Listl, P. Mengel, *ISSCC Digest of Technical Papers*, 252, (2001).
5. D. Stoppa, L. Viarani, A. Simoni, L. Gonzo, M. Malfatti, G. Pedretti, *Proc. IEEE ESSCIRC 2004*, Leuven, Belgium, 419 (2004).
6. DESSIS 8.0 Reference Manual. ISE Integrated Systems Engineering AG, Zürich, Switzerland, (2002).

HIGH-RESOLUTION TEMPERATURE/STRAIN DISTRIBUTED MEASUREMENTS BY FIBER-OPTIC BRILLOUIN SENSING

R. BERNINI
IREA- CNR, Via Diocleziano 328, 80124 Napoli, Italy

A. MINARDO, L. ZENI
Dipartimento di Ingegneria dell'Informazione, Seconda Università di Napoli, via Roma, 29, 81031 Aversa (CE), Italy

A reconstruction algorithm employing an accurate modelling of the stimulated Brillouin scattering (SBS) interaction in a single-mode optical fibre is experimentally demonstrated. Distributed strain/temperature measurements are performed by using a Brillouin optical frequency-domain analysis configuration. Reconstructions are carried out by fully taking into account the influence of the modulation of the acoustic wave involved in the SBS interaction.

1. Introduction

Stimulated Brillouin scattering (SBS) in optical fibers permits to measure temperature and/or strain on a truly distributed basis, over kilometric ranges with high resolution. SBS effect is the result of the interaction between two counterpropagating lightwaves with frequency shift ν and an acoustic wave of frequency ν. In this three-wave mixing process, power is transferred from the pump lightwave to the Stokes lightwave (that is the lightwave having a lower frequency) and also to the acoustic wave. The interaction process is described by the Brillouin gain coefficient $g(\nu)$, which depends on the frequency shift ν and attains its maximum at the so-called Brillouin frequency shift ν_B. As the Brillouin frequency shift changes linearly with temperature and strain, a distributed temperature-strain sensor can be realized using stimulated Brillouin scattering.

A method to spatially resolve the Brillouin frequency shift along the fiber, consists in using a sinusoidally intensity modulated pump beam: This latter interacts with a counter-propagating CW probe beam, so that this latter is intensity-modulated at the same frequency. By measuring the induced complex AC component for a range of modulation frequencies, the base-band transfer function of the sensing fiber is achieved [1]. We demonstrated in a recent paper [2] that the small-signal Brillouin gain coefficient depends on the modulation frequency at which the SBS interaction is measured. In particular, the spectral

dependence of the Brillouin gain, as a function of the pump-probe frequency shift, does not follow any longer a Lorentzian function, rather it assumes a multiple-peaked shape. This behavior is due to the AC component of the acoustic wave, which modifies the spectral characteristics of the Brillouin gain coefficient when the modulation frequency exceeds the natural Brillouin gain spectrum linewidth. Hence, when dealing with high-resolution measurements, the exact relationship between measured data and Brillouin frequency shift profile has to be considered for accurate reconstructions.

In this work, we show for the first time the use of the dynamic frequency-domain SBS model for the reconstruction of temperature profiles along single-mode optical fibers. The unknown profile is determined by representing it with Fourier harmonics, whose coefficients are determined by numerical fitting between measured data and model data.

2. Frequency domain theory

When the modulation frequency exceeds the natural Brillouin gain spectrum linewidth, the three-waves model of SBS interaction has to be considered [2]:

$$\partial E_p/\partial t + \partial E_p/\partial z = -E_s E_a - \alpha/2 E_p \tag{1a}$$

$$\partial E_s/\partial t - \partial E_s/\partial z = E_p E_a^* - \alpha/2 E_s \tag{1b}$$

$$\partial E_a/\partial t + [1 + i\Delta(z)]E_a = E_p E_s^* \tag{1c}$$

where E_p, E_s, and E_a are the normalized pump, Stokes, and acoustic field amplitudes, respectively. The coefficient α takes into account the optical intensity losses, $\Delta(z)$ is the detuning, i.e., the difference between the pump-probe frequency shift and the Brillouin frequency shift, normalized to the acoustic damping rate γ_a. For the frequency-domain approach, the boundary conditions correspond to the injection of a CW pump wave at $z = 0$, i.e. $E_p(0,t) = E_{p0}(0)$, and a Stokes wave at $z = L$, which is the sum of a stationary component $E_{s0}(L)$ and a small AC component at a given angular frequency ω, i.e. $E_s(L,t) = E_{s0}(L) + \mathrm{Re}[E_{s3}(L)\exp(j\overline{\omega}t)]$, where $\overline{\omega}$ is the modulation angular frequency normalized to the acoustic damping rate. We search for solutions of the problem as:

$$E_j(z,t) = \mathrm{Re}\left[E_{j0}(z) + E_{j1}(z)e^{j\overline{\omega}t} + E_{j2}^*(z)e^{-j\overline{\omega}t}\right] \qquad j = p,s,a \tag{2}$$

where $E_{p0}(z)$, $E_{s0}(z)$, and $E_{a0}(z)$ are the steady-state solutions of eq.s (1). At each section z along the fiber, the total AC complex component of the field amplitude is $E_{j3}(z) = E_{j1}(z) + E_{j2}(z)$. By substitution of eq.s (2) in eq.s (1), we obtain a set of four coupled linear equations of the variables E_{p1}, E_{p2}, E_{s1}, and E_{s2}, which are given in [2]. These equations can be numerically solved by setting the boundary conditions $E_{p1}(0) = E_{p2}(0) = 0$. The total AC components of the optical fields at z=L are calculated as $E_{p3}(L,\overline{\omega}) = E_{p1}(L,\overline{\omega}) + E_{p2}(L,\overline{\omega})$ and $E_{S3}(L,\overline{\omega}) = E_{S1}(L,\overline{\omega}) + E_{S2}(L,\overline{\omega})$, whereas the correspondent complex AC intensity components are given, in the small-signal model, by $I_P(L,\overline{\omega}) = 2 \cdot k \cdot E_{p0}(L) \cdot E_{p3}(L,\overline{\omega})$ and $I_S(L,\overline{\omega}) = 2 \cdot k \cdot E_{S0}(L) \cdot E_{S3}(L,\overline{\omega})$ (K is a Brillouin coupling constant [3]). Finally, the baseband transfer function (TF) is given by the ratio between the AC component of the pump wave intensity and the AC component of the input Stokes wave intensity at z = L, i.e. $H(\overline{\omega}) \equiv I_P(L,\overline{\omega})/I_S(L,\overline{\omega})$.

3. Reconstruction technique

The model described in the previous Section can be employed in order to perform accurate reconstructions of temperature/strain profiles, by representing these latter as the sum of a finite number of harmonic components. A detailed description of the harmonic reconstruction technique can be found in [3]. Here we report briefly its operation. The profile to be determined is represented as:

$$f_B(z) = \sum_{n=-N}^{N} f_n e^{jn\omega_f z} = f_0 + 2\,\mathrm{Re}\left(\sum_{n=1}^{N} f_n e^{jn\omega_f z}\right) \qquad 0 \le z \le L \tag{3}$$

where L is the length of the fibre, $\omega_f = 2\pi/L$ is the fundamental spatial frequency and $\underline{f} = \{f_n\}_{n=0}^{N}$ is the sequence of the unknown complex coefficients. The algorithm searches for the complex coefficients f_n which minimize a cost-function defined as the square norm, in the ω space, of the difference between the measured signals and the model signals, that is:

$$F(\underline{f}) = \sum_{i=1}^{M}\sum_{j=1}^{K}\left|H_{(Model)}(\underline{f},\omega_j,\nu_i) - H_{(Measured)}(\omega_j,\nu_i)\right|^2 \tag{4}$$

where M is the number of processed signals and K is the number of modulation frequencies ω_j. The model data are generated by numerically solving the model described in the previous Section. The number of harmonic components is progressively increased during the minimization procedure. The expansion is

arrested when the norm of the profile estimate differs from the norm of the previous one, by a quantity less then a definite threshold.

4. Experimental measurements

Experimental measurements were performed in order to validate the harmonic reconstruction technique. To this aim, the experimental configuration shown in Fig. 1 was employed. The semiconductor laser was a pigtailed DFB module emitting at 1550 nm with an output power of about 40 mW. The output light was first split by a fiber-fused coupler, which directed the 1% of the power to a first electro-optic modulator (EOM1) for the AC-modulated pump signal generation, whereas the remaining 99% was launched into a second high-bandwidth electro-optic modulator (EOM2). This latter was employed for the generation of a CW light having an opportune frequency offset (around 10 GHz), by means of the sideband technique described in [4]. A pass-band optical filter (OF) is placed after the EOM in order to suppress one of the two generated sidebands. The polarization scrambler (PS) is used in order to eliminate the Brillouin gain fluctuations due to changes in the state of polarization (SOP) of the two beams. The measured input optical powers are $P_{P0}(0)$=1 mW and $P_{S0}(L)$=30 μW. Measurements were taken by employing a modulation frequency ranging from 40 KHz to 250 MHz. We compare the reconstruction provided by the harmonic approach, with the one achieved by local fitting of the Brillouin gain spectrum at each section along the fiber. In the latter case, Brillouin gain spectra are extracted by inverse-Fourier-transform of the frequency-domain data.

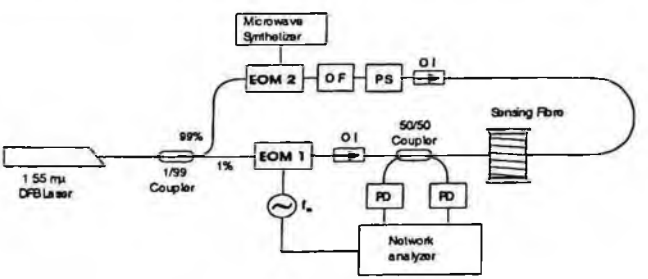

Figure 1. Experimental setup for Brillouin Optical Frequency-domain analysis

A standard single-mode 30-m long optical fiber has been employed for the measurements. The fiber had a nominal Brillouin frequency of 10865 MHz at room temperature. A 5-m long region of the sensing fiber was immerged in a water bath containing melting ice at T = 0°C. Two additional 40-cm long strands of fiber, separated by a central 2-m long strand of fiber, were also immerged in the same water bath. The mean Brillouin frequency shift measured along the 5-m

long cold region is measured to be 10829 MHz. This latter value is used as a reference, in order to verify the capability of the sensor in measuring correctly the Brillouin shift in correspondence of the narrower perturbed regions. The profile provided by the proposed reconstruction algorithm, together with the profile provided by the local fitting approach, are shown in Fig. 2a. The two reconstructions are identical along the fiber, except for the fiber regions corresponding to the two narrower cold spots. The error on their peaks estimation is 1.5 MHz and 3.6 MHz for the harmonic reconstruction, against the values of 18.7 MHz and 20.7 MHz relative to the classical reconstruction. A zoom over the fiber length comprising the two narrower cold spots is shown in Fig. 2b.

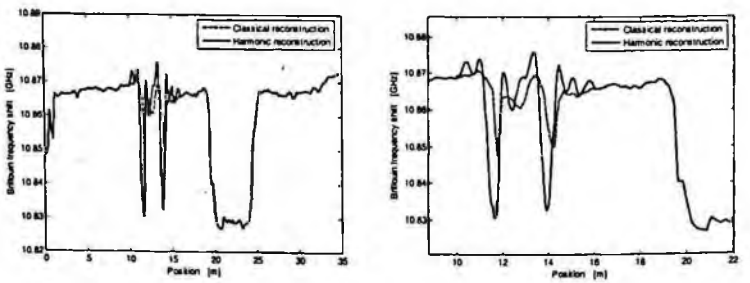

(a) (b)

Figure 2 (a). Temperature profile reconstruction by the local fitting approach (dashed line) and the harmonic approach (solid line). (b). Zoom of the reconstruction of Figure 2a over the narrower cold spots.

References

1. D. Garus, T. Gogolla, K. Krebber, F. Schliep, "Brillouin optical-fiber frequency-domain analysis for distributed temperature and strain measurements", *J. Lightwave Technol.*, vol. 15, no. 4, pp. 654-662, 1997.
2. R. Bernini, A. Minardo and L. Zeni, "Stimulated Brillouin scattering frequency-domain analysis in a single-mode optical fiber for distributed sensing", *Optics Letters,* vol. 29, no. 17, pp. 1977-1979, 2004.
3. R. Bernini, L. Crocco, A. Minardo, F. Soldovieri, L. Zeni, "A new frequency domain approach to distributed fiber-optic Brillouin sensing", *Opt. Lett.*, vol. 27, no. 5, pp. 288-290, 2002.
4. M. Nikles, L. Thevenaz, P. A. Robert, "Brillouin gain spectrum characterization in single-mode optical-fibers", *J. Lightwave Technol.,* vol. 15, no. 10, pp. 1842-1851, 1997

DYNAMIC MEASUREMENTS ON A STAR TRACKER PROTOTYPE OF AMS USING FIBER OPTIC SENSORS

A. CUSANO, P. CAPOLUONGO, S. CAMPOPIANO, C. AMBROSINO, A. CUTOLO
Optoelectronic Division – Eng. Dept. University of Sannio Benevento, Italy

M. GIORDANO
Institute for Composite and Biomedical Materials National Research Council (IMCB-CNR) Naples, Italy

M. CAPONERO,
Centro di Ricerche ENEA, Via Enrico Fermi 45, 00044 Frascati (Roma), Italy

A. PAOLOZZI, F. FELLI
Univ. "La Sapienza, 00184 Roma, Italy

An aluminum prototype of the AMICA (Astro Mapper for Instrument Check of Attitude) Star Tracker Support (ASTS) of the AMS_02 (Alpha Magnetic Spectrometer) space experiment has been instrumented with Fiber Bragg Gratings (FBGs). In this work the use of FBGs in the acquisition of strains during a dynamic test on the ASTS prototype is reported. The excitation has been provided by an instrumented impact hammer, the response has been given by bonded FBGs and accelerometers nominally in the same location. All time histories have been recorded, transformed in the frequency domain to determine resonant frequencies and displacements (strain) shapes of the ASTS. Numerical simulations of this structure have been performed to predict the aforementioned dynamic features.

1. Introduction

AMS_02 is a particle detector in space [1]. The subsystem considered is the AMICA Star Tracker Camera (ASTC) developed by the Center for Advanced research in Space Optics, (CARSO), in Trieste (Italy) and the analysis is addressed to the mechanical support structure, the ASTS (designed by Italian National Institute for Nuclear Physics, INFN, of Rome). A qualification process for space flight is required to check if modal characteristics of such a system are compatible with space environmental conditions. So, a critical aspect is represented by a proper choice of a sensing system. It must exhibits features like reliability, robustness, low complexity implementation. Fiber optic sensors seems to be a good candidate: they are able to measure static and dynamic strains when embedded or stuck on a structural component.

In this work, a particular class, FBGs, have been chosen: they codify strain variations in wavelength and they are able to retrieve the strain distribution of a structure. A proper interrogation system, exhibiting adequate features of passing band, reliability, robustness and low complexity implementation [2], has been utilized. To retrieve modal resonant frequencies and vibrational shapes the frequency response function (FRF) approach has been adopted. Instrumented hammer's impacts or shakers are input signals, while displacements or

accelerations are the common output signals. Experimental results demonstrated than FBG strain sensors can be a valid alternative to the most useful sensing system for this application.

2. Methodology: frequency response function (FRF)

The FRF, H(jω), can be considered like a ratio between the FFT of the dynamic response of the system, typically expressed as displacements in the different directions, and the FFT of the excitation. This normalization of the effect in comparison to the cause gives, for every frequency, an information in terms of amplitude and phase, relative to a proper characteristic of the system. It can be shown that natural frequencies can be evaluated from zero crossings of the real part of FRF or, otherwise, from frequencies corresponding to peaks of its imaginary part. This latter component gives a second information: for each excitation point, the corresponding amplitude of the vibrational shape is proportional to it. The FRF can be expressed directly in terms of the modal parameters [3]

$$[H(j\omega)] = \sum_{k=1}^{n} \left[\frac{u_k u_k^{l}}{j\omega - \lambda_k} + \frac{u_k^{*} u_k^{*l}}{j\omega - \lambda_k^{*}} \right] \tag{1}$$

where: u_k is the k-th modal displacement vector and λ_k the relative system pole, strongly related to the natural frequency of vibration.
In the common practice, responses of accelerometers are output signals and so the term FRF is adopted. Since FBGs are strain sensors, the response of the system is called strain frequency response (SFRF).

3. Fiber Bragg gratings as strain sensors

A Fiber Bragg Grating (FBG) is a periodic or semi-periodic permanent perturbation of the refractive index of the core of an optic fiber. So, when this structure is irradiated with a broadband optical source, a narrow band pass spectrum signal is reflected. The central wavelength of this signal, "Bragg wavelength", λ_B, is related to the physical parameters of the grating by the relationship [2]:

$$\lambda_B = 2\, n\, \Lambda \tag{2}$$

where: n is the effective refractive index of the mode propagating inside the fiber; Λ the pitch of FBG. Each external cause, like strain, able to modify right

hand terms of eq. (2), causes a shift of the Bragg wavelength. Relative variation of the λ_B as a function of applied axial strain is:

$$\frac{\Delta\lambda_B}{\lambda_B} = \left(1 - \frac{n^2}{2}\left[p_{12} - \nu\left(p_{11} + p_{12}\right)\right]\right) \cdot \varepsilon \qquad (3)$$

where ε is the applied strain, p_{11}, p_{12} are two components of the strain optic matrix [4], ν is the Poisson's ratio. It results by eq. (3) that FBGs are linear strain transducers.

4. Experimental set up

Reported tests have been performed on a mock up of the ASTS made using an Al Alloy 5083. An experimental grid, constituted by 32 points, included 5 points placed at the constrained edge of the sample, has been used to perform modal analysis. In Fig. 1 the protecting jackets of two optical fibers where FBGs are written are visible. Jackets are removed in correspondence of FBGs for a better bonding on the structure. Near to each FBG an accelerometer was placed as reference sensor so, nominally, the two different sensors are in the same location. FBGs measure strain component orthogonal to the plane of the constraint; accelerometers transduce the acceleration component perpendicular to the plane of the lower side of the ASTS. The exploited interrogation system relies on a low cost ratiometric technique based on optical filtering, realized in FBG technology, combined with broadband interrogation [2].

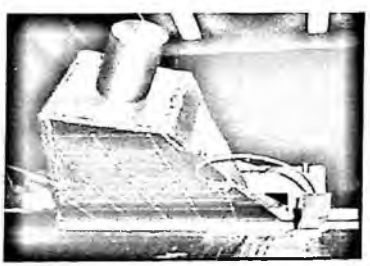

Fig. 1. Prototype structure with excitation grid

In light of the passive nature of the proposed technique, system bandwidth is only limited by the electronic circuitry involved in the receiving unit. Static and dynamic resolutions of 1pm and 40nε/(Hz)0.5 can be achieved up to 50KHz. For this application, the system bandwidth was limited to 400Hz. A Data Acquisition (DAQ) system is responsible for data storage and elaboration.

5. Results and discussion

In order to predict resonant frequencies and modal shapes of this structure, a numerical simulation was performed, for the first two flexural modes. Obtained resonance frequencies are 41.74 Hz and 120.14 Hz. Experimental modal analysis was performed by using instrumented impact hammer in each location of the excitation grid. Here, the results of FBG bonded on the left of the structure in Fig.1 and of the accelerometer near located are reported. By applying the classical modal analysis techniques [3] from the SFRFs (FRFs) the strain (displacement) shapes for the first two flexural modes were obtained. The resonant frequencies for the first two detected modes were 38.33 Hz and 123.78 Hz for both the sensors. Strain and displacement modal shapes can be observed with a suitable offset, in Fig. 2 and Fig. 3, respectively. Since the FBG sensor is subject to a purely axial strain field, such deformations are proportional to the curvature along the y axis and to the distance from the neutral plane. In other words they represent the second partial derivative of the vertical displacement with respect to the spatial coordinate. This circumstance is approximately verified in our results as can be seen in Fig. 2 and Fig. 3. The strain distribution for the first mode shape is approximately constant (Fig. 2) as one can expect from a deformed shape with approximately constant curvature.

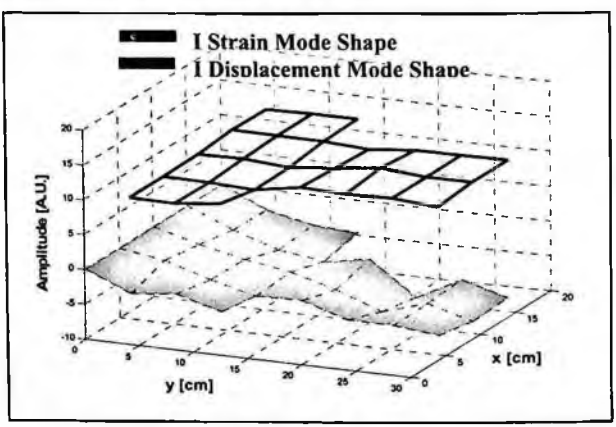

Fig. 2. I mode strain and displacement vibrational shapes

On the other hand the second mode shape (Fig. 3) shows a variable curvature that reduces towards the tip until it becomes negative. A closer view to Fig. 2 and Fig. 3 shows that the experimental grid used for displacement has five more points. Those points are relevant to the clamped end and cannot be reported for strain shapes because at the clamped end the values of this magnitude cannot be guessed while displacements along the vertical axis are null. Finally, these

experimental results, both for resonant frequencies and for vibrational shapes, are in good agreement with numerical ones.

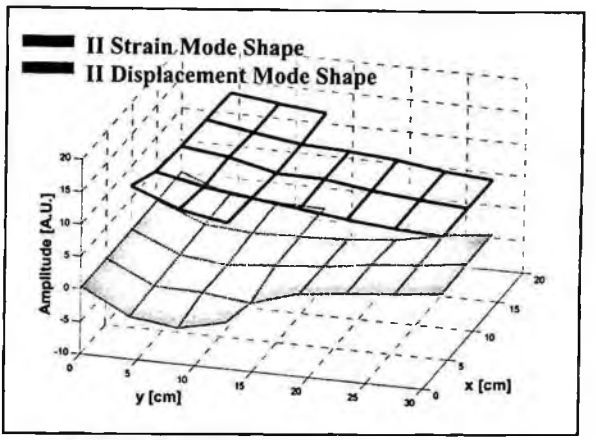

Fig. 3. II mode strain and displacement vibrational shapes.

6. Conclusions

Experimental results obtained with FBG sensors and conventional accelerometers are in excellent agreement for the first two natural frequencies: the strain mode shapes (obtained by FBGs) exhibit a behavior like the second space derivative of the displacement modes obtained by accelerometers. A good level of agreement was obtained comparing experimental results with numerical ones. This means that FBG sensors can be exploited for modal analysis tests. As a future work, the measurement and analysis of the responses in all the external surfaces of the ASTS is planned. Also a Single-Input-Multi-Output (SIMO) test will be performed, exploiting the FBG multiplexing property and an automatic procedure for data acquisition and analysis will be prepared.

References

1. T. Martin, JSC-28792 **Rev.B**, NASA Space and Life Sciences Directorate Flight Project Division, December 2001.
2. A. Cusano A. Cutolo, M. Giordano, A. Calabrò, Sensors and Actuators A, **110(1-3)**, 276-281, 2003.
3. Heyelen W., Lammens S., Sas P., "Modal Analysis Theory and Testing", Katholieke Universiteit Leuven, 1997
4. Measures R. , Structural monitoring with fiber optic Technology, Academic Press, London, 2001

PRESSURE SENSITIVE PAINTS: TOP-DOWN VERSUS BOTTOM-UP APPROACHES FOR NANOSILICON POWDER FABRICATION

ANNA CASTALDO
Enea, UTS MAT-NANO, Portici Research Center
Portici (Na), Italy, 80055, Via Vecchio Macello

GIROLAMO DI FRANCIA
Enea, UTS MAT-NANO, Portici Research Center
Portici (Na), Italy, 80055, Via Vecchio Macello

ETTORE MASSERA
Enea, UTS MAT-NANO, Portici Research Center
Portici (Na), Italy, 80055, Via Vecchio Macello

LUIGI QUERCIA
Enea, UTS MAT-NANO, Portici Research Center
Portici (Na), Italy, 80055, Via Vecchio Macello

GIUSEPPE FAMELI
Enea, UTS ENE-FOTO, Portici Research Center
Portici (Na), Italy, 80055, Via Vecchio Macello

PAOLA DELLI VENERI
Enea, UTS ENE-FOTO, Portici Research Center
Portici (Na), Italy, 80055, Via Vecchio Macello

We propose an innovative PSP formulation in which pressure sensitive element is nanostructured silicon obtained in two different approaches and the binder is a polysilsesquioxane. The first approach is named top-down and consists in the dimension reduction of porous silicon powders assisted by a stain etching step. The other is a bottom-up one and consists in synthesizing nanometric silicon by metatheses reaction between silicon dioxide and carbon black, conducted in a ball milling reactor. We describe powders fabrication methods, formulation of our PSP and characterize paints performance.

1. Introduction

Pressure Sensitive Paints (PSP) play an important role in aerodynamic testing. They are polymeric formulations consisting of an oxygen permeable polymer matrix into which a photoluminescent material is either dispersed or dissolved. The photoluminescence of the material is quenched in presence of molecular oxygen and this quenching can determine the pressure through the Stern-Volmer equation. Detailed explanation of the principle of PSP have been previously presented in the literature [1]. Following the initial publication of the use of luminescent paint for pressure measurement, in connection with wind tunnel research, many different formulations of polymer with different luminophores have been tried [2]. Testing of these formulations, however, has led to discovery of a number of problems and limitation, e.g. photodegradation of the complexes, response time and temperature dependency [3]. In an attempt to eliminate these problems we propose an innovative formulation in which sensible element luminophore is nanostructured silicon obtained by two different methods and the binder is a polysilsesquioxane with nanosized cages, which could contain the luminophore. Performance of our PSP is compared to that of the paints realized in the work by Mclachlan and coworkers [4]. As we show in the following, our PSP formulation exhibits a strong response to pressure variation, with a response time suitable for aerodynamic testing.

2. Experimental

Nanostructured powders are obtained by the ball milling technique [5]. The ball milling is carried out in a planetary ball mill. In the bottom-up experiment Carbon black (Black Pearls Cabot, GP-2831) and pure silica (average particle size less than 0,5 mm) in equimolecular ratio are put in an hard steel jar of 25 mL volume. The total weight of the powder is 1,13 g. The ball milling is performed with 5 hard steel balls. The rotation rate is 400 rpm. Time of reaction is 295 hours. The ball milled powder are characterized by X-ray diffraction, Raman scattering, FT-IR, SEM, micro-photoluminescence. In the bottom-up experiment ball milling of crystalline silicon wafer grossland fragmented is carried out in an agate jar. Single-crystal <100> p-type silicon wafers with $0{,}429*10^2$ Ω cm resistivity are used. Ball milling is performed in various conditions, up to a dimension of few hundreds of nanometers. Nanostructured powder samples are finally obtained by chemical etching, using an activated HF-HNO_3 solution (50:1, wt %). After the etching, samples are rinsed and stored in pentane.

Poly [(propylmethacryl-heptaisobutyl-POSS)-*co*-(*n*-butylmethacrylate)] is solubilized in toluene and cast on the test surface, where the selected powder is dispersed by means of spraying. PL quenching measurements are performed in a pressure chamber equipped with mass flow controller, turbomolecular vacuum

pump and with an accurate pressure sensitive measurement system. Through a quartz window, PL is excited by He-Cd laser radiation (442 nm). Emission spectra are collected and recorded on a CCD spectrometer by an optical fiber.

3. Results and discussion

Silicon nanostructures, in dependence of their size confinement, could have a resonant level with respect to triplet state of oxygen [6]. This justifies the high oxygen quenching of their photoluminescence and represents the reason of our choice of nanosilicon powder as luminophore. Moreover, the photoluminescence of silicon nanostructures is stable at the low temperature, at difference of the organometallic complexes previously used in PSP. We obtain nanosilicon powders in two different approaches. The first one is a top-down approach, consisting in the dimension reduction of porous silicon powders suited by the stain etching method. The other is a bottom-up one, consisting in the synthesis of nanometric silicon by metatheses reaction between silicon dioxide and carbon black, conducted in a ball milling reactor [7].

Both approaches are based on the ball milling technique. They produce very different powders, as we show in SEM photograph of Fig 1. In the top-down approach we have a micrometric nanostructured powder, with average pores dimension of 60 Å and a specific area of 3,18 m^2/g. From the bottom-up approach derives a nano-powder whose average dimension is 100 nm. This powder is inhomogeneous, because methateses reaction proceeds with other secondary reactions to obtain silicon, silica and silicon carbide.

Figure 1. SEM photograph of top-down (a) and bottom-up (b) powders.

Powder obtained by the top-down approach exhibits an higher PL level more appropriate to construct an oxygen sensor. Starting from this powder we formulate our paint with a polysilsesquioxane as a binder. This polymer is permeable to oxygen, has a good transparence in the emission region of the nanostructured silicon and an high decomposition temperature, i.e. useful for aerodynamic applications. We obtain films of the binder and above we deposit the selected powder, to avoid diffusion time in the polymeric matrix. In an

opportune pressure chamber we carry out our measurements. Our paint is sensible to variations of pressure. In Figure 2 we report the correlation between photoluminescence intensity and pressure: PL intensity decreases with an increase of pressure. This correlation enables us to the utilization of such paint in the PSP technique.

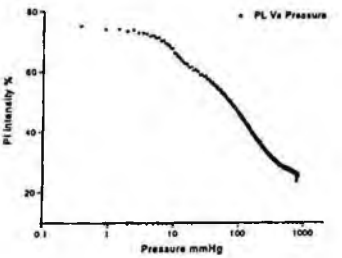

Figure 2. Diagram of correlation between photoluminescence intensity and pressure: PL intensity decreases with an increase of pressure in the range 0.1-1000 mmHg.

In another experiment, in which our paint is placed in vacuum and then in nitrogen, a response time of only 5 seconds could be estimated (10 s is the response time of the paints reported by McLachlan, [*Cfr* ref. 4]).
Figure 3 reports calibration characteristic of our paint in comparison to two paints obtained at NASA Ames Research Center from Mc Lachlan and colleagues. In our case, calibration is not linear, probably because our system is inhomogeneous.

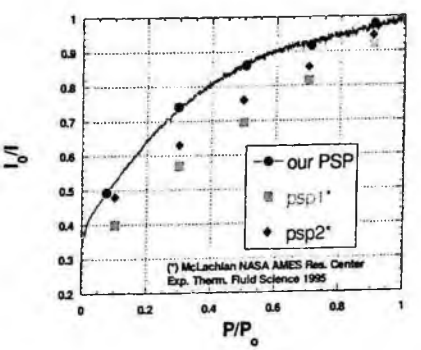

Figure 3. Calibration characteristic of our PSP in comparison to PSP1-PSP2 from a study of McLachlan et al [see ref. 4].

It is noticeable that we synthesize, at the moment, our paint far from test chamber, with unavoidable loss of sensing activity during transportation. Clearly we will tend to ameliorate this aspect, for example with the aid of gloves box and appropriate storage media. We are studying how to deposit an optimal polymeric shield over the paint, in order to face the problem of preserving performance before measurements.

4. Conclusion

In this study silicon nanostructures have been obtained by two approaches: top-down and bottom-up. The top-down approach conduces to a nanostructured micrometric powder, the bottom-up to a nanosized powder containing silicon. Moreover we show the complex pattern of nanosized byproducts of a simple methatesis reaction conducted in a ball milling reactor, in particular evidencing a possible synthesis of silicon carbide.

We formulate a new pressure sensitive paint based on a selected silicon nanostructured powder. Formulation we propose is very simple in making and cover a wide range of applications, responding in few seconds to oxygen concentrations variations.

References

1. J.H. Bell, E.T. Schairer, L.A. Hand, R.D. Mehta, *Ann.Rev. of Fluid Mechanics* **33**, 155 (2001).
2. V. Mosharov, M. Kuzmin, A. Orlow, V. Radchenko, N. Sadovskii, I. Troyanovsky, *EP 0558771* A1 (f.d. 01.03.92).
3. M. H. Nayfeh, J. Therrien , Z. H. Yamani, *US 6585947* (f.d. 01.07.2003).
4. B. G. McLachlan, J.H. Bell, J. Espina et al, NASA *TM-103970* (October 1992).
5. H. Mio, J. Kano, F. Saito, K. Kaneko, *Mat. Science and Engineering* **A 332**, 75 (2002)
6. G. Di Francia et al EUROSENSORS XVIII *Digest of technical papers*, 155 (2004).
7. C. Lam, Y.G. Zhang, Y.H. Tang, C.S. Lee, I. Bello, S.T. Lee, *J. Cryst. Gr.* **220**, 446 (2000).

ETCHED FIBER BRAGG GRATINGS BASED MEASUREMENTS FOR REFRACTIVE INDEX AND TEMPERATURE

A. IADICICCO, S. CAMPOPIANO, A. CUTOLO, A. CUSANO
Optoelectronic Division, Engineering Department, University of Sannio, Benevento, Italy

M. GIORDANO
Institute for Composite and Biomedical Materials, CNR, Napoli, Italy

In this work, a new device based on non-uniform thinned Fiber Bragg Gratings (ThFBGs) for the simultaneous measurements of temperature and refractive index is presented. The proposed structure relies on the use of a single and partially thinned FBG. The perturbation leads to a wavelength-splitting of the unperturbed grating spectral response in two separate peaks dependent on the surrounding refractive index and the local temperature. The simultaneous measurements of the Bragg wavelengths of the two peaks allow the accurate measurements of the refractive index and the temperature by using a single sensing element, simultaneously. Here, wet chemical etching in a buffered hydrofluoric acid (HF) solution was used for sensor fabrication. Experimental characterization for a 7.6μm etched cladding sensor is presented.

1. Introduction

In the last years, the needs of reliable and robust sensors for chemical sensing applications have indicated in the fiber optic technology a valid alternative. Interesting configurations of fiber optic refractometers have been proposed including long period gratings [1], Fabry-Perot configurations [2] and thinned fiber Bragg gratings [3-4]. Among them, only ThFBGS and LPGs allow high sensitivity combined with easy multiplexing capability.

However, the in situ operation in typical control and diagnosis applications requires the compensation of the thermal changes especially when long time monitoring is necessary. In this work, the use of a single non-uniform ThFBG for the simultaneous measurements of refractive index and temperature is presented [5]. The structure relies on a standard grating: in part of the sensing element the cladding layer is partially or totally removed, while the remaining part is practically unchanged, as show the figure 1. The perturbation leads to a wavelength-splitting of the unperturbed spectral response in two separate peaks. The first one, related to the thinned region, exhibits a spectral response dependent on the local temperature and the surrounding refractive index (SRI),

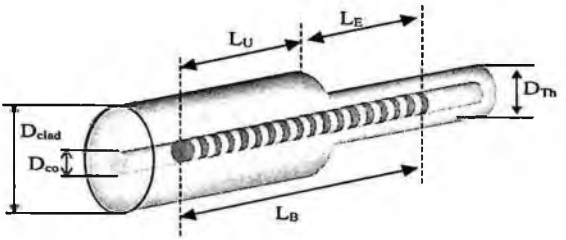

Fig. 1 (a) Schematic diagram of the structure under investigation (not in scale

while the other one responds only to the thermal changes. Here, numerical and experimental results on the use of a non-uniform ThFBG for multi-parameter sensing are presented. A sensor prototype was fabricated by using standard SMF-28 optical fibers and wet chemical etching in a buffered hydrofluoric acid (HF) solution [3-5]. Experimental characterizations of the sensor response to external refractive index and temperature varying in the range 1.333-1.450 and 15-50°C, respectively, are presented.

2. Principle of operation

In common optical fibers, the effective refractive index, n_{eff}, of the fundamental mode is practically independent of the SRI. However, according to ThFBG operation [4], if the cladding diameter is reduced, the effective refractive index n_{eff} of the fundamental mode will show a non linear dependence on the SRI. Here, a non-uniform ThFBG is considered, as shown in figure 1, where the cladding layer is partially or totally removed only in a part of the FBG. The key parameters of the device are the thinned region length L_{Th}, the unperturbed region length L_U, the core diameter D_{co}, the cladding diameter D_{clad}, the thinned diameter D_{Th} and the SRI. The main effect of the perturbation is the splitting of the spectral response of the original grating in two peaks located at two distinct wavelengths depending on the etching features and SRI. The Bragg wavelengths of the two peaks are:

$$\lambda_U = 2 \cdot n_{effU} \Lambda \qquad \lambda_{Th} = 2 \cdot n_{effTh} \Lambda$$

where λ_U and λ_{Th} are the Bragg wavelengths and n_{effU} and n_{effTh} are the effective refractive indices of the unperturbed and thinned grating region, respectively, and Λ is the grating pitch. It's worth to note that the Bragg wavelength related to the unperturbed region λ_U is sensitive only to local thermal changes. Whereas, the Bragg wavelength related to the thinned region λ_{Th} responds to thermal variation and surrounding refractive index changes [5]. The dependence of the n_{eff} on the SRI is achieved through the interaction of the evanescent field

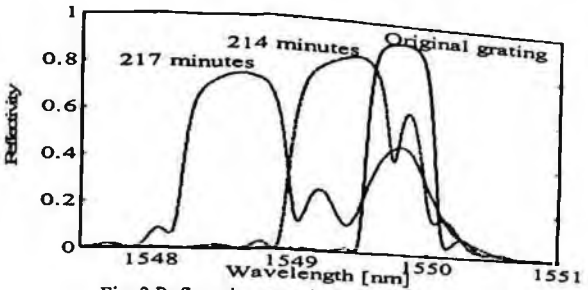

Fig. 2 Reflected spectra during the etching process

with the surrounding medium. Since the evanescent field in the surrounding medium increases as the SRI increases and/or the cladding layer decreases, maximum sensitivity are carried out when the SRI is close to the cladding one and the cladding layer is completely removed [4].

3. Experimental results

In this section, the sensor fabrication steps and the experimental results are reported. The thinned region was obtained by wet chemical etching using an aqueous hydrofluoric acid (HF) solution at 24% [3-5]. The optoelectronic set-up, involved for both fabrication process monitoring and for further refractive index measurements, comprises a broadband superluminescent diode (2mW), operating at 1550nm with 40nm FWHM (Full Width Half Maximum), a directional 3dB coupler and an optical spectrum analyzer, with resolution of 10pm, for spectral measurements. A commercial 8mm long FBG demonstrating a central wavelength of 1549.81nm and a bandwidth (FWHM) of 0.51nm, was used. The holder for the etching step was realized with a plastic tube for fiber arrangement. In particular, the FBG is arranged in the etching holder positioning about half sensing element inside the plastic tube. Then it is filled up with epoxy resin to prevent the etching of the entire sensing element. Finally a test tube with dual functionalities pipes is arranged around the holder. Fig. 2 shows the spectral responses of the device during the etching process, compared to the original one. According to the theoretical analysis, during the etching process the Bragg reflected signal splits in two lobes. The peak at lower wavelengths corresponds to the thinned region and is sensitive to the SRI and the local temperature, while the peak at longer wavelength is related to the unperturbed structure and thus is dependent only on the local temperature. Then the sensor diameter was measured by using microscopic analysis revealing a residual diameter of approx. 7-8μm.

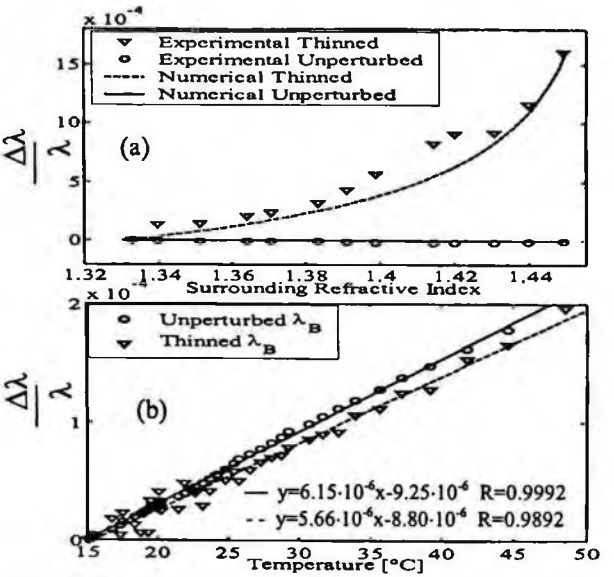

Fig. 3 Experimental results: (a) Relative shift for the thinned and the unperturbed wavelengths versus the external refractive index; (b) Relative shift for the thinned and the unperturbed wavelengths versus the temperature;

In order to characterize the sensor sensitivities to SRI, aqueous-glycerine solutions at different concentrations and with known refractive index were used as surrounding media maintaining the holder in a thermo-stated bath. Fig. 3a shows the relative Bragg wavelength shifts of the two peaks induced by SRI changes at a temperature of 25°C. Centroid analysis was used for Bragg wavelength identification with a wavelength resolution less than 10pm over the whole investigated range. As expected, the wavelength corresponding to the etched region exhibits a non-linear behaviour versus SRI. Sensitivities of $7.8 \cdot 10^{-2}$ and $3.4 \cdot 10^{-3}$ have been obtained for SRI around 1.45 and 1.33, respectively. On the other side, no changes in the wavelength corresponding to the unperturbed grating region occur. Numerical analysis has been carried out by using the three layer fiber model and multiplayer approach [4-5] for a 7.6μm residual diameter, very close to the value obtained by the microscopic analysis. From these results and in the case of interrogation unit able to discriminate wavelength shifts with a resolution of 1pm at 1550nm, refractive index resolutions of $\approx 10^{-5}$ and $\approx 10^{-4}$ for SRI around 1.45 and 1.333, respectively, are possible. Finally, the thermal characterization has been carried out by using water as surrounding medium with a thermo-optic coefficient of about -10^{-4}/°C. Fig. 3b shows the thermal responses of the two peaks in the range 15-48°C. The thermal sensitivity of the thinned region is slightly lower than the unperturbed

region one due to the negative thermo-optic coefficient of the water compared with the positive one of the cladding. In addition, in both cases, linear behaviour was found with sensitivities of $6.15 \cdot 10^{-6}$/°C and $5.66 \cdot 10^{-6}$/°C for the unperturbed and thinned regions, respectively. In this case, resolution of 0.1°C can be obtained by using the same detection units with 1pm resolution. Based on the obtained results, the proposed configuration involving non-uniform ThFBGs demonstrated the potentiality to perform simultaneous and accurate measurements of refractive index and temperature.

4. Conclusions

A novel in fiber sensor based on non-uniform thinned fiber Bragg grating for simultaneous measurements of temperature and refractive index has been demonstrated. The principle of operation relies on the splitting of the original grating spectral response in two distinct peaks due to a selective etching over the grating length. A sensor prototype was realized by low cost technique based on wet chemical etching and epoxy resin masking procedure. The experimental characterization shows refractive index resolutions of $\approx 10^{-5}$ and $\approx 10^{-4}$ for the SRI around 1.45 and 1.333, respectively, and resolution in temperature of 0.1°C is possible by using easily available interrogation units.

References

1. A.G. Mignani, A.A. Mencaglia, "Direct and Chemically-Mediated Absorption Spectroscopy Using Optical Fiber Instrumentation", IEEE Sensors Journal, vol. 2, 52-57, 2002.
2. M. Giordano, M. Russo, A. Cusano, A. Cutolo, G. Mensitieri, L. Nicolais, "Optical Sensor Based On Ultra Thin Film of δ-Form Syndiotactic Polystyrene for Fast and High Resolution Volatile Organic Compounds Detection", Applied Physics Letters, (in press).
3. A. Iadicicco, A. Cusano, A. Cutolo, R. Bernini, M. Giordano, "Thinned Fiber Bragg Gratings as High Sensitivity Refractive Index Sensor", IEEE Photonics Technology Letters, Vol. 16, No. 4, April 2004.
4. A. Iadicicco, A. Cusano, S. Campopiano, A. Cutolo, M. Giordano, "Thinned Fiber Bragg Gratings as Refractive Index Sensors", IEEE Sensors Journal (in press).
5. A. Iadicicco, S. Campopiano, A. Cutolo, M. Giordano, A. Cusano, "Non-Uniform Thinned Fiber Bragg Gratings for Simultaneous Refractive Index and Temperature Measurements", IEEE Photonics Technology Letters 2005 (in press).

PHYSICAL SENSORS

A STRAIN GAUGE SENSOR BASED ON AN ORGANIC FIELD EFFECT TRANSISTOR

ILEANA MANUNZA, ALESSANDRA SULIS
INFM-University of Cagliari Department of Electric and Electronic Engineering, piazza d'Armi
09123 Cagliari, Italy

ANNALISA BONFIGLIO
INFM-University of Cagliari Department of Electric and Electronic Engineering, piazza d'Armi
09123 Cagliari, Italy
INFM-S3 "nanoStructures and bioSystems at Surfaces", Modena, Italy

An organic, completely flexible strain gauge sensor based on a field effect devise has been fabricated. The proposed device consists in a "bottom contact" structure assembled on a flexible free standing insulating layer, without any substrate, with source, drain contacts and the active semiconductor layer on one side and the gate on the opposite side. The main advantage consists in avoiding the presence of a substrate thus allowing to apply a mechanical stimulus directly on the channel area. Thanks to the flexibility of the substrate and the low cost of the employed technology, this device opens up a new perspective for producing strain gauge devices from organic field effect transistors.

1. Introduction

Since late 70's organic thin-film transistors based on conjugated oligomers and polymers have been fabricated since they are inherently flexible and ultralow in cost even for large area[1]. So far, great progress has been made in the field of optoelectronic devices, like Organic Light-Emitting Diodes (OLEDs)[2] and for switching functions by means of Organic Field Effect Transistors (OFETs)[3].

Organic semiconductors offer several advantages due to easy processing, good compatibility with a wide variety of substrates including flexible plastics, and great opportunities in terms of structural modifications. Nevertheless, only few examples of organic semiconductor based field effect strain sensors have been presented[4,5] so far. The concept of the strain gauge sensor derived from a fied effect device is based on the reproducible variation in channel conductivity recorded when a mechanical stimulus is applied to the channel area of the device. The realization of flexible devices based on organic semiconductors is

particularly interesting in this perspective, because these materials are inherently soft and can be assembled in a flexible structure that can be applied on whatever substrate to measure its mechanical deformation.

2. Experimental

2.1. *Device Fabrication*

Recently, a fully flexible structure for field effect devices has been produced[6]. The main advantage of this structure is that it is assembled starting from a flexible insulating film, but without any substrate. In this way, it is possible to apply a mechanical stimulation to the channel area of the device by directly contacting the gate side of the insulating film.

The basic structure of the device is shown in Figure 1

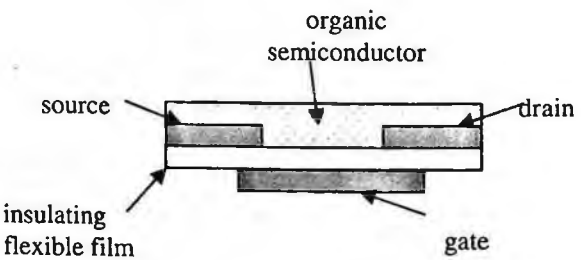

Figure 1. Basic structure of the device

A 900 nm-thick MylarTM sheet (Du Pont), stuck to a plastic frame, works as insulator and, at the same time, as a free-standing surface for device assembling. The Mylar™ sheet has a dielectric constant close to that of silicon dioxide (3.3) and a dielectric rigidity of 10^5 V/cm that allows to apply a gate bias sufficiently high to induce a field-effect in the organic semiconductor

Bottom-contact Au source and drain electrodes have been patterned on one side of the dielectric using a standard photolithographic technique whilst the Au gate electrode has been thermally evaporated on the opposite side of the insulating layer. W/L ratio of 250 (W and L are the channel width and length, respectively), with L = 25 μm, have been used.

Prior to organic deposition, the substrate has been cleaned with acetone, washed with deionized water, and dried with a Nitrogen flux.

Pentacene (Sigma Aldrich) has been used as received. Pentacene films have been grown by vacuum-sublimation at a nominal deposition flux of about 1 Å/s.

2.2. *Experimental Test*

Measurements of drain-source current (Ids) versus drain-source and gate-source voltages have been carried out at room temperature in air, by means of a HP 4155 Semiconductor Parameter Analyzer.

In order to avoid ageing effects, all measurements have been performed immediately after pentacene deposition.

Mechanical stimulus has been applied by means of a step motor that bears a small metal sphere on top of it. The film with the device on it is suspended on a plastic frame and the sphere is in contact with the bottom (gate) side of the film. In this way by extending or retracting the step motor, it is possible to apply a variable mechanical pressure on the film.

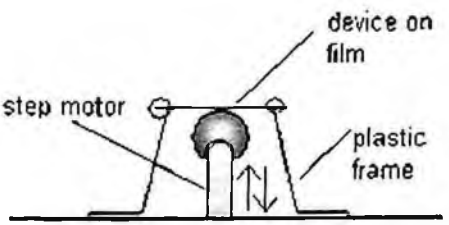

Figure 2 Scheme of the measurement setup.

3. Results and discussion

The device has the typical behaviour of organic p-type field effect transistors, working in accumulation mode, with increasing negative values of Ids with increasing negative Vds values and with a clear field effect induced by the Vgs voltage. Figure 3 shows the output characteristic of the unstrained device. Typical recorded values of hole mobilities are, in the range of 10^{-3}-10^{-2} cm^2/Vs, while threshold voltages are of the order of a few Volts.

Before applying the mechanical stress cycle, the devices were biased with a fixed value of V_{DS} and V_{GS} and left several minutes for complete stabilization of the electrical characteristics.

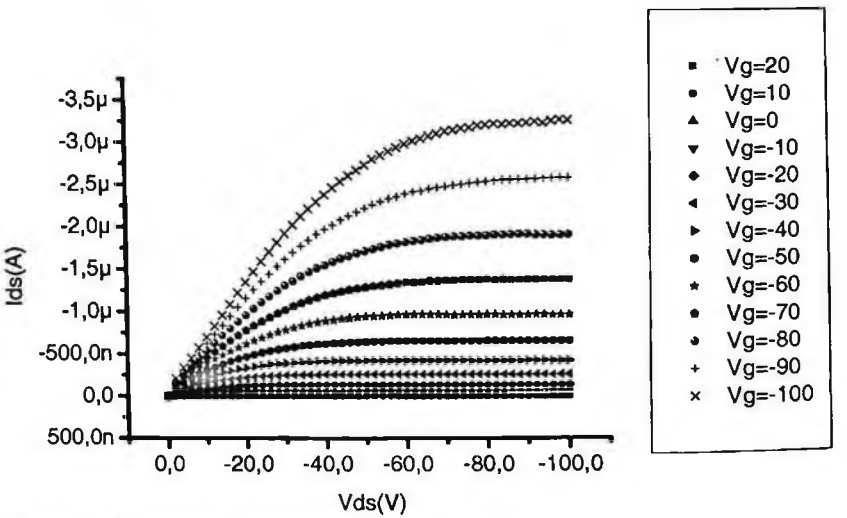

Figure 3 Output characteristic of the unstrained device.

Figure 4 shows Ids versus time during a complete strain/unstrain cycle (at Vds = -80V and Vgs=-80V)

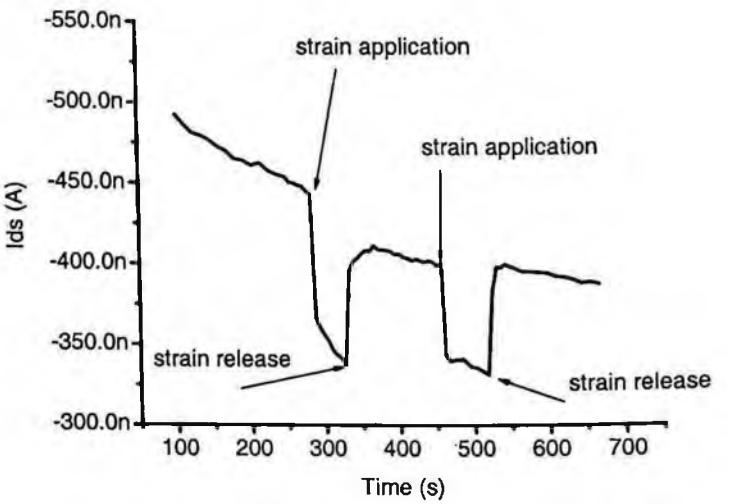

Figure 4 I_{ds} versus time during a complete strain/unstrain cycle (bias conditions: Vds = -80 V, Vgs = -80 V). Arrows indicate the instant in which the strain was applied (or released). Initially the device was unstrained.

When a mechanical stimulus (a pressure) is applied to the gate side of the device, there are modifications of the geometrical dimensions of the channel (W/L ratio) and a stretching of both insulating and semiconductor layers.

Altogether, these modifications reflect on the intensity of the current through the channel. As a matter of fact variation of W and L are similar, being Mylar an isotropous film. As a consequence the W/L ratio should not contribute to the current variation. The stretching of the insulating film should produce a thinning effect on the layer, thus producing an increase of capacitance. If this would happen we should observe a current increase, that is not verified. Therefore it seems more plausible that the observed effect of current decreasing after the application of the mechanical stimulus, is mainly due to the stretching of the semiconductor layer, that produces a reduction in the carrier mobility. A possible explanation of this phenomenon can be tempted: as pentacene layers have a granular morphology (that is known[7] to strongly affect the mobility properties), it is likely that, by stretching the insulating layer, the grains are forced to separate, thus making more difficult the propagation of charge between adjacent grains.

4. Conclusions

In conclusion, we have proven the possibility of obtaining a strain gauge sensor completely flexible based on pentacene films grown on bottom-contact Au-patterned on 900 nm-thick Mylar™ gate dielectric. The electrical characteristics indicate that the device behaves as a typical p-channel transistor working in accumulation mode. Output current is modulated by a mechanical stimulus applied on the gate side of the device. Taking advantage of the full mechanical flexibility of the insulating sheet, attractive developments of the device structure can be envisaged.(e.g "robot skin" applications) .

References

1. S. R. Forrest, Nature **428**, 911 (2004).
2. 2.T. Tsujimura, SID 2003 Technical Digest Vol.XXXIV, Book 1,6 (2003).
3. C. Dimitrakopoulos and P. R. L. Malenfant, Adv. Mater. **14**, 99 (2002).
4. T. Someya, T. Sekitani, S. Iba,Y. Kato, H. Kawaguki, R. Teramoto,T. Sakurai, PNAS, **101**, 27 (2004)
5. Sciligno et al, IEEE Sens Journ , **3**, 4 (2003).
6. A. Bonfiglio, F. Mameli, and O. Sanna, Appl. Phys. Lett. 82, 3550 (2003).
7. G. Horowitz and M. E. Hajlaoui, Synthetic Metals 122 (2001) 155-189

POROUS SILICON MATRICES FOR RADIOISOTOPIC PHANTOMS

G. DI FRANCIA, V. LA FERRARA, I. NASTI
Portici Research Centre, ENEA, Naples, Italy

L. MONTANI, G. IURLARO, F. MARRACINO, R. SCAFÈ*
Casaccia Research Centre, ENEA, Rome, Italy

The feasibility of radioisotopic planar sources made by absorption of an active solution in Porous Silicon (PS) matrices has been studied. To this aim two PS samples, characterized by different pore dimension and shape, have been made and tested. The ^{99m}Tc radiotracer, commonly used in nuclear medicine departments, has been loaded into the pores by immersion, and the radioactivity distribution over the porous areas has been measured by an Imaging Probe (IP). Using a solution with the low specific activity of 5.8 MBq/cc, counting rates of 96±3 and 36±2 counts/s per pixel (area 3.5x3.5 mm^2) have been measured, showing good emission homogeneity for both PS samples. A mean activity ratio of 2.6±0.4 has been found between the two samples. Further studies are in progress to optimize matrices treatment and loading techniques and to design porous phantoms having appropriate surface areas, shapes and absorbance.

1. Introduction

Nuclear medicine imaging requires phantoms with standard patterns and geometries whose specific activity is known with adequate precision to perform detectors quality assurance tests [1,2,3]. A more recent request for precise small area patterns is emerging in techniques such as small-animal imaging and coded aperture imaging, mainly dedicated to radiopharmaceutical studies and to spatial resolution improvement, respectively [4,5]. Using PS matrices with particular structures, previously impregnated with ^{99m}Tc pertechnetate, it would be possible to make radio-emitting phantoms of different activity, shape and dimension.

* Corresponding author: scafe@casaccia.enea.it; Ph: +3906-3048-3434; Fax: +3906-3048-3989

2. Materials and Methods

2.1. *Fabrication of Porous Silicon matrices*

Two PS samples have been fabricated by electrochemical etching, in a HF based solution, of p and n type <100> oriented crystalline silicon with a resistivity of 10 Ω×cm and 1 Ω×cm for P10 and N1 samples respectively. Figure 1 shows SEM images of PS samples concerning $7x10^{-3}mm^2$ and $7x10^{-5}mm^2$ areas of P10 and N1, respectively. Table 1 summarizes the etching condition and PS samples main specifications.

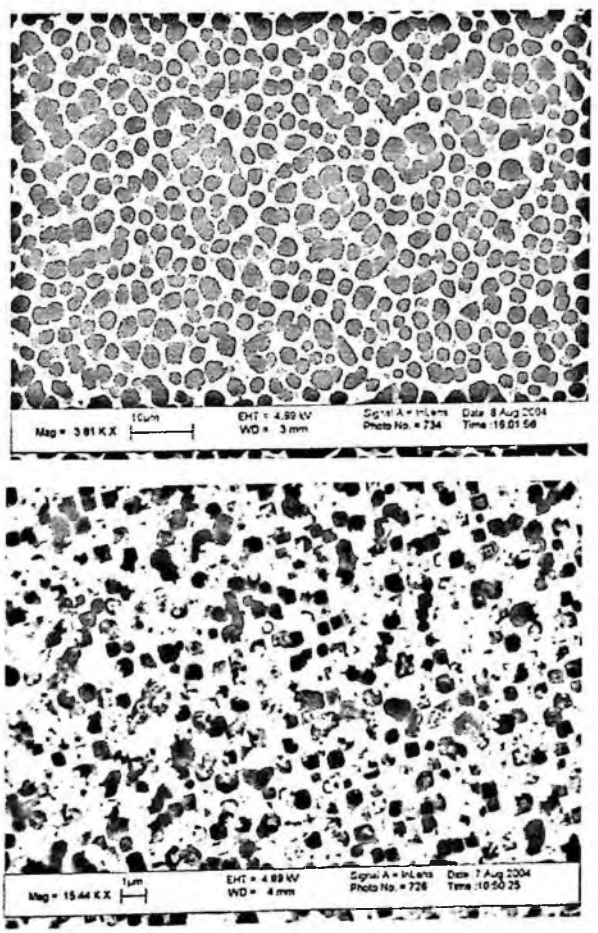

Figure 1. SEM images of PS samples concerning $7x10^{-3}$ mm^2 and $7x10^{-5}$ mm^2 areas of P10 (top) and N1 (bottom), respectively.

Electrochemical anodization was performed using a typical cell arrangement [6]. To ensure good ohmic contact, the back side of P10 sample was coated using 5000 Å e-gun evaporated aluminum while N1 sample was coated by 900 Å e-gun evaporated Indium Thin Oxide.

Table 1. Etching conditions and PS samples main parameters.

Sample	P10	N1
Etching Solution	2M HF/ acetonitrile/H_2O	HF (MOS, 50% in weight):IPA =7:3 + illumination by 250 W Hg Lamp
Current Density (mA/cm^2)	7	40
Etching Time (min)	120	2
Sample diameter (mm)	45	47
Pore Shape	Circular (Φ = 3.2 μm)	Square (L = 0.6μm)
Pore density (μm^{-2})	9.47	1.06

After the etching samples were rinsed in pentane and dried in air. Freshly prepared PS surface is hydrophobic so it has been immersed in a solution of 10% NaOH in water to make the surface hydrophilic and to be able to absorb the radiotracer.

2.2. *Radioisotope Loading*

^{99m}Tc is the most popular radionuclide in diagnostic nuclear medicine departments and therefore $^{99m}TcO^-_4$ solution has been used for phantom loading. The ^{99m}Tc pertechnetate is sterile, without anti-microbe conserving, tested for apyrogenicity and with physiological pH. It can be obtained directly from a ^{99}Mo - ^{99m}Tc generator ELUMATIC III which utilizes saline solution (NaCl at 0.9% in H_2O) for elution [1,7].

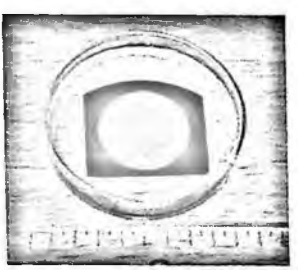

Figure 2. P10 sample soaked in $^{99m}TcO_4^-$ solution.

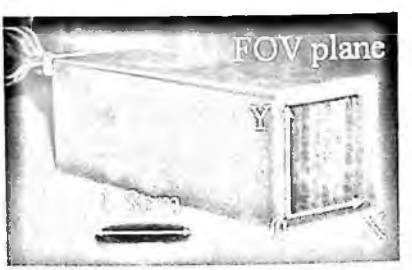

Figure 3. Detector used for radioactivity measurements.

To perform measurements with a proper count rate, a 5.8 MBq/cc specific activity $^{99m}TcO^{-}_{4}$ solution has been prepared. PS matrices have been loaded by immersion in the radioactive solution for two hours using a polystyrene non-pyrogenic dish (Figure 2). Thereafter each PS sample has been dried out with a lamp and coated with a thin plastic film to avoid detector contamination during measurements.

2.3. *Radioactivity Measurements*

Radioactivity spatial distribution has been analyzed using an IP [8] with a $26\times26mm^2$ field of view (FOV). The IP is characterized by an integrated collimator-scintillator matrix made of a tungsten parallel collimator with 49 parallelepiped CsI(Tl) crystal pixels (by Hilger Crystals, UK) inserted in its square holes. Septa are 6mm height and 0.2mm thick and crystal pixels are 5mm thick. Each CsI(Tl) element has five faces fine machined, wrapped in a white carbon polymeric film, and the output face polished.

Light detection is performed through a Hamamatsu R8520-00-C12 position sensitive photomultiplier tube [9] coupled to the crystal array via a planar Perspex light guide. Charge multiplication is obtained with 11 metal channel dinodic stages and charge readout is performed through 12 crossed anode strips.

The experimental result consists of a 7×7 counts matrix corresponding to 49 counters each measuring a $3.5\times3.5mm^2$ sample area.

To analyze a PS surface more extended than the FOV, three experimental conditions have been studied: a) PS samples centered on the detector FOV; b) samples shifted 1cm along X axis; c) samples rotated by 90° on the XY plane (Figure 4). Activity measurements have been performed at the minimum applicable sample to detector distance. To compute the imager uniformity corrections a calibrated Co^{57} planar source has been used; its activity is uniformly distributed over a dish with a diameter of 50mm and 4mm height.

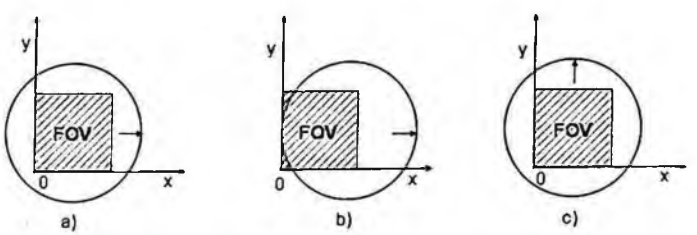

Figure 4. Schematic drawing of measurement geometry in three experimental conditions. The circle represents the PS sample and the square is the imager; the arrow symbolizes the sample orientation: a) sample centred on the FOV; b) sample shifted 1cm along X axis; c) sample rotated by 90° on the XY plane.

3. Results and Conclusions

In Figure 5 are reported images of the two PS samples obtained in experimental condition type a (Figure 4). In the images each pixel corresponds to a crystal element of the scintillation matrix.

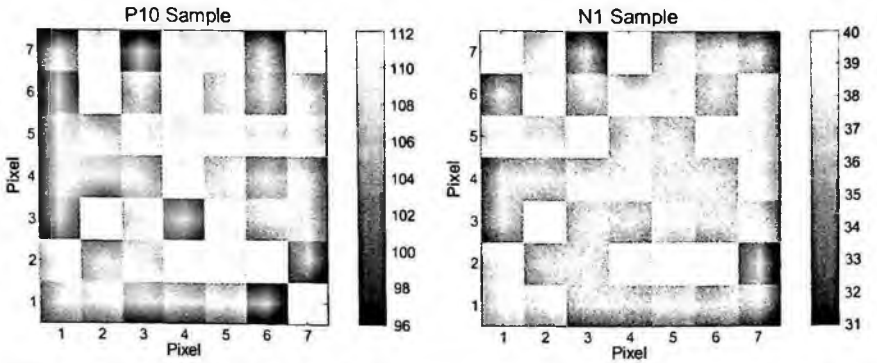

Figure 5 Images obtained with P10 and N1 samples centered on the detector FOV. Each pixel represents a 3.5x3.5 mm^2 sample area and the gray-scale corresponds to the measured counts in it.

Radioactivity emission measurements on P10 and N1 samples have been corrected for detector non homogeneity, radioactive decay and background. Mean counting rates per pixel and their standard deviations are reported on Table 2; counting ratio (P10/N1) is the same in the three experimental conditions within the uncertainties.

Table 2. Mean counting rates per pixel and standard deviations.

Position	a)		b)		c)	
Sample	P10	N1	P10	N1	P10	N1
Mean ± St.Dev. (cps/pixel)	104±4	35±2	88±4	34±2	106±8	44±4
Counting ratio (P10/N1)	2.9±0.5		2.6±0.3		2.4±0.4	

We have measured 96±3 and 36±2 cps/pixel mean counting rates, on P10 and N1 respectively, showing a good homogeneity within 2σ. PS samples activity ratio has been evaluated as the mean counting ratio, giving a value of 2.6±0.4.

Note that, even if the experimental setup could be optimized as below specified, the uncertainties on measured homogeneity are comparable to that of reference radioisotopic source used for calibration. The experimental setup for

homogeneity measurements can be improved increasing: (a) the detector FOV to analyze a more extended area, (b) the collimator length to better select the source zones and (c) the detector lateral shielding.

Some theoretical parameters have been considered to relate this experimental value to pore geometry and a good agreement has been found with a parameter related to pore internal area. Further studies will be performed to confirm this hypothesis. Moreover, to understand the mechanism of radioisotope absorption, the very low absolute percentage by weight of Tc in the solution has to be taken into account. In fact, in the present experiment, 0.5ng of ^{99m}Tc were used corresponding to a 0.03 ppb concentration.

Acknowledgments

This work was supported by ENEA under project P466 "Functional Imaging in Nuclear Medicine and Biology".

References

1. R.Chandra: "Nuclear Medicine Physics – The basics" – sixth edition, Lippincott Williams & Wilkins, Philadelphia (USA), pp.34-38, (2004).
2. International Commission on Radiological Units: "Medical Imaging - The Assessment of Image Quality", Report 54, Bethesda (USA), (1996) pp.11-22.
3. A.Rose: "The Sensitivity Performance of the Human Eye on an Absolute Scale", Journal of the Optical Society of America, Vol.38, N.2 (1948), pp.196-208.
4. J.R.English et al.: "Sub-Millimeter Technetium-99m Calibration Sources", Molecular Imaging and Biology, Vol.4, N.5, pp.380-384, (2002).
5. R.Accorsi et al.: "Optimal coded aperture patterns for improved SNR in nuclear medicine imaging" Nucl. Instr. Meth. A 474 (2001) 273–284.
6. A.Halimaoui, In: Canham L. (Ed.), "Properties of Porous Silicon", INSPEC Publisher, London (UK), pp. 12-22, (1997).
7. CIS bio international, Filiale di Schering S.A.: "ELUMATIC III® Generatore di Tecnezio [^{99m}Tc] - Istruzioni per l'uso", (2001).
8. R.Massari et al.: "New Imaging Probe with Crystals Integrated in Square Holed Collimator", 2004 IEEE NSS-MIC, Conf. Record, M10-236 (2004).
9. Hamamatsu Photonics K.K.: "Position Sensitive Photomultiplier Tube R8520-00-C12", Technical Data Sheet, Japan, (2000).

DESCRIPTION AND POSSIBLE APPLICATIONS OF A TABLETOP LASER SYSTEM

C. BELLECCI, P. CIUFFA, M. FRANCUCCI, P. GAUDIO, S. MARTELLUCCI, M. RICHETTA, A. RYDZY

Dipartimento di Ingegneria dell'Impresa, Facoltà di Ingegneria, Università di Roma "Tor Vergata", Via del Politecnico 1, 00133 Roma, Italy

S. BOLLANTI, F. FLORA, P. DI LAZZARO, D. MURRA

ENEA, Dipartimento Innovazione, Settore Fisica Applicata, 00044 Frascati (Roma), Italy

Tabletop pulsed laser systems have been demonstrated to be of great relevance in many applications and studies. They have been widely used in several fields. Among them one can mention: generation of plasma on solid, liquid or gaseous targets; spectroscopic X rays analyses; imaging; microlithography; microscopy; radiographies (in particular of biological samples); conversion efficiency studies (laser to X or UV radiation); radiation matter interaction studies; plasma parameter determination; astrophysical studies, and so on. In this article it is reported a description, characterization and performance study of our Nd:YAG/Glass ultraintense tabletop pulsed laser system. It is located at University of Rome "Tor Vergata" and it used to produce X and UV rays by means of laser induced plasma.

1.1. *Introduction*

The laser–plasma interaction is presently a subject of large and growing interest [1]. It attracts not only the attention of plasma physics community, but also of others communities like those of laser physics, spectroscopy, multiphoton physics and so on. This growing interest is due to the availability of laser systems with unique properties [2, 3] and powerful computing means in many basic research laboratory, and its the perspective of several new possible applications [4 – 7], besides the traditional area of inertial confinement fusion [8, 9]. Nowadays laser plasma techniques are specializing in several branches concerning astrophysics [5, 6], inertial confinement fusion [8, 9], quantum electrodynamics and high energy physics [10 – 12], atomic physics [13] and solid state physics [14], X ray spectroscopy [15 – 20], radiographies [21] and imaging [22, 23].

A high temperature plasma is created when an intense laser pulse is focused onto the surface of a solid target. The intensity of the laser pulse must reach or exceed the threshold for plasma formation, which is typically of about 10^7Watt/cm^2.

The intense laser light is absorbed initially in a thin layer of material (of the order of skin depth) which is heated, melted and vaporized. An expanding plasma cloud is then generated at the solid surface. Working with pulse width larger than 10ps, the timescale of plasma expansion is shorter than the pulse duration and the hydrodynamics effect becomes important. A gradient develops inside the plasma density and laser energy can be absorbed by this plasma while it propagates through the target when laser radiation reaches the critical surface. In this situation plasma frequency equals laser frequency. Laser induced plasmas emit visible, UV and X radiation due to line transitions, radiative recombination and bremmssthralung radiation [24, 25].

Radiative properties represent a classical example of non-interfering probe. Plasma information can be obtained directly from its emission spectrum as ionization balance, density, temperature and chemical composition.

Such consideration can explain the growing interest addressed to radiative properties of hot and dense matter. X ray spectroscopy of multicharged ions appears as one of most powerful techniques available for investigating high temperature plasmas.

For example, the X ray emission spectrum from He−like ions has been used as diagnostic for several type of hot plasmas (magnetically confined plasmas, laser induced plasmas, astrophysical plasma) [26 − 29].

The apparatuses described above are called *ultraintense tabletop pulsed laser systems* and have dimensions comparable with those of an optical table. In this paper a description, characterization and performance study of our laser facility, located at University of Tor Vergata, is reported. It is based on four solid state Nd:YAG/Glass active mediums that produce an ultraintense laser pulse. The system will be improved for obtaining an EUV ray source by laser induced plasma for microlithography applications.

1.2. *Apparatus description*

The apparatus is shown in figure 1 and consists of: a four-amplification stages nanosecond laser source emitting in the near infrared, a lens system that focuses the laser beam on the target and a two-stage vacuum chamber where plasma is generated.

The laser is a no commercial Q-switching solid-state source which can work at a maximum frequency of 1shot/2min, to minimize thermal lens effects growing inside the various amplifier rods.

The oscillator (type Nd:YAG) emits pulsed laser radiation with the following features:

1) wavelength $\lambda = 1064$nm (infrared); 2) pulse width $\tau = 15$ns; 3) energy $E_p = 36$mJ; 4) TEM_{00} emission mode; 5) polarization (P) parallel to optical table; 6) maximum pulse repetition rate PRR = 10Hz.

The first and second amplifiers (#A) (type Nd:YAG) can work at a maximum pulse frequency of 10Hz and their output energy per pulse is of about 220mJ and 780mJ respectively.

The third and fourth amplifier are made of Nd:Glass. For this reason they must exceed 1 shot / 2 minutes as repetition rate, otherwise thermal lens effects will occur. The maximum output energy is about respectively 3.94J and 10J at the output of the final stage.

The laser beam focusing system is made of a single convergent lens with a focal length of about 20cm and it is located inside the double vacuum chamber. The laser beam, after the forth amplifier, enters into the vacuum chamber passing through a glass flange and the single lens and it is focused onto the target (generally solid) to generate plasma. The spot dimension is of about 100μm.

Inside the vacuum chamber there are a spectrometer to analyze the plasma radiation and one or more detectors to measure soft X radiation emitted by plasma.

At the moment in our laser setup, there are also two optical isolators, the first of which is positioned between the oscillator and the 1°A, while the second one is set between the 1°A and the 2°A.

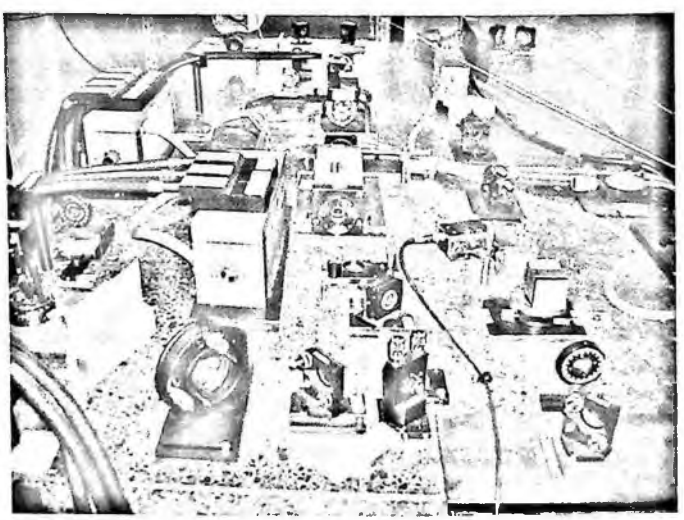

Figure 1. Setup of apparatus.

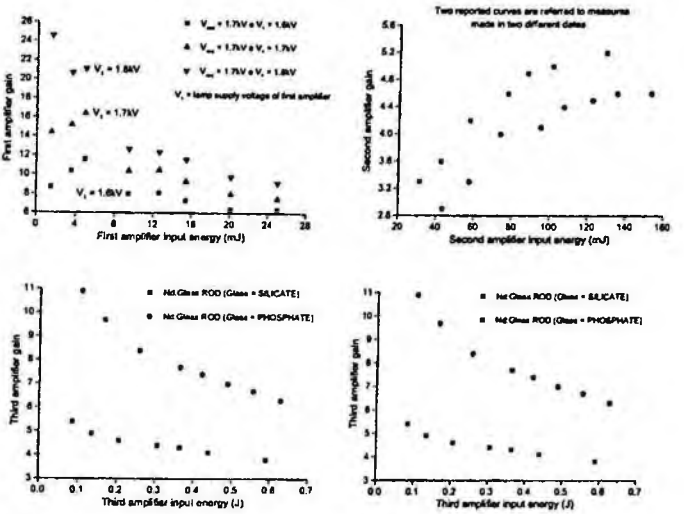

Figure 2. Performance study of four amplifiers of our Nd:YAG/Glass laser source.

1.3. *IR → soft X ray conversion efficiency estimation for different solid targets*

A study concerning the conversion efficiency η from infrared (IR) laser radiation to soft X rays emitted by various solid targets has been carried out to find targets with the better IR → soft X ray conversion efficiency, results are reported in fig. 3. Soft X rays emitted in the region between 1.3keV and 1.55keV (8Å ÷ 9.56Å) has been selected through an aluminium filter of total thickness of 45μm, placed in front of the detector, which consists in a PIN photodiode. The solid targets utilized in measurements were: Mg, Ti, Fe, Cu, Zn, Y. bNext figure shows the laser energy (E_{laser}) and the laser intensity range, respectively (3.25J - 9.91J) and ($2.76*10^{12}W/cm^2$ - $8.41*10^{12}W/cm^2$) for the lens located in the focus position.

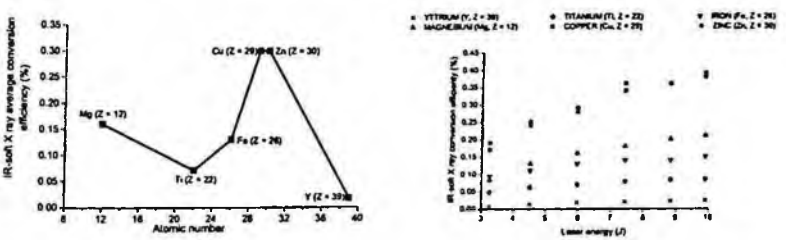

Figure 3. IR → soft X ray conversion efficiency estimation for six different solid targets.

1.4. *Conclusions*

In this paper we have described the Tor Vergata Nd:YAG/Glass ultraintense laser facility, that is an example of *ultraintense tabletop pulsed laser system.* This apparatus is used to generate plasmas on solid targets with various conditions as different electron or ion temperatures, different electron density, different optical thickness and charge state, etc.

So we have demonstrated that our apparatus is able to produce soft X rays from laser induced plasma through the estimation of conversion efficiency (η) from infrared (IR) laser radiation to soft X rays for six different solid targets in the X ray spectral region 1.3–1.55keV (that is 8–9.56Å). In the future we intend to improve our setup for working with gas targets and produce EUV radiation (about 13 nm) for microlithography applications.

References

1. W. L. Kruer, *Physics of Laser Plasma Interaction*, Addison Wesley, Redwood City, CA (1988).
2. M. D. Perry and G. Morou, *Science* **264**, 917 (1994).
3. G. Morou, J. Barty and M. D. Perry, *Physics Today* Jan 1998.
4. I.C.E. Turcu and J.B. Dance, *X ray from laser plasma: Generation and Applications*, Wiley, London (1998).
5. B. A. Remington, D. Arnett, R. P. Drake and H. Takabe, *Science* **284**, 1488(1998).
6. B. A. Remington, D. Arnett, R. P. Drake and H. Takabe, *Phys. Plasmas* **7**, 1641 (2000).
7. E. P. Liang, S. C. Wilks, and M. Tabak, *Phys. Rev Lett.* **81**, 4887 (1998).
8. J. D. Lindl, *Phys. Plasmas* **2**, 3933(1995).
9. W. Hogan et al., *Energy from Inertial Fusion, IAEA*, Vienna (1994).
10. K. W. D. Ledingham and P. A. Norreys, *Contemp. Phys.* **40**, 367 (1999).
11. T. Tajima and J. M. Dawson, *Phys. Rev. Lett.* **43**, 267 (1979).
12. A. Pukhov , Z. M. Sheng, and J. Meyer ter –Vehn, *Phys. Fluids* **6**, 2847 (1999).
13. M. Gavrila, *Adv. At. Mol. Opt. Phys. Suppl.* **1**, 435 (1992)
14. P. Celliers et al, *Phys Rev. Lett.* **84**, 5564 (2000).
15. K. B. Fournier, A. Ya. Faenov, T. A. Pikuz, I. Yu. Skobelev, F. Flora, S. Bollanti, P. Di Lazzaro, D. Murra, A. Grilli, A. Reale, L. Reale, G. Tomassetti, A. Ritucci, I. Bellucci, S. Martellucci, G. Petrocelli, *J. Phys. B: At. Mol. Phys.* **35**, 3347 (2002).
16. I. Yu. Skobelev, A. Ya. Faenov, T. A. Pikuz, A. I. Magunov, F. Flora, S. Bollanti, P. Di Lazzaro, D. Murra, A. Reale, L. Reale, G. Tomassetti, A.

Ritucci, G. Petrocelli, S. Martellucci, N. Lisi, F. B. Rosmej, *Journal of Experimental and Theoretical Physics* **95**, 421 (2002).

17. K. B. Fournier, A. Ya. Faenov, T. A. Pikuz, I. Yu. Skobelev, F. Flora, S. Bollanti, P. Di Lazzaro, D. Murra, A. Reale, L. Reale, G. Tomassetti, , A. Ritucci, I. Bellucci, S. Martellucci, G. Petrocelli, V. S. Belyaev, V. I. Vinogradov, A. S. Kyrilov, A. P. Matafonov, *Journal of Quantitative Spectroscopy & Radiative Transfer* **81**, 167 (2003).
18. K. B. Fournier, A. Ya. Faenov, T. A. Pikuz, A. I. Magunov, I. Yu. Skobelev, V. S. Belyaev, V. I. Vinogradov, A. S. Kyrilov, A. P. Matafonov, F. Flora, S. Bollanti, P. Di Lazzaro, D. Murra, A. Reale, L. Reale, G. Tomassetti, A. Ritucci, M. Francucci, S. Martellucci and G. Petrocelli, *J Phys. B: At. Mol. Opt. Phys.* **36**, 3787 (2003).
19. K. B. Fournier, A. Ya. Faenov, T. A. Pikuz, A. I. Magunov, I. Yu. Skobelev, F. Flora, S. Bollanti, P. Di Lazzaro, D. Murra,, V. S. Belyaev, V. I. Vinogradov, A. S. Kyrilov, A. P. Matafonov, M. Francucci, S. Martellucci, G. Petrocelli, *Physical Review E* **70**, 016406 (2004).
20. A. Ya. Faenov, T. A. Pikuz, I. Yu. Skobelev, A. I. Magunov, V. P. Efremov, M. Servol, F. Quéré, M. Bougeard, P. Monot, Ph. Martin, M. Francucci, G. Petrocelli, P. Audebert, *JETP Letters* **80**, 730 (2004).
21. L. Reale, A. Lai, A. Tucci, A. Poma, A. Faenov, T. Pikuz, F. Flora, L. Spano, T. Limongi, L. Palladino, A. Ritucci, G. Tomassetti, G. Petrocelli, M. Francucci, S. Martellucci, *Microscopy Research and Technique* **64**, 21 (2004).
22. T. Pikuz, A. Faenov, I. Skobelev, A. Magunov, M. Sanchez del Rio, L. Alianelli, G. Baldacchini, F. Flora, S. Bollanti, P. Di Lazzaro, D. Murra, G. Tomassetti, A. Ritucci, A. Reale, L. Reale, M. Francucci, S. Martellucci, G. Petrocelli, *Proceedings of SPIE 5196*, 362 (2004).
23. T. Pikuz, A. Faenov, I. Skobelev, A. Magunov, L. Labate, L. A. Gizzi, M. Galimberti, A. Zigler, G. Baldacchini, F. Flora, S. Bollanti, P. Di Lazzaro, D. Murra, G. Tomassetti, A. Ritucci, A. Reale, L. Reale, M. Francucci, S. Martellucci, G. Petrocelli, *Laser and Particle Beams* **22**, 289 (2004).
24. R. Falkone and M. Murname, *AIP Conf. Proc.* **147**, 81 (1986).
25. M. Murname, H. C. Kapteyn, M. D. Rosen, and R. Falkone, *Science* **251**, 531 (1991).
26. E. Kallne, J. Kallne, and A.K. Pradhane, *Phys. Rev. A* **28**, 467 (1983).
27. K.J. Phillips, F.P. Keenan, L.K. Harra, S.M. McCann, E. Rachlew-Kallne, J.E. Rice, and M. Wilson, *J.Phys. B* **27**, 1939 (1994).
28. A.H. Gabriel, Mon. Not. R. Astron. Soc. **160**, 99 (1972).
29. T. Kato, T. Fujiwara, and Y. Hanaoka, *Astrophys. J.* **492**, 822 (1998).

TEMPERATURE-COMPENSATED FBG SENSOR FOR EXTENDED STRAIN RANGE MEASUREMENTS

RICCARDO FALCIAI, COSIMO TRONO

Istituto di Fisica Applicata N. Carrara (IFAC) - CNR,
Via Panciatichi 64, 50127 Florence, Italy

In this work a temperature-compensated configuration for extending the working range of fiber Bragg grating (FBG) strain sensors has been proposed. This technique consists of the application of two FBGs to the opposite surfaces of a straight elastic beam which was bent in a horizontal direction. Pushing nearer of beam ends produced the beam curvature variation measured by means of the two FBG wavelength difference The difference of the two FBG wavelengths depends on the beam curvature, while the mean value is taken in order to compensate for the temperature effects.
The sensitivity of the system was obtained for different beam lengths. Decreasing the beam length increases the sensitivity, but decreases the working range.
The sensor proposed is less fragile than the bare fiber and constitutes a displacement sensor particularly suited for applications to breaks or separate elements of structures where it is impossible to affix the bare fiber.

1. Introduction

Since the development of an efficient writing technique[1], fiber Bragg gratings (FBG) have been considered excellent sensor elements, that are suitable for measuring temperature, strain or pressure[2]. Myriad applications have been discussed in the open literature: applications to civil engineering structural monitoring[3], aircraft and aerospace[4], and composite materials[5], are only a few examples of FBG applications in sensing. Applications to the cultural heritage have also been reported recently, in particular for the monitoring of deformations in wooden panel paintings[6]. The monitoring of these wooden structures could be very difficult in certain situations, for example on breaks in the wood in which the deformations should be very large: greater than the range of FBGs on a bare fiber. In such a situation, the fiber must be fixed in two points before and after the gratings, and should be pretensioned by taking into account the estimated break contraction. The measurement is limited by the FBG measurement range, which is approximately 8 mstrain (mε).

We propose an original temperature-compensated configuration for extending the working range of fiber Bragg grating (FBG) strain sensors and particularly suited for application as displacement sensor.

2. Working principle

Two gratings (FBG_{up} and FBG_{lo}) were glued in a central position to the opposite surfaces of a straight elastic beam, with length L and thickness h, which was bent in a horizontal direction (Figure1).

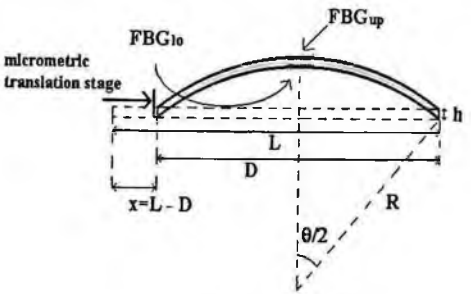

Figure 1. Experimental setup.

Two gratings (FBG_{up} and FBG_{lo}) were glued in a central position to the opposite surfaces of a straight elastic beam, with length L and thickness h, which was bent in a horizontal direction (Figure 1). If R is the curvature radius and θ the arc angle, the chord length D will be:

$$D = 2R \cdot sin\left(\frac{\theta}{2}\right) \tag{1}$$

If θ is sufficiently small, it is possible to approximate the *sin* function with the first two terms of the Taylor series:

$$sin\left(\frac{\theta}{2}\right) \approx \frac{\theta}{2} - \frac{\theta^3}{48} + \ldots \tag{2}$$

and equation (1) becomes:

$$D = 2R \cdot \left(\frac{\theta}{2} - \frac{\theta^3}{48}\right) \tag{3}$$

By writing the arc angle as a function of the beam length L and the curvature $c=1/R$ and by combining equations (1) and (2) it is possible to express the horizontal displacement $x=L-D$ as a function of the beam curvature:

$$x = L - D = \frac{L^3}{24} \cdot c^2 \tag{4}$$

On the other hand, by measuring the strain ε on the beam surface at a distance $h/2$ from the neutral axis, the curvature can be written as $c=2\varepsilon/h$ and, by representing the Bragg wavelength shift as $\Delta\lambda_{Bragg} = k_\varepsilon \cdot \varepsilon$ and introducing the wavelength shift difference $\Delta\lambda_{up\text{-}lo}$ between FBG_{up} and FBG_{lo} and h' (effective distance between the two fiber cores), it results:

$$x = L - D = \frac{L^3}{24 \cdot h'^2 \cdot k_\varepsilon^2} \cdot \Delta\lambda_{up-lo}^2 \tag{5}$$

and, by introducing coefficient a:

$$a = \frac{L^3}{24 \cdot h'^2 \cdot k_\varepsilon^2} \tag{6}$$

we can write:

$$x = a \cdot \Delta\lambda^2_{up-lo} \tag{7}$$

which means a quadratic relation between the horizontal displacement and the Bragg wavelength shift.

3. Experimental validation

For the experimental validation, two FBGs were glued in a central position on the upper and lower surfaces of a 19 cm long and 0.3 mm tick bronze beam. The beam was bent by means of a micrometer translation stage (1 μm precision), and the Bragg wavelengths were measured with a precision of 1 nm. Afterwards the beam ends were cut symmetrically (two centimeters per side), obtaining a 15-cm-long beam with the grating glued in the same condition. The measurement was then repeated.

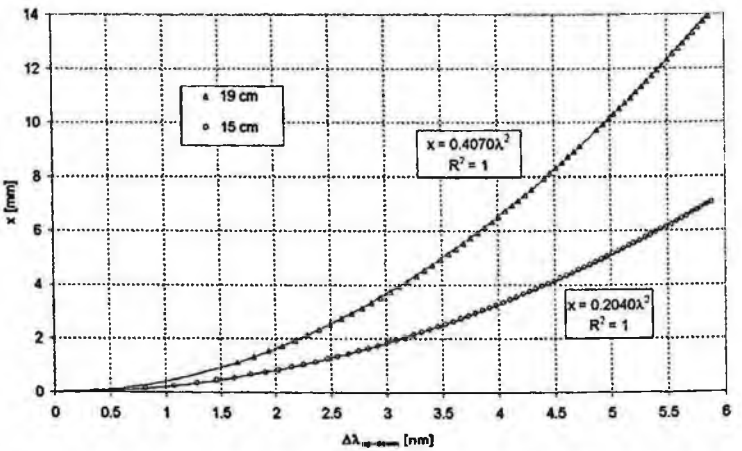

Figure 2. Calibration curves for 19 cm and 15 cm long beams.

The data from the two cases are reported in Figure 2 (symbols Δ and o, respectively) and fitted by least-square fit to a second order polynomial, which gives the most probable coefficient *a*. The obtained coefficients a_{15} and a_{19} from the fits are:

a_{15} *(measured)* = (0.2040±0.0004) mm*nm^{-2},

a_{19} *(measured)* = (0.407±0.002) mm*nm^{-2},

respectively.

If the beam length and thickness and the fiber diameter (250 μm) are known, it is also possible to calculate the theoretical value of these coefficients

from equation (6). With the following numerical values: L_{15} = 15 cm, L_{19} = 19 cm, h = 0.3 mm, h' = 0.55 mm and k_ε = 1200 nm*ε^{-1}, we obtain:

a_{15} *(calculated)* = 0.33 mm*nm^{-2}

a_{19} *(calculated)* = 0.67 mm*nm^{-2}

These values are somewhat different from the fitted values. This is probably due to an error in the evaluation of the quantity h', because of an unknown layer of glue between the beam and the fibers. The same values would be obtained for h' = 0.7 mm, which means a 75 μm thick layer of glue between both the upper and lower fibers and the beam surface, which is plausible. A better validation of equation (6) can be obtained by considering that the only difference between the two cases is the beam length L. This means that it should be:

$$\frac{L_{19}^3}{L_{15}^3} = 2.02 = \frac{a_{19}}{a_{15}} \tag{8}$$

By replacing the measured values, we obtain:

$$\frac{a_{19}}{a_{15}} = \frac{0.407}{0.204} = 1.995 \tag{9}$$

The experimental data are in good agreement with the theoretically predicted behavior, and confirm a cubic dependence on the beam length for the parabola coefficients.

The sensitivity of the sensor is given by:

$$S = \frac{d\left(\Delta\lambda_{up-lo}\right)}{dx} = \frac{1}{dx/d\left(\Delta\lambda_{up-lo}\right)} = \frac{12 \cdot h'^2 \cdot k_\varepsilon^2}{L^3 \cdot \Delta\lambda_{up-lo}} \tag{10}$$

It is directly proportional to the square of the beam thickness and inversely proportional to the cube of the beam length. For a given beam it depends on the inverse of the Bragg difference shift $\Delta\lambda_{up\text{-}low}$ and, hence, on the beam curvature. For example, for the 19-cm-long beam, and for a starting curvature corresponding to x = 7 mm and D = 18.3 mm ($\Delta\lambda_{up\text{-}lo} \approx$ 4.2 nm from equation (7)), the sensitivity for sufficiently small Δx variation, will be S = 0.29 pm*μm^{-1}. By considering a minimum detectable wavelength shift of 1 pm, the minimum detectable distance variation in this configuration is 3.4 μm. We obtained a working range for the sensor of ≈14 mm, without damage, against a range of ≈ 2 mm of a linear FBG sensor of the same length.

4. Temperature compensation

The proposed sensor configuration can make possible an automated temperature compensation. If the gratings are glued in the same position and at the same distance from the beam neutral axis, a curvature variation will produce the same Bragg wavelength shift but in opposite directions for the upper and lower gratings. If, moreover, the beam thermal expansion coefficient was zero,

the temperature effect would be only on the grating refractive indices and in the same way for the two gratings, and automatically compensated by taking the difference $(\Delta\lambda_{up}-\Delta\lambda_{lo})$. However, as the beam thermal expansion is not negligible, a temperature variation will produce two effects: the same Bragg wavelength shift for the two gratings, due to the temperature effects on the fibers and to the expansion of the beam, and, in the meanwhile, the physical elongation ΔL of the beam which produces a curvature variation, following the equation (4), when replacing L with $L+\Delta L$. By supposing that the variations in length are negligible with respect to the beam length L, i.e. $\Delta L<<L$, the dependence between ΔL and the square of the curvature c^2 is linear. This means that a variation in distance ΔD (the parameter that we want to measure) and a thermal expansion ΔL produce the same effect on the curvature and, as a consequence of equation (5), on the quantity $\Delta\lambda_{up-lo}$. In order to compensate this temperature-dependent shift, it is possible to measure the expansion ΔL by means of the Bragg wavelength mean value shift $\Delta\overline{\lambda} = \Delta\left(\frac{\lambda_{up}+\lambda_{lo}}{2}\right)$. In fact, if the two gratings are exactly symmetrical, $\Delta\overline{\lambda}$ will be linearly dependent on temperature T, and ΔL will be proportional to this quantity, so that:

$$\Delta L(T) = \beta \cdot \Delta\overline{\lambda}(T) \tag{11}$$

In considering the thermal expansion, equation (7) can be modified as follows:

$$x + \Delta L(T) = a \cdot \Delta\lambda_{up-lo}^2 \tag{12}$$

and, by combining equation (11) and equation (12), we can write:

$$x = a \cdot \Delta\lambda_{up-lo}^2 - \beta \cdot \Delta\overline{\lambda}(T) \tag{13}$$

The idea is to use the same sensor proposed in this work to obtain parameter β. The beam was heated in a oven and then affixed with a particular curvature on a glass support at room temperature (20 °C). In this way the quantity D, and hence $x=L-D$, in equation (13) remains constant and the variation $\Delta\lambda_{up-lo}$ is produced only by the beam length decrease ΔL during the cooling.

The measurements were made on the 15 cm long beam. The calibration parameter a_{15} was already experimentally obtained above. By measuring the variation $\Delta\lambda_{up-lo}$, the quantity ΔL was obtained from equation (12), with x constant, and related to $\Delta\overline{\lambda}$ in order to obtain the correction coefficient β (equation (11)). Three different values for x (and thus for the beam curvature), were considered: 4.5 mm, 7.2 mm and 8.7 mm. The experimental results for x=4.5 mm are reported in Figure 3.

The obtained coefficients were 0.206 mm*nm^{-1}, 0.213 mm*nm^{-1} and 0.210 mm*nm^{-1}, respectively. This result confirms that β is practically independent from the starting value of $x=L-D$, and that by considering at the same time the

quantities $\Delta\lambda_{up\text{-}lo}$ and $\Delta\bar{\lambda}$, we can obtain from equation (13) measurements directly compensated with respect to the temperature effect.

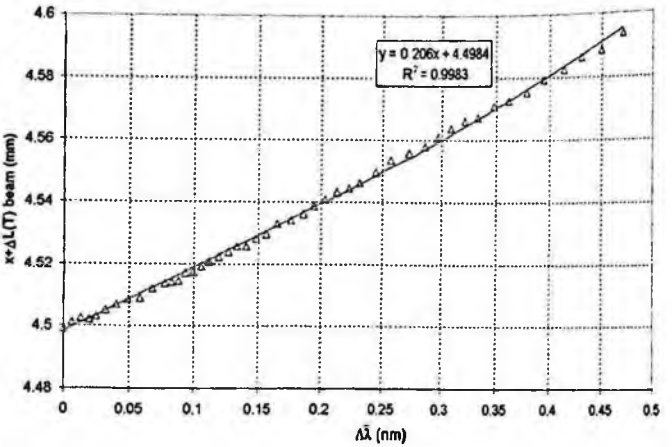

Figure 3. Beam thermal expansion as a function of the FBGs mean value. Displacement (parameter x) at room temperature: 4.5 mm.

The mean value from the three coefficients can be calculated, obtaining: $\bar{\beta} = 0.210 \pm 0.004$ mm*nm^{-1}, taking as error the maximum difference. Substituting this experimental value in equation (13), the sensor displacement response for the 15 cm long beam is given by equation (14):

$$x = 0.2040 \cdot \Delta\lambda_{up\text{-}lo}^2 - 0.210 \cdot \Delta\bar{\lambda}(T). \quad (14)$$

5. Conclusions

In this work an original configuration for extending the working range of FBG strain sensors was presented which is particularly suited for application as displacement sensor. Two gratings were glued in a central position to the opposite surfaces of a straight elastic beam. Pushing nearer of beam ends produced the beam curvature variation measured by means of the two FBG wavelength difference.

The sensitivity of the system was directly proportional to the square of the beam thickness and inversely proportional to the cube of the beam length, and depended on the inverse of the beam curvature. Decreasing the beam length increases the sensitivity, but decreases the working range, which was, for example, ~14 mm for the 19 cm long beam, and ~8 mm for the 15 cm long beam.

A temperature compensation technique was also proposed. Compensation was possible by considering the variation of the mean value of the two Bragg grating wavelengths, which depends linearly only on the temperature.

The proposed sensor is particularly suited for structures in which it is impossible to affix the bare fiber, such as breaks or separate elements.

References

1. G. M. Meltz, W. W. Morey, W. H. Glenn; "Formation of Bragg gratings in optical fibers by a transverse holographic method"; *Optics Letters*, Vol. 14, n. 15, pp 823-825, 1989.
2. A. D. Kersey et al.; "Fiber grating sensors" ; *Journal of Lightwave Technology*, Vol. 15 n. 8, pp. 1442-1463, 1997.
3. W. Lee et al.; "Railroad bridge instrumentation with fiber optic sensors"; *Proceedings of the Optical Fiber Sensors Conference (OFS-12)*, Williamsburgh, Va, USA, pp. 412-415, 1997.
4. A. R. Huntley; "Optical sensors network"; *Avionics conference and Exhibition "Systems Integration: Is the Sky the Limit?"*, November 1994.
5. E. J. Friebele et al. ;"Distributed strain sensing with fibre Bragg grating arrays embedded in CRTM composites"; *Electronics Letters*, Vol. 30, pp. 1783-1784, 1994.
6. R. Falciai, C. Trono, G. Lanterna, C. Castelli; "Continuous monitoring of wooden works of art using fiber Bragg-grating sensors"; *Journal of Cultural Heritage*, Vol. 4, pp. 285-290, 2003.

HIGHLY SENSITIVE THERMOELECTRIC TRANSDUCERS WITH CMOS MATERIALS[1]

F. MANCARELLA, A. RONCAGLIA, G.C. CARDINALI, G. PIZZOCHERO, S. GUERRI, M. SEVERI

IMM Sezione di Bologna, CNR, Via Gobetti 101, Bologna, I-40129, Italy

Thermoelectric transducers fabricated with both p and n-type heavily doped polysilicon thermoelements are presented. The devices are realized on front-side micromachined membranes obtained with typical CMOS passivation and intermetal dielectric layers, namely thermal silicon oxide, LPCVD silicon nitride and oxide. The polysilicon layers constituting the thermocouples are deposited on different interconnection levels and connected with Al/Si paths.

1. Introduction

In these last years, the demand of transducers which permit to convert a thermal radiation into an electrical signal has known a wide increase. Non-dispersive (NDIR) infrared spectroscopy [1], AC-DC power converters and alarm systems are some examples of such applications. Moreover, the possibility to employing a CMOS technology in conjunction with post-process-micromachining makes these applications truly attractive. In such a context, we propose a low-cost CMOS-compatible infrared transducer employing thin heavily doped polysilicon films as active elements and typical CMOS passivation layers.

2. Device fabrication

The transducer is realized by means of thermocouples implemented onto a dielectric suspended membrane obtained as a stack of dielectric layers typically employed in CMOS technology as proposed in [3], [4] (in this case also LPCVD silicon nitride is used, differently than in the cited papers).

It is well-known that in bulk micromachining realizing a stress free or slightly tensile stressed membrane is one of the most important aims. In order to

[1] This work is supported by Netgas project- EC V framework program, proposal IST-2001-37802

obtain that, the thickness of the dielectric layers have been properly chosen. The low thermal conductivity and reduced thickness of the membrane layers guarantees a good thermal isolation between the hot and the cold junctions of the thermocouples.

Fig 1. shows a schematic view of the thermal converter. As may be seen, the thermocouples are realized onto the legs of an open membrane. The hot junctions are placed close to the center and the cold junctions, instead, are placed onto the silicon bulk, supposed at a constant temperature.

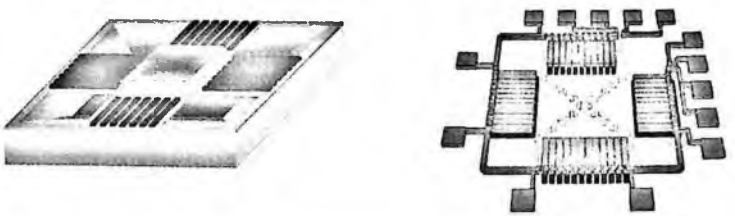

Figure 1. Schematic view of the thermal converter.

Two materials combination have been used to form thermocouples: heavily doped polysilicon (n type and p type), and aluminum. Thin polysilicon layers (160 nm and 320 nm thick) are deposited by LPCVD technique at a temperature of 620 °C on different interconnection levels and doped by ion implant with phosphorus and boron. The doses have been activated by annealing at 900 °C in nitrogen atmosphere for about 60 minutes. The layers are patterned by photolithography and dry etched. The measured sheet resistances for n-type and p-type polysilicon were about 130 Ω/sq and 200 Ω/sq respectively. The thermocouples are connected by means a 1 μm thick Al/Si layer deposited by sputtering and patterned by reactive ion etching. Low temperature oxide (LTO), deposited at a temperature of 420 °C, is used as a passivation layer.

Front-side bulk micromachining has been used to fabricate the suspended membrane, because removal of silicon underlying the dielectric stack is crucial for thermal insulation [2]. For such a purpose an anisotropic wet etchant has been employed. Besides, the lateral underetching of silicon below the membrane and the vertical etching of the underlying cavity has been carefully controlled. In order to guarantee a good compatibility with CMOS technology, a 5 wt% Tetra-Methyl-Ammonium-Hydroxide (TMAH)-water etching solution has been used.

During front-side bulk post-processing, etching of aluminum pads needs to be prevented. The addition of silicon powder to the solution permits to passivate aluminum during the etching. Moreover, in order to avoid one troublesome property of TMAH (formation of hillock), ammonium peroxydisulfate has been added to the etchant.

Fig 2. shows optical micrographs of a front-side etched thermoelectric transducer. The membrane of this device is roughly 1 mm^2 wide but wider membranes have been realized also without any difficulty.

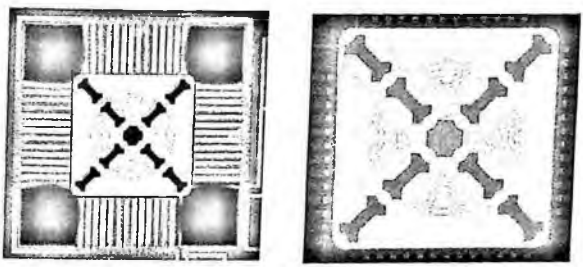

Figure 2. Front-side etched polysilicon/Al thermoelectric transducer (left) and a particular of the spiral-shape heater (right).

3. Results

The performance of a thermopile can be evaluated by means of a few proper parameters. These are responsivity R, normalized detectivity D^* and noise equivalent power NEP. Concerning the latter parameter, Johnsson noise V_N has been considered as the main noise source (referred to a 1 Hz wide band).

The measurements have been carried out in air, without any type of atmosphere conditioning. The incident radiation has been substituted by heating the thermopile by a spiral-shaped heavily doped polysilicon heater placed at the center of the device (see Fig. 2). Heater and thermopile resistances had been previously measured using a wafer-level characterization apparatus.

Thermopiles with different kinds of thermoelements have been measured: n/p polysilicon, n-polysilicon/aluminum and p-polysilicon/aluminum. Tab 1. summarizes the most important figures of merit calculated for such devices. The measurements, as might be expected, confirm that the thermopile realized by means of heavily doped p/n polysilicon layers has the highest responsivity. On the other hand, the electrical resistance of such a thermopile is higher with respect to the polysilicon/Al one, increasing in such a way the electrical noise.

However that is compensated by the much higher responsivity, as the NEP value demonstrates.

Table 1. Figures of merit about different kinds of thermopiles

	n/p polysilicon	p-poly/Al	n-poly/Al
NEP [W]	6.8×10^{-10}	4.9×10^{-9}	3.8×10^{-9}
D [cm·Hz$^{1/2}$/W]	2×10^{8}	2×10^{7}	4×10^{7}
Noise Voltage	6.4×10^{-8}	3.9×10^{-8}	3.3×10^{-8}
R [V/W]	90	-7.8	8.5

Figures 3a and 3b. show the thermopile output voltage versus current and power heater, respectively. The shape of the latter curve is fairly linear, as expected from theory. From the curves' slope an estimation of the transducer responsivity may be derived. Figure 3c shows a comparison among different thermopiles.

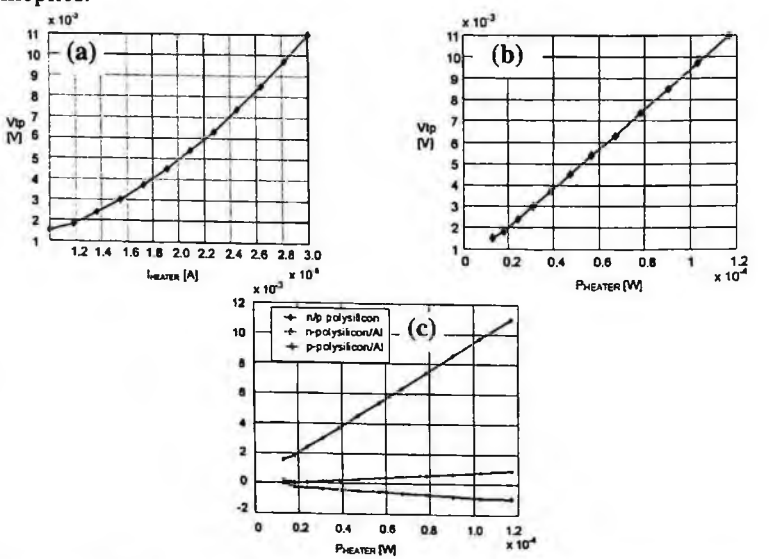

Figures 3. (a) Thermopile output voltage measured against the heater current (b) and power dissipated by heater. (c) Comparison of test curves concerning n/p poly, n-poly/Al and p-poly/Al thermopiles.

4. Conclusions

CMOS-compatible thermoelectric transducers, realized onto a suspended dielectric membrane, have been presented. The devices are realized employing heavily doped polysilicon films of both p- and n-type. Several kinds of thermocouples have been used: p/n-polysilicon, p-polysilicon/Al and n-polysilicon/Al. Silicon micromachining is performed as a post-processing step, with a dual doped TMAH solution in order to preserve the aluminum pads and avoid hillock formation.

The thermopile voltage output V_{tp} has been measured by heating the devices by a spiral-shaped polysilicon heater. The most important figures of merit (responsivity, normal detectivity and noise equivalent power) have been calculated by means of the V_{tp} – heating power measured dependence, by knowing the heater and thermoelements resistance from previously performed measurements. The achieved results confirm that the thermopile with the highest responsivity is the one realized by means of heavily doped p/n polysilicon layers. Despite this device also presents the highest voltage noise, the NEP is much lower with respect to the other thermopiles.

References

1. D. Rossberg, *Sensors and actuators A,* 47 (1995), 413
2. R. Lenggenhager, H. Baltes, T. Elbel, *Sensors and actuators A,* 37 (1993), 216
3. T. Akin, Z . Olgun, O. Akar, H. Kulah, *Sensors and actuators A*, 66 (1998), 218
4. E. Socher, O. Bochobza-Degani, Y. Nemirovsky, *Journal of microelectromechanical systems* 9 (2000), 38

WAFER-LEVEL MEASUREMENT OF THIN FILMS THERMOELECTRIC POWER[1]

A. RONCAGLIA, F. MANCARELLA , G.C. CARDINALI, S. CRISTIANI, M. SANMARTIN, M. SEVERI

IMM Sezione di Bologna, CNR, Via Gobetti 101, Bologna , I-40129, Italy

The possibility to perform wafer level probing measurement of thin films thermoelectric power is demonstrated by using test structures realized with dielectric cantilevers suspended over a silicon substrate and equipped with heavily n-doped polysilicon heaters and thermistors. The measurements presented are performed on p and n-doped polysilicon thin films without the need of any atmosphere conditioning, and, consequently, in a fully automatic fashion. An ad hoc extraction procedure is proposed in order to compensate for instrumental offsets and sensitivity limits typically existing in a standard wafer-level test instrumentation.

1. Introduction

Infrared detectors are covering a growing range of applications, among which alarm systems and non-dispersive infrared spectroscopy are only two simple examples. A widely used type of such device, the thermopile detector, employs the well-know Seebeck effect to convert a temperature gradient into an electric signal. Other kinds of transducers and actuators also employ the thermoelectric (Seebeck) effect as a working principle, such as physical sensors based on heat exchange (flow sensors, temperature sensors), micro thermoelectric generators and Peltier cells. Heavily doped polycrystalline silicon films are well suited materials to realize thermoelements in these devices, for their high thermoelectric figure of merit and good compatibility with microelectronic processes (CMOS in particular). As a consequence of that, precise measurement of polysilicon thermoelectric properties is of concern in many sensor applications. The most important parameter, in this respect, is thermoelectric power, that can be defined as the ratio between the voltage arising across a sample of the considered material (polysilicon in this case) as a consequence of an imposed temperature difference on it and the temperature difference itself.

[1] This work is supported by Netgas project-EU V framework program, proposal IST-2001-37802.

The absolute thermoelectric power of a conductive material is, generally speaking, not straightforwardly measurable with simple methods, since the presence of a reference layer is always necessary in order to realize a test thermocouple. In that case, what is measured is a relative thermoelectric power, or Seebeck coefficient, resulting from the sum of the thermoelectric powers of the individual layers. For polysilicon in particular, the use of a highly conductive reference layer as aluminum is advantageous because in that case the thermoelectric power of polysilicon is completely dominating in the measurement, so that the measured Seebeck coefficient is practically coincident with the absolute thermoelectric power.

Different methods have been proposed for thermoelectric power measurement of layers like doped silicon or polysilicon. The simplest one exploits a bulk sample that is heated at its extremes by two metal blocks (copper in example), whose temperature is controlled by a system that maintains a defined temperature difference between them [1]. By placing the test sample across the blocks, a temperature difference arises on it, as well, and the corresponding thermoelectric voltage can be measured by using a proper sample wiring and a voltmeter. This method is rather slow, requires a bulky equipment and, above all, does not allow to appreciate the local variation of the measured thermoelectric power at the microscale level, because of the sample size.

More evolved methods have also been proposed, based on micromechanical test structures in which the measured layer can be heated at one end [2]. The produced thermoelectric voltage and the temperature difference can be measured independently (with plain electrical measurements), and thermoelectric power quite straightforwardly calculated. In this case, however, the measurements shown in the literature are never performed at the wafer level, as the samples are always diced, bonded and placed in vacuum (often within a cryostatic apparatus), in order to well control their temperature and, at the same time, eliminate the influence of undesired convective heat exchange that may affect the measurement precision.

We propose here a method to execute the above described measurement at the wafer level, without any atmosphere conditioning and with no strict temperature control of the samples. The described measurements are operated by means of a standard semiconductor device characterization apparatus, in a simple and fast fashion. In order to obtain a sufficiently precise result, an extraction procedure is proposed in order to overcome typical offset problems due to switching interconnections in automated probe stations.

2. Test structure fabrication

The wafer-level measurement proposed is based on an appropriate micromachined test structure (see figures 1 and 2). The device is in essence a dielectric cantilever micromachined on a silicon substrate by anisotropic etching performed from the wafer front side. As can be observed in the figures, it consists of a 75 μm wide and 190 μm long rectangle suspended over a micromachined cavity, with four narrow arms connected to the silicon bulk. Two resistors are integrated into the tip of the cantilever in order to execute the measurement. The resistor closest to the end is used as a heater, the second one, instead, as a temperature monitor (see the layout in figure 1). In order to determine polysilicon thermoelectric power, an Al/polysilicon thermocouple is also integrated on the beam, realized by superimposing an aluminum layer over a polysilicon one. The two layers are separated by an LPCDV oxide passivation. As may be seen in the figure, the hot junction is placed close to the heater, while the cold one is on the silicon bulk. Since aluminum thermoelectric power is negligible (less then 2 μV/K) with respect to polysilicon one, the latter can be extracted from the thermocouple output voltage without introducing notable errors, as already explained in the introduction.

Both the resistors and the thermocouple have been realized employing heavily doped polysilicon layers. Thin undoped polysilicon has been deposited by LPCVD technique at a temperature of 620 °C and subsequently doped by ion implantation with boron and phosphorous (at a chemical concentration of 2×10^{20} cm^{-3} roughly). The implantation has been followed by an annealing process at a temperature of 900°C in nitrogen atmosphere for about one hour. Then the layers have been photolithographically patterned and RIE etched using a $SiCl_4$ based process.

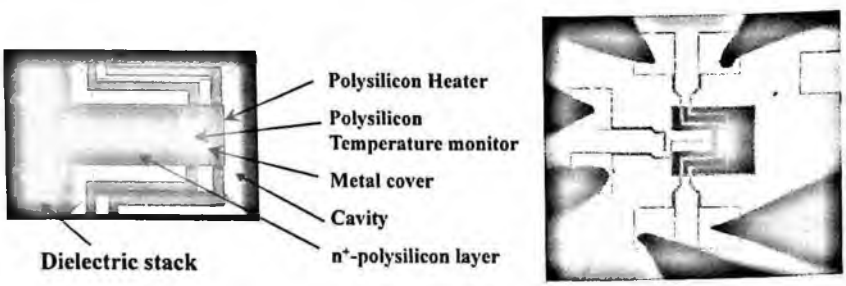

Figure1. Micromachined test structure layout (left) and device optical micrograph (right).

The interconnections are realized by a 1 μm thick, RIE etched Al/Si layer, that also enables a good electrical contact with heavily doped polysilicon. Moreover,

in order to homogenize the temperature between the sensor and heater resistor, an integrated rectangular cover made of aluminum has been introduced on the polysilicon resistors present on the cantilever tip.

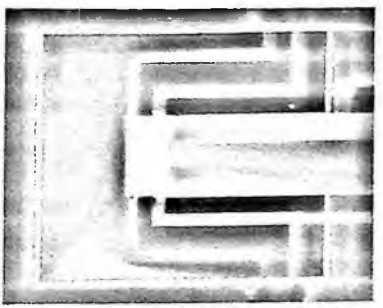

Figure 2. SEM image of the micromachined test structure

3. Results

The tests were carried out by driving current through the heater and, at the same time, measuring the consequent thermoelectric voltage across the poly/Al thermocouple and the thermistor resistance. In order to overcome the presence of the instrumental offset, which can introduce errors in the measurements, the thermistor current has been ramped up in order to extract a precise, offset-corrected value of the temperature resistance variation. By calculating the slope of the resulting $V_{seasor}(I_{sensor})$ curve, the thermistor resistance (R_{sensor}) can be extracted, thus eliminating the effect of the offset.

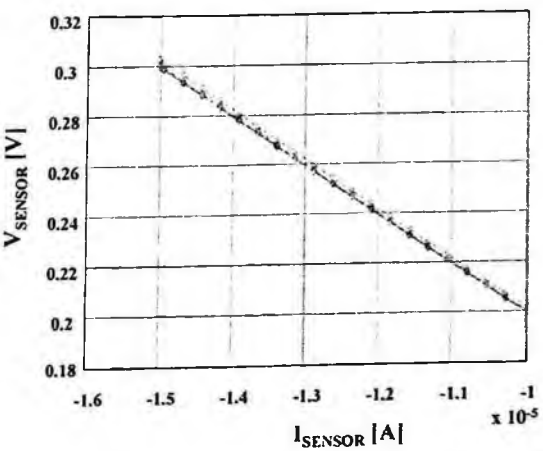

Figure 3. Measurement of the thermistor resistance for different values of the heater current.

The procedure has been repeated for different values of the heater current (see Figure 3) and, consequently, for different temperatures.

By knowing the n-type polysilicon temperature coefficient of resistance (TCR), previously determined by wafer-level sheet resistance measurements, the temperature close to the thermocouple hot contact can be estimated by using the following formula:

$$\Delta T = \left(\frac{R(I_0 + \Delta I_0) - R(I_0)}{R(I_0)} \right) \frac{1}{\beta}$$

where β is the TCR of polysilicon and ΔI_0 the current heater increment. Simultaneously, the thermoelectric voltage V_{tp} of the thermoelement has been measured for each current heater value. In such a manner, the trend of V_{tp} vs. the temperature difference imposed on the thermocouple is extracted.

By knowing the temperature difference ΔT , the thermoelectric power α can be calculated by means of the following simple expression:

$$V_{tp} = \alpha \cdot \Delta T$$

Figure 4 shows the thermoelectric power $\alpha(I_{heater})$ plotted as a function of the heater current (therefore indirectly as function of the temperature) extracted by means the above explained procedure, on n-type and p-type heavily doped polysilicon layers. Typical obtained values are summarized in Tab.1; the measured values of the layer resistivity (obtained with van der Pauw test structures and thickness profilometry) is also reported. As may be seen, the absolute values are comparable, despite the difference in resistivity.

Table 1. Measured thermoelectric powers

Layer	α (μV/K)	ρ ($\mu\Omega$cm)
n-polysilicon	–230	2.1
p-polysilicon	235	6.4

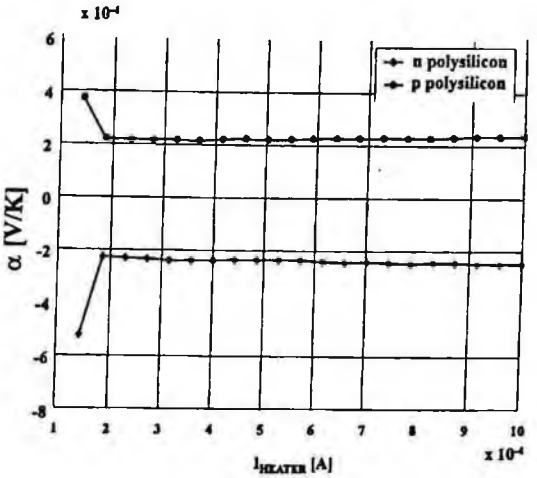

Figure 4. Thermoelectric power for p-type and n-type polysilicon vs. heater current.

4. Conclusions

A wafer-level technique for the measurement of thermoelectric power on conductive thin films has been described. The method exploits micromachined test structures with a thermocouple containing the measured layer and placed over a suspended dielectric cantilever. In order to overcome the intrinsic offset voltage of the instrument that could affect the measurement precision, the thermistor resistance has been calculated by means of the slope of a V_{sensor} (I_{sensor}) curve. Thanks to the robust extraction method proposed, the measurement can be performed with a standard wafer-level device characterization apparatus without resorting to vacuum environment. The technique has been validated on heavily doped polysilicon layers. Its use enables quick and inexpensive measurement of thermoelectric power on whole wafers and, consequently, statistical evaluation of this parameter variation at the microscale level.

References

1. M. Boutchic, K. Ziouche, P. Godts, D. Leclercq, *IEEE Electron Device Letters* **23**, 139 (2002)

2. M. von Arx, O. Paul, H. Baltes, *IEEE Transaction on Semiconductor Manufacturing* **10**, 201 (1997)

A BIOMIMETIC SENSING SKIN: CHARACTERIZATION OF PIEZORESISTIVE FABRIC-BASED ELASTOMERIC SENSORS

G. PIOGGIA, M. FERRO, F. CARPI, E. LABBOZZETTA, F. DI FRANCESCO
F. LORUSSI, D. DE ROSSI
Interdepartmental Research Centre "E. Piaggio"
Faculty of Engineering, University of Pisa, via Diotisalvi 2, Pisa – Italy

This article presents a deformable poroelastic bidimensional elastomeric architecture that responds to deformations along various directions thanks to an integrated sensorized fabric. The sensors exploit the piezoresistivity of the loaded rubbers as a principle of strain transduction. Using this architecture, sensors have been characterized in terms of their quasistatic and dynamic electromechanical transduction properties.

1. Introduction

Key points for biologically inspired artificial implementations are the materials, the sensing elements and the control.

Rigid structures are evolving toward flexible architectures characterized by redundant sensing and actuation nets. Development and selection of materials is mandatory. The new breakthroughs made in the past few decades in material science in order to develop intelligent materials built in compliance, non-linearity and softness allow to mimic the multi-component and bi-phasic nature of biological tissues [1]. Moreover, intelligent algorithms allow dynamics to be effectively reconstructed [2,3,4]. In this work we present a electromechanical characterization and modelling of piezoresistive fabric-based elastomeric sensors which properties are suitable for applications in various sectors: health care, rehabilitation and biomimetic robotics [3,4].

2. Sensors

The artificial sensing skin is a 3D latex foam, under which lies a sensing layer.

The sensing layer responds to simultaneous deformations in different directions by means of a piezoresistive network which consists of a Conductive Elastomers (CEs) composites rubber screen printed onto a cotton lycra fabric. CE composites show piezoresistive properties when a deformation is applied and can be easily integrated into fabric or other flexible substrate to be employed as strain sensors (figure 1). They are elastic and do not modify the mechanical behaviour of the fabric. CEs consist in a mixture containing graphite and silicon rubber. Resistance, Gauge Factor, Temperature Coefficient Ratio

and Reactive Properties have been classified [3]. In the production process of sensing fabrics, a solution of CE and trichloroethylene is smeared on a lycra substrate previously covered by an adhesive mask. The mask is designed according to the desired topology of the sensor network and cut by a laser milling machine. After the deposition, the cross-linking process of the mixture is obtained at a temperature of 130°C. Furthermore, by using this technology, both sensors and interconnection wires can be smeared by using the same material in a single printing and manufacturing process.

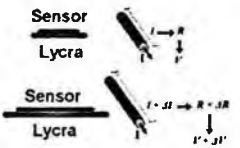

Figure 1 – Transduction principle of the strain sensor

3. Methods

From the technical viewpoint, a piezoresistive woven sensing fabric is a system whose local resistivity is a function of the local strain.

In a discrete way, it can be thought of as a two dimensional resistive network where single resistors have a non-linear characteristic that depends on the local strain. The integral impedance pattern is a function of the overall shape of the sensorised fabric and allows mapping between the electrical space and the shape space. For the characterisation of the sensors in terms of their quasi-static and dynamic electromechanical transduction properties sensors were serially connected. In this case, a current is superimposed in the circuit and high impedance differential voltages are acquired from each sensor. A block scheme of the acquisition hardware is presented in figure 2. Two multiplexers allow a sensor to be selected and the relative signal is acquired by a differential amplifier. A microprocessor drives the whole system, performs the analogous/digital conversion and exchanges data via USB interface. The device is provided with an automatic calibration subsystem which allows gain and offset to be tailored to each sensor.

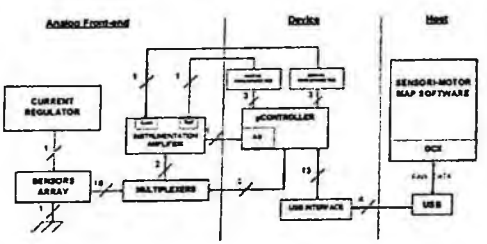

Figure 2 – Block schema of the acquisition hardware

A pushing punch driven by a stepper motor was used to apply alternate mechanical deformations (by indentation) to each fabric based sensor. Several tests were carried out, by using rectangular-wave mechanical stimulations (series of pressure impulses). In order to model the electromechanical response of each sensor, an equivalent circuit based on the equivalence between the electrical response (current variation) of the circuit and the response (resistance variation) of the sensor was proposed.

4. Results

Each sensor was tested by applying a series of pressure impulses (figure 3a) and by acquiring the voltage drop across the sensor as its response (figure 3b).

Pressure impulses result in a typical differential voltage behaviour showed in figure 3b. Sensor response shows a peak in correspondence to every mechanical transition. Data acquired were filtered, peaks were detected and relative maximum and minimum, and time constants were selected as features (figure 3b).

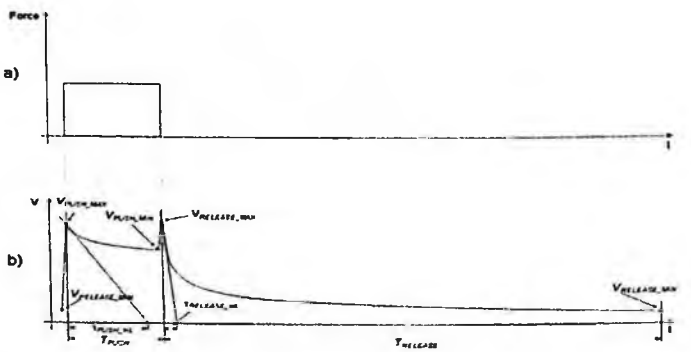

Figure 3 – a) A pressure impulse; b) sensor response a pressure impulse and selected features

Sensor responses during constant pressure time intervals were approximated by decreasing exponentials, assuming the local minimum as the steady-state value. This approximation results as true as long is the pressure time interval. In order to remove the contribution of high order exponentials, first order time constants were calculated discarding the first 5% of each curve. This choice allowed quantization errors introduced by the acquisition device in response to rapid transitions to be avoided and sensor steady state deformation, related to slower frequency components, to be maintained.

During a series of pressure impulses, the time constants of the deformation phases presented an average value of 9.32 seconds, while the time constants during the deformation recovery showed an average value of 4.72 seconds.

Figure 4a shows the acquired signal during pressure deformations (continuous line) and the extracted exponential discharging law (dashed line); figure 4b shows the quadratic error. Close to the mechanical transitions the differences between the signal and the exponential law is high; during the constant pressure phases the differences are very low ($< 3\times10^{-5}$ V).

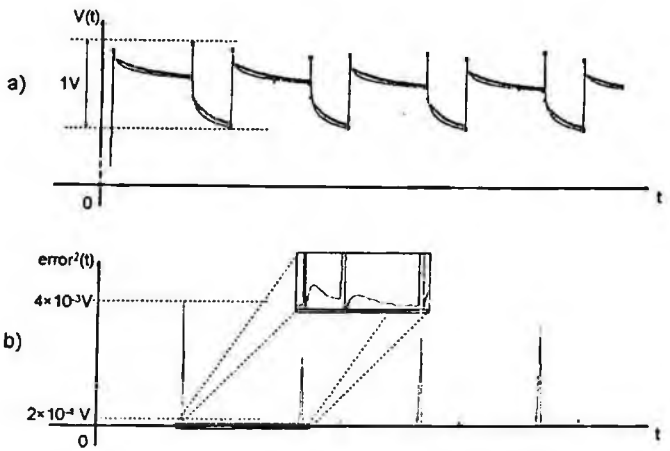

Figure 4 – a) acquired signal during pressure deformations (thin line) and extracted exponential law (bold dotted line); b) quadratic error

In order to model the first-order components of the sensor response (resistance variation) to a rectangular stimulation (applied deformation), the equivalent circuit represented in figure 5 was considered.

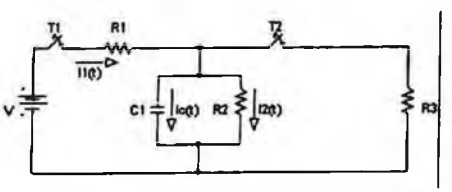

Figure 5 – Proposed equivalent electric model of each sensor

The power supply V is the electrical analogous of the imposed deformation. The switch T1 (initially open) is closed and open in correspondence of, respectively, the beginning and the end of the imposed deformation. The switch T2 (initially open) is closed when T1 is open again. Following a simple analysis of this circuit, it is easy to recognise that the variation of the charging and discharging currents of the circuit in consecutive phases of stimulation are analogous to the variation of the resistance of the

sensor during, respectively, its deformation and the following release. The circuit parameters R_1, R_2, R_3 and C can be derived by using the features, extracted from reference experimental signals, listed in Table 1.

Feature of the variation of the sensor resistance	Feature of the variation of the charging/discharging currents of the circuit	Symbol
Initial peak [kΩ]	Initial peak [A]	$I_1(0)$
Steady-state value for the deformation phase [kΩ]	Steady-state value for the charging phase [A]	$I_1(\infty)$
Time constant of the first-order exponential components for the deformation phase [s]	Time constant for the charging phase [s]	τ_1
Time constant of the first-order exponential components for the release phase [s]	Time constant for the discharging phase [s]	τ_2

Table 1 – Considered analogous features

A circuit voltage of 1 V was assumed as the analogous of a deformation of 1 mm, while a circuit current of 1 A was assumed to correspond to a variation of the sensor resistance of 1 kΩ. Values of the features listed above were extracted from ten cycles of a reference experimental signal and were used to derive the circuit parameters by means of the following system of equations:

$$\begin{cases} \tau_1 = C(R_1 \,//\, R_2) \\ I_1(0) = \dfrac{V}{R_1} \\ I_1(\infty) = \dfrac{V}{R_1 + R_2} \\ \tau_2 = C(R_2 \,//\, R_3) \end{cases}$$

The solution of this system provided, for the considered ten cycles of stimulation, the results reported in figure 6.

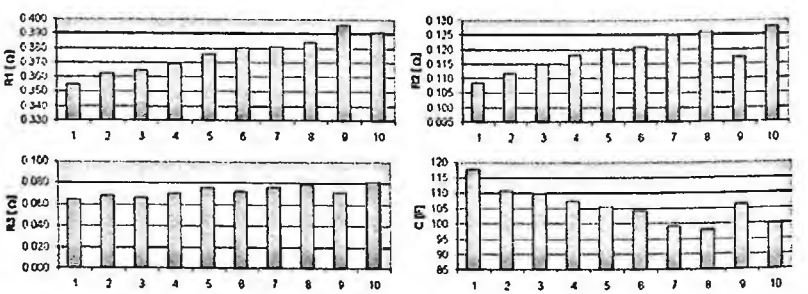

Figure 6 – Values of the parameters of the equivalent electric model extracted from ten cycles of a reference experimental signal

In consideration of the limited number of tests considered so far, definitive assessments and interpretations of the trends reported in figure 6 are premature at the moment. Accordingly, we are approaching a second phase of tests, in order to validate such an electrical equivalent model by subjecting each sensor to an extensive campaign of measurements, by applying deformations consisting of rectangular-wave signals with variable amplitudes, frequencies and duty-cycles.

5. Conclusions

In this paper sensors exploiting the piezoresistivity of the loaded rubbers as a principle of strain transduction have been preliminarily characterized in terms of their quasistatic and dynamic electromechanical transduction properties. Moreover, in order to model the first-order components of the sensor response to a rectangular stimulation, an electrical equivalent circuit was proposed.

References

1. Y. Osada, D. De Rossi (Editors), Springer-Verlag, Berlin Heidelberg, 440, (2000).
2. F. Di Francesco, B. Lazzerini, F. Marcelloni, G. Pioggia, Atmospheric Environment **35(7)**, 1225-1234, (2001).
3. D. De Rossi, F. Lorussi, A. Mazzoldi, P. Orsini, E.P. Scilingo, in Sensor and sensing in biology and engineering, Eds. Barth/Humphrey/Secomb, Springer-Verlag, 379-392, (2003).
4. G. Pioggia, A. Ahluwalia, F. Carpi, A. Marchetti, M. Ferro, W. Rocchia, D. De Rossi, Applied Bionics and Biomechanics, **1(2)**, 91-100, (2004).

ANALYSIS OF THE PHASE RESPONSE OF FIBER BRAGG GRATINGS TO LONGITUDINAL ULTRASONIC FIELDS IN THE HIGH FREQUENCY REGIME: TOWARDS NEW INTERROGATION STRATEGIES

VINCENZO ITALIA, ANDREA CUSANO, STEFANIA CAMPOPIANO, ANTONELLO CUTOLO

Eng. Dept. - University of Sannio, C.so Garibaldi 107, 82100 Benevento- Italy

MICHELE GIORDANO

Institute for Composite and Biomedical Materials, P.le Tecchio, 80 -80125 Napoli – Italy

In this work, the analysis of the phase response of fiber Bragg gratings (FBGs) subjected to longitudinal ultrasonic (US) field has been carried out. Numerical results reveal high sensitivity of the FBG phase response to US waves. The potentialities of the proposed approach to extend the sensing capability of fiber Bragg grating sensors as high frequency ultrasonic detectors are discussed with regard to new interrogation strategies based on time delay measurements.

1. Introduction

Fiber Bragg gratings have been widely investigated as temperature and strain sensors in many applications. They have unique advantages over classical sensors, by intrinsic features of fiber optic sensors, electromagnetic interference immunity, low mass and volume, stability in harsh environments. Moreover, the spectral encoding of the sensor output provides measurements free of intensity fluctuations. The employment of FBGs as detectors in ultrasonic measurements is potentially advisable for many application areas, including the non-destructive evaluation of materials by ultrasonic inspection technique, and medical applications.

In spite of this, there are only few studies concerning the response of a FBGs under fast-varying perturbations. Theoretical and experimental results demonstrated the capability of this class of sensors to detect ultrasonic fields if the US wavelength is larger than the grating length in order to avoid the generation of dynamic US dependent chirping along the sensor [1-4]. In all the investigated cases, intensity based measurements based on narrowband

interrogation and edge operation have been proposed. Here, for the first time, the analysis of the FBG phase response to longitudinal US fields in the high frequency regime has been carried out. The changes induced on the phase spectrum and thus on the time delay due to US waves with different amplitudes and frequency have been investigated. Results indicate that for particular optical wavelengths, the phase spectrum and thus the time delay exhibit a significant sensitivity to the high frequency US wave in the low amplitude regime (few micro-strains). The interesting results here reported indicate the possibility to develop new interrogation strategies in order to extend the sensing capability of this class of sensors for applications where only few technologies can compete.

2. FBG Ultrasonic Wave Interaction

In this section, the interaction between a uniform FBG of length L, written into the core of a standard single-mode fiber, and a ultrasonic wave, with the acoustic wavefront normal to optical fiber, is theoretically analyzed [4]. The unperturbed FBG is described by a modulation of the effective refractive index of the fundamental guided mode along the fiber axis z

$$n(z)=n_0\left\{1+\frac{\overline{\delta n_0}}{2n_0}[1+\cos(K_0 z)]\right\} \tag{1}$$

where n_0 is the fiber core refractive index, $K_0=2\pi/\Lambda_0$ is the reference Bragg wavevector (Λ_0 is the reference Bragg period) and $\overline{\delta n_0}$ is the peak to peak amplitude of the index modulation. The time dependence of the strain field, associated to the us field, is assumed to be sinusoidal and can be modelled as: $\varepsilon(z,t)=\varepsilon_m\cos(k_S z-\omega_S t)$,

where, ε_m denotes the strain wave amplitude, ω_S its angular frequency and k_S its wavenumber related to its wavelength by $k_S=2\pi/\lambda_S$. We evaluate the new effective refractive index n' of the Bragg grating under the ultrasonic wave action as the sum of two contributions. The first one is a mechanical contribution, due to the modulation of the grating pitch under the strain wave, the second one is an optical contribution due to the change in refractive index via the elasto-optic effect. The Bragg effective refractive index profile under the ultrasonic wave action can be expressed as

$$n'(z',t)=n_0\left\{1+\frac{\overline{\delta n_0}}{2n_0}-\left(\frac{n_0^2}{2}\right)\cdot[P_{12}-\nu(P_{11}+P_{12})]\cdot\varepsilon_m\cos(K_S z'-\omega_S t)+\right. \tag{2}$$

$$\left.+\frac{\overline{\delta n_0}}{2n_0}\cos\left(K_0 z'-K_0\frac{\varepsilon_m}{K_S}\left[\sin(K_S z'-\omega_S t)+\sin\left(K_S\frac{L'}{2}+\omega_S t\right)\right]\right)\right\}.$$

Were P_{ij} are the stress-optic coefficients and ν is the Poisson ratio.

3. FBG Ultrasonic Wave Interaction

The effective refractive index profile of the FBG under ultrasonic excitation, $n'(z)$, can be used to determine the FBG spectral characteristics, by means of the transfer matrix approach. This latter performs a sampling of $n'(z)$, allowing to model any non-uniformities along the grating with high accuracy[4]. In particular, we refer to a FBG having a length L=1mm, a pitch Λ_0=535nm, and $\overline{\delta n_0} = 2\times10^{-3}$. The attention of our analysis has been focused on the intensity spectrum, indicated with $\Gamma(\lambda)$, and the phase spectrum, $\Phi(\lambda)$, reflected form the grating. Figure 1.a shows the amplitude spectrum of the reflected signal for a FBG subjected to US waves in the range 10-100με in the case L=λ_S. The spectra here reported are referred to the time t=0s. As expected, the time dependent non uniform distribution of the strain field along the grating length is responsible for a shape distortion of the amplitude spectra, in this case the wavelength shift can not be considered as a proper parameter for the US detection.

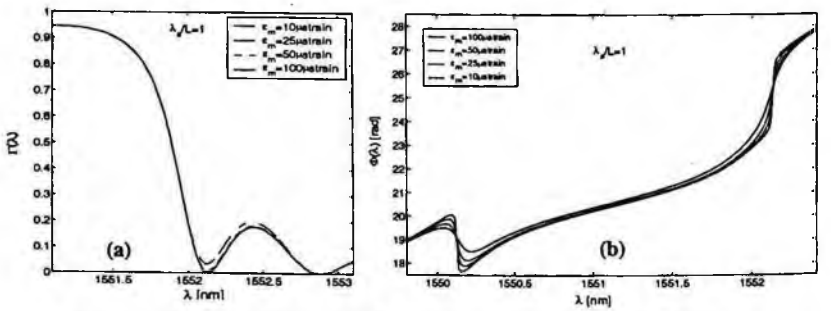

Figure 1. Complex reflectivity of US perturbed grating. (a) reflectivity (b) phase.

Fig. 1.b shows the phase spectrum of the sensing grating in the same operative conditions. In the investigated case interesting US sensitivity can be observed in two spectral regions corresponding to the first nulls of the main lobe of the reflected spectrum. This result could be explained on the basis of the theory developed by Sipe et al [5]. The reflectance nulls can be interpreted as the resonances of an equivalent Fabry-Perot cavity in which the light is trapped in and thus a relevant interaction with the US wave occurs. Fig.2 shows the time delay response for various value of λ_S and ε_m. The behaviour of the phase spectrum is emphasized in the time delay plot, due to the derivative based relation between the two functions expressed as:

$$\tau(\lambda) = \frac{d\Phi}{d\omega} = -\frac{\lambda^2}{2\pi \cdot c}\frac{d\Phi}{d\lambda} \tag{3}$$

Another important feature is the notch character of the high sensitivity regions as function of the optical wavelength.

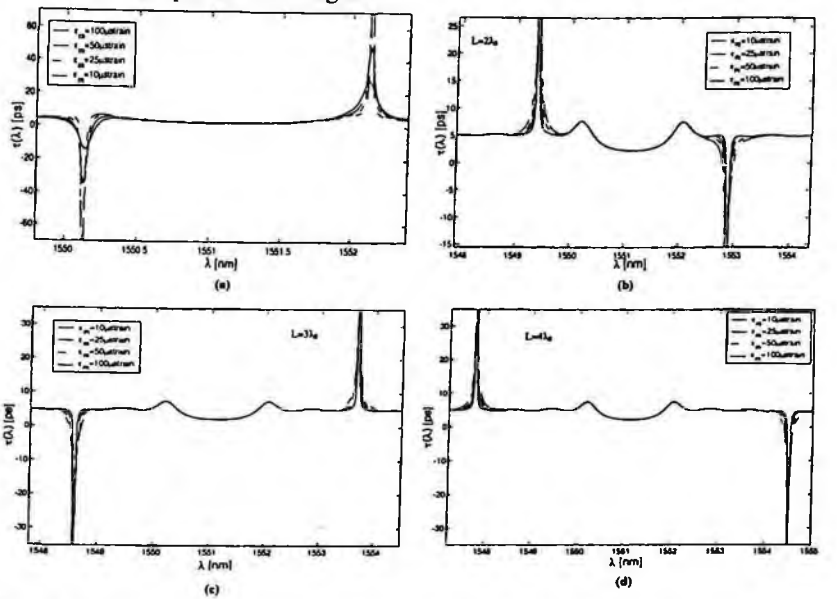

Figure 2. Group delay response as function of the optical wavelength for different strain amplitudes in the cases: (a) $L=\lambda_S$, (b) $L=2\lambda_S$ and (c) $L=3\lambda_S$ and (d) $L=4\lambda_S$.

This aspect play an important role in the design of interrogation systems employing the time delay sensitivity as discussed later. Figure 3.a shows the time delay-US strain sensitivity defined as $d\tau/d\varepsilon$ in correspondence of the two high sensitivity wavelengths in the case $L=\lambda_S$. Numerical results indicate an extremely high US sensitivity in terms of time delay especially for low amplitudes US waves, that drops to low values as the US strain approaches the value of $50\mu\varepsilon$. Figure 3.b shows, as previously mentioned, that the sensitivity regions exhibit a notch like behaviour, decaying significantly as the optical wavelength differs from the null-reflectivity ones. Based on the analysis here reported, the choice of the time delay as key parameter for US detection in the high frequency and low amplitude regime seems to be promising. The key point is the choice of the operating wavelength, the power budget and the detection technique[6,7] in order to obtain the required sensitivity.

4. Conclusions

In this work, the investigation of the fiber Bragg grating phase response to ultrasonic waves in the high frequency and low amplitude regime is reported.

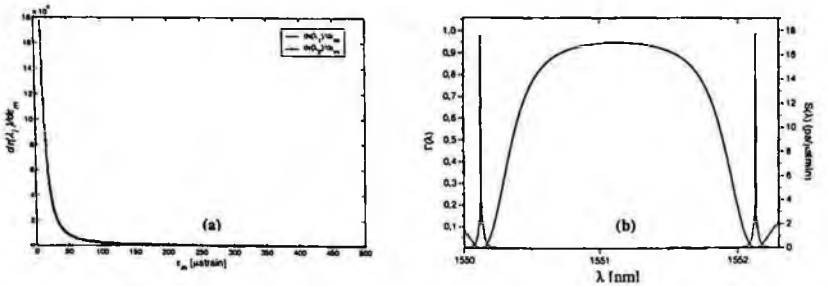

Figure 3. Sensitivity of US perturbed grating: (a) time delay-US strain sensitivity, (b) sensitivity as function of the optical wavelength with the amplitude spectrum of the grating.

Numerical results show that high US sensitivity is obtained at well defined optical wavelengths dependent on the US wavelength but located in correspondence of the nulls in the amplitude spectrum of the reflected light. In conclusions, this analysis indicate in the time delay the proper parameter to be used in the high frequency and low amplitude regime. This means that a proper choice of the operating wavelength and the time delay based interrogation strategy would enable this class of sensors to be used in applications where the US detection is required, including non destructive testing, structural health monitoring, medical and biomedical fields.

References

1. N.E. Fisher, D.J. Webb, C.N., Pannell, D.A. Jackson, L.R. Gavrilov, J.W. Hand, L. Zhang, I. Bennion, *Applied Optics* Vol. 37, No. 34, (1998)
2. N. Takahashi, K. Yoshimura, S. Takahashi, K, Imamura, *Ultrasonics* 38 581-585 (2000)
3. D.C. Betz, G.Thursby, B. Culshaw, W.J. Staszewski, *Journal of Smart Materials and Structures*, vol.12, pp.122-128, (2003).
4. A.Minardo, A.Cusano, R.Bernini, L.Zeni, M.Giordano, *IEEE Trans. on Ultrasonics, Ferroelectrics, and Frequency Control*, in press (2004)
5. J. E. Sipe, L. Poladian, C. M. de Sterke, *J. Opt. Soc. Amer. A*, vol. 11, pp. 1307-1320, (1994)
6. E. I. Petermann, J. Skaar, B. E. Sahlgren, R. A. H. Stubbe and A. T. Friberg, *Journal of Lightwave Technology*, Vol. 17, No. 11.
7. S. D. Dyer, K. B. Rochford and A. H. Rose, *Opt. Exp.*, vol. 5, pp. 262–266, November 1999.

A CALIBRATION SYSTEM FOR SURFACE TEMPERATURE SENSORS

L. ROSSO, V.C. FERNICOLA
Istituto di Metrologia "G. Colonnetti" (IMGC – CNR), Strada delle Cacce 73
10035 Torino, Italy

The calibration of contact surface temperature probes greatly depends on the interaction between the sensor and the reference measurement surface. A dedicated calibration system for such probes has been developed at IMGC. It enables the calibration on a temperature-controlled reference surface in the temperature range from ambient to 350°C. The paper describes the prototype, its main metrological features as well as the thermal-fluid-dynamic model of the system for simulating the impact of the various influence parameters on the measurement. The preliminary results of the comparison between the numerical predictions and the experimental values, as obtained from the metrological characterisation of the system, are also reported.

1. Introduction

Contact temperature probes are convenient and practical means for measuring the surface temperature of solid bodies[1]. However, measurement results obtained with such probes are reliable only if they have been previously subjected to a traceable calibration. Different methods and facilities are used for the calibration of contact surface thermometers [2-4]. A widely used reference calibration system is based on a temperature controlled hot plate, which provides a stable and reproducible temperature. The actual surface temperature is calculated by extrapolation of the temperatures measured through two or more calibrated thermometers, which are embedded in the plate at different depths. In other calibration systems the reference block is partially immersed in a thermostatic bath - the level of the liquid is maintained under the block's surface - in order to ensure a uniform temperature field. In this case the surface temperature is measured by means of a calibrated thermometer embedded into the block just behind the calibration surface [5]. When the above mentioned facilities are not available, contact thermometers are calibrated by total immersion in a thermostatic bath [2]. This calibration procedure completely elude contact probe operating conditions, i.e., its direct application to the body under test, and makes

it almost impossible to correlate the calibration results with the subsequent measurements.

At present, the best measurement capability for surface temperature measurements available at European NMI facilities varies between 0.2 °C and 2 °C in the range from ambient temperature to about 300 °C [3-5]. An EUROMET comparison of European reference standards for surface temperature, in the range between 50 °C and 300 °C, has been recently carried out for the mutual recognition of national standards [6].

In order to meet industrial traceability needs, a dedicated system for the calibration of contact temperature probes was designed and constructed at IMGC. It was subjected to a detailed characterisation in order to evaluate the temperature uniformity of the reference surface.

The design of a calibration system must take into account the problems related to surface temperature measurements, i.e., the interactions which occur between the sensor, the surface and the surrounding fluid as well as the measurement errors due to the perturbation of the temperature field from the sensor. These errors depends on different parameters (measurement conditions, geometric and physical properties of the surface, technical features of the sensor, etc.) and have been widely investigated; nevertheless, their experimental evaluation is quite difficult [7-10]. At present, several mathematical model are available in literature; but most of them are based on simplified assumptions and don't allow an accurate evaluation of the whole range of phenomena involved.

This paper describes the main features of the calibration system prototype as well as the thermo-fluid-dynamic model that has been developed for simulating the impact of the various influence parameters on the measurement. The preliminary results of the comparison between the numerical model predictions and the experimental values, as obtained from the metrological characterisation of the system, are also reported.

2. Design of the calibration system

A block diagram of the calibration system designed at IMGC is shown in Figure 1. It is based on a temperature controlled aluminium block (25 mm thick, 100 mm in diameter), whose upper surface acts as reference surface. At present, it covers the range from ambient temperature up to 350 °C. The block is mounted on a flat round heater and is surrounded by thermal insulation. In this configuration a *quasi-linear* temperature gradient is obtained across the block. Three calibrated thermometers, which are radially inserted at different depths,

enable the measurement of the temperature profile as well as the extrapolation of the surface temperature.

The temperature of the block is controlled by an active control system which consists of a separate Pt100 sensor, a PID controller and a DC power supply. The reference block is also fitted with a guard ring heater in order to reduce radial heat loss and to ensure an even surface temperature.

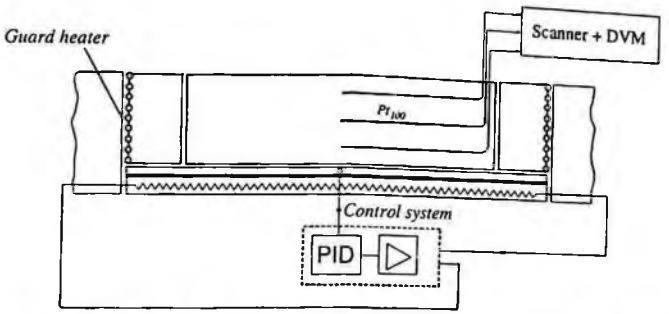

Figure 1: Schematic of the calibration system for contact temperature measurement probes

3. Numerical model

A numerical model of a calibration system, based on the finite element method, has been implemented in order to simulate the heat transfer mechanisms involved in contact surface temperature measurements. From a physical point of view, the heat transfer phenomena to be considered are:

- convection between the surrounding fluid and the measurement surface and between the fluid and the sensor;
- heat conduction through the measurement surface;
- radiative and convective heat transfer in the measurement region.

The experimental apparatus was modelled as a bi-dimensional domain. It was divided into sub-domains for taking into account the presence of materials with different thermal conductivities. The grid, which consists of about 20,000 triangular elements, was obtained by using an auto-adaptative procedure. The mesh resolution was increased where the temperature gradients are higher, as can be seen in Figure 2.

In order to simulate the operating conditions the following assumption were also made: *i*) the lateral surface of the apparatus exchanges heat with the surrounding environment by convection and radiation, *ii*) the temperature of the

ambient air and the surrounding surfaces is at 23°C, *iii*) the thermal contact resistance between the reference block and the heater is constant; *iv*) the heater can be approximated by a disk with an internal heat generation.

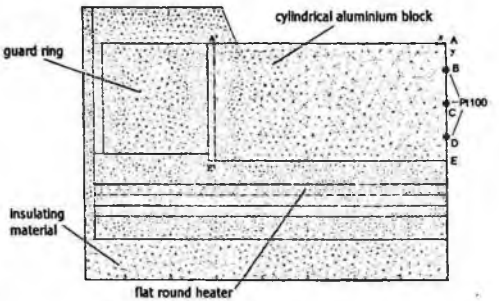

Figure 2: Grid used for the thermal modelling of the reference calibration system.

4. Numerical and experimental results

The simulation of the experimental apparatus was performed at several temperatures in the range from ambient temperature to 400°C. Figure 3a shows the surface temperature profile along the radial direction AA', from the center to the edge (point A is at x=0), as obtained from the numerical simulation. The temperatures of the surface are plotted with reference to the edge point A' (at x=50mm, y=0). A surface temperature uniformity over the whole reference surface to within 0.34°C at 400°C was predicted from the model.

The thermal profile across the aluminium reference block was also investigated, both theoretically and experimentally, through the temperatures measured by three thermometers embedded into the cylindrical aluminium block at different depths. The comparison of numerical and experimental results along the AE axis of the block is plotted in Figure 3b. In this case, point B (at x=0, y=6.25 mm in Figure 2 was used as reference point. Experimental data and numerical simulation showed a good agreement, within the experimental uncertainty, up to 200°C; for higher temperatures they disagreed.

A characterisation of the system prototype was also performed in order to evaluate the surface temperature uniformity. To this end, fluorescent film thermometry was exploited. A two-dimensional matrix of fluorescent point sensors was deposited on the reference surface. An optical fibre, which was placed near to the surface but not in contact with it, was used for the sensor excitation and for the gathering of the fluorescent signal in correspondence to the

various point sensors, thus scanning the whole reference surface. A temperature uniformity of better than 0.15°C was obtained over the whole temperature range.

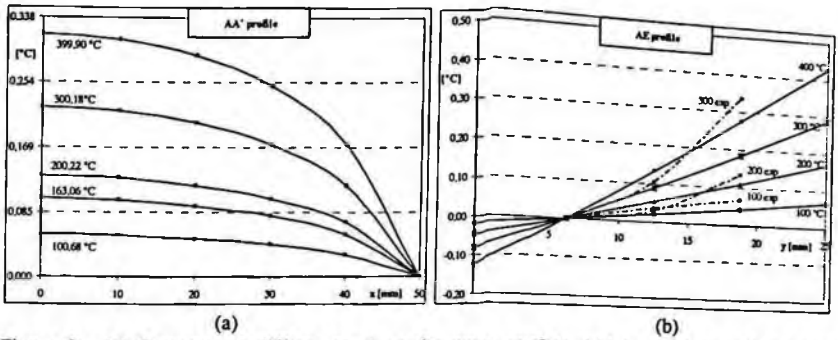

Figure 3: (a) Temperature differences along the upper surface AA' (point A is at 0 mm) for different surface temperatures; (b) comparison of numerical and experimental results along the AE axis of the cylindrical aluminium block.

Further investigations, using a commercial contact surface temperature sensor and the fluorescent point sensor array described above, were carried out for the evaluation of its impact on the surface itself. The effect of the contact sensor on the surface reference temperature was evaluated as a function of the radial position. The temperatures in correspondence to the fluorescent point sensors were measured before (T_b) and after (T_a) applying the contact probe in the centre of the reference block. Figure 4 shows the variation $DT = T_a - T_b$ measured at several temperatures. As expected, the perturbating effect of the contact probe on the surface temperature uniformity is maximum near the probe (at x=0) and decreases with distance.

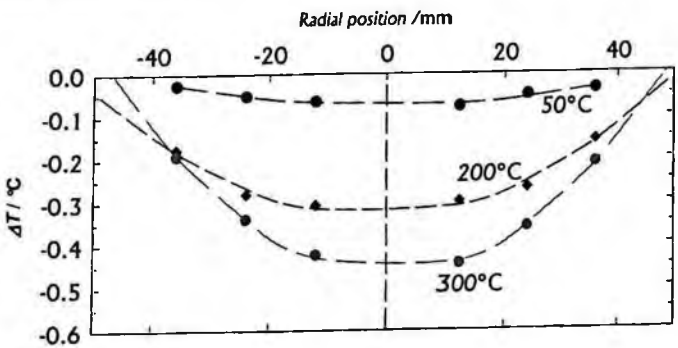

Figure 4: Surface temperature variation due to contact-probe applied in the centre of reference block at various temperatures.

Conclusions

The paper describes the design and modelling of a reference calibration system for contact surface temperature sensors developed at IMGC. The system is based on a high thermal capacity block, whose surface can be controlled in the temperature range between ambient temperature to about 350 °C. A dedicated numerical model for simulating the operating conditions of the system has been implemented, with the aim of improving the features of the unit and identifying the critical points during the actual operation. A mechanical design was performed on the basis of the numerical calculations and a prototype was constructed. Numerical simulation and experimental data were also compared.

The vertical thermal profile across the cylindrical aluminium block, as obtained from the numerical simulation, was compared to experimental values measured by three thermometers embedded into the block, showing a good agreement up to 200°C; for higher temperatures the agreement was lower. This discrepancy is probably due to the approximations and simplifications used for simulating the calibration system and can be reduced with a more detailed model. The numerical simulation also predicted a temperature uniformity to within 0.34°C at 400°C over the whole reference surface. Fluorescent film thermometry was used for measuring the actual surface uniformity. An array of fluorescent point sensors was placed on the reference surface and a remote fibre optic system was used for gathering the excitation and the fluorescence signals. An experimental temperature uniformity of better than 0.15°C was obtained over the investigated temperature range (25°C to 350°C). The change in surface temperature uniformity was also investigated as a function of the working temperature when a contact sensor was loading the surface. The peak-to-peak changes amounted to 0.3°C at 200°C and about 0.4°C at 400°C.

References

1. M.J. De Groot, *High Temperature High Pressure* **29**, 591 (1997).
2. European co-operation for Accreditation, Temperature and Humidity Expert Group, *Questionnaire on surface contact thermometry* (1999).
3. *Surface thermal measurements*, Proceedings of the Workshop, Ed. IMEKO Secretariat, Budapest, Hungary (1995).
4. F. Edler, M. Gorgieva, J. Hartmann, M. Wagner, Proc. of TEMPMEKO 2001, Vol. 2, Berlin, Germany, 1105 (2002).
5. R. Morice, E. Andras, E. Devin, T. Kovacs, Proc. of TEMPMEKO 2001,Vol. 2, Berlin, Germany, 1111 (2002).

6. EUROMET Project no. 635 – *Comparison of the reference surface temperature apparatus at NMIs by comparison of transfer surface temperature standards* (2001).
7. L. Michalski, K. Eckersdorf and J. Mc Ghee., *Temperature Measurement*, 2nd Ed., John Wiley & Sons, New York (2001).
8. D.K. Hennecke and E.M. Sparrow, *Int. Journal of Heat and Mass Transfer* **13**, 287 (1970).
9. E.M. Sparrow, *Measurement in Heat Transfer*, 2nd Ed., edited by E.R.G. Eckert, R.J. Goldstein, Hemisphere Publishing Corp., Washington (1976).
10. B. Cassagne, G. Kirsch, and J.P. Bardon, *Int. Journal of Heat and Mass Transfer* **23**, 1207 (1980).

MULTI-FREQUENCY ICE DETECTION SYSTEM

EROS PASERO, MARCO RICCARDI, TASSILO MEINDL

Department of Electronics, Polytechnic of Turin, Corso Duca degli Abruzzi 24
Turin, 10129, Italy

This paper presents the design and performance evaluation of a new sensor system for detecting the presence of water or ice films on its surface. The system is based on a multi-frequency capacitive measurement and the effect that water and ice have different dielectric constants. Accumulation of ice or water on the electrodes of the sensor leads to a change of the effective capacitance value of the sensor. This change is measured using a sophisticated, high-sensitive, differential capacitance measurement circuit.

1. Introduction

In many fields, exact and fast information about the specific environmental conditions are required so as to initiate an appropriate response to the detected environmental conditions. For instance, an adequate assessment of the environmental conditions on road surfaces may significantly contribute to enhanced traffic safety, since corresponding decisions made by road administrators may be based on this information. In particular, any information on road sections having ice or moisture formed thereon may help to significantly improve traffic safety.

Thus, one of the key components of modern road information systems (RIS) is the monitoring of the current road surface conditions, wherein the detection of the presence of water, snow, ice and the beginning formation of ice, is one of the most important pieces of information for traffic safety. [1]

We provide an enhanced sensor system and methods for detecting a capacitive change of a sensor element, for instance in view of surface monitoring, with enhanced accuracy and reliability, especially with regard to water, snow, and ice detection on exposed surfaces and the detection of ice formation at an early stage. The measurement techniques and the sensor circuit are explained in section two. Some interesting experimental results are presented in section three.

2. Device Description

The dielectric constant of H_2O (including water and ice) changes dependent on the actual temperature and the measurement frequency [3, 4], as shown in figure 1.

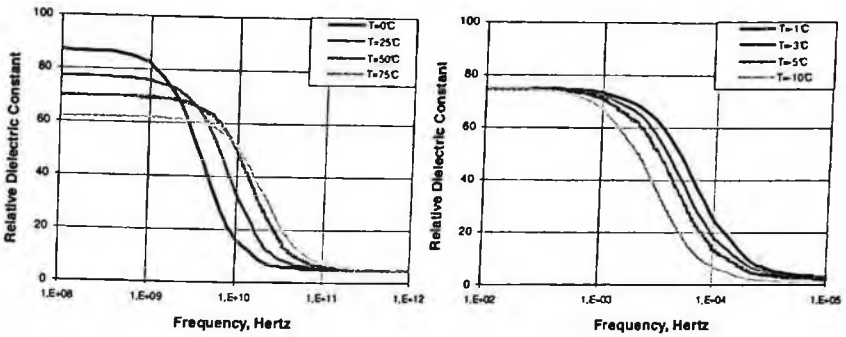

(a) (b)

Fig. 1. Relative dielectric constant of H_2O as a function of temperature and measurement frequency,(a) water, (b) ice.

Small amounts of contaminations such as dirt, fuel or salt can quiet easily modify the dielectric constant of the substance [2, 5]. Further on, the effective dielectric constant depends strongly on the thickness of the water or ice layer on the surface of the sensor. Therefore, at low frequencies the dielectric constant of water and ice can be similar and at high frequencies that of ice and air. For this reason, a capacitive measurement at a single frequency is obviously not sufficient. For an exact classification of the material on the sensor, distinguishing among ice, water or air (in our case clean sensor), it is necessary to measure the dielectric constant of the material on the surface of the sensor in the frequency domain. An enhanced system performs measurements at two frequencies, namely below 1 kHz and in a range of 10 kHz to 10 MHz. This ensures that the measurements are performed above and below the relaxation time and therefore water and ice can be detected accurately. To allow a more accurate system, we implemented a multi-frequency measurement system able to classify the substance on the surface of the sensor in the complete interesting frequency domain, namely in the range of 50 Hz to several MHz.

2.1. *Basic Measurement Circuit*

The sensor system comprises a pair of exposed conductive electrodes, which are the sensing device, a frequency generator and a charge detector (see figure 2). In our case the frequency generator is realized by a reference voltage source V_R

and a controllable switch S_1 for periodically connecting the reference voltage source with the electrode assembly to provide different frequencies.

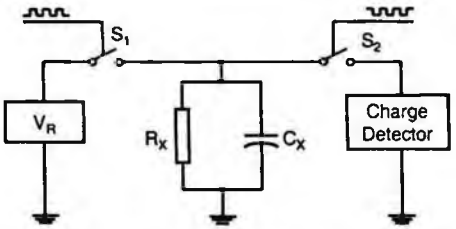

Fig. 2. Schematic layout of capacitance measurement circuit connected to the sense electrode (C_X, R_X).

In the basic measurement circuit the charge detector comprises only a capacitance C_S of value well known that is connected after each charge cycle towards the sensors electrodes by closing switch S_2.

$$C_X << C_S \tag{1}$$

In this way, part of the charge Q_X stored in the electrode assembly may be transferred to the sense capacitor.

$$Q_X = C_X \times V_R = (C_X + C_S) \times V_S \tag{2}$$

Anyhow, from (1) and (2) follows that nearly all charge is transferred towards the larger detection capacitance C_S:

$$Q_X = C_X \times V_R = C_S \times V_S \tag{3}$$

In order to increase accuracy, the charge transfer process can be repeated *n* times (without considering saturation effects), and therefore, the value of the sensor's electrodes C_X can be evaluated easily by counting the number of pulses and measuring the voltage level of the detection capacitance.

$$C_X = C_S \times (V_S / V_R) / n \tag{4}$$

An associated microcontroller evaluates the voltage level V_S reached by the detection capacitance, after several charge-transfer cycles between the sensor and the detector. This measurement is performed by an analog to digital converter (ADC) of the microcontroller in order to allow for further data processing

2.2. *Differential Capacitance Measurement*

The sensitivity of the capacitance measurement can be extended if a differential capacitance measurement with afterwards amplification is used. This could be

done e.g. if another pair of electrodes with the same geometrical parameters like those of the sensor's electrodes is added, on that no material disposition can occur. If this reference capacitance is now charged with the same pulses, the resulting voltage level can be subtracted from that of the sensor, resulting in a differential voltage signal. The drawback of this solution is that also wires add additional capacitances to the sensor, rendering the compensation not exact, and further space and power consumption is required.

Therefore, we perform a different method. We extend the charge detector only by a differential operation amplifier and a digital to analog converter (DAC). During a calibration phase we charge the clean sensor electrodes (no material disposition) like mentioned above and monitor the occurring voltage levels V_S after certain amounts of pulses. During later measurements we can then provide only this calibration information to the differential amplifier in order to allow a differential measurement with higher resolution (see figure 3).

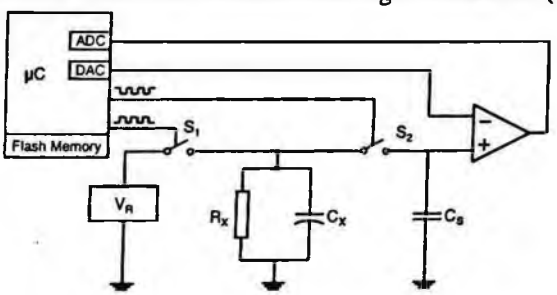

Fig. 3. Schematic layout of the differential capacitance measurement circuit connected to the detection capacitance.

This solution significantly reduces both space and power consumption, because a reference capacitor is not necessary, saving respectively the power that should be used to charge it at every measurement cycle.

3. Experimental Results

Experimental results reveal that the system can successfully detect ice and water films on the surface. Figure 4 (a) shows a typical cycle, starting from the surface under test being clean (T_0), then with water (T_1) and finally with ice (T_3). In this experiment only two frequencies of measurement are used (100 Hz and 22 kHz), so the curves in the graphs represent the values acquired by the system at those frequencies.

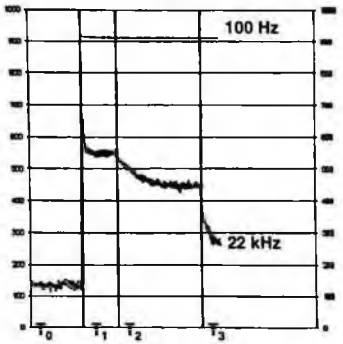

(a)

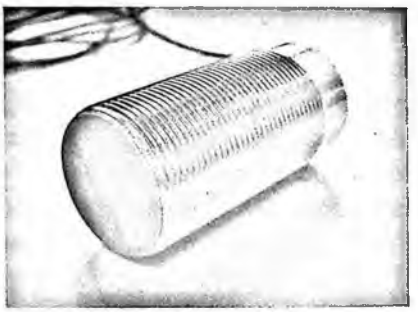

(b)

Fig. 4. Experimental results, (a) change of dielectric constant during a typical measurement cycle and (b) test sensor system.

As can be seen in figure 4 (a) the presence of water causes a great variation of both measured values, indicating the presence of water. Until the sensor's situation changes the measured values remain constant. Then the temperature of the sensor is decreased (T_2) and the changing of water in ice is suddenly revealed (T_3). In fact the upper track doesn't present variation, because both water or ice relative dielectric constant at the frequency of 100 Hz is not appreciated, but the lower track changes drastically, because the relative dielectric constant of ice is very different from that of water (between 1 and 5 instead of 80) as shown in figure 1.

4. Conclusion

The paper describes a sensor system able to detect different substances, by means of a characterization of the dielectric constant at different frequencies. This application shows good performances in detecting water and ice on a road surface. But in future, increasing the number of frequencies the same sensor could be used in other fields.

References

1. N.S.T. Lee, H.A. Karimi, E.J. Krakiwsky, Vehicle Navigation and Information Systems Conference, Canada, 1989.
2. V.V. Tikhonov, International Geoscience and Remote Sensing Symposium, Firenze, Italy, July 10-14, 1995.
3. C.H. Collie, J.B. Hasted, R.M. Ritson, Proc. Physical Society Vol. 60 (1948) 145-160.
4. A. von Hippel, IEEE Trans. Electrical Insulation Vol. 23 (1988) 817-823.
5. C.D. Lu and J.W. Yu, Chinese Journal of Physics Vol. 40 (2002) 60-68

USE OF ELECTRIC TRANSDUCERS FOR CONTINUOUS MONITORING OF GROUNDWATER LEVEL VARIATIONS IN A LANDSLIDE AREA*

P.P.LIMONI, P. LOLLINO, J. WASOWSKI

CNR IRPI - Sez. di Bari, Via Amendola 122/I, , Bari, Italy 70126,

This paper concerns the application of electric transducers for studying the instability of peri-urban slopes in Caramanico Terme, a hilltop town located in the Apennine Mountains of the Abruzzi region (Central Italy). We describe the functioning of three types of piezometers located within different geologic materials and their response to the variations of the slope boundary conditions in terms of time lag and data reliability. The Caramanico area is characterised by a long record of historical landsliding activity typical of a high mountainous setting subjected to a relatively high average rainfall and seismic activity. Following previous landslide surveys and a careful evaluation of slope movements case records, we argue that a systematic and periodic monitoring of both ground deformation and causal factors of instability using integrated ground-based techniques, including subsurface monitoring, is necessary to advance the understanding of recurrent landslide hazards. In particular, electric transducers installed within both an oper-pipe piezometer and a Casagrande cell, together with electric piezometers, have been recognised as useful to gain a deeper insight on local groundwater variations. A very small acquisition timestep (6 hours) of the data-logging is aimed at obtaining nearly continuos pore water pressure measurements during intense rainfall and future earthquake events.

1. Introduction

Caramanico is a small but important thermal center and holiday resort located in the Abruzzi region (Central Italy). It is surrounded by steep slopes reaching over 30 degrees.

Following previous landslide surveys [1] [2] and a careful evaluation of slope movements case records, we argue that systematic ground monitoring is now necessary to advance the understanding of recurrent landslide phenomena in this and other peri-urban hilltop settings [3]. In addition to such field observations, aerial photography and new EO techniques such as Synthetic Aperture Radar (SAR) interferometry and other image processing, which employs ground surface change, can also provide an useful contribution by: 1) detecting and

* This work was supported in part by European Community (Contract No. EVGI 2001-00055)

measuring ground deformations and 2) monitoring the on-surface and sub-surface slide causal factors.
This paper addresses these problems and presents some results from an EU funded R&D project (LEWIS), which is aimed at integrating ground-based techniques and Earth-Observation methods to provide warning of potential slope instabilities at selected test sites. From preliminary results of this project, it comes out that in peri-urban areas landslides are more likely to occur due to extreme rainfalls, seismic events or anthropogenic interference at locations which have experienced a permanent reduction of the limit equilibrium factors of safety in the past. Here we outline the functioning and the first results of in situ ground monitoring at one of the test sites of LEWIS project. In particular, we discuss the significance of groundwater level/pore pressure monitoring for hazard assessment at slope-specific scale.

2. Geological and hydrogeological characteristics

The lithologies shown in Fig. 1 which can be classified from a geotechnical point of view as rocks have been divided into three main groups: stratified and highly fractured limestones; marly mudstones including sandstone intercalations; carbonate megabreccias which form the caprock of the Caramanico hillslopes.
There are three groups of Quaternary/Holocene age sediments, which can be classified as soils, i.e.: a shallow layer of heterogeneous carbonate clasts with or without a clayey-silty-sandy "matrix" which mantle large portions of the hillslope areas, a mixture of cohesionless and cohesive materials made of eluvial sediments and a layer of artificial ground in some urbanized areas.
The widespread instabilities of the Caramanico hillslopes seem to be broadly related to the spatial distribution of these geological units and their hydrogeological properties. From the hydraulic point of view, three important units can be distinguished, i.e.:
1) A low hydraulic conductivity mudstone substratum with local sandstone beds, intensely fractured horizons, shear zones and folding;
2) A highly-permeable megabreccia slopecaprock which acts as an aquifer;
3) A medium to low hydraulic conductivity shallow deposit also acting as an aquifer. The rapid lateral and vertical changes of lithofacies/porosity in these loose deposits imply that the groundwater flow pattern is locally complex.

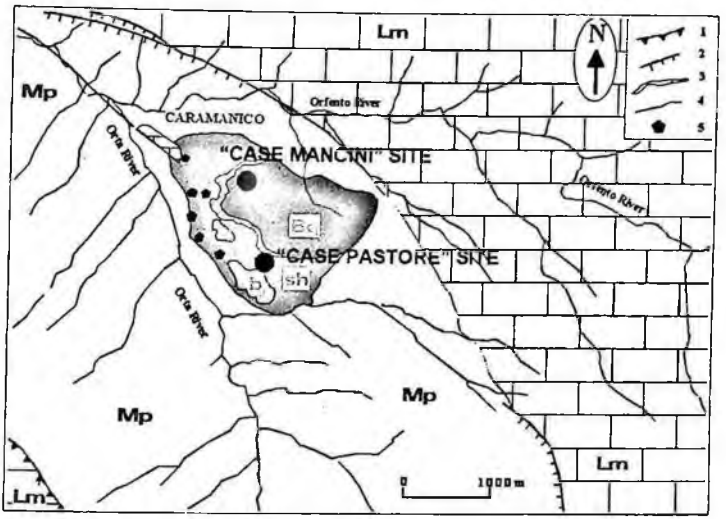

Fig.1 - Geological outline of the Caramanico area. Explanation: Lm = carbonate succession made mainly of stratified and fractured limestones - Miocene; Mp = marly mudstones, including rare sandstone intercalations - Early Pliocene; Bq = carbonate megabreccias – Quaternary (?); Sh = soils, represented mainly by thick colluvial materials including talus and landslide deposits, and secondarily by water-laid and elluvial sediments and artificial ground - Holocene; b = two major bodies of carbonate breccias (Quaternary); 1 = overthrust front of the Morrone Mt; 2 = fault (concealed or probable when dashed); 3 = steep scarp of the megabreccia caprock; 4 = lithological limit; 5 = spring.

3. In situ monitoring

Three continuous recording piezometers were installed in two boreholes (Fig. 2) to investigate the local groundwater level and pore water pressure variations. Borehole CMS (Case Mancini Site), which is located upslope an active landslide area, was instrumented with an open pipe piezometer equipped with an electric transducer at a fixed depth of 44 m to investigate groundwater table fluctuations within a 47 m thick limestone megabreccia caprock. An electric piezometer was also installed in the same borehole at 51.5 m depth to monitor pore pressure changes within the upper weathered part of the underlying mudstone substratum. Borehole CPS (Case Pastore Site), located within an apparently inactive deep-seated landslide, was equipped with a Casagrande piezometer. The cell, which contains an electric transducer, was positioned at 14 m depth to measure piezometric level data in a remoulded landslide material (silty clay containing limestone clasts) which is characterised by medium permeability.

All the instruments, whose technical features are reported in Table 1, are recording with an acquisition timestep of 6 hours and the data are transferred to data-loggers located at ground surface.
The electric signal (in mA) is converted into a pressure value using the conversion factor (mA/kPa or mA/m). The measured data are then processed by plotting a pressure-time or water head-time diagram, which shows the variation of pore pressures (kPa) or water level (m) with time.

Tab. 1 - Technical features of instruments

Instruments	Measure field	Precision	Filter type
Electric transducer	0 – 200 kPa	< 0, 3% F.S	Sintered polyethylene
Electric piezometer	0 – 500 kPa	< 0, 3% F.S	Sintered steel
Casagrande piezometer	0 – 200 kPa	< 0, 3% F.S	Sintered polyethylene

The preliminary results of the monitoring campaign carried out by means of the piezometers above described are shown in Fig. 2. Although limited to a short observation period, the piezometric data are offering some indications on the local hydraulic boundary conditions. In particular, the data recorded by the electric piezometer in borehole CMS indicate a higher piezometric level (of about 1 m) respect to that revealed by the open pipe electric transducer, this suggests that there may be confined flow in the mudstone stratum. The Casagrande piezometer in borehole CPS, which is located in a shallow remoulded clay stratum, reveals piezometric head variations that can be related directly to rainfall events, thus suggesting unconfined hydraulic conditions. Moreover the data logged by the CMS electric piezometer, which is installed in very-low permeability clays, confirm that these instruments need long time (up to 6 months) to reach the equilibrium value in such materials; the end of this lag-time can be considered as the real initial value of the data representative of the pore pressures in the soil mass.
The CMS electric piezometer data suggest that the pore water pressure regime in the slopes seems to follow a seasonal trend, with an increase of groundwater pressures during rainy winter and a decrease during the dry seasons (Fig. 3). Relatively low variations of water level have been observed in the megabreccia debris cover at Case Mancini, probably as a consequence of the presence of a well-functioning horizontal drain downslope; low variations of pore pressure have also been noticed for the electric piezometer. On the contrary, higher fluctuations of the piezometric level have been recorded by the Casagrande piezometer at Case Pastore. This indicates a more direct influence of rainfalls on the piezometric regime of this slope.

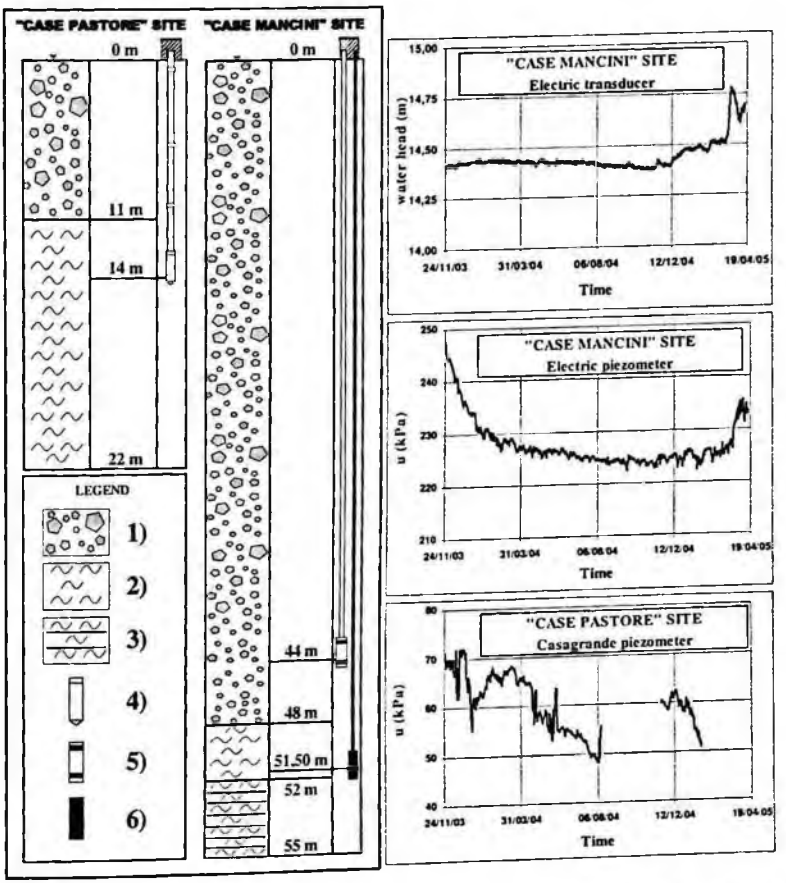

Fig.2 Lithological characteristics of two boreholes in the test sites, instruments installed and monitoring piezometric/groundwater level trends with time; Legend: 1) carbonate megabreccias, 2) remoulded clay, 3) stratified clay substratum, 4) casagrande piezometer, 5) electric transducer, 6) electric piezometer.

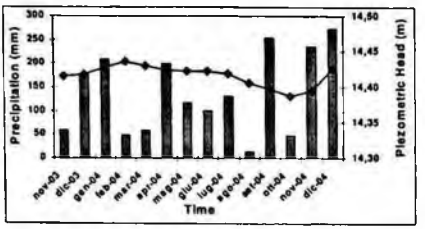

Fig.3 - Relationship between electric transducer data and monthly rainfall, in the "Case Mancini" site.

4. Conclusions

Nowadays the use of electric transducers for continuous monitoring of pore water pressure regime within slopes susceptible to landsliding is becoming indispensable in order to understand the hydraulic behaviour of slopes with time and to relate the pore pressure variations to the changes of slope boundary conditions (natural or anthropic). Furthermore, when also used for investigation and modelling of seismic slope stability, continuous-logging electric transducers are fundamental to provide informations on possible pore water pressure variations induced by earthquakes, both during shaking and afterwards. At Caramanico, preliminary data acquired by means of continuous-logging piezometers are considered to be reliable and consistent with the geometry of the slopes and the hydraulic boundary conditions.

References

1. R. Almagià. Studi geografici sulle frane in Italia. *Mem. Soc. Geog. It.*,13-431 (1910).
2. J. Wasowski. Understanding rainfall-landslide relationships in man-modified environment: a case history from Caramanico Terme (Italy). *Env. Geol.*, **35**, 197-209 (1998).
3. J. Wasowski, P. Lollino, P.P. Limoni,. V. Del Gaudio, G. Lollino and P. Gostelow. Towards an integrated field and EO-based approach for monitoring peri-urban slope instability. *Landslides: Evaluation and Stabilization*, Lacerda, Ehrlich, Fontura & Sayao (eds.), 809-816 (2004).

COMPARISON BETWEEN OPTIC AND ELECTRONIC SENSORS IN REINFORCED CONCRETE BEAMS EXTERNALLY BONDED WITH COMPOSITES SUBJECTED TO CYCLIC LOADS

P.CAPOLUONGO, C.AMBROSINO, S. CAMPOPIANO, A.CUSANO, A.CUTOLO
Optoelectronic Division - Engineering Department, University of Sannio, C.so Garibaldi N°107 82100, Benevento, Italy.

F.CERONI, M.R.PECCE
Engineering Department, University of Sannio, C.so Garibaldi N°107 82100, Benevento, Italy.

M.GIORDANO
Institute for Composite and Biomedical Materials, Italian National Research Council, P.le Tecchio N°80, 80100, Naples, Italy

In this paper a comparison between performances of optic sensors based on fiber Bragg gratings and electric strain-gauges has been carried out. Both sensing systems are used to measure strains on strengthening reinforced concrete beams with fiber reinforced plastic laminates, an innovative and effective technique to increase loading capacity of already existing structural elements. Fiber Bragg gratings represent an alternative solution for strain measurements in the field of civil engineering to strain gauges, widely exploited and well assessed for these applications. Advantages of optic sensors in multi-point sensing systems for great numbers of sensors will be evidenced in terms of costs and performances.

1. Introduction

Actually, the use of fiber reinforced plastic (FRP) laminates externally bonded to reinforced concrete (RC) elements is a very common technique for strengthening, rehabilitation and seismic assessment of civil structures. FRPs materials are usually made by fibers (carbon, glass, aramid) with high mechanical properties (tensile strength and elastic modulus) and by an epoxy matrix that impregnates fibers and bonds them to concrete surface. RC elements strengthened with FRP can have a typical failure due to the detachment of laminate from concrete surface and is generally due to a stress concentration [1]. Since the modality of this failure is strictly related to the bond behavior developed at the concrete-adhesive-laminate interface [1], an adequate monitoring is required. This task can be accomplished by a rugged and in situ sensing system. In the common practice strain-gauges are exploited. A good alternative can be represented by a particular class fiber optic sensors: fiber Bragg gratings (FBGs). They are optical strain transducers and have several good features like low intrusivity, good mechanical robustness, electromagnetic interferences immunity and high multiplexing capability [2]. Here the performances of FBGs are compared with the ones of electric strain-gauges for

monotonic and cyclic load tests performed on reinforced concrete beams externally bonded with FRP layers.

2 Strain Sensors

A FBG is a periodic permanent perturbation of the refractive index of the core of an optic fiber. It reflects, when irradiated by an optical broad band source, a narrow band pass spectrum centered at "Bragg's wavelength", λ_B, related to the physical parameters of the grating by Eq.1 [2]:

$$\lambda_B = 2\, n\, \Lambda \tag{1}$$

where n is the effective refractive index of the propagating mode of the fiber; Λ the spatial period of the FBG. The axial strain sensitivity of these devices is reported in Eq.2 [2]

$$\frac{\Delta\lambda_B}{\lambda_B} = \left(1 - \frac{n^2}{2}\left[p_{12} - \nu\left(p_{11} + p_{12}\right)\right]\right) \cdot \varepsilon = S_\varepsilon \cdot \varepsilon \tag{2}$$

where ε is the applied strain, p_{11}, p_{12} are two components of the strain optic matrix, ν is the Poisson's ratio [2]. Whereas strain-gauges (SGs) are electric devices, they change their resistance as a consequence of geometric variation induced by strain application. Equation (3) relates the relative resistance variation for an uni-axial SG to the applied strain [2]:

$$\frac{\Delta R}{R} = K \cdot \varepsilon \tag{3}$$

where R is the resistance of the device and K is a calibration factor. This expression is formally very similar to Eq.(2).

3. Experimental Set Up

Monotonic and cyclic load tests require the utilization of two set up. For the monotonic one, a RC beam with a rectangular section (100mm x 180mm), 2400mm long and with asymmetrical internal steel reinforcement is exploited. External reinforcement is made by two high strength superimposed carbon fibers layers bonded with an epoxy resin on the bottom side of the beam. This sample is placed on two supports at the ends and vertically loaded in two points 300mm spaced respect to the midspan. Bending loads are applied by pressing the middle section of the top side of the beam with a mechanical system connected to a load cell. To check the strain distribution on the FRP laminate on the bottom face thirteen strain gauges are placed along carbon fiber strip: one at the central section (where maximum normal stress is reached in the laminate), six at left and right ends. Wheatstone bridge circuits, internal to three commercial HBM Spider 8 digital acquisition boards, are exploited to interrogate strain-gauges. This system has a resolution of 1$\mu\varepsilon$.

A FBG, with a central wavelength, λ_B, free at 1549.9nm, a 0.2nm FWHM passing bandwidth, oriented along the beam's length direction is applied aside the central strain - gauge, in order to sense the same strain. The exploited interrogation systems for this sensor has an optic filter, realized with a chirped and strongly apodized FBG [3], with a nominal linearity range of 10nm, centered at 1550 nm. A static resolution of 1με is achieved with this system [3]. FBG sensors responses are acquired, as SGs signals, by the same digital acquisition systems.

The beam utilized for the cyclic load test has the same features as the one exploited for previous one. In this case two reinforcement fibers layers (carbon fiber with epoxy resin) are placed on the top and on the bottom side of the beam, symmetric respect to the midspan. The excitation mechanism is modified in order to apply a bi-directional load. On this sample seven strain-gauges are placed on the top and seven on the bottom side. The FBG, (0.43nm FWHM passing bandwidth @ λ_B=1549.8nm) is located aside the central SG of the bottom side.

4. Results and Discussion

A proper calibration procedure is carried out in order to obtain the FBG response expressed as applied strain. A preliminary step is devoted to the measurements of the relative wavelength shift - strain sensitivity referred to the free FBG, obtaining a value of $0.75*10^{-6}\mu\varepsilon^{-1}$, and the conversion between the wavelength shift and the normalized output provided by the interrogation systems.

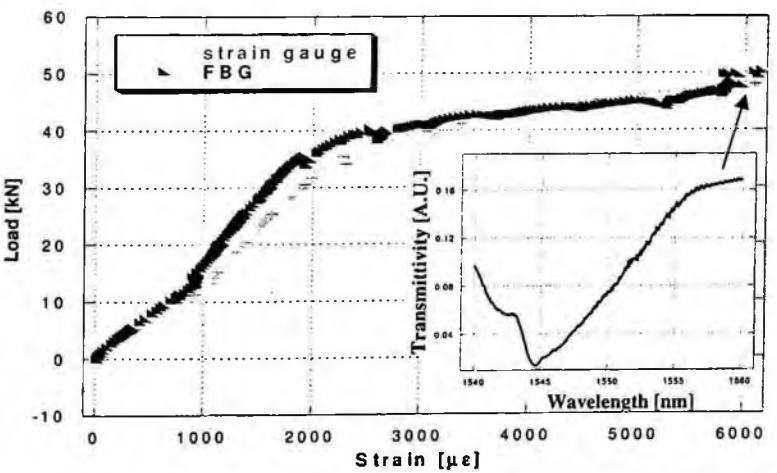

Figure 1. Load - strain diagram for the monotonic test. The inset on the right side represent the transmictivity of the linear filter exploited to interrogate the FBG.

A second step is devoted to the conversion between the wavelength shift and the normalized output provided by the interrogation systems. In Figure 1 the load - strain curve for the monotonic test is reported. For low load values a small disagreement is obtained between the results of FBG and reference SG. Probably this is due to the strong inhomogeneities of the material, which cause the two device to sense a different strain. FBG data for very high strain exhibit a slope smaller than SG's ones. This is a consequence of the great right shift of the FBG, leading it outside the linearity range of the adopted filter (see the inset of Figure 1, representing the transmittivity of the filter). This drawback can be overcame by using a filter with a greater linear range. The failure of the beam in this case is caused by the delamination of laminate at one end at a load of 53.0kN.
For the second test, the breaking of the sample happens after nine cycles of bi-directional load application. The preliminary strain characterization for the exploited FBG leads to a sensitivity of $0.77*10^{-6}\mu\varepsilon^{-1}$. The time history of the two sensors is reported in Figure 2. Also in this case, for both compressive and tensile load, a good level of agreement can be observed for the two sensors during each performed cycle. The failure of the beam is caused by delamination at a load of 31.3kN.

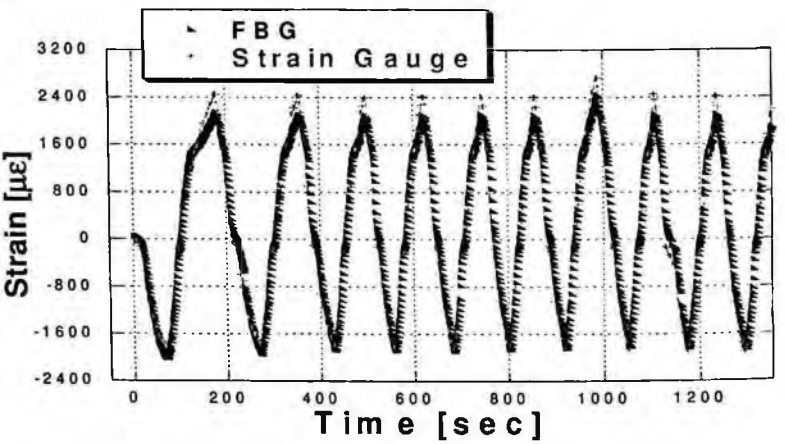

Figure 2. Time history of both SG and FBG sensors for the cyclic test

The good results obtained comparing both SGs and FBGs responses witness the potentialities of these latter devices in this field. Real systems for civil engineering applications need a great number of sensors. Strain-gauges are cheap, but require delicate Wheatstone bridge based interrogation systems. They are electrical, their wires are not shielded from electromagnetic interferences. Moreover, at the rising up of the number of sensors, a great amount of electric wires, cumbersome for the structure, is necessary.

Whereas, for the FBG based sensor, at the rising up of the number of sensors a narrow band tunable laser can be used to interrogate several sensors multiplexed on the same fiber instead of a broad band interrogation system by using an only photodetector [3]. Such a system can achieve a resolution of 1με. A comparison between two commercial SG based systems (HBM Spider 8, Vishay 5100) and a FBG one has been performed. Costs at the rising up of the number of sensing systems are reported in Figure 3: FBG based one, for 41 devices become more convenient than SGs ones.

5. Conclusions

Performances of SG, a traditional sensing system for strain measurement, and FBG based ones for the monitoring of reinforcement composite bars application on concrete beams have been presented. The two sensors exhibit a good agreement both for the monotonic and the cyclic test, except for some discrepancies due to the inhomogeneities of the material. Moreover, a comparison of the costs of SG and FBG sensing systems has been made. At the rising of the number of sensors, FBG results as more competitive. This, in union with other good features of these sensors, makes them ideal candidates for this application.

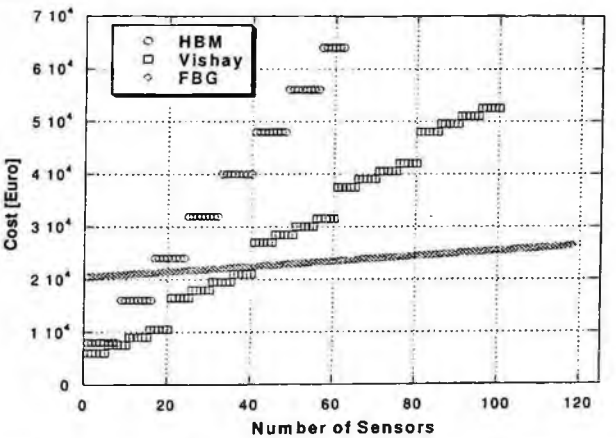

Figure 3. Cost of multi-point sensing systems at the rising up of channels number

References

1. J. Teng et al., "FRP Strengthened RC Structures", Wiley & Sons Ltd, pp.11-101, 2002;
2. R. Measures, "Structural monitoring with fiber optic Technology", Academic Press, London, 2001;
3. A. Cusano, G. Breglio, M. Giordano, L. Nicolais, A. Cutolo, IEEE/ASME Transactions on Mechatronics , Vol.9, No.1, pp. 40-49, 2004;

REVIEW OF NON DESTRUCTIVE TESTING TECHNIQUES FOR COMPOSITES MATERIALS AND NEW APPLICATIONS OF PIEZO-POLYMER INTERDIGITAL TRANSDUCERS

F. BELLAN, A. BULLETTI, L. CAPINERI,
A. CASSIGOLI, L. MASOTTI, O. OCCHIOLINI

Department of Electronic and Telecommunications, University of Florence, S. Marta 3, 50139 Florence, Italy

F. GUASTI, E. ROSI

Alenia Spazio - Laben, Einstein 35, 50013 Campi Bisenzio (Florence), Italy

The paper reviews the techniques employed for non destructive testing (NDT) on Carbon Fiber Reinforced Plastic (CFRP) materials from the perspective of the sensors characteristics and compares the different methods, even the most recently developed by the authors, based on guided acoustic waves generated/detected with piezopolymer intergitated transducers (piezo-IDT). These devices transmit and receive ultrasonic guided waves traveling inside the material and are able to detect any accidental defect or damage occurred to the material itself. New application of piezopolymer IDT for NDT on different types of composites will be presented and the very good defect detection capability will be demonstrated by exciting a symmetric mode S_0 at 350 kHz.

1. Introduction

The importance of composite materials for designing and manufacturing high-tech products is a matter a fact. Nowadays we find composite materials employed in the space, avionic, transport and sport equipment industry as parts of vehicles (cars, motorbikes and bicycles), of boats, skis and snowboards etc.
In the applications where material health and safety is of great concerns (parts of spacecrafts or airplanes) non destructive testing methods are necessary for quality control and monitoring during service.
Several methods are commonly used for NDT on CFRP and recently authors [1][2], developed a method, based on guided acoustic waves generated/detected with piezopolymer intergitated transducers (piezo-IDT). The first objective is to use these sensors in ultrasonic non-destructive testing for defect detection on composite spacecraft parts [3]. One of the key advantages of this technology with respect to a traditional piezoceramic sensor is the conformability of such devices - based on the soft piezoelectric polymer material – to non-planar

surfaces of complex shaped products. The sensor manufacturing technology is rather new and is based on a laser microfabrication (laser ablation of gold layer) of electrodes over metallized PVDF film. The results of the study demonstrate the feasibility of using the piezo-polymer sensors for NDT of carbon fiber reinforced plastic (CFRP) composites.
The flexibility of the design and use of piezo-IDT has stimulated some other applications as the measurement of the stress. Recent results on 4 mm thick cross-ply CFRP are presented and compared with expected values from theory of acoustoelasticity [4]. Another application under development is the health monitoring of sandwich composites that require piezo-IDT operating at lower frequency (50 – 100) kHz.

2. Comparison of different NDT techniques

The results of NDT state of the art research is summarize in the table shown in Figure 1, where standard and new techniques are compared. In particular we observe that there are two candidate methods for devising in-service NDT system that are the ultrasonic Lamb wave and Optical fibers with a Bragg grating. Both are currently explored by many research groups.

3. Lamb waves NDT ultrasonic methods based on PVDF interdigital transducers

The first objective of the design of an IDT is the definition of the electrode pattern, which under certain hypothesis defines the frequency response, and the selection of a propagation mode according to the laminate dispersion curves [5]. The IDT interlaced electrodes geometry has been adopted. This transducer configuration is differential, because the two series of electrodes (also called fingers) are driven with opposite phase signals (V+ and V-) and they have the same reference ground electrode (GND). The basic transducer design parameters are: width (W), length (L), piezopolymer film thickness (t), fingers separation (S) and number of fingers (N). The interlaced configuration requires that finger separation S, must be half of the wavelength λ relative to the selected guided wave mode [2].
The material used for the sensors design is a commercial copolymer P(VDF-TrFE) film (PiezoTech s.a., St. Louis, France) with thickness t = 100 μm and a gold metallization with approximate thickness of 0.1 μm, mass density 1780 kg/m, and longitudinal velocity 2200 m/s. For electrodes design on the PVDF film we have used a fast manufacturing process based on laser ablation of the thin film metallization on both film surfaces.

Main advantages using PVDF instead of commercial piezoceramic (PZT) material are:

- Conformable to non planar surfaces.
- Potentially to be embedded inside the composite material.
- Low-cost (material and design).

The interaction between guided (Lamb) waves and an embedded defect can be simulated by Finite Element Methods [6][7] and the main effects that can be measured experimentally are:

- Phase velocity variation
- Reflection, Refraction and diffraction of waves from damaged area.

4. New applications of piezopolymer IDT for NDT on CFRP

There are several NDT applications for piezopolymer IDT that has been experimented by the authors [3][4][8]:

- Defect detection in CFRP laminates
- Joint breakage.
- Traveling waves around a CFRP cylinder.
- Surface perturbation on propagation velocity
- Stress measurements
- Applications to marine reinforced composites.

Some examples of signals acquired by the diagnostic system formed by some couples of Transmitter/Receiver piezopolymer transducers excited with sine wave burst at 350 kHz are shown in section 6 and described below.

Figure 2 shows the acquired signal of a failure induced in a bonding between an aluminum and a composite laminate. The couple of sensors are installed on the aluminum plate. The first signal on the left corresponds to the excitation signal received by Rx, the centered one is the signal reflected by the aluminum edge and reduced (in amplitude) by the presence of the composite laminate bonded on the aluminum. After the debonding this signal increases in amplitude because there is no more energy transfer to the composite laminate. The last signal (on the right) represents the reflection from the opposite edge of aluminum plate that and remains unchanged in the two cases.

The Figure 3 shows the condition of signal acquired both across a not damaged and a damaged area in the delamination presence; as foreseen in the literature [7], there is an evident shift in phase and a decrease of amplitude of the signal.

5. Conclusions

The research activity focused on the development of piezopolymer interdigital transducers has produced a design and manufacturing process which is repeatable and easy to be adapted for different NDT applications. It is of interest now to investigate the capability of new NDT diagnostics for composites based on a network of these transducers. In the short term the research will be addressed to avionic and hi-tech marine composites.

6. Figures

	Method	Strengths	Limitations	Structural Health Monitoring potential
STANDARD METHODS	Ultrasonic (C-scan)	Portable Sensitive to small damage	Mechanical movement Specialized software	Currently none
	X-radiography	Small defects with penetrant No data analysis	Expensive equipment Safety hazard	Currently none
	Acoustic emission	Surface mountable Sensitive to small damage	Very complex results Specialized software	Lightweight Results for large area
	Thermography	Sensitive to small damage	Expensive equipment Specialized software	Currently none
NEW METHODS	Optical fibers (Bragg grating)	Inexpensive equipment Embeddable Quick scan of large area	Expensive to implement Specialized software Accuracy in defect localization	Lightweight Large area coverage Must be embedded Requires laser source
	Ultrasonic (Lamb waves)	Inexpensive equipment Inexpensive to implement Surface mountable Portable Sensitive to different damages Quick scan of linear space (No probe movement)	Very complex results Specialized software Continuous/frequent monitoring	Lightweight Comformable Medium power draw Linear scan results (single-twin probe) Triangulation possible (multi probe)

Figure 1. Comparison of NDT techniques for CFRP.

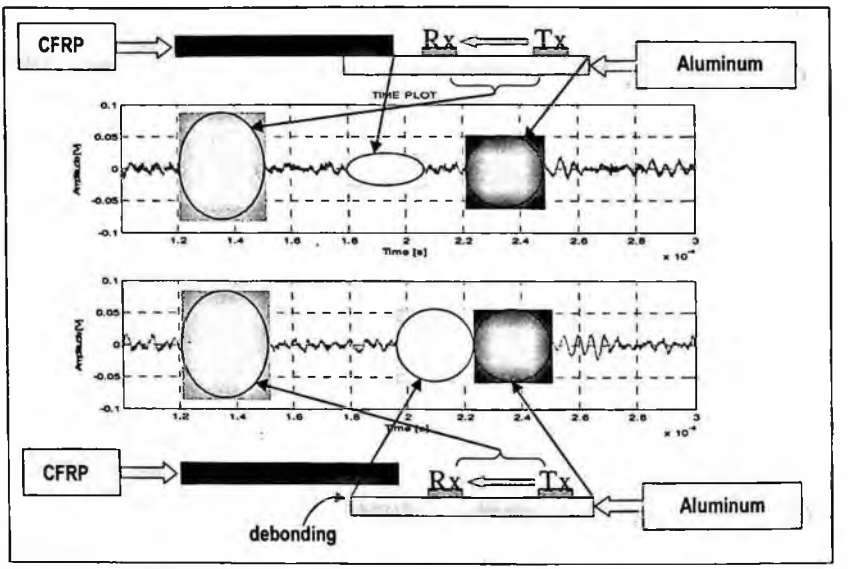

Figure 2. Acquired signal before and after a debonding action induced by debonding a piece of Aluminum glued to a composite laminate.

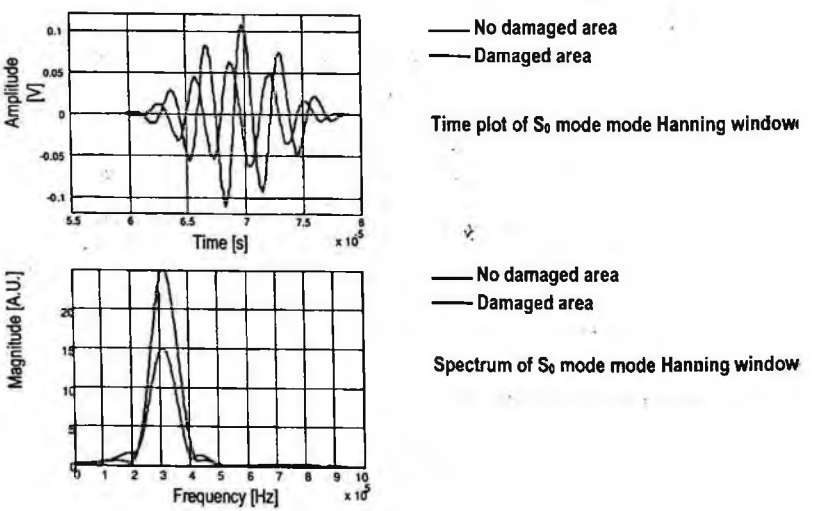

Figure 3. Signal acquired both across a not damaged and a damaged area in a delamination presence and relative frequency spectra.

Acknowledgments

ESA Innovation Triangle Initiative (Contract n. 16938/02/NL/MV).

References

1. F. Bellan, A. Bulletti, L. Capineri, L. Masotti, F. Guasti, E. Rosi, "A new design and manufacturing process for lamb waves interdigital transducers based on piezopolymer film" sent to Sensors and Actuators A, 2004.
2. F. Bellan, A. Bulletti, L. Capineri, L. Masotti, F. Guasti, E. Rosi, "Acoustic guided waves interdigital transducers for non destructive testing of carbon epoxy composites for spacecraft structures", AISEM 2003-2004 Proceedings, Ferrara, 8-11 February 2004.
3. ESA-ESTEC Contract n.16938/02/NL/MV.
4. O. Occhiolini, "Studio, sviluppo e sperimentazione di un metodo di misura dello stato di sforzo di laminati compositi mediante onde di Lamb", Thesis submitted to the Faculty of Engineering of the Università di Firenze to obtain the degree in Electronic engineering, April 2005.
5. G. S. Kino, Acoustic Waves – Devices, Imaging, & analog signal processing, Prentice-Hall, Englewood Cliffs New Jersey, Processing Series, 1987, Chapter. 2.
6. S. Kessler and S. M. Spearing, "In-situ sensor-based damage detection of composite materials for structural health monitoring", AIAA-2002-1545.
7. V. Agostini, P. del Santo, I. Genesio, D. Olivero, "Simulation of Lamb Wave Propagation for the Characterisation of Complex Structures", IEEE Trans. On UFFC, pp. 441-448, April 2003.
8. Internal Report "Prove effettuate presso la ditta VEGA srl di Barberino del Mugello – Firenze", 28 December 2004.

OPTIMIZATION OF FOREST FIRE DETECTION BY INTRAFRAME ADPTIVE FILTERING

G. Lorusso, M. Dongiovanni, F. Intini, G. Nacci, E. Celiberti

SMA High Tech S. p. A., Via Repubblica 36/f, 70015 Noci (BA)

Abstract

The PAIS system, based on IR technology, was developed by SMA (Sistemi per la Meteorologia e l'Ambiente) for forest fire detection.

The application of a new adaptive filter is here presented, in order to allow an optimal recognition of emergency situations, avoiding not really dangerous alarms due to sudden disturbances of the environment.

A variable threshold is computed, based on the Hyperbolic filter algorithm, which is inversely proportional to the mean value obtained by moving a selected window through the matrix derived as two contiguous acquisitions difference.

The main advantages of this filter are a reduction of the response time and the threshold independence on the variability of meteorological conditions.

The results show that this filter is able to significantly reduce the number of false fire alarms inside the investigated area.

1 Introduction

In the field of devices for Environmental Monitoring, the PAIS (Prevenzione Antincendio e Salvaguardia) system has developed by S.M.A. S.p.A. to allow an efficient fight against forest fire.

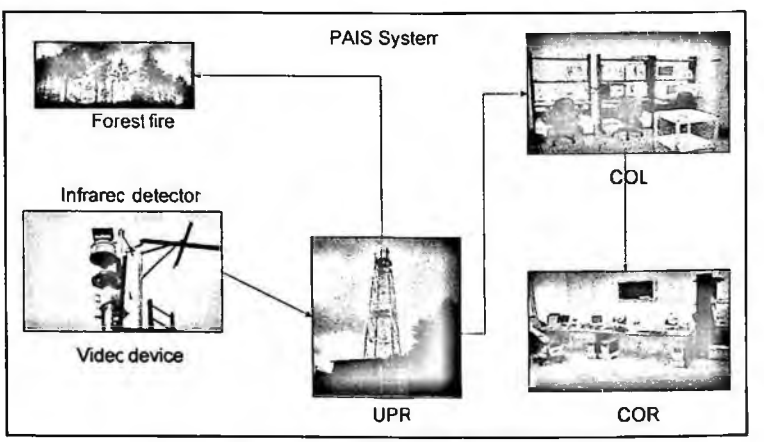

Figure 1: PAIS architecture

PAIS consists of three fundamental blocks.

- a peripheral device for detecting forest fires named *U.P.R.*. (Unità Periferica di Rilevamento);
- a local operational centre named *C.O.L.* (Centro Operativo Locale);
- a regional operational centre named C.O.R. (Centro Operativo Regionale).

U.P.R. is the principal component of PAIS system and is composed of

- a sensing element (PbSe) ranging from 3,3 to 5 μm;
- a motion system which allows a 360° azimuthal rotation (with steps of 0,3°) and 30° zenithal rotation (with steps of 1°);
- A video device working in the visible spectral region.

All the data and images related to the zone under surveillance are collected by the local center (*C.O.L.*) operators and regularly analysed so that, actually, a maximum delay of about 3 minutes is achieved between the fire start and the system-alarm.

2 The Hyperbolic Adaptive Filter

All the elements composing the *U.P.R.*. system are shown in fig. 2 in a block diagram form.

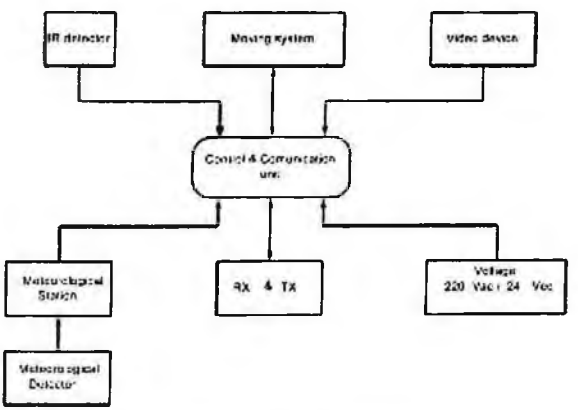

Figure 2: U.P.R. architecture

The target, the object of main interest, is usually the incoming fire. The system detects the presence of the target and tracks it as it moves.

The operational range of the system (3,3-5) assure a lower water vapour absorption [1] so that a realistic signal processing can be performed in spite of the very small part of the radiation emitted by the target reaching the sensible element of the system.

Even though a very small part of the radiation emitted by the target is able to reach the sensible element of the system, both because of its transverse direction of propagation with respect to the direction of maximum emission and because of the travelling across different layers of earth's atmosphere characterized by different moisture contents causing differential attenuations of it, a realistic signal processing can be performed thanks to the operational range of the system (3,3-5) assuring a lower water vapour absorption [1]

The optical receiver collects some of the radiation coming from the target and delivers it to the detector which converts it into an electrical signal. The electrical signal from the detector is transmitted to the processor where it is amplified and the coded target information is extracted. The purpose of signal processing is not only recognizing fires against the background but, above all, discriminating real fires from not real dangerous alarms (figure 3).

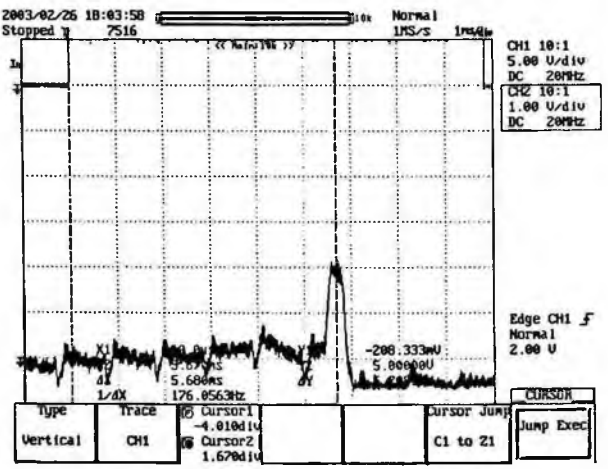

Figure 3: Analogic signal

The application of an adaptive filter is here presented, in order to allow an optimal recognition of emergency situations, not due to sudden disturbances of the environment. This new algorithm is especially designed for maximizing fire detection probability against false alarms.

Because IR level, shown in fig., is not constant a variabile threshold is computed based on the *Hyperbolic Filter Algorithm*, which is inversely proportional to the mean values obtained by moving a two-dimensional selector window applied to two contiguous acquisitions difference. The window has to be correctly selected depending on the particular features of the fire (form, dimensions, developing, vegetation cover...).

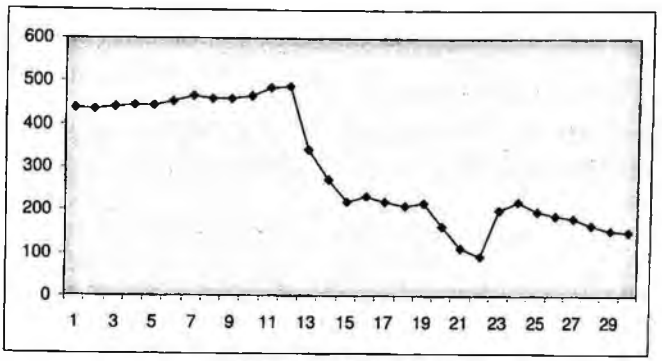

Figure 4: IR levels graph

This filter can be performed using the following procedure

- storage of numeric voltage values recorded during the first acquisition into a reference matrix (RM);
- storage of numeric voltage values recorded during the next acquisition into a current matrix (CM);
- computation of the difference between the current scene (CM) and the reference scene (RM);
- threshold computation by

$$T = \frac{2\,k \cdot N}{M + 1} \qquad [3],$$

where

k is the variable gain factor;

N is the instrument full scale value;

M is the mean value of observation window.

- comparison between the threshold and the difference matrix.

The algorithm shows that every time the window selects a sample of low IR values, the filter produces a consequently low mean value causing a high value of the threshold, and vice versa.

The real advantage of this filter is that, even when the sample of IR values selected by the moving window contains a few higher values (corresponding to spurious sources) respect to the background, the mean value is not affected and the threshold is kept high; in these conditions the system does not produce any alarm condition.

3 Results and Conclusions

The results obtained by applying the Hyperbolic adaptive filtering show an increased *U.P.R.*'s stability, in the sense that the system is able to detect a significantly reduced number of false alarms.

In particular, the experience shows that this technique presents the following advantages

- 67% reduction of false alarms
- 81% delay time reduction (actual filtering delay time is 850 ms, whereas Hyperbolic filtering's delay time is 150 ms)

The pictures below show the difference between the number of the not real alarms produced by the actual filtering (a) and the hyperbolic filtering(b).

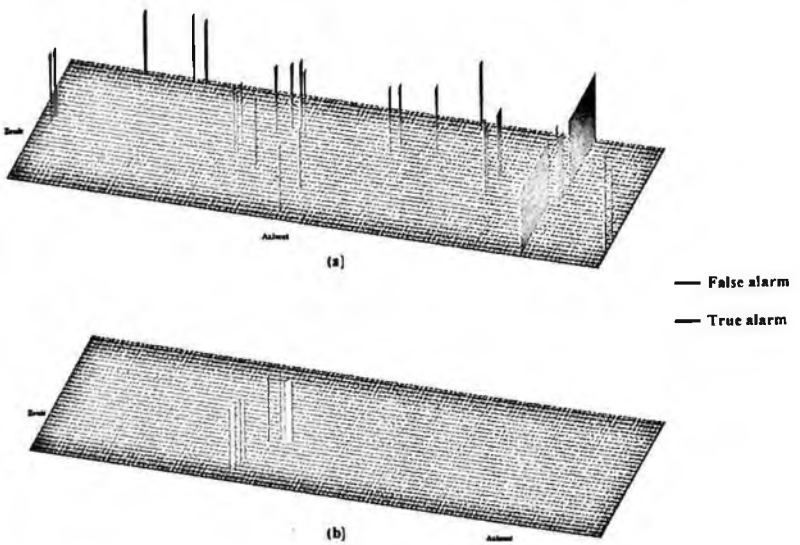

Figure 5: Difference between old filter (a) and Hyperbolic filter (b) answer

The Hyperbolic filtering is able to improve significantly the recognition of emergency situations, avoiding not really dangerous alarms.

References

1. Hudsonn Jr. R. D., *Infrared System Engineering*, Wiley-Interscience, 1970
2. Derin H., Elliot H., *Modelling and segmentation of noisy and textured images using Gibbs fields*, IEEE Trans, 1987
3. G. Mastronardi, Image comparison in integrated safety system, Atti del Simposio Internazionale su Robotic and Automation, Lugano, 1985

FOREST FIRE LOCALIZATION WITHOUT USING DIGITAL TERRAIN MODEL

M. Dongiovanni, G. Lorusso, F. Intini, G. Nacci, E. Celiberti

SMA High Tech S. p. A., Via Repubblica 36/f, 70015 Noci (BA)

Abstract

The PAIS system, developed by SMA (Sistemi per la Meteorologia e l'Ambiente) for forest fire detection, mainly uses Digital Terrain Model in trying to determine the exact position of the fire site. A theoretic study is here proposed, based on a new technique for determining the distance between the IR sensor and the target. The distance is computed by using both the hypothesis of black body with spherical emissivity in free space and the Bourget-Lambert-Beer law which takes the attenuation related to the atmospheric variability into consideration.

The computed distance is then used to determine UTM coordinates of the target. The real advantages of this technique are a reduction of the main memory and a more precise fire target localization.

1 Introduction

The PAIS is an automatic vegetation fire detection system which has been developed by SMA. It is, at present, one of the most validated and reliable detection systems, since it became operational in different sites in Sicilia, Puglia, Toscana, Basilicata, Campania, where the places present particularly severe vegetation fire problems. PAIS consists of an operational console and a computer set with an embedded territorial database for topological and thematic information retrivial and suitable software programs for overall fire risk evaluation and evolution forecasting.

The principal features of the PAIS are

- High sensitivity: the sensor can detect fire developing over small areas typically 5 m^2 at a distance of 10 Km;
- Wide sectorial coverage of areas 30x30 km using infrared detectors and cameras in visible spectral region;
- The system can work day and night in a fully automatic way;
- The detected fire can be localised on the ground with a precision of 0.5 degree.

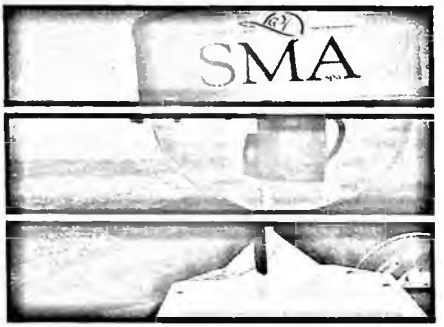

Figure 1: PAIS detector

2 Fire Localization

The main problem for the control of forest fire is to discover fire as soon as possible and locate it with good precision on the ground. Experience confirms that the efficiency of fire suppression procedures is highly dependent on the delay time of the intervention. PAIS computes the position of the fires sites using Digital Terrain Model for the zones under surveillance.

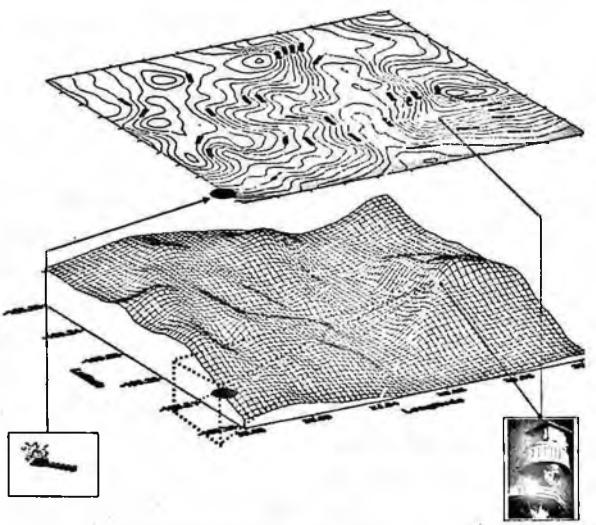

Figure 2: Fire localization

A theoretic study is here proposed, based on a technique for determining the distance between the IR sensor and the target. The distance is computed by using both the hypothesis of blackbody with spherical emissivity in free space and the Bourget-Lambert-Beer law which takes the attenuation related to the atmospheric variability into consideration.

The spectral distribution of the radiation emitted by a fire is the same as the one of a blackbody at 800 K, so it is perfectly known thanks to *Planck's*. Integrating Planck's law over a wavelength range extending from 3.3 to 5 micrometers (the operative sensor range) we obtain an expression for the radiant emittance, the flux radiated into a hemisphere above a fire extending over an area of 1 cm².
Since the radiation emitted by the fire is obliged to travel across different layers of the atmosphere, with different moisture contents, it will be partially attenuated depending on a particular meteorological conditions.
Moreover before reaching the infrared sensor, the radiant energy flux from the fire may be reflected, scattered or absorbed according to the *Bouguer-Lambert-Beer's law*.

$$P = P_0 \, e^{-\sigma x}$$

where:

P_o is the flux entering dispersive medium;

P is the flux remaining after the beam traversed a distance x;

σ the *extinction coefficient* including the effect of scattering and the absorption of the atmosphere; its values are experimentally determined by dependence on meteorological parameters.

The optical receiver collects some of the radiation from the target-fire and delivers it to a detector which converts it into an electrical signal. The data acquired are sampled, digitized and processed.

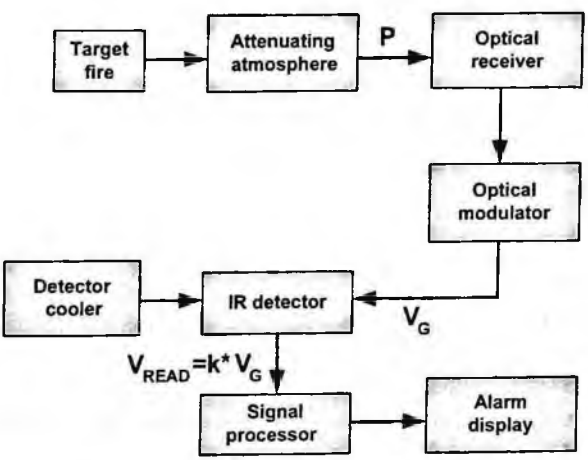

Figure 3: The elements of the infrared sensor

The target-fire distance is determined by:

$$D = \frac{1}{\sigma} \cdot \ln\left(\frac{P_0 \cdot (\sin(\frac{ifov}{2}))^2 \cdot R \cdot G \cdot k}{P_{READ}}\right)$$

where:

P_o is the flux remaining after the target beam has traversed D;

P is the flux entering the atmosphere;

ifov is the istantaneus view of the detector (angular amplitude);

R is the detector responsivity;

G is the voltage gain;

k is the digital factor;

σ is the *extinction coefficient.*

The computed distance is then used to determine Universal Transverse Mercatore coordinates of the target in an appropriate coordinate system.

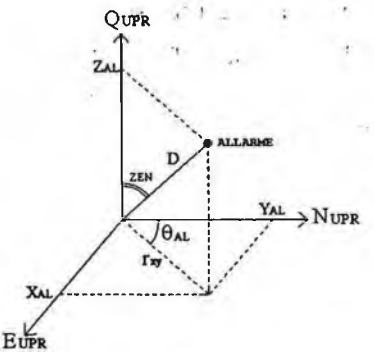

$$\begin{cases} x\_alarm = x\_al\_upr + x\_upr \\ y\_alarm = x\_al\_upr + x\_upr \\ z\_alarm = x\_al\_upr + x\_upr \end{cases}$$

3 Conclusion

This method is particulary interesting for the improvement introduced in localizing fire's site.

The real advantages of this technique are represented by

- a fire target localization carried out avoiding the problems related to DTM use;
- a more precise localization performed by taking into account local weather conditions.

References

1. Cambursano C., *Cartografia Numerica*, Progetto Leonardo, 1997
2. Flotron A. & Kölbl O., *Precision Terrain Models for civil Engineering*, OEEPE Publication, 32-134, 2000
3. [3] Hudson D. R., *Infrared System Engineering*, Wiley-Interscience, 1970

SYSTEMS, NETWORKS AND ELECTRONIC INTERFACES

AN INTEGRATED WIDE-RANGE RESISTANCE-TO-TIME CONVERTER WITH DECOUPLED OSCILLATOR

MARCO GRASSI, PIERO MALCOVATI

Department of Electrical Engineering, University of Pavia,
Via Ferrata, 27100, Pavia, ITALY; [marco.grassi, piero.malcovati]@unipv.it

GIANPIERO DE IACO, ANDREA BASCHIROTTO

Department of Innovation Engineering, University of Lecce,
Via Arnesano, 73100, Lecce, ITALY; [gianpiero.deiaco, andrea.baschirotto]@unile.it

In this paper we present an integrated wide-range resistance-to-time converter. The circuit in transistor level simulations achieves a precision of about 0.5% over a range of 5 decades (1kΩ-100MΩ) without requiring any calibration or autoranging. The presented technique exploits an integrator-based controlled oscillator, whose main time constant is function of the applied resistance value, named R_{sens}. The state of the art [1] of this measurement method has been improved by separating the oscillator circuit from the sensing device, leading to higher linearity performance. Indeed, the sensor response takes advantage of the fact that the device is biased between a fixed buffered reference voltage V_{REF}=1V and ground. A couple of high-linearity current mirrors replicate the current V_{REF}/R_{sens} and alternately push it into or pull it from the virtual ground of a resettable Miller integrator. The output of this block is connected to a couple of comparators which compare V_{OUT} with two fixed boundary voltages V_H and V_L (V_H–V_L=1V), producing the control signals for the switches that shunt the mirrored current. A small logic grants that the comparators switch alternately; furthermore it feeds an internal counter whose transition period is proportional to the value of R_{sens}. In the resistance range of interest the internal oscillator frequency will vary between f_{min}=50Hz and f_{max}=5MHz if the integrator feedback capacitance is set to 10pF and the mirrored current is scaled by a factor of 1:10 in order to reduce the operational amplifier output current, leading also to a lower total power consumption. The ratio between a reference counter, whose clock frequency is fixed at the midrange value $f_{mid}=(f_{min}\cdot f_{max})^{1/2}$=16kHz and the resistance dependent one represents the digitized value of R_{sens}. The measurement ends when the slower of the two counters reaches a fixed value N^* which is enough to achieve the desired accuracy, i.e. 8 equivalent bits (N^*=256). The maximum conversion time is 5 seconds, when sensing the highest resistance values, i.e. R_{sens}=100MΩ, while for the lower half-range values conversion (R_{sens}<320kΩ) requires only 16ms.

1. Introduction

The proposed resistance-to-time converter can be used either as a wide-range portable ohmmeter or as a smart front-end circuit for resistive sensor read-out. Regarding this second application the device will be optimized as electronic interface for gas sensor arrays for indoor monitoring purpose. In this case the

digitized outputs of the several different unitary elements of the sensor array will be properly processed with suitable digital pattern recognition algorithms. If the aim is to design a low-cost and wide-range integrated interface, a successful solution may be a partially re-configurable circuit without a complex calibration system. In the case of this work, considering an array of N different sensors, a strong cost reduction is guaranteed if a single front-end circuit is able to process the analog information from all sensor types included in the array, thus requiring a wide dynamic range circuit and multiplexing technique. Indeed, even if each of the N sensing devices is optimized to detect a particular kind of gas, they provide important information also on the concentration of other gas types which are then used by traditional and dynamic pattern recognition techniques [2]. The latter technique, which gathers information also from the derivative of the sensor response, requires an electronic interface which must be fast enough, i.e. that provides at least 10 accurate samples of the resistance value for every element of the array per second (overall system sample rate >10 Hz). Moreover, wide dynamic range performance is needed because the sensors resistance value (R_{sens}) may vary through several decades, being the combination of three variable components: the baseline R_{bl} (which mainly depends on the fabrication technique), the deviation from the baseline ΔR_{bl}, due to technological and aging spread and temperature as well as the resistance variation ΔR_{gas}, which depends on gas concentration, negative for most gas types. Its value can be as large as a couple of decades from the actual baseline value. At the present state of art in sensors manufactory, depending on device type, technology spread and sensor age, the baseline usually varies from a very low value [3], i.e. 10kΩ, to a very high one, i.e. 100MΩ and the sensor resistance has to be measured with a 0.5% precision in order to be sure to detect every gas type presence with enough accuracy for indoor gas monitoring purposes. The dynamic range required for the front-end circuit is then 5 decades [1kΩ-100MΩ]. The large baseline variation together with the large measurement accuracy would require, without any range compression, to use a linear front-end circuit with a resolution so high to be unpractical. For this reason alternative read-out structures have to be developed [4]. For example, an oscillator approach can be tried [1]. In this case the circuit main time constant is function of sensor impedance: this technique allows the measurement of higher resistance values with respect to traditional interfaces, but it is slower and of course affected by the parasitic capacitance of the sensor layers. Furthermore, linearity may be reduced by the fact that the sensor is exposed to the large voltage variation of the oscillating circuit itself. In fact, in Figure 1, it is shown that the sensor (R_{sens}) is biased by a voltage which

may vary of a quantity $2|V_{REF}|$ when the oscillator output crosses the threshold voltage V_{TH}.

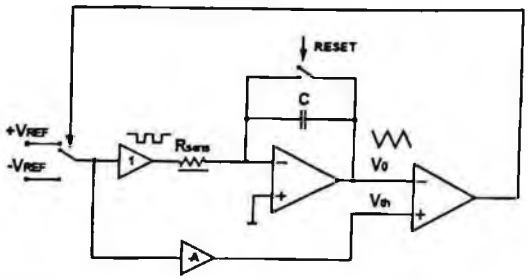

Figure 1 - Example (simplified circuit) of possible oscillator approach for R_{sens} estimation

Figure 2, instead, shows an example of logarithmic compression [5] of the R_{sens} value. The current $I_{sens}=V_{REF}/R_{sens}$ flowing trough the sensor is mirrored into the diode D1, while a reference current I_{REF} flows through a matched diode D2. Due to exponential behavior of these devices the difference between the two voltage drops across the diodes is:

$$V_0 = -V_T \cdot \ln\left(R_{sens} \cdot \frac{I_{REF}}{V_{REF}}\right) \qquad (1)$$

leading to desired logarithmic compression of the R_{sens} value. This circuit measures resistance values with a precision up to 1% over 5 decades using a single scale.

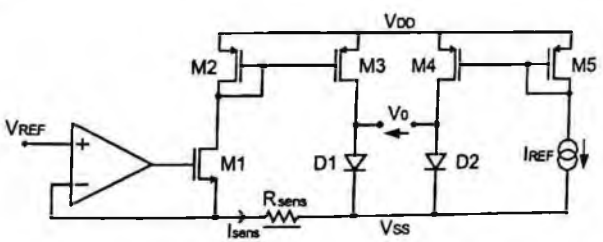

Figure 2 - Example of logarithmic compression of R_{sens} and I_{sens} values

2. The resistance-time converter with decoupled oscillator approach

In this paper we present an improved oscillator approach for resistive gas sensors read-out, whose simplified schematic is shown in Figure 3.

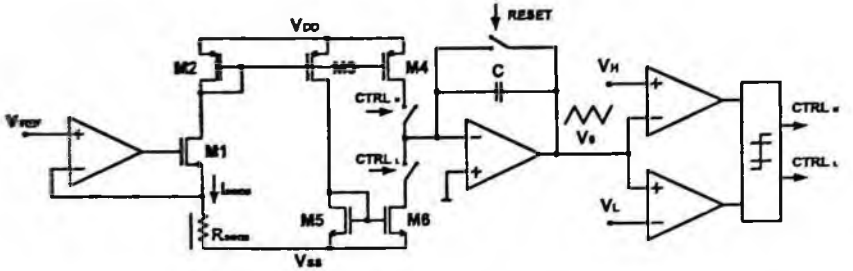

Figure 3 – Simplified schematic of the proposed enhanced oscillator approach

The resistive sensor, R_{sens}, is biased with a fixed buffered voltage V_{REF}, which is set to 1V. A couple of high-linearity cascoded current mirrors (reported as regular mirrors for simplicity) replicate the current V_{REF}/R_{sens} and alternately push it into or pull it from the virtual ground of a resettable Miller integrator. The output of this block is connected to a couple of comparators which compare V_{OUT} with two fixed boundary voltages V_H and V_L ($\Delta V=V_H-V_L=1V$), producing the control signals for the switches that shunt the mirrored current. A small logic grants that the comparators switch alternately; furthermore it feeds a counter whose transition period is proportional to the value of R_{sens}. Thus the triangular oscillator frequency is given by:

$$f_{osc} = \frac{\delta \cdot V_{REF}}{2C \cdot \Delta V \cdot R_{sens}} \tag{2}$$

where δ is the scaling ratio of the current mirrors, that in this circuit is set to 1:10 in order to moderate the bandwidth requirements for the integrator operational amplifier and the overall power consumption. Setting the capacitance value of the integrator to C=10pF, in the resistance range of interest, the oscillator frequency will vary between f_{min}=50Hz and f_{max}=5MHz. Behavioral and transistor level simulations in 0.35μm technology show that, in this context, an acceptable bandwidth for the integrator amplifier is B=50MHz. The ratio between a reference counter, whose clock frequency is fixed at the midrange value $f_{mid}=(f_{min} \cdot f_{max})^{1/2}$=16kHz and the resistance dependent one represents the A/D converted value of R_{sens}. The measurement ends when the slower of the two counters reaches a fixed value N^* which is enough to achieve the desired accuracy, i.e. N^*=256 for a 8-bit equivalent accuracy. Thus the absolute measured resistance value is given by:

$$R_{meas} = \alpha \cdot R_{mid} \cdot \frac{N_{(ref)}}{N_{(osc)}} + \beta \tag{3}$$

where $N_{(ref)}$ and $N_{(osc)}$ indicate respectively the reference and the oscillator frequency dependent counters register values at the end of conversion, while α and β represent front-end circuit gain-error and offset-error terms. If the end-user is not interested in absolute measurements of the R_{sens} value, as happens in gas sensing, there is no need to compensate these kind of non-idealities since they do not affect linearity in gas concentration extraction. Of course, if the applied R_{sens} value is lower than midrange $R_{mid}=(R_{min}\cdot R_{max})^{1/2}=320k\Omega$, the slower of the two counters reaching N^* will be the reference one, while, for $R_{sens}>R_{mid}$, the slower counter will be the oscillator controlled by R_{sens}, as shown in Table 1. Then, the minimum number of bits for each of the two registers is given by:

$$N_{bit} > \log_2\left(N^* \cdot \frac{R_{max}}{R_{mid}}\right) \equiv \log_2\left(256 \cdot \frac{100M\Omega}{320k\Omega}\right) > 16 \qquad (4)$$

$R_{nominal,applied}$	$N_{(ref)}$	$N_{(osc)}$	$R_{measured\ (sim)}$	Lin. Error
1 kΩ	256	80448	1.0183 kΩ	- 0.30881 %
2 kΩ	256	40261	2.0347 kΩ	- 0.40381 %
5 kΩ	256	16008	5.1175 kΩ	+ 0.21120 %
10 kΩ	256	8031	10.201 kΩ	- 0.12878 %
20 kΩ	256	4003	20.466 kΩ	+ 0.19125 %
50 kΩ	256	1597	51.296 kΩ	+ 0.45333 %
100 kΩ	256	801	102.27 kΩ	+ 0.13148 %
200 kΩ	256	399	205.31 kΩ	+ 0.51676 %
500 kΩ	409	256	511.25 kΩ	+ 0.11263 %
1 MΩ	817	256	1.0212 MΩ	- 0.01593 %
2 MΩ	1634	256	2.0425 MΩ	- 0.00806 %
5 MΩ	4082	256	5.1025 MΩ	- 0.07443 %
10 MΩ	8165	256	10.206 MΩ	- 0.05005 %
20 MΩ	16320	256	20.400 MΩ	- 0.08129 %
50 MΩ	40778	256	50.972 MΩ	- 0.05101 %
100 MΩ	81520	256	101.90 MΩ	- 0.04878 %

Table 1 – Enhanced (decoupled from sensor) oscillator approach simulation results summary for R_{sens} measurement. $R_{measured}$ column values have been reported as given by counter registers, while *Lin. Error* column data have been calculated canceling offset and gain error contributions

From the values reported in Table 1 it is evident that the conversion time is 5 seconds when sensing maximum resistance values, while for low resistances ($R_{sens}<320k\Omega$), using the proposed measurement technique, the conversion time will be fixed and equal to 16ms. Therefore, for using dynamic pattern recognition techniques (assuming a sensor array consisting of 5 elements) it is

necessary that sensors have moderated baseline value, i.e. R_{bl}<1MΩ. For using dynamic pattern recognition with higher resistance values programmability in the integrator capacitance value have to be introduced to increase the oscillation frequency and reduce the measurement time (B_{dyn}>50MHz).

3. Conclusions

In Figure 4 the relative error in R_{sens} estimation obtained with transistor level simulations, based on the data summarized in Table 1, is plotted. Unfortunately the very long time needed by each parametric simulation (varying applied R_{sens} value) limited the number of examined discrete R_{sens} points (16). Observing the plot appears that, for resistance values higher than midrange (R_{sens}>320kΩ), the relative precision for R_{sens} estimation is better than 0.1%, while, for lower values, the accuracy goes down to 0.5%. This is caused by the non-idealities introduced by the higher oscillation frequency of the circuit. Furthermore, in the last decade, the growing of inaccuracy is due to the leakage current of the switches that shunt the mirrored current, that is not any longer negligible. The circuit anyway shows a worst-case accuracy of 0.5% over a range of 5 decades (1kΩ-100MΩ), while the RMS error is lower than 0.2%.

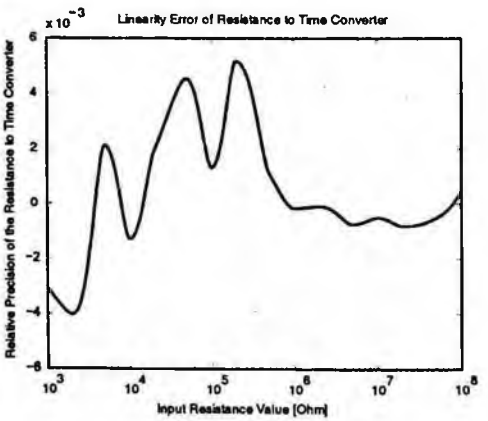

Figure 4 – Relative error in R_{sens} estimation at transistor simulation level

References

1. A. Flammini et al., IMTC'03 proceedings, p.726, IEEE (2003).
2. E. Martinelli et al., AISEM'03 proceedings, p.334, World Scientific (2003).
3. A. Baschirotto et al., PRIN'03 project, *http://ims.unipv.it/prin03* (2003).
4. M. Grassi et al., GMEE'04 meeting proceedings, p.79, GMEE (2004).
5. D. Barrettino, Ph.D. dissertation, p.61, ETH-Zurich (2004).

THERMAL ΣΔ MODULATION FOR QUARTZ CRYSTALS MICROBALANCES

EMILIANO ZAMPETTI, CHRISTIAN FALCONI, SIMONE PANTALEI, EUGENIO MARTINELLI, CORRADO DI NATALE, ARNALDO D'AMICO

Department of Electronic Engineering, Tor Vergata, via del Politecnico 1, Roma, Italy

Quartz crystals are used for a variety of applications; in particular, if the quartz is coated by a chemically interactive material, it behaves as a microbalance and may be used as a chemical sensor. Since the properties of quartz crystals and of chemically interactive materials strongly depend on temperature, it is often necessary to control the temperature of quartz microbalances. Furthermore, during the measurement, it may be important to measure the speed of the flow to which the microbalance is exposed. Here we present a new ΣΔ interface for controlling the temperature of the microbalance and measuring the flow speed when an auxiliary terminal is properly added to one electrode of the quartz.

1. Introduction

Quartz crystals covered by chemically interactive materials may be used as chemical sensors; depending on the molecules adsorbed by the chemically interactive material, the mass of the "microbalance" is modified, resulting in variations of the oscillating frequency of the oscillator comprising the quartz. Quartz microbalances generally have significant cross-sensitivities toward the temperature of the microbalance itself; furthermore it may be important to measure the flow speed. For these reasons the measurement and control of the temperature and of the flow speed are very important. Here we present a simple technological solution and a novel electronic interface which allow both an accurate measurement and control of the microbalance temperature and the measurement of the flow speed.

Figure 1 shows the modified microbalance; the auxiliary terminal allows to use the top electrode as a resistor, which may be used both as a temperature sensor and as an heater. Furthermore, the power required for generating a given overheat depends on the flow speed, according to King's law; as a result the measurement of the overheat and of the average heating power can also give the flow speed. In conclusion, the top electrode of the quartz crystal is used as the temperature sensor, heater, flow sensor and electrical contact for the resonator (to be included in the oscillator).

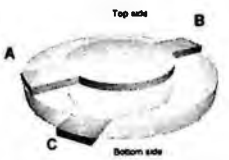

Fig. 1. Quartz microbalance with an auxiliary terminal. The electrodes are constituted by a gold/chromium film whose thickness is about 1500 Å. The gold/chromium top electrode is used as a temperature sensor, heater, flow sensor and electrical contact for the resonator.

The traditional approach for controlling the temperature of a temperature dependent resistor (hot wire anemometer) requires the control of a non linear system; such problem may be circumvented by applying thermal $\Sigma\Delta$ modulation [2], which also provides a digital signal related to the flow speed. The basic principle of thermal $\Sigma\Delta$ modulation is shown in figure 2. The comparator compares the output voltages of two temperature to voltage transducers (TS_1 and TS_2) which are in thermal contact with, respectively, the heated object and the environment. Depending on the output of the comparator, the D type flip flop enables or disables the heater. The thermal filter (R_{TH}, C_{TH}) acts as the integrator in the $\Sigma\Delta$ modulator (noise shaping). The desired temperature may be fixed by applying a proper voltage to the non inverting input of the comparator. Since the thermal resistance R_{TH} depends on the flow, flow speed may be deduced from the (digital) output of the flip flop.

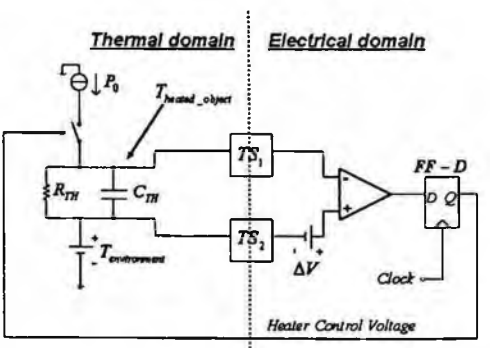

Fig. 2. Thermal ΣΔ modulation: R_{TH} and C_{TH} are the thermal resistance and the thermal capacitance.

2. ΣΔ interface for hot-wire anemometers

2.1 Characterization of the microbalance

In order to determine the thermal resistance and capacitance of the microbalance, first the temperature sensor constituted by the gold-chromium top electrode has been calibrated; afterwards, an heating current has been injected into the heater, resulting in an overheat which may be measured by means of the (calibrated) temperature sensor. If both the heating current and the voltage developed across the top electrode are measured, the ratio between the overheat and the heating power (in absence of flow) gives the thermal resistance (in absence of flow).

After the thermal resistance has been obtained, the thermal capacitance has been estimated by extracting the time constant $\tau = R_{TH} C_{TH}$ of the free cooling after the heating power is removed. For our microbalance, we have found C_{TH} = *58,3 mJ / °C* and R_{TH} = *270 °C/ W*.

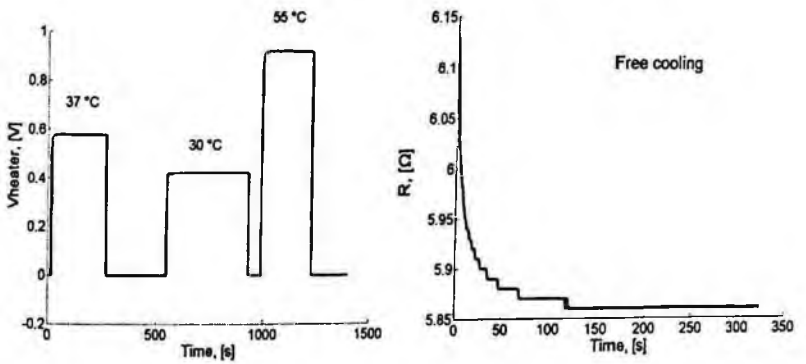

Fig. 3. Measurements for the evaluation of the thermal capacitance and resistance. On the left it is shown the voltage across the temperature sensor when three different heating currents are used. On the right it is shown the heater resistance (R_{Heater}) during free cooling.

2.2 Electronic interface design and simulation

Traditional circuits for hot-wire anemometers require the control of a non-linear feedback loop; here we propose a novel electronic interface which removes this complication by means of thermal ΣΔ modulation. Figure 4 shows how thermal

$\Sigma\Delta$ modulation may be applied to an hot-wire anemometer; the feedback loop will try to equate the ratios R_A /R_B and R_{REF} /R_{Heater}. After the system is calibrated, this corresponds to keep a desired temperature of the quartz microbalance. In practice, if $V_{S1} > V_{S2}$, the output of the comparator is low and, therefore, M_1 is switched on by the flip-flop D, thus heating the quartz, so that R_{Heater} increases (metal resistors have positive TCs). On the contrary, if $V_{S1} < V_{S2}$, the output of the comparator is high and, therefore, M_1 is switched off by the flip-flop D; ideally, under these circumstances, the free cooling of the microbalance is desired; although this could be done by a more complex circuit, it is more simple to add a (large) resistance R_{AUX} which allows a reliable start up and, also, a reliable comparison when M_1 is off; these advantages are obtained at the cost of a non-zero current flowing through the top electrode even when the temperature is higher than the desired temperature; this is not an issue if this current is enough small (i.e. if the resistance R_{AUX} is enough large).

An equivalent electric circuit of the thermal system has been developed in order to perform SPICE simulations; figure 5 shows these simulations, showing a very small ripple around the set point (see figure 5). In this case we had $T_{set\ point} = 65{,}3°C$ and the ripple was as low as $\pm\, 6m°C$ (neglecting the input equivalent noise voltage of the comparator).

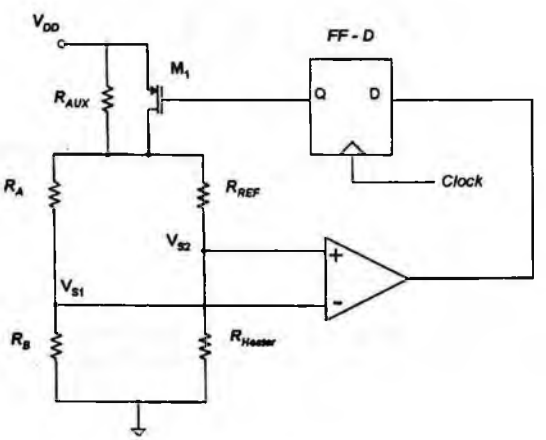

Fig. 4. Proposed $\Sigma\Delta$ interface for the hot-wire anemometer. The (digital) output of the *FF-D* allows to extract the flow speed.

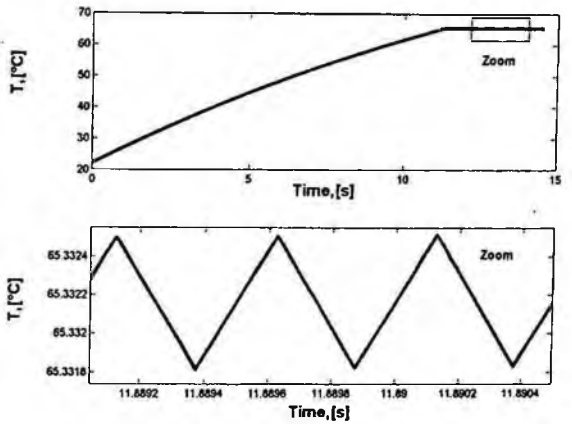

Fig. 5. SPICE simulation. The temperature of the quartz microbalance shows a small ripple around the set value (as it is typical in thermal $\Sigma\Delta$ modulation systems).

2.3 Measurements

The circuit has been fabricated and tested; figure 6 shows the output voltage of a thermocouple in thermal contact with the top electrode. After the equilibrium is reached, the temperature fluctuations are very small (i.e. good precision). In order to achieve a good accuracy, the system must be calibrated; since the reference resistor and the heater resistors have low resistances, a 4-wires technique must be used, as shown in figure 7; a proper use of chopper switches allows to reduce the effects of the input offset voltage of the instrumentation amplifier.

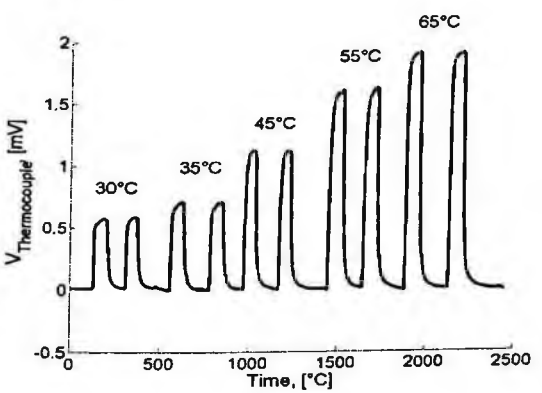

Fig. 6. Thermocouple output voltage; the thermocouple is in thermal contact with the quartz microbalance.

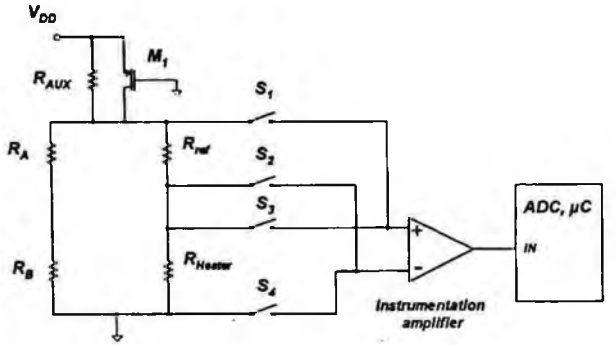

Fig. 7. System for 4-wire auto-calibration.

3. Conclusions

In this work we have introduced a new $\Sigma\Delta$ interface for the thermal control of an hot-wire anemometer; the technique has been used for the temperature control of a quartz microbalance, having a modified top electrode which is used as temperature sensor, heater, flow sensor and electrical contact for the resonator (to be included in the oscillator). In comparison with traditional electronic interfaces for how-wire anemometer, there is no need for controlling a non-linear system. As an additional advantage, the thermal $\Sigma\Delta$ modulation approach also provides a digital signal related to the flow speed. The system has been fabricated and tested and show correct operation.

References

1. E. Zampetti, S. Pantalei, C. Di Natale, R. Paolesse, A, Macagnano, A. D'Amico," *Recovery time improvement of QMB sensors by integrated simple micro heater*" Aisem 2004
2. H. J. Verhoeven, "*Smart thermal flow sensors*", Ph.D. Thesis, Delft University of Technology, Delft, 1995.
3. B. W. van Oudheusden, "*Thermal flow sensors*" in G. C. M. Meijer, A. W. van Herwaarden (Editors), Institute of Physics Publishing Bristol and Philadelphia, London, 1994.

A NOVEL TEMPERATURE CONTROL SYSTEM FOR RESISTIVE GAS SENSOR

GIUSEPPE FERRI[†],
CARLO CATALANI, NICOLA GUERRINI, VINCENZO STORNELLI
Dipartimento di Ingegneria Elettrica, Università di L'Aquila, Monteluco di Roio, L'Aquila, 67100, Italia

In this paper we present a CMOS integrated system for the temperature control of resistive gas sensor array. The circuit has been designed in AMS 0.35μm CMOS integrated technology. The general solution proposed performs the heating control exploiting a signal provided from a resistance-to-frequency converter. The sensor interface signal, by a digital conditioning sub-system, manages the heater circuit. The structure allows high sensibility and precision and performs good stability in temperature, power supply drift and low power characteristics so it can be used also in portable applications.

1. Introduction

In sensor system research, there is actually a great demand in micro-systems and technologies which combine a low power consumption with excellent general performance. The main fields of applications are the following: environment, medicine, biotechnology, automotive, consumer electronics, etc..

In particular, chemical sensor array targets are the detection of the presence of odours or gases, among which the most common pollutants, such as the sulphur dioxide (SO_2), nitrogen oxides (NO and NO_2), the carbon oxide (CO_2) and volatile organic compounds like toluene, chloride of methylene etc..

The interfacing of the sensitive element with a suitable integrated circuit is a fundamental characteristic. CMOS technology is widely used, because it allows to match the reduction of costs of the silicon technology with the possibility of designing new low voltage low power interface circuits.

An important problem is the accurate control of the sensor operating temperature. The sensor, which typically operates at temperatures ranging from 150 to 300°C, is heated through a use of the circuit, which fixes the sensor

[†] E-Mail: ferri@ing.univaq.it, tel. +39 0862 434446, fax: +39 0862 434403.

temperature at about 200°C, by a constant power supply. The feedback control is completed by a digital sub-system, that provides more free grades to the user for custom applications.

2. *Temperature control system*

The basic principle of the temperature control is shown in fig.1.

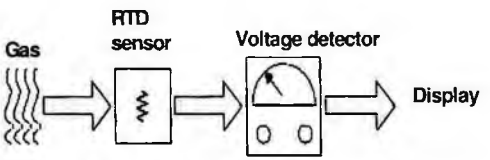

Figure 1. A typical resistive gas sensor temperature control scheme.

The problem of the system temperature control through the heater has been here reduced to the control of a resistance. The current (or more generally) the power delivered to the heater resistance must be such that the temperature has to remain constant. This task is made easy thanks to the presence of a second resistance, close to the heater one, which remains at the same temperature. Finally the insertion of a third resistance also close to the heater and the thermometer resistance allows, through a "resistance to frequency" (R/f) conversion, the measurement and control of the resistance and therefore of the temperature. A suitable control logic evaluates the frequency (and, consequently, the resistance) and generates a feedback signal to maintain the sensor at the desired temperature. The power delivered to the heater is electrically controlled by the digital sub-system. This solution has been demonstrated to be the most interesting and affordable in front of the 3.3V available power supply. The implemented topology only maintains the power delivered to the heater resistance constant and controls it by a suitable loop (see fig.2). In this figure, the *Logic Control* allows pointing out and processing the temperature value.

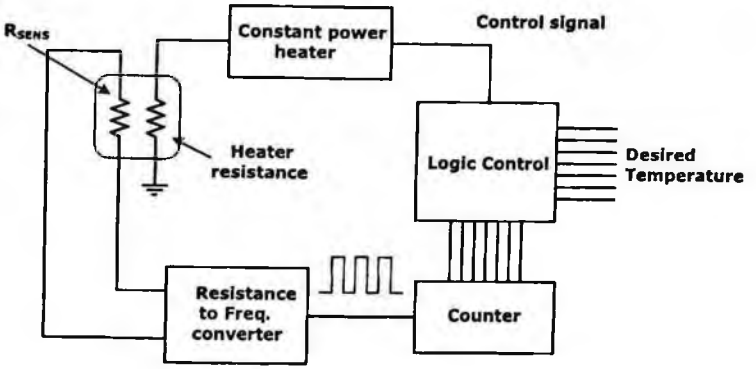

Figure 2. Basic block control system.

3. *R/f conversion*

The proposed R/f converter [1] is based on phase shifters (fig.3) [2] in oscillator configuration (*In* and *Out* terminals are connected in short circuit).

In fig.3, capacitance C is loaded and unloaded at a constant current, implemented through traditional current mirrors. An inverter stage (MpOut, MnOut) gives a squared output wave.

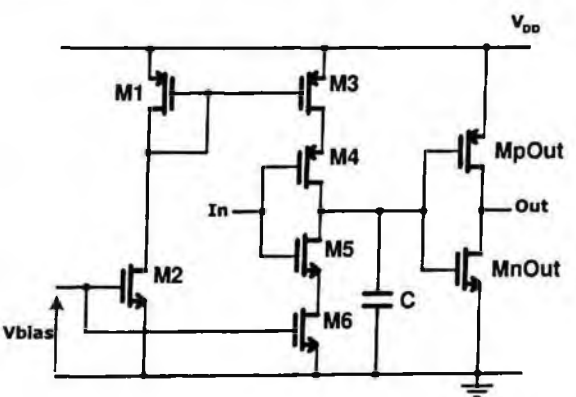

Figure 3. Phase shifter basic block.

The delay at the output of the shifter is proportional to the C/I ratio, as follows:

$$T_{Delay} = \frac{1}{2} V_{DD} \frac{C}{I}$$

Fig.4 shows the complete shifter topology, formed by a cascade of three basic shifters. This allows to obtain a phase shift up to 360°.

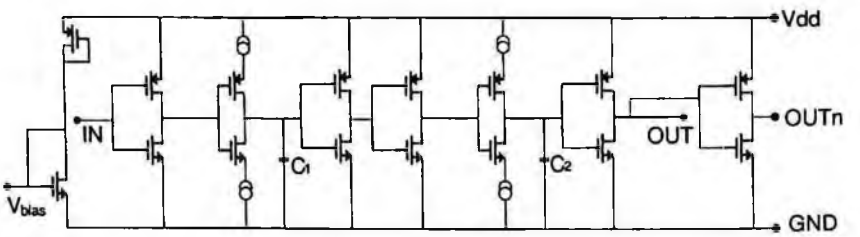

Figure 4. The complete shifter topology.

When *In* and *Out* terminals are connected together, the phase shifter becomes an oscillator, having as output signal a periodic waveform whose period is proportional to the sensor resistance.

The R/f converter (fig.5) is formed by a voltage to current circuit which gives the current to the shifter-based oscillator.

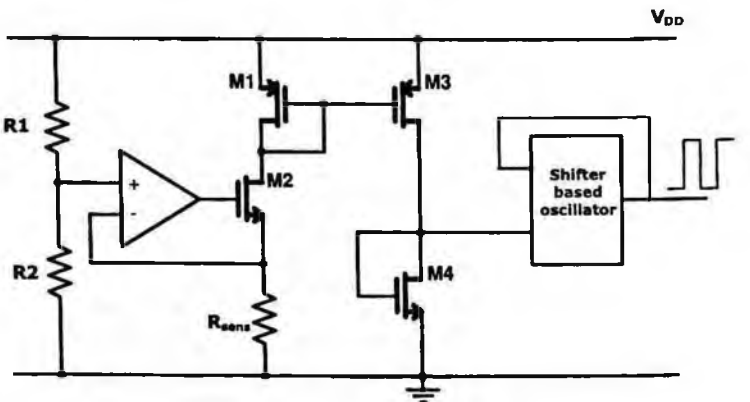

Figure 5. R/f converter scheme.

For this circuit we have:

$$f = \frac{1}{6 \cdot C \cdot R_{SENS}\left(1+\frac{R_1}{R_2}\right)}$$

For the following values of the components we obtain a frequency oscillation of 3.17MHz: R_{SENS} = 1KΩ; C = 10pF; R_1 = 8KΩ; R_2 = 2KΩ. The signal is shown in fig.6.

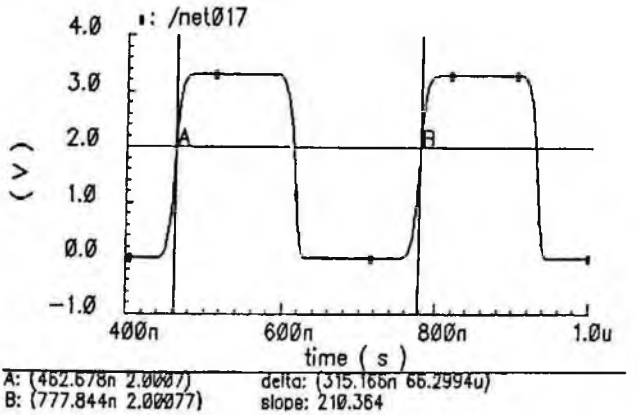

Figure 6. Output squared wave signal of R/F converter.

4. *Heater*

The power generator (heater), shown in fig.7, allows the control of the power in the circuit. The heating resistance is represented by R_{HEATER}. Fig.8 shows the power vs. heater resistance at different temperatures. Typical R_{HEATER} value is 100 Ω, while power, which gives the required heating level to the sensor, is 25 mW. Fig.9 shows the power furnished by the heater vs. heater resistance value at different reference currents I_{REF} (see fig.7). The typical I_{REF} value is 8.2μA.

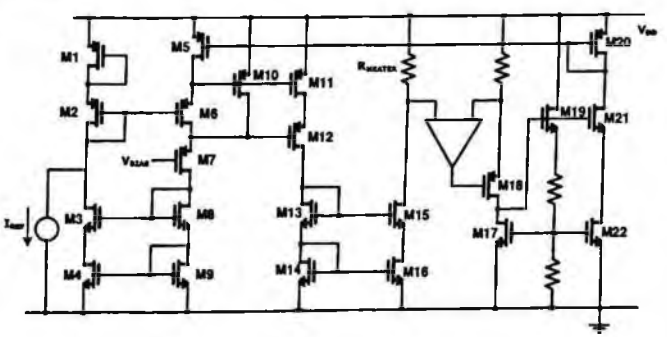

Figure 7. Heater schematic.

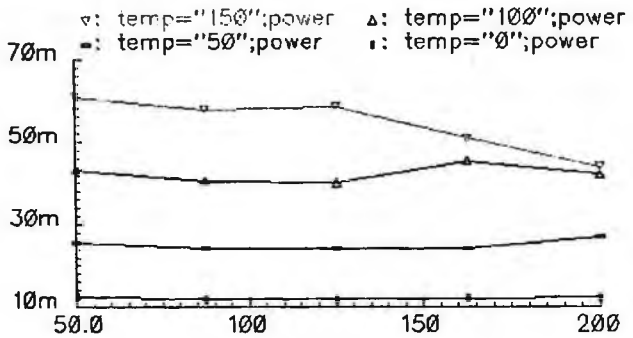

Figure 8. Power vs. R_{HEATER} (at different temperatures, power level 25mw).

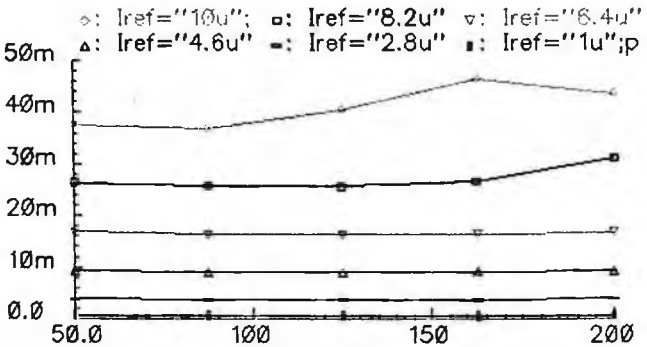

Figure 9. Power level vs. R_{HEATER} (at different references currents).

Acknowledgments

The activity reported in this paper has been carried out within the PRIN project n.2003091427, funded by Italian Government in 2003. The authors want to thank all the participants to this project.

References

1 G.Ferri, P.De Laurentiis, "A low voltage CMOS phase shifter as a resistive sensor transducer", Proc. IEEE ISCAS, Geneve (Switzerland), May 2000.
2 G.Ferri, P.De Laurentiis, "A low voltage low power CMOS phase shifter", International Journal of Circuit Theory and Applications, vol.28 n.2, March-April 2000, pp.187-191.

RESONANT FREQUENCIES IN MONO AND BI-DIMENSIONAL LC,CL,R NETWORK FOR APPLICATION IN SENSOR ARRAY

A. ORSINI, A. CATINI
I.M.M., P.S.M., Via fosso del Cavaliere, 100
Rome , 00133 , Italy

F.CARUSO, D.CECILI, S.INNOCENZI
Electronic Engineering Department, University "Tor Vergata", V.le del Politecnico, 1
Rome , 00133 , Italy

Resonators are proven to be interesting transducers for sensing applications especially in the chemical sensor domain. The sensors have been represented by capacitors/inductors in a ladder network formed from a cascade of n identical elementary cells in a mono dimensional arrangement or in a N x N array, once the type of cell impedances and the number of cells are known.. This work considers these two kinds of networks and for each of them calculates the resonant frequencies generated in each node. This study demonstrates the existence of interesting frequency distributions which have remarkable characteristics.

1. Introduction

Much attention has been paid to ladder networks (LN) as they represent good equivalent models for numerous mechanical, chemical and thermal systems, interconnection networks, analogue neural networks and distributed high-frequency amplifiers [1]-[4].

In order to determine the electrical characteristics of these networks, numerous methods, based upon known circuits, are applied. These methods give, in general, the network solution through processes that are strictly and univocally related to the type of the components of the elementary cell and they become particularly onerous, from both a symbolic and numerical point of view, as the number of cells increases.

Some ad hoc methods that exploit the intrinsic network symmetry has also been developed [5], but they have a recursive structure that severely limits the symbolic elaboration or, from the numerical point of view, have a slow response time.

2. Mono-Dimensional Network

The general form of a ladder network consists of n L-sections in cascade, each consisting of series resistance R1 and parallel resistance R2. (Fig.1)

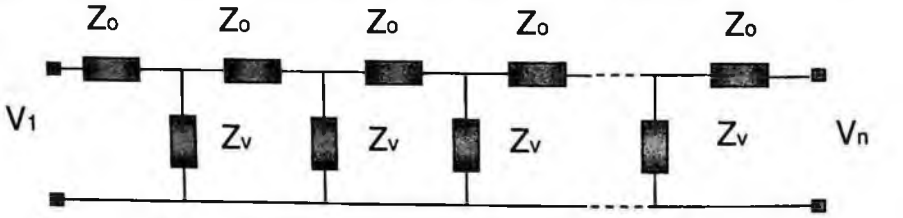

Figure 1. General form of a ladder network with equal L-sections.

It is possible to describe the network transfer characteristics of impedance and attenuation by means of a constant K, defined as the ratio of Z_o and Z_v, $K = Z_o/Z_v$. From $Z_o = K*Z_v$, the parallel arm Z_v may be normalized to unity. It has been found possible to describe the output impedance in a generalized form as a function of K, thus: $Z_{output}(n) = 1/1, b_1/B_1, b_2/B_2, b_3/B_3, b_4/B_4 \ldots$ where any term in the series b_n/B_n is defined in terms of the previous terms b_{n-1} and B_{n-1} as:

$$b_n = K B_{n-1} + b_{n-1} \qquad B_n = (K+1) B_{n-1} + b_{n-1} \tag{1}$$

It follows that the series of output impedance may be evaluated directly in terms of K, using the values of bn and Bn given; thus:

$$\frac{1}{1}, \frac{K+1}{K+2}, \frac{K^2+3K+1}{K^2+4K+3}, \frac{K^3+5K^2+6K+1}{K^3+6K^2+10K+1}, \ldots \tag{2}$$

Also for the Transfer Function the solutions are represented by polynomials fraction in the form of:

$$\gamma K^3 + \beta K^2 + \alpha K + 1 \tag{3}$$

whose coefficients are reported in Table 1:

Table 1: List of coefficients.

n	α	β	γ	...			
1	1	1					
2	1	3	1				
3	1	6	5	1			
4	1	10	15	7	1		
5	1	15	35	28	9	1	
6	1	21	70	84	45	11	1

These numbers are not casual but came from *Tartaglia's Triangle*, in particular from even columns of the triangle:

$$c_i = \binom{n+i}{2i} \qquad 0 \le i \le n$$
$$P(n) = \sum_{i=0}^{n} c_i \cdot K^i \tag{4}$$

Then the tension in every node of the ladder network is calculated with the following formula:

$$V_n(i) = \frac{P(n-i)}{P(n)} \cdot V_0 \tag{5}$$

2.1. *Resistive Networks and Fibonacci Numbers*

An interesting mathematical relationship is demonstrated between the transfer characteristics of ladder networks and the Fibonacci series of numbers. This relationship, apart from possible academic interest, has been found to simplify network analysis by enabling the network transfer functions to be stated in the form of a simple arithmetic series. Examination of the transfer function of the network can be carried out by assuming a network constructed of one-ohm resistors (i.e., $Z_o=Z_v=1$, K=1) and by varying the number, *n*, of L-sections.

Table 2: Fibonacci numbers in ladder network.

n	V_1	V_2	V_3	V_4	V_5	...	V_n
1	1/2						
2	2/5	1/5					
3	5/13	2/13	1/13				
4	13/34	5/34	2/34	1/34			
5	34/89	13/89	5/89	2/89	1/89		
N	F_{2N-1}/F_{2N+1}	F_{2N-3}/F_{2N+1}	F_{2N-5}/F_{2N+1}	F_{2N-7}/F_{2N+1}	F_{2N-9}/F_{2N+1}	...	F_1/F_{2N+1}

2.2. *Resonant Networks*

Utilizing the results showed in the first paragraph, we can write node tensions with equation (5):

$$V_n(i) = \frac{\sum_{j=0}^{n-i} \binom{n-i+j}{2j} (s^2LC)^j}{\sum_{j=0}^{n} \binom{n+j}{2j} (s^2LC)^j} \cdot V_0 \qquad (6)$$

To find the resonance frequencies of the circuit, we can analyze, for a n-L network, the polynomial p(n). These frequencies can be expressed in the closed form:

$$f^{(i)} = \frac{f_0}{\sqrt{2 - 2\cos\left(\frac{2i+1}{2N+1}\pi\right)}} \qquad 0 \le i \le n-1 \qquad (7)$$

It is possible to graph the complex unitary circle and to show how it is mapped from the resonance frequencies. For every N there will be a different polygon circumscribed (for example: n=1 triangle, for n=3 eptagon) with odd late number. In the case of N=2 they form a pentagon with solutions proportional to gold number:

$$f^{(0)} = f_0 / \phi$$
$$f^{(1)} = f_0 \cdot \phi \qquad (9)$$

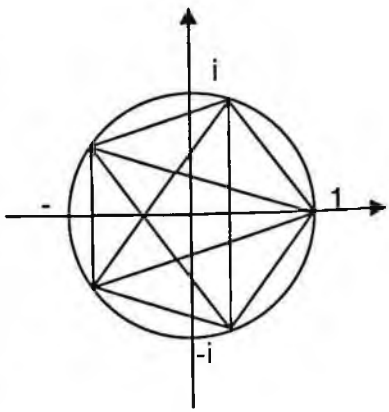

Figure 2: Unitary circle and pentagon (n=2).

The periodicity of frequencies is determined by superimposition of polygons and is represented in the following table, where $[\omega_n]$ represent classes of ω, which cardinality is equal to N.

Nearby to Table 3 there are the distribution of frequencies (normalized) for CL networks (Fig. 3) and LC networks (Fig. 4).

Table 3: resonant frequencies periodicity with N.

$[\omega_1]$	N=1	N=4	N=7	N=1+3h
$[\omega_2]$	N=2	N=7	N=12	N=2+5h
$[\omega_3]$	N=3	N=10	N=17	N=3+7h
$[\omega_4]$	N=4	N=13	N=22	N=4+9h
$[\omega_5]$	N=5	N=16	N=27	N=5+11h
$[\omega_6]$	N=6	N=19	N=32	N=6+13h
$[\omega_n]$	N=n	....	....	N=n+(2n+1)h

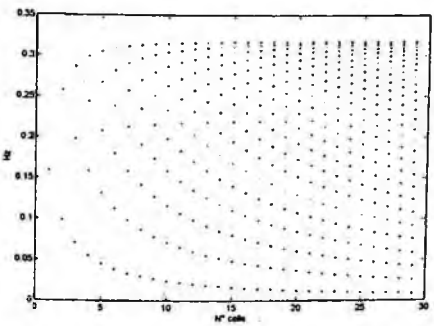

Figure 3: $f^{(i)}$ for Low-pass Network.

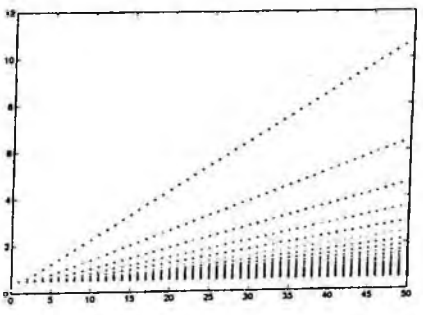

Figure 4: $f^{(i)}$ for High-pass Network

2.3. *Element Variation in Resonant Networks*

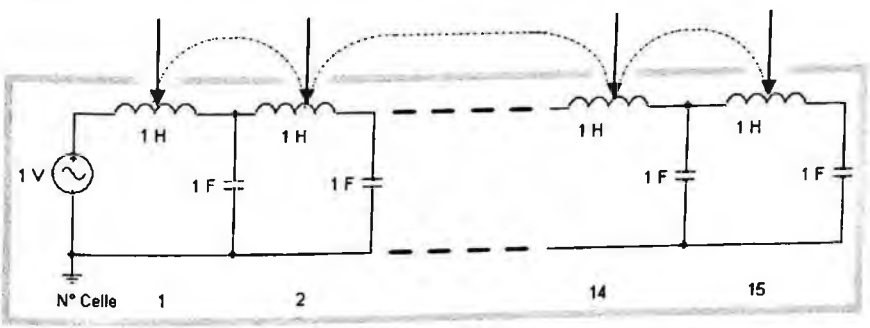

Figure 5: Chain of changing elements in mono-dimensional Network.

Under Capacitance or Inductance change of only one network cell, whatever the position of it may be, the sum of all Δf, detected in each node, is a constant and equal to 0.5. In the case of simultaneous changes ΔC-ΔL the sum is equal to 1.
Regarding the sign of variations, a positive change of one element shifts all frequencies to a smaller value, while a negative change makes all frequencies bigger.
The position of the varied element determinates the number of maximum variations between old and new frequencies.

3. Bi-dimensional Network

Definition of a bi-dimensional ladder network is a problem with multiple answers. The realization of different electrical outlines can be obtained by two steps: adding other impedances to branches and nodes of mono-dimensional network and growing the circuit with the repetition of the new elementary cell in two directions; in this way, the quotient between the cross-sectional impedances number (Na) and the longitudinal impedances number (Nb) is different from 1. The grid in figure 6, geometrically half of a square of side n cells divided along diagonal, represent a first example that follows precedent rules, in fact for symmetry a grid which elementary cell is a square, can be reduced to this one applying Miller Theorem.

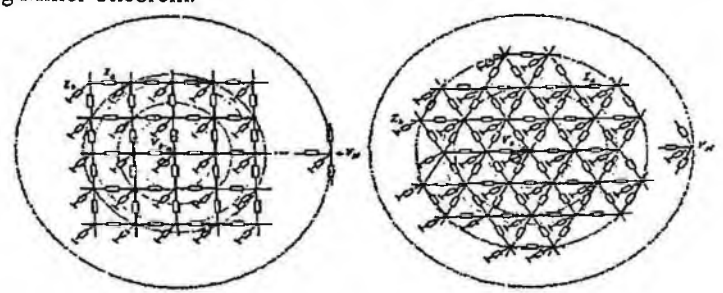

Figure 6: Development of two dimensional grid.

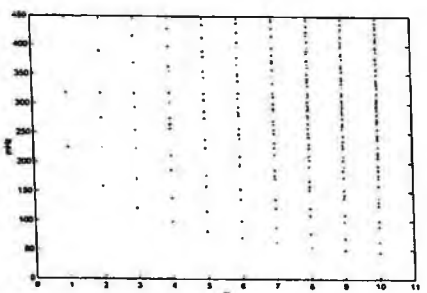

Figure 7: $f^{(6)}$ for 2-D LC Networks.

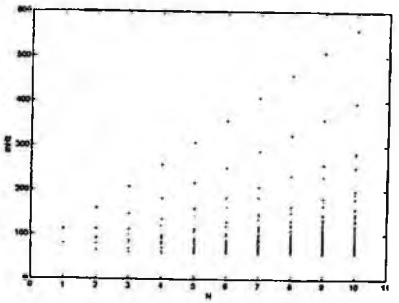

Figure 8: $f^{(i)}$ for 2-D CL Networks.

The results of electrical simulation for bi-dimensional grid show interesting values analogous to one dimensional curves. As seen in figure we can evidence:

- Frequencies distribute on straight lines (LC) or hyperboles (CL);
- Many values tend on repeating;
- Two values are always present: $f_0/2$ in LC arrangement and $2f_0$ in the dual one;
- The resonance has an inferior limit for LC configuration, while is a superior limit for the other one. The limit is $f_0/2\sqrt{2}$ in CL arrangement and $2\sqrt{2}/f_0$ in the dual one.

Acknowledgments

The authors would like to thank Prof. D'Amico and all the reviewers for their advice.

Appendix

FIBONACCI NUMBERS

The Fibonacci series of numbers' may be defined, in general terms, in the form of an infinite sequence, thus: where F_1 and F_2 may be given any value and each successive term is the sum of the two previous terms. It follows that there are an infinite number of possible Fibonacci series.

Possibly the most interesting Fibonacci series, often called the basic Fibonacci numbers, is that, in which $F_1 = 1$ and $F_2 = 2$, thus:

1, 1, 2, 3, 5, 8, 13, 21, 34, 55, 89, ;

this series has quite remarkable arithmetic properties. Development gives:

l/1, 2/3, 5/8, 13/21, 34/55, 89/144, etc.,

consisting of successive terms of series (2) expressed as a ratio. It is of interest that each successive term in the series rapidly approaches a maximum value; it

can be shown that the value of the nth term is (√5 - 1)/2: it is given as the value of "a" in the quadratic equation a^2 + a = 1.
A study of this number, 0.618, and of its Fibonacci derivation, has received considerable attention in the field of pure mathematics for some hundreds of years.

References

1. W. A. Blackwell, *Mathematical modeling of Physical Networks.* New York: Macmillan, 1968.
2. G. C. Temes and S. K. Mitra, *Modern Filter Theory and Design.* New York: Wiley, 1973.
3. M. A. Maher, S. DeWeerth, M. Mahowald and C. Mead, *Implementing neural architectures using analog VLSI circuits. IEEE Trans. Circuits Sys,.* Vol. 36, no. 5, pp. 643-652 1989.
4. R. Goyal, Ed., *Monolithic Microwave Integrated Circuits: Technology and Design.* Norwood, MA: Artec House, 1989.
5. M. N. S. Swamy and B. B. Bhattacharyya, *A study of recurrent ladders using the polynomials defined by Morgan-Voice. IEEE Trans. Circuit Theory* Vol. CT-14, pp.260-264, Sept. 1967.
6. M.Faccio, G.Ferri, A.D'Amico, *A new fast method for Ladder Networks Characterization. IEEE Trans.Circ.Syst.* Vol.38, no.11, pp.1377-82, 1991.
7 H.Weiss, V.Weiss, *The Golden Mean as a clock cycle of brain vawes. Chaos, Solitons and Fractals*, (2003) Artiche in press
8 A.Mojsilovic, E.Soljanin, *Color quantization and processing by Fibonacci lattices. IEEE Trans Image Process;* Vol.10, pp.:1712–25, 2001.

MULTI-SENSOR CONTINUOUS DATA ACQUISITION IN PHYSICAL ACTIVITY MONITORING

DOTT. RIC. G. GELAO, PROF. ING. A. GIORGIO, PROF. ING. A. G. PERRI
DOTT. M. QUINTO

Dipartimento Elettrotecnica ed Elettronica, Politecnico,
Via Orabona 4, Bari 70125, Italia
E-mail: perri@poliba.it; http://www.dispositivielettronici.com

In physical activity monitoring often only one parameter at a time is detected, since otherwise patient movement capabilities would be compromised. This is unsatisfactory since correlation among parameters is necessary to reject parameters alteration due to everyday life, but also it is necessary to detect correlated parameter alteration due to medical causes. Let's think about how everyday activities could modify heart rhythm and body temperature. We stress the importance of multi-sensor continuous data acquisition in biomedical studies also for the importance of correlated parameter changes coming from medical causes.

Our group has developed a new system for acquiring simultaneously a group of parameters which are strongly correlated: breathing rate, heart electrical activity, kinetic activity. Preliminary results on the prototypes are encouraging.

We should avoid to transform this measurement in a torture for the patient, so we need to pay attention to the non-invasivity and comfortable wearability of the sensors. To reduce device's weight we are developing a remote logger that gets signal from smaller on-body board.

1. Introduction

We are developing an apparatus for medical monitoring, consisting in a wearable multi sensors attached to a small board which is connected via the GPRS net to a computer in the hospital. This system would allow 24 hours logging and warning dispatching, for home diagnostic and in intensive care unit.

But while monitoring devices are very effective in intensive care units, they are quite oppressive and difficult to apply to 24 hours home monitoring for diagnostic purposes. Heart rate monitoring requires sensors attached on the skin, but there are more oppressive sensors such some of those used for breath sensing and those for energetic expenses measuring. For hearth rate monitoring we use the standard method, for breathing sensing we use an already known methods involving a belt to sense the thorax dilatation, but we apply a new kind

of belt dilatation sensor on the belt. For physical activity monitoring we use an accelerometer.

Signals from these sensors are amplified filtered and elaborated and feed to the ADC of a micro-controller. Since our complete system architecture is widely discussed in [1], and since hearth rate monitoring is a standard application, here we present the breathing sensor and the physical activity sensor.

2. Breathing monitoring

Breathing monitoring is an important parameter to study patient's health. Between the methods suggested by literature [2-6], we select the breast elastic belt method: sensing the belt stress it is possible to sense the breathing.

2.1. *Sensor*

Aside from several stress sensor we found interesting conductive rubbers sensors since it is quite cheap and could be easy tailored. Conductive rubbers have been applied as flexible conductors and as pressure sensors, but we did not found application as dilatation sensors. Conductivity of these rubbers are sensitive to stress, but among the large kind of conductive rubbers available, not all are suited for this application.

We describe more detail about our dilatation sensor for breathing monitoring application in [2] from the same authors, so here we summarize the results.

We took a sample of conductive rubber 120mm long, 20mm large and 0.3mm thick that was fit in the breast belt. Since the sample was not capable to stand all the belt stress, a non conductive rubber was added in parallel to our conductive rubber. It is not feasible a full belt made only with this kind of conductive rubber since it is not strong enough.

Two couples of small iron plates where tightened to each end of the rubbers sandwich to ensure the electrical connection.

2.2. *Experimental results*

The conductive rubber resistance is measured with the four wires method, two to inject a constant current, two to sense voltage. We did not used the Weston bridge method because of the sensor resistance drift due to the ageing.

Since breathing rate ranges from 0.1Hz to 3Hz and breast movement spectrum is impulsive with frequency in the range coming from 0.4Hz to 3Hz,

our front end amplifier was connected to the sensor through a capacitor with a low frequency cut off at 0.4Hz, the upper cut off is set at 3Hz.

The amplified signal is sent to a peak detector (tuned for breathing rate frequencies) whose output pulses are sent to a peak shaper to have standard length pulses.

This output is already a good signal for breathing rate measurement, but since we preferred to measure a voltage than a frequency, we feed the pulses in a frequency/voltage converter.

To have a faster conversion we used a simple circuit whose key element are a exponential-pulse generator and a sample and hold. For each pulses coming from the previous circuit the exponential pulse generator is triggered, then the tail of this pulses is sampled just before the generator is re-triggered. The synchronization between the S&H and the generator is controlled by a negative edge triggered pulse generator which sends delayed pulses to the exponential generator. Since the exponential pulse is sampled before the reset, the voltage held to the output of the S&H is one to one function of the time length of the last breath act, that is, in our case, a map from [0Hz;∞Hz] to [0V; 2.5V].

As benefit no average between consecutive pulses is done, while the drawbacks are the staircase waveform of the output and the impossibility of warning in case of breathing stop. Whether this warning would be needed, the output of the pulse shaper (or output of exponential generator) would be used.

Using exponential generator, the map between the frequency and the voltage is nonlinear. This is not so bad, since nonlinearity could be corrected on the remote computer display and the exponential allows to map any time length to a finite voltage. Furthermore, since the output voltage is fed to an ADC, and because of the nonlinearity, the best resolution would be given at the most common breathing rate, while the uncommon rates would have lower resolution.

Of course, noise and time delay would cut off the far ends of the interval [0Hz; ∞Hz] from the map, but the remaining interval is still wide: the system has been tested on the wide interval [0.05Hz; 6Hz].

For signal diagrams please look at [2], by the same authors.

2.3. *Perspectives*

The system has been successfully test on a wide rates interval, but ageing problems still remain.

Indeed the rubber resistivity raised tenfold after few hour of usage, when the rubber was fit in the belt with the dilatation method. While this could be

compensated with an automatic gain control at the front end amplifier, better would be to measure compression effects on rubber conductivity.

A second problem is the sensibility to the arms movements, which could trigger false breathing pulses. This is intrinsic to the belt method, but the effect is not so frequent compared to the breathing rate.

In conclusion, our sensor has been successfully tested, the remaining problems are minor. We still are looking for other kind of conductive rubbers, cheaper or with better ageing.

3. Physical activity sensor monitoring

The physical activity is important per se, but also to understand the medical meaning of heart rate dynamics. For example consider how could be different the meaning of an high heart rate whether the subject is running or standing.

Physical activity is useful to understand objectively the lifestyle of a patient, and to evaluate his daily energetic expenses.

3.1. *Sensor*

We observed that r.m.s. values of acceleration (passed through a high pass filter) is fully correlated with walking speed. Experimental data collected in previous experiences with other accelerometer, shows that vertical acceleration on the shoulder of a running patient peaks from -1g to 2g, while power spectrum spans up to 20Hz. Peaks comes from each impact of foots on ground.

This signal includes a contribute coming from the gravity that is $g\cos\theta$ where θ is the angle between the sense direction of the accelerometer and the gravity. The variable θ is not constant at all when the accelerometer is fixed on the clothes of a patient, and varies widely when a subject bows or stand up. Fortunately the power spectrum of θ is concentrated at frequency below 1Hz (typical), much lower than the frequencies of the acceleration of a walking (running) patient. In conclusion it's necessary and also enough to use a high pass filter to cut off the gravity.

We chose the accelerometer ADXL103 (by Analog Devices) whose characteristics are ideal for our application. While the band is much larger than what we need (but this is not a problem), the noise density is low, $10^{-4}g/Hz^{1/2}$, useful for good measurements. Its power dissipation is low, it takes 0.7mA at 5V, very useful since our system is battery powered. It is also quite cheap, 10$.

A particular explanation should be deserved to our interest in the sensitivity range: $\pm 1.7g$. This is a bit lower than maximum measurement on a running patient, so this would cause accelerometer signal clipping and would create a

progressive saturation of our circuit output signal. We do not foresee a complete saturation, since this would happen only patients runs in a very heavy way.

This is not a real limitation, since a running patients could be statistically marginal and signal partial saturation would be marginal, furthermore for athletic application would be necessary a new device with larger sensitivity range. On the other hand, the cut at $\pm 1.7g$ is interesting since it cut off the high acceleration peaks coming from collisions of accelerometer with the environment where acceleration peaks could reach several tens of g. In absence of clipping, high g peaks would severely ruin the 24 hour averages of r.m.s. acceleration.

3.2. *Electronic interface*

The signal chain is quite simple, it requires a band pass filter to cut off low frequencies at 0.7Hz (related to gravity) and high frequencies at 20Hz to clean unforeseen unwanted signal outside the signal band, output signal is shown in figure 1, upper part.

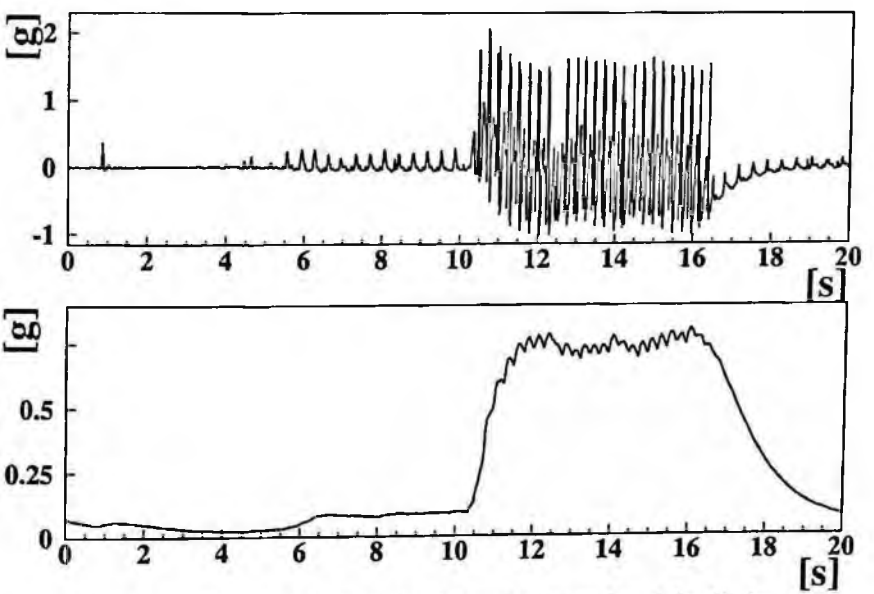

Figure 1: Upper trace: accelerometer signal. Lower trace: rms filtered signal in the.

The filtered signal pass to a cheap and effective r.m.s. converter, the AD737, whose precision is enough for our purposes. The r.m.s. converter output

is filtered to cut off frequencies over 0.1Hz to kill off the residual ripple observed on running patients, this signal is shown in figure 1, lower part.

The signal is clean and spanned voltage range is matched to input span of the ADC of our wearable unit.

3.3. *Tests and perspectives*

This kinetic sensor has been tested on several subjects, for each patient it was clearly possible to recognized whether the subject was standing, walking or running.

The observed signal is correlated to the physical activity but also to the weight of the subject, and (we suppose) also the way subject walks. For simple qualitative analysis this is not a problem, if a quantitative analysis were required then a subject by subject calibration would be used, or more simply a statistical parametrization of calibration on some biological parameter (weight, height, sex, age).

With this calibration, we hope that this physical activity measurement would allow a also good quantitative estimator of the energetic expenses to what concern walking and running, and we hope that (using also other biological parameters to evaluate basic metabolism) could be possible to estimate the daily energetic expenses.

This would be very interesting since available method that measure the CO2 (with mouth and nose tubing, see [6]) and the heat production (in a calorimetric box) are not suited for 24 hour measurements.

References

1. A. Convertino, A. Giorgio, A. G. Perri, "An innovative remote health monitoring system", in these proceedings
2. G. Gelao, A. Giorgio, A.G. Perri, M. Quinto "A new dilatation sensor for the respiration rate measurement", in these proceedings
3. J. G. Webster ed., *Medical instrumentation*, J. Wiley (1998)
4. J. Moore ed., Zouridakis ed., *Biomedical technology and devices handbook*, CRC (2004)
5. F. P. Branca, *Fondamenti di ingegneria clinica*, Springer (2000)
6. T. Togawa, T. Tamura, P. A. Öberg, *Biomedical transducers and instruments*, CRC (1997)

A MULTI PROCESSOR CONTROL SYSTEM FOR A GAS SENSING ARRAY

L. BISSI†, P. PLACIDI, M. PICCIONI, M. CICIONI, A. SCORZONI, L. ROSELLI,
Dipartimento di Ingegneria Elettronica e dell'Informazione, Università di Perugia, via G.Duranti 93, 06125 Perugia, Italy

L. MASINI, I. ELMI, S. ZAMPOLLI AND G.C. CARDINALI
CNR – IMM, Sezione di Bologna, via Gobetti 101, 40129 Bologna, Italy

In this paper we describe the structure of a multiprocessor control system for a gas sensing array. After a brief illustration of the sensor structure, a system overview will be given. Then, preliminary experimental results will be described.

1. Introduction

Nowadays microsystems based on gas sensing arrays with suitable electronic interfaces are being increasingly adopted for monitoring the presence of pollutant gases in the air (e.g. CO, C_6H_6, NO_2). The system described in this paper controls and acquires data from a gas sensor which exploits an array of four metal-oxide thin films deposited on thin dielectric membranes. The system is based on a microcontroller local network. An advantage of this architecture is the modularity of the system. A multisensor system is preferred because a single sensor does not react selectively to a singular target gas inside a mixture, but also to other interfering gases, therefore sensor redundancy helps in improving the performance of the gas detector.

2. Sensor structure

In each sensor the heater, the sensing layer and the contacts are deposited on a membrane of silicon nitride (Si_3N_4). The structure of the sensor is shown in Fig. 1.

The sensing layer changes its electric conductivity, and so its resistance, when it reacts with gas molecules. The heater function is to maintain the sensing

†*Corresponding Author: E-mail: bissi@diei.unipg.it, Ph: +39-75-5853636, Fax:+39-75-5853654*

layer at the operating temperature (T_{op}) where the sensor features its maximum sensitivity and selectivity, typically in the temperature range between 100°C and 450°C.

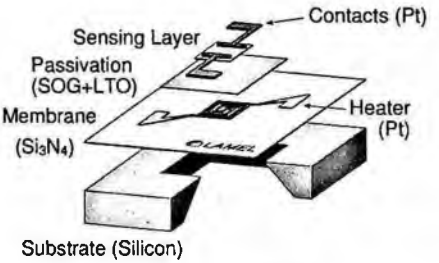

Figure 1. Sensor structure.

3. System architecture

The system architecture (Fig. 2) has been conceived by exploiting a modular approach: a central controller is connected via I^2C (Inter-IC bus) interface to four "monosensor" subsystems [1,2].

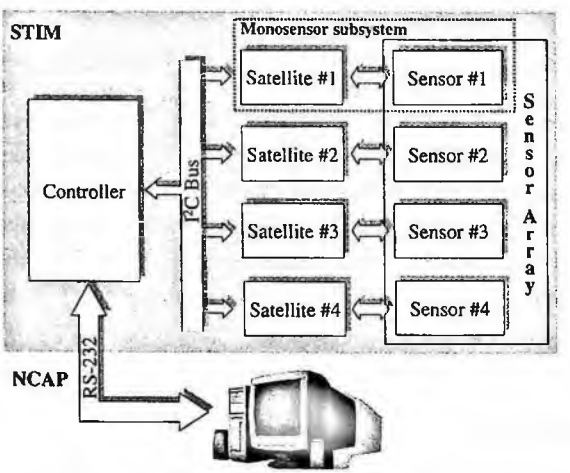

Figure 2. Block diagram of the system.

The management of the system follows the IEEE 1451 directives that are specially designed for the control of a transducer network. The controller manages the subsystem network and acts as an interface between the sensors

array and a host user PC which emulates the Network Capable Application Processor (NCAP) of the 1451.1 standard [3].

The controller is a microcontroller (μC) Microchip PIC16F876A which implements a Smart Transducer Interface Module (STIM) as defined in the IEEE 1451.2 [4] directive. It includes a Transducer Electronic Data Sheet (TEDS), i.e. an electronic datasheet permanently stored in the PIC Flash memory that contains information and parameters of the system. However, differently from the IEEE 1451.2, the interface between the STIM module and the NCAP (the so-called Transducer Independent Interface TII), in this project is replaced by a RS-232 serial interface. In particular, the TII hardware signals (e.g. NINT) have been replaced by simple messages running on the RS-232 interface.

The NCAP module emulator is realized through a LabView Virtual Instruments (VI) on a personal computer. It presently allows the user to control and monitor the sensors system through a local PC. In the future we plan to connect the system to the Internet with Ethernet protocol.

3.1. *Monosensor subsystem*

Each monosensor subsystem (shown in Fig. 3) is composed by a sensor and a satellite.

A satellite can be further divided into the following blocks:

- a μC featuring I^2C interface; In this project a Microchip PIC16F873 μC is used to manage all the operations.
- a Temperature Control Circuit;
- a DAC block which provides a reference voltage (V_{ref}) for the control of the temperature T_{op};
- a Conditioning Circuit for translating the resistance of the Sensing Layer into a voltage suitable for the A/D conversion of the μC.

The I^2C interface, managed by the μC, allows the satellite to communicate with the controller. The controller sends the commands and the operating parameters to the satellites and they reply accordingly.

The Temperature Control Circuit is in charge of maintaining a uniform temperature T_{op} of the sensing layer. The Heater is characterized by a calibration curve between the heater resistance (R_H) and T_{op}. So the T_{op} can be kept constant by comparing the value of R_H (or, equivalently, V_H) with a reference resistance R_{ref} (or, equivalently, a V_{ref}) which corresponds to the chosen T_{op} in the calibration curve.

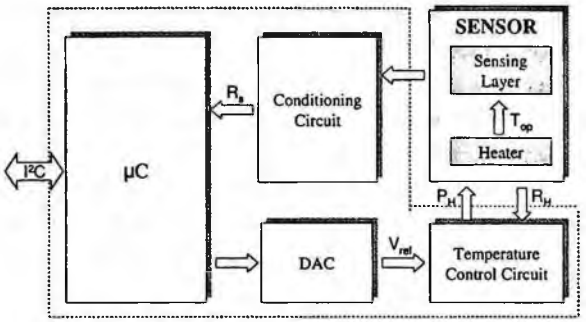

Figure 3. Block diagram of a monosensor subsystem.

In the satellite the output of a PWM module of the µC is filtered by a low pass filter in order to emulate a DAC, providing the V_{ref} voltage to the Temperature Control Circuit.

The resistance of the Sensing Layer (R_s) is measured with a potentiometric method. Suitable analog components are adopted in the Conditioning Circuit for the pre-elaboration of the acquired signal before the A/D conversion and the subsequent calculation of the R_s value. A wide dynamic measurement range (5kΩ, 15MΩ) of R_s was obtained using two ranging resistors. The appropriate ranging resistor is chosen through an auto-range procedure managed by the µC.

Two kinds of temperature control are provided: "continuous" when the temperature T_{op} of the sensing layer is kept constant, "pulsed" when heating periods of the Sensing Layer (at temperature T_{op}) are interleaved with cooling periods at ambient temperature (T_{amb}). The choice of the temperature control depends on the particular sensor material and on the particular type of gas to be detected.

The R_s value, after appropriate elaborations, provides the concentration of a particular kind of gas we want to detect.

The electrical behavior of the system is influenced by device tolerances and drift of parameters with respect to nominal values. In order to compensate for the effects of these variations, an automatic self-calibration procedure has been implemented, managed by the µC firmware.

4. Results

The system has been debugged and tested in suitable environmental chambers.

For example with a continuous operating temperature of 250°C, a 300 sccm (standard cubic centimeters per minute) flow and a gas sequence of 5 ppm of Benzene, 30 ppm of CO and 0.5 ppm of NO_2, when the duration of the injections

is 10 minutes, with 20 minutes of synthetic air between two subsequent injections, we obtained the resistance values shown in Fig. 4. The peak corresponds to the NO_2 injection.

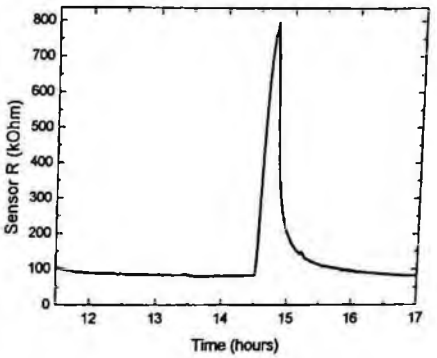

Figure 4. Sensor resistance in continuous temperature mode.

5. Conclusions

This paper describes a multiprocessor control system based on a microcontroller local network that detects ambient pollutant species through metal-oxide chemical gas sensors.

Thanks to its modularity, the system can be expanded including additional monosensor subsystems while keeping the same architecture.

The system, realized following the IEEE 1451 directives, is presently composed by a controller and four satellites. Each satellite acquires resistance values from a single gas sensor.

After debugging, the system has been tested in environmental chambers under a known gas sequence. Promising results were obtained.

Acknowledgments

This research work was partially funded by the Italian Ministry of Research and Education (MIUR) under FISR and FIRB projects and by the European Union in the frame of the GoodFood IP project.

References

1. M. Brugia et al., Microcontroller-Based Interface Circuit for Metal-Oxide Gas Sensors, Proc. AISEM 2002, Feb. 2002, BO (Italy), World Scientific Pub., pp. 365-369.

2. M. Baroncini et al., Accurate Analytical Thermal Model of the Heating Element in Micromachined Gas Sensors, Proc. 7th AISEM (Bologna, Italy), 2002.
3. IEEE Org., IEEE Standard for a Smart Transducer Interface for Sensors and Actuators – Network Capable Application Processor (NCAP) Information Model, IEEE Std 1451.1 - 1999.
4. IEEE Org., IEEE Standard for a Smart Transducer Interface for Sensors and Actuators - Transducer to Microprocessor Communication Protocols and Transducer Electronic Data Sheet (TEDS) Formats, IEEE Std 1451.2 - 1997.

Proceedings of the 10th Italian Conference

Sensors and Microsystems

This book contains a selection of papers presented at the 10th Italian Conference on Sensors and Microsystems. It provides a unique perspective on the research and development of sensors, microsystems and related technologies in Italy. The scientific values of the papers also offers an invaluable source to analysts intending to survey the Italian situation about sensors and microsystems. In an interdisciplinary approach, many aspects of the disciplines are covered, ranging from materials science, chemistry, applied physics, electronic engineering and biotechnologies.

ISBN-13 978-981-283-352-5
ISBN-10 981-283-352-8

World Scientific
www.worldscientific.com
6962 hc